

# LOW-CARBON TECHNOLOGIES FOR THE PETROLEUM INDUSTRY

EDITED BY: Kaiqiang Zhang, Rameshwar D. Srivastava, Wei Yu, Songyan Li  
and Zhiming Chen

PUBLISHED IN: Frontiers in Energy Research





# frontiers

## Frontiers eBook Copyright Statement

The copyright in the text of individual articles in this eBook is the property of their respective authors or their respective institutions or funders. The copyright in graphics and images within each article may be subject to copyright of other parties. In both cases this is subject to a license granted to Frontiers.

The compilation of articles constituting this eBook is the property of Frontiers.

Each article within this eBook, and the eBook itself, are published under the most recent version of the Creative Commons CC-BY licence.

The version current at the date of publication of this eBook is CC-BY 4.0. If the CC-BY licence is updated, the licence granted by Frontiers is automatically updated to the new version.

When exercising any right under the CC-BY licence, Frontiers must be attributed as the original publisher of the article or eBook, as applicable.

Authors have the responsibility of ensuring that any graphics or other materials which are the property of others may be included in the CC-BY licence, but this should be checked before relying on the CC-BY licence to reproduce those materials. Any copyright notices relating to those materials must be complied with.

Copyright and source acknowledgement notices may not be removed and must be displayed in any copy, derivative work or partial copy which includes the elements in question.

All copyright, and all rights therein, are protected by national and international copyright laws. The above represents a summary only. For further information please read Frontiers' Conditions for Website Use and Copyright Statement, and the applicable CC-BY licence.

ISSN 1664-8714

ISBN 978-2-88971-667-8

DOI 10.3389/978-2-88971-667-8

## About Frontiers

Frontiers is more than just an open-access publisher of scholarly articles: it is a pioneering approach to the world of academia, radically improving the way scholarly research is managed. The grand vision of Frontiers is a world where all people have an equal opportunity to seek, share and generate knowledge. Frontiers provides immediate and permanent online open access to all its publications, but this alone is not enough to realize our grand goals.

## Frontiers Journal Series

The Frontiers Journal Series is a multi-tier and interdisciplinary set of open-access, online journals, promising a paradigm shift from the current review, selection and dissemination processes in academic publishing. All Frontiers journals are driven by researchers for researchers; therefore, they constitute a service to the scholarly community. At the same time, the Frontiers Journal Series operates on a revolutionary invention, the tiered publishing system, initially addressing specific communities of scholars, and gradually climbing up to broader public understanding, thus serving the interests of the lay society, too.

## Dedication to Quality

Each Frontiers article is a landmark of the highest quality, thanks to genuinely collaborative interactions between authors and review editors, who include some of the world's best academicians. Research must be certified by peers before entering a stream of knowledge that may eventually reach the public - and shape society; therefore, Frontiers only applies the most rigorous and unbiased reviews.

Frontiers revolutionizes research publishing by freely delivering the most outstanding research, evaluated with no bias from both the academic and social point of view. By applying the most advanced information technologies, Frontiers is catapulting scholarly publishing into a new generation.

## What are Frontiers Research Topics?

Frontiers Research Topics are very popular trademarks of the Frontiers Journals Series: they are collections of at least ten articles, all centered on a particular subject. With their unique mix of varied contributions from Original Research to Review Articles, Frontiers Research Topics unify the most influential researchers, the latest key findings and historical advances in a hot research area! Find out more on how to host your own Frontiers Research Topic or contribute to one as an author by contacting the Frontiers Editorial Office: [frontiersin.org/about/contact](https://frontiersin.org/about/contact)



# LOW-CARBON TECHNOLOGIES FOR THE PETROLEUM INDUSTRY

Topic Editors:

**Kaiqiang Zhang**, Imperial College London, United Kingdom

**Rameshwar D. Srivastava**, National Energy Technology Laboratory (DOE),  
United States

**Wei Yu**, University of Texas at Austin, United States

**Songyan Li**, China University of Petroleum (Huadong), China

**Zhiming Chen**, China University of Petroleum, China

**Citation:** Zhang, K., Srivastava, R. D., Yu, W., Li, S., Chen, Z., eds. (2021).

Low-Carbon Technologies for the Petroleum Industry. Lausanne: Frontiers Media  
SA. doi: 10.3389/978-2-88971-667-8

# Table of Contents

- 05    *Mathematical Characterization of Inorganic Salt Precipitation From the Reaction of CO<sub>2</sub> With Formation Brine and Its Application***  
Zhou Yuan, Xinwei Liao, Kuaile Zhang, Xiaoliang Zhao, Hongyang Chu and Jiandong Zou
- 15    *An Interpretation Model for the Production Profile on the Same Angle of a Horizontal Well Trajectory***  
Wenguang Song, Na Jia and Qiongqin Jiang
- 23    *Transient Temperature Distribution of Underground Carbon Dioxide Salt Cavern Storage With State Space Model***  
Zhou Yuan, Yanxi Zhou, Minghui Wei and Xinwei Liao
- 32    *Experimental Investigation on the Role of Clays in Low Salinity Water Flooding***  
Xuemei Wei, Yanyu Zhang, Wenchao Jiang, Zhao Wang, Xiaojun Li and Feipeng Wu
- 42    *Investigation of the Heat Transfer Mechanism of CO<sub>2</sub>-Assisted Steam Injection via Experimental and Simulation Evaluation***  
Zhengxiao Xu, Zhaomin Li, Binfei Li, Songyan Li, Teng Lu, Mingxuan Wu and Hao Bai
- 53    *Optimization Simulation Research on Middle-Deep Geothermal Recharge Wells Based on Optimal Recharge Efficiency***  
Song Deng, Dingkun Ling, Huijun Zhao, Xin Shen, Huajun Du and Lu Liu
- 64    *Productivity Prediction Model for Stimulated Reservoir Volume Fracturing in Tight Glutenite Reservoir Considering Fluid-Solid Coupling***  
Leng Tian, Xiaolong Chai, Peng Wang and Hengli Wang
- 80    *Research on Mechanism of Enhancing Recovery of Heavy Oil With N<sub>2</sub> Huff-n-Puff Assisted by Viscosity Reducer***  
Lei Tao, Sen Huang, Yali Liu, Hao Cheng, Huajun Du, Cheng Wang, Na Zhang and Jinlong Li
- 94    *Effect of Stress-Sensitive Fracture Conductivity on Transient Pressure Behavior for a Multi-Well Pad With Multistage Fractures in a Naturally Fractured Tight Reservoir***  
Zhan Meng, Honglin Lu, Xiaohua Tan, Guangfeng Liu, Lianhe Wang and Daoyong Yang
- 115    *Investigation of Clay Type on Low Salinity Water Flooding Using a Glass Micromodel***  
Xuemei Wei, Wenchao Jiang, Yanyu Zhang, Zhao Wang, Xiaojun Li and Feipeng Wu
- 126    *Numerical Simulation of a Horizontal Well With Multi-Stage Oval Hydraulic Fractures in Tight Oil Reservoir Based on an Embedded Discrete Fracture Model***  
Zhi-dong Yang, Yong Wang, Xu-yang Zhang, Ming Qin, Shao-wen Su, Zhen-hua Yao and Lingfu Liu

- 138 ***Experimental Study on the Cyclic Steam Stimulation Assisted by Flue Gas Under Shallow Heavy-Oil Reservoir Conditions: Optimization of the Steam-Flue Gas Ratio***  
Songyan Li, Zhoujie Wang, Rui Han, Lei Wang and Zukang Hu
- 150 ***Effects of Dissociation Water Retention on Pore Structure Disintegration in Hydrate Sediments***  
Liu Yang, Shuo Wang, Hongfeng Lu, Ling Liu and Rina Sa
- 163 ***Transient Pressure Analysis of Inclined Well in Continuous Triple-Porosity Reservoirs With Dual-Permeability Behavior***  
Sheng-Zhi Qi, Xiao-Hua Tan, Xiao-Ping Li, Zhan Meng, You-Jie Xu and Daming Tang
- 174 ***Implementation of Ion Exchange Processes for Carbon Dioxide Mineralization Using Industrial Waste Streams***  
Steven Bustillos, Abdulaziz Alturki, Dale Prentice, Erika Callagon La Plante, Mitchell Rogers, Mark Keller, Raghavendra Ragipani, Bu Wang, Gaurav Sant and Dante A. Simonetti
- 191 ***Evaluating the Effect of Oil-Displacing Agents Using Computer Graphics and Visualization Glass Plate Model Experiments***  
Xiangyu Sun, Jijiang Ge, Shang Ren and An Zhao
- 203 ***Study of Rheological Property and Flow Behavior for Nanoparticles Enhanced VES System in Porous Media***  
Zhaoxia Liu, Qiang Wang, Ming Gao, Wenli Luo and Hongyan Cai
- 211 ***Emulsion Characterization of the Heavy Oil-Alkaline Water System in Alkaline Flooding Mechanism Investigation Using a Combination of Modified Bottle Test and Sandpack Flooding***  
Zhiyu Xi, Na Jia and Ezeddin Shirif
- 228 ***Effects of Fracturing Parameters on Fracture Unevenness During Large-Stage Multi-Cluster Fracturing in Horizontal Wells***  
Rui Yong, Fu-Jian Zhou, Ming-Hui Li, Yi Song, Xiao-Jin Zhou, Zhi-Heng Zhao, Ben Li and Shi-Yong Qin



# Mathematical Characterization of Inorganic Salt Precipitation From the Reaction of CO<sub>2</sub> With Formation Brine and Its Application

Zhou Yuan\*, Xinwei Liao, Kuaile Zhang, Xiaoliang Zhao, Hongyang Chu and Jiandong Zou

School of Petroleum Engineering, China University of Petroleum, Beijing, China

## OPEN ACCESS

### Edited by:

Wei Yu,  
The University of Texas at Austin,  
United States

### Reviewed by:

Hongbing Xie,  
Beijing Karst Technology Co., Ltd.,  
China

Mauricio Xavier Fiallos Torres,  
The University of Texas at Austin,  
United States

### \*Correspondence:

Zhou Yuan  
yuanz1987@163.com

### Specialty section:

This article was submitted to  
Advanced Fossil Fuel Technologies,  
a section of the journal  
Frontiers in Energy Research

**Received:** 13 April 2020

**Accepted:** 10 June 2020

**Published:** 14 July 2020

### Citation:

Yuan Z, Liao X, Zhang K, Zhao X,  
Chu H and Zou J (2020) Mathematical  
Characterization of Inorganic Salt  
Precipitation From the Reaction  
of CO<sub>2</sub> With Formation Brine and Its  
Application. *Front. Energy Res.* 8:141.  
doi: 10.3389/fenrg.2020.00141

In the process of CO<sub>2</sub> enhanced oil recovery (CO<sub>2</sub>-EOR), CO<sub>2</sub> interacts with formation brine containing high concentrations of scale-forming ions to produce inorganic salt precipitation, which blocks the rock pore throats, changes the characteristics of the reservoir, and thereby reduces the oil recovery rate. In this study, a series of experiments on the static reaction of CO<sub>2</sub>-formation brine was conducted. The amounts of precipitation formed from the interaction of CO<sub>2</sub>-formation brine under various conditions were tested. Using the PHREEQC software, the mathematical characterization formulas between the precipitation amount and various environmental factors (e.g., temperature, pressure difference, scale-forming ion concentration, and pH) were established. On this basis, a numerical simulation model of CO<sub>2</sub> flooding in a typical area of oil field C was established. The distribution of inorganic salt precipitation during continuous gas flooding was predicted, and the effect of inorganic salt precipitation on oil field recovery was analyzed.

**Keywords:** CO<sub>2</sub>-formation brine, inorganic salt precipitation, mathematical characterization formula, numerical simulation, CO<sub>2</sub>-EOR

## INTRODUCTION

As indicated by relevant studies on CO<sub>2</sub> flooding for enhanced oil recovery (EOR), the injected CO<sub>2</sub> is involved in strong chemical reactions with the formation brine, and the generated precipitates block the rock pore throats and reduce the porosity and the permeability of the reservoir. This leads to significant changes in the physical properties of the formation rocks (Fischer et al., 2010; Zhao et al., 2010; Liu et al., 2012; Yu et al., 2012; Alam et al., 2014; Lu et al., 2016) and thereby lowers the oil recovery rate.

The laboratory experiment is the most commonly used method to investigate the CO<sub>2</sub>-brine interaction. The research results by Wigand et al. (2008), Ketzer et al. (2009), Fischer et al. (2010), and Wandrey et al. (2011) are the most representative. Studies have shown that the reaction between CO<sub>2</sub> and formation brine is reversible, the equilibrium of which is affected by temperature, pressure, and the mineralization degree of the formation brine. Inorganic carbonate precipitates are formed in the case of over-equilibrium.

Upon dissolving in the formation brine, most CO<sub>2</sub> still exist in the form of free molecules, while only a small fraction of CO<sub>2</sub> combines with the formation brine to form carbonic acid (H<sub>2</sub>CO<sub>3</sub>).

Due to the dissociation of H<sub>2</sub>CO<sub>3</sub>, bicarbonate (HCO<sub>3</sub><sup>-</sup>) and carbonate (CO<sub>3</sub><sup>2-</sup>) ions are further generated, which then interact with scale-forming ions in the formation brine to produce inorganic carbonate precipitation (e.g., CaCO<sub>3</sub> and MgCO<sub>3</sub>).

Sbai (2011) described the kinetic mechanism of solid particle suspension in porous media and suggested that these particles may cause clogging of the pores. Shiraki and Dunn (2000), Assayag et al. (2009), Bacci et al. (2010), and Luquot et al. (2012) conducted a series of CO<sub>2</sub> core displacement experiments under reservoir conditions. The experiments indicated that when CO<sub>2</sub> is injected into geological reservoirs, it reacts with the formation brine to form carbonates, and the precipitation of carbonates significantly affects the porosity and the permeability of the formation rocks.

Employing numerical simulation technology, Zeidouni (2009) simulated the carbonate precipitation phenomenon during the CO<sub>2</sub> flooding process and evaluated the impact of salt precipitation on oil field development. Yang et al. (2010) and Delshad et al. (2010) also conducted corresponding studies to simulate CO<sub>2</sub> distribution during the CO<sub>2</sub>-EOR process.

At present, most studies are qualitative research studies that have not quantified the influencing factors of the precipitation amount. Based on previous research results, in this paper, the influences of various environmental factors (e.g., pressure difference, temperature, and scale-forming ion concentration) on precipitation formation from the reaction of CO<sub>2</sub> and brine were investigated quantitatively. Meanwhile, using the PHREEQC software, the effect of pH values was also simulated, and the corresponding exponential mathematical characterization formula was established *via* mathematical regression. On this basis, the Eclipse E300 module was used with the mathematical characterization formula to correct mathematical model parameters, optimize reservoir engineering parameters, simulate the distribution pattern of inorganic salt precipitation generated during the CO<sub>2</sub>-EOR process in a block of oil field C, and determine the effect of precipitation on the oil field's ultimate recovery rate.

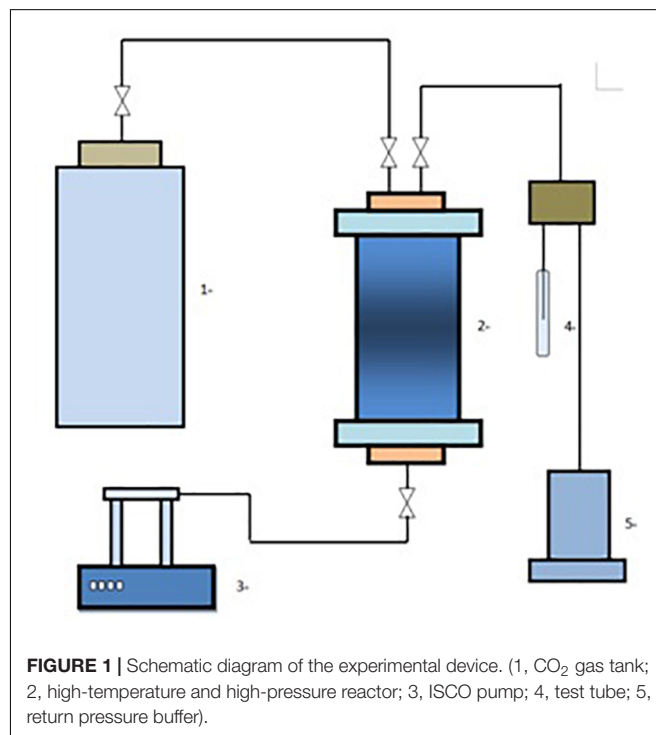
## DETERMINATION OF PRECIPITATION AMOUNT AFTER THE INTERACTION OF CO<sub>2</sub> AND FORMATION BRINE

### Experimental Method and Procedure

In this experiment, formation water, taken from three wells in a block of oil field C (the water properties are shown in Table 1), was used as the medium. Afterward, CO<sub>2</sub> was injected into a high-temperature and high-pressure reaction device (Figure 1) filled with 100 ml formation water until saturation was reached. Using the ISCO pump to raise the pressure of the device to the target pressure (8–16 MPa), it was put into the thermostat, and the pressure and the temperature (20–80°C) were kept stable and left to stand for 6 days. Subsequently, the pressure was released to atmospheric pressure and the system was left still for 1 day, followed by the determination of ion concentrations, precipitation composition, and precipitation amount.

**TABLE 1 |** The scale-forming ion analysis of the formation of brine sample.

Sample	Ca (mg/L)	Mg (mg/L)	Ba (mg/L)	Sr (mg/L)
1	2,012	198	0.006	19.4
2	5,145	209	0.057	25.4
3	10,590	222	0.028	18.8



The scale-forming ions in the formation brine sample were mainly Ca<sup>2+</sup>, Mg<sup>2+</sup>, Ba<sup>2+</sup>, and Sr<sup>2+</sup>. Among them, Ca<sup>2+</sup> was the main component, taking up 95% of the total scale-forming ions, followed by Mg<sup>2+</sup>. The concentrations of Ba<sup>2+</sup> and Sr<sup>2+</sup> were very low.

### Experimental Results

According to the principle of orthogonal experiment design, three brine samples with varied properties were employed for static experiments under different temperature (20, 30, 50, and 80°C) and pressure difference (8, 10, 12, and 16 MPa) conditions.

The concentrations of Ca<sup>2+</sup> in the initial formation brine and the liquid samples taken out of the system each time were determined by inductively coupled plasma emission spectrometry. By subtracting the Ca<sup>2+</sup> concentration in the initial formation brine from the Ca<sup>2+</sup> concentration of each liquid sample, the variation of the Ca<sup>2+</sup> concentration under different temperature and pressure conditions was obtained, which was then used to calculate the mass of CaCO<sub>3</sub> precipitation based on the molecular weight of the precipitate.

Since the experimental pressure was too high to measure the pH value of the solution, the PHREEQC software was applied to fit the experimental and the simulation results of the precipitation amount under different pH conditions to obtain a complete set of



data. The experimental and the simulation results are shown in Table 2.

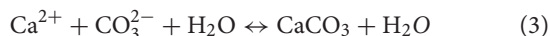
In order to confirm the presence of inorganic carbonate, the precipitates produced in the experiment were processed and tested for elemental composition (Figure 2). The main elements in the precipitates were C, O, and Ca and a small amount of Mg. The main inorganic salt precipitate produced by the reaction was CaCO<sub>3</sub>, with the rest being CaCl<sub>2</sub> and MgCl<sub>2</sub>. The ratio of the three precipitates (CaCO<sub>3</sub>:CaCl<sub>2</sub>:MgCl<sub>2</sub>) was 10:0.25:1. The specific concentrations are shown in Table 3.

## PRECIPITATION FACTOR ANALYSIS AND MATHEMATICAL CHARACTERIZATION METHOD OF CO<sub>2</sub>-FORMATION BRINE INTERACTION

### Analysis of Mechanism and Influencing Factors of Precipitation Formation From CO<sub>2</sub>-Formation Brine Interaction

#### Reaction Mechanism

The precipitation formation from CO<sub>2</sub>-formation brine interaction can be described by the following chemical reactions:



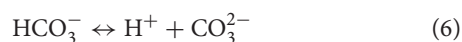
The precipitation and the dissolution of inorganic salts is a chemical equilibrium process. According to the chemical equations, the reversible reactions are affected by the concentrations of HCO<sub>3</sub><sup>-</sup>, CO<sub>3</sub><sup>2-</sup>, Ca<sup>2+</sup>, and H<sup>+</sup> in the solution.

Therefore, the conversion form of the CO<sub>2</sub>-brine system must be clarified first.

Gaseous CO<sub>2</sub> dissolves in brine and forms H<sub>2</sub>CO<sub>3</sub>:



H<sub>2</sub>CO<sub>3</sub> then further ionizes:



Based on Eqs (4–6), the following equations can be obtained:

$$K_{\text{CO}_2} = \frac{[\text{H}_2\text{CO}_3]}{P_{\text{CO}_2}} \quad (7)$$

$$K_1 = \frac{[\text{H}^+] + [\text{HCO}_3^-]}{[\text{H}_2\text{CO}_3]} \quad (8)$$

$$K_2 = \frac{[\text{H}^+] + [\text{CO}_3^{2-}]}{[\text{HCO}_3^-]}$$

**TABLE 2 |** The experimental and the simulation results of the precipitation amount.

Sample	Temperature (°C)	Pressure difference (MPa)	pH value	Precipitation capacity (mg/L)
1	20	8	5.5	90
	20	10		130
	20	12		100
	20	16		150
	30	16		120
	50	16		50
	80	16		20
	20	8		160
2	20	12	6.2	180
	20	16		200
	20	18		240
	30	16		130
	50	16		70
	80	16		10
	20	8		140
	20	10		220
3	20	12	7	220
	20	16		270
	30	16		230
	50	16		110
	80	16		30
	20	8		170
	20	10		200
	20	12		170
1	20	16	6.2	240
	30	16		190
	50	16		100
	80	16		50
	20	8		310
	20	12		330
	20	16		390
	20	18		510
2	30	16	7	220
	50	16		150
	80	16		70
	20	8		300
	20	10		470
	20	12		480
	20	16		570
	30	16		480
3	50	16	7	240
	80	16		80
	20	8		210
	20	10		260
	20	12		220
	20	16		300
	30	16		230
	50	16		110
1	80	16	7	60
	20	8		370
	20	12		410

(Continued)

**TABLE 2** | Continued

Sample	Temperature (°C)	Pressure difference (MPa)	pH value	Precipitation capacity (mg/L)
3	20	16		490
	20	18		650
	30	16		280
	50	16		190
	80	16		40
	20	8		410
	20	10		720
	20	12		790
	20	16		920
	30	16		750
	50	16		370
	80	16		190

$K_{CO_2}$  is the equilibrium constant for the dissolution of CO<sub>2</sub>, while  $K_1$  and  $K_2$  are the equilibrium constants for H<sub>2</sub>CO<sub>3</sub> dissociation and HCO<sub>3</sub><sup>−</sup> dissociation, respectively. The values in the square brackets represent the activity of each ion.

Under ambient temperature conditions, only H<sub>2</sub>CO<sub>3</sub> exists in acidic (pH < 4.5) brine, while CO<sub>3</sub><sup>2−</sup> mainly exists in an alkaline (8.34 < pH < 12) environment. As for neutral, weakly acidic, and weakly alkaline brine, the main species is HCO<sub>3</sub><sup>−</sup>, without the presence of CO<sub>3</sub><sup>2−</sup>. Moreover, this phenomenon is very weakly affected by temperature or fluid pressure (Zai-Hua and Dreybrodt, 2005).

The pH value of the formation brine used in this study is 6.2 at normal temperature and pressure. Thus, the ionization of Eq. 6 would not proceed. Therefore, it can be determined that the precipitation mechanism of the CO<sub>2</sub>–formation brine interaction is as described by reactions (1) and (2).

It is generally considered that as long as the ion product of CaCO<sub>3</sub> is greater than its solubility product, CaCO<sub>3</sub> will precipitate. However, in actuality, CaCO<sub>3</sub> will only precipitate

**TABLE 3** | Elemental composition of the precipitates generated from CO<sub>2</sub>–formation brine interaction.

Element	Concentration (m)	Unit
C	10.08	wt. %
O	44.87	wt. %
Mg	1.91	wt. %
Cl	7.56	wt. %
Ca	34.57	wt. %
Total	100.00	wt. %

and deposit when the supersaturated state is exceeded. This is because CaCO<sub>3</sub> is a slightly soluble inorganic salt, and in its saturated solution, the supersaturation is often significantly greater than the solubility, causing the crystal nuclei to cease growing after nucleation. Therefore, only extremely high ion concentrations in the solution enable the growth and the precipitation of crystal nuclei.

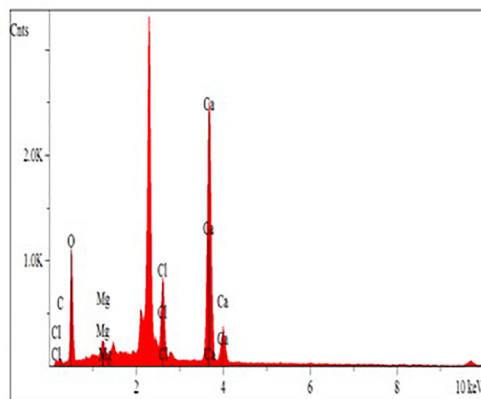
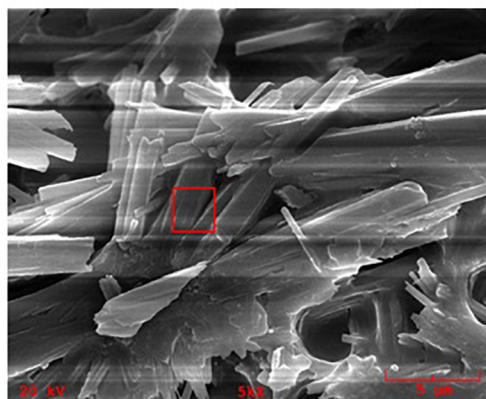
## Analysis of Influencing Factors

### Influence of temperature

**Figure 3** shows that temperature has a significant impact on the production of precipitation; the higher the temperature, the less precipitation there is. Moreover, the amount of precipitation is more sensitive to temperature when the scale ion content is high.

The phenomenon is evidently closely related to the solubility of the CO<sub>2</sub>–formation brine system (i.e., temperature has a significant influence on H<sub>2</sub>CO<sub>3</sub> formation from the dissolution of CO<sub>2</sub> in brine).

With a constant  $P_{CO_2}$ ,  $K_{CO_2}$  is inversely proportional to temperature. This is because temperature is inversely proportional to CO<sub>2</sub> solubility in brine, and the activity of H<sub>2</sub>CO<sub>3</sub> decreases when temperature increases, leading to a lower HCO<sub>3</sub><sup>−</sup> concentration from its dissociation. Even if the chemical reaction rate increases upon temperature elevation (Shukla et al., 2010), the total amount of CaCO<sub>3</sub> precipitates will still decrease.

**FIGURE 2** | SEM images and energy spectrum of the precipitates.

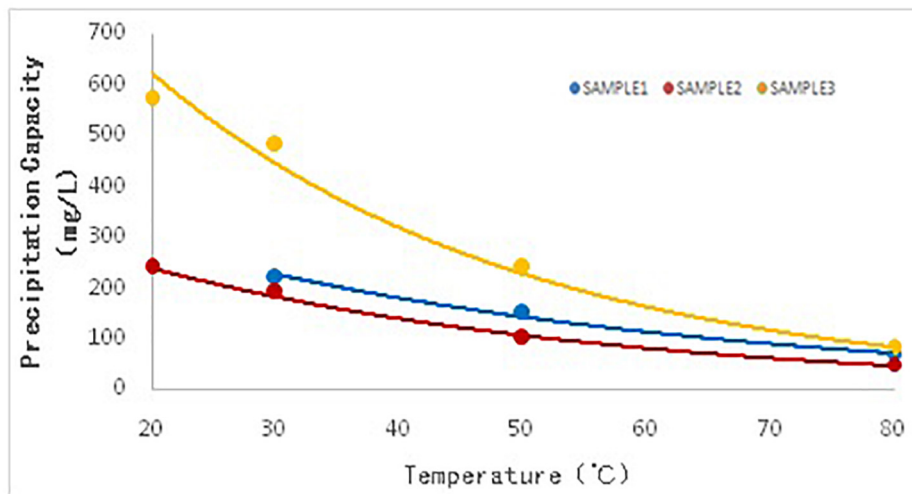


**FIGURE 3** | The relationship between temperature and the precipitation capacity of inorganic salt.

### Influence of pressure difference

A pressure increase does not lead to precipitation; conversely, precipitates appear upon lowering the pressure. This is because a higher pressure means a higher  $P_{CO_2}$ , under a constant temperature. The activity of  $H_2CO_3$  in the  $CO_2$ -formation brine system improves with a higher  $P_{CO_2}$ , which indirectly results in a higher activity of  $H^+$  and thus increased acidity of the solution. Moreover, the solubility product of  $CaCO_3$  is proportional to  $P_{CO_2}$ . Thereby, even if the amount of  $CaCO_3$  produced increases, it will only reach a saturated stable state without precipitation.

When the pressure starts to decrease,  $P_{CO_2}$  decreases, implying a lower solubility product of  $CaCO_3$ . Thus,  $CaCO_3$  crystals grow and precipitate out of the solution.

### Influence of scale-forming ion concentration

From **Figure 5**, we can see that the greater the scale ion content, the more sediment will be formed.

This is caused by the oversaturation of  $CaCO_3$ . The  $CaCO_3$  saturation formula is:

$$S_C = \frac{[Ca^{2+}][CO_3^{2-}]}{K_C} \quad (9)$$

where  $S_C$  is the saturation degree of  $CaCO_3$ ,  $K_C$  is the activity product of  $CaCO_3$ , and the values inside the square brackets represent the activity of each ion.

The increased concentration of scale-forming ions implies a higher concentration of free  $Ca^{2+}$  ions, and the solution is highly supersaturated in terms of  $Ca^{2+}$ , which results in higher nucleation and growth rate of  $CaCO_3$  (Al Nasser and Al Salhi, 2014). According to formula (10),  $S_C$  increases, promoting the generation and the precipitation of  $CaCO_3$ . The activity of  $H^+$  decreases rapidly with the increase of  $Ca^{2+}$  concentration, which is also very beneficial to the formation of  $CaCO_3$ .

It needs to be noted that in "Practical Aspects of  $CO_2$  Flooding," Perry and Charles (2002) pointed out that the salinity of the brine also affects the solubility of  $CO_2$ ; specifically, the

higher the salinity, the lower the solubility. However, in the current experiment,  $CO_2$  dissolves in brine to form  $H_2CO_3$ , which then dissociates to generate  $HCO_3^-$ . The  $HCO_3^-$  ions then react with the large amount of  $Ca^{2+}$  in the solution to form  $CaCO_3$ , which in turn causes more  $CO_2$  to dissolve in brine and promotes the formation of more  $CaCO_3$ . The  $CaCO_3$  generated will then precipitate after supersaturation is reached.

### Influence of pH

Glenn and Reginald (2003) believes that the dissolution of  $CO_2$  in formation brine from the formation fluids lowers the pH value of the formation brine and that  $CaCO_3$ , a weak acid salt, is greatly affected by the pH value, which is the main controlling factor of generation from  $H_2CO_3$  dissociation. A higher pH value leads to increased  $HCO_3^-$  concentration and enhanced  $HCO_3^-$  activity and thereby an increase in the amount of  $CaCO_3$ .

## Mathematical Characterization Method of Precipitation Amount From $CO_2$ -Formation Brine Interaction

According to **Figures 4–6**, the inorganic salt precipitation amount has an exponential relationship with temperature, pressure difference, and scale-forming ion concentration. The following mathematical formulas can be used:

$$y = ae^{bx} \quad (11)$$

Take the logarithm of both sides of (Eq. 11):

$$\lg y = \lg a + bx \quad (12)$$

Assign  $Y$  as  $\lg y$ :

$$Y = \lg a + bx \quad (13)$$

Equation 13 is a linear equation where  $Y$  changes linearly with  $X$ , and the data in **Table 3** were substituted into Eq. 13 for linear regression. Each  $X$  value has a corresponding actual value  $Y_1$  and predicted value  $Y_2$ . In order to minimize the square of the difference between the two values, set:

$$Q(a, b) = \sum_{i=1}^n (Y_i - (aX_i + b))^2 \quad (14)$$

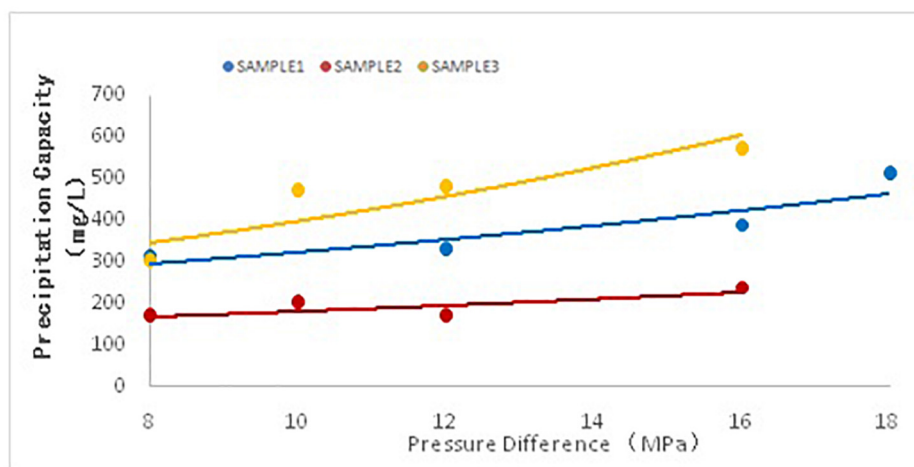


**FIGURE 4 |** The relationship between pressure difference and precipitation capacity.

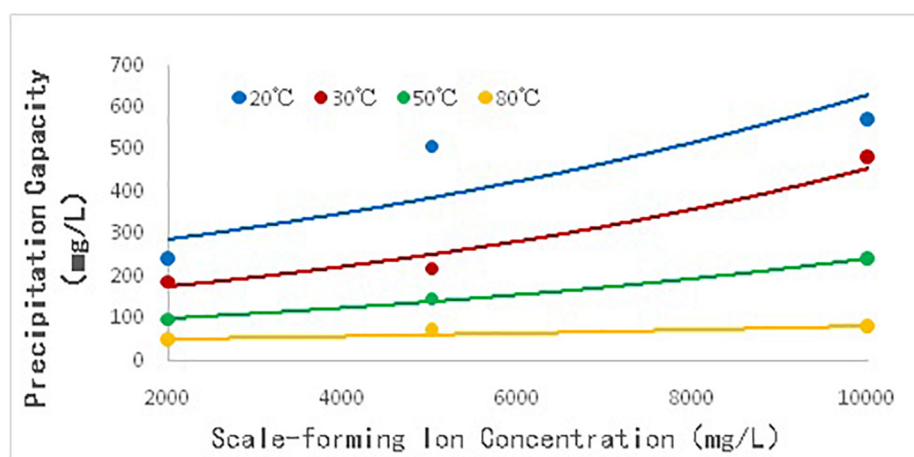


**FIGURE 5 |** The relationship between scale-forming ion content and precipitation capacity.

**TABLE 4 |** Regression parameters.

	Coefficients	Standard error	t statistic	P-value	Lower 95%	Upper 95%
Intercept	0.836256	0.380804	2.196027	0.032174	0.073709	1.598803
Scale-forming ion content	9.7E-05	9.58E-06	10.12754	2.36E-14	7.79E-05	0.000116
Temperature	-0.03435	0.001776	-19.3443	1.01E-26	-0.03791	-0.03079
Pressure Difference	0.062037	0.01211	5.122985	3.72E-06	0.037788	0.086286
pH value	0.667493	0.054766	12.18805	1.64E-17	0.557825	0.77716

Expand the brackets and take the average value:

$$Q(a, b) = n\bar{Y}^2 - 2an\bar{X}\bar{Y} - 2bn\bar{Y} + a^2n\bar{X}^2 + 2abn\bar{X} + nb^2 \quad (15)$$

By solving the partial derivatives of  $Q$  toward  $a$  and  $b$ , respectively, and assigning 0 to the partial derivatives, the solution formulas of  $a$  and  $b$  were obtained:

$$\begin{aligned} a &= \frac{\bar{X}\bar{Y} - \bar{X}\bar{Y}}{(\bar{X})^2 - \bar{X}^2} \\ b &= \bar{Y} - a\bar{X} \end{aligned} \quad (16)$$

As suggested by **Table 4**, the standard error is very small, indicating a high parameter accuracy. The corresponding  $P$ -value is less than 0.05–0.0001, and the confidence of the model is as high as 95–99.99%.

Therefore, the quantitative characterization equation of inorganic salt precipitation can be obtained:

$$y = 2.30771e^{(0.0000097M - 0.03435T + 0.062037\Delta P + 0.667439pH)} \quad (10)$$

**TABLE 5 |** Model parameters.

Parameter	Value	Parameter	Value
Crude oil viscosity (mPa's)	1.81	Reservoir temperature (°C)	80
Permeability ( $\times 10^{-3} \mu\text{m}^2$ )	0.2	Rock density (kg/m <sup>3</sup> )	2,500
Porosity (%)	10	Dissolved gas-oil ratio (m <sup>3</sup> /m <sup>3</sup> )	43
Initial brine saturation	53%	Initial oil saturation	0.6
Reactant H <sub>2</sub> O coefficient	1,280	Chemical reaction rate constant	$5 \times 10^{-6}$

where  $y$  is the precipitation amount (mg),  $T$  is the temperature (°C),  $\Delta P$  is the pressure difference (MPa),  $M$  is the concentration of scale-forming ions (mg/L), and pH is the pH value of the solution.

## ANALYSIS OF INFLUENCE OF PRECIPITATION FROM CO<sub>2</sub>-FORMATION BRINE INTERACTION ON OIL FIELD DEVELOPMENT

### Establishment of Reservoir Numerical Model Considering Inorganic Salt Precipitation

The reservoir in a block of oil field C has an average porosity of 10.01% and a permeability of 0.3 mD. It is classified as an ultra-low permeability reservoir with an extremely low asphaltene concentration. The formation brine contains a high concentration of calcium ions (12,150 mg/L). The burial depth of

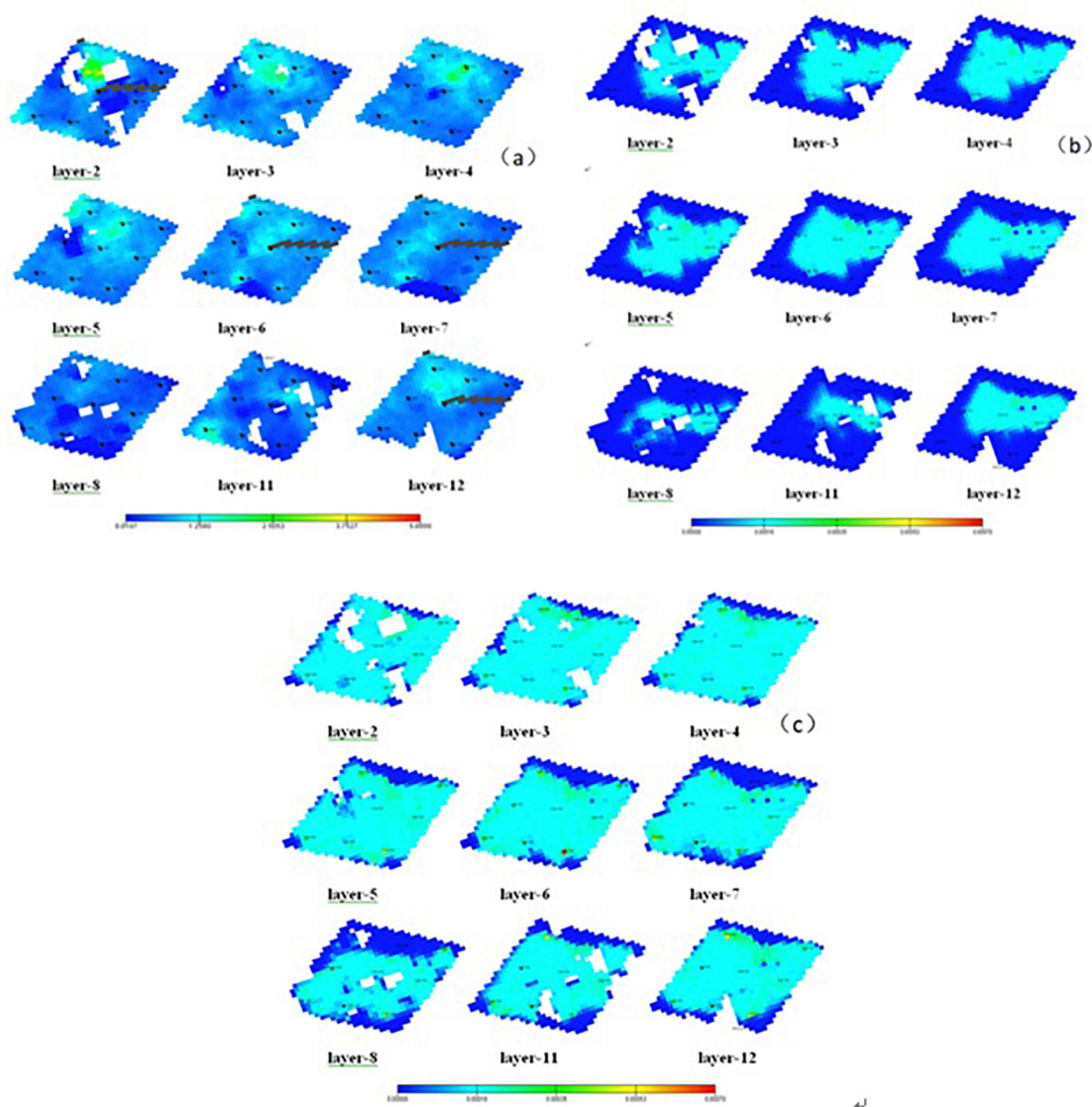


**FIGURE 6 | (A)** Formation permeability at different horizons. **(B)** Inorganic salt precipitation distribution after 10 years of production. **(C)** Inorganic salt precipitation distribution after 40 years of production.



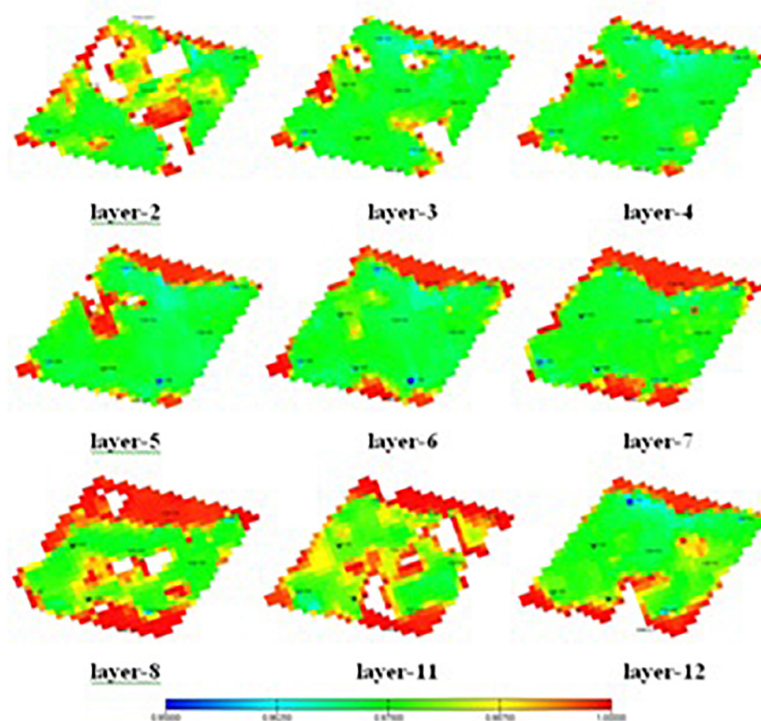


**FIGURE 7 |** Coefficient of fluidity change at the 40th year of the CO<sub>2</sub> enhanced oil recovery.

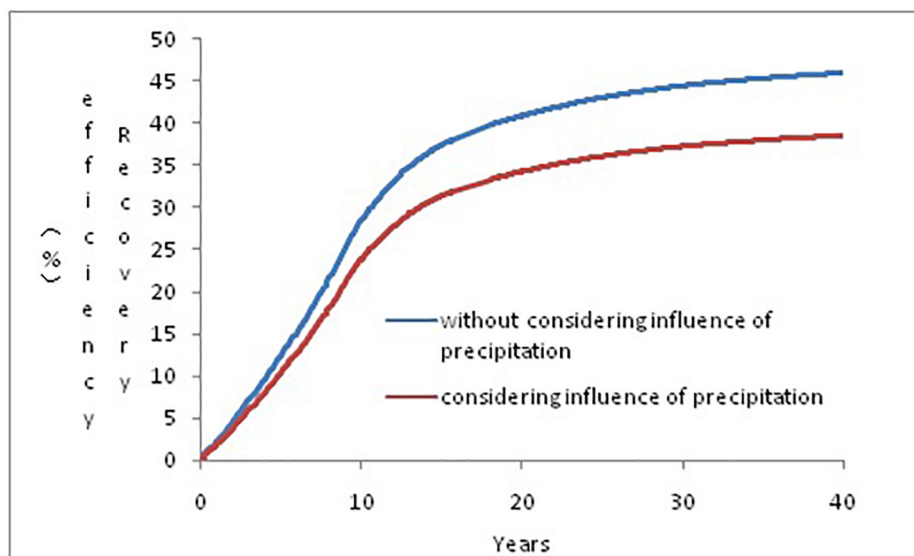


**FIGURE 8 |** Recovery rate at the 40th year with and without considering the influence of precipitation.

the reservoir is 2,700–2,900 m, with the formation temperature and pressure being 80°C and 21 MPa, respectively. Meanwhile, the comprehensive brine cut is 53%. The research block is a rhombic anti-nine-point well pattern with a water drive recovery

factor of 35.4%, and there is a high permeability zone connecting the injection and the production well inside the well pattern.

First, a suspended precipitation module was established, which simulated the precipitation formation with the production

well. Thereby, the precipitation amount generated by the CO<sub>2</sub>-brine interaction could be directly output through the software. Then, the precipitation amount was fitted using Eq. 17 to obtain the key parameter: the reactant H<sub>2</sub>O coefficient and the chemical reaction rate constant. On this basis, an adsorbed precipitation module was established for simulating the precipitation effect.

The CaCO<sub>3</sub> precipitation reaction is determined by the chemical reaction equation and the reaction rate. The chemical reaction equation is realized by adjusting the chemical reaction coefficient of the reactant and the product, and the specific process is as follows.

Chemical reaction equation:

$$\sum (S_{Rri} \cdot C_i) \rightarrow \sum (S_{Pri} \cdot C_i) \quad (11)$$

$S_{Rri}$ : reaction coefficient of reactant  $C_i$

$S_{Pri}$ : reaction coefficient of product  $C_i$

Reaction rate:

$$R_r = V_b \cdot A_r \cdot \exp(-E_r/(RT)) \cdot \prod_{c_{ri}}^{n_{ri}} \quad (12)$$

$V_b$ : rock pore volume

$A_r$ : reaction rate constant

$E_r$ : reaction energy

$R$ : gas constant

$T$ : temperature

$n_{ri}$ : component index

Suppose the initial solid saturation is 0 and the final output solid saturation is the resulting precipitation saturation, the effect of solid deposition on fluidity is obtained. Changes in fluidity can also reflect changes in permeability.

$$M_p^c = x_p^c \Delta k_s \Delta k_{rp} (S_p) \Delta \frac{b_p}{\mu_p} \quad (13)$$

$x_p^c$ : molar fraction of components

$k_s$ : fluidity multiplier in the presence of solids

$k_{rp}$ : relative permeability of phase  $p$

$S_p$ : saturation of phase  $p$

$b_p$ : molar density of phase  $p$

$\mu_p$ : viscosity of phase  $p$

$k_s$ : reduced mobility caused by solid adsorption blocking pore throat

The model parameters are shown in Table 5.

## Evaluation of the Influence of Inorganic Salt Precipitation on Development

By simulating the production situation after 10 and 40 years, the inorganic salt precipitation distribution and its influence on the reservoir were obtained, as shown in Figure 6.

Figure 6 displays the precipitation distribution in the reservoir after production. Upon CO<sub>2</sub> injection, precipitation first occurs near the high-permeability zone. After 10 years of production, precipitates are gradually formed in the area, with relatively high permeability. In the 40th year, the precipitates are widely distributed in a large area in the research block

and reach a maximum value at the production well and its surrounding area. This precipitation trend is because CO<sub>2</sub> is first injected along the high-permeability zone where the fluid pressure is relatively high and the CO<sub>2</sub> solubility is large in brine. Then, the soluble bicarbonate [Ca(HCO<sub>3</sub>)<sub>2</sub>] is formed rapidly from the reaction of CO<sub>2</sub> and scale-forming ions in the formation brine. In the presence of a pressure difference in the formation, the reaction equilibrium shifts toward the direction of precipitation, thereby generating calcium carbonate precipitates. The pressure difference at the production well and its surrounding area is the largest, which explains the highest precipitation amount.

Figure 7 shows the distribution of fluidity change in the reservoir at the 40th year of CO<sub>2</sub>-EOR. The fluidity of the study block decreases generally. This is because, during gas flooding, the pressure in the formation decreases gradually, resulting in the gradual generation of precipitation, which blocks the pore throats and reduces the fluidity.

Figure 8 illustrates the recovery rate change during the CO<sub>2</sub>-EOR process with and without considering precipitation. As suggested by the figure, precipitation already has a great impact from the early stage of oil field development, which is mainly due to the rapid reaction of CO<sub>2</sub>-brine. As the development continues, more and more precipitates are generated, blocking the pore throats and reducing the recovery rate. The recovery rate excluding the influence of precipitation was 46%, and it dropped by 7 to 39% when the influence of precipitation was considered.

## CONCLUSION

- (1) In this paper, based on the static CO<sub>2</sub>-brine immersion experiment, the reaction laws of the CO<sub>2</sub>-formation brine system under various pressure difference, temperature, and scale-forming ion concentration conditions were studied. A greater pressure difference led to a larger amount of precipitation, while a higher temperature favored a smaller precipitation amount. Meanwhile, under constant pressure and temperature, greater concentrations of scale-forming ions in the formation brine led to the formation of larger amounts of precipitation.
- (2) Quantitative research was conducted on the precipitation amount, and the corresponding exponential mathematical characterization formula was obtained.
- (3) According to the numerical model, upon CO<sub>2</sub> injection, precipitation first occurs near the injection well. As CO<sub>2</sub> continues to migrate to the production well, the corresponding area has the highest precipitation amount.
- (4) By employing the modified numerical model, the oil recovery in a block of oil field C was predicted. The recovery rate considering precipitation was 39%, while that excluding the influence of precipitation was 46%, with the difference being 7%. The poor development of the oil field considering precipitation is due to the universal deposition of the precipitates generated from the CO<sub>2</sub>-formation brine interaction in the reservoir.

## DATA AVAILABILITY STATEMENT

The raw data supporting the conclusions of this article will be made available by the authors, without undue reservation.

## REFERENCES

- Al Nasser, W. N., and Al Salhi, F. H. (2014). Kinetics determination of calcium carbonate precipitation behavior by inline techniques. *Powder Technol.* 270, 548–560. doi: 10.1016/j.powtec.2014.05.025
- Alam, M., Hjuler, M., Christensen, H., and Fabricius, I. (2014). Petrophysical and rock-mechanics of CO<sub>2</sub> injection for enhanced oil recovery: experimental study on chalk from South Arne field. *North Sea. Pet. Sci. Eng.* 122, 468–487. doi: 10.1016/j.petrol.2014.08.008
- Assayag, N., Matter, J., Ader, M., Goldberg, D., and Agrinier, P. (2009). Water-rock interactions during a CO<sub>2</sub> injection field-test: Implications on host rock dissolution and alteration effects. *Chem. Geol.* 265, 227–235. doi: 10.1016/j.chemgeo.2009.02.007
- Bacci, G., Korre, A., and Durucan, S. (2010). An experimental and numerical investigation into the impact of dissolution/precipitation mechanisms on CO<sub>2</sub> injectivity in the wellbore and far field regions. *Int. J. Greenh. Gas Control* 5, 579–588. doi: 10.1016/j.ijggc.2010.05.007
- Delshad, M., Wheeler, M. F., and Kong, X. (2010). *A Critical Assessment of CO<sub>2</sub> Injection Strategies in Saline Aquifers*. Tulsa: Society of Petroleum Engineers.
- Fischer, S., Liebscher, A., Wandrey, M., and The CO<sub>2</sub> Sink Group, (2010). CO<sub>2</sub>-brine-rock interaction -First results of long-term exposure experiments at in situ P-T conditions of the Ketzin CO<sub>2</sub> reservoir. *Chem. Erde* 70, 155–164. doi: 10.1016/j.chemer.2010.06.001
- Glenn, T. H., and Reginald, T. (2003). The experimental determination of solubilities. *Chem. Int.* 25, 30–33.
- Ketzer, J. M., Iglesias, R., Einloft, S., Dullius, J., Ligabue, R., and Lima, V. (2009). Water-rock-CO<sub>2</sub> interactions in saline aquifers aimed for carbon dioxide storage: experimental and numerical modeling studies of the Rio Bonito Formation (Permian), southern Brazil. *Appl. Geochem.* 24, 760–767. doi: 10.1016/j.apgeochem.2009.01.001
- Liu, F., Lu, P., Griffith, C., Hedges, S. W., Soong, Y., Hellevang, H., et al. (2012). CO<sub>2</sub>-brine-cap rock interaction: reactivity experiments on Eau Claire shale and a review of relevant literature. *Int. J. Greenh. Gas Control* 7, 153–167. doi: 10.1016/j.ijggc.2012.01.012
- Lu, J., Nicot, J.-P., Mickler, P. J., Ribeiro, L. H., and Darvari, R. (2016). Alteration of Bakken reservoir rock during CO<sub>2</sub>-based fracturing—an autoclave reaction experiment. *Unconv. Oil Gas Resour.* 14, 72–85. doi: 10.1016/j.juogr.2016.03.002
- Luquot, L., Andreani, M., Gouze, P., and Camps, P. (2012). CO<sub>2</sub> percolation experiment through chlorite/zeolite—rich sandstone (Pretty Hill Formation—Otway Basin—Australia). *Chem. Geol.* 294–295, 75–88. doi: 10.1016/j.chemgeo.2011.11.018
- Perry, J., and Charles, F. (2002). *Practical Aspects of CO<sub>2</sub> Flooding*. Tulsa: Society of Petroleum Engineers.
- Sbai, M. A. (2011). Numerical modeling of formation damage by two-phase particulate transport processes during CO<sub>2</sub> injection in deep heterogeneous porous media. *Adv. Water Resour.* 34, 62–82. doi: 10.1016/j.advwatres.2010.09.009
- Shiraki, R., and Dunn, T. L. (2000). Experimental study on water-rock interactions during CO<sub>2</sub> flooding in the Tensleep Formation, Wyoming, USA. *Appl. Geochem.* 15, 265–279. doi: 10.1016/s0883-2927(99)00048-7
- Shukla, R., Ranjith, P., Haque, A., and Choi, X. (2010). A review of studies on CO<sub>2</sub> sequestration and caprock integrity. *Fuel* 89, 2651–2664. doi: 10.1016/j.fuel.2010.05.012
- Wandrey, M., Fischera, S., Zemke, K., Liebscher, A., Scherfb, A. K., Hillebrandb, A. V., et al. (2011). Monitoring petrophysical, mineralogical, geochemical and microbiological effects of CO<sub>2</sub> exposure—Results of long-term experiments under in situ conditions. *Energy Procedia* 4, 3644–3650. doi: 10.1016/j.egypro.2011.02.295
- Wigand, M., Carey, J. W., Schütt, H., Spangenberg, E., and Erzinger, J. (2008). Geochemical effects of CO<sub>2</sub> sequestration in sandstones under simulated in situ conditions of deep saline aquifers. *Appl. Geochem.* 23, 2735–2745. doi: 10.1016/j.apgeochem.2008.06.006
- Yang, F., Bai, B. J., Tang, D. Z., Shari, D. N., and David, W. (2010). Characteristics of CO<sub>2</sub> sequestration in saline aquifers. *Pet. Sci.* 7, 83–92.
- Yu, Z. C., Liu, L., Yang, S. Y., Li, S., and Yang, Y. Z. (2012). An experimental study of CO<sub>2</sub>-brine-rock interaction at in situ pressure-temperature reservoir conditions. *Chem. Geol.* 326–327, 88–101. doi: 10.1016/j.chemgeo.2012.07.030
- Zai-Hua, L., and Dreybrodt, W. (2005). Equilibrium chemistry of the CaCO<sub>3</sub>-CO<sub>2</sub>-H<sub>2</sub>O system and discussions. *Carsol. Sin.* 24, 1–14.
- Zeidouni, M. (2009). Analytical solution to evaluate salt precipitation during CO<sub>2</sub> injection in saline aquifers. *Energy Procedia* 1, 1775–1782. doi: 10.1016/j.egypro.2009.01.232
- Zhao, R. B., Sun, H. T., Wu, Y. S., Zhao, C. F., and Xue, X. A. (2010). Influence of CO<sub>2</sub> corrosion on rock structure and its mechanical characteristics. *Sci. China Tech. Sci.* 53, 822–828.

## AUTHOR CONTRIBUTIONS

All authors listed have made a substantial, direct and intellectual contribution to the work, and approved it for publication.

**Conflict of Interest:** The authors declare that the research was conducted in the absence of any commercial or financial relationships that could be construed as a potential conflict of interest.

Copyright © 2020 Yuan, Liao, Zhang, Zhao, Chu and Zou. This is an open-access article distributed under the terms of the Creative Commons Attribution License (CC BY). The use, distribution or reproduction in other forums is permitted, provided the original author(s) and the copyright owner(s) are credited and that the original publication in this journal is cited, in accordance with accepted academic practice. No use, distribution or reproduction is permitted which does not comply with these terms.



# An Interpretation Model for the Production Profile on the Same Angle of a Horizontal Well Trajectory

Wenguang Song<sup>1</sup>, Na Jia<sup>2</sup> and Qiongqin Jiang<sup>1\*</sup>

<sup>1</sup> School of Computer Science, Yangtze University, Jingzhou, China, <sup>2</sup> Petroleum Systems Engineering, Faculty of Engineering and Applied Science, University of Regina, Regina, SK, Canada

## OPEN ACCESS

### Edited by:

Zhiming Chen,

China University of Petroleum, China

### Reviewed by:

Sen Wang,

China University of Petroleum, China

Haitao Li,

Southwest Petroleum  
University, China

### \*Correspondence:

Qiongqin Jiang

17617100@qq.com

### Specialty section:

This article was submitted to

Advanced Fossil Fuel Technologies,

a section of the journal

Frontiers in Energy Research

**Received:** 12 April 2020

**Accepted:** 31 July 2020

**Published:** 23 September 2020

### Citation:

Song W, Jia N and Jiang Q (2020) An Interpretation Model for the Production Profile on the Same Angle of a Horizontal Well Trajectory. *Front. Energy Res.* 8:203. doi: 10.3389/fenrg.2020.00203

An accurate interpretation of the fluid production profile is the essential scientific step required for the dynamic monitoring and management of a reservoir. Currently, an accurate interpretation of conventional logging is generally available for vertical wells. However, high-accuracy interpretation is still a blank for horizontal wells, especially for those wells with low production. Therefore, it is of great importance to develop a new model that can efficiently improve the interpretation accuracy of horizontal wells' production profiles. Practically, it was observed from experiments that, for multiphase flow in a horizontal well, the flow pattern changes significantly with the varied inclination angle along the well trajectory. This is because the flow pattern is critically related to the flow rate and the measured phase flow data (i.e., the production data of oil, gas, and water), which varies with the inclination angle along the horizontal well trajectory. Based on the above observations, a new methodology is proposed to interpret horizontal wells' production profiles with the same inclination angle. A comparison of the measured data and numerically calculated results indicates that the newly established method can significantly improve the interpretation accuracy of horizontal wells' production fluid profile. The interpretation method is, therefore, enriched by production logging for different types of wells. By comparing the experimentally measured data and the calculated results, the newly established method is indicated to be capable of significantly improving the interpretation accuracy of horizontal wells' fluid production profile. The interpretation method is further extended to production logging for different well types. By applying this new methodology, the main water-producing layer can be precisely identified to prevent and control the water burst from horizontal wells as well as the formation of water plugging. Consequently, oil and gas recovery can be effectively enhanced.

**Keywords:** production logging, flow pattern, horizontal well, well trajectory, interpretation of fluid production profile

## INTRODUCTION

In recent decades, more horizontal wells have been drilled worldwide to enhance production from various types of hydrocarbon reservoirs. So far, existing logging interpretation models that were originally developed and utilized for vertical wells have not been utilized efficiently for horizontal wells with desirable interpretation accuracy. Due to the gravity effect,



the fluid flow patterns inside horizontal wells change significantly compared with those in vertical wells. Although a lot of research has been performed to examine the mechanisms of flow patterns and interpretation of production logging for horizontal wells, the advances are still very limited. Obviously, those logging interpretation models cannot be utilized efficiently for horizontal wells with acceptable interpretation accuracy. Due to gravity segregation, the fluid flow patterns within horizontal wells are changed significantly compared with those of vertical wells. Many scientists have done research on the oil–water two-phase flow holdup of horizontal wells. Chang Ya proposes a method for measuring the phase holdup of gas–liquid two-phase flow based on c-4d technology at Zhejiang University (Wang et al., 2006). Zhao Xin does research work on phase holdup of oil–water two-phase flow at Tianjin University (Lum et al., 2004). Xue Ting analyzes the cause of the error in measuring oil content at Tianjin University (Yue et al., 2015) and puts forward a method of measuring oil–water two-phase flow oil content based on thermal diffusion (Lian et al., 2013). Dong Yong points out, through experiments, that the change phenomenon of well-deviation angle, water-holding capacity, water cut, and total flow exists in horizontal wells (Ji, 2012). They did not carry out in-depth analysis and study on the relationship between them, nor did they give a solution method for the slippage speed of oil–water two-phase flow. Wang Haiqin analyzes the flow characteristics of oil–water two-phase flow (Xu et al., 2012), studies nine flow patterns, and describes their phase distribution and flow characteristics (Zhai et al., 2012). Wang Haiqin's experiment is carried out in a small diameter of 50 mm. Whether it is accurate to apply his conclusion to a large diameter needs further analysis. Zhao Xin designed a BP neural network water-cut prediction model for oil–water two-phase flow in a vertical pipe diameter (Tang, 2013) under the condition that the water cut in the vertical well is 51–91% and the flow rate is within 60 m<sup>3</sup>/day. The calculation result is more accurate. Zheng Xike analyzes the difficulty of water-cut calculation for the oil–water two-phase flow in horizontal wells (Zong, 2009) and puts forward a support vector machine regression model (SVR model; Tian et al., 2015) of response time domain and frequency domain eigenvalues of a water-cut meter. This model is only for capacitance- and impedance-measuring instruments. Other measuring instruments are not described. Zhai Lusheng studies the correction algorithm of liquid holdup in a static oil–water two-phase stratified flow (Lian et al., 2015). In recent years, many scholars have put forward some interpretation models for horizontal well production logging interpretation, such as the variable coefficient drift model by Lovick and Angeli (Li et al., 2013) and the Vedapuri three-layer flow model of an oil–water mixture (Tan et al., 2019). These also include Peebles and Garber's improved one horizontal well slippage speed calculation model (Li et al., 2018), the Harmthy slippage speed calculation model (Luo et al., 2015), Duckler's (Luo et al., 2020a) liquid gas correction model (Luo et al., 2020b), the Nicolas correction model (Yue et al., 2020), the Choquette correction model (Pang et al., 2020), the Abb deviated model (Xie et al., 2020), the Beggs and Brill model (Wu et al., 2020), the CTE slippage model (Jinghong et al., 2020), and the statistical model prediction split phase flow calculation

method. Song Yufeng proposes a data fusion expert knowledge base logging interpretation method (Keles et al., 2020). Guo Liejin's team has done numerical simulation analysis of stratified turbulence in horizontal wells (Liu et al., 2020). These models or methods have been verified by production tests (Hayati-Jafarbeigi et al., 2020), and their application in high-productivity horizontal wells can meet the requirements of accuracy (Tian et al., 2020). But the accuracy and interpretation conclusions in low-productivity horizontal wells are worth studying. Therefore, in view of the low production of horizontal wells, it is necessary to study the relevant interpretation model of the production profile. In this study, a new logging interpretation model has been developed based upon analysis of the relationship between water holdup and water content from the flow-pattern perspective (Wu et al., 2020). The newly developed methodology for horizontal wells combines the existing interpretation methods with the consideration of flow at the same horizontal angle. Functionally simulating software is specifically developed for this interpretation model, and the interpretation accuracy of the horizontal wells is considerably improved.

## EXPERIMENTING ON THE HORIZONTAL WELL TILT ANGLE INFLUENCES FLOW PATTERN

The pilot-scale experimental tests to mimic multiphase fluid flow within horizontal wells are performed in the laboratory of



**FIGURE 1** | Photos of experimental setup at Yangtze University.



**TABLE 1** | Measured liquid volume and water cut of oil–water two-phase flow experiments.

Test number	Total liquid (stere)	Water content (%)	Test number	Total liquid (stere)	Water content (%)
1	10	30	17	200	30
2		50	18		50
3		70	19		70
4		90	20		90
5	30	30	21	300	30
6		50	22		50
7		70	23		70
8		90	24		90
9	50	30	25	400	30
10		50	26		50
11		70	27		70
12		90	28		90
13	100	30	29	500	30
14		50	30		50
15		70	31		70
16		90	32		90

Yangtze University (Song et al., 2015) as shown in **Figure 1**. The experimental oil–water distribution is shown in **Table 1**.

The fluids utilized in the experiments include diesel (with a light brown color), tap water, and air. The density and viscosity of diesel oil are, respectively, at standard temperature and pressure. A Newtonian fluid flow behavior is displayed (Xu et al., 2020). The density and viscosity of tap water is 0.9884 g/cm<sup>3</sup> and 1.16 mPa·s at standard temperature and pressure, respectively (Pang et al., 2020). The air density is 0.001223 g/cm<sup>3</sup> at standard temperature and pressure (Vollestad et al., 2020). **Table 1** lists the experimental measurements of total liquid and water cut for each test.

A simulation wellbore and bench are used with the experimental equipment as shown in **Figure 1**. The simulated wellbore is 159 mm (7 inches) in diameter and 124 mm (5.5 inches) in diameter. The simulated well in the laboratory is 12 m long, and there are 10-m transparent wells in the middle. Each section of the transparent well is 2 m long, and there are 1-m stainless steel wells at both ends of the well. The center distance between the two shafts is 800 mm, and the bottom of the shaft and the height of 5 m are equipped with a gas–liquid mixer. Three pressure sensors and three temperature sensors are arranged uniformly from top to bottom in each wellbore, and they are used to measure the pressure and temperature changes in the wellbore simulated by glass. The procedures for each experimental test can be described as follows: (1) design the ratio of different phases based on data listed in **Table 1**, (2) fill up the fluids in the experiment platform, (3) run the equipment through a computer controlling system, (4) observe transformations of flow pattern directly through the transparent glass pipe and capture the images (as shown in **Figure 2**) of such transformations by a digital camera. The flow rates of oil, gas, and water in the experiments are specifically designed according to field data. The

experimental oil–water distribution is shown in **Table 1**. Under the current circumstances, the oil–water flow is a common flow pattern. The images of the gas–water two- and three-phase flow are captured during the tests. The experiment is conducted at standard temperature and pressure. Specifically, a transparent glass pipe with an inner diameter of 124 mm and length of 5.2 m is installed for visual observation of fluid morphology within the flow line (Feng et al., 2017).

The experimental platform consists of an orientation-adjustable pipeline, which can be adjusted with an angle from vertical (0°) to horizontal (90°) so that multiphase fluid flow analyses based on various angles can be conducted within this pipe. In the meantime, the fluid phase transmission can be directly observed from the translucent pipeline. **Figure 2** shows the captured images of a flow pattern of the multiphase flow.

As shown in **Figure 2**, different angles represent different orientations of the pipeline, e.g., 89° and 91°, respectively, mean an upswept pipeline and a sloping-down pipeline, and 90° indicates that the pipeline is in a standard horizontal direction. We can take pictures of two- and three-phase flow. For a fixed proportion of fluid mixtures with a low flow volume as shown in experiments 1–12 in **Table 1**, a tiny change of angle (e.g., 1°) could lead to a significant variation of the flow pattern. More specifically, at 90°, the fluid pattern is laminar with a flat fluid interface (i.e., water–gas, water–oil, and oil–gas) that can be clearly observed; however, the interface becomes more indistinct and uneven when the tilt angle changes to 91° or 89°. It appears to be a mixed color when the tilt angle changes for different zones' flow volume. It is also observed from the experiments that, for a system with a fixed fluid proportion, no change of flow pattern can be observed if the tilt angle stays unchanged.

## THE PRODUCTION PROFILE INTERPRETATION MODEL

In practice, a real horizontal well is not absolutely horizontal in that a certain fluctuation exists on the well trajectory of the production section as shown in **Figure 3**. As demonstrated in **Figure 2**, when the tilt angle changes, the flow pattern also changes without the flow volume, velocity, and phase fraction of each component kept the same. Based on this observation, a calculation model using the same tilt angle is presented to calculate the fluid distribution profile of each phase by utilizing the optimized method. The same tilt angle is at A1 and A2 or B1 and B2 as shown in **Figure 3**. This is the interpretation model for the production profile on the same angle of the horizontal well trajectory. By using this methodology, we can design a model to calculate the value of the production layer. The differences among the different layers are used to calculate the production of each interpretation layer.

The calculation model is summarized below. In **Figure 3**, the oil, gas, and water are flowing simultaneously from left to right. The wave line in **Figure 3** is the horizontal well trajectory. The rightward direction of the arrow indicates the flow direction. First, the production value of each interpretation layer is calculated according to the marked signs (i.e., A1, A2, B1, B2)

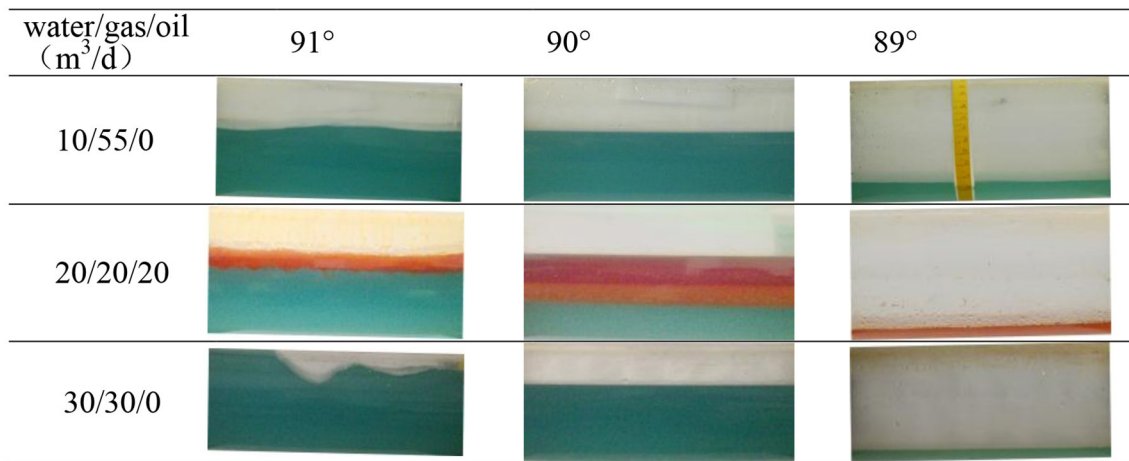


**FIGURE 2** | Experimental Images of the Multiphase Flow within a Horizontal Well.

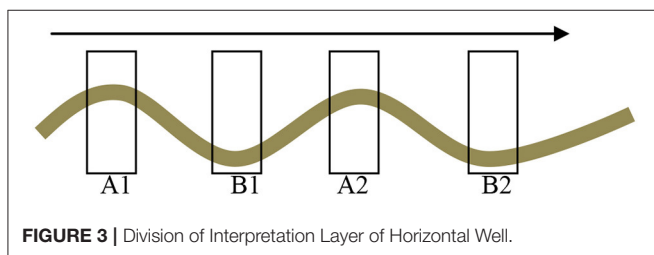


**FIGURE 3** | Division of Interpretation Layer of Horizontal Well.

in the graph; all these layers are horizontal (i.e., 90°), and the flow patterns are laminar as indicated in **Figure 2**. Then, the flow difference between every interval is calculated.

$$\begin{aligned}\Delta_1 &= Q_{A2} - Q_{A1} \\ \Delta_2 &= Q_{B2} - Q_{B1}\end{aligned}\quad (1)$$

where  $Q_{A1}$ ,  $Q_{A2}$ ,  $Q_{B1}$ , and  $Q_{B2}$  are the production value of each layer;  $\Delta_1$  is the production value of  $Q_{A2}$  minus  $Q_{A1}$ ; and  $\Delta_2$  is the production value of  $Q_{B2}$  minus  $Q_{B1}$ .

Three interpretations for the calculated values of  $\Delta$  are presented as follows: (1)  $\Delta = 0$  means there is no production value between these two layers, (2)  $\Delta > 0$  means production exists with a value of  $\Delta$  between those two layers, and (3)  $\Delta < 0$  means there is a suction value of the layer. In this way, the producing layer can be identified, and the production rate of each layer can be calculated more precisely.

According to the formula (1) of the multiphase production  $Q$ , the key point of the interpretation methods is to precisely calculate the apparent velocity of fluid ( $V_a$ ) and the velocity correction factor ( $C_v$ ) (Zeng and Yao, 2020). The  $V_a$  can be determined from the measurement of turbine flow velocity, tracer measurement, etc.  $V_a$  value is a relied-upon measurement (China University of Petroleum-Beijing, 2020). The  $V_a$  value method depends on the difference in the measuring instrument. For example, in turbine flow measurement,  $V_a$  is obtained by

turbine measures. In tracer flow measurement,  $V_a$  value is the tracer measurement value.

The new interpretation method proposes a back calculation to generate the value of  $V_a$ . The formula is as follows:  $V_a = Q/C_v \times P_c$ . In this formula,  $Q$  represents the set-point value of the production layer,  $C_v$  is the fluid velocity profile correction factor, and  $P_c$  is the pipe diameter constant. If the correct  $C_v$  value is utilized, the calculated  $V_a$  is equal to the measured value, which indicates that the correct production value of  $Q$  is achieved. If the calculated  $V_a$  is not matched with the experimental data, the value of  $Q$  is optimized until matching is achieved.

In order to calculate  $C_v$ , several important parameters, such as the inner diameters of casing pipes ( $D$ , unit: m), mean velocity of fluid ( $V_m$ , unit: m/s), fluid density (unit: kg/m<sup>3</sup>), and fluid viscosity (unit: mPa·s), are calculated. Furthermore, the Reynolds number is calculated, and the corresponding  $C_v$  value is determined by using the interpolation algorithm.

Upon completion of the aforementioned calculations, the production value of each fluid phase,  $Q$  (where  $Q$  is the calculation value; the previous  $Q$  is a set-point value), can be calculated. Upon completion of the calculation of  $Q$ , the output of every interpretation layer can be determined.

## Design of the Calculation Principle

For this study, an algorithm that is designed to automatically recognize the true slope angle of the horizontal well trajectory was developed. The slope angle is according to the same tilt angle value, and the same tilt angle value directly affects the interpretation accuracy of the model. At the same tilt angle, the design scheme to calculate the production value of each phase of the horizontal well is shown in **Figure 4**. The values of  $Q_w$ ,  $Q_o$ , and  $Q_g$  were calculated by using the respective fluid physical properties, velocity profile correction factor, and tilt angle interpretation model. The process includes the inversion calculations of oil, gas, and water phase holdup, flow velocity, density, and apparent flow velocity contour. These values can

be obtained from measuring production data. The flow pattern includes both the laminar and turbulent flow.

The water/oil/gas holdup represents the fraction of the flowing volume of water/oil/gas with respect to the total volume of the pipe per unit length. In **Figure 4**, the  $Q_w$  is initially the set-point water value of the producing layer,  $Q_o$  is initially the set-point oil value of the producing layer, and  $Q_g$  is initially the set-point gas value of the producing layer. The water, oil, and gas holdup is  $Y_w^*$ ,  $Y_o^*$ , and  $Y_g^*$ , respectively. The water, oil, and gas flow rate is  $V_w^*$ ,  $V_o^*$ , and  $V_g^*$ . The flow density is  $P^*$ , and the apparent

fluid velocity is  $V_{app}^*$ . They are all calculated from the inversion method in formula (2) to formula (11). In **Figure 4**, the water, oil, and gas holdup is  $Y_w$  ( $Y_w$  is measured by an instrument),  $Y_o$  ( $Y_o$  is measured by an instrument), and  $Y_g$  ( $Y_g$  is measured by an instrument), respectively. Water, oil, and gas flow rates are  $V_w$  ( $V_w$  is measured by an instrument),  $V_o$  ( $V_o$  is measured by an instrument), and  $V_g$  ( $V_g$  is measured by an instrument). The flow density is  $P$  ( $P$  is measured by an instrument), and the apparent fluid velocity is  $V_{app}$  ( $V_{app}$  is measured by an instrument). The values for each variable are initially assumed and then the values are calculated and compared with the measured data. If the retrieved calculation data are consistent with the measured values, the results of the inversion calculation are treated as accurate. The initial production values for the water, oil, and gas phases ( $Q_w$ ,  $Q_o$ ,  $Q_g$ ) of the interpretation layer are established, and the value of each phase is optimized until the calculated value and the measured data are matched. The key point is to design the same-angle calculation model or a related algorithm through the analysis of the relevant experimental data.

A calculation model of the production logging profile under the same tilt angle is developed, and the specific process is presented below.

In step 1, the horizontal well track is drawn, the near horizontal level is found qualitatively according to the track, and the interpretation of each layer is determined for different tilt angles.

In step 2, an initial production value for the whole zone flow layer is assumed. The mean fluid velocity of each phase of the well is calculated, and the production value is the flow value within the well. The  $V_a$  is calculated according to the relationship between the Reynolds number and the velocity profile, and then the value of apparent velocity of fluid is determined.

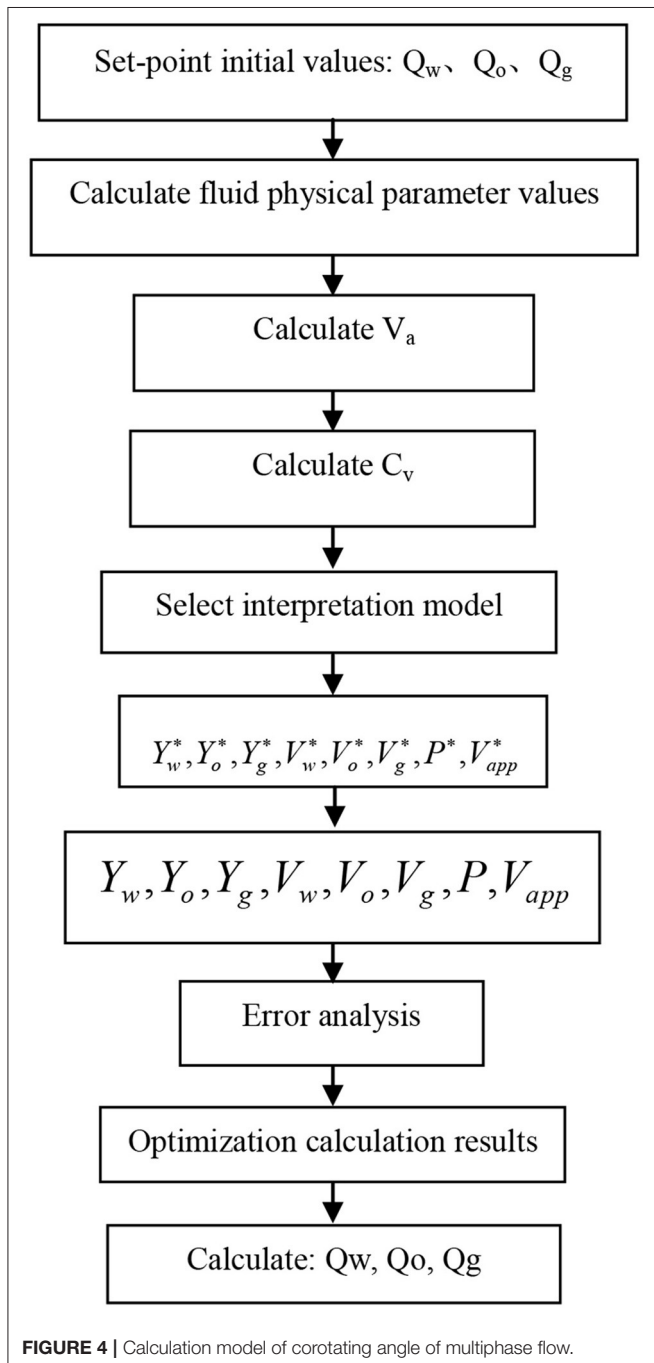


**TABLE 2 |** Comparison of interpreted single-phase flow with the measured data.

Well ID	Interpretation layer (m)	Output (m <sup>3</sup> )		
		Interpretation	Measured	Error (%)
1#	Whole flow layer	169.30	168.10	0.70
	1602.99–1607.43	49.90	48.80	2.20
	1633.40–1641.09	55.38	59.72	7.80
2#	Whole flow layer	482.56	489.72	1.50
	1388.9–1395.5	131.60	135.00	2.50
	1408.45–1411.25	59.30	60.10	1.30
3#	Whole flow layer	1233.50	1251.70	1.45
	1627.25–1632.95	200.31	210.54	4.86
	1660.45–1673.15	415.75	401.59	3.53
4#	Whole flow layer	826.30	838.30	1.43
	1966.45–1984.95	551.10	565.80	2.59
	2042.65–2054.80	272.00	278.20	2.23
5#	Whole flow layer	900.50	921.50	2.28
	1,419–1,421	187.26	192.19	2.57
	1,655–1,658	667.58	703.14	5.06

In step 3, the drift and slip velocities are calculated according to the drift and slip models. Then, the value of each water holdup for each layer is calculated. If the calculated value is the same as the practical value, the assumed initial total production value should be consistent with the practical production value. If not, the calculated holdup value is used as a known parameter for further calculation. Then, the initial production value is reset, and the value of each water holdup is recalculated. Next, repeat steps 1 and 2.

In step 4, the value of flow velocity of each phase is calculated after the water holdup. If the velocity stays the same as the practical value, the density value of each phase is calculated. Otherwise, the initial production value is reset, and the water holdup and flow velocity values are recalculated. Repeat steps 3 and 4 until the holdup value and the density value of each phase match the practical value.

In step 5, based on the correct holdup and flow velocity values, the density value is calculated. If the calculated density value is the same as the practical value, cease the calculation process. If not, reset the initial production value and repeat steps 2–5 until the values of the water holdup, flow velocity, and density are similar to the practical values. Then the process is terminated, and the values are finalized, which includes mean flow velocity, apparent velocity, slip velocity, drift velocity, water holdup, fluid velocity, and fluid density.

In step 6, based on the calculated parameters from the expert fluid property database and combined with the values from step 5, the flow value (the flow can mean flux) of each phase is calculated by decreasing the whole flow layer by layer.

The method is demonstrated by using the water–oil case as an example. The interpretation model for the production profile on the same angle of horizontal well trajectory is used to calculate the whole flow layer production, average flow velocity, apparent velocity, slip velocity, drift velocity, water holdup of each phase, each phase's fluid velocity, and fluid density.

According to the well track, the initial values ( $Q_o$ ,  $Q_w$ , unit per day) of the oil and gas phase flows are set on the full flow layer, the apparent flow velocity ( $V_a$ , unit  $m/min$ ), the slip velocity ( $V_s$ , unit  $m/min$ ), the oil holdup  $Y_o$ , water holdup  $Y_w$ , actual flow

velocity of oil ( $V_o$ , unit  $m/min$ ), and the actual flow velocity of water ( $V_w$ , unit  $m/min$ ); the other data are the pipe diameter constant ( $P_c$ ,  $(m^3/d)/(m/min)$ ), the external diameter ( $D$ , unit  $mm$ ), the density of water ( $\rho_w$ , unit  $g/cm^3$ ), the density of oil ( $\rho_o$ , unit  $g/cm^3$ ), which are determined by using the inversion optimization method.

Formula (2) is used to calculate the pipe diameter constant.

$$P_c = \frac{1}{4} \pi D^2 \times 60 \times 24 \times 10^{-6} \quad (2)$$

Then formula (3) is used to calculate the mean fluid velocity.

$$V_m = \frac{Q_o + Q_w}{P_c} \quad (3)$$

After that, according to the initial values of  $Q_o$  and  $Q_w$ , by combining the expert knowledge database and the fluid-producing profile by using the method of optimized iteration computation, the value of  $C_v$  is obtained. Formula (4) is used to calculate the apparent fluid velocity  $V_a$ , and formulas (5) and (6) are used to calculate the superficial velocity of the oil and gas. The relationship is that  $C_v$  multiplied by  $V_a$  makes the velocity profile ( $V_m$ ).

$$v_a = \frac{v_m}{C_v} \quad (4)$$

$$v_{so} = \frac{Q_o}{P_c} \quad (5)$$

$$v_{sw} = \frac{Q_w}{P_c} \quad (6)$$

Combine the known parameters  $v_{so}$ ,  $v_{sw}$ ,  $v_m$ ,  $\rho_w$ ,  $\rho_o$ ,  $\theta$ , and formulas (7) and (8) to calculate the values of  $v_s$  and  $Y_w$ .

$$v_s = 12.013(\rho_w - \rho_o)^{1/4} \exp[-0.788(1 - Y_w) \ln \frac{1.85}{\rho_w - \rho_o}] (1 + 0.04 * \theta), \quad (7)$$

$$V_{so} = (1 - Y_w)V_m + Y_w(1 - Y_w)V_s. \quad (8)$$

**TABLE 3 |** Comparison of interpreted wellhead multiphase flow results with measured data.

Well ID	Interpretation interval	Production value ( $m^3/d$ )								
		Interpretation data			Measured data			Error (%)		
		Oil	Gas	Water	Oil	Gas	Water	Oil	Gas	Water
A1	2091.93–2099.82	63.34	215.36	0	66.63	226.20	0	5.10	5.10	0
	2124.76–2127.98	52.74	179.32	0	56.37	191.70	0	6.80	6.90	0
A2	1879.93–1886.3	47.53	123.58	0	52.52	135.57	0	9.50	9.70	0
	1911.13–1915.08	41.07	106.79	0	45.67	118.94	0	9.20	9.30	0
A3	3810.39–3816.2	120.37	12131.22	80.59	123.72	12640.56	80.59	2.70	4.10	0.50
	3840.15–3846.67	101.42	12112.27	61.64	104.76	12621.61	61.64	3.30	4.20	0.0
A4	3047.715–3057.617	91.33	7903.52	41.16	95.14	8205.81	53.79	0.10	0.10	0.30
	3068.741–3079.743	72.38	7884.57	22.21	76.19	8186.86	24.84	5.20	3.80	9.80



In formula (7), the density values of water and oil are obtained from the expert database, and  $\theta$  is the tilt angle of the horizontal well (unit  $^{\circ}$ ). The oil holdup can be calculated by using formula (9).

$$Y_o = 1 - Y_w, \quad (9)$$

$$V_o = \frac{V_{so}}{1 - Y_w} = \frac{Q_o}{P_c(1 - Y_w)}, \quad (10)$$

$$V_w = \frac{V_{sw}}{Y_w} = \frac{Q_w}{P_c Y_w}. \quad (11)$$

Finally, formulas (9) and (10) are used to calculate the actual velocity of oil and water. The density also can be found from using a measuring tool to measure.

By comparing the data obtained from the inversion method and the measured value, the initial production values of oil and water are determined to be correct or not. If the data from the inversion analogy are similar to those of the measured values, the production value is the target value. Otherwise, the production value is optimized.

The production profile  $Q_{A1}$ ,  $Q_{A2}$ ,  $Q_{B1}$ , and  $Q_{B2}$  values of the horizontal well are compared with those data generated by using formula (1) to obtain the difference between tilt angles  $\Delta_1$ ,  $\Delta_2$  values for the purpose of finding the productive interval and the corresponding parameters.

## PRECISE VERIFICATION OF THE INTERPRETATION RESULT

In order to verify the rationality of the interpretation results, a total of five horizontal wells' production logging data were analyzed, and the interpretation results were further compared with the actual measured values. **Table 2** shows the difference of the single-phase flow between the interpretation results and the measured data by using the logging tool. The measured data were calculated by using the model to get the interpretation values. The model is the interpretation model for the production profile on the same angle of the horizontal well trajectory.

**Table 2** shows that for the actual measured data in the wellhead area, the maximum and minimum errors of layer flow are 7.8 and 0.7%, respectively. The error is the difference between the measured data and the interpreted values divided by the measured value.

**Table 3** shows that the maximum error of the simulated result is 9.8% in a three-phase flow horizontal well, and the maximum error of the two-phase flow is 0.5%.

## REFERENCES

China University of Petroleum-Beijing (2020). *Patent Issued for Apparatus for Physical Simulation Experiment for Fracturing in Horizontal Well Layer by Layer by Spiral Perforation and Method* (USPTO 10,550,688). Electronics Newsweekly.

## CONCLUSIONS

In this paper, a multiphase flow pattern mechanism for a horizontal well is studied and analyzed by a proposed calculation methodology that uses the same tilt angle for a highly deviated well. The main innovation point of this research is the interpretation method with the same tilt angle. The production logging interpretation method and the model proposed in this paper are only applicable to the production logging interpretation of a single well and not applicable for cluster wells.

The change of the tilt angle has great influence on the flow pattern when the flow rate is low. Thus, an interpretation method for calculating the production profile with the same tilt angle was developed. The algorithm flow chart of the interpretation model was constructed and the relevant algorithm model and formula was deduced based on the two-phase example. This study designs an inclined angle interpretation method by studying the horizontal flow pattern. Furthermore, it leads to the development of a series of interpretation models for production logging of a horizontal well by studying relevant calculation methods and models. Therefore, interpretation accuracy of horizontal wells is significantly improved. Further study will be focused on the study for multiphase flow and improvement of the current calculation model.

## DATA AVAILABILITY STATEMENT

All datasets generated for this study are included in the article/supplementary material.

## AUTHOR CONTRIBUTIONS

WS: conceptualization, funding acquisition, investigation, and writing—original draft. NJ and WS: data curation and writing—review and editing. QJ: formal analysis, methodology, project administration, resources, software, supervision, validation, and visualization. All authors contributed to the article and approved the submitted version.

## ACKNOWLEDGMENTS

The author would like to thank the support received from Xinjiang Uygur Autonomous Region Innovation Environment (talent, base) Construction Foundation (Xinjiang NSFC Program Foundation 2020D01A132): Research and implementation of horizontal well inversion optimization interpretation method. Jingzhou Science Technology Foundation (2019EC61-06) and Hubei Science and Technology Demonstration Foundation (2019ZYYD016).

Feng, Q., Xia, T., Wang, S., and Singh, H. (2017). Geofluids; research institute of petroleum exploration and development researchers report recent findings in geofluids (transient pressure analysis for multifractured horizontal well with the use of multilinear flow model in shale gas reservoir). *Sci. Lett.* 111–117.

Hayati-Jafarbeigi, S., Mosharaf-Dehkordi, M., Ziaei-Rad, M., and Dejam, M. (2020). A three-dimensional coupled well-reservoir flow model for



- determination of horizontal well characteristics. *J. Hydrol.* 585:124805. doi: 10.1016/j.jhydrol.2020.124805
- Ji, B. (2012). Progress and prospects of enhanced oil recovery technologies at home and abroad. *Oil Gas Geol.* 33, 111–117.
- Jinghong, H., Ruofan, S., and Yuan, Z. (2020). Investigating the horizontal well performance under the combination of micro-fractures and dynamic capillary pressure in tight oil reservoirs. *Fuel* 269:117375. doi: 10.1016/j.fuel.2020.117375
- Keles, C., Tang, X., Schlosser, C., Louk, A. K., and Ripepi, N. S. (2020). Sensitivity and history match analysis of a carbon dioxide “huff-and-puff” injection test in a horizontal shale gas well in Tennessee. *J. Nat. Gas Sci. Eng.* 77:103226. doi: 10.1016/j.jngse.2020.103226
- Li, G., Qin, Y., Liu, L., He, Q., Chen, F., and Zhang, Y. (2013). Application of overall fracturing technology for cluster horizontal wells to the development of low permeability tight gas reservoirs in the Daniudi Gas Field, Ordos Basin. *Nat. Gas Industry* 33, 49–53.
- Li, H., Tan, Y., Jiang, B., Wang, Y., and Zhang, N. (2018). A semi-analytical model for predicting inflow profile of horizontal wells in bottom-water gas reservoir. *J. Petrol. Sci. Eng.* 160, 351–362. doi: 10.1016/j.petrol.2017.10.067
- Lian, L., Qin, J., Yang, S., Yang, Y., and Li, Y. (2013). Analysis and evaluation on horizontal well seepage models and their developing trends. *Oil Gas Geol.* 34, 821–827. doi: 10.11743/ogg20130616
- Lian, Z., Zhang, Y., Zhao, X., Ding, S., and Lin, T. (2015). Establishment and application of mechanical and mathematical models for multi-stage fracturing strings in a horizontal well. *Nat. Gas Industry* 35, 85–91.
- Liu, S., Zhu, Z., and Balint, S. (2020). Application of composite deflecting model in horizontal well drilling. *Hindawi* 2020:4672738. doi: 10.1155/2020/4672738
- Lum, J. Y. L., Lovick, J., and Angeli, P. (2004). Dual continuous horizontal and low inclination two-phase liquid flows. *Canad. J. Chem. Eng.* 83, 303–315. doi: 10.1002/cjce.5450820211
- Luo, H., Li, H., Lu, Y., and Zhenhua, G. (2020a). Inversion of distributed temperature measurements to interpret the flow profile for a multistage fractured horizontal well in low-permeability gas reservoir. *Appl. Math. Model.* 77, 360–377. doi: 10.1016/j.apm.2019.07.047
- Luo, H., Li, H., Tan, Y., Li, Y., Jiang, B., Lu, Y., et al. (2020b). A novel inversion approach for fracture parameters and inflow rates diagnosis in multistage fractured horizontal wells. *J. Petrol. Sci. Eng.* 184:106585. doi: 10.1016/j.petrol.2019.106585
- Luo, W., Li, H., Wang, Y., and Wang, J. C. (2015). A new semi-analytical model for predicting the performance of horizontal wells completed by inflow control devices in bottom-water reservoirs. *J. Nat. Gas Sci. Eng.* 27, 1328–1339. doi: 10.1016/j.jngse.2015.03.001
- Pang, Z., Jiang, Y., Wang, B., Cheng, G., and Yu, X. (2020). Experiments and analysis on development methods for horizontal well cyclic steam stimulation in heavy oil reservoir with edge water. *J. Petrol. Sci. Eng.* 188:106948. doi: 10.1016/j.petrol.2020.106948
- Song, W., Jiang, Q., Li, J., and Li, M. (2015). Equal-tilt-angle production profile calculation model of horizontal wells. *Oil Gas Geol.* 36, 688–694.
- Tan, Y., Li, H., Zhou, X., Wang, K., Jiang, B., and Zhang, N. (2019). Inflow characteristics of horizontal wells in sulfur gas reservoirs: a comprehensive experimental investigation. *Fuel* 238, 267–274. doi: 10.1016/j.fuel.2018.10.097
- Tang, Q. (2013). Application of geosteering technology in the development of Sulige gas field—case studies of the Su10 and Su53 blocks. *Oil Gas Geol.* 34, 388–393. doi: 10.11743/ogg20130316
- Tian, Q., Cui, Y., Luo, W., Liu, P., and Ning, B. (2020). Transient flow of a horizontal well with multiple fracture wings in coalbed methane reservoirs. *Energies* 13:1498. doi: 10.3390/en13061498
- Tian, Z., Shi, L., and Qiao, L. (2015). Research of and countermeasure for wellbore integrity of shale gas horizontal well. *Nat. Gas Industry* 35, 70–76. doi: 10.3787/j.issn.1000-0976.2015.09.010
- Vollestad, P., Angheluta, L., and Jensen, A. (2020). Experimental study of secondary flows above rough and flat interfaces in horizontal gas-liquid pipe flow. *Int. J. Multiphase Flow* 125:103235. doi: 10.1016/j.ijmultiphaseflow.2020.103235
- Wang, X., Yu, G., and Li, Z. (2006). Productivity of horizontal wells with complex branches. *Petrol. Explor. Dev.* 33, 729–733.
- Wu, Z., Dong, L., Cui, C., Cheng, X., and Wang, Z. (2020). A numerical model for fractured horizontal well and production characteristics: comprehensive consideration of the fracturing fluid injection and flowback. *J. Petrol. Sci. Eng.* 187:106765. doi: 10.1016/j.petrol.2019.106765
- Xie, D., Huang, Z., Ma, Y., Vaziri, V., Kapitaniak, M., and Wiercigroch, M. (2020). Nonlinear dynamics of lump mass model of drill-string in horizontal well. *Int. J. Mech. Sci.* 174:105450. doi: 10.1016/j.ijmecsci.2020.105450
- Xu, J., Dong, N., Zhu, C., Liu, J., and Chen, T. (2012). Application of seismic data to the design of horizontal well trajectory in tight sandstone reservoirs. *Oil Gas Geol.* 33, 909–913.
- Xu, Y., Li, X., and Liu, Q. (2020). Pressure performance of multi-stage fractured horizontal well with stimulated reservoir volume and irregular fractures distribution in shale gas reservoirs. *J. Nat. Gas Sci. Eng.* 77:103209. doi: 10.1016/j.jngse.2020.103209
- Yue, M., Zhang, Q., Zhu, W., Zhang, L., Song, H., and Li, J. (2020). Effects of proppant distribution in fracture networks on horizontal well performance. *J. Petrol. Sci. Eng.* 187:106816. doi: 10.1016/j.petrol.2019.106816
- Yue, P., Du, Z., Chen, X., Zhu, S. Y., and Jia, H. (2015). Critical parameters of horizontal well influenced by semi-permeable barrier in bottom water reservoir. *J. Central South Univer.* 22, 1448–1455. doi: 10.1007/s11771-015-2662-z
- Zeng, Q., and Yao, J. (2020). Production calculation of multi-cluster fractured horizontal well accounting for stress shadow effect. *Int. J. Oil Gas Coal Tech.* 23:293. doi: 10.1504/IJOGCT.2020.105773
- Zhai, L., Jin, N., and Zheng, X. (2012). The analysis and modeling of measuring data acquired by using combination production logging tool in horizontal simulation well. *Chin. J. Geophys.* 55, 1411–1421. doi: 10.6038/j.issn.0001-5733.2012.04.037
- Zong, Y. (2009). *Measurement of the Properties of Oil-Water Two-Phase Flow in Inclined and Horizontal Pipes*. Tianjin: Tianjin University.

**Conflict of Interest:** The authors declare that the research was conducted in the absence of any commercial or financial relationships that could be construed as a potential conflict of interest.

Copyright © 2020 Song, Jia and Jiang. This is an open-access article distributed under the terms of the Creative Commons Attribution License (CC BY). The use, distribution or reproduction in other forums is permitted, provided the original author(s) and the copyright owner(s) are credited and that the original publication in this journal is cited, in accordance with accepted academic practice. No use, distribution or reproduction is permitted which does not comply with these terms.



# Transient Temperature Distribution of Underground Carbon Dioxide Salt Cavern Storage With State Space Model

Zhou Yuan<sup>1,2†</sup>, Yanxi Zhou<sup>1†</sup>, Minghui Wei<sup>1\*</sup> and Xinwei Liao<sup>2</sup>

<sup>1</sup> School of Mechanical and Electrical Engineering, Southwest Petroleum University, Chengdu, China, <sup>2</sup> State Key Laboratory of Petroleum Resources and Prospecting, China University of Petroleum, Beijing, China

## OPEN ACCESS

### Edited by:

Kaiqiang Zhang,  
Imperial College London,  
United Kingdom

### Reviewed by:

Wengang Zhang,  
Chongqing University, China  
Na Wei,  
Southwest Petroleum  
University, China  
Jie Chen,  
Chongqing University, China

### \*Correspondence:

Minghui Wei  
wmh881988@163.com

<sup>†</sup>These authors have contributed  
equally to this work

### Specialty section:

This article was submitted to  
Advanced Fossil Fuel Technologies,  
a section of the journal  
Frontiers in Energy Research

**Received:** 27 March 2020

**Accepted:** 30 July 2020

**Published:** 20 October 2020

### Citation:

Yuan Z, Zhou Y, Wei M and Liao X  
(2020) Transient Temperature  
Distribution of Underground Carbon  
Dioxide Salt Cavern Storage With  
State Space Model.  
Front. Energy Res. 8:201.  
doi: 10.3389/fenrg.2020.00201

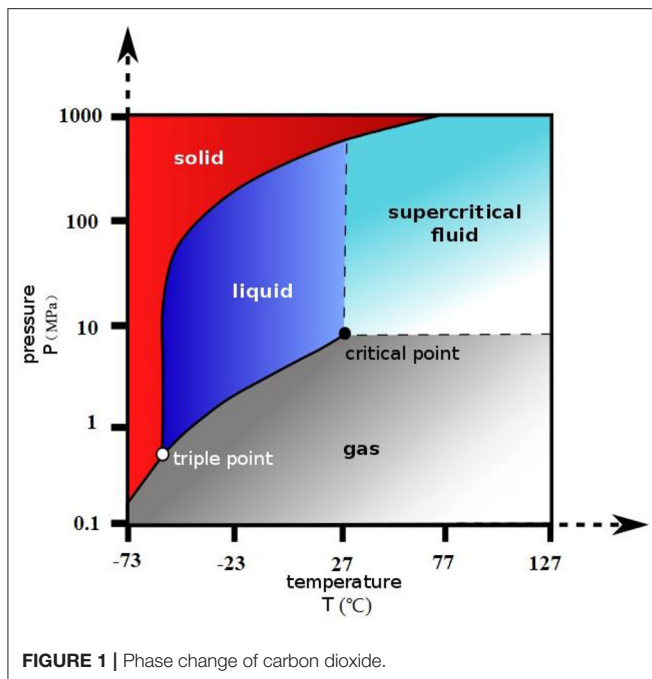
Underground salt caverns have become one of the potential methods for carbon dioxide (CO<sub>2</sub>) storage due to its advantages including high storage capacity and easy construction. The wellbore and salt cavern heat transfer models for the CO<sub>2</sub> injection process was developed and solved by the state space method. This method can not only solve the partial differential equation, but can also be used as the basic model of automatic control. The results indicate that the temperature of annulus and the salt cavern are significantly influenced by the injection rate during the injection process, while the brine temperature in tubing remains almost unchanged. When the injection process stops, the temperature of annulus and the salt cavern are dominated by the formation temperature. The temperature of tubing brine mainly changes after a few hours, causing crystals to separate out from the brine, which can also explain why the tubing is blocked when the gas injection stops.

**Keywords:** salt cavern, CO<sub>2</sub> storage, heat transfer, state space method, injection process

## INTRODUCTION

With the advent of industrial development, carbon dioxide (CO<sub>2</sub>) has an increasingly high concentration in the atmosphere as a result of the combustion of fossil fuels, such as coal, petroleum, and natural gas, which has caused the rising trend in the Earth's average temperature. There are nearly  $1.03 \times 10^9$  tons of CO<sub>2</sub> emissions in China every year (Li et al., 2017). How to deal with carbon dioxide emissions has become a global problem. Carbon capture and storage (CCS) is a technique of lower carbon utilization for fossil fuels on a large scale (Li et al., 2015). This technique was developed in the 1970s and has been used in enhanced oil recovery with CO<sub>2</sub> (CO<sub>2</sub>-EOR), in enhanced geothermal systems with CO<sub>2</sub> (CO<sub>2</sub>-EGS), CO<sub>2</sub> storage with gas recovery (CO<sub>2</sub>-EGR), and CO<sub>2</sub> storage with saline water recovery (CO<sub>2</sub>-EWR) (Wang et al., 2012; Sun et al., 2013; Boot-Handford et al., 2014; Li et al., 2014; Luo et al., 2014; Middleton et al., 2015; Wei et al., 2020). In recent years, a group of underground salt cavern storages with various advantages have been built in China (Zhang and Goh, 2012). Firstly, man-made salt caverns can be sized by specific demands by water-jet and the capacity of one salt cavern is usually  $2-5 \times 10^5$  m<sup>3</sup> (Bérest, 2019). Furthermore, using a salt cavern as CO<sub>2</sub> storage is different from traditional methods, where CO<sub>2</sub> can be drawn from all the time. Therefore, the salt cavern has extensive application properties for CO<sub>2</sub> storage (Kushnir et al., 2012).

The accurate prediction of wellbore and cavern temperature plays an important role in keeping the storage a safe and smooth process. It has great significance for judging the strength and



stability of wellbore and salt caverns. For the underground salt cavern system, while the injection has stopped for a few hours, the crystal in tubing brine may separate out as the temperature changes, which would block the tubing, and affect the CO<sub>2</sub> storage system performance. What is more, when CO<sub>2</sub> approaches a supercritical state (31.1°C, 7.38 MPa) drastic change would occur somewhere along the wellbore and in the salt cavern, which would not be expected during the injection process (Li et al., 2017).

Studies on wellbore temperature distribution have been conducted since the 1950s. Both numerical and analytical approaches have been adopted to estimate the wellbore temperature (Hasan and Kabir, 1996; Wei et al., 2020). The earliest study of wellbore temperature was by Ramey. He drew charts for predicting bottom-hole circulating temperatures (Ramey, 1962; Wei et al., 2020) and proposed a steady-state model for obtaining the hole wellbore temperature distribution, which could not be applied to transient behavior (Hasan and Kabir, 2002; Yang et al., 2017; Wei et al., 2020). Raymond proposed the first numerical model for predicting temperature distributions for both transient and pseudo-steady-state conditions (Raymond, 1969). Hasan proposed the analytic methods for wellbore temperature prediction (Hasan et al., 1997, 1998). For CO<sub>2</sub> injection, the flow and thermal behavior in the wellbore involves some unique characteristics. Many researchers also developed CO<sub>2</sub> two-phase flow models under isothermal conditions (Wang et al., 2011a,b; Guo and Zeng, 2015; Li et al., 2016; Wei et al., 2020). Although using a salt cavern for CO<sub>2</sub> storage is not equal to injecting CO<sub>2</sub> into the wellbore. It needs to consider the heat transfer of annulus, tubing, and the salt cavern (Zhang and Goh, 2015; Wang et al., 2019). There have been few research topics that have focused on this field before (Kyuro and Yuichi, 2011; Goh and Zhang, 2012).

This study develops mathematical models to calculate the wellbore and salt cavern heat transfer models during CO<sub>2</sub> injection and injection-stopped periods, and models were solved by the state space method. This method can not only be used for solving partial differential equations, but also as an automatic control model. The results demonstrated that wellbore and cavern temperatures were significantly influenced by the injection rate during the injection process, and the tubing brine temperature had remained approximately constant. When the injection stopped, the wellbore and cavern temperatures were dominated by the formation temperature. The main variation in the tubing brine temperature occurred a few hours after the injection had stopped which would cause crystals to separate out from the brine. This is the reason why the tubing may be blocked after the injection process is stopped. The model can be used to design CO<sub>2</sub> injection parameters and monitor salt cavern states, and reduce the risk to the underground salt cavern system.

## MATHEMATICAL MODEL

**Figure 1** shows the phase change of CO<sub>2</sub>, when CO<sub>2</sub> approaches the supercritical state (31.1°C, 7.38 MPa), which is likely to occur somewhere along the wellbore and in the salt cavern (Li et al., 2017; Wei et al., 2020).

**Figure 2** describes the process of injecting CO<sub>2</sub> into the salt cavern storage which can be divided into two parts. The first part: the fluid of CO<sub>2</sub> is injected into the salt cavern storage through annulus. The second part: the fluid of brine in the salt cavern storage flows through the tubing to the ground. Based on the principle of the conservation of energy, the dynamic mathematical model of heat transfer in the process of injecting CO<sub>2</sub> into the salt cavern storage is established (Wei et al., 2020).

### The Heat Transfer Model of Annulus

According to **Figure 2**, in the CO<sub>2</sub> heat transfer model of annulus, the energy change is equal to the heat generated by the axial flow of CO<sub>2</sub>, the heat transfer between the CO<sub>2</sub> of annulus and the tubing, and that between the well wall and the CO<sub>2</sub> of annulus. Therefore, the heat transfer model is Li et al. (2017) and Wei et al. (2020):

$$\rho_a A_a C_a \frac{\partial T_a}{\partial t} = -M_a C_a \frac{\partial T_a}{\partial z} + 2\pi r_1 \lambda_1 [T_f - T_a] + 2\pi r_2 \lambda_2 [T_w - T_a] \quad (1)$$

where  $T_a$  is the annulus fluid temperature of CO<sub>2</sub>, °C.  $T_w$  is the tubing temperature, °C.  $T_f$  is the well wall temperature, °C.  $\rho_a$  is the CO<sub>2</sub> density of annulus, kg/m<sup>3</sup>.  $A_a$  is the area of annulus, m<sup>2</sup>.  $C_a$  is the CO<sub>2</sub> specific heat of the annulus fluid, J/kg.°C.  $M_a$  is the mass flow of injected CO<sub>2</sub>, kg/s.  $r_1$  is the radius of annulus, m.  $r_2$  is the outer radius of tubing, m.  $\lambda_1$  is the convective heat transfer coefficient of annulus CO<sub>2</sub> and the well wall, W/m<sup>2</sup>.°C.  $\lambda_2$  is the convective heat transfer coefficient of annulus CO<sub>2</sub> and tubing, W/m<sup>2</sup>.°C.

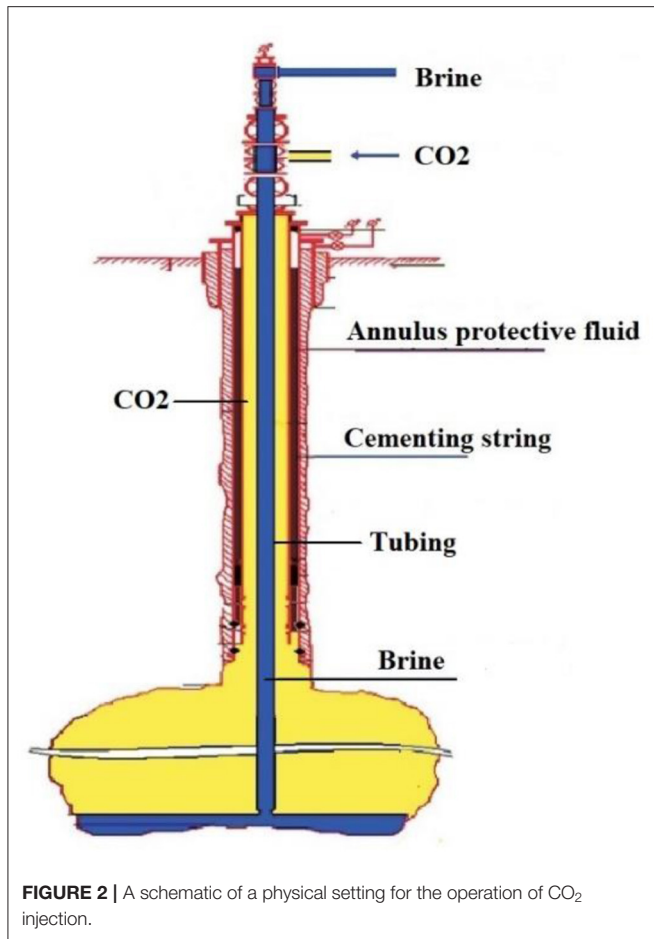


**FIGURE 2** | A schematic of a physical setting for the operation of CO<sub>2</sub> injection.

## The Heat Transfer Model of Tubing Fluids

The fluid in the tubing is brine, the energy change of it is equal to the heat generated by the axial flow of the brine, and the heat exchange with the tubing brine and the tubing. Therefore, the heat transfer model is:

$$\rho_p A_p C_p \frac{\partial T_p}{\partial t} = \rho_p A_p C_p v_p \frac{\partial T_p}{\partial z} + 2\pi r_3 \lambda_3 [T_w - T_p] \quad (2)$$

where  $T_p$  is the tubing fluid temperature of brine, °C.  $\rho_p$  is the density of the tubing fluid, kg/m<sup>3</sup>.  $A_p$  is the area of the tubing, m<sup>2</sup>.  $C_p$  is the specific heat of tubing brine, J/kg·°C.  $r_3$  is the inner radius of tubing, m.  $v_p$  is the fluids flow velocity in the tubing, m/s.  $\lambda_3$  is the convective heat transfer coefficient between the tubing brine and tubing, W/m<sup>2</sup>·°C.

## The Heat Transfer Model of Tubing

For the tubing, the energy change is equal to the convection heat transfer between the annulus CO<sub>2</sub> and the tubing, and that between the brine and the tubing. Therefore, the heat transfer model is:

$$\rho_w A_w C_w \frac{\partial T_w}{\partial t} = 2\pi r_2 \lambda_2 [T_a - T_w] + 2\pi r_3 \lambda_3 [T_p - T_w] \quad (3)$$

where  $\rho_w$  is the density of tubing, kg/m<sup>3</sup>.  $A_w$  is the area of tubing, m<sup>2</sup>.  $C_w$  is the specific heat of tubing, J/kg·°C.

## Heat Transfer Model of Salt Cavern Storage

For the CO<sub>2</sub> which is stored in the salt cavern storage, the energy change is equal to the heat transfer between the CO<sub>2</sub> and the salt cavern storage wall, and that between the CO<sub>2</sub> and the brine in the salt cavern storage, and the energy entered from the annulus. Therefore, the heat transfer model is:

$$m_c C_c \frac{\partial T_c}{\partial t} = A_{f1} \lambda_{f1} [T_{fc} - T_c] + A_c \lambda_{bc} [T_b - T_c] + M_a C_c [T_{ab} - T_c] \quad (4)$$

where,  $T_c$  is a cavern's CO<sub>2</sub> temperature, °C.  $T_{fc}$  is a cavern's formation temperature, °C.  $T_b$  is the brine in the salt cavern storage temperature, °C.  $T_{ad}$  is the CO<sub>2</sub> temperature that flows into the cavern from the annulus, °C.  $m_c$  is the CO<sub>2</sub> quality in the salt cavern storage, kg.  $C_c$  is the CO<sub>2</sub> heat capacity in the salt cavern storage, J/kg·°C.  $A_{f1}$  is the contact area of the CO<sub>2</sub> and the salt cavern storage wall, m<sup>2</sup>.  $A_c$  is the contact area of the brine in the salt cavern storage and the CO<sub>2</sub> in the salt cavern storage, m<sup>2</sup>.  $\lambda_{f1}$  is the heat transfer coefficient between the CO<sub>2</sub> and the salt cavern storage wall, W/m<sup>2</sup>·°C.  $\lambda_{bc}$  is the heat transfer coefficient between the CO<sub>2</sub> and the brine in the salt cavern storage, W/m<sup>2</sup>·°C.  $M_a$  is the mass flow rate of injected gas, kg/s.  $T_{ad}$  is the temperature of the CO<sub>2</sub> which is injected into the salt cavern storage from annulus, °C.

The brine energy change in the salt cavern storage is equal to the heat transfer between brine and the salt cavern wall, and that between the brine and the CO<sub>2</sub>. Therefore, the heat transfer model is:

$$m_b C_b \frac{\partial T_b}{\partial t} = A_{f2} \lambda_{f2} [T_f - T_b] + A_c \lambda_{cb} [T_c - T_b] \quad (5)$$

where,  $m_b$  is the quality of brine in the salt cavern storage, kg.  $C_b$  is the heat capacity of the brine in the salt cavern storage, J/kg·°C.  $A_{f2}$  is the contact area of the brine and the salt cavern storage wall, m<sup>2</sup>.  $A_c$  is the contact area of the CO<sub>2</sub> in the salt cavern and the brine in the salt cavern, m<sup>2</sup>.  $\lambda_{f2}$  is the heat transfer coefficient of the brine and the salt cavern storage wall, W/m<sup>2</sup>·°C.  $\lambda_{cb}$  is the heat transfer coefficient of the brine and CO<sub>2</sub> in the salt cavern storage, W/m<sup>2</sup>·°C.

## INITIAL CONDITION AND BOUNDARY CONDITION AND STATE-SPACE METHOD FOR THE WELLBORE

In the process of gas injection, mass flow and injection temperature is measured on the ground. The formation temperature is attained using the surface temperature and the formation temperature gradient, the formation temperature gradient is 3°C/100 m, thus  $T_f = T_{f0} + yz$ ,  $T_{f0}$  is the formation



temperature,  $\gamma$  is the formation temperature gradient, and  $z$  represents depth.

The state space method is a basic model of modern control theory. So it can not only solve the partial differential equation, but can also be used as the basic model of automatic control.

For Equations (1–4), using difference instead of integral, therefore:

$$\frac{\partial T}{\partial t} = \frac{T(k+1, 1) - T(k, 1)}{\Delta t} \quad \frac{\partial T}{\partial z} = \frac{T(1, j) - T(1, j-1)}{\Delta z} \quad (6)$$

Equation (1) can be expressed as:

$$\rho_a A_a C_a \frac{T_a(k+1, j) - T_a(k, j)}{\Delta t} = -M_a C_a \frac{T_a(k, j) - T_a(k, j-1)}{\Delta z} + 2\pi r_2 \lambda_2 [T_w(k, j) - T_a(k, j)] + 2\pi r_3 \lambda_3 [T_f(k, j) - T_a(k, j)] \quad (7)$$

The depth of wellbore is divided into  $L$  nodes, each discrete time is represented by  $k$ , according to the linear system theory, each grid temperature in the tubing and annulus is an independent state. Set the gas injection temperature as  $T_a(k, 0)$ , and set  $x_1 = -\frac{M_a \Delta t}{\rho_a A_a \Delta z}$ ,  $x_2 = \frac{2\pi r_2 \lambda_2 \Delta t}{\rho_a A_a C_a}$ ,  $x_3 = \frac{2\pi r_3 \lambda_3 \Delta t}{\rho_a A_a C_a}$ , and the state space model for the wellbore heat transfer system can be obtained. Equation (1) converts to Wei et al. (2020):

$$T_A(k+1) = A_a T_A(k) + B_a T_W(k) + C_a T_F(k) + D_a U_d(k) \quad (8)$$

where,

$$\begin{aligned} T_A(k) &= [T_a(k, 1), T_a(k, 2), T_a(k, 3), \dots, T_a(k, L)]_{L \times 1}^T \\ T_W(k) &= [T_w(k, 1), T_w(k, 2), T_w(k, 3), \dots, T_w(k, L)]_{L \times 1}^T \\ T_F(k) &= [T_f(k, 1), T_f(k, 2), T_f(k, 3), \dots, T_f(k, L)]_{L \times 1}^T \\ U_d(k) &= [T_a(k, 0), 0, 0, \dots, 0]_{L \times 1}^T \end{aligned}$$

$$A_a = \begin{bmatrix} x_1 + 1 - x_2 - x_3 & 0 & 0 & \dots & 0 \\ -x_1 & x_1 + 1 - x_2 - x_3 & 0 & \dots & 0 \\ 0 & -x_1 & \ddots & \ddots & 0 \\ \vdots & 0 & \ddots & x_1 + 1 - x_2 - x_3 & 0 \\ 0 & 0 & 0 & -x_1 & x_1 + 1 - x_2 - x_3 \end{bmatrix}_{L \times L}$$

$$B_a = x_2, C_a = x_3, D_a = -x_1$$

where,  $T_A$  is the state vector of the heat transfer state space model for annulus fluid of  $\text{CO}_2$ ,  $T_W$  is the state vector of tubing temperature,  $T_F$  is the state vector of formation temperature,  $U_d$  is the input vector for the state space model, and  $A_a$  is the system matrix. In the same way, set  $z_1 = -v_p \frac{\Delta t}{\rho_p A_p C_p}$ ,  $z_2 = \frac{2\pi r_1 \lambda_1 \Delta t}{\rho_p A_p C_p}$ , and the brine temperature from the cavern that entered into the tubing as  $T_p(k, 0)$ , we can get the state space model of the brine temperature in the tubing (Wei et al., 2020).

$$T_P(k+1) = A_p T_P(k) + B_p T_W(k) + D_p U_P(k) \quad (9)$$

where,

$$\begin{aligned} T_P(k) &= [T_p(k, 1), T_p(k, 2), T_p(k, 3), \dots, T_p(k, L)]_{L \times 1}^T \\ T_W(k) &= [T_w(k, 1), T_w(k, 2), T_w(k, 3), \dots, T_w(k, L)]_{L \times 1}^T \\ U_P(k) &= [T_p(k, 0), 0, 0, \dots, 0]_{L \times 1}^T \\ A_p &= \begin{bmatrix} z_1 + 1 - z_2 & 0 & 0 & \dots & 0 \\ -z_1 & z_1 + 1 - z_2 & 0 & \dots & 0 \\ 0 & -z_1 & \ddots & \ddots & 0 \\ \vdots & 0 & \ddots & z_1 + 1 - z_2 & 0 \\ 0 & 0 & 0 & -z_1 & z_1 + 1 - z_2 \end{bmatrix}_{L \times L} \\ B_a &= z_2, D_a = -z_1 \end{aligned}$$

where,  $T_P$  is the state vector of the heat transfer state-space model for the tubing fluid of brine,  $U_P$  is the input vector, and  $A_p$  is the system matrix.

Salt cavern storage temperature state space model:

Set  $y_1 = \frac{A_{f1} \lambda_{f1} \Delta t}{m_c C_c}$ ,  $y_2 = \frac{A_{c} \lambda_{bc} \Delta t}{m_c C_c}$ ,  $y_3 = \frac{M_a C_c \Delta t}{m_c C_c}$ ,  $z_1 = \frac{A_{f2} \lambda_{f2} \Delta t}{m_b C_b}$ ,  $z_2 = \frac{A_{c} \lambda_{cb} \Delta t}{m_b C_b}$ , So (3), (4) can be transformed into the state space model for calculating the temperature of gas and brine in salt cavern storage

$$\begin{bmatrix} T_c(k+1) \\ T_b(k+1) \end{bmatrix} = \begin{bmatrix} 1 - y_1 - y_2 - y_3 & y_3 \\ z_2 & 1 + z_1 + z_2 \end{bmatrix} \begin{bmatrix} T_c(k) \\ T_b(k) \end{bmatrix} + \begin{bmatrix} y_1 & 1 \\ z_1 & 0 \end{bmatrix} \begin{bmatrix} T_f \\ T_{ad} \end{bmatrix} \quad (10)$$

The  $\text{CO}_2$  gas in the salt cavern storage satisfies the gas equation. Before calculation, the initial density of gas in the salt cavern storage can be calculated according to the initial pressure of the gas in the salt cavern storage and the gas state equation.

$$\rho_c = \frac{P_c M}{8.314 Z T_c} \quad (11)$$

where  $M$  is the molecular mass of natural gas, and  $Z$  is the pressure factor, which can be obtained by:

$$Z = 0.702 e^{-2.5 T_r} p_r^2 - 5.524 e^{-2.5 T_r} p_r + (0.044 T_r^2 - 0.164 T_r + 1.15) \quad (12)$$

$$p_r = \frac{p}{p_e}, T_r = \frac{T}{T_e} \quad (13)$$



**TABLE 1** | Calculation parameters.

Parameter	Value	Parameter	Value
Well depth, m	500	Mass flow rate, kg/s	16
Tubing inner diameter, mm	100	Initial injection pressure, MPa	5
Tubing outer diameter, mm	114	Injection temperature, °C	21
Well-bore diameter, mm	178	Surface earth temperature, °C	20
Salt cavern volume, m <sup>3</sup>	$2 \times 10^5$	Brine density, kg/m <sup>3</sup>	1,200
Salt cavern's sectional area, m <sup>2</sup>	2,500	Salt cavern's height, m	80
Thermal conductivity of formation, W/m.°C	0.52	Thermal conductivity of tubing, W/m.°C	44.7
Thermal conductivity of Salt cavern, W/m.°C	0.08		

where  $Pr$  is the pseudo-reduced pressure, dimensionless;  $Tr$  is the pseudo-reduced temperature, dimensionless;  $P_c$  is the critical pressure of CO<sub>2</sub> gas, Pa;  $T_c$  is the critical temperature of gas, K (Ren et al., 2016).

After every step, the mass of CO<sub>2</sub> gas in the cavern is:  $m_c(k+1) = M_a \Delta t + m_c(k)$ . The density of natural gas in the cavern is:

$$\rho_c(k) = m_c(k) / V_c \quad (14)$$

According to Equations (11–14), the pressure of the cavern can be obtained. To ensure that the carbon dioxide in the salt cavern storage will not have a phase change, the allowed pressure of the cavern is generally <7 MPa.

## CASE STUDY

The state space model was used to show the transient temperature distribution of underground CO<sub>2</sub> salt cavern storage, supposing the salt cave's shape is cylindrical and its simulation data were shown in **Table 1** (Zhang and Goh, 2012; Bérest, 2019).

The wellbore temperature profiles, as a function of well depth under different injection times, are calculated by the state space method. As shown in **Figure 3A**, the temperature decreases with injection and reaches a quasi-stable state temperature of 27.5°C at the bottom of annulus. The time needed to reach the quasi steady state is about 20 min. Therefore, special attention should be paid to monitoring in the first 20 min during the injection process. **Figure 3B** signifies the annulus temperature profiles after injection for 0.1, 1, and 2 h. With the increase of injection time, the annulus temperature decreases, its temperature variation is 1.5°C at the bottom of the annulus. **Figure 3C** manifests the effect of different gas injection times on the brine temperature distribution in the tubing. The steady state temperature of the tubing brine remains almost unchanged at two injection times. Therefore, the crystal separating out from brine due to the temperature changes would not occur during the injection process.

The tubing heat transfer effect was neglected in the Raymond model while tubing's influence on temperature distribution of the annulus was considered in the state space model. The material of the tubing used is steel which is used in petroleum and matches the American Petroleum Institute (API) specifications. **Figure 3D** displays the tubing heat transfer effect on the annulus temperature distribution. More heat would enter the annulus from the formation transferring without considering it. The annulus CO<sub>2</sub> temperature calculated by the Raymond model is about 3–4°C lower than that by the state space model. Therefore, when calculating the annulus CO<sub>2</sub> temperature, the influence of tubing heat transfer could not be ignored.

**Figure 4** presents the change of the salt cavern temperature and pressure during the injection process. The pressure prediction is also very important for stable operation of the gas storage. For salt cavern gas storage, the general pressure range is about 5–25 MPa. As shown in **Figure 4A**, salt cavern pressure increases from 5 to 6.1 MPa in an 80-h injection. It is in the allowable operating pressure range. **Figure 4B** shows the temperature variation of salt cavern CO<sub>2</sub> and brine in a 60-h injection, and CO<sub>2</sub> temperature decreases to a new quasi-steady state. According to **Figure 1**, there is no CO<sub>2</sub> phase change during the injection process so it meets the design requirement. We can calculate that the CO<sub>2</sub> mass is  $1.9978 \times 10^7$  Kg.

**Figure 5** is the effect of the gas injection rate on CO<sub>2</sub> storage system operation state. **Figure 5A** demonstrates the annulus CO<sub>2</sub> temperature profiles in CO<sub>2</sub> injection rates of 13, 16, and 20 kg/s. Different CO<sub>2</sub> injection rates have little influence on the annulus temperature above 100-m depth. The annulus temperature in the middle and lower part gradually decreased with the increased injection rate. **Figure 5B** shows the temperature variation of the brine in the tubing. When the CO<sub>2</sub> injection rate changed, the brine temperature changed very little. **Figure 5C** manifests the CO<sub>2</sub> gas pressure in the salt cavern at different CO<sub>2</sub> injection rates. When the CO<sub>2</sub> injection rates were 13, 16, and 20 kg/s, the CO<sub>2</sub> gas pressure in the salt cavern was 5.9, 6.1, and 6.4 MPa, respectively, after an 100-h CO<sub>2</sub> injection. The CO<sub>2</sub> gas pressure in the salt cavern increased significantly with the increase of the gas injection rate. **Figure 5D** shows the variation of CO<sub>2</sub> gas temperature in the salt cavern at different injection rates. As the injection rate increased, the CO<sub>2</sub> gas temperature in the salt cavern decreased significantly, and reached new and different quasi-steady states.

**Figure 6** is the change of the temperature in the wellbore and salt cavern when the well was shut in. **Figure 6A** signifies the change of CO<sub>2</sub> gas temperature in the salt cavern storage when the well was shut in. During the injection process, the temperature of injection CO<sub>2</sub> plays a dominant role in the salt cavern's temperature. When CO<sub>2</sub> injection stops, the heat transfer between the formation and salt cavern's CO<sub>2</sub> plays a dominant role in the salt cavern's temperature. The CO<sub>2</sub> gas temperature in the salt cavern storage increases after the well is shut in, but the increasing trend slows and gradually approaches the formation temperature. **Figure 6B** shows the change of CO<sub>2</sub> gas pressure in salt cavern storage when the well is shut in. When the well was shut in, the CO<sub>2</sub> gas

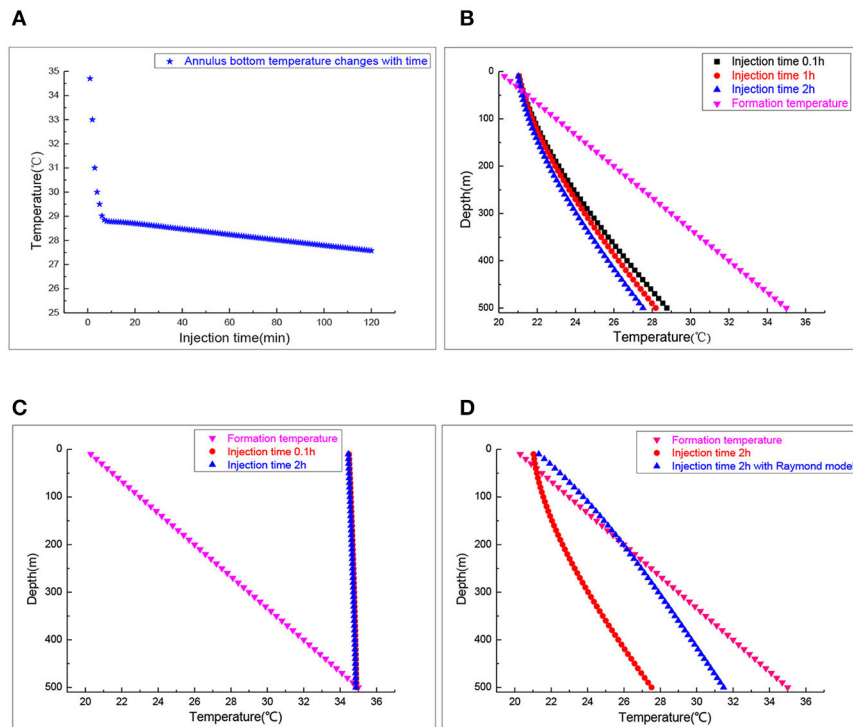


**FIGURE 3 |** The wellbore temperature profile during the injection process. **(A)** Annulus bottom temperature. **(B)** Annulus temperature profiles. **(C)** Inside tubing brine temperature profiles. **(D)** Annulus temperature profiles.

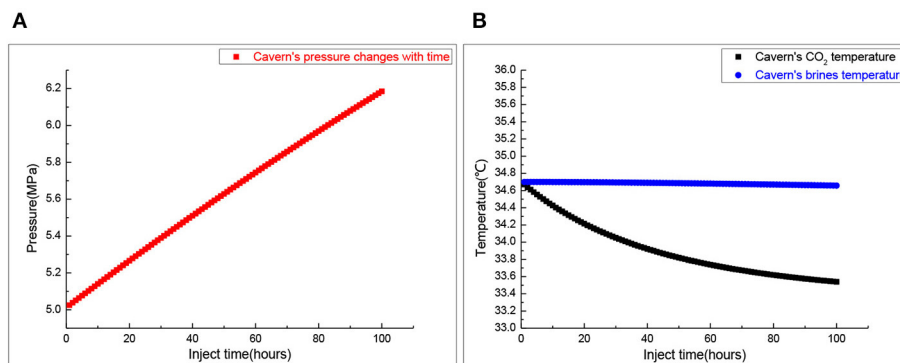


**FIGURE 4 |** The cavern's pressure and temperature during the injection process. **(A)** Salt cavern pressure. **(B)** Salt cavern temperature.

pressure in salt cavern storage changes with the temperature change, but the change is very small. **Figure 6C** shows the distribution of annulus CO<sub>2</sub> temperature at different time points when the well is shut in. Due to the heat transfer between the formation and the brine in the tubing, the annulus temperature firstly increases and then decreases. At first, the annulus temperature is lower than the formation temperature, then it becomes higher than it, and finally approaches the current formation temperature. **Figure 6D** shows the brine temperature in the tubing in 1, 5, and 20 h after the well was shut in, and the brine temperature in the tubing gradually approached

the formation temperature. The result shows that heat transfer between the wellbore and formation play a dominant role in the brine temperature distribution in the tubing after the well is shut in.

**Figure 7** shows the distribution of the temperature variation between the temperature when the well was shut in for 20 h and the temperature just after gas injection was stopped. The change of brine temperature in the tubing mainly occurs when the well was shut in. The change of temperature will cause crystals to separate out from the brine, which can explain the blockage of the tubing when the well was shut in.

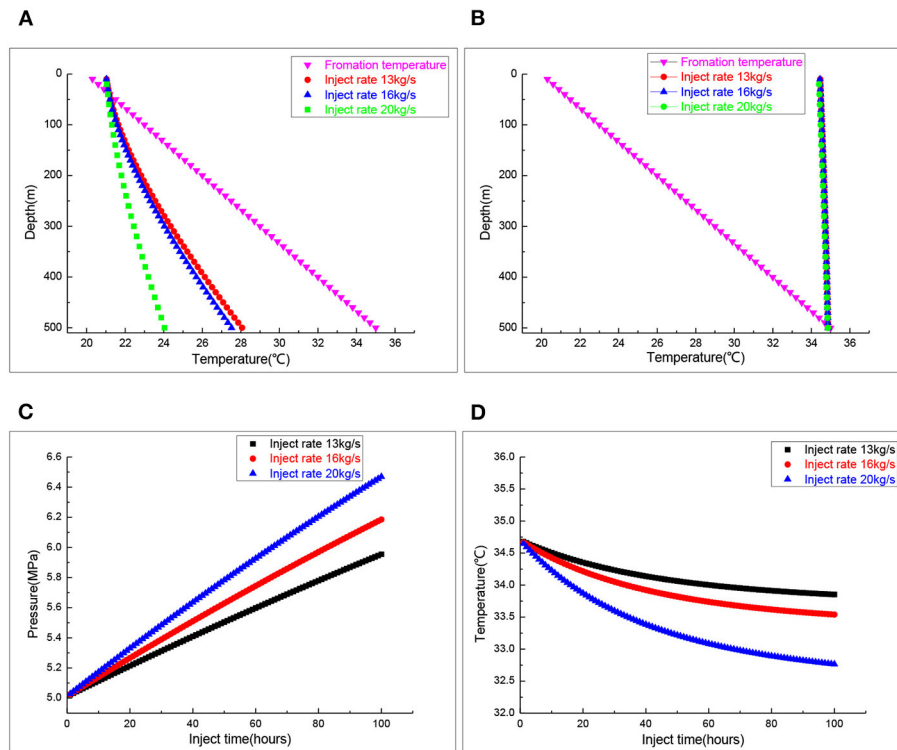


**FIGURE 5 |** The wellbore and cavern's temperature at different injection rates. **(A)** Annulus temperature profiles. **(B)** Inside tubing temperature profiles. **(C)** Salt cavern pressure. **(D)** Salt cavern temperature.

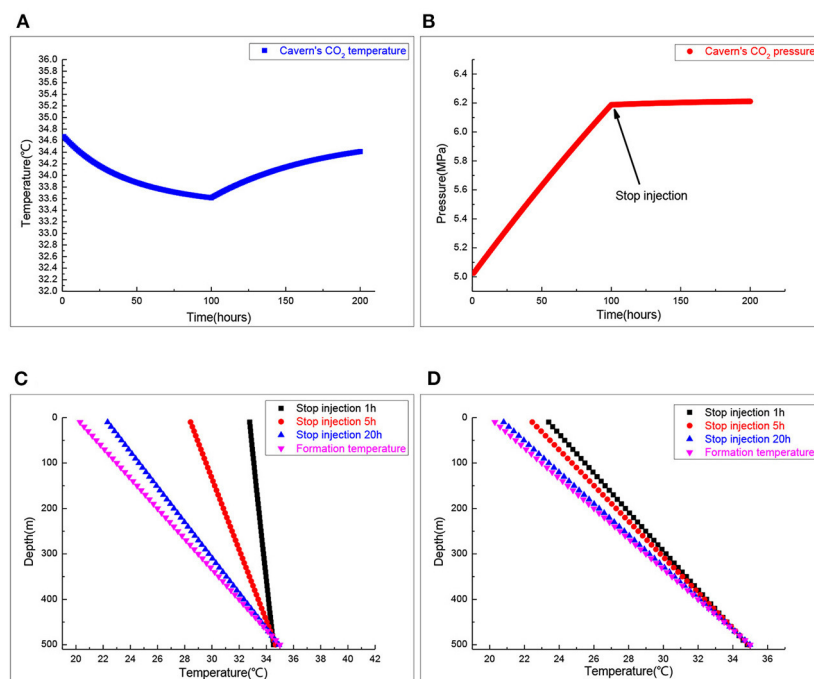
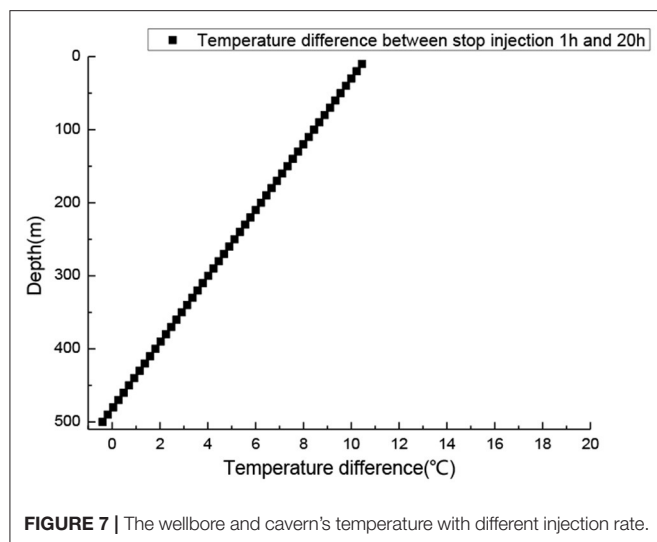


**FIGURE 6 |** The wellbore and cavern's temperature when injection stops. **(A)** Salt cavern CO<sub>2</sub> temperature. **(B)** Salt cavern CO<sub>2</sub> pressure. **(C)** Annulus CO<sub>2</sub> temperature profiles. **(D)** Inside tubing brine temperature.



## CONCLUSION

This thesis proposes a new method (using underground salt cavern storage) for CO<sub>2</sub> storage and a mathematical model for transient temperature distribution during the CO<sub>2</sub> injection process. Furthermore, state space method is used for solving this model, where CO<sub>2</sub> storage's temperature-pressure can be predicted, and parameters of CO<sub>2</sub> storage can be monitored and optimized during the CO<sub>2</sub> injection process.

The operating parameters analysis manifests that flow rates have a significant impact on the temperature of the wellbore

## REFERENCES

- Bérest, P. (2019). Heat transfer in salt caverns. *Int. J. Rock Mech. Rock Eng. Min. Sci.* 120, 82–95. doi: 10.1016/j.ijrmms.2019.06.009
- Boot-Handford, M., Abanades, J. C., Anthony, E., Blunt, M., and Brandani, S. (2014). Carbon capture and storage update. *Energy Environ. Sci.* 7, 130–189. doi: 10.1039/C3EE42350F
- Goh, A. T., and Zhang, W. (2012). Reliability assessment of stability of underground rock caverns. *Int. J. Rock Mech. Mining Sci.* 55, 157–163. doi: 10.1016/j.ijrmms.2012.07.012
- Guo, J., and Zeng, J. (2015). A coupling model for wellbore transient temperature and pressure of fracturing with supercritical carbon dioxide. *Shi You XueBao/ActaPet. Sin.* 36, 203–209. doi: 10.7623/syxb201502009
- Hasan, A. R., and Kabir, C. S. (1996). A mechanistic model for computing fluid temperature profiles in gas-lift wells. *SPE Prod. Facil.* 11, 179–185. doi: 10.2118/26098-PA
- Hasan, A. R., and Kabir, C. S. (2002). *Fluid Flow and Heat Transfer in Wellbores*. Richardson, TX: SPE.
- Hasan, A. R., Kabir, C. S., and Wang, X. (1997). *Development and Application of a Wellbore/Reservoir Simulator for Testing Oil Wells*. SPEFE.
- Hasan, A. R., Kabir, C. S., and Wang, X. (1998). *Wellbore Two-Phase Flow and Heat Transfer During Transient Testing*. SPEJ.
- Kushnir, R., Dayan, A., and Ullmann, A. (2012). Temperature and pressure variations within compressed air energy storage caverns. *Int. J. Heat Mass Transfer* 55, 5616–5630. doi: 10.1016/j.ijheatmasstransfer.2012.05.055

and the cavern. In addition, when the injection is stopped, heat transfer is dominated by the formation temperature, resulting in a remarkable increase in annulus temperature. The temperature of tubing brine mainly changes when injection stops, which is very important in preventing blockages in the tubing.

This research may help interpret the mechanism of wellbore and cavern heat transfer during CO<sub>2</sub> injection. This heat transfer model of wellbore and cavern is our primary work. Future work will be focused on the CO<sub>2</sub> releasing process and the phase variation in the process.

## DATA AVAILABILITY STATEMENT

The raw data supporting the conclusions of this article will be made available by the authors, without undue reservation.

## AUTHOR CONTRIBUTIONS

ZY and YZ: stimulation, data curation, and writing manuscript. MW: construction of thesis ideas, establish mathematical model, and provide research fund. XL: manuscript review. All authors contributed to the article and approved the submitted version.

## FUNDING

This research was funded by the State Key Laboratory of Petroleum Resources and Prospecting, China University of Petroleum, Beijing, grant number PRP/open-1610 and the National Natural Science Foundation of China, grant number 51804267.

- Kyuro, S., and Yuichi, S. (2011). Heat Transfer and Phase Change in Deep CO<sub>2</sub> Injector for CO<sub>2</sub> Geological Storage. *Two Phase Flow, Phase Change and Numerical Modeling*. Fukuoka: InTech.
- Li, Q., Wei, Y. N., Liu, G., and Lin, Q. (2014). Combination of CO<sub>2</sub> geological storage with deep saline water recovery in western China: insights from numerical analyses. *Appl. Energy* 116, 101–110. doi: 10.1016/j.apenergy.2013.11.050
- Li, X., Li, G., Wang, H., Lu, P., Tian, S., and Song, X. (2017). A unified model for wellbore flow and heat transfer in pure CO<sub>2</sub> injection for geological sequestration, EOR and fracturing operations. *Int. J. Greenhouse Gas Control* 42, 602–614. doi: 10.1016/j.ijggc.2016.11.030
- Li, X., Li, G., Wang, H., Lu, P., Tian, S., Yang, R., et al. (2016). “A coupled model for predicting flowing temperature and pressure distribution in drilling ultra-short radius radial wells,” in *IADC/SPE Asia Pacific Drilling Technology Conference*, (Singapore), 22–24.
- Li, X., X. R., Wei, L., and Jiang, P. (2015). Modeling of wellbore dynamics of a CO<sub>2</sub> injector during transient well shut-in and start-up operations. *Int. J. Greenhouse Gas Control* 42, 602–614. doi: 10.1016/j.ijggc.2015.09.016
- Luo, F., Xu, R. N., and Jiang, P. X. (2014). Numerical investigation of the doublet enhanced geothermal system with CO<sub>2</sub>as working fluid (CO<sub>2</sub>-EGS). *Energy* 64, 307–322. doi: 10.1016/j.energy.2013.10.048
- Middleton, R. S., Carey, J. W., Currier, R. P., Hyman, J. D., Kang, Q., Karra, S., et al. (2015). Shale gas and non-aqueous fracturing fluids: opportunities and challenges for supercritical CO<sub>2</sub>. *Appl. Energy* 147, 500–509. doi: 10.1016/j.apenergy.2015.03.023
- Ramey, H. J. (1962). Wellbore heat transmission. *J. Pet. Technol.* 14, 427–435. doi: 10.2118/96-PA

- Raymond, L. R. (1969). Temperature distribution in a circulating drilling fluid. *J. Pet. Technol.* 21, 333–341. doi: 10.2118/2320-PA
- Ren, W., Li, G., Tian, S., Sheng, M., and Fan, X. (2016). An analytical model for real gas flow in shale nanopores with non-circular cross-section. *AIChE J.* 62, 2893–2901. doi: 10.1002/aic.15254
- Sun, H., Yao, J., Gao, S. H., Fan, D. Y., Wang, C. C., and Sun, Z. X. (2013). Numerical study of CO<sub>2</sub> enhanced natural gas recovery and sequestration in shale gas reservoirs. *Int. J. Greenh. Gas Control* 19, 406–419. doi: 10.1016/j.ijggc.2013.09.011
- Wang, H., Li, G., and Shen, Z. (2012). A feasibility analysis on shale gas exploitation with supercritical carbon dioxide. *Energy Sources Part A* 34, 1426–1435. doi: 10.1080/15567036.2010.529570
- Wang, H., Shen, Z., and Li, G. (2011a). Influences of formation water invasion on the wellbore temperature and pressure in supercritical CO<sub>2</sub> drilling. *Pet. Explor. Dev.* 38, 362–368. doi: 10.1016/S1876-3804(11)60039-6
- Wang, H., Shen, Z., and Li, G. (2011b). Wellbore temperature and pressure coupling calculation of drilling with supercritical carbon dioxide. *Pet. Explor. Dev.* 38, 97–102.
- Wang, Z., Wang, L., and Zhang, W. (2019). A random angular bend algorithm for two-dimensional discrete modeling of granular materials. *Materials*. 12:2169. doi: 10.3390/ma12132169
- Wei, M., Wu, C., and Zhou, Y. (2020). Study on wellbore temperature and pressure distribution in process of gas hydrate mined by polymer additive CO<sub>2</sub> jet. *Adv. Polymer Technol.* 2020, 1–7. doi: 10.1155/2020/2914375
- Yang, M., Zhao, X., and Meng, Y. (2017). Determination of transient temperature distribution inside a well bore considering drill string assembly and casing program. *Appl. Thermal Eng.* 118, 299–314. doi: 10.1016/j.applthermaleng.2017.02.070
- Zhang, W., and Goh, A. T. (2012). Reliability assessment on ultimate and serviceability limit states and determination of critical factor of safety for underground rock caverns. *Tunnel. Undergr. Space Technol.* 32, 221–230. doi: 10.1016/j.tust.2012.07.002
- Zhang, W. G., and Goh, A. T. C. (2015). Regression models for estimating ultimate and serviceability limit states of underground rock caverns. *Eng. Geol.* 188, 68–76. doi: 10.1016/j.enggeo.2015.01.021
- Conflict of Interest:** The authors declare that the research was conducted in the absence of any commercial or financial relationships that could be construed as a potential conflict of interest.
- The reviewer NW declared a shared affiliation, with no collaboration, with with several of the authors YZ and MW to the handling editor.
- Copyright © 2020 Yuan, Zhou, Wei and Liao. This is an open-access article distributed under the terms of the Creative Commons Attribution License (CC BY). The use, distribution or reproduction in other forums is permitted, provided the original author(s) and the copyright owner(s) are credited and that the original publication in this journal is cited, in accordance with accepted academic practice. No use, distribution or reproduction is permitted which does not comply with these terms.





# Experimental Investigation on the Role of Clays in Low Salinity Water Flooding

Xuemei Wei<sup>1,2\*</sup>, Yanyu Zhang<sup>1,2\*</sup>, Wenchao Jiang<sup>1,2</sup>, Zhao Wang<sup>1,2</sup>, Xiaojun Li<sup>3</sup> and Feipeng Wu<sup>1,2</sup>

<sup>1</sup> Key Laboratory of Unconventional Oil and Gas Development, China University of Petroleum (East China), Ministry of Education, Qingdao, China, <sup>2</sup> School of Petroleum Engineering, China University of Petroleum (East China), Qingdao, China, <sup>3</sup> Dongxin Oil Production Plant, Shengli Oilfield, Dongying, Shandong, China

## OPEN ACCESS

### Edited by:

Wei Yu,  
University of Texas at Austin,  
United States

### Reviewed by:

Hongna Ding,  
Northeast Petroleum University,  
China

Lei Zhang,  
China University of Geosciences  
Wuhan, China

Xiao Wang,  
Southwest Petroleum University,  
China

### \*Correspondence:

Yanyu Zhang  
yyzhang@upc.edu.cn  
Xuemei Wei  
307725687@qq.com

### Specialty section:

This article was submitted to  
Advanced Clean Fuel Technologies,  
a section of the journal  
Frontiers in Energy Research

**Received:** 11 August 2020

**Accepted:** 22 September 2020

**Published:** 22 October 2020

### Citation:

Wei X, Zhang Y, Jiang W, Wang Z, Li X  
and Wu F (2020) Experimental  
Investigation on the Role of Clays in  
Low Salinity Water Flooding.  
Front. Energy Res. 8:593639.  
doi: 10.3389/fenrg.2020.593639

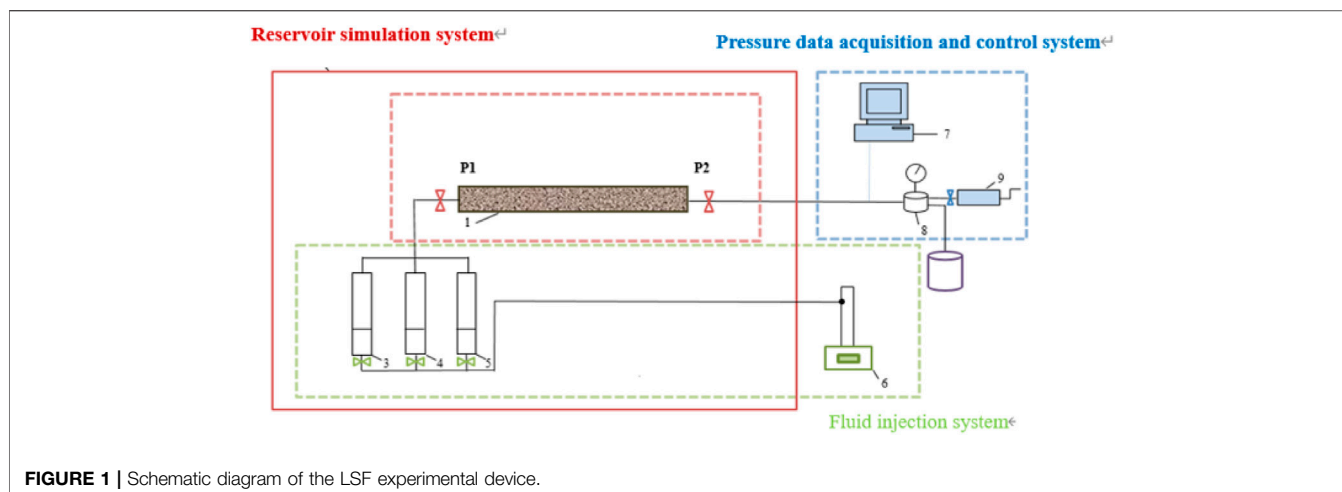
Clay minerals are regarded as an important factor affecting the results of low salinity water (LSW) flooding. However, most researchers put great attention on their microscopic properties, only few of them investigated the influence of clay minerals by the sand pack flooding experiments. This paper quantifies the effects of clay minerals on LSW flooding with artificial sand pack samples. We used three kinds of sand pack samples (100% quartz sand; 90%/10% quartz sand/kaolinite or montmorillonite) and heavy oil in the LSW flooding experiments. For the samples made of montmorillonite, results show that there exists an optimal salinity range for the LSW flooding. The best salinity range of Na<sup>+</sup> is between 1,000 mg/L and 5,000 mg/L, and Ca<sup>2+</sup> is between 500 mg/L and 1,000 mg/L. As for kaolinite, a better result will be produced with lower salinity. In addition, using CaCl<sub>2</sub> solution floods samples made of montmorillonite has a better result. A similar phenomenon was also observed when NaCl solution was used to flood kaolinite samples. Respect of flooding modes, the continuous injection of high-low salinity water is more effective, but the LSW flooding method is better considering the economy and time cost.

**Keywords:** sandstone reservoir, low salinity water flooding, enhanced oil recovery, clay minerals, sandpack displacement

## INTRODUCTION

With the exploitation of oil and gas resources, the development of oilfield becomes harder. Although chemical flooding method can help to improve the oil recovery, it needs a huge cost and causes great environmental concerns (Guo, 2020). Under this situation, researchers are eager to develop new enhanced oil recovery (EOR) technologies. Recently, they realized that the saturation of residual oil can be effectively reduced by injecting LSW. As a new oil recovery technology (Zhang et al., 2007), LSW flooding is widely used in the field due to its advantages of high efficiency, environment-friendly and low cost. Up to now, it has been used in Burgan oilfield, North Sea oilfield, Powder River basin in Wyoming and Endicott oilfield (Idowu et al., 2011; Nasralla et al., 2011).

LSW flooding can alter the physical and chemical properties of reservoir by injecting water with a low concentration of soluble ions. It can reduce the saturation of residual oil and improve oil recovery as a result (Wu et al., 2015; Li et al., 2016; Wu et al., 2016). However, the salinity of LSW has a threshold value. If the salinity is too low, it may cause swelling or flocculation of the clay minerals. And if it is too high, it will lose its function. A large number of experiments have proved the positive effect of LSW on EOR and revealed a lot of relevant mechanisms. However, different testing methods produced different dominant mechanisms, some mechanisms are contradictory to others. Meanwhile, it is generally believed that clay minerals are necessary factors that would affect the



result of LSW flooding (Bernard, 1967; Tang and Morrow, 1999; Zhang and Morrow, 2006; Zhang et al., 2007; loahardjo et al., 2010). Lots of studies on mechanisms of clay minerals were conducted. First, in terms of microcosmic mechanism, the main mechanisms include the diffusion of double electron layer (Ligthelm et al., 2009; Cui et al., 2020), cation exchange of clay minerals (Almada et al., 2013; Amirian et al., 2017) and changes in wettability (Nasralla et al., 2011; Amirian et al., 2017). The study of micro percolation mainly focuses on the particle migration of clay minerals. Tang and Morrow (1999) first discovered that the migration of clay mineral particles is important for the flooding of residual oil adsorbed in the pore wall. Song and Kovscek (2016) observed the migration of clay mineral particles with crude oil. There are also many studies through the core flooding experiment. Lebedeva and Fogden (2011) found LSW flooding can increase oil recovery in kaolinite; Kim and Lee (2017) showed the influence of clay type and relative permeability with sandstone cores. Al-Saedi and Flori (2018) prepared sandstone cores with a controllable percentage of clay and carried out the flooding experiment. All of them have investigated the EOR mechanisms of LSW flooding.

From the micro point, most researchers think that the influence of clay minerals is caused by the change of wetting angles and the migration of particles. However, experiment results are quite different under reservoir conditions due to the influence of clay occurrence mode and fluid properties. Also, relevant research on clay minerals is mainly in the qualitative stage, without quantitative evaluation and analysis on the influence of LSW flooding. Moreover, the LSW flooding experiment has special requirements on ion composition and

concentration of injected water (Yang et al., 2020). Up to now, there is no study conducted on the optimal ion and concentration of LSW for different types of clay minerals. At the same time, the artificial cores used in the experiments are simply made through the mixing of clay and cores, which can not simulate the cementation state of clay minerals in natural cores. As a result, the accuracy of the experimental data and conclusions is hard to guarantee. In this paper, two kinds of popular clay minerals (kaolinite and montmorillonite) were used to make synthetic sand cores that can simulate the adhesion of clay minerals in natural cores. Through the LSW flooding experiments, the macroscopic flooding effects in different cores were observed, the adaptability evaluation of different clay minerals was obtained and the influence law of clay minerals was summarized. In this way, this paper can provide basic guidance for the use of LSW flooding in the oilfield.

## EXPERIMENTAL SECTION

### Equipment

The LSW flooding equipment can be seen in **Figure 1**. It consists of three systems: reservoir simulation system, fluid injection system and the acquisition and control system for pressure data. The reservoir simulation system includes customized mineral-filled sand filling pipe and thermostat, which can accurately simulate the production process of real reservoir; the fluid injection system can maintain a constant flow rate for the injection of various fluids; the pressure data acquisition and control system can simulate the formation and

**TABLE 1 |** Components and physical properties of crude oil.

Oil sample			GD2-23X602
Components/wt%	Saturated hydrocarbon	36.12	
	Aromatic hydrocarbon	31.13	
	Resin	22.42	
	Asphaltene	10.33	
Viscosity/mPa s	60°C (reservoir temperature)	2,530	

**TABLE 2 |** Composition of Na<sup>+</sup> solution (mg/L).

No	Na <sup>+</sup>	K <sup>+</sup>	Mg <sup>2+</sup>	Cl <sup>-</sup>	SO <sub>4</sub> <sup>2-</sup>	Salinity
1	500	50	50	550	50	1,200
2	1,000	100	100	1,100	100	2,400
3	5,000	500	500	5,500	500	12,000
4	20,000	2000	2000	22,000	2000	48,000

**TABLE 3** | Composition of  $\text{Ca}^{2+}$  solution (mg/L).

No	$\text{Ca}^{+}$	$\text{K}^{+}$	$\text{Mg}^{2+}$	$\text{Cl}^{-}$	$\text{SO}_4^{2-}$	Salinity
1	500	50	50	550	50	1,200
2	1,000	100	100	1,100	100	2,400
3	5,000	500	500	5,500	500	12,000
4	20,000	2000	2000	22,000	2000	48,000

bottom hole pressure and collect the pressure during the injection process.

## Materials

Materials used in the experiment include quartz sand, clay minerals, crude oil, and LSW with different salinity.

Oil used in the experiment is the heavy oil from Shengli oilfield. The viscosity, resin content and asphaltene of it are pretty high. Its composition and basic physical properties are listed in **Table 1**.

Two kinds of water, including  $\text{Na}^{+}$  and  $\text{Ca}^{2+}$  solution, with four different concentration were prepared: 500, 1,000, 5,000, 20000 mg/L. The compositions of these water are listed in **Tables 2 and 3**. High salinity water (HSW 20,000 mg/L) was used to measure the permeability of sand packs and form the connate water in sand packs before flooding. The salinity of injected water used in LSW is less than 12,000 mg/L.

Synthetic sand packs are made of quartz sand and clay minerals. The ratio of the 10–20 mesh coarse quartz sand, the 40–60 mesh fine quartz and clay is 4.5:4.5:1. First, mixed the clay and deionized water with a ratio of 1:15, then degraded by a 15 Hz acoustic wave for 30 min. After that, added NaOH to adjust the pH value to 9.8 (consistent with the injected water in the research

oil field), centrifuged the solution for 3 min, removed the sediment, took out the suspension, quickly stirred and degraded for 10 min, centrifuged 3 min again, repeated the above step for three times. Took the suspension attached to the surface of quartz sand and placed it in the oven at 120°C. Finally, the quartz sand with clay was filled in the sand filling pipe to complete the sand pack production process. The scanning electron microscope (SEM) of the sand pack surface is shown in **Figure 2**. The physical properties and experimental parameters of the sand packs are listed in **Table 4**.

## Procedure

1) Make different kinds of synthetic sand packs: 100% quartz sand; 90%/10% quartz sand/kaolinite or montmorillonite. 2) Measure the porosity of each sand pack using the weighing method. 3) Test the permeability of each sand pack under simulated reservoir conditions. 4) Saturate HSW and crude oil in sequence under the pressure of 10 MPa and reservoir temperature of 60°C with a liquid injection rate of 0.2 ml/min, after that, leave the sand packs in the holder for 1 week to make the oil, water and rock contact sufficiently. 5) Inject water at 0.2 ml/min according to designed scheme. During the sand pack flooding experiments, produced oil and water were recorded at each 0.2 PV. 6) Calculate the oil recovery factor and water content in produced fluid. When the water content became 98%, the sand pack flooding process was finished.

## Schemes

A single variable was controlled in the experiment. Clay minerals were divided into kaolinite, montmorillonite and non-clay minerals,

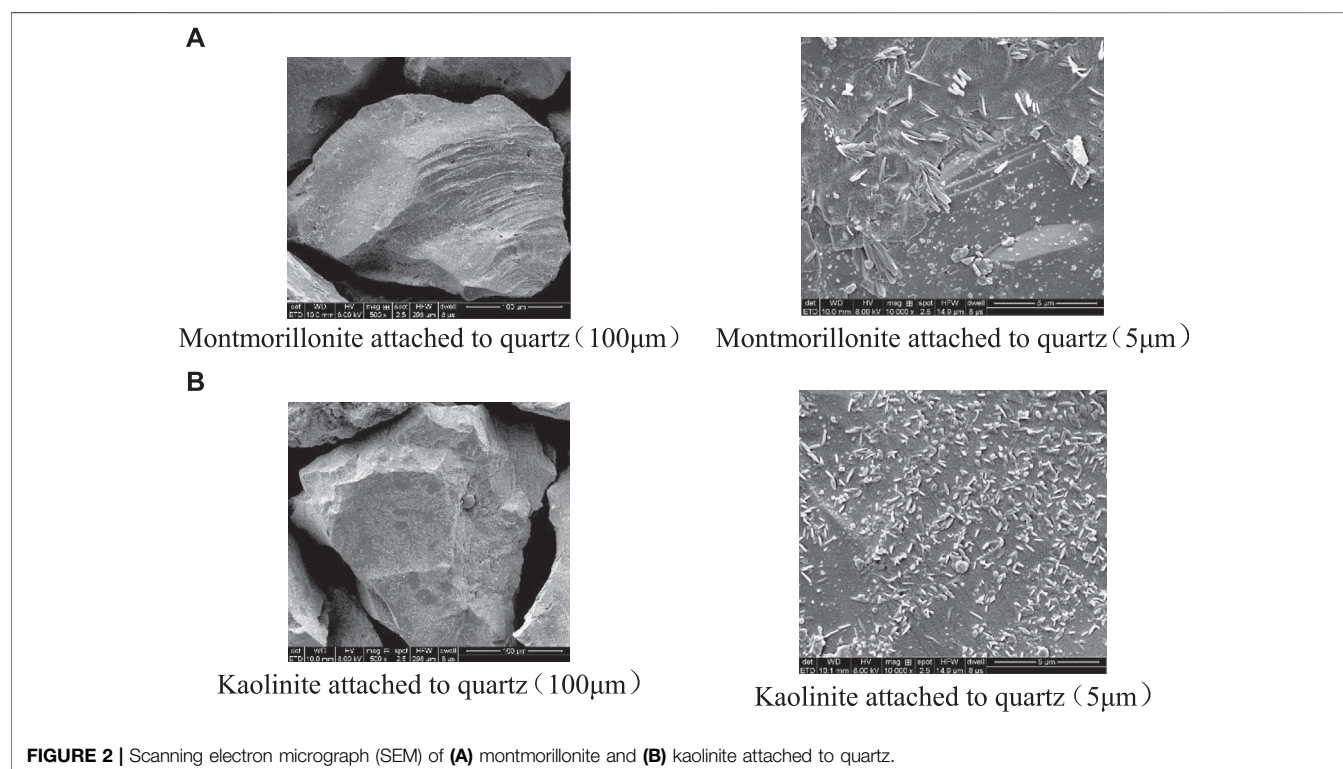


**TABLE 4 |** Sand pack properties.

Sand pack	L (cm)	D (cm)	Clay	Content (%)	$\Phi$ (%)	K (mD)	So (%)
1	30	5	Kaolinite	10	27.37	550	85.32
2	30	5	Kaolinite	10	28.04	640	86.13
3	30	5	Kaolinite	10	27.56	510	84.98
4	30	5	Kaolinite	10	26.89	620	85.88
5	30	5	Kaolinite	10	27.32	560	85.65
6	30	5	Kaolinite	10	27.61	610	86.21
7	30	5	Montmorillonite	10	28.20	660	85.79
8	30	5	Montmorillonite	10	27.66	580	86.27
9	30	5	Montmorillonite	10	27.24	580	86.06
10	30	5	Montmorillonite	10	27.37	570	85.23
11	30	5	Montmorillonite	10	28.15	560	85.49
12	30	5	Montmorillonite	10	27.72	530	86.12
13	30	5	—		28.86	650	87.56
14	30	5	—		29.32	690	86.56
15	30	5	—		29.25	700	88.45
16	30	5	—		28.65	680	87.64
17	30	5	—		29.03	690	88.13
18	30	5	—		28.96	680	87.25
19	30	5	Kaolinite	10	28.36	540	86.33
20	30	5	Montmorillonite	10	28.27	630	86.18
21	30	5	—		28.89	690	88.02

the ion type of the flooding fluid was set to  $\text{Ca}^{2+}$  and  $\text{Na}^+$ . First, 18 groups of experiments were designed with LSW with a concentration of 5,000, 1,000, and 500 mg/L, respectively. Then, each kind of sand pack was flooded by HSW-LSW (20,000, 5,000, 1,000, 500 mg/L) in sequence to see the effect of flooding mode on oil recovery.

## EXPERIMENT RESULTS AND DISCUSSION

### Performance of Enhanced Oil Recovery

Results of sand pack flooding are shown in Table 5, including injection water, flooding mode and oil recovery. During the

successive LSW injection, more and more oil was produced with the decrease of salinity of the injected water. This phenomenon successfully proves the EOR performance of LSW injection.

### Analysis of Montmorillonite Flooding Results

The comparison of oil recovery in different sand pack-flooding runs can be seen in Figures 2 and 3. With the rise of injected volume of LSW, the recovery degree increases rapidly at first, then gradually tends to be stable. The result of oil recovery with a

**TABLE 5 |** Experimental results of sand pack flooding.

Sand pack	Injection water	Concentration/(mg/L)	Flooding mode	Oil recovery factor/%
1	NaCl	5,000	LSW	52.32
2	NaCl	1,000	LSW	60.14
3	NaCl	500	LSW	62.82
4	$\text{CaCl}_2$	5,000	LSW	50.59
5	$\text{CaCl}_2$	1,000	LSW	55.73
6	$\text{CaCl}_2$	500	LSW	60.27
7	NaCl	5,000	LSW	53.82
8	NaCl	1,000	LSW	58.91
9	NaCl	500	LSW	59.03
10	$\text{CaCl}_2$	5,000	LSW	51.11
11	$\text{CaCl}_2$	1,000	LSW	57.68
12	$\text{CaCl}_2$	500	LSW	58.06
13	NaCl	5,000	LSW	71.54
14	NaCl	1,000	LSW	72.65
15	NaCl	500	LSW	72.25
16	$\text{CaCl}_2$	5,000	LSW	71.54
17	$\text{CaCl}_2$	1,000	LSW	72.12
18	$\text{CaCl}_2$	500	LSW	70.25
19	CaCl <sub>2</sub> :20,000		HSW-LSW	69.42
20	NaCl:5,000–1,000–500			63.75

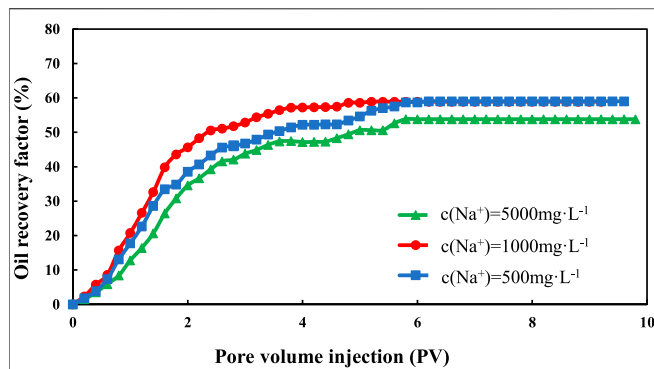


**FIGURE 3 |** Oil recovery of montmorillonite sand packs of different salinity of NaCl.

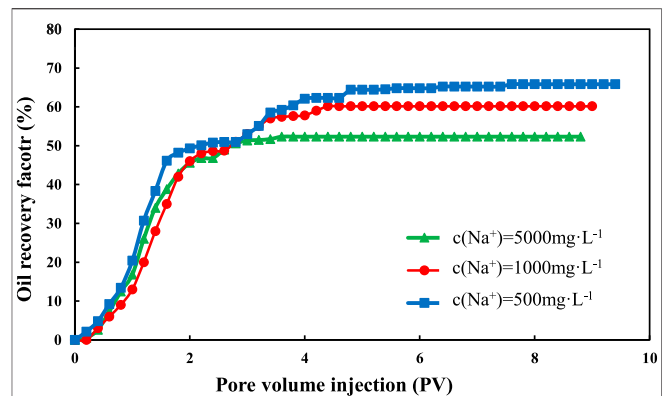


**FIGURE 6 |** Oil recovery of kaolinite sand packs of different salinity of NaCl.

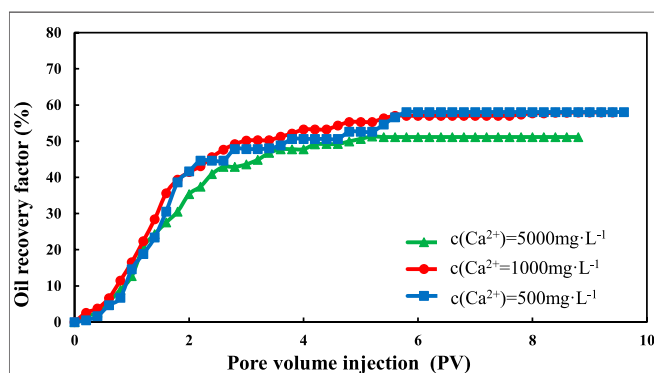


**FIGURE 4 |** Oil recovery of montmorillonite sand packs of different salinity of  $\text{CaCl}_2$ .

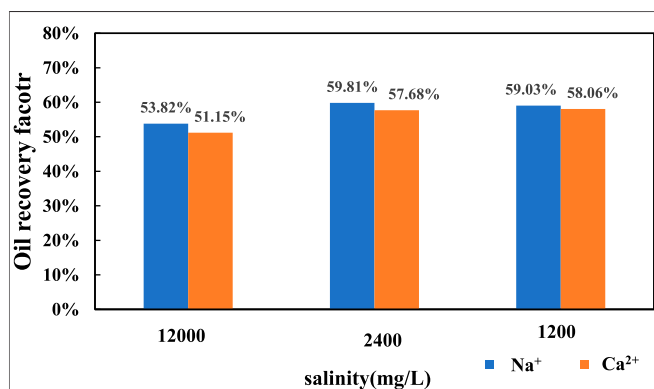


**FIGURE 5 |** Oil recovery of montmorillonite sand packs of different salinity brine.

salinity of 1,200 mg/L is similar to that of 2,400 mg/L, which is much higher than that of 12,000 mg/L.

The final oil recovery of montmorillonite is shown in Figure 4. For  $\text{Na}^+$ , when the salinity of injected water decreased from 12,000 to 2,400 mg/L, the final oil recovery increased from 53.82 to 58.91%, which increased by 5.09%. When the salinity of

injected water decreased from 2,400 to 1,200 mg/L, the final oil recovery increased from 58.91 to 59.03%, which increased by only 0.21%. It can be seen that the increase is pretty obvious in the range of 12,000–2,400 mg/L, however, the recovery in the range of 2,400–1,200 mg/L had little change. The  $\text{Ca}^{2+}$  flooding had a similar situation. When the salinity of injected water decreased from 12,000 to 2,400 mg/L, the final oil recovery increased from 51.15 to 57.68%, which increased by 6.53%. When the salinity decreased from 12,400 to 1,200 mg/L, the final oil recovery increased from 57.68 to 58.06%, which increased by only 0.38%.

This indicates that under the condition of montmorillonite sand pack, the oil recovery increases with the decrease of salinity, but there is a limit for the salinity content. As a result, the oil recovery cannot keep increasing with the decrease of the salinity of LSW. And there exists an optimum salinity to maximize oil recovery. This is because montmorillonite is pretty expansive and has great expansibility under acidic conditions. When the ion concentration becomes higher, the diffusion electron layer of montmorillonite will be compressed and the expansion volume will decrease (Zadaka et al., 2010), which is helpful to increase the

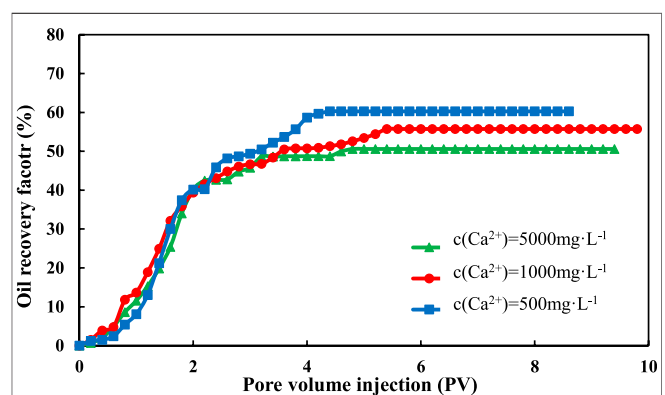
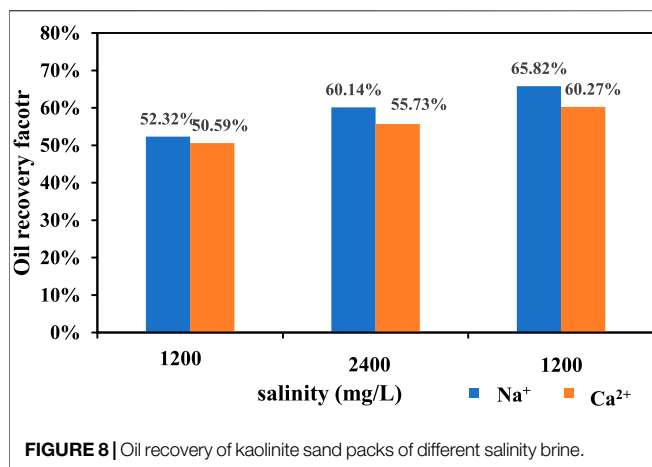


**FIGURE 7 |** Oil recovery of kaolinite sand packs of different salinity of  $\text{CaCl}_2$ .





permeability of the reservoir. However, when the ion concentration is too low, the compression capacity of metal cation ions on the electric double layer decreases rapidly, and the expansion capacity of montmorillonite increases rapidly, which leads to the expansion and dispersion of clay and block the seepage channel.

### Analysis of Kaolinite Flooding Results

The comparison of oil recovery of kaolinite is shown in Figures 4 and 5. Like montmorillonite, the oil recovery increases rapidly first, then tends to be stable slowly. However, what is different from the montmorillonite sand pack is that the oil recovery increases with the decrease of salinity of injected water.

The final oil recovery of kaolinite is shown in Figure 7. For Na<sup>+</sup>, when the salinity of injected water decreased from 12,000 to 2,400 mg/L, the final oil recovery increased from 52.32 to 60.14%, which increased by 7.82%. When the salinity of injected water decreased from 2,400 to 1,200 mg/L, the final oil recovery increased from 60.14 to 65.82%, which increased by 5.86%. The Ca<sup>2+</sup> flooding had a similar situation. When the salinity of injected water decreased from 12,000 to 2,400 mg/L, the final oil recovery factor increased from 50.59 to 55.73%, which increased by 5.14%. When the salinity decreased from 12,400

to 1,200 mg/L, the final oil recovery factor increased from 55.73 to 60.27%, which increased by 4.54%.

Regardless of the replacement of the kaolinite sand packs by NaCl solution or CaCl<sub>2</sub> solution, the increase of oil recovery in the range of 1,200–2,400 mg/L is higher than that in the range of 2,400–12,000 mg/L. It shows that the oil recovery increase with the decrease of salinity, and a lower salinity will have a faster increase rate. This is because kaolinite is non-expansive, which will not expand and migrate when meets water, and does not need the inhibition of cations. When the salinity of the displacement fluid decreases in pore throat, the diffusion of double electron layer between clay particles promotes the migration of clay particles, and the oil droplets adsorbed on the surface of clay particles migrate as well. With the increase of negative zeta potential and electrostatic repulsion, the oil droplets on the surface of clay particles gradually move from the surface of clay particles, eventually leading to the enhancement of water wettability to enhance oil recovery.

### Analysis of Quartz Sand Flooding Results

Figures 8 and 9 show the change of oil recovery with the change of injection volume for sand packs that are only made from quartz sand. From these two figures, we can see that the quartz sand packs also underwent three stages: rapid growth, slow growth and stabilization. However, the recovery degree of these quartz sand packs is pretty high even under low salinity conditions. This phenomenon means that the low salinity condition does not affect the recovery factor. The ultimate recovery factor of the quartz sand packs is about 70%, which cannot be achieved by water flooding with low salinity water.

### Analysis of the Influence of Ion

In this study, different kinds of NaCl and CaCl<sub>2</sub> solutions are used to flood the montmorillonite and kaolinite, respectively. The comparison of the oil recovery is shown in Figure 10. It can be seen from Figure 10 that when the CaCl<sub>2</sub> solution displacement montmorillonite, the result is better, and the NaCl solution is better for kaolinite.

Under same condition, using different kinds of LSW for the flooding of the same type of sand packs, the result of univalent

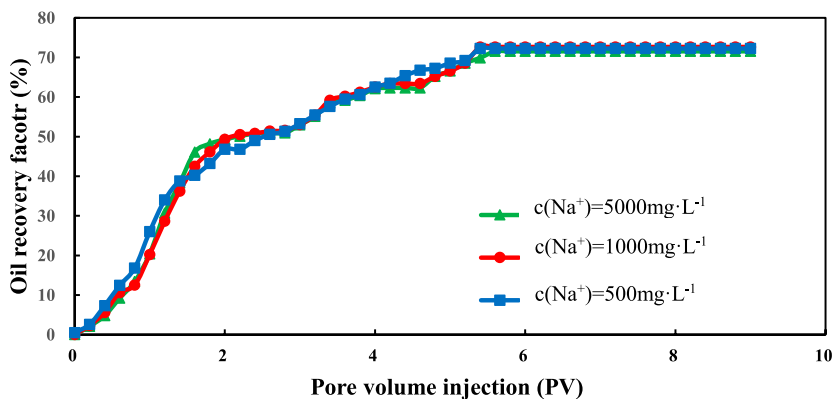


**FIGURE 9 |** Oil recovery of quartz sand packs displaced by different salinity of CaCl<sub>2</sub>.

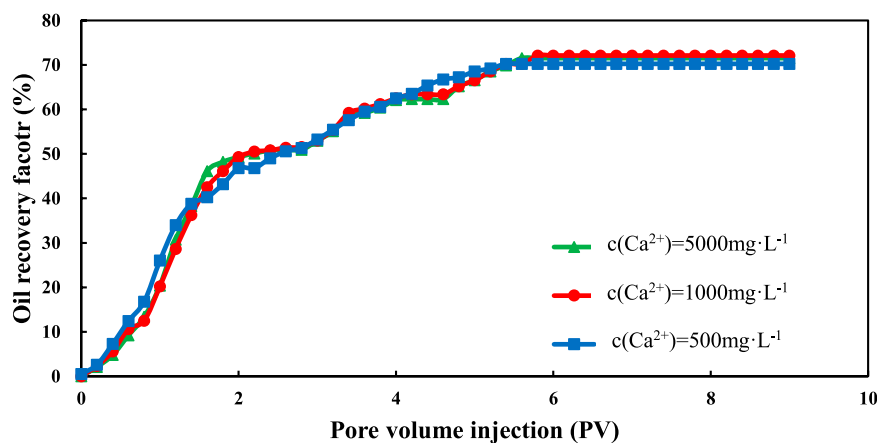


FIGURE 10 | Oil recovery of quartz sand packs displaced by different salinity of  $\text{CaCl}_2$ .

ions ( $\text{Na}^+$ ) is always better than that of divalent ions ( $\text{Ca}^{2+}$ ). The reason is that the  $\text{Ca}^{2+}$  just like a bridge between clay particles and crude oil, which is not conducive to crude oil desorption. However,  $\text{Na}^+$  can replace the high valence ions for the water in the pore, and the substitution of the high valence ions will behave as a bridge making the crude oil desorb from the surface of clay particles easily. Univalent ions can induce the diffusion of double electron layers on the surface of clay particles and oil-water interface, increase the negative zeta potential on the surface of clay particles and the oil-water interface, and enhance the electrostatic repulsion between the interfaces, thus promote the desorption of crude oil on the surface of clay particles. The change of zeta potential at the interface also makes the wettability of clay particles to be more hydrophilic. Therefore, under different valence states, if ions have an impact on the recovery of LSW flooding, the displacement effect of the solution containing monovalent ion is more obvious than that of the solution containing divalent ion.

Additionally, it can be seen that when the montmorillonite is flooded by LSW, the increasing rate of  $\text{CaCl}_2$  solution is faster and its result is more obvious. Compared with monovalent ions, divalent ion needs a lower concentration to compress the dielectronic layer. This is mainly due to the characteristic absorption of divalent ions (Ma et al., 2011), which reacts with hydroxyl groups on the surface of montmorillonite to form hydroxyl compounds and enters into the Stern layer. So  $\text{Ca}^{2+}$  still has a better compression effect on the double electron layer than  $\text{Na}^+$  when the salinity of the water is low.

## Analysis of the Influence of Displacement Mode

Figure 11 shows the results of kaolinite sand packs under different displacement modes. When the  $\text{Na}^+$  concentration of LSW is 5,000, 1,000, 500 mg/L, the oil recovery is 10.95, 18.77, and 24.45% higher than that of HSW. The final oil recovery of continuous injection of high-low salinity water (H-LSW) can reach 69.42%, which is 28.05% higher than that of direct injection

of HSW, and 17.1, 9.28, 3.6% higher than the direct injection of 5,000, 1,000, 500 mg/L.

The oil recovery curve of the montmorillonite sand pack under different displacement modes is shown in Figure 12. When the concentration of LSW is 5,000, 1,000, 500 mg/L, the recovery is 10.57, 15.66, 15.78%, respectively, higher than that of HSW with the concentration of 20,000 mg/L. However, the oil recovery can be as high as 63.75% with continuous injection of H-LSW, which is 20.5% higher than that of direct injection of high salinity water with a concentration of 5,000 mg/L. The oil recovery of low salinity water with a concentration of 5,000, 1,000, 500 mg/L, is 9.93, 4.84 and 2.96% higher than the direct injection of 5,000, 1,000, 500 mg/L.

To sum up, the final oil recovery under different displacement modes is in order of H-LSW > LSW > HSW. This is because when the H-LSW is injected continuously, the concentration of brine reduces gradually, besides, the long inject time and large injection volume are conducive to the interaction among brine, crude oil

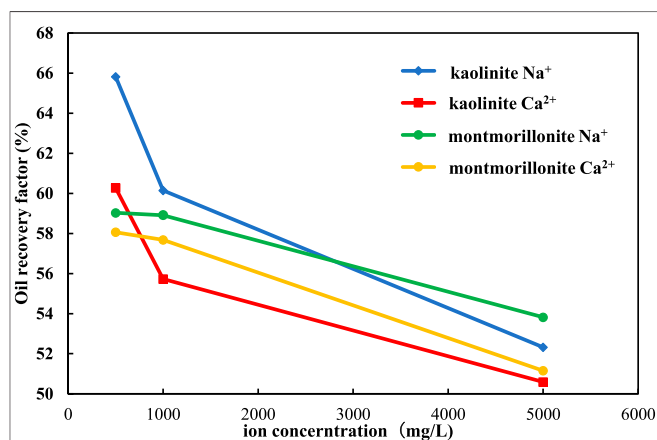
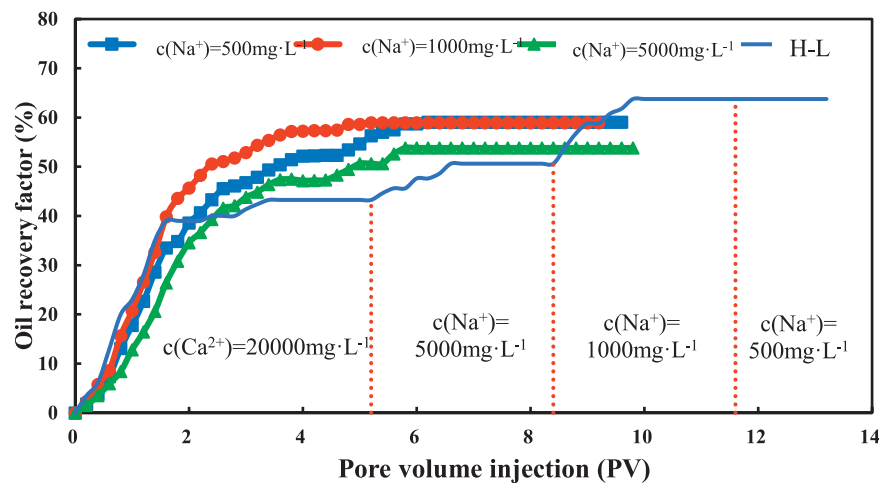
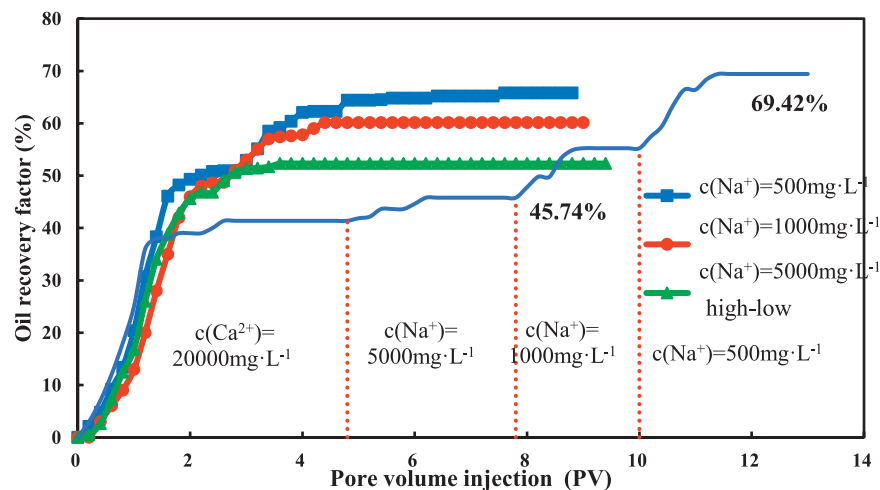


FIGURE 11 | Oil recovery of montmorillonite sand packs displaced by different salinity of  $\text{CaCl}_2$ .



**FIGURE 12 |** Variation curve of the recovery degree of kaolinite sand packs under different displacement methods.



**FIGURE 13 |** Variation curve of the recovery degree of montmorillonite sand packs under different displacement methods.

and clay minerals. Therefore, to achieve maximum oil production, the continuous injection of H-LSW is the best choice. However, this method requires a large amount of brine, and its injection volume is larger than the volume required by the direct injection of LSW to achieve optimal production. As a result, the displacement mode of direct injection of LSW can achieve an ideal recovery in a short time.

## CONCLUSIONS

In this paper, experiments were conducted with synthetic sand packs that contain different types of clay and different kinds of LSW to determine the relationship between clay minerals and LSW. From the results, the following conclusions have been drawn:

- (1) LSW flooding can improve the oil recovery of sand packs made from clay minerals, including montmorillonite and kaolinite, but it cannot increase the oil recovery of sand packs that do not contain clay minerals.
- (2) For expansive clays such as montmorillonite, the oil recovery is higher with  $\text{CaCl}_2$  solution. And the best displacement concentration of  $\text{Ca}^{2+}$  is between 500 mg/L and 1,000 mg/L. The reason is that the cations in LSW can inhibit the expansion and migration of expansive clay minerals. If the concentration is too low, it will lead the migration of clay mineral particles, block the pores and increase the residual oil.
- (3) For non-expansive clays, such as kaolinite, the oil recovery is higher with the  $\text{CaCl}_2$  solution. And when the ion concentration is lower, the recovery will be higher. That is because when the ion concentration is lower, the water

wettability of the sand pack will be higher, and the oil displacement efficiency will be higher.

- (4) No matter whether the montmorillonite or kaolinite is contained in the sand packs, the final oil recovery under different displacement modes is in the order of H-LSW > LSW > HSW.
- (5) As for field production, for sand packs rich in montmorillonite, CaCl<sub>2</sub> solution should be used as displacement fluid, and ion concentration should be 1,000 mg/L. For sand packs rich in kaolinite, NaCl solution should be used as displacement fluid, and solution with lower ion concentration will have better results. In terms of displacement modes, from the perspective of maximizing oil production, continuous injection of H-LSW is the best choice; from the perspective of achieving ideal recovery in a short time, the direct LSW flooding mode is more attractive.

## REFERENCES

- Al-Saedi, H. N., and Flori, R. E. (2018). Enhanced oil recovery of low salinity water flooding in sandstone and the role of clay. *Petrol. Explor. Dev.* 45 (5), 927–931. doi:10.1016/s1876-3804(18)30096-x
- Almada, M. B. P., Pieterse, S. G. J., Marceliset, A. H. M., Brussee, N. J., and van der Linde, H. A. (2013). “Experimental investigation on the effects of very low salinity on Middle Eastern sandstone core floods,” in SPE European formation damage conference and exhibition, Noordwijk, The Netherlands, June 5–7, 2013 (Society of Petroleum Engineers), SPE165180. Available at: <https://www.onepetro.org/conference-paper/SPE-165180-MS> (Accessed 2013).
- Amirian, T., Haghighi, M., and Mostaghimi, P. (2017). Pore scale visualization of low salinity water flooding as an enhanced oil recovery method. *Energy Fuels*. 31 (12), 13133–13143. doi:10.1021/acs.energyfuels.7b01702
- Amirian, T., Haghighi, M., and Mostaghimi, P. (2017). Pore scale visualization of low salinity water flooding as an enhanced oil recovery method. *Energy Fuels*. 31 (12), 13133–13143. doi:10.1021/acs.energyfuels.7b01702
- Bernard, G. G. (1967). “Effect of floodwater salinity on recovery of oil from cores containing clays,” in SPE California regional meeting, Los Angeles, California. October 26–27, 1967 (Society of Petroleum Engineers), SPE1725. Available at: <https://www.onepetro.org/conference-paper/SPE-1725-MS> (Accessed, 1967).
- Cui, C. Z., Wei, Z. Z., and Wu, Z. J. (2020). Influence of low salinity water flooding on rock wettability based on DLVO theory. *J. China Univ. Petrol.* 44 (01), 106–114. doi:10.3969/j.issn.1673-5005.2020.01.012
- Guo, S. (2020). Application and development analysis of EOR flooding technology in oilfield. *Chem. Eng. Equip.* (04), 40–41.
- Idowu, J., Somerville, J., Adebare, D., and Meshioye, O. (2011). “Effect of salinity changes of the injected water on water flooding performance in carbonate reservoirs,” in Nigeria annual international conference and exhibition, Abuja, Nigeria. July 30–August 3, 2011 (Society of Petroleum Engineers), SPE 150816. Available at: <https://www.onepetro.org/conference-paper/SPE-150816-MS> (Accessed 2011).
- Kim, C., and Lee, J. (2017). Experimental study on the variation of relative permeability due to clay minerals in low salinity water-flooding. *J. Petrol. Sci. Eng.* 151, 292–304. doi:10.1016/j.petrol.2017.01.014
- Lebedeva, E. V., and Fogden, A. (2011). Micro-CT and wettability analysis of oil recovery from sand packs and the effect of waterflood salinity and kaolinite. *Energy Fuels*. 25 (12), 5683–5694. doi:10.1021/ef201242s
- Li, H. T., Ma, Q. R., and Li, D. H. (2017). Micro mechanism of low salinity water injection to improve oil recovery of sandstone reservoir. *J. Pet. Explor. Drill. Prod. Technol.* 39 (2), 151–157. doi:10.13639/j.odpt.2017.02.005
- Li, Y. J., Xia, N., and Li, Y. P. (2016). Oil displacement of low salinity water and hexaalkyl hydroxypropyl sulfobetaine surfactant. *Oilfield Chem.* 33 (03), 487–491. doi:10.19346/j.cnki.1000-4092.2016.03.022
- ## DATA AVAILABILITY STATEMENT
- All datasets presented in this study are included in the article.
- ## AUTHOR CONTRIBUTIONS
- XW: Conceptualization, methodology, validation, formal analysis and writing - original draft. YZ: Supervision, guidance and resources. WJ: Writing - original draft and data graph drawing. ZW: Experiment operation and data graph drawing. XL: Investigation and resources. FW: Methodology, validation and formal analysis.
- ## FUNDING
- This study was supported by the Natural Science Foundation of China (Project Number: 51874339).
- Ligthelm, D. J., Gronsveld, J., Hofman, J., Brussee, N., Marceils, F., and van der Linde, H. (2009). “Novel waterflooding strategy by manipulation of injection brine composition,” in EUROPEC/EAGE conference and exhibition, Amsterdam, The Netherlands, June 8–11, 2009 (Society of Petroleum Engineers), SPE119835. Available at: <https://www.onepetro.org/conference-paper/SPE-119835-MS> (Accessed 2009).
- loahardjo, N., Xie, X., and Morrow, N. R. (2010). Oil recovery by sequential waterflooding of mixed-wet sandstone and limestone. *Energy Fuels*. 24 (9), 5073–5080. doi:10.1021/ef100729b
- Ma, L., Peng, C. S., and Fan, C. (2011). Effect of water chemical properties on swelling property of montmorillonite suspension. *J. Ocean Univ. China*. (S1), 379–385.
- Nasralla, R. A., Alotaibi, M. B., and Nasr-El-Din, H. A. (2011). “Efficiency of oil Recovery by low salinity water flooding in sandstone reservoirs,” in SPE Western North American region meeting, Alaska, United States, 7–11 May (Society of Petroleum Engineers), SPE 144602. Available at: <https://www.onepetro.org/conference-paper/SPE-144602-MS> (Accessed 2011).
- Nasralla, R. A., Bataweel, M. A., and Nasr-El-Din, H. A. (2011). Investigation of wettability alteration by low salinity water,” in SPE Offshore Europe oil and gas conference and exhibition, Aberdeen, United Kingdom. September 6–8, 2011 (Society of Petroleum Engineers), SPE146322. Available at: <https://www.onepetro.org/conference-paper/SPE-146322-MS> (Accessed 2011).
- Song, W., and Kovscek, A. R. (2016). Direct visualization of pore-scale fines migration and formation damage during low-salinity waterflooding. *J. Nat. Gas Sci. Eng.* 34, 1276–1283. doi:10.1016/j.jngse.2016.07.055
- Tang, G. Q., and Morrow, N. R. (1999). Influence of brine composition and fines migration on crude oil/brine/rock interactions and oil recovery. *J. Petrol. Sci. Eng.* 24 (2–4), 99–111. doi:10.1016/s0920-4105(99)00034-0
- Wu, J., Chang, Y. W., and Li, J. (2015). Mechanism and application conditions of low salinity water drive technology. *J. Southwest Petrol. Univ.* 37 (05), 145–151.
- Wu, X. Y., Lv, P., and Wang, C. S. (2016). Research on the influence of injection timing on low salinity water flooding effect. *Sci. Technol. Eng.* 16 (04), 12–15.
- Yang, Z. H., Yin, T. H., Kang, S., and Shen, H. (2020). Influence mechanism of ionic composition of brine on rock surface wettability. *J. Northeast Petrol. Univ.* 44(02):113–118.
- Zadaka, D., Radian, A., and Mishael, Y. G. (2010). Applying zeta potential measurements to characterize the adsorption on montmorillonite of organic cations as monomers, micelles, or polymers. *J. Colloid Interface Sci.* 352 (1), 171–177. doi:10.1016/j.jcis.2010.08.010
- Zhang, Y. S., and Morrow, N. R. (2006). “Comparison of secondary and tertiary recovery with change in injection brine composition for crude-oil/sandstone combinations,” in SPE/DOE symposium on improved oil recovery, Oklahoma, United States, April 22–26, 2006 (Society of Petroleum Engineers), SPE99757, Available at: <https://www.onepetro.org/conference-paper/SPE-99757-MS> (Accessed 2006).

- Zhang, Y. S., Xie, X. N., and Morrow, N. R. (2007). "Waterflood performance by injection of brine with different salinity for reservoir cores," in SPE annual technical conference and exhibition, California, United States, November 11–14, 2007 (Society of Petroleum Engineers), SPE109849, Available at: <https://www.onepetro.org/conference-paper/SPE-109849-MS> (Accessed 2007).
- Zhang, Y., Xie, X., and Morrow, N. R. (2007). "Waterflood performance by injection of brine with different salinity for reservoir cores," in SPE annual technical conference and exhibition, California, United States, November 11–14, 2007 (Society of Petroleum Engineers), SPE 109849. Available at: <https://www.onepetro.org/conference-paper/SPE-109849-MS> (Accessed 2007).

**Conflict of Interest:** The authors declare that the research was conducted in the absence of any commercial or financial relationships that could be construed as a potential conflict of interest.

*Copyright © 2020 Wei, Zhang, Jiang, Wang, Li and Wu. This is an open-access article distributed under the terms of the Creative Commons Attribution License (CC BY). The use, distribution or reproduction in other forums is permitted, provided the original author(s) and the copyright owner(s) are credited and that the original publication in this journal is cited, in accordance with accepted academic practice. No use, distribution or reproduction is permitted which does not comply with these terms.*





# Investigation of the Heat Transfer Mechanism of CO<sub>2</sub>-Assisted Steam Injection via Experimental and Simulation Evaluation

Zhengxiao Xu<sup>1,2</sup>, Zhaomin Li<sup>1,2\*</sup>, Binfei Li<sup>1,2</sup>, Songyan Li<sup>1,2</sup>, Teng Lu<sup>1,2</sup>, Mingxuan Wu<sup>1,2</sup> and Hao Bai<sup>1,3</sup>

<sup>1</sup>Key Laboratory of Unconventional Oil & Gas Development (China University of Petroleum (East China)), Ministry of Education, Qingdao, China, <sup>2</sup>School of Petroleum Engineering, China University of Petroleum (East China), Qingdao, China, <sup>3</sup>Department of Engineering Management, China National Aviation Fuel Southwest Storage & Transportation Co., Ltd., Chongqing, China

## OPEN ACCESS

### Edited by:

Simona Liguori,  
Clarkson University, United States

### Reviewed by:

Ahmet Ansoy,  
Istanbul Technical University, Turkey  
Bo Jiang,  
Nanjing University of Science and  
Technology, China

### \*Correspondence:

Zhaomin Li  
lizhm@upc.edu.cn

### Specialty section:

This article was submitted to  
Advanced Clean Fuel Technologies, a  
section of the Frontiers in Energy  
Research

**Received:** 06 August 2020

**Accepted:** 29 September 2020

**Published:** 30 October 2020

### Citation:

Xu Z, Li Z, Li B, Li S, Lu T, Wu M and  
Bai H (2020) Investigation of the Heat  
Transfer Mechanism of CO<sub>2</sub>-Assisted  
Steam Injection via Experimental and  
Simulation Evaluation.  
*Front. Energy Res.* 8:592142.  
doi: 10.3389/fenrg.2020.592142

Steam injection is an important process for the thermal recovery of heavy oil reservoirs. As a non-condensable gas CO<sub>2</sub>-assisted steam injection can not only improve the development effect but also reduce carbon emissions. In this study, the simulation method was combined with the experimental method. Based on an experiment using steam condensation with or without CO<sub>2</sub>, the influence of the condensation mode on steam heat transfer was considered. The effect of changes in the steam flow rate on phase transition and steam quality were analyzed. The heat transfer effects of the gas-steam mixture with different contents of CO<sub>2</sub> were compared. The results show that the surface condensation mode changes from dropwise condensation to film condensation with the addition of CO<sub>2</sub>, and the average temperature of the condensation block decreases by 20.05%. With increases in the steam flow rate, the quality of steam increases, and the heat transfer coefficient of steam on the condensation surface increases. With increase in CO<sub>2</sub> content, the temperature of the gas-steam mixture decreases, and the inhibition effect on steam heat transfer is more obvious.

**Keywords:** steam injection, simulation method, experimental method, condensation mode, CO<sub>2</sub> content, heat transfer inhibition

## INTRODUCTION

The development of heavy oil reservoirs is at a stage of high energy consumption and high cost. The green and efficient development of heavy oil resources strongly relies on breakthroughs in related theories and technological innovations. At present, thermal oil recovery, including steam flooding, steam huff and puff, SAGD, etc., are commonly used. However, the economic benefits of these development methods are often poor, with issues such as high steam loss, low effective heat, and a large number of greenhouse gases produced in the process (Lawal, 2014; Zhang et al., 2018; Xu et al., 2020a). New methods developed for the recovery of heavy oil reservoirs may, in some cases, be an economically viable alternative to steam (Li et al., 2019; Xu et al., 2019; Xu et al., 2020b). For oil sand or heavy oil reservoirs, the recovery efficiency of pure steam injection is low. Non-condensable gases (NCGs) such as flue gas can be used to assist steam injection, which would make conventional steam recovery more economical, and the production of each well would also be higher (Li et al., 2017; Pang et al., 2017; Wu et al., 2018). Taking the Dover Project (formerly the Underground Test Facility) as an

example, the addition of an appropriate amount of NCG improves the development effect of steam injection and has good economic benefits (Yee and Stroich, 2004). Since 2011, the field testing of NCG-assisted steam injection has also been carried out in Liaohe Oilfield in China. The results show that NCG injection is an effective method to regulate the development of the steam chamber and improve oil recovery (Erpeng et al., 2015).

Similarly, as an important and economical method of carbon capture, utilization and storage (CCUS), this technology is of great significance for reducing carbon emissions by injecting and storing a large amount of greenhouse gases into the reservoir (Zhang et al., 2019; Chen et al., 2020b; Li et al., 2020). It is well known that the presence of a small amount of NCGs greatly reduces condensation performance. When the steam condenses on the liquid surface, the NCG accumulates at the liquid-gas interface and forms a gas layer, thereby increasing heat transfer resistance (Othmer, 1929). Many scholars have conducted experimental studies on the condensation heat transfer in various tubes (Briggs and Sabaratnam, 2003) and walls (Othmer, 1929) with the addition of an NCG. These studies mainly focus on the influence of NCG concentration (Su et al., 2014), composition (Ge et al., 2013), temperature (Ren et al., 2015) and pressure (Ali et al., 2013) on the condensation effect.

In addition to the most recognized mechanism by which heat loss can be reduced with an insulation layer enriched with NCGs, a large number of theoretical models have also been established (Oh and Revankar, 2006; Lu et al., 2019b). Some studies have found that NCGs can promote the expansion of the steam chamber when steam is injected with NCGs (Yuan et al., 2011). At the same time, the influence of NCGs on the reservoir energy supplement is also studied. After the gas-steam mixture is added to the steam chamber, the formation pressure first increases and then remains stable. The partial pressure of the steam at the interface is lower than that of the steam in the gas-steam mixture. Even if the average temperature drops, the steam chamber does not collapse because the NCG reduces the partial pressure of the steam (Law, 2004). There are few studies on the heat transfer of CO<sub>2</sub> assisted steam injection. With the change of temperature and pressure conditions, the phase change of CO<sub>2</sub> also occurs. CO<sub>2</sub> is considered to be an important environmentally friendly alternative refrigerant due to its unique properties at low temperatures. At the same time, pressure has a great influence on the heat transfer of CO<sub>2</sub>. The heat transfer characteristics of CO<sub>2</sub> are also different under sub-atmospheric pressure, near critical pressure and supercritical conditions (Cabeza et al., 2017; Lu et al., 2019a; Baik and Yun, 2019).

In previous studies, the main characteristics of steam condensation in the presence of NCGs are as follows: In most of the studies, the NCG is air, while CO<sub>2</sub> is rare, and the influence of a high concentration of gas is not considered. Most research focuses on the average heat transfer coefficient, and local influencing factors such as a liquid film or a gas film are rarely considered. In this study, a steam condensation experiment was carried out to calculate the heat transfer coefficient of a pure steam injection. After adding CO<sub>2</sub>, the

changes in the condensation modes were compared, and the heat transfer mechanism in the dropwise condensation and film condensation modes was summarized. Then, the simulation model was established, and the experimental results were verified. The effect of steam flow rate on the phase change and steam quality was analyzed, and the heat transfer effect of the gas-steam mixture with different contents of CO<sub>2</sub> was compared. This study is helpful for understanding the development of a steam chamber with an NCG injection and has important guiding significance for the development of heavy oil reservoirs with steam injection to reduce costs and increase efficiency. In addition, this result is also enlightening for low-carbon technology in the petroleum industry.

## CONDENSATION EXPERIMENT

### Experimental Materials

The steam used in this research is produced by water injection preheating by a steam generator, and the ultrapure water used was made by the UPT-I-10T water purifier (Sichuan Youpu ultrapure Technology Co., Ltd.), the resistivity of ultrapure water is 18.2 MΩ cm. The high-purity CO<sub>2</sub> used in the experiment was from Qingdao Tianyuan Gas Manufacturing, with a purity of 99.9 mol%. Both alcohol (purity ≥ 99.7%) and sulfuric acid (purity between 95% and 98%) were provided by Sinopharm Chemical Reagent Co., Ltd.

### Experimental Device

The steam generator is the GL-1 produced by Hai'an Petroleum Scientific Research Instrument Company. The maximum output temperature of the steam is 350°C, and the maximum pressure is 25 MPa. The high-precision plunger pump is the 100DX type from Teledyne ISCO, USA, with a maximum output pressure of 66 MPa, a maximum output flow of 60 ml/min, and an accuracy of 0.001 ml/min. The heating band is used to insulate the pipeline between the steam generator and the condenser chamber to reduce the heat loss during steam injection. The gas flow controller is the Brooks SLA5850S, with a flow range of 0–50 ml/min and an accuracy of 0.1 ml/min. It has long-term zero stability and annual variation is less than ±0.5% of full scale.

The condensation chamber used in the experiment is made of stainless steel to avoid rusting due to the humid environment produced by the experiment. The size of the condensation chamber is 140 × 20 × 300 mm. In the main condensation position of the steam, a brass block is embedded as a reference for comparison, as shown in **Figure 1**. The condensation surface was pretreated before the experiment. After the surface was polished with sandpaper, it was soaked in a mixture of pure alcohol and 20% sulfuric acid to ensure a good surface smoothness. The contact side of the brass block and stainless steel were heat-insulated with PTFE. Evenly distributed detection holes were made on the right side of the brass block; one end was open to the middle of the brass block, and the other end was open to the outside of the stainless steel condenser. The thermocouple adopted in the experiment is K-type thermocouple with a diameter of 0.4 mm and an accuracy of ±0.1 K. The

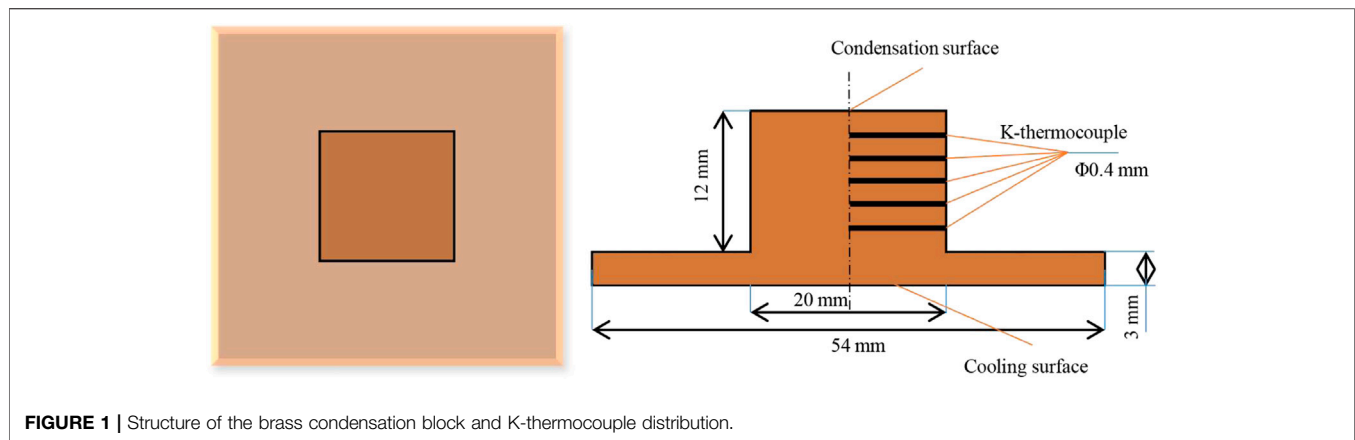


**FIGURE 1** | Structure of the brass condensation block and K-thermocouple distribution.

thermocouples in the condensation block were distributed with a spacing of 2 mm, a diameter of 0.5 mm, and a penetration depth of 10 mm. The temperature of condensation surface is obtained by linear fitting, and the standard error is less than 10%.

## Experimental Steps

A flow chart of the condensation experiment is shown in **Figure 2**. It includes four parts: the steam and CO<sub>2</sub> injection system, the condensation system, the cooling cycle system and the experimental data acquisition system. The specific steps are as follows:

- (1) Start the steam generator, preheat for 3 h until the steam blowout is stable, and adjust the CO<sub>2</sub> flow rate as required.
- (2) Keep the cooling water (at a constant temperature of 20°C) circulating on the back of the condensation block. Record the temperature of the condensation block using the data acquisition device.
- (3) Keep the connecting pipeline of the condensation chamber unblocked, monitor the pressure of the condensation chamber in real time, and defog the visual window.
- (4) Turn on the switch for the condensation chamber, and pass steam or a gas-steam mixture into the condensing chamber.

- (5) The experimental phenomena on the surface of the condensate are recorded by camera in real time.

## SIMULATION MODEL

### Model Simplification and Simulation Conditions

**Figure 3** shows a local simplified model to simulate the heat transfer process between the condensation block and chamber. The size of the condensation model is set to be the same as the real object, and the internal dimension of the condensation chamber is set at 220 × 90 × 20 mm.

### Simulation Method and Numerical Parameters

The simulation module used is the heat transfer of solids and fluids. A solver is established for calculation based on the coupling of the heat transfer field and the flow field. The adaptive drawing method adopted for mesh division, the maximum cell size is 22 mm, the minimum cell size is 3.96 mm, and local encryption is performed on the condensate block. In the transient simulation, in order to

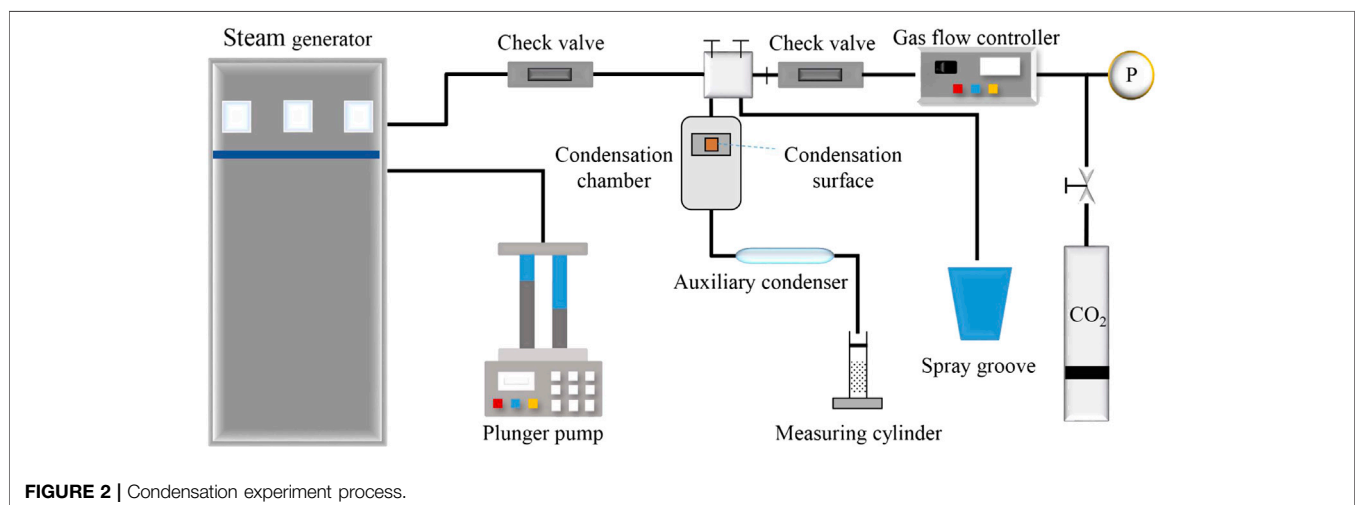
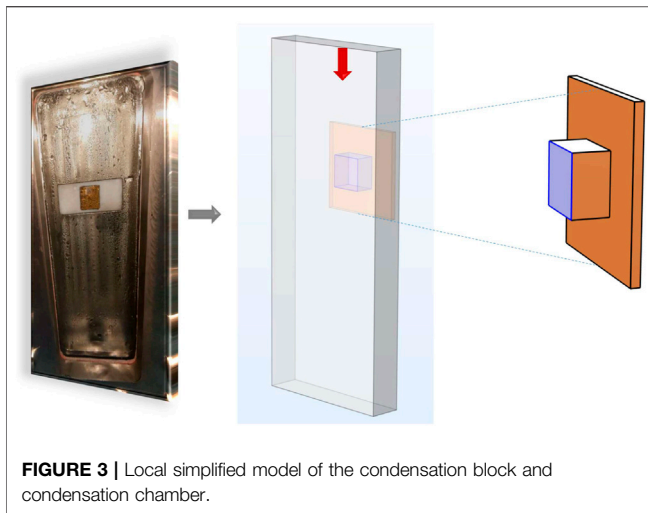


**FIGURE 2** | Condensation experiment process.



make the flow boundary clearer, the mesh was encrypted. Taking the temperature value at the same time point on the condensing surface, it is found that the number of grids has little effect on the change of temperature value, achieving mesh independence.

### Assumptions

- (1) During the condensation heat transfer process, the surfaces other than the specific heat exchange surface are thermally insulated from the outside.
- (2) During the simulations of dropwise condensation and film condensation, the morphology of the condensation surface remains stable without a phase change.
- (3) When comparing the influence of factors such as steam flow rate and CO<sub>2</sub> content, only changes in the condensation surface temperature are considered, and changes in condensation mode are not considered.

### Numerical Parameters

The condensation block is constructed of brass material, and its specific parameters are shown in **Table 1**.

Considering changes in the properties under different CO<sub>2</sub> content conditions in the gas-steam mixture, the corresponding numerical parameter settings are shown in **Table 2**.

## RESULTS AND DISCUSSION

### Condensation Experiments With Steam and a Gas-Steam Mixture

Pure steam is introduced into the condensation chamber from top to bottom; the steam temperature is 100°C, the injection rate is 0.35 m/s, and the steam is blown out for 3 h in advance. During

the experiment, it was observed that the condensed water appeared dropwise on the condensed surface, as shown in **Figure 4**.

**Figure 4** shows that during the steam condensation process on the brass surface, the condensed water cannot wet the surface well and is evenly distributed on the surface in the form of small droplets. The small droplets further condense, expand, collide and gather into large droplets. When the gravity of the water droplet is greater than the adhesion force between it and the wall, the droplet slides down and carries other, smaller water droplets in the same vertical direction on the wall surface so that the wall surface is exposed again. Relative to the size of the water droplets, the exposed area is large, and as the condensation process continues, the water droplets periodically regroup in the exposed area.

The concept of temperature difference is introduced here, and it refers to the difference between saturation temperature and condensate temperature under the corresponding pressure. There is a relationship between temperature difference and the condensation heat transfer coefficient. The experiment was carried out under atmospheric pressure. The saturation temperature of pure steam under atmospheric pressure is denoted as  $\bar{T}$ , and the ideal temperature is 100°C. During the experiment, the temperature difference **Eq. (1)** is obtained:

$$\Delta T = \bar{T} - T_i \quad (1)$$

In the formula,  $\Delta T$  is the temperature difference, °C.  $\bar{T}$  is the temperature of pure steam under atmospheric pressure, °C.  $T_i$  is the actual temperature of the condensate, °C.

Suppose that the temperature distribution **Eq. (2)** in the horizontal direction of the condensation block is as follows:

$$T_x = mx + n \quad (2)$$

In the formula,  $T_x$  is the temperature of the thermocouple when the distance between the condensate block and the wall is  $x$ , °C,  $m$  is the slope, and  $n$  is the intercept.

The temperature measured by the thermocouples uniformly distributed on the condensate block at the same time is selected to verify the accuracy of the above fitting formula, as in **Eq. (3)**:

$$F(m, n) = \sum_{i=1}^j (mx_i + n - T_i)^2 \quad (3)$$

Verification **Eq. (4)**

$$\frac{\partial F}{\partial m} = \frac{\partial F}{\partial n} = 0 \quad (4)$$

If the conditions are met, a linear curve is fit to the curve to calculate the slope  $m$  and wall temperature  $n$ .

**TABLE 1 |** Parameters of the brass block.

Density (kg/m <sup>3</sup> )	Constant pressure heat capacity (kJ/(kg·K))	Thermal conductivity (W/(m·K))	Young's modulus (Pa)	Poisson's ratio	Temperature coefficient of resistivity (1/K)
0.598	2.080	0.0250	$1.1 \times 10^{11}$	0.35	0.0039

**TABLE 2 |** Numerical parameters with different CO<sub>2</sub> contents in the gas-steam mixture (100°C, 1 atm).

CO <sub>2</sub> content (%)	Density (kg/m <sup>3</sup> )	Constant pressure heat capacity (kJ/(kg·K))	Thermal conductivity (W/(m·K))
0	0.598	2.080	0.0250
20	0.766	1.575	0.0246
40	0.934	1.307	0.0242
60	1.103	1.135	0.0238
80	1.271	1.012	0.0234
100	1.441	0.919	0.0230

From the combination of Eqs (1) and (2), it can be concluded that:  $T_0 = \bar{T} - \Delta T = n$ ,  $\partial T_x / \partial x = m$ .

From this, the heat flux density of the steam on the condensation block can be calculated, as in Eq. (5):

$$q = \lambda \frac{\partial T_x}{\partial x} \quad (5)$$

In the formula,  $q$  is the heat flux density, W/m<sup>2</sup>.  $\lambda$  is the thermal conductivity of the brass block, W/(m·K).

Finally, the heat transfer coefficient of the steam on the condensate can be calculated as the ratio of the heat flux to the temperature difference, as shown in Eq. (6):

$$h = \frac{q}{\Delta T} \quad (6)$$

In the formula,  $h$  is the heat transfer coefficient, W/(m<sup>2</sup>·K).

Based on the data collected by the thermocouples in the condensation process, the temperature difference and heat transfer coefficient of the condensation surface at each time point during steam injection can be obtained from the above calculation steps. The relation curve between the heat transfer coefficient and temperature difference is plotted as shown in Figure 5.

The trend of the temperature curve of each thermocouple in Figure 5 shows that at the beginning of steam injection, the temperature of the condensation surface is the normal temperature 20°C, and the temperature difference between the steam and condensation surface is large. Therefore, the heat transfer between steam and condensation is obvious, and the temperature rises rapidly. However, with increasing surface temperature, the rate of temperature change gradually decreases, and the heat transfer process gradually tends to become stable. The temperature measured by each thermocouple is different and remains unchanged at a

constant value. As the distance between the thermocouple and the condensation surface increases, the thermocouples are sequentially numbered K1, K2, K3, K4, and K5. Among them, K1 has the fastest temperature increase and the highest temperature value after stability. With increasing distance between the heat source and the thermocouple, the heating rate at the thermocouple gradually decreases, and the final stable temperature value decreases in turn and tends to a linear distribution. The relationship curve between the heat transfer coefficient and the change in temperature difference indicate that the heat transfer coefficient increases with decreasing temperature difference, and the growth rate becomes faster. In the initial stage of steam condensation, the greater the temperature difference is, the lower the actual condensation surface temperature, and the shorter the period from water droplets forming to falling off. With the development of condensation heat transfer, the temperature difference gradually decreases, the condensation surface temperature gradually approaches the temperature of injected steam, the condensation speed of steam on the surface becomes slower, the heat transfer coefficient is large, and more heat is transferred to the condensation surface.

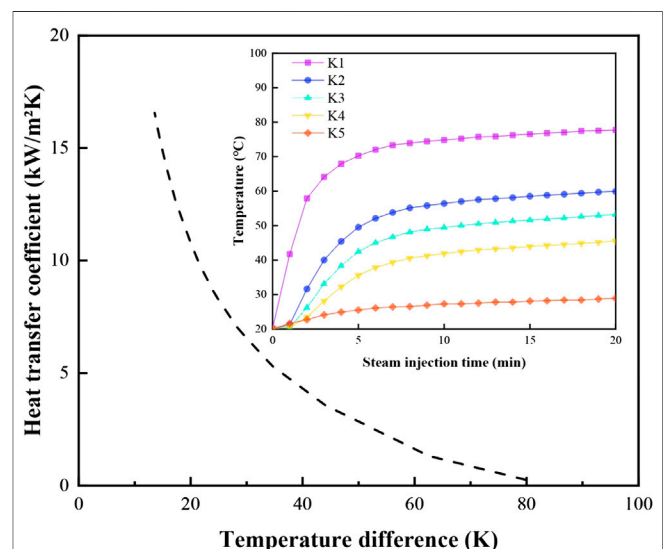
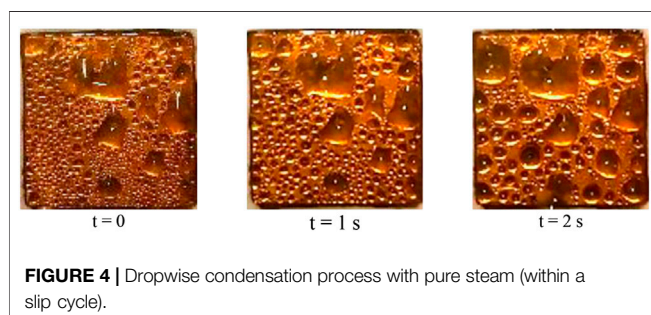
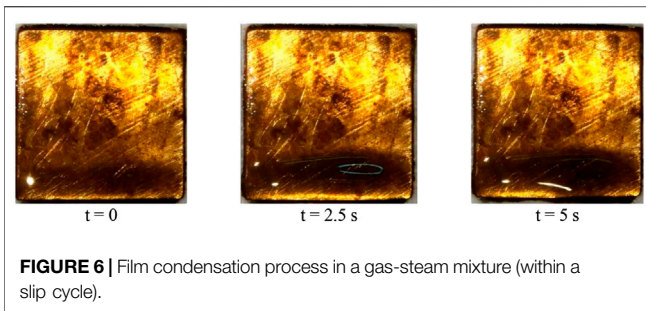


**FIGURE 5 |** Variation in the heat transfer coefficient of steam on the condensation surface with temperature difference (the attached figure shows the change of temperature at thermocouple position with steam injection time).

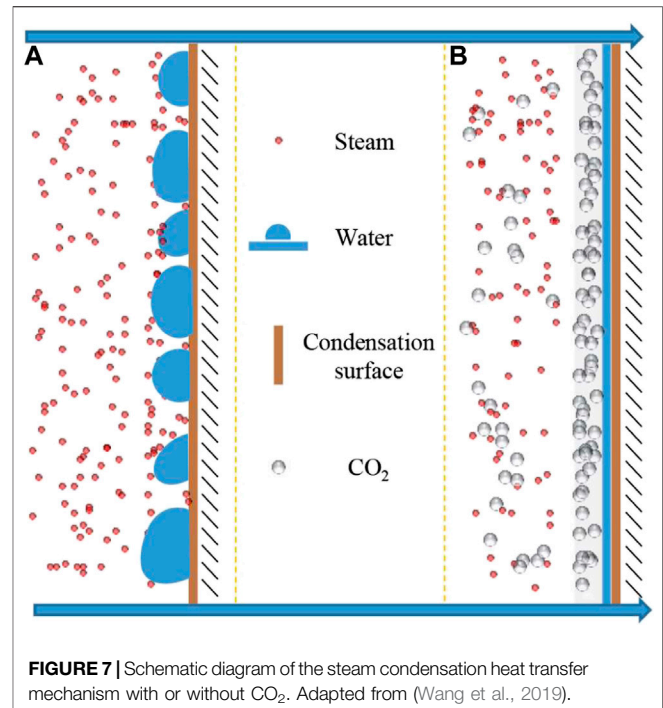




CO<sub>2</sub> was added to pure steam to form a gas-steam mixture without changing other conditions. After the condensation experiment, it was found that the condensation mode on the surface changed significantly. The experimental process is shown in **Figure 6**.

**Figure 6** shows that no small water droplets appear on the condensation surface. A layer of water film is attached to the surface and thickens gradually with the introduction of a gas-steam mixture until the water film falls down and accumulates at the bottom layer due to the influence of gravity and falls off. The condensation is repeated throughout the process of the mixed steam entering the condensing chamber (Yuan et al., 2011). It is obvious that there is water film on the surface during steam condensation, and the thickness of the water film changes. However, the time that the surface is exposed to the steam is very short.

The most direct impact of this phenomenon is that the addition of CO<sub>2</sub> inhibits the condensation heat transfer of steam. The heat transfer coefficient on the condensation surface of the gas-steam mixture is lower than that of pure steam with the same temperature difference. The mechanism explanation is shown in **Figure 7**. In the dropwise condensation mode with pure steam, the surface, except for the part covered by the liquid droplets, is exposed to the steam. Therefore, the heat exchange process is carried out between steam and liquid droplets and exposed surface. Since the surface area of the liquid droplet is much larger than the area it occupies and there is no liquid film thermal resistance on the exposed surface, dropwise condensation has a fast surface heat transfer rate. Even if a small amount of an NGC such as CO<sub>2</sub> is added, the condensation mode on the condensation surface is film condensation. The heat transfer coefficient of the gas-steam mixture with CO<sub>2</sub> is small due to the thermal resistance effect, on the one hand. According to the theory of convective heat transfer, in the process of film condensation heat transfer, there is liquid membrane resistance in the heat transfer resistance. As some of the CO<sub>2</sub> molecules penetrate the liquid membrane layer, CO<sub>2</sub> will accumulate continuously on the gas-liquid interface. There is also gas-phase membrane resistance, so the direct contact time between the steam and the surface is reduced. On the other hand, partial pressure of steam is less due to presence of CO<sub>2</sub> in the mixture. The decrease in the saturation temperature of the steam causes the energy of the mixed steam to decrease. The combination of the two effects results in film condensation when the gas-steam mixture is added. The heat transfer coefficient of



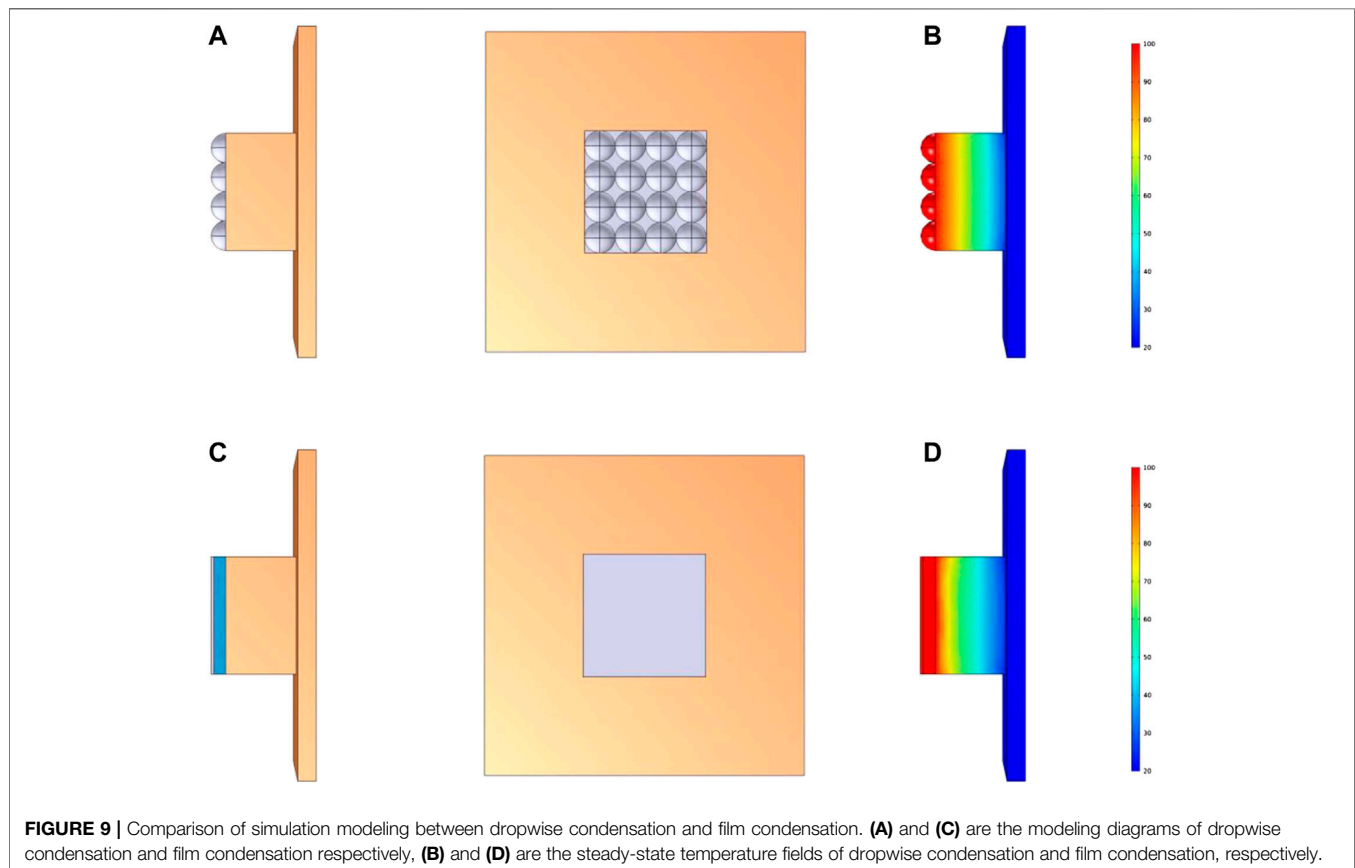
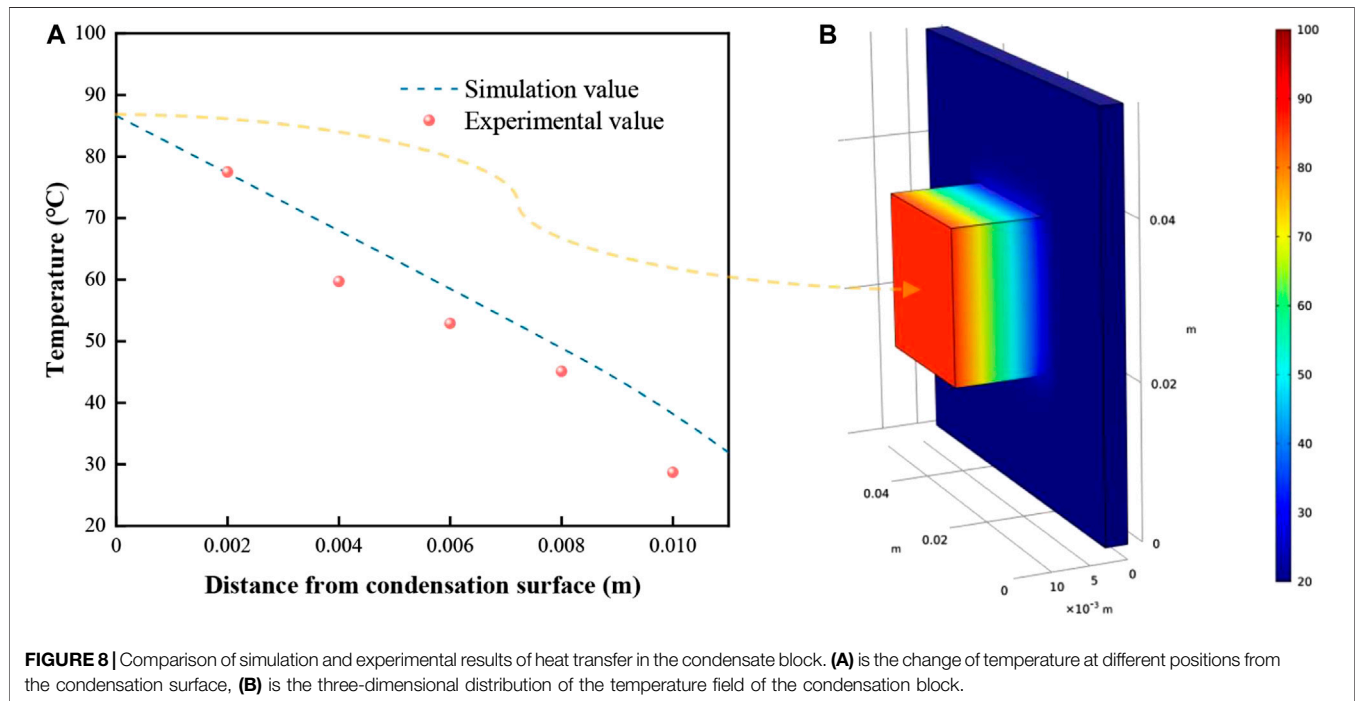
the film condensation mode under the same temperature difference is smaller than that of dropwise condensation (Chen et al., 2020a).

The process of NCG-assisted steam injection is essentially a dynamic continuous process of condensation heat transfer. After the mixture is injected into the reservoir, the steam flows and transfers heat to the rocks and heavy oil. When the steam temperature is lower than the saturation temperature, it condenses on the rock surface and produces a phase transition (Wang et al., 2019).

From a microscopic view of the gas-steam mixture, both molecules move to the surface of the brass block, but the steam molecules are condensed into water, while the gas molecules are retained and gathered near the surface of the brass block. Therefore, it can be considered that in the schematic diagram of **Figure 7**, a non-condensable gas layer is formed between the steam molecules and the brass surface on a macroscopic level. Under pure steam injection conditions, the condensation heat flux is large. The mass transfer and phase transition of steam molecules are relatively fast. Under the action of gravity, the condensate droplets frequently fall off and wash the condensation surface. The gas-liquid interface is completely dynamic. With the increase of CO<sub>2</sub> content, the falling off frequency of droplets is obviously slowed down, and the condensation morphology gradually transits to film condensation.

## Steady State Simulation of Heat Transfer on the Condensation Surface

The boundary conditions are set. In the steady state of steam injection, the condensation surface temperature is 86.4°C



according to the measured value of the experimental thermocouple. Therefore, the temperature of the simulated condensation surface is set at 86.4°C, the temperature of the cooling surface is 20°C, and the initial temperature of the condensate is 20°C. After reaching the steady state, the temperature distribution is shown in **Figure 8B**. Considering the connection between the measured position of the thermocouple and the comparison result of the corresponding simulated temperature value, the experimental value is shown in **Figure 8A**.

**Figure 8** shows that from the condensation surface to the cooling surface, the temperature distribution in the condensate is decreasing. The inside of the condensing block is made of uniform brass, and the vertical surfaces are isothermal when heat conduction occurs. The experimental value measured by the thermocouple is less than or equal to the simulation value because the condensate is not completely insulated from the outside during the experiment. The heat loss from this part of the process is not considered in the simulation process, which is solved under ideal conditions. The trends in the simulation values and experimental values are basically the same, so more factors are considered in the follow-up research.

## Heat Transfer Simulation Under Different Condensation Modes

Combined with the different phenomena on the condensation surface obtained from the experiment, dropwise condensation appears with pure steam injection, and film condensation appears with gas-steam mixture injection with CO<sub>2</sub>. Considering the difference in thermal resistance caused by the two condensation modes, ignoring the change of steam partial pressure and assuming that the condensation surface is in a dynamic stable state, the models are established as shown in **Figures 9A,C**. In **Figure 9A**, a total of 16 water droplets are uniformly distributed on the condensation surface, each of which

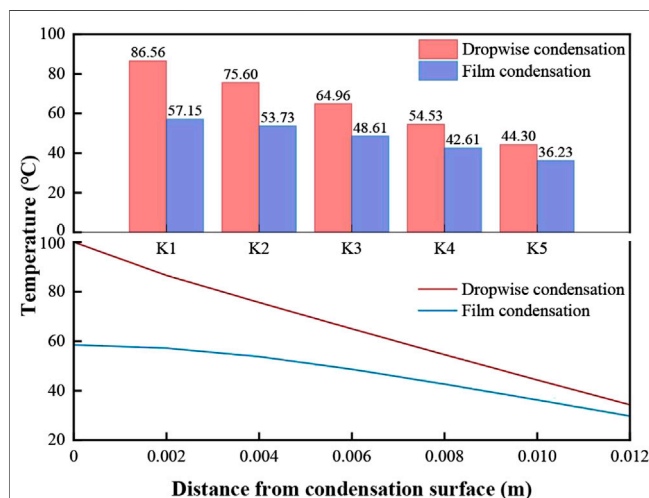


**FIGURE 10** | Comparison of the temperature at each thermocouple in dropwise condensation and film condensation.

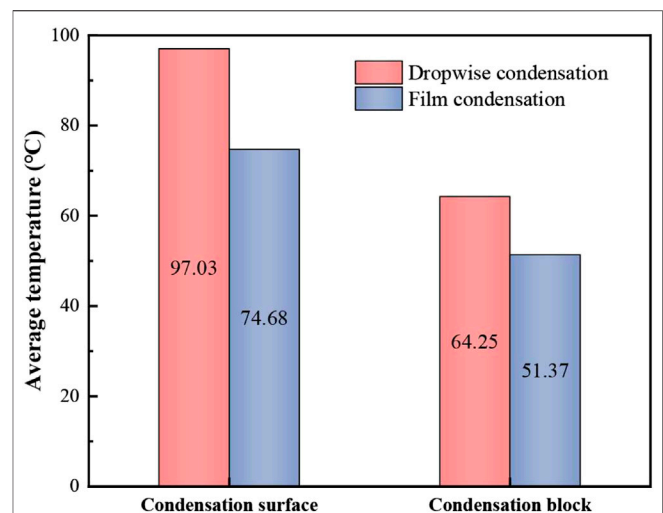


**FIGURE 11** | Comparison of the average temperature between dropwise condensation and film condensation.

has a diameter of 5 mm. In **Figure 9C**, a CO<sub>2</sub> gas film with a thickness of 0.5 mm is distributed, and a water film with a thickness of 2 mm is distributed between the gas film and the condensation surface. The condensation surface is set to be in thermal contact with the steam, and the steam temperature is 100°C. After reaching the steady state, the temperature distributions of the condensation block are shown in **Figures 9B,D**.

**Figure 9** shows that the temperature gradient in the dropwise condensation mode is larger than that in the film condensation mode. The temperature change curves along the thermocouple connection under the two condensation modes are compared, as shown in **Figure 10**. The presence of gas in the steam chamber, reservoir rocks and heavy oil may reduce the heat transfer efficiency, which affects the expansion of the steam cavity (Pang et al., 2017).

**Figure 10** shows that the temperature at the condensation surface in the dropwise condensation mode is 100°C, and the temperature at the condensation surface in the film condensation mode is less than 60°C. The reason for this difference is that at the measured position, the surface in the dropwise condensation mode directly contacts the steam for heat exchange. With the gas film and liquid film barriers, the temperature transferred to the surface in the film condensation mode is greatly reduced. From thermocouple K1 to K5, the temperature in the dropwise condensation mode is greater than the temperature in the film condensation mode at each position, but as the distance between the thermocouple and the condensation surface increases, the temperature difference between the two modes decreases.

It should be noted that although the film condensation has a good inhibition effect on the steam heat transfer because the thermal resistance layer is a pre-set immovable unit, the temperature at the location of the thermocouple cannot represent the whole condensation heat transfer process, which needs further comprehensive analysis. The area of the

condensation surface is calculated to obtain the average temperature, and the volume of the condensation block is calculated to obtain the average temperature. The comparison of the average temperature in the two modes is shown in **Figure 11**.

**Figure 11** shows that in the dropwise condensation and film condensation modes, the average temperature difference on the condensation surface is smaller than the average temperature difference in the condensation block. This is because in the dropwise condensation mode, there is an exposed area on the condensation surface that directly contacts the steam. The thermal conductivity of metal is greater than that of the gas film and the liquid film, and the distance between gas molecules is relatively large. The gas depends on the irregular thermal movement of molecules and the collision between molecules, which causes energy transfer within the gas, thus forming a macroscopic heat transfer. The average temperature of the condensate is the most representative of heat transfer. The average temperature of the condensate in the film condensation mode is 12.88°C lower than that in the dropwise condensation mode, and the decrease range is 20.05%, which is less than the 23.03% on the condensation surface. This shows that the addition of CO<sub>2</sub> indirectly inhibits the heat transfer of steam by changing the condensation mode (Xu et al., 2016).

## Influence of Steam Flow Rate and CO<sub>2</sub> Content

In this section, the change in condensation mode and flow regime is not considered; only the influence of the steam flow rate and CO<sub>2</sub> content change on the condensation surface temperature is considered.

The free interface between gas and liquid can be obtained by surface tracking. The gas volume fraction  $F_g$  and liquid volume fraction  $F_l$  are defined as the sum of the gas volume fraction and the liquid volume fraction, respectively. The sum of the gas-liquid two-phase volume fractions in a single grid is one and can track the gas-liquid interface. In the model, liquid water and pure steam are set as the initial phase and the second phase, respectively. When the volume fraction of the gas phase  $F_g = 0$ , the grid is filled with the liquid phase; when  $F_g = 1$ , the grid is filled with mixed gas; when  $0 < F_g < 1$ , gas and liquid coexist in the grid.

$$F_g + F_l = 1 \quad (7)$$

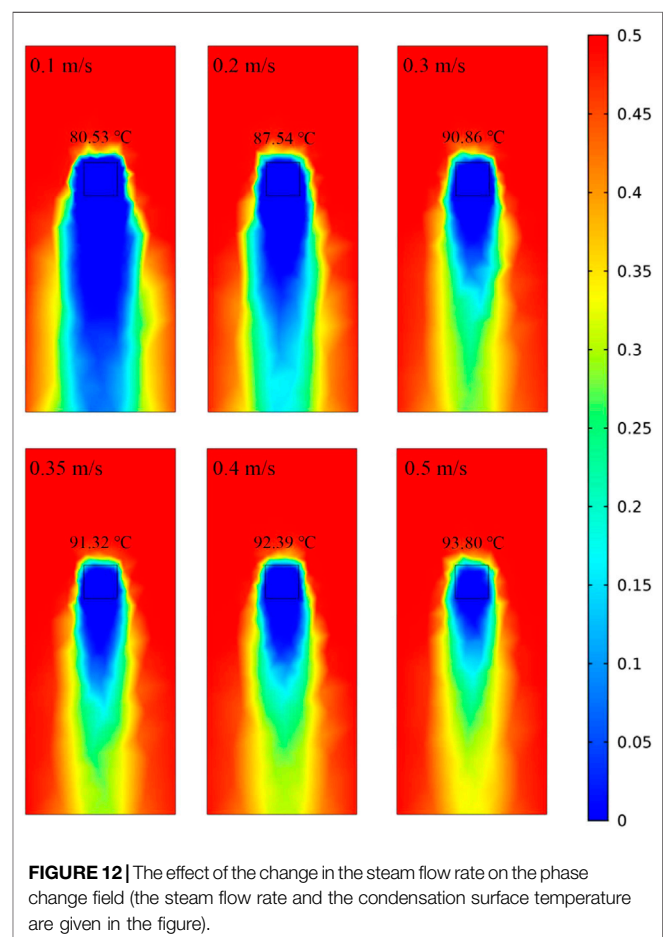
With the steam temperature set at 100°C, the phase transition temperature between the water phase and steam phase is 100°C, and the latent heat from the water phase to the steam phase is 2,257.2 kJ/kg. By changing the injection rate of the steam, changes in the condensation surface temperature and phase change field of the condensation chamber are studied, as shown in **Figure 12**.

**Figure 12** shows that the phase transition of steam occurs after the steam is injected into the condensation chamber, where gas and liquid phases coexist. This leads to a decrease in steam quality, and the condensation phenomenon is concentrated on the condensation surface and its lower part. The results of this study are similar to those found by Wu and Vierow (Wu and Vierow, 2006) that the condensation heat transfer coefficient at

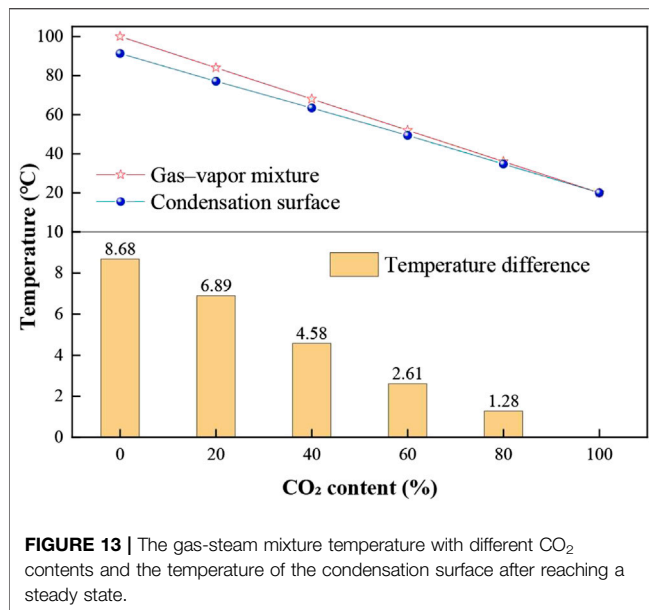
the top is greater than that at the bottom. As the steam flow rate increases, the steam in the condensing chamber can still maintain a high degree of quality. The temperature of the condensing surface gradually increases, and the increase rate becomes slower, eventually approaching 100°C.

During the process of steam injection, there are three heat transfer modes, steam condensation at the interface, significant convection heat transfer from steam to the interface, and conduction through liquid condensate (Dehbi, 2015). Under the same pressure condition, the heat transfer rate and heat transfer coefficient increase with the increase of steam flow rate at the inlet. A higher inlet flow leads to a larger interfacial shear force, which reduces the thickness of the liquid phase on the condensing surface and accelerates the shedding speed of the liquid phase, both are reasons for reducing the heat transfer resistance of the liquid phase. At the same time, the high steam flow rate brings a large heat flux, which also promotes heat transfer. It is worth noting that the velocity change caused by the increase in flow affects the flow regime, which also has an important impact on the heat transfer process. This is the focus of our next research.

To explore the influence of carbon dioxide content on the inhibition of steam heat transfer, the constant mixed steam flow rate was 0.35 m/s, the CO<sub>2</sub> contents were set as 0% (pure steam),







20%, 40%, 60%, 80%, and 100% (pure CO<sub>2</sub>), and the initial CO<sub>2</sub> temperature was 20°C. After mixing with steam, the partial pressure of steam and the temperature of the gas-steam mixture are affected. In this process, changes in other physical parameters are ignored. The temperature of the gas-steam mixture under different CO<sub>2</sub> contents and the temperature of the condensation surface after reaching the steady state are compared, as shown in **Figure 13**.

As shown in **Figure 13**, with an increase in CO<sub>2</sub> content, the temperature of the gas-steam mixture decreases linearly, and the temperature difference between the gas-steam mixture and the condensation surface gradually decreases after reaching the steady state. This indicates that heat transfer requires a temperature difference as the spontaneous power, and the addition of CO<sub>2</sub> reduce the partial pressure of the steam. The condensation heat transfer coefficient decreases with increasing CO<sub>2</sub> mass fraction and decreases with decreasing total system pressure.

The partial pressure of steam decreases with the increase of CO<sub>2</sub> content. The accumulation of CO<sub>2</sub> reduces the interface saturation temperature (corresponding to the interface steam partial pressure) at the gas-liquid interface, which leads to a decrease in the temperature difference between the steam and the condensation surface, that is, the driving force for condensation decreases, and the condensation effect becomes worse. In the reservoir developed by steam injection, whether the heat of steam acts on the reservoir is the key to determine the development effect. When steam and CO<sub>2</sub> are injected into the reservoir together, due to the low heat transfer coefficient of the gas-steam mixture in the rock formations along the way, the steam can maintain the gas phase through a longer flow distance, which increases the sweep range. At the same time, when acting on the cold oil zone, the residual heat of steam is higher, which can effectively heat the crude oil to reduce viscosity and improve its fluidity. Moreover, due to the slowing down of condensation process,

the water content in the production process is relatively low, which is one of the key reasons for enhanced oil recovery.

## CONCLUSION

NCG-assisted steam injection has an impact on the expansion of the steam chamber, which in turn affects the development of heavy oil reservoirs. The following four major conclusions were drawn from the results of this study:

- (1) When pure steam is injected, the heat transfer coefficient increases with the decrease of temperature difference, and is affected by the steam flow rate. After the addition of CO<sub>2</sub>, the condensation mode changes from dropwise condensation to film condensation, which inhibits the condensation heat transfer of the steam.
- (2) Film condensation has a high thermal resistance when composed of a gas film and a liquid film. Compared with dropwise condensation, after the heat is transferred to the condensation surface, the temperature decreases by 23.03%, and the average temperature of the entire condensation block decreases by 23.03%.
- (3) A phase transition occurs after the steam is injected into the condensation chamber, and the condensation is concentrated near the brass block surface and its lower part. As the steam flow rate increases, the steam in the condensation chamber can still maintain a high degree of quality, the temperature of the condensation surface gradually increases, and the increase rate becomes slower.
- (4) With the increase of CO<sub>2</sub> content, the temperature of the gas-steam mixture decreases linearly. The high CO<sub>2</sub> content brings a small heat flux, which also inhibits heat transfer process. The co-injection of steam and CO<sub>2</sub> is beneficial to improve the development effect of steam in the reservoir.

## DATA AVAILABILITY STATEMENT

The raw data supporting the conclusions of this article will be made available by the authors, without undue reservation.

## AUTHOR CONTRIBUTIONS

All authors listed have made a substantial, direct and intellectual contribution to the work, and approved it for publication.

## FUNDING

This project was financially supported by the National Natural Science Foundation of China (No. 51774306 and No. 51974346), National Key Scientific and Technological Project for the Oil & Gas Field and Coalbed Methane of China (2016ZX05031002-004-002), and the Youth Innovation of University in Shandong Province under (No. 2019KJH002). We are grateful to the



Shandong Engineering Research Center for Foam Application in Oil and Gas Field Development and UPC-COSL Joint Laboratory

on Heavy Oil Recovery for their assistance with the experimental research.

## REFERENCES

- Ali, H., Sheng Wang, H., Briggs, A., and Rose, J. W. (2013). Effects of vapor velocity and pressure on marangoni condensation of steam-ethanol mixtures on a horizontal tube. *J. Heat Trans.* 135 (3), 10. doi:10.1115/1.4007893
- Baik, W., and Yun, R. (2019). In-tube condensation heat transfer characteristics of CO<sub>2</sub> with N<sub>2</sub> at near critical pressure. *Int. J. Heat Mass Tran.* 144, 118628. doi:10.1016/j.ijheatmasstransfer.2019.118628
- Briggs, A., and Sabaratnam, S. (2003). Condensation of steam in the presence of air on a single tube and a tube bank. *Int. J. Energy Res.* 27 (4), 301–314. doi:10.1002/er.876
- Cabeza, L. F., de Gracia, A., Fernández, A. I., and Farid, M. M. (2017). Supercritical CO<sub>2</sub> as heat transfer fluid: a review. *Appl. Therm. Eng.* 125, 799–810. doi:10.1016/j.applthermaleng.2017.07.049
- Chen, H., Wang, Z., Wang, K., Li, Z., and Li, S. (2020a). Investigation of EOR mechanism for flue gas assisted SAGD. *J. Petrol. Sci. Eng.* 193, 107420. doi:10.1016/j.petrol.2020.107420
- Chen, L., Huang, M., Li, Z., Liu, D., and Li, B. (2020b). Experimental study on the characteristics of foam flow in fractures. *J. Petrol. Sci. Eng.* 185, 106663. doi:10.1016/j.petrol.2019.106663
- Dehbi, A. (2015). A generalized correlation for steam condensation rates in the presence of air under turbulent free convection. *Int. J. Heat Mass Tran.* 86, 1–15. doi:10.1016/j.ijheatmasstransfer.2015.02.034
- Erpeng, G., Youwei, J., Yongrong, G., Hongzhuang, W., and Pengbo, Y. (2015). “Discussion on the first N-SAGD pilot test in China,” in SPE Asia Pacific Enhanced Oil Recovery Conference. Kuala Lumpur, Malaysia. 11–13 August, 2015 (Society of Petroleum Engineers). doi:10.2118/174655-ms
- Ge, M., Zhao, J., and Wang, S. (2013). Experimental investigation of steam condensation with high concentration CO<sub>2</sub> on a horizontal tube. *Appl. Therm. Eng.* 61 (2), 334–343. doi:10.1016/j.applthermaleng.2013.08.013
- Law, D. H.-S. (2004). “Disposal of carbon dioxide, a greenhouse gas, for pressure maintenance in a steam-based thermal process for recovery of heavy oil and bitumen,” in SPE International Thermal Operations and Heavy Oil Symposium and Western Regional Meeting. Bakersfield, CA. 16–18 March 2004 (Society of Petroleum Engineers). doi:10.2118/86958-ms
- Lawal, K. A. (2014). Economics of steam-assisted gravity drainage for the Nigerian Bitumen deposit. *J. Petrol. Sci. Eng.* 116, 28–35. doi:10.1016/j.petrol.2014.02.013
- Li, S., Li, Z., and Sun, X. (2017). Effect of flue gas and n-hexane on heavy oil properties in steam flooding process. *Fuel* 187, 84–93. doi:10.1016/j.fuel.2016.09.050
- Li, S., Wang, Q., Zhang, K., and Li, Z. (2020). Monitoring of CO<sub>2</sub> and CO<sub>2</sub> oil-based foam flooding processes in fractured low-permeability cores using nuclear magnetic resonance (NMR). *Fuel* 263, 116648. doi:10.1016/j.fuel.2019.116648
- Li, Z., Xu, Z., Li, B., Wang, F., Zhang, Z., Yang, H., et al. (2019). Advances in research and application of foam flooding technology. *J. of China Univ. of Pet.* 43(5), 118–127. doi:10.3969/j.issn.1673-5005.2019.05.013
- Lu, J., Cao, H., and Li, J. (2019a). Experimental study of condensation heat transfer of steam in the presence of non-condensable gas CO<sub>2</sub> on a horizontal tube at sub-atmospheric pressure. *Exp. Therm. Fluid Sci.* 105, 278–288. doi:10.1016/j.expthermflusci.2019.04.004
- Lu, J., Cao, H., and Li, J. (2019b). Theoretical modeling of vapor condensation in the presence of noncondensable gas on a horizontal tube. *J. Heat Trans-T ASME.* 141 (12), 9. doi:10.1115/1.4044703
- Oh, S., and Revankar, S. T. (2006). Experimental and theoretical investigation of film condensation with noncondensable gas. *Int. J. Heat Mass Tran.* 49 (15), 2523–2534. doi:10.1016/j.ijheatmasstransfer.2006.01.021
- Othmer, D. F. (1929). The condensation of steam. *Ind. Eng. Chem.* 21 (6), 576–583. doi:10.1021/ie50234a018
- Pang, Z., Wu, Z., and Zhao, M. (2017). A novel method to calculate consumption of non-condensate gas during steam assisted gravity drainage in heavy oil reservoirs. *Energy* 130, 76–85. doi:10.1016/j.energy.2017.04.078
- Ren, B., Zhang, L., Cao, J., Xu, H., and Tao, Z. (2015). Experimental and theoretical investigation on condensation inside a horizontal tube with noncondensable gas. *Int. J. Heat Mass Tran.* 82, 588–603. doi:10.1016/j.ijheatmasstransfer.2014.11.041
- Su, J., Sun, Z., Ding, M., and Fan, G. (2014). Analysis of experiments for the effect of noncondensable gases on steam condensation over a vertical tube external surface under low wall subcooling. *Nucl. Eng. Des.* 278, 644–650. doi:10.1016/j.nucengdes.2014.07.022
- Wang, Z., Li, Z., Sarma, H. K., Xu, Y., Wu, P., Yang, J., et al. (2019). A visualization experimental study on gas penetration through interlayer to improve SAGD performance. *J. Petrol. Sci. Eng.* 177, 959–970. doi:10.1016/j.petrol.2019.03.001
- Wu, T., and Vierow, K. (2006). Local heat transfer measurements of steam/air mixtures in horizontal condenser tubes. *Int. J. Heat Mass Tran.* 49 (15), 2491–2501. doi:10.1016/j.ijheatmasstransfer.2006.01.025
- Wu, Z., Liu, H., and Wang, X. (2018). 3D experimental investigation on enhanced oil recovery by flue gas coupled with steam in thick oil reservoirs. *Energy Fuels.* 32(1), 279–286. doi:10.1021/acs.energyfuels.7b03081
- Xu, H., Sun, Z., Gu, H., and Li, H. (2016). Forced convection condensation in the presence of noncondensable gas in a horizontal tube; experimental and theoretical study. *Prog. Nucl. Energy.* 88, 340–351. doi:10.1016/j.pnucene.2016.01.013
- Xu, Z., Li, S., Li, B., Chen, D., Liu, Z., and Li, Z. (2020b). A review of development methods and EOR technologies for carbonate reservoirs. *Petrol. Sci.* 17 (4), 990–1013. doi:10.1007/s12182-020-00467-5
- Xu, Z., Li, B., Zhao, H., He, L., Liu, Z., Chen, D., et al. (2020a). Investigation of the effect of nanoparticle-stabilized foam on EOR: nitrogen foam and Methane foam. *ACS Omega.* 5 (30), 19092–19103. doi:10.1021/acsomega.0c02434
- Xu, Z., Li, Z., Jing, A., Meng, F., Dang, F., and Lu, T. (2019). Synthesis of magnetic graphene oxide (MGO) and auxiliary microwaves to enhance oil recovery. *Energy Fuels.* 33 (10), 9585–9595. doi:10.1021/acs.energyfuels.9b01841
- Yee, C. T., and Stroich, A. (2004). Flue gas injection into a mature SAGD steam chamber at the dover project (formerly UTF). *J. Can. Petrol. Technol.* 43 (01), 8. doi:10.2118/04-01-06
- Yuan, J., Chen, J., Pierce, G., Wiwchar, B., Golbeck, H., Wang, X., et al. (2011). Noncondensable gas distribution in SAGD chambers. *J. Can. Petrol. Technol.* 50 (03), 11–20. doi:10.2118/137269-PA
- Zhang, K., Jia, N., Li, S., and Liu, L. (2018). Millimeter to nanometer-scale tight oil-CO<sub>2</sub> solubility parameter and minimum miscibility pressure calculations. *Fuel* 220, 645–653. doi:10.1016/j.fuel.2018.02.032
- Zhang, K., Jia, N., and Liu, L. (2019). CO<sub>2</sub> storage in fractured nanopores underground: phase behaviour study. *Appl. Energy.* 238, 911–928. doi:10.1016/j.apenergy.2019.01.088

**Conflict of Interest:** Author HB was employed by the company China National Aviation Fuel Southwest Storage & Transportation Co., Ltd.

The remaining authors declare that the research was conducted in the absence of any commercial or financial relationships that could be construed as a potential conflict of interest.

Copyright © 2020 Xu, Li, Li, Lu, Wu and Bai. This is an open-access article distributed under the terms of the Creative Commons Attribution License (CC BY). The use, distribution or reproduction in other forums is permitted, provided the original author(s) and the copyright owner(s) are credited and that the original publication in this journal is cited, in accordance with accepted academic practice. No use, distribution or reproduction is permitted which does not comply with these terms.



# Optimization Simulation Research on Middle-Deep Geothermal Recharge Wells Based on Optimal Recharge Efficiency

Song Deng<sup>1</sup>, Dingkun Ling<sup>1</sup>, Huijun Zhao<sup>1\*</sup>, Xin Shen<sup>1</sup>, Huajun Du<sup>2</sup> and Lu Liu<sup>1</sup>

<sup>1</sup>School of Petroleum Engineering, Changzhou University, Changzhou, China, <sup>2</sup>Shandong Ruiheng Xingyu Petroleum Technology Development Co. Ltd, Qingdao, China

## OPEN ACCESS

### Edited by:

Songyan Li,  
China University of Petroleum  
(Huadong), China

### Reviewed by:

Zhengming Xu,  
China University of Geosciences,  
China  
Zhi Ye,  
University of Oklahoma,  
United States

### \*Correspondence:

Huijun Zhao  
cczuzhj.geo@foxmail.com

### Specialty section:

This article was submitted to  
Advanced Clean Fuel Technologies,  
a section of the journal  
Frontiers in Energy Research

**Received:** 24 August 2020

**Accepted:** 30 September 2020

**Published:** 12 November 2020

### Citation:

Deng S, Ling D, Zhao H, Shen X, Du H  
and Liu L (2020) Optimization  
Simulation Research on Middle-Deep  
Geothermal Recharge Wells Based on  
Optimal Recharge Efficiency.  
Front. Energy Res. 8:598229.  
doi: 10.3389/fenrg.2020.598229

In order to solve the low recharge efficiency of middle and deep geothermal Wells, a thermo-hydro-mechanical (THM) model integrating geothermal production and reinjection was established, and the relationship model between recharge efficiency and production well temperature was built to obtain the optimal recharge efficiency. In view of the different well spacing between reinjection and production wells, the different well spacing between production wells and different reinjection well types, numerical simulation and comparative analysis were carried out under the optimal recharge efficiency. The results show that under the optimal recharge efficiency, the change in well spacing has the greatest impact on the exploitation of production wells. The well spacing of production wells is gradually reduced from 600 m to 20 m, and the time of thermal breakthrough in production wells is getting earlier and earlier. However, when the spacing between the production wells reach 200 m, thermal breakthrough hardly occurs. Compared with different well spacings, different reinjection well types have less impact on the exploitation of production wells, and the situation of production wells under one reinjection and two production is better than one reinjection and one production. Therefore, it is proposed that under the optimal recharge efficiency of 40.41–72.52%, the most suitable approach is to use one reinjection and two production as this well spacing between the reinjection and production well above 400 m, the well spacing between the production wells above 200 m and the reinjection wells of horizontal wells are optimal and most suitable for geothermal exploitation.

**Keywords:** Recharge efficiency, Well spacing, Thermal breakthrough, Reinjection well type, One reinjection and two production

## INTRODUCTION

In recent years, the decrease of traditional fossil energy storage and the environmental pollution that accompanies it has attracted widespread attention. The harmful substances produced by these traditional energy consumption processes are far more serious than expected (Mei et al., 2018; Shen et al., 2016; Kong et al., 2017). Renewable energy and geothermal energy could be widely used in many aspects such as heating, tourism and aquaculture by virtue of large energy potentials, sustainability, and convenient development and utilization (Gao, 2018; Xu, 2018). Geothermal resources can be divided into three types: bedrock fissure thermal storage, solution fissure thermal storage and sandstone pore thermal storage according to different thermal storage media and

recharge performance (Olasolo et al., 2016). Among them, unconsolidated sandstone reservoirs have a poor degree of rock cementation. During the development process, some problems may occur such as sand-carrying sand production and low recharge efficiency (Sedghi and Zhan, 2020). It is, therefore, necessary to study optimized designs for reinjection wells to improve the recharge efficiency of sandstone geothermal reservoirs. Reinjection is an effective protective measure: first, it can effectively treat the wastewater produced by geothermal heat, and to a certain extent, can avoid thermal pollution or pollution to the environment; second, it can help the geothermal reservoir to recover heat production and effectively improve the utilization rate of geothermal resources; third, it can maintain the pressure of geothermal reservoirs, effectively stabilizing the mining conditions of geothermal resources, and preventing ground subsidence (Liu, 2003).

Scholars all over the world have researched the optimal design for the layout of reinjection wells. For example, Yan Fang Ping compared the recharge efficiency under two different recharge modes, and different reinjection layout schemes according to the results of a simulation (Yan, 2020). Sun Jian ping and Xu Rui jian used different recharge arrangements to conduct single-well recharge tests for confined aquifers in a certain area (Sun et al., 2020). CHÁVEZ Oscar and GODÍNEZ Francisco performed numerical simulations on the thermal behavior of Mexico's geothermal reservoirs, calculated the optimal reinjection-production well distance and a variety of different configuration methods (Chávez and Godínez, 2020). In order to reduce the probability of thermal breakthrough in production wells, Liu G and Wang G proposed the arrangement of clustered wells, and the results showed that the clustered well pattern would have better results (Liu et al., 2020). Alexandros Daniilidis analyzed the influence of physical parameters, design parameters and operating parameters on the productivity performance of the geothermal system, and summarized the best parameter settings (Daniilidis et al., 2020). Zhu Jialing studied the influence of the pressure difference between geothermal reinjection wells on the recharge efficiency, and proposed guidelines on 'the appropriate spacing of the extraction and reinjection wells for porous thermal storage (Zhu et al., 2012).

Most of them study the layout of reinjection wells aimed to improve the utilization rate of geothermal resources or the heat recovery rate, but research on the optimal design of the reinjection well layout based on the optimal recharge efficiency has rarely been studied. The numerical simulation of geothermal production and recharge involves multiple processes, including the heat transfer process between geothermal water, the thermal reservoir and wellbore, the heat transfer process between the wellbore and thermal reservoir, and the flow process of geothermal water and thermal reservoir and wellbore, etc. These require multiphysics coupling but these studied rarely involve multiphysics coupling. COMSOL users are more inclined to study the impact of fractures on geothermal production. There is less researches on the optimization design of well type and well spacing for the efficiency of middle-deep

geothermal recharge. In response, this paper established a THM multi-field coupling model for medium and deep geothermal recovery and irrigation. According to the fitting equation of the recharge efficiency and the temperature of the production well, an optimal recharge efficiency range was obtained. Using COMSOL software, the geothermal recovery was performed under the optimal recharge efficiency. The layout of the reinjection wells was simulated, and the well type, well spacing and well layout method were optimized to provide guidance for solving the problem of low recharge efficiency of middle-deep sandstone thermal storage.

## GEOHERMAL MULTI-FIELD COUPLING MODEL ESTABLISHMENT

### Hypothesis Conditions

Based on sandstone fractured thermal reservoirs, this paper establishes a THM model for reservoir reconstruction. The reservoir is divided into three layers with different hydraulic and thermal properties. The sandstone fractured thermal reservoir is simplified as a rock block-fracture dual medium. The rock block is used as a porous medium with low permeability, and the physical property changes of the rock block are not considered. The fracture can also be used as the main flow channel of geothermal water. Assuming that the water in the hydrothermal reservoir is saturated with single-phase water, the flow of water is laminar, which conforms to Darcy's law. The geothermal water in the cracks produces heat exchange and transfer by convection and conduction, which conforms to Fourier's law. It is Assumed that the temperature difference between the solid and liquid phases is small, that it is locally in a state of thermal equilibrium that gravity, the capillary force has no effect on the flow, and that the fluid does not react chemically with the rock mass.

### Governing Equation

According to the theory of THM, the seepage and heat transfer in the model are described, including the seepage field, temperature field equation and water flow continuity equation, as shown below:

#### (1) Seepage field equation

The seepage field equation of the rock:

$$S \frac{\partial p}{\partial t} + \nabla \cdot u = - \frac{\partial e}{\partial t} + Q \quad (1)$$

$$u = - \frac{\kappa}{\eta} (\nabla p + \rho g \nabla z) \quad (2)$$

The seepage field equation of the fracture:

$$d_f S_f \frac{\partial p}{\partial t} + \nabla_r \cdot \left( - d_f \frac{\kappa_f}{\eta} \nabla p \right) = - d_f \frac{\partial e_r}{\partial t} + Q_r \quad (3)$$

**TABLE 1** | Control equation parameters.

Type	Symbol/(Unit)	Type	Symbol/(Unit)
Time	$t/(s)$	Specific heat capacity	$c/(J/(kg \cdot K))$
Flow rate	$u/(m/s)$	Heat source	$W/(W/m^3)$
Permeability	$\kappa/(m^2)$	Density	$\rho/(kg/m^3)$
Dynamic viscosity	$\eta/(Pa \cdot s)$	Thermal conductivity	$\lambda/(W/(m \cdot K))$
Water storage coefficient	$S/(Pa^{-1})$	Fracture water specific heat capacity	$c_s/(J/(kg \cdot K))$
Volume strain	$e$	Fracture water temperature	$T_f/(K)$
Seepage sink source	$Q/(s^{-1})$	Fracture water absorbs heat	$W_f/(W/m^2)$
Crack width	$d_f/(m)$	Fracture water density	$\rho_f/(kg/m^3)$
Heat exchange	$Q_f$	Water heat transfer coefficient	$\lambda_f/(W/(m \cdot K))$
Crack surface normal	$n$	Heat transfer coefficient	$h/(W/(m^2 \cdot K))$
Derivation along crack tangent	$\nabla_\tau$		

$$Q_\tau = \frac{\kappa_r}{\eta} \frac{\partial p}{\partial n} \quad (4)$$

In the formula, the subscript  $f$  is expressed as fracture.

## (2) The temperature field equation

### The Rock Temperature Field Equation:

$$c_s \rho_s \frac{\partial T_s}{\partial t} = \lambda_s \nabla^2 T_s + W \quad (5)$$

In the formula, the subscript  $s$  represents rock.

Because of the low porosity, the flow rate of water in the rock is low, and the water temperature can be considered equal to the temperature of the rock, so the convection in the pores of the rock is not considered.

### The Fracture Water Temperature Field Equation

$$d_f \rho_f c_f \frac{\partial T_f}{\partial t} + d_f \rho_f c_f \nabla_\tau T_f = d_f \nabla_\tau \cdot (\lambda_f \nabla_\tau T_f) + W_f \quad (6)$$

$$W_f = h(T_s - T_f) \quad (7)$$

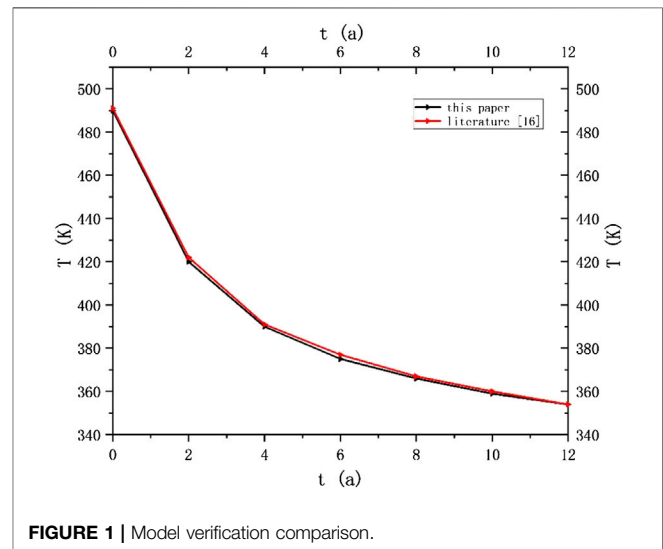
## (3) Continuity equation

$$\frac{\partial(\varepsilon \rho)}{\partial t} + \nabla \cdot (\rho u) = 0 \quad (8)$$

The parameters in the formula are shown in **Table 1**:

### Coupling Relationship

The coupling effect of the temperature field on the seepage field is mainly reflected in the change of the physical parameters of the fluid. Under the action of high temperature and high pressure, the

**FIGURE 1** | Model verification comparison.

density of water will not be a constant, and can generally be expressed as a function of temperature and pressure (Zhao, 2010):

$$\frac{1}{\rho_f} = 3.086 - 0.899017(4014.15 - T)^{0.147166} - 0.39(658.15 - T)^{-1.6}(p - 225.5) + \delta \quad (9)$$

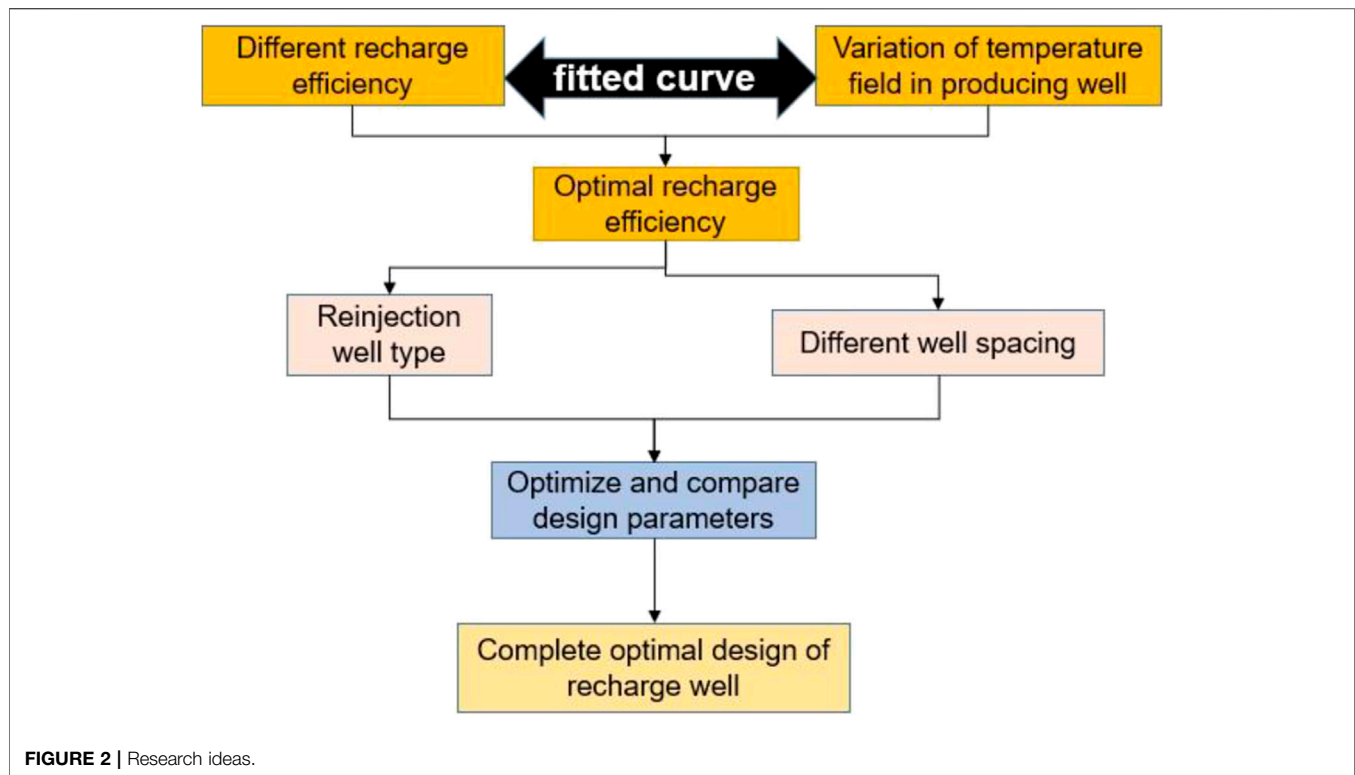
In the formula,  $T$  represents the absolute temperature of water;  $\delta$  represents the function of water temperature and pressure;  $p$  represents pressure.

The influence of water temperature on the dynamic viscosity of water cannot be ignored. The dynamic viscosity of water:

$$\eta = \nu \rho_f \quad (10)$$

In the formula,  $\nu$  represents the kinematic viscosity coefficient of water.

Both the density and viscosity of water are related to temperature, and temperature changes will directly affect the two processes of seepage and heat transfer, and their role is a strong coupling relationship.



## Model Reliability Verification

To verify the reliability of the model, it was applied to Tang classic THM model (the fluid heat transfer between fracture and fault is the process of heat transfer by convection and heat conduction) to calculate the output temperature (Tang et al., 2016), the model parameters are the same as those, and the calculation results are shown in **Figure 1**. By comparison, it is found that the calculation results in this paper are similar to the calculation results in (Tang et al., 2016), and the numerical difference is small, which, to some extent, proves the reliability of this model.

## Concept

### (1) Thermal breakthrough

The so-called Thermal Breakthrough refers to the production wells' pumping of groundwater and recharging of low-temperature water in the reinjection area. Due to the production wells' pumping, the low-temperature water will generate convection, which will lead to the migration of the cold water front to the hot water area at a certain speed, and eventually lead to the decrease of the temperature at the production wells. The occurrence of thermal breakthrough will reduce the operating efficiency of production well, so the occurrence of thermal breakthrough should be avoided or the time of thermal breakthrough should be delayed.

### (2) "One reinjection and one production" and "One reinjection and two production"

"One reinjection and one production" means that the number of reinjection wells and production well is 1:1, and "One reinjection and two production" mean that the number of reinjection wells and production wells is 1:2. For the sake of convenience, "One reinjection and one production" and "One reinjection and two production" are used to replace these two statements.

## EXAMPLE MODEL

### Research Methods

This paper studies the influence of different well type designs on recharge efficiency. The calculation method of recharge efficiency is listed as follows:

$$\gamma = \frac{Q_1}{Q_2} \cdot \frac{\eta_2}{\eta_1} \quad (11)$$

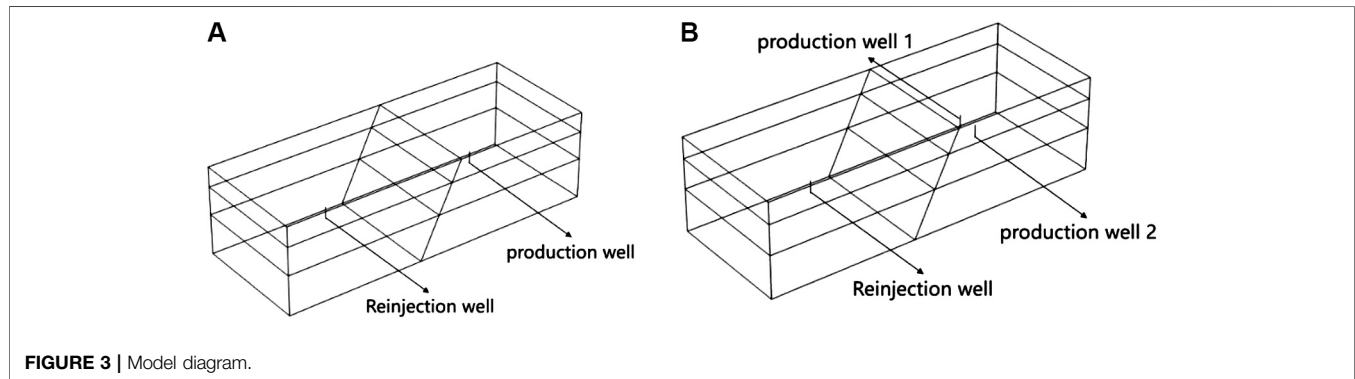
In the formula,  $Q_1$ ,  $Q_2$  represents the recharge volume and pumping volume respectively, and  $\eta_1$ ,  $\eta_2$  represents the number of production wells and reinjection wells respectively.

The specific idea of the study is shown in **Figure 2**. The main method is to change the recharge efficiency, fit the relationship between different recharge efficiency and the temperature change of the production well, calculate the optimal recharge efficiency according to the fitted curve, and study under the optimal recharge efficiency. Different reinjection well types, different well spacing and different design parameters, and finally the best design plan is selected.



**TABLE 2** | Geological parameters.

	Upper strata	Middle strata	Lower strata	Fracture
Thermal Conductivity ( $W/(m \cdot K)$ )	2	2	3.5	3
Density ( $kg/m^3$ )	1500	1800	2300	1200
Constant pressure heat capacity ( $J/(kg \cdot K)$ )	900	850	910	800
Porosity	0.26	0.25	0.12	0.60
Permeability ( $m^2$ )	$6.75 \times 10^{-11}$	$6.25 \times 10^{-11}$	$9 \times 10^{-12}$	

**FIGURE 3** | Model diagram.

## Calculation Model

Taking the geothermal exploitation and utilization development zone in North China as the research area, and based on the thermal storage depth of 1100 m in this area, a geothermal thermal reservoir model was established. The model includes three geological layers and a fracture surface as well as different numbers of production wells and reinjection wells.

The three geological layers and fractures have different thermal and hydraulic characteristics, and the specific parameters are shown in **Table 2**. The top and bottom boundaries are both defined as impervious layers. The different design methods of the two wells for irrigation and irrigation are shown in **Figure 3**, including one reinjection and one production (as shown in **Figures 3A**), one reinjection and multiple productions (as shown in **Figures 3B**).

The model uses a free tetrahedron for finer mesh division. The full mesh of the one reinjection and one production model contains 36,797 domain elements, 5,033 boundary elements and 426 edge elements; the full mesh of the one reinjection and multiple production model contains 37,463 domain elements, 5,067 boundary elements and 429 edge elements. The full mesh of the one reinjection and multiple production model contains 37,463 domain elements, 5,067 boundary elements, and 429 edge elements. Among them, the configuration of reinjection wells includes vertical well, inclined well, and horizontal well. The production wells are only vertical wells. The spacing between production and reinjection well includes 20, 100, 200, 300, 400, 500, and 600 m. The pumping volume is always maintained at 5 kg/s, and the recharge volume will be changed according to a change in recharge efficiency. There are three settings for the recharge efficiency: 100, 80, and 60%. The thermal breakthrough time is limited to 2 K.

**TABLE 3** | Model parameters.

Size(m)	800*300*300	Surface temperature (K)	285
Upper depth (m)	880–930	Ground ladder temperature (K/m)	0.03
Middle depth (m)	930–1000	Head (mm/m)	$1 \times 10^{-3}$
Lower depth (m)	1000–1100	Recharge water temperature (K)	280
Well radius (m)	0.25	Crack thickness (m)	$2 \times 10^{-3}$
Well section length (m)	30	Well depth (m)	910

## Parameter Setting

The relevant parameters of the model, the thermal and hydraulic characteristics of geological layers and fractures are shown in **Table 3** and **Table 2** below.

## THE RELATIONSHIP BETWEEN RECHARGE EFFICIENCY AND TEMPERATURE FIELD CHANGES

**Figure 4** shows the temperature curves of production wells at different levels of recharge efficiency when the spacing between production and reinjection well (vertical well) is 100, 300, and 500 m and the spacing between production wells is 100 m. It can be seen from **Figure 4** that the temperature change curves of production well 1 and production well 2 in the case of one reinjection and two production almost overlap, so the production well in the case of one reinjection and one production and the temperature change curve of the above production well 1 are selected for analysis.

As is shown in **Figure 4**, the temperature decline trend is almost the same, but the decline is greater in the case of one

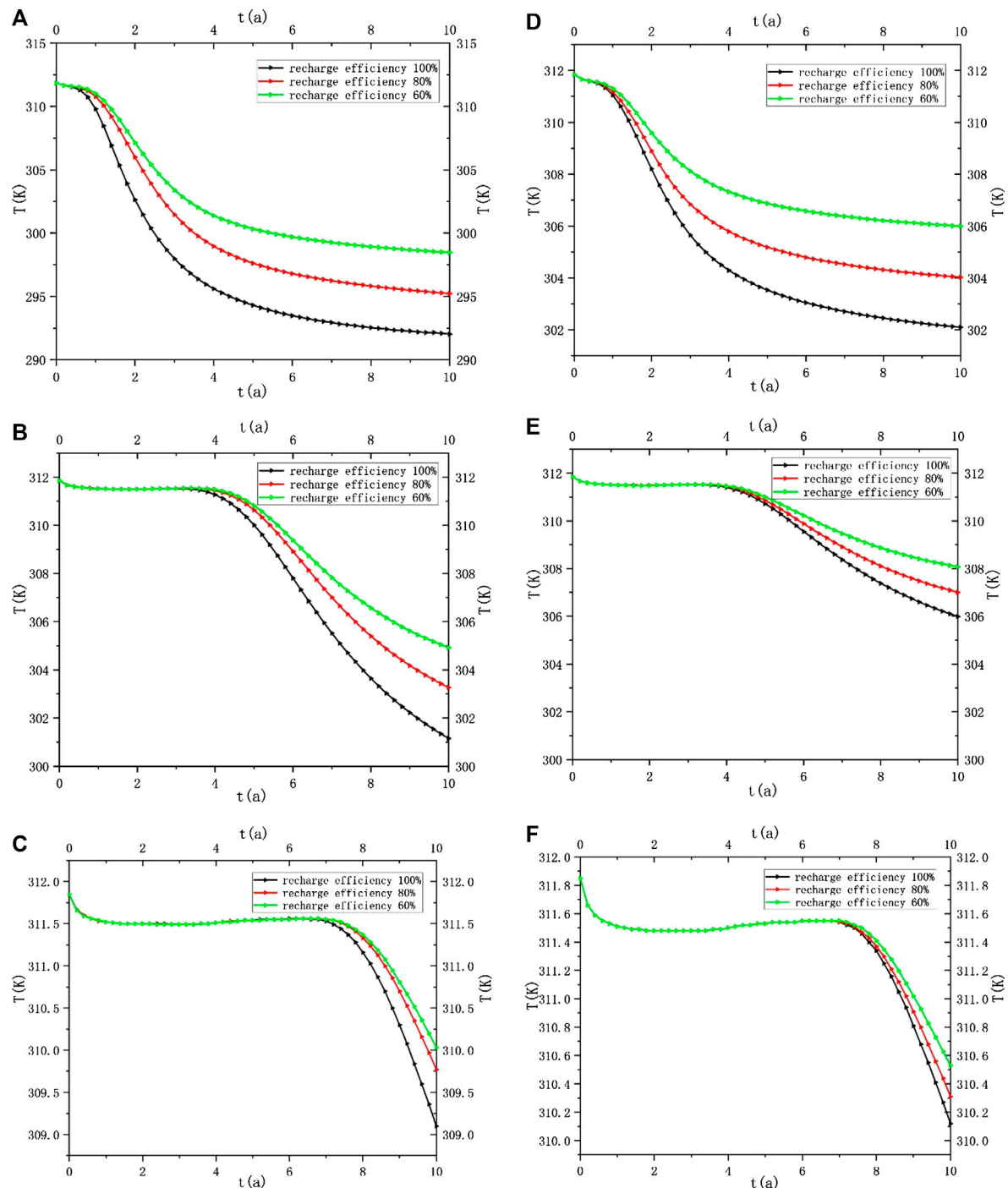
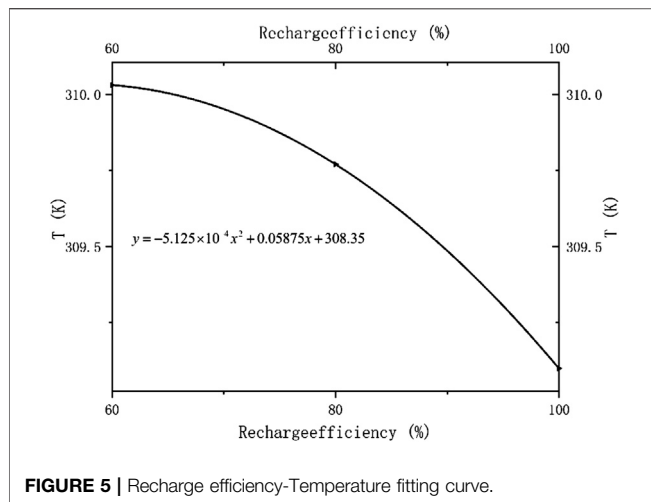


**FIGURE 4 |** Temperature changes of production wells under different recharge efficiency. **(A)** Temperature change of one reinjection and one production with a well spacing of 100 m. **(B)** Temperature change of one reinjection and one production with a well spacing of 300 m. **(C)** Temperature change of one reinjection and one production with a well spacing of 500 m. **(D)** Temperature change of one reinjection and two production with a well spacing of 100 m. **(E)** Temperature change of one reinjection and two production with a well spacing of 300 m. **(F)** Temperature change of one reinjection and two production with a well spacing of 500 m.

reinjection and one production. When the well spacing is 500 m, the water temperature in the reinjection well has little effect on the water temperature of the production well. It took 8 years to see a significant drop in temperature and the drop was only about

2 K. However, with the reduction of the well spacing to 100 m, the influence of the water temperature of the reinjection wells on the production wells became greater and greater, and even thermal breakthroughs occurred.



It can be seen from **Figure 4** that the temperature decrease trend of production wells is the same, but the temperature drop of production wells will decrease as the recharge efficiency increases. Compared with 60% recharge efficiency, at 100% recharge efficiency, the minimum temperature of production well 1 under the condition of one reinjection and one production is 6.44 K lower, and the lowest temperature of production well 1 under the condition of one reinjection and two production is also 3.91 K lower. This is because the setting of the recharge efficiency is determined by the ratio of recharge volume to pumping volume. In the case of one reinjection and one production, and one reinjection and two production, the lower the recharge efficiency, the lower the recharge volume. The increase in the amount of recharge will shorten the time for the cold front to reach the production well and accelerate the occurrence of thermal breakthroughs in the production well, resulting in a larger drop in its temperature. However, with the increase of the well spacing, the decrease is getting smaller and smaller.

To better characterize the relationship between recharge efficiency and temperature field, take different recharge efficiencies as the abscissa and the lowest temperature of the production well as the ordinate, and use the trend line to fit the data to get the Recharge efficiency-Temperature fitting equation. Fitting equation:

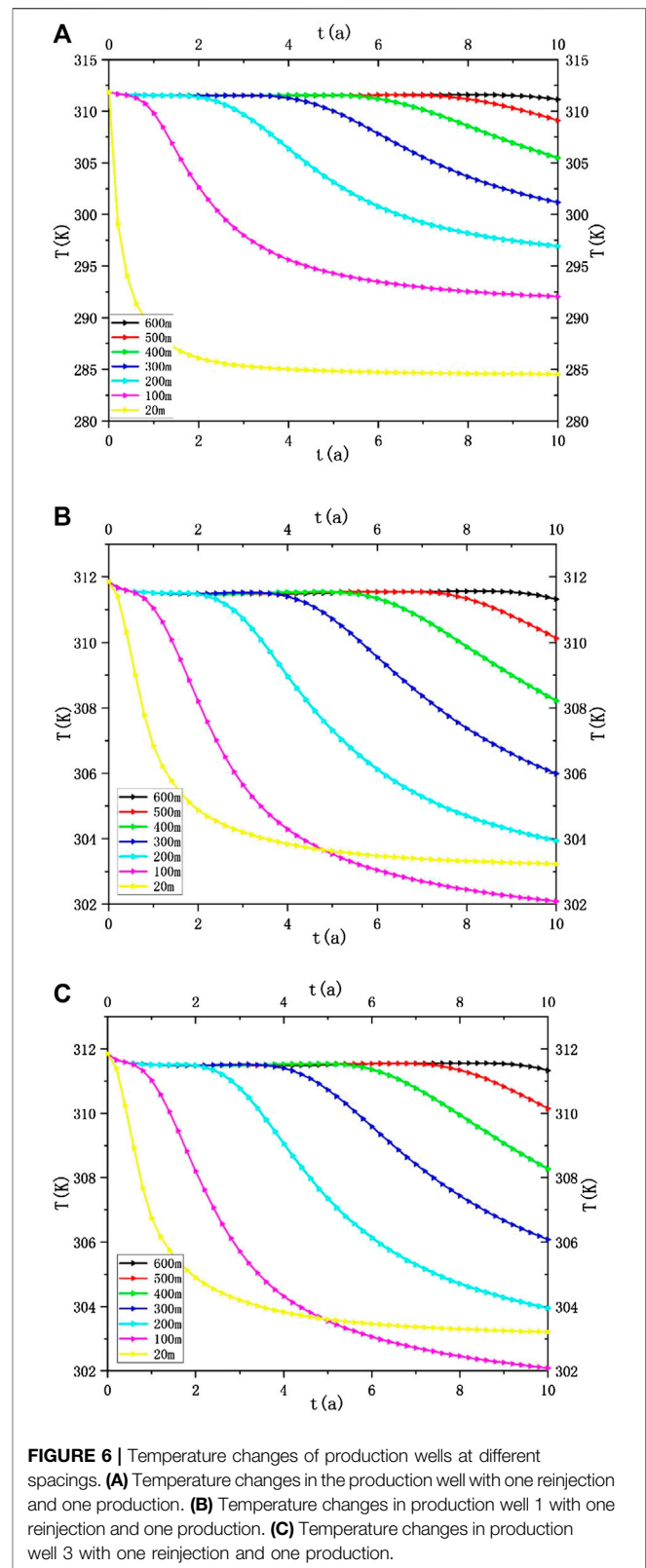
$$y = -5.125 \times 10^{-4}x^2 + 0.05875x + 308.35$$

Decisive factor:

$$R^2 = 0.998$$

**Figure 5** shows the fitting curve of recharge efficiency and temperature change. The fitting equation can be used to calculate when the temperature of the production well is reduced by 2 K. The optimal recharge efficiency that can avoid thermal breakthrough is 40.41–72.52%.

The following research is based on the optimal recharge efficiency obtained by the curve and analyzes the relationship between different well spacing, well type, and temperature field



and thus, obtains the well spacing between the production and reinjection well, and the well spacing between the production and production well under the optimal recharge efficiency. The best

design plan for the well spacing between the well and the well type of the reinjection well.

## RESULTS AND DISCUSSION

### Analysis of Temperature Field Changes in Different Well Spacing

#### Temperature Changes Under Different Well Spacings Between Production and Reinjection Wells

In order to analyze the influence of different production and reinjection wells on the temperature field of the reservoir under different well spacings, the situation of one irrigation and one production, one irrigation and two production was simulated, and the temperature changes of production wells under different production and rejection well spacings were simulated. It is fixed as a vertical well, and the calculation result is shown in **Figure 6**.

It can be seen from **Figure 6A** that in one reinjection and one production, after the well spacing reaches 600 m, the water temperature of the production well has a very small drop within 10 years, about 1 K, and no thermal breakthrough occurred. When the well spacing reached 500 m, the production well had a thermal breakthrough at 9.50 a. As shown in **Figures 6B, C**, in the case of one reinjection and two production, the decline of the two production well is smaller than that of one reinjection and one production, only 0.50 K, and the curves of production well 1 and production well 2 almost overlap, with only slight differences. Thermal breakthrough did not occur when the well spacing was 500 m, but after the well spacing was reduced to 400 m, a thermal breakthrough occurred in 8 a. Compared with one reinjection and one production, the overall temperature change range of the production well with one reinjection and two production is relatively small, with a temperature difference ranging from 0 to 9.76 K, while the former reaches 27.32 K. The difference is that one reinjection and two production have the lowest temperature when the well spacing is 100 m, while the one reinjection and one production reaches the lowest temperature when the well spacing is 20 m.

It can be seen from **Figure 6** that when the well spacing reaches 20 m, the thermal breakthrough takes place very quickly in both cases, and both occurred within a short period of 1 a. When the well spacing is gradually reduced from 600 to 400 m, the temperature of the production wells does not change significantly. This is because the migration resistance of the recharged water is large, and the water flow rate is slow, so interference in the production wells is small. At the same time, the larger the well spacing, the longer it takes for the recharged water to absorb the heat in the thermal reservoir during the migration process, which can fully exchange heat with geothermal fluid, and prolong the thermal breakthrough time. When the well spacing was reduced to 100 m, the water temperature in both cases dropped significantly after 2 a. This is because the circulation channel between the recharge water and the geothermal water was greatly shortened, and the cold front reached production. The speed of the well became faster, and a thermal breakthrough occurred, resulting in a significant drop in the water temperature of the production well.

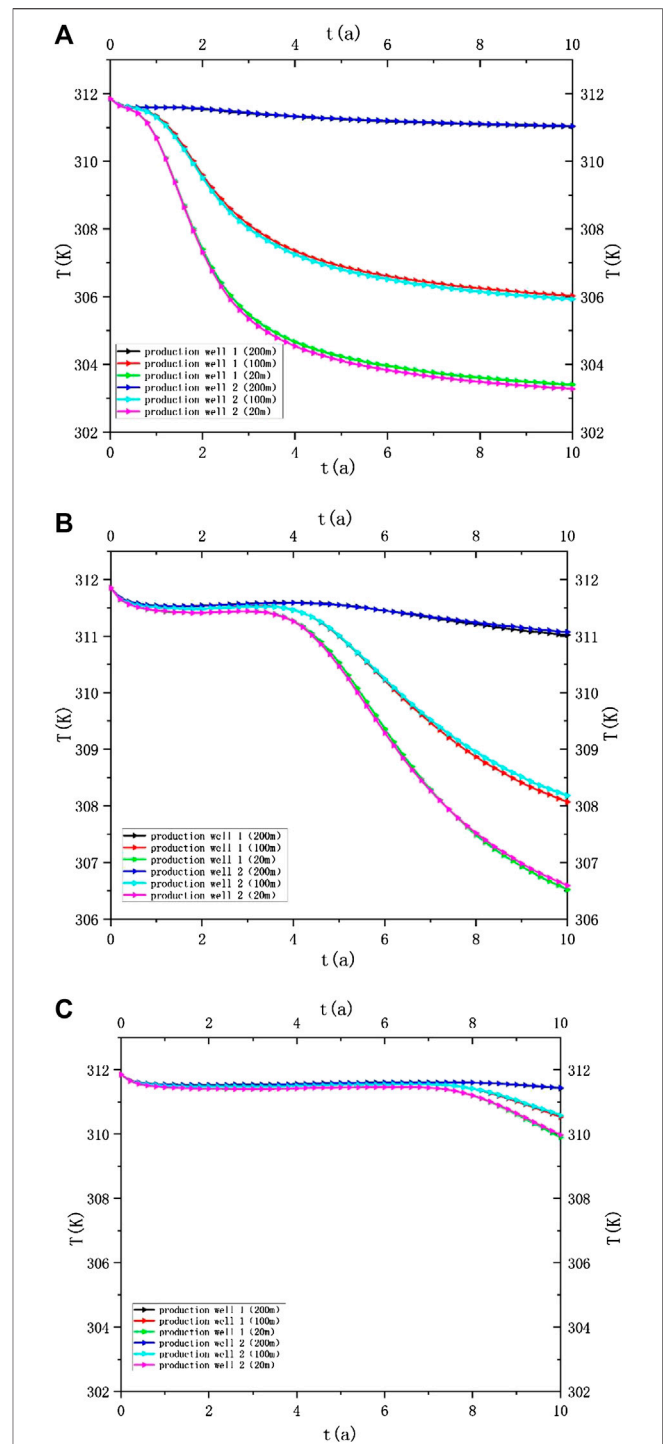


**FIGURE 7 |** Temperature changes of production wells 1 and 2 under different spacings between production wells. **(A)** Temperature changes of production well 1 and 2 at a distance of 100 m between production and reinjection wells. **(B)** Temperature changes of production well 1 and 2 at a distance of 300 m between production and reinjection wells. **(C)** Temperature changes of production well 1 and 2 at a distance of 500 m between production and reinjection wells.

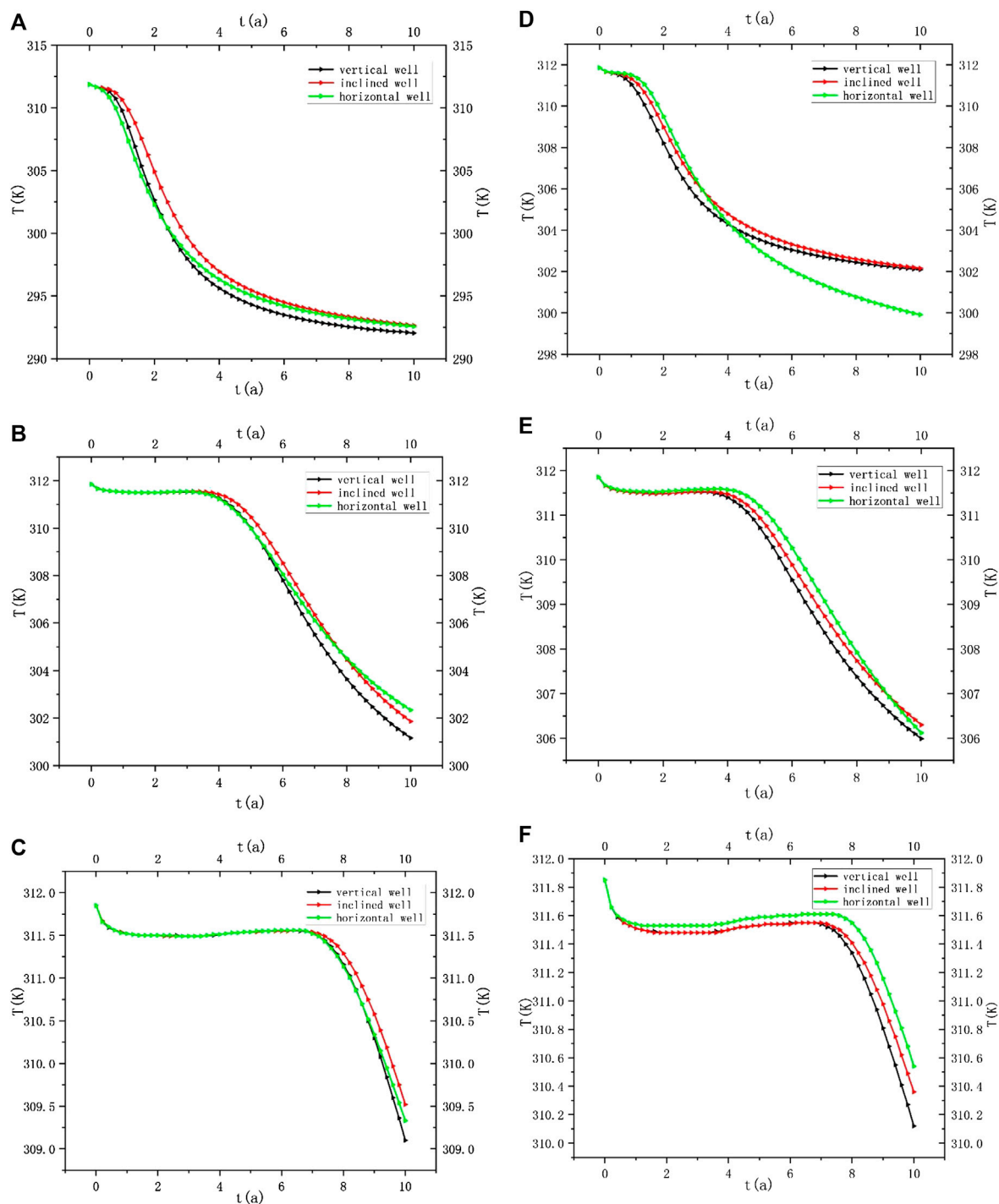


**FIGURE 8 |** Temperature changes of production wells under different reinjection well types. **(A)** Temperature change of one reinjection and one production with a well spacing of 100 m. **(B)** Temperature change of one reinjection and one production with a well spacing of 300 m. **(C)** Temperature change of one reinjection and one production with a well spacing of 500 m. **(D)** Temperature change of one reinjection and two production with a well spacing of 100 m. **(E)** Temperature change of one reinjection and two production with a well spacing of 300 m. **(F)** Temperature change of one reinjection and two production with a well spacing of 500 m.



## Temperature Changes of Production Wells Under Different Spacings Between Production Wells

**Figure 7** shows the relationship between temperature changes in production wells that are caused by different spacings between production wells when the well spacing between the production and reinjection well is 100, 300, and 500 m, and the reinjection well is a vertical well, in the case of one reinjection and two production.

It can be seen from **Figure 7** that the temperature change curves of the two production wells in the case of one reinjection and two production basically overlap, and the length of the thermal breakthrough is mainly determined by the well spacing between the production and reinjection well. It can be seen that as the well spacing between the production wells increases to 500 m, the thermal breakthrough time of the production wells is greatly delayed. However, the increase in the spacing between the production wells also causes a delay in the thermal breakthrough time of the production wells, especially after reaching 200 m, after which point the temperature of the production wells hardly changes, and the change range is only 0.82 K. When the spacing between production and reinjection wells is 500 m and the spacing between production wells is 200 m, the temperature variation of the production wells is the smallest. This is because the time for the recharge water to move to the production well becomes longer, which leads to a longer time for its heat absorption in the thermal reservoir, and the distance between the two production wells also provides certain conditions for the warming of the recharge water.

The well spacing between production wells has no less impact on the thermal breakthrough time of production wells than the well spacing between production wells. Therefore, when designing the layout of production wells, attention should be paid to the setting of well spacing between production wells and should be maintained above 200 m.

## Analysis of Temperature Field Changes of Different Reinjection Well Types

Due to the complexity of stratum properties, there are many choices for well types of reinjection wells. To study the impact of reinjection well types on the temperature changes of a production well, we simulated the well spacing between reinjection and production well at 500, 300, and 100 m, and the spacing between production wells at 100 m, examining different reinjection well types (vertical, 45° inclined and horizontal well). The calculation results are shown in **Figure 8** for the temperature changes of production wells under the vertical, 45° inclined, and horizontal wells.

As shown in **Figure 8**, different reinjection well types have a certain impact on the temperature of the production well, and the trend of the temperature change curves of the production wells are similar. However, compared with different recharge efficiency and different well spacing, the influence law of the reinjection well type is not uniform. As shown in **Figures 8A–C** in the case of one reinjection and one production, the 45° inclined well has the smallest impact on the temperature change of the production well under different well spacings, while **Figures 8D–F** show one

reinjection and two production, and horizontal wells have the least impact. In short, the temperature variation range of vertical downhole production wells is the largest, and this becomes more obvious as the well spacing increases.

The three different reinjection well types have little effect on the temperature change of production wells under high well spacing because the change range is only 0.41 K in 10 a, and the change curves before 10 a are almost coincident. Compared with the well spacing, the reinjection well type has a smaller effect on the temperature of the production well, but when the well spacing reaches 500 m, the use of horizontal wells is best.

In the process of geothermal exploitation, the scheme of one reinjection and two production is adopted, and the well spacing between the reinjection and production well is maintained at more than 400 m, and the well spacing between production wells is maintained at more than 200 m. The use of horizontal wells for reinjection wells is more conducive to geothermal exploitation.

## CONCLUSION

This comprehensive analysis examines well spacings, well types, and different well layout methods under the optimal recharge efficiency change relationship diagram. The fitting equation between the recharge efficiency and the temperature change of the production well was established by COMSOL, and an optimal recharge efficiency was obtained. The optimal recharge efficiency is determined for different well spacings between reinjection and production wells, different well types, and production well layout methods. The simulation was performed under recharge efficiency, and the following conclusions were obtained:

- (1) The well spacing between the reinjection and production wells has the greatest impact on the temperature changes of the production wells. When it is gradually reduced from 600 to 400 m, the temperature change of the production wells is not obvious, but when it is further reduced to 20 m, a thermal breakthrough occurred at 0.20 a, and the temperature change range increased sharply. The well spacing between production wells also has a certain effect on temperature change. When the well spacing of the production well reaches 200 m, a thermal breakthrough hardly occurs. The closer the spacing of the production well, the faster a thermal breakthrough will occur faster.
- (2) Although different reinjection well types will have a certain impact on the temperature changes of production wells, as the well spacing increases, the impact will become smaller and smaller. However, the situation of one reinjection and two production is better than one reinjection and one production. Regardless of whether it is from a different well spacing or different well types, the production wells with one reinjection and one production have a faster thermal breakthrough than one reinjection and two production.
- (3) Based on the above research, to improve the recharge efficiency of geothermal wells, attention should be paid to the configuration of the well spacing, as well as the number ratio of production

wells and reinjection wells. Within the range of the optimal recharge efficiency of 40.41–72.52%, the design scheme for using one reinjection two production, the well spacing between reinjection and production wells is more than 400 m, the well spacing between production wells is more than 200 m, and the reinjection wells are horizontal wells is optimal.

## DATA AVAILABILITY STATEMENT

The original contributions presented in the study are included in the article/supplementary materials, further inquiries can be directed to the corresponding author/s.

## AUTHOR CONTRIBUTIONS

SD, DL, and HZ participated in the design of this study. DL performed the statistical analysis and carried out the study. XS and LL collected important background information. HD provided

assistance for data acquisition. DL drafted the manuscript. All authors read and approved the final manuscript.

## ACKNOWLEDGMENTS

The authors gratefully acknowledge the financial support from: (1) Study on deep geothermal wellbore instability under large temperature difference of Changzhou Applied Basic Research Program (fund number CJ20190060); (2) The National Natural Science Foundation of Jiangsu Province under the project Study on deformation behavior and instability mechanism of surrounding rock in medium-deep geothermal drilling (fund number BK20180959); (3) State key Research and development program Unconsolidated sandstone thermal reservoir protection and efficiency drilling and completion technology and materials (fund number 2019YFB1504201).

## REFERENCES

- Chávez, O., and Godínez, F. (2020). Polygeneration study of low-to-medium enthalpy geothermal reservoirs in Mexico. *J. Therm. Sci.* doi:10.1007/s11630-020-1271-9
- Daniilidis, A., Nick, H. M., and Bruhnac, D. F. (2020). Interdependencies between physical, design and operational parameters for direct use geothermal heat in faulted hydrothermal reservoirs. *Geothermics* 86, 101806. doi:10.1016/j.geothermics.2020.101806
- Gao, X. (2018). *Research on evaluation Model of pore sandstone thermal storage and recharge capacity in Tianjin*. Beijing, China: China University of Geosciences.
- Kong, Y., Pang, Z., Shao, H., and Kolditz, O. (2017). Optimization of well-doublet placement in geothermal reservoirs using numerical simulation and economic analysis. *Environ. Earth Sci.* 76, 118. doi:10.1007/s12665-017-6404-4
- Liu, G., Wang, G., Zhao, Z., and Ma, F. (2020). A new well pattern of cluster-layout for deep geothermal reservoirs: case study from the Dezhou geothermal field, China. *Renew. Energy* 155, 484–499. doi:10.1016/j.renene.2020.03.156
- Liu, J. R. (2003). Development status of geothermal recharge. *Shuiwen Dizhi Gongcheng Dizhi* 30 (3), 100–104. doi:10.3969/j.issn.1000-3665.2003.03.025
- Mei, B., Guo, L., Wang, P., et al. (2018). Technology and Application progress of Geothermal well tail water recharge. *CN Res Comprehensive Util.* 36 (01), 168–170. doi:10.3969/j.issn.1008-9500.2018.01.061
- Olasolo, P., Juárez, M. C., Morales, M. P., D'Amico, S., and Liarte, I. A. (2016). Enhanced geothermal systems (EGS): a review. *Renew. Sustain. Energy Rev.* 56, 133–144. doi:10.1016/j.rser.2015.11.031
- Sedghi, M. M., and Zhan, H. (2020). Semi-analytical solutions of discharge variation of a qanat in an unconfined aquifer subjected to general areal recharge and nearby pumping well discharge. *J. Hydrol.* 584, 124691. doi:10.1016/j.jhydrol.2020.124691
- Shen, J., Wang, L., and Zhao, Y.-T. (2016). Exploration and Analysis of well formation technology for Sandstone pore type recharging Wells--A Case study of guantao Formation heat storage in Binhai New District, Tianjin. *CN Real Estate* 21, 75–80. doi:CNKI:SUN:GFCD.0.2016-21-010
- Sun, J.-P., Xu, R.-J., Jiang, Z.-B., et al. (2020). Study on single-well atmospheric recharge at confined aquifer site in Jinan. *J Shandong Jianzhu Univ.* 35 (03), 7–12. doi:10.12077/sdjz.2020.03.002
- Tang, Z., Changhua, M., Zhang, X., et al. (2016). Numerical Simulation and Analysis of Thermal-solid flow coupling in enhanced geothermal systems. *Beijing Gongye Daxue Xuebao* 42 (10), 1560–1564.
- Xu, Y. (2018). *Simulation and Prospect of pore-type geothermal tailwater recharge in sanqiao area, xi'an*. Xi'an, China: Chang'an University.
- Yan, F. (2020). Numerical Simulation study on improving recharge rate of porous geothermal reservoirs. *Neimenggu Shiyu Huagong* 46 (02), 9–13. doi:CNKI:SUN:NMSH.0.2020-02-004
- Zhao, Y. (2010). *Multi-field coupling of porous media and its engineering response*. Beijing, China: Science Press.
- Zhu, J., Zhu, X., and Lei, H. (2012). Analysis of the influence of pressure difference compensation between geothermal recharging Wells on recharging efficiency. *Acta Solar Energy* 33 (01), 56–62. doi:10.3969/j.issn.0254-0096.2012.01.010

**Conflict of Interest:** Author HD employed by the company Shandong Ruiheng Xingyu Petroleum Technology Development Co. Ltd.

The remaining authors declare that the research was conducted in the absence of any commercial or financial relationships that could be construed as a potential conflict of interest.

Copyright © 2020 Ling, Deng, Zhao, Shen, Du and Liu. This is an open-access article distributed under the terms of the Creative Commons Attribution License (CC BY). The use, distribution or reproduction in other forums is permitted, provided the original author(s) and the copyright owner(s) are credited and that the original publication in this journal is cited, in accordance with accepted academic practice. No use, distribution or reproduction is permitted which does not comply with these terms.



# Productivity Prediction Model for Stimulated Reservoir Volume Fracturing in Tight Glutenite Reservoir Considering Fluid-Solid Coupling

Leng Tian<sup>1,2</sup>, Xiaolong Chai<sup>1,2,\*</sup>, Peng Wang<sup>1,2</sup> and Hengli Wang<sup>1,2</sup>

<sup>1</sup> State Key Laboratory of Petroleum Resources and Prospecting, China University of Petroleum (Beijing), Beijing, China, <sup>2</sup> Institute of Petroleum Engineering, China University of Petroleum (Beijing), Beijing, China

## OPEN ACCESS

### Edited by:

Kaiqiang Zhang,  
Imperial College London,  
United Kingdom

### Reviewed by:

Cong Xiao,  
Delft University of Technology,  
Netherlands  
Yulong Zhao,  
Southwest Petroleum University,  
China  
Jinghong Hu,  
China University of Geosciences,  
China

### \*Correspondence:

Xiaolong Chai  
982026645@qq.com

### Specialty section:

This article was submitted to  
Advanced Clean Fuel Technologies,  
a section of the journal  
Frontiers in Energy Research

**Received:** 18 June 2020

**Accepted:** 24 August 2020

**Published:** 13 November 2020

### Citation:

Tian L, Chai X, Wang P and Wang H  
(2020) Productivity Prediction Model  
for Stimulated Reservoir Volume  
Fracturing in Tight Glutenite Reservoir  
Considering Fluid-Solid Coupling.  
Front. Energy Res. 8:573817.  
doi: 10.3389/fenrg.2020.573817

At present, the main development mode of “horizontal well + volume fracturing” is adopted in a tight glutenite reservoir. Due to the existence of conglomerate, the seepage characteristics are more complex, and the production capacity after volume fracturing is difficult to predict. In order to solve this problem, a dual media unstable seepage model was established for matrix seepage and discrete fracture network seepage when considering the trigger pressure gradient. By considering the Poisson’s ratio of stress sensitivity in an innovative way, the coupling model of permeability and stress is improved, and the production prediction model of volume fracturing horizontal well in a tight glutenite reservoir based on the fluid-solid coupling effect is formed. The finite element method is used to numerically solve the model, and the fitting verification of the model is carried out; the impact of stress sensitivity, producing pressure difference, fracture length, number of fracture clusters and fracture flow capacity conductivity on productivity is analyzed, which has certain guiding significance for the efficient development of volume fracturing in a tight glutenite reservoir.

**Keywords:** tight glutenite reservoir, volume fracturing, stress sensitivity, productivity prediction model, fluid-solid coupling

## INTRODUCTION

Horizontal well productivity prediction is very important in tight reservoir development. Especially for reservoirs with ultra-low permeability and tight reservoirs, unstable well-production systems may increase the difficulty of well production prediction (Ren et al., 2019; Zhang et al., 2019c). Friauf et al. (2009) developed a new productivity prediction model that calculates the productivity of a hydraulically fractured well, taking into account the effect of damage of the fracture face from fluid leak-off. Results of the new productivity prediction model are compared with McGuire, Prats and Raymond models. The existing models assume either elliptical or radial flow around the well with permeability varying azimuthally. He found that there were significant differences in the calculated well productivity, which indicate that earlier assumptions made about the flow geometry lead to a serious overestimation of the well PI. The new productivity prediction model can be used to quickly calculate the productivity of wells that have both a finite-conductivity fracture and damage in the invaded zone. Considering the characteristics of unconventional oil and gas seepage, the trilinear flow model was first adopted in the study of volume fracturing horizontal well seepage. The pressure and production dynamics could be analyzed based on the trilinear analytical model, which was adopted by Brown et al. (2011). The two-hole three-region composite analytical model of volume

fracturing horizontal wells was established by Brohi et al. (2011). The model described an oil reservoir in the inner region with dual porosity media, oil reservoir in the exterior region with single porosity media. The model was used for the study on tight gas reservoirs, shale gas reservoirs and tight oil reservoirs. Sennhauser et al. (2011) established the multistage fracturing horizontal well productivity model. The model can accurately describe the reservoir in terms of geology, fluid characteristics and pressure profile. It is also demonstrated that the overall productivity of multistage fracturing horizontal wells is determined by a number of parameters, including well spacing, fracture spacing, fracture size and characteristics, and the location of the first and last fractures. The model was applied to the study of tight gas reservoirs, shale gas reservoirs and tight oil reservoirs. Based on the seepage characteristics of porous media in unconventional reservoirs and geological data. Na Zhang and Abushaikh (2019) presented a new fully-implicit mimetic finite difference method (FDM) to simulate reservoir fluid flow. It had been applied to many fields due to its local conservativeness and applicability of any shape of polygon. The principle of the MFD method and the corresponding numerical formula for discrete fracture model are described in detail. The new fully-implicit mimetic finite difference method is tested through some examples to show the accuracy and robustness and the model can be used to predict the well production. Jackson et al. (2013) presented a new approach to simulate fluid flow by adopting Control-Volume-Finite-Element Method (CVFM). The new approach disposes of the pillar-grid concept that has persisted since reservoir simulation began. The new approach promotes the representation of multi-scale geological heterogeneity and the prediction of flow through that heterogeneity significantly. Multiphase flow is simulated using a novel mixed finite element formulation centered on a new family of tetrahedral element types,  $PN(DG) - PN + 1$ , which has a discontinuous  $N$ th-order polynomial representation for velocity and a continuous (order  $N + 1$ ) representation for pressure. The new approach preserves key flow features associated with realistic geological features that are usually lost. Li and Li. (2012) derived a new production prediction model theoretically with the pressure sensitivity of permeability being considered, and used the production data from a low permeability oil field to test and verify the model. The pressure sensitivity coefficient of permeability has been calculated by using the new model with the field data. He founded that the permeability near the well bottom decreased significantly because of the drop in pressure in low permeability reservoirs. An obvious permeability decline funnel could be formed even if the formation was homogeneous before development. It was found that the productivity index is no longer a constant in low permeability reservoirs with serious pressure sensitivity of permeability. The pressure sensitivity of permeability should be considered when low permeability reservoirs are being developed. Otherwise, the production will be greatly overestimated. Doe et al. (2013) carried out discretization of complex fracture network in the fractured region, established the productivity model of multiple porosity media, and calculated the contribution rate of natural fractures in the productivity. Cao et al. (2015) established a full analytical

mathematical productivity model considering friction, and compared and analyzed the difference between the analytical method and the finite-difference solution results, proving that the model is more accurate in spatial discretization and other aspects (Johansen et al., 2015). Taking the tight reservoir of Daqing Oilfield as the study object, Hu et al. (2017) established a numerical model of production capacity based on the theory of unsteady seepage mechanics and superposition principle, which was used to calculate and analyze the production capacity of fracturing horizontal wells. Yang et al. (2019) and Zhang et al. (2019a) established the productivity model of the shale reservoir to optimize the fracture spacing, considering the linear flow in the reservoir and the linear flow coupling model in hydraulic fractures, and proved that the productivity of multi-fracture horizontal wells are inversely proportional to the fracture spacing. The maximum capacity after volume fracturing can be achieved by reducing the fracture spacing. The production capacity of the production well can be doubled by reducing the cluster spacing from 70 to 15 ft.

Compared with the Poisson's ratio of conventional tight sandstone, the Poisson's ratio of tight glutenite reservoir, a mechanic parameter of stone, is greatly different. In this paper, a productivity prediction model for volume fracturing horizontal well considering fluid-solid coupling was established, combining the principle of effective stress and constitutive relation of rock skeleton, while fully taking into account the fluid-solid coupling effect of the tight reservoir; the impact of Poisson's ratio of stress sensitivity and lithological characteristic parameters on the fluid-solid coupling effect was considered in an innovative manner, and a fluid-solid full coupling productivity model suitable for the characteristics of glutenite oil reservoir was established. The accuracy and reliability of the model was validated by comparing the mathematical model of stress field and seepage field of volume fracturing horizontal well in a tight reservoir with the actual production well (Zhang et al., 2019b).

## ESTABLISHMENT OF PRODUCTIVITY PREDICTION MODEL

### Seepage Field Model of Volume Fracturing Horizontal Well in Tight Reservoir

#### Geometric Model of Volume Fracturing Horizontal Well

In the "Five-region Model" proposed by Stalgorova and Mattar. (2012), and the "Composite Flow Model" proposed by Su Yuliang et al., it is believed that the main fracture and natural fracture are formed by fracturing form complex fracture clusters after volume fracturing of horizontal wells, and there are non-fractured regions between the clusters. The reservoir area of volume fracturing horizontal wells are composed of three parts: reservoir matrix, natural fracture (unmodified) region, artificial fracture and natural fracture interlaced fracture network region. Based on the above conclusions, a volume fracturing horizontal well model for a tight glutenite reservoir is established, as shown in **Figure 1**.

The formation and fluid meet the following conditions: 1) thickness of the reservoir is  $h$ , with outer boundary closed, and with natural fracture; 2) rocks and fluids are slightly compressible;



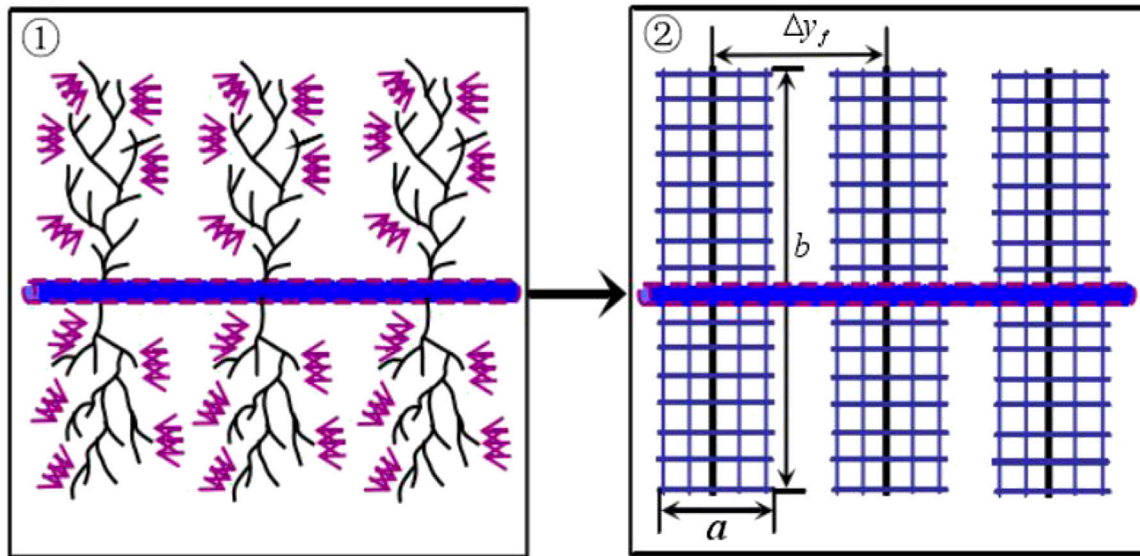


FIGURE 1 | Schematic diagram of geometric model.

3) the impact of gravity and temperature changes are not considered for the seepage process.

### Mathematical Model for Seepage of Volume Fracturing Horizontal Well

#### Mathematical Model for Seepage of Matrix–Natural Fracture System

The fluid motion equation in a matrix system considering the trigger pressure gradient:

$$v_m = -\frac{K_m}{\mu} (\nabla P_m - \lambda) \quad (1)$$

Equation for state of rock skeleton and fluid in matrix system

$$\phi = \phi_0 e^{-C_p (P_i - P_m)}, \rho = \rho_0 e^{-C_L (P_i - P_m)} \quad (2)$$

Equation for continuity of a single phase compressible fluid

$$\nabla(\rho v_m) + Q_m = \frac{\partial(\rho \phi)}{\partial t} \quad (3)$$

Eqs (1) and (2) were substituted into the continuity Eq. (3):

$$\nabla^2 P_m + C_L (\nabla P_m)^2 - \lambda C_L \nabla P_m - \frac{\phi \mu C_m}{K_m} \frac{\partial P_m}{\partial t} - \alpha (P_m - P_n) = 0 \quad (4)$$

$$C_m = C_p + C_L \quad (5)$$

Since the  $\nabla P_m$  is very small, Eq. (3) can be reduced to the following equation.

$$\nabla^2 P_m - \lambda C_L \nabla P_m - \frac{\phi \mu C_m}{K_m} \frac{\partial P_m}{\partial t} - \alpha (P_m - P_n) = 0 \quad (6)$$

Eq. (6) is the equation for the seepage governing differential of single-phase micro-compressible fluid in bedrock when the trigger pressure gradient is considered. Similarly, the governing differential equation of the natural fracture system can be obtained as follows.

$$\nabla^2 P_n - \frac{\phi \mu C_m}{K_m} \frac{\partial P_m}{\partial t} + \alpha \frac{K_m}{K_n} (P_m - P_n) = 0 \quad (7)$$

The initial and boundary conditions:

$$\begin{cases} P_m(x, y, z, t=0) = P_n(x, y, z, t=0) = P_i \\ P_n(x, y, z, t) = P_f(x, y, z, t) \\ \left. \frac{\partial P_m}{\partial x} \right|_{x=x_e} = \left. \frac{\partial P_m}{\partial y} \right|_{y=y_e} = \left. \frac{\partial P_m}{\partial z} \right|_{z=z_e} \\ \left. \frac{\partial P_n}{\partial x} \right|_{x=x_e} = \left. \frac{\partial P_n}{\partial y} \right|_{y=y_e} = \left. \frac{\partial P_n}{\partial z} \right|_{z=z_e} = 0 \end{cases} \quad (8)$$

### Seepage Model of Fracture Network System

The fluid motion equation:

$$v_f = -\frac{K_f}{\mu} P_f \quad (9)$$

The equation for state:

$$\phi_f = \phi_{f0} e^{-C_0 (P_i - P_f)}, \rho = \rho_0 e^{-C_L (P_i - P_m)} \quad (10)$$



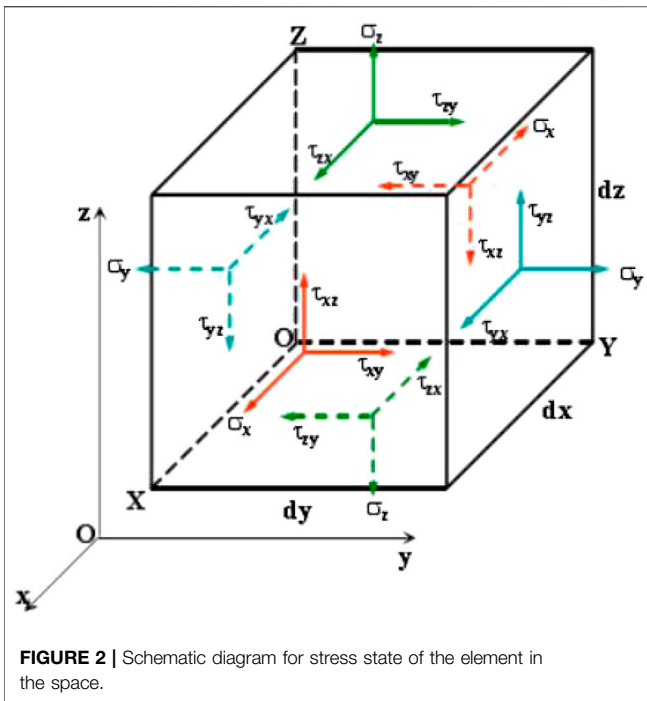


**FIGURE 2** | Schematic diagram for stress state of the element in the space.

The equation for continuity

$$\nabla(\rho v_f) - Q_f = \frac{\partial(\rho \phi_f)}{\partial t} \quad (11)$$

Similarly, the seepage governing differential equation:

$$\nabla^2 P_f - \frac{\phi_f \mu C_f}{K_f} \frac{\partial P_f}{\partial t} = 0 \quad (12)$$

The initial and boundary conditions

$$\begin{cases} P_f(x, y, z, t = 0) = P_i \\ P_f(x, y, z, t) = P_m(x, y, z, t) = P_n(x, y, z, t) \end{cases} \quad (13)$$

### Definite Conditions for Solution of Seepage Field

In order to solve the nonlinear equations, some fixed value conditions are set. These conditions are definite conditions. For example, the fixed pressure condition is that the well is produced under a certain flow pressure. For the mathematical model for the seepage field of volume fracturing horizontal wells in tight reservoirs, the definite conditions mainly include the initial formation pressure conditions, the definite pressure production.

Initial conditions:

$$p_m(x, y, z, t = 0) = p_n(x, y, z, t = 0) = p_f(x, y, z, t = 0) = p_i \quad (14)$$

Boundary conditions:

$$p|_{r=r_w} = p_w \quad (15)$$

## Model for Stress Field of Volume Fracturing Horizontal Well in Tight Reservoir

Assumptions: 1) The rock is the deformation of porous media; 2) The rock particles are incompressible, while particle pores can be compressed; 3) The impact of temperature change on rock deformation is not considered; 4) Rock deformation is a small elastoplastic deformation; 5) The compression coefficient of pore changes (Jianjun et al., 2002; Liu et al., 2018; Zhao and Du, 2019).

### Equation for Constitutive Relation

$$d\sigma_{ij} = D_{ijkl} d\epsilon_{kl} \quad (16)$$

### Geometric Equation

$$\epsilon_{ij} = \frac{1}{2} (u_{i,j} + u_{j,i}) \quad (17)$$

### Differential Equation for Stress Equilibrium

Before the reservoir is developed, any unit (infinitely small) in the reservoir is in static equilibrium. When the reservoir is developed, the pore pressure of the reservoir will change. Meanwhile the effective stress also changes. This change can be expressed by the stress equilibrium differential equation. A hexahedral differential element is used to represent the stress state in the space, as shown in **Figure 2** and the length of each side is  $dx, dy, dz$  respectively.

The equilibrium equation of the element in the  $x$  direction:

$$\begin{aligned} & \left( \sigma_x + \frac{\partial \sigma_x}{\partial x} \right) dydz - \sigma_x dydz + \left( \tau_{xy} + \frac{\partial \tau_{xy}}{\partial y} \right) dzdx - \tau_{xy} dzdx \\ & + \left( \tau_{xz} + \frac{\partial \tau_{xz}}{\partial z} \right) dxdy - \tau_{xz} dxdy + f_x dxdydz = 0 \end{aligned} \quad (18)$$

So if we simplify **Eq. (18)**, we get **Eq. (19)**.

$$\frac{\partial \sigma_x}{\partial x} + \frac{\partial \tau_{xy}}{\partial y} + \frac{\partial \tau_{xz}}{\partial z} + f_x = 0 \quad (19)$$

Similarly, the differential equation for equilibrium in the  $y$  and  $z$  directions:

$$\frac{\partial \sigma_y}{\partial y} + \frac{\partial \tau_{xy}}{\partial x} + \frac{\partial \tau_{yz}}{\partial z} + f_y = 0 \quad (20)$$

$$\frac{\partial \sigma_z}{\partial z} + \frac{\partial \tau_{xz}}{\partial x} + \frac{\partial \tau_{yz}}{\partial y} + f_z = 0 \quad (21)$$

### Definite Conditions for Solution of Stress Field

For the mathematical model for stress field of horizontal well in a tight reservoir, its definite conditions can be divided into initial conditions and boundary conditions, and the boundary conditions can be divided into stress boundary conditions and displacement boundary conditions (Zhang et al., 2018). The initial conditions for the stress field are consistent with those for the model for seepage field.

Stress field displacement boundary conditions:

$$u|_{\Omega_e} = \bar{u} \quad (22)$$

Stress field stress boundary conditions:

$$\sigma_{ij} \cdot n|_{\Omega_e} = \bar{T}_i \quad (23)$$

## Dynamic Cross Coupling Model of Seepage Field and Stress Field

### Permeability Coupling Relationship

Yin et al. (2019) studied the permeability coupling of tight glutenite reservoirs by considering the influence of young's modulus and initial permeability comprehensively. However, he did not consider the influence of Poisson's ratio which is a rock characteristic parameter. Young's modulus can reflect the changing relationship of longitudinal strain stress. Compared with Young's modulus, Poisson's ratio reflects the longitudinal and transverse strain ratio and better reflects the overall strain of the rock. In this paper, the initial permeability, Young's modulus and Poisson's ratio are considered.

$$\alpha = c_1 \alpha_E + c_2 \alpha_k + c_3 \alpha_v \quad (24)$$

$$\alpha_E = 1.465 - 0.3553 \ln E \quad (25)$$

$$\alpha_K = 0.4834 K_0^{-0.3422} \quad (26)$$

$$\alpha_v = \ln v \quad (27)$$

Substitute the data into Eqs 24-27:

$$K_f = K_{f0} \exp[-0.087(\sigma_n - p)]$$

### Coupling Relation of Porosity

Ran and Li. (1997) derived the porosity strain model through the definition of porosity. The volumetric strain parameters themselves imply the mechanical properties of rocks, and the derived porosity coupling model is as follows:

$$\phi = \frac{\phi_0 + \varepsilon_v}{1 + \varepsilon_v} \quad (28)$$

## SOLUTION OF PRODUCTIVITY PREDICTION MODEL

### Finite Element Solution of Seepage Model

The whole reservoir is considered as a continuous calculation domain, including porous media seepage considering the trigger pressure gradient and the fracture network seepage of the volume fracturing region, and fracture fluid flow within the volume fracture system (Zhang et al., 2020). For fracture fluid seepage in the fracture network system, the actual a three-dimensional fracture is equivalent to two-dimensional fracture with certain fracture openness with a discrete fracture network model. So, the whole calculation domain governing equation  $\Omega_{i,m}$  of three-dimensional integral form can be reduced as.

$$\iiint_{\Omega} F d\Omega = \iiint_{\Omega_f(3D)} F d\Omega_f + \iiint_{\Omega_{m,n}(3D)} F d\Omega_{m,n} = \int \int_{\Omega_f(2D)} F d\Omega_f + \iiint_{\Omega_{m,n}(3D)} F d\Omega_{m,n} \quad (29)$$

The approximate expression of the pressure field function is obtained by taking any element in the system:

$$P_m \approx P_{i,m} N_{i,m} \quad (30)$$

Eq. (30) is substituted into Eq. (6) to obtain the expression of characteristic matrix of element  $\Omega_{i,m}$

$$\begin{aligned} & \iiint_{\Omega_{i,mn}} (\nabla N_{i,mn}^T \nabla N_{i,mn} + \lambda \nabla N_{i,mn}^T \nabla N_{i,mn}) d\Omega_{i,mn} P_{i,m} \\ & + (1 - \omega_n) \iiint_{\Omega_{i,mn}} N_{i,mn}^T \nabla N_{i,mn} d\Omega_{i,mn} \frac{\partial P_{i,m}}{\partial t} P_{i,m} \\ & + \alpha \iiint_{\Omega_{i,mn}} N_{i,mn} (P_{i,m} - P_{i,n}) N_{i,mn}^T d\Omega_{i,mn} = 0 \end{aligned} \quad (31)$$

Similarly, the element characteristic matrix expression of natural fracture seepage model  $\Omega_{i,n}$ :

$$\begin{aligned} & \iiint_{\Omega_{i,mn}} \nabla N_{i,mn}^T \nabla N_{i,mn} d\Omega_{i,mn} P_{i,m} + \omega_n \iiint_{\Omega_{i,mn}} N_{i,mn}^T N_{i,mn} d\Omega_{i,mn} \frac{\partial P_{i,m}}{\partial t} \\ & - \alpha \iiint_{\Omega_{i,mn}} N_{i,mn} (P_{i,m} - P_{i,n}) N_{i,mn}^T d\Omega_{i,mn} \\ & = 2\pi h \iiint_{\Omega_{i,m}} q_n N_{i,mn}^T d\Omega_{i,mn} \end{aligned} \quad (32)$$

The element characteristic matrix expression of network fracture seepage  $\Omega_{i,f}$  in volume fracturing region:

$$\begin{aligned} & K_f \iint_{\Omega_{i,f}} \nabla N_{i,f}^T \nabla N_{i,f} d\Omega_{i,f} P_{i,f} + \omega_f K_f \iint_{\Omega_{i,f}} N_{i,f}^T N_{i,f} d\Omega_{i,f} \frac{\partial P_{i,f}}{\partial t} \\ & = 2\pi h \iint_{\Omega_{i,f}} q_f N_{i,f}^T d\Omega_{i,f} \end{aligned} \quad (33)$$

Assuming that the initial reservoir flow occurs in the natural fracture system  $\Omega_{i,n}$  and flows into the fracture network system  $\Omega_{i,f}$ , the solution can be obtained by the implicit backward difference scheme, and finite element closed equations with unknown quantities in the next time step  $\Omega_{i,f}$  can be obtained:

$$\begin{aligned} & \left\{ \iiint_{\Omega_{i,mn}} \nabla N_{i,mn}^T \nabla N_{i,mn} d\Omega_{i,mn} + K_f \iint_{\Omega_{i,f}} \nabla N_{i,f}^T \nabla N_{i,f} d\Omega_{i,f} \right\} P_n^{k+1} \\ & + \frac{\omega_n \iiint_{\Omega_{i,mn}} N_{i,mn}^T N_{i,mn} d\Omega_{i,mn} + \omega_f K_f \iint_{\Omega_{i,f}} N_{i,f}^T N_{i,f} d\Omega_{i,f}}{t^{k+1} - t^k} P_n^{k+1} \\ & + \alpha \iiint_{\Omega_{i,mn}} N_{i,mn} N_{i,mn}^T d\Omega_{i,mn} P_n^{k+1} \\ & = Q_n^{k+1} + \frac{\omega_n \iiint_{\Omega_{i,mn}} N_{i,mn}^T N_{i,mn} d\Omega_{i,mn} + \omega_f K_f \iint_{\Omega_{i,f}} N_{i,f}^T N_{i,f} d\Omega_{i,f}}{t^{k+1} - t^k} P_n^k \\ & + \alpha \iiint_{\Omega_{i,mn}} N_{i,mn} N_{i,mn}^T d\Omega_{i,mn} P_n^k \end{aligned} \quad (34)$$

The pressure at the next time step of the matrix system is calculated according to the matrix natural fracture equilibrium equation of the entire reservoir:

$$\left\{ \begin{aligned} & \iiint_{\Omega_{i,mn}} (\nabla N_{i,mn}^T \nabla N_{i,mn} + \lambda \nabla N_{i,mn}^T \nabla N_{i,mn}) d\Omega_{i,mn} \\ & + K_f \iint_{\Omega_{i,f}} \nabla N_{i,f}^T \nabla N_{i,f} d\Omega_{i,f} \end{aligned} \right\} P_m^{k+1} \\ + \frac{(1 - \omega_n) \iiint_{\Omega_{i,mn}} N_{i,mn}^T N_{i,mn} d\Omega_{i,mn} + \omega_f K_f \iint_{\Omega_{i,f}} N_{i,f}^T N_{i,f} d\Omega_{i,f}}{t^{k+1} - t^k} P_m^{k+1} \quad (35) \\ + \alpha \iiint_{\Omega_{i,mn}} N_{i,mn} N_{i,mn}^T d\Omega_{i,mn} P_m^{k+1} \\ = \frac{(1 - \omega_n) \iiint_{\Omega_{i,mn}} N_{i,mn}^T N_{i,mn} d\Omega_{i,mn} + \omega_f K_f \iint_{\Omega_{i,f}} N_{i,f}^T N_{i,f} d\Omega_{i,f}}{t^{k+1} - t^k} P_m^k \\ + \alpha \iiint_{\Omega_{i,mn}} N_{i,mn} N_{i,mn}^T d\Omega_{i,mn} P_m^k$$

The whole continuous calculation domain can be solved through Eqs (34) and (35).

## Finite Element Solution for Fluid-Solid Coupling Productivity Model

Differential equation for stress field:

$$A(U) = 0, \quad \forall x \in \Omega \quad (36)$$

Boundary conditions:

$$B(U) = 0, \quad \forall x \in \Gamma \quad (37)$$

The unknown function  $U$  is the field function that needs to be solved.  $A$  and  $B$  in Eqs (36) and (37) are differential operators for independent variables such as spatial coordinates and time. The equivalent integral form of differential Eq. (36) and boundary conditions Eq. (37) can be written by the Galerkin equation as follows:

$$\int_{\Omega} v^T A(U) d\Omega + \int_{\Gamma} v^T B(U) d\Gamma = 0 \quad (38)$$

According to the principle of effective stress, the total stress of reservoir rock is composed of effective stress and pore fluid pressure:

$$\sigma = \sigma' + mp \quad (39)$$

$$m^T = [111000] \quad (40)$$

It is assumed that the displacement vector at any point in the calculation domain satisfies the following equation:

$$U^T = [u, v, w] \quad (41)$$

The above equation can be expressed as:

$$u = [IN_i, IN_j, IN_m, IN_p]^T a' = Na' \quad (42)$$

The following equation can be obtained by the combination of Eqs (17) and (41):

$$\varepsilon = Ba' = [B_i, B_j, B_m, B_p]^T a' \quad (43)$$

$$B_i = \begin{bmatrix} \frac{\partial N_i}{\partial x} & 0 & 0 \\ 0 & \frac{\partial N_i}{\partial y} & 0 \\ 0 & 0 & \frac{\partial N_i}{\partial z} \\ \frac{\partial N_i}{\partial y} & \frac{\partial N_i}{\partial z} & 0 \\ 0 & \frac{\partial N_i}{\partial z} & \frac{\partial N_i}{\partial y} \\ \frac{\partial N_i}{\partial z} & 0 & \frac{\partial N_i}{\partial x} \end{bmatrix} \quad (44)$$

By substituting Eqs (19)-(23) and Eq. (36) into Eq. (38), the following equation can be obtained:

$$\int_{\Omega} \delta u_i (\sigma_{ij,j} + f_i - \rho u_i) d\Omega - \int_{\Gamma} \delta u_i (\sigma_{ij} n_j - \bar{T}_i) d\Gamma = 0 \quad (45)$$

The above equation is integrated by parts and substituted into Eq. (42), Eq. (17) and the elastic constitutive matrix of rock to obtain the overall equilibrium equation of the fluid-solid fully coupled stress field:

$$M \frac{d\bar{u}}{dt} + C \frac{d\bar{u}}{dt} + \sum_e \int_{\Omega_e} B^T \sigma d\Omega_e = F_{\Gamma} \quad (46)$$

$$M = \sum_e \int_{\Omega_e} \rho N^T N d\Omega, C = \sum_e \int_{\Omega_e} \mu N^T N d\Omega F_{\Gamma} \\ = \sum_e \int_{\Omega_e} N^T f d\Omega + \sum_e \int_{\Gamma_e} N^T \bar{T} d\Gamma \quad (47)$$

The Galerkin weighted residual method is applied to the seepage field model and the following equations can be obtained:

$$K_p^T a + Sp + Hp = F_f \quad (48)$$

$$K_p = \sum_e \left( \int_{\Omega_e} B^T m N_p d\Omega_e \right) \quad (49)$$

$$S = \sum_e \int_{\Omega_e} N_p^T \frac{1}{Q} d\Omega_e, H = \sum_e \int_{\Omega_e} (\nabla N_p)^T k \nabla N_p d\Omega_e \quad (50)$$

To sum up, the matrix form of the equilibrium equations for the fluid-solid coupling mathematical model of porous media based on the full-coupling finite element method can be obtained as follows:

$$\begin{bmatrix} M & 0 \\ 0 & 0 \end{bmatrix} \begin{bmatrix} \bar{u} \\ P \end{bmatrix} + \begin{bmatrix} C & 0 \\ K_p^T & S \end{bmatrix} \begin{bmatrix} \bar{u} \\ P \end{bmatrix} + \begin{bmatrix} K & -K \\ 0 & H \end{bmatrix} \begin{bmatrix} \bar{u} \\ P \end{bmatrix} = \begin{bmatrix} F_{\Gamma} \\ F_f \end{bmatrix} \quad (51)$$

Eq. (51) is substituted into COMSOL and the result is obtained.

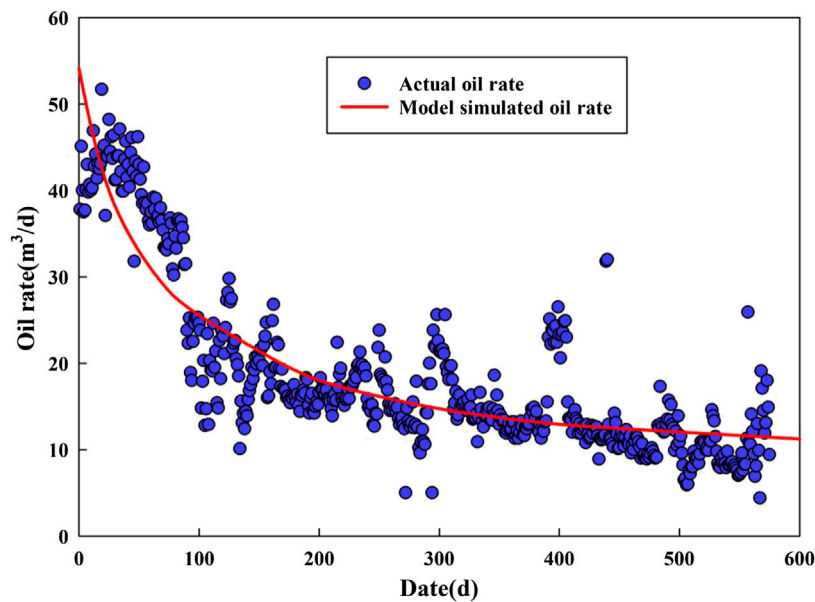


**FIGURE 3 |** Comparison between actual production and model production.

entire formation flows around the wellbore of the horizontal well elliptically.

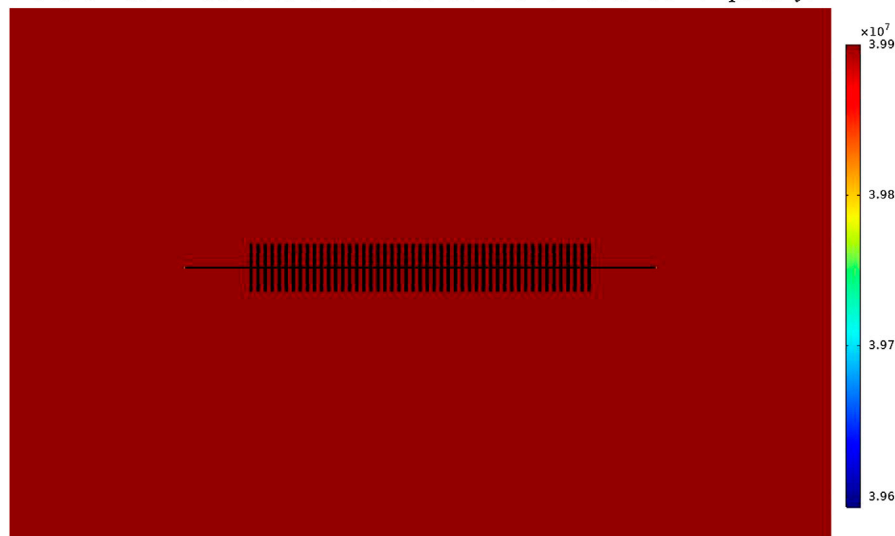


**FIGURE 4 |** Formation pressure distribution in volume fracturing horizontal well (0 days).

## EXAMPLE FOR CALCULATION OF PRODUCTIVITY PREDICTION MODEL

### Comparison of Actual and Model Production

After establishing and solving the fluid-solid coupling model, the required parameters of the model are input into COMSOL (Table 1). Then the trend of the model simulated oil rate is obtained by using the full coupling of finite elements. Combined

with the actual oil rate changes of production well, the trend of model simulated oil rate can be analyzed as shown in Figure 3. It can be seen from Figure 3 that the fitting error between the actual daily production and the simulation result of fluid-solid coupling model is small.

### Pressure Distribution of Model

Figures 4-6 show the variation of pore pressure around the well with production time. Figures 46 show the pressure

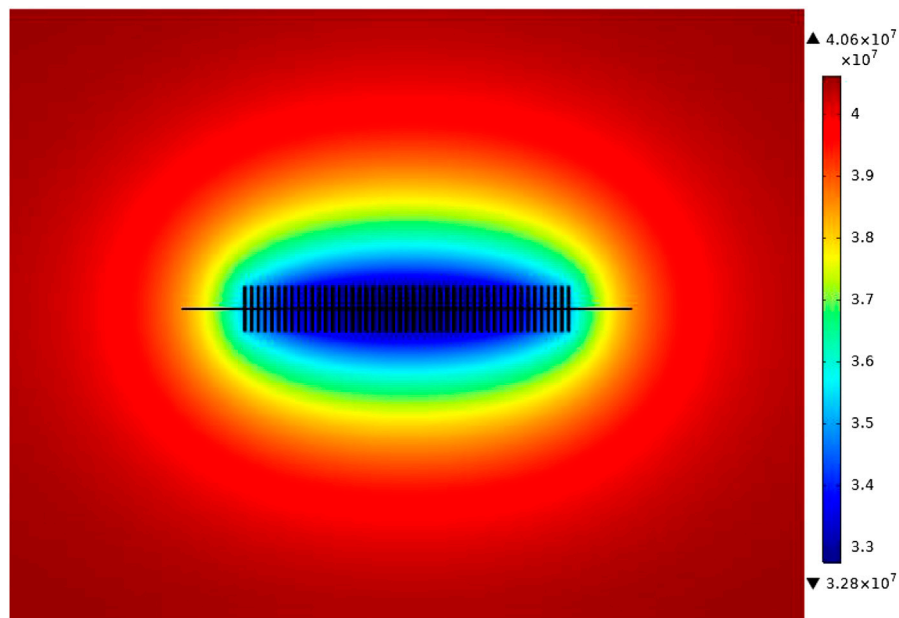


**FIGURE 5 |** Formation pressure distribution in volume fracturing horizontal well (300 days).

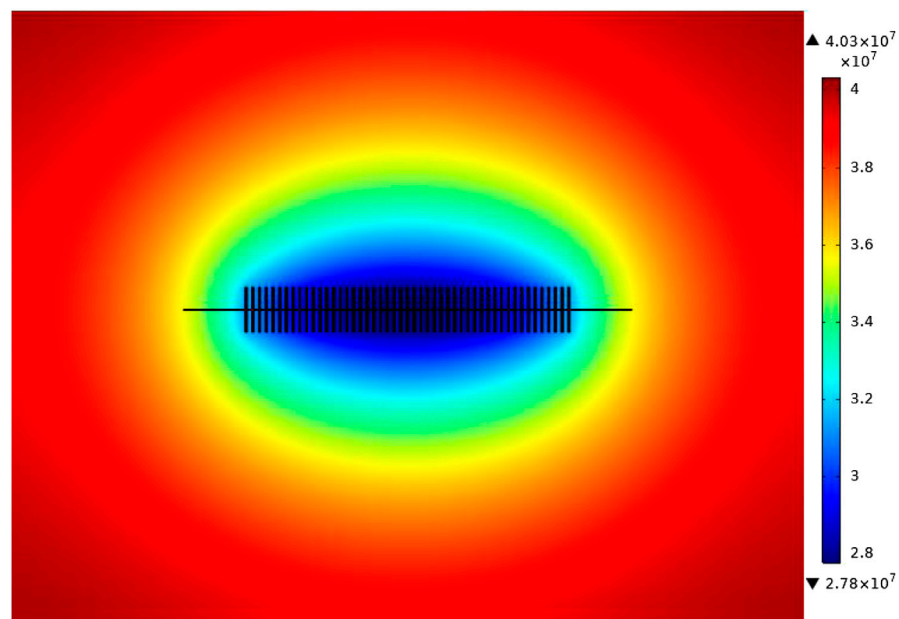


**FIGURE 6 |** Formation pressure distribution in volume fracturing horizontal well (600 days).

distribution at 0, 300 and 600 days of production, respectively. As can be seen from the Figures, formation pressure gradually decreases in the horizontal well simulation production process, and the pressure change range is as follows: area near the wellbore of horizontal well  $\geq$  volume fracturing region  $\geq$  unmodified region of matrix. Globally, the reservoir fluid

flow first occurs around the wellbore with a fast flow speed. After the fluid flows away, the supply fluid of the volume fracturing region and matrix flows into the wellbore from the fracturing region and matrix flow into the wellbore. The fluid of the entire formation flows around the wellbore of the horizontal well elliptically.



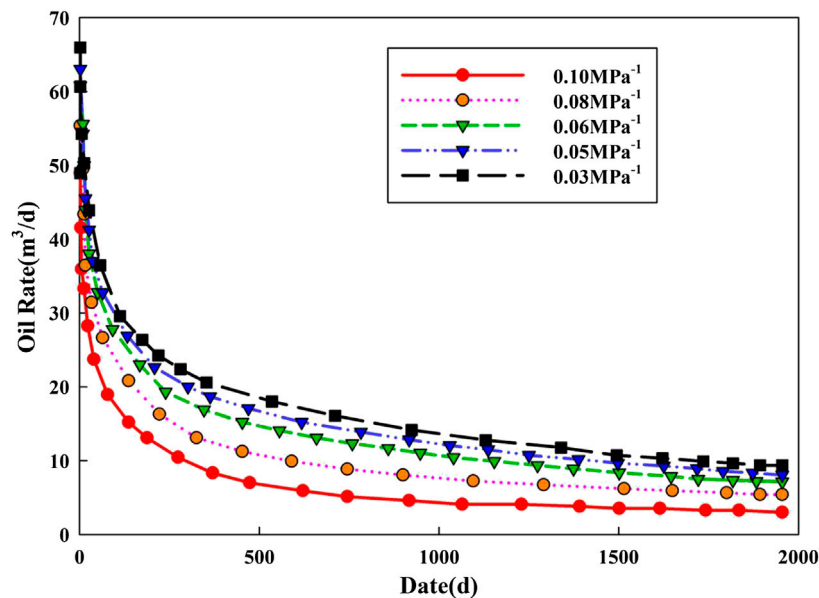


FIGURE 7 | Daily oil production curve of different stress sensitivity coefficient.

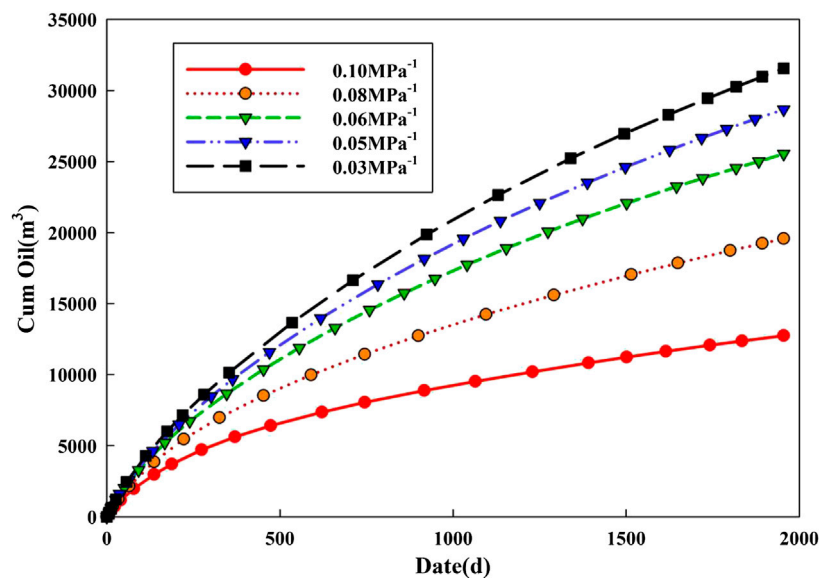


FIGURE 8 | Cumulative oil production curve of different stress sensitivity coefficient.

## Sensitivity Analysis

By sensitivity analysis of different parameters, the impact of each factor on production can be understood. These parameters mainly include stress sensitivity, producing pressure, fracture half length, number of fracture clusters and fracture flow capacity.

### Stress Sensitivity

The fluid-solid coupling effect is mainly due to the change of reservoir pressure in the production process, which leads to the

change of pore and permeability. And the change of permeability is obvious. Based on the rock mechanics characteristics of the glutenite, the stress sensitivity coefficient is a parameter to reflect the influence of stress change on permeability. The flow pressure is set to 26 MPa and other parameters remained unchanged by single factor analysis. The variation of the oil rate under different stress sensitivity coefficients is simulated.

As can be seen from **Figures 7, 8**, with the increase of the stress sensitivity coefficient, the production of the horizontal well is

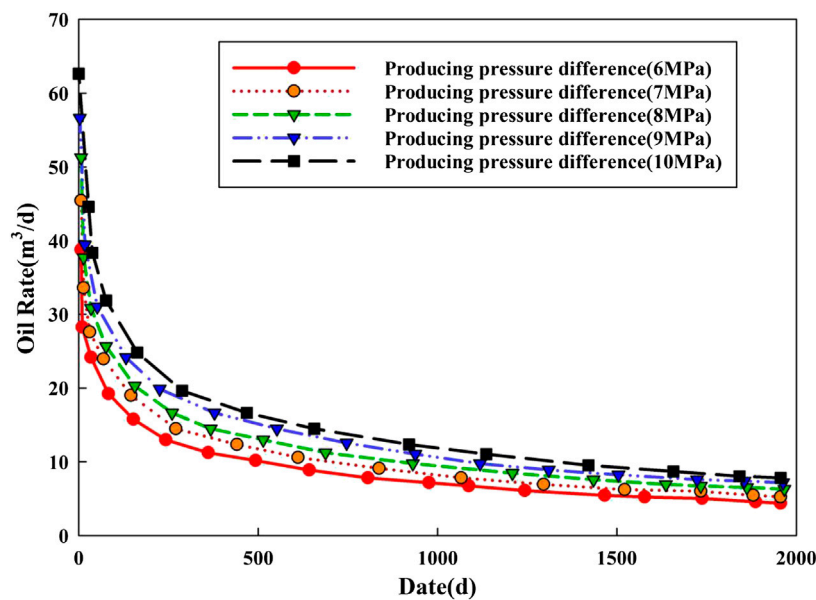


FIGURE 9 | Daily oil production curve of different producing pressure difference.

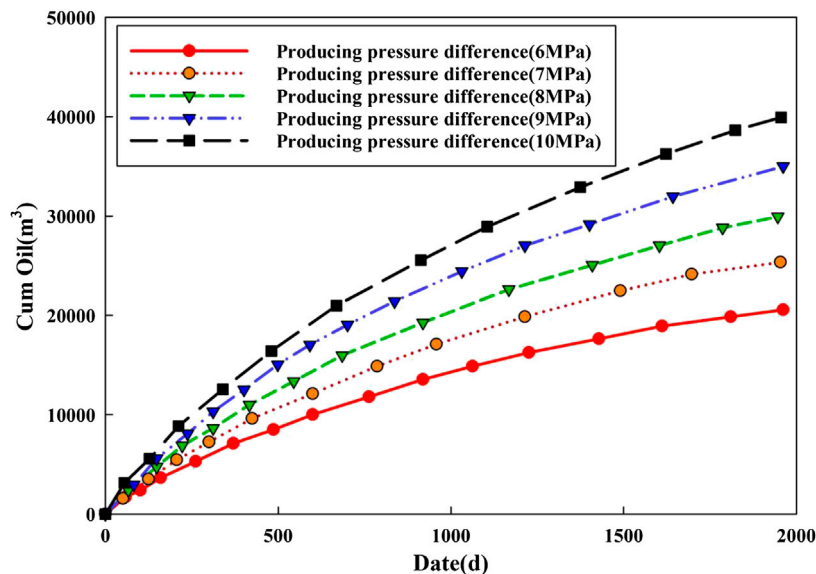


FIGURE 10 | Cumulative oil production curve of different producing pressure difference.

reduced. Under the effect of stress, the initial permeability of the reservoir, especially the volume fracturing region, is high, and the permeability loss with the change of stress is large, resulting in the decrease of production. In the actual production process, the control of the producing pressure should be considered to reduce the fluid-solid coupling effect on the productivity.

### Producing Pressure Difference

The change of pressure in the production process will also lead to the change of pore and permeability of reservoir. The fluid-solid

coupling can be reflected by controlling the producing pressure difference of the model. The stress sensitivity coefficient is set to  $0.06 \text{ MPa}^{-1}$  and other parameters remained unchanged by single factor analysis. The variation of oil rate under varying producing pressure differences is simulated.

As can be seen from **Figures 9, 10**, the daily production of volume fracturing horizontal well increases with the increase of producing pressure difference. The increase of producing pressure difference leads to a large drop in formation pressure, which will obviously affect the loss of formation porosity and

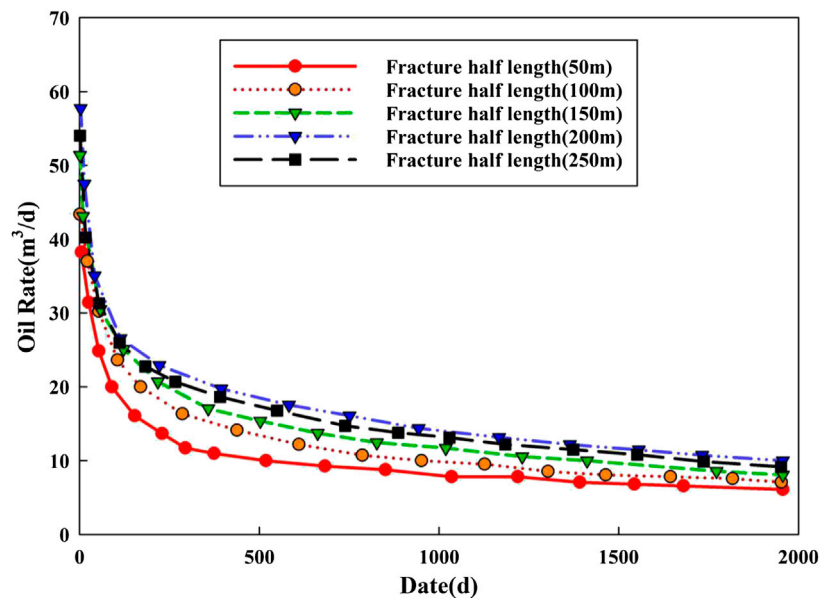


FIGURE 11 | Daily oil production curve of different fracture half length.

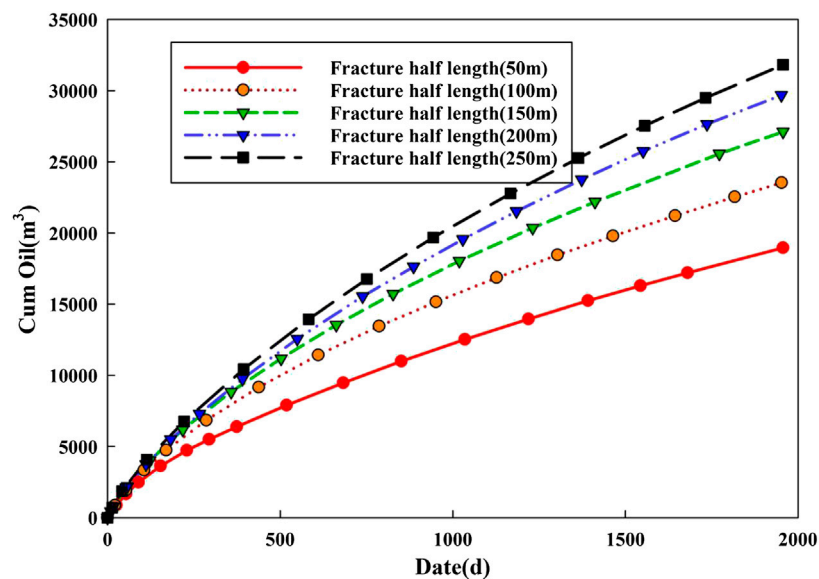


FIGURE 12 | Cumulative oil production curve of different fracture half-lengths.

permeability. Increasing the producing pressure difference will increase the cumulative production of the horizontal well, but the increasing rate will decrease. After increasing the producing pressure difference, the reservoir's available range increases, leading to higher production. However, it also enhances the fluid-solid coupling effect, resulting in a decrease in fluid flow capacity, which has some impact on the actual production of the horizontal well.

### Fracture Half Length

Fracture half length is one of the important parameters to control the area of SRV zone. By extending the fracture half length, the SRV zone of the reservoir can be expanded effectively. Therefore, fracture half-length has a great influence on horizontal well production. The variation of the oil rate under different fracture half lengths is simulated by single factor analysis.

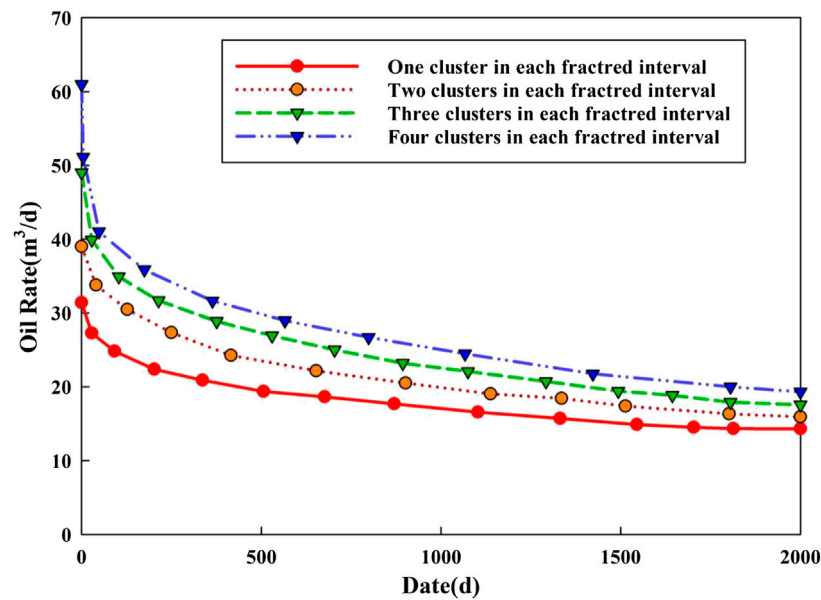


FIGURE 13 | Daily oil production curve of different number of fracture clusters.

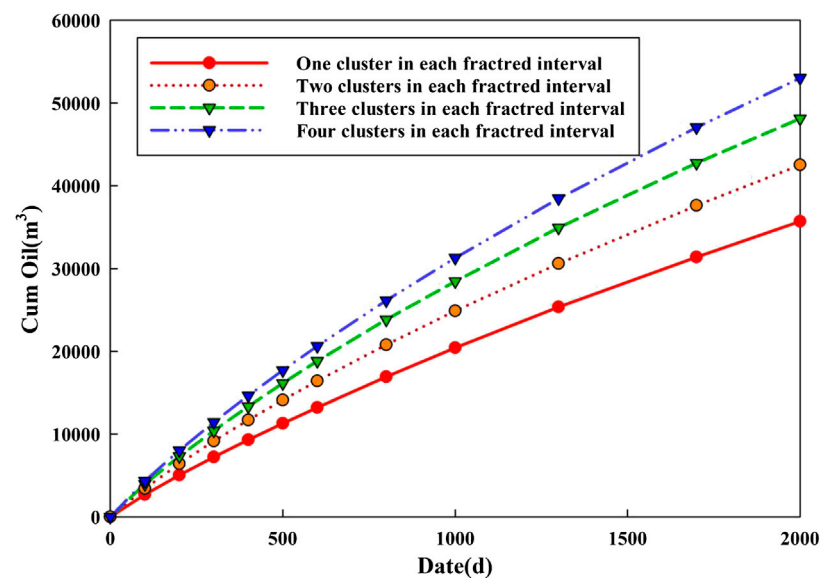


FIGURE 14 | Cumulative oil production curve of different number of fracture clusters.

As can be seen from Figures 11, 12, the increase of fracture half length has a small impact on the early productivity of the horizontal well. With the increase of fracture half-length, the growth trend of cumulative production is obvious. However, although the fracture half-length increases in a linear manner, the growth rate of cumulative production decreases to some extent. At the same time, considering the economic cost of on-site fracturing, there is some room for optimization of fracture half-length.

### Number of Fracture Clusters

The number of fracture clusters could control the area of SRV zone. Therefore, the number of fracture clusters has a great influence on horizontal well production. The variation of oil the rate under different numbers of fracture clusters is simulated by single factor analysis.

As can be seen from Figures 13, 14, with the increase of fracture clusters, the growth trend of cumulative production is obvious. The increasing of fracture clusters has a great impact on the production of

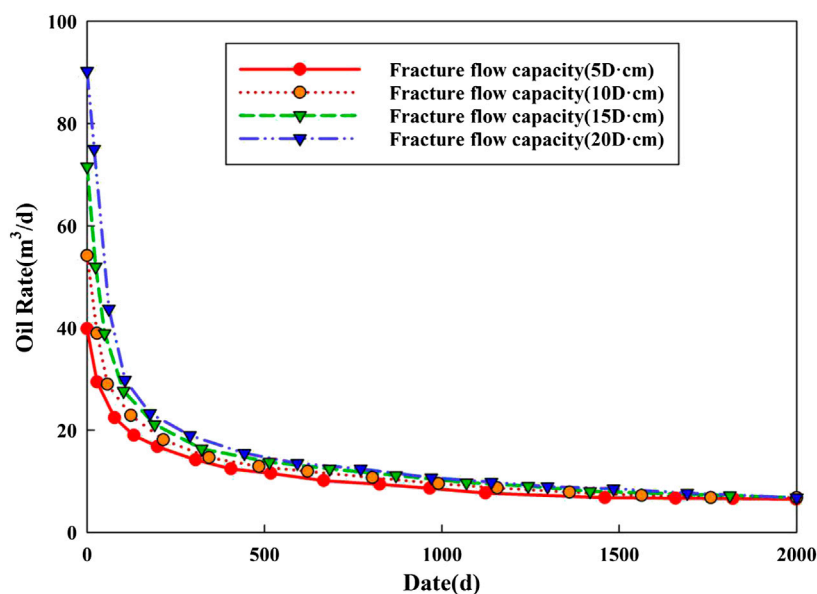


FIGURE 15 | Daily oil Production Curve of Different Fracture Flow Capacity.

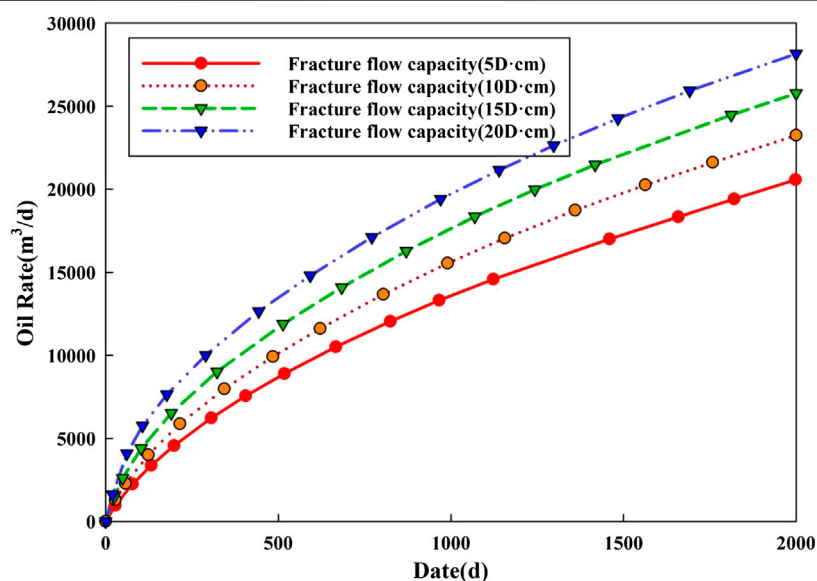


FIGURE 16 | Cumulative oil production curve of different fracture flow capacity.

the horizontal well in the early stage and a small impact in the later stage. In the early production of the horizontal well, the oil supply is mainly from the volume fracturing region to the horizontal wellbore, and the oil supply is from the reservoir matrix region in the later stage. Due to the unmodified reservoir matrix, the seepage condition is poor and the oil supply capacity is relatively weak, resulting in little difference in the daily production at the later stage.

### Fracture Flow Capacity

Fracture flow capacity is another important parameter to control horizontal well production. The variation of the oil rate under

different fracture flow capacities is simulated by single factor analysis.

As can be seen from **Figures 15, 16**, the fracture flow capacity has a great impact on the early production stage of the horizontal well and a small impact on the later stage. In the early stage of horizontal well production, the wellbore of the horizontal well is mainly supplied from the volume fracturing region, which results in a high fracture flow capacity and fast fluid flow in the effective modification area. In the later stage, oil is supplied from the reservoir matrix region, which is not modified, has low permeability and relatively weak oil supply capacity, resulting



**TABLE 1** | Basic parameters of tight reservoir used in calculation.

Parameter	Unit	Value
$P_i$	[MPa]	40
$\mu$	[m Pa·s]	6
$L$	[m]	2000
$\rho$	[kg/m <sup>3</sup> ]	800
$C_L$	[MPa <sup>-1</sup> ]	0.01
$C_p$	[MPa <sup>-1</sup> ]	0.00075
$C_n$	[MPa <sup>-1</sup> ]	0.0075
$\phi$	—	0.07
$K_m$	10 <sup>-3</sup> $\mu\text{m}^2$	1.66
$\lambda$	MPa/m	0.01
$K_n$	10 <sup>-3</sup> $\mu\text{m}^2$	16.6
$\phi_n$	—	0.0001
$E$	GPa	44
$\nu$	—	0.24
$\sigma_{\max}$	[MPa]	55
$\sigma_{\min}$	[MPa]	25

in little difference in daily production in the later stage. However, although the fracture flow capacity increased in a linear manner, the growth rate in cumulative production decreased.

## CONCLUSION

According to the seepage characteristics, the mathematical model of multiple media seepage in volume fracturing horizontal wells is established. The model takes into account the dual media composed of the fracture grid and the matrix formed by the coupling of artificial fracture and natural fracture, and a seepage model for the matrix region considering the trigger pressure gradient is established. In addition, the fluid-solid coupling effect in the tight reservoir is considered in the model, and the basic mathematical model of the stress field is established based on the principle of effective stress and the

constitutive relation of rock skeleton. In addition, the mathematical model of stress field-seepage field for volume fracturing horizontal wells in tight reservoir is formed by combining with the seepage model. Finally, based on the rock mechanics characteristics of glutenite and taking into account the impact of Young's modulus, Poisson's ratio, initial permeability value and other parameters, the permeability stress crossing dynamic model is improved, and the fluid-solid coupling productivity model for volume fracturing horizontal wells is formed.

## DATA AVAILABILITY STATEMENT

The raw data supporting the conclusions of this article will be made available by the authors, without undue reservation.

## AUTHOR CONTRIBUTIONS

All the authors have contributed to the conception and design of the productivity model. LT was mainly responsible for the construction of the capacity model, XC and PW were responsible for the solution and validation of the capacity model, and HW was responsible for the sensitivity analysis of the capacity model. The first draft was written by XC, and was revised and confirmed by all the authors.

## ACKNOWLEDGMENTS

The authors would like to acknowledge the funding by the project (51974329) sponsored by the National Natural Science Foundation of China and the project (2016ZX05047-005-001) sponsored by the National Major Science and Technology Projects of China.

## REFERENCES

- Brohi, I. G., Pooladi-Darvish, M., and Aguilera, R. (2011). *Modeling fractured horizontal wells as dual porosity composite reservoirs-application to tight gas, Shale gas and tight oil cases*. Fairbanks, AK: Society of Petroleum Engineers.
- Brown, M., Ozkan, E., Raghavan, R., and Kazemi, H. (2011). Practical solutions for pressure-transient responses of fractured horizontal wells in unconventional shale reservoirs. *SPE Reservoir Eval. Eng.* 14 (06), 663–676. doi:10.2118/125043-pa
- Cao, J., James, L. A., and Johansen, T. E. (2015). *A new coupled axial-radial productivity model for horizontal wells with application to high order numerical modeling*. Abu Dhabi, UAE: Society of Petroleum Engineers.
- Doe, T., Lacazette, A., Dershowitz, W., and Knitter, C. (2013). "Evaluating the effect of natural fractures on production from hydraulically fractured wells using discrete fracture network models." in *Unconventional Resources Technology Conference*, Denver, CO, August 12–14, 2013. doi:10.1190/urtec2013-172
- Friehauf, K. E., Suri, A., and Sharma, M. M. (2009). A simple and accurate model for well productivity for hydraulically fractured wells. *SPE Prod. Oper.* 25 (04), 453–460. doi:10.2118/119264-pa
- Hu, J., Zhang, C., Rui, Z., Yu, Y., and Chen, Z. (2017). Fractured horizontal well productivity prediction in tight oil reservoirs. *J. Petrol. Sci. Eng.* 151, 159–168. doi:10.1016/j.petrol.2016.12.037
- Jackson, M. D., Gomes, J. L. M. A., Mostaghimi, P., Percival, J. R., Tollit, B. S., Pavlidis, D., et al. (2013). *Reservoir modeling for flow simulation using surfaces, adaptive unstructured meshes, and control-volume-finite-element methods*. Austin, TX: Society of Petroleum Engineers. doi:10.2118/163633-MS
- Jianjun, L., Xiangui, L., Yareng, H., and Shengzong, Z. (2002). Study on fluid-solid coupling seepage in low permeability reservoir. *J. Rock Mech.* 21 (1):88–92 [in Chinese].
- Johansen, T. E., James, L., and Cao, J. (2015). Analytical coupled axial and radial productivity model for steady-state flow in horizontal wells. *IJPE* 1 (4), 290–307. doi:10.1504/ijpe.2015.073538
- Li, K., and Li, L. (2012). *A new production model by considering the pressure sensitivity of permeability in oil reservoirs*. Abu Dhabi, UAE: Publisher Society of Petroleum Engineers.
- Liu, R., Jiang, Y., Huang, N., and Sugimoto, S. (2018). Hydraulic properties of 3D crossed rock fractures by considering anisotropic aperture distributions. *Adv. Geo-Energy Res.* 2 (2), 113–121. doi:10.26804/ager.2018.02.01
- Ran, Q., and Li, S. (1997). Study on dynamic model of physical property parameters in numerical simulation of fluid-solid coupled oil reservoirs. *Petrol. Explor. Dev.* 024 (003), 61–65 [in Chinese].
- Ren, L., Su, Y. L., Zhan, S. Y., and Meng, F. K. (2019). Progress of the research on productivity prediction methods for stimulated reservoir volume (SRV)-fractured horizontal wells in unconventional hydrocarbon reservoirs. *Arab. J. Geosci.* 12 (6), 184. doi:10.1007/s12517-019-4376-2

- Sennhauser, E. S., Wang, S., and Liu, M. X. (2011). *A practical numerical model to optimize the productivity of multistage fractured horizontal wells in the cardium tight oil resource*. Alberta, Canada: Society of Petroleum Engineers.
- Stalgorova, E., and Mattar, L. (2012). *Analytical model for history matching and forecasting production in multistage composite systems*. Alberta, Canada: Society of Petroleum Engineers.
- Yang, X., Guo, B., and Zhang, X. (2019). *Use of a new well productivity model and post-frac rate-transient data analysis to evaluate production potential of refracturing horizontal wells in shale oil reservoirs*. Charleston, VA: Society of Petroleum Engineers.
- Yin, D., Liu, K., and Sun, Y. (2019). A new model for pressure sensitive effect calculation considering rock characteristic parameters of tight reservoirs. *Spe. Reservoirs*. 26 (05), 71–75, 117 [in Chinese].
- Yuliang, S., Wendong, W., and Guanglong, S. (2014). Composite flow model for horizontal Wells with SRV fracturing. *J. Pet. Sci.* 35 (3) [in Chinese].
- Zhang, K., Jia, N., Li, S., and Liu, L. (2019a). Static and dynamic behavior of CO<sub>2</sub> enhanced oil recovery in shale reservoirs: experimental nanofluidics and theoretical models with dual-scale nanopores. *Appl. Energy*. 255, 113752. doi:10.1016/j.apenergy.2019.113752
- Zhang, K., Jia, N., Li, S., and Liu, L. (2018). Thermodynamic phase behaviour and miscibility of confined fluids in nanopores. *Chem. Eng. J.* 351, 1115–1128. doi:10.1016/j.cej.2018.06.088
- Zhang, K., Jia, N., and Liu, L. (2019b). CO<sub>2</sub> storage in fractured nanopores underground: phase behaviour study. *Appl. Energy*. 238, 911–928. doi:10.1016/j.apenergy.2019.01.088
- Zhang, K., Jia, N., and Liu, L. (2019c). Generalized critical shifts of confined fluids in nanopores with adsorptions. *Chem. Eng. J.* 372, 809–814. doi:10.1016/j.cej.2019.04.198
- Zhang, K., Liu, L., and Huang, G. (2020). Nanoconfined water effect on CO<sub>2</sub> utilization and geological storage. *Geophys. Res. Lett.* 47 (15). doi:10.1029/2020GL087999
- Zhang, N., and Abushaikh, A. S. (2019). *Fully implicit reservoir simulation using mimetic finite difference method in fractured carbonate reservoirs*. Abu Dhabi, UAE: Society of Petroleum Engineers.
- Zhao, K., and Du, P. (2019). Performance of horizontal wells in composite tight gas reservoirs considering stress sensitivity. *Adv. Geo-Energ. Res.* 3 (3), 287–303. doi:10.26804/ager.2019.03.07

**Conflict of Interest:** The authors declare that the research was conducted in the absence of any commercial or financial relationships that could be construed as a potential conflict of interest.

Copyright © 2020 Tian, Chai, Wang and Wang. This is an open-access article distributed under the terms of the Creative Commons Attribution License (CC BY). The use, distribution or reproduction in other forums is permitted, provided the original author(s) and the copyright owner(s) are credited and that the original publication in this journal is cited, in accordance with accepted academic practice. No use, distribution or reproduction is permitted which does not comply with these terms.

## GLOSSARY

$K_m$  matrix permeability,  $10^{-3} \mu\text{m}^2$

$v_m$  fluid flow rate in matrix,  $10^{-3}\text{m/s}$

$\mu$  fluid viscosity,  $\text{mPa} \cdot \text{s}$

$\nabla P_m$  the pressure gradient of the pore system in bedrock,  $\text{MPa/m}$

$\lambda$  trigger pressure gradient,  $\text{MPa/m}$

$\phi$  matrix porosity, %

$\phi_0$  initial formation porosity, %

$C_L$  fluid compressibility,  $\text{MPa}^{-1}$

$C_p$  pore compressibility,  $\text{MPa}^{-1}$

$P_1$  initial reservoir pressure,  $\text{MPa}$

$\rho$  fluid density,  $\text{kg/m}^3$

$\rho_0$  initial fluid density,  $\text{kg/m}^3$

$Q_m$  cross flow rate,  $\text{kg/m}^3 \cdot \text{s}$

$\alpha = = L_m^2/12$  form factor

$L_m$  matrix rock size,  $\text{m}$

$C_m$  matrix composite compressibility,  $\text{MPa}^{-1}$

$P_n$  natural fracture system pressure,  $\text{MPa}$

$P_m$  matrix system pressure,  $\text{MPa}$

$K_n$  natural fracture permeability,  $10^{-3} \mu\text{m}^2$

$C_n$  natural fracture compressibility,  $\text{MPa}^{-1}$

$\phi_n$  natural fracture porosity

$K_f$  artificial fracture permeability,  $10^{-3} \mu\text{m}^2$

$C_f$  artificial fracture compressibility,  $\text{MPa}^{-1}$

$\phi_f$  artificial fracture porosity

$p_w$  bottom hole flowing pressure,  $\text{MPa}$

$d\sigma_{ij}$  effective stress increment

$D_{ijkl}$  elastic-plastic coefficient matrix tensor

$d\epsilon_{kl}$  strain increment

$\epsilon_{ij}$  strain tensor

$\mu$  displacement component

$f_i$  volume force on one side

$\sigma$  normal stress

$\tau$  shearing strength

$\tau_{xy}$  the component of stress in the  $y$  direction on the  $x$  plane

$\alpha$  effective stress sensitivity coefficient,  $\text{MPa}^{-1}$

$E$  Young's modulus,  $\text{GPa}$

$\nu$  Poisson's ratio

$\alpha_E$  relationship between Young's modulus and effective stress sensitivity coefficient

$\alpha_\nu$  relationship between Poisson's ratio and effective stress sensitivity coefficient

$\alpha_K$  relationship between initial permeability value and effective stress sensitivity coefficient

$c_1$  Young's modulus influence coefficient

$c_2$  Poisson's ratio influence coefficient

$c_3$  initial permeability value influence coefficient

$\epsilon_v$  volumetric strain

$N_{i,mn}$  system element basis function matrix of  $\Omega_{m,n}$

$\nabla N_{i,mn}^T, \nabla N_{i,mn}$  transpose of matrix

$P_{i,m}$  element node pressure matrix of  $\Omega_m$

$V$  any function on the boundary

$\sigma$  total stress of reservoir rock

$\sigma'$  effective stress

$\mathbf{M}$  System mass matrix

$F_T$  load vector

$\mathbf{C}$  System damping matrix

$L$  horizontal well length,  $\text{m}$

$\sigma_{\max}$  maximum principal stress,  $\text{MPa}$

$\sigma_{\min}$  minor principal stress,  $\text{MPa}$



# Research on Mechanism of Enhancing Recovery of Heavy Oil With N<sub>2</sub> Huff-n-Puff Assisted by Viscosity Reducer

Lei Tao<sup>1</sup>, Sen Huang<sup>1</sup>, Yali Liu<sup>2</sup>, Hao Cheng<sup>1</sup>, Huajun Du<sup>3</sup>, Cheng Wang<sup>1</sup>, Na Zhang<sup>4\*</sup> and Jinlong Li<sup>4</sup>

<sup>1</sup>School of Petroleum Engineering, Changzhou University, Changzhou, China, <sup>2</sup>College of Petroleum Engineering, China University of Petroleum (East China), Qingdao, China, <sup>3</sup>Shandong Ruiheng Xingyu Petroleum Technology Development Co., Ltd., Qingdao, China, <sup>4</sup>School of Petrochemical Engineering, Changzhou University, Changzhou, China

## OPEN ACCESS

### Edited by:

Songyan Zhu,  
China University of Petroleum  
(Huadong), China

### Reviewed by:

Qian Sun,  
Chengdu University of Technology,  
China  
Renyi Cao,  
China University of Petroleum, China

### \*Correspondence:

Na Zhang  
zhangna3021@126.com

### Specialty section:

This article was submitted to  
Advanced Clean Fuel Technologies,  
a section of the journal  
Frontiers in Energy Research

**Received:** 31 August 2020

**Accepted:** 06 October 2020

**Published:** 16 November 2020

### Citation:

Tao L, Huang S, Liu Y, Cheng H, Du H,  
Wang C, Zhang N and Li J (2020)  
Research on Mechanism of Enhancing  
Recovery of Heavy Oil With N<sub>2</sub> Huff-n-  
Puff Assisted by Viscosity Reducer.  
Front. Energy Res. 8:601186.  
doi: 10.3389/fenrg.2020.601186

In this paper, viscosity reducers with viscosity reduction ability and foaming ability and the recovery efficiency in N<sub>2</sub> huff-n-puff were studied. The optimal 4# viscosity reducer was selected by evaluating the viscosity reduction ability, emulsion stability, interfacial performance, and foaming. The huff-n-puff experiments of single sandpack and dual sandpack were carried out under the reservoir conditions. The results showed that the viscosity reduction rate of 4# viscosity reducer was more than 90% at 50–90°C, and it could form a stable oil/water emulsion when applied to heavy oil. Under the action of 4# viscosity reducer, the interfacial tension between oil and water decreased to 0.41 and 0.19 IFT/mN·m<sup>-1</sup> at 50 and 80°C, respectively. In the single sandpack huff-n-puff experiment, the 4# viscosity reducer could inhibit N<sub>2</sub> bubbles coalesced in large channels and improve the mobility of heavy oil. Compared with N<sub>2</sub> huff-n-puff, the recovery rate of N<sub>2</sub> huff-n-puff assisted by 4# increased by 8.53%. In the dual sandpack huff-n-puff experiment, the N<sub>2</sub> was inhibited to flow from the low permeability sandpack to the high permeability sandpack by 4# viscosity reducer, and the gas production of the low permeability sandpack increased by 284.71%. Under the combined action of viscosification and plugging, the total oil production of the sandpack increased by 7.88%. Therefore, N<sub>2</sub> huff-n-puff assisted by viscosity reducer has a significant effect on enhancing oil recovery in heavy oil reservoirs.

**Keywords:** heavy oil, N<sub>2</sub> huff-n-puff, viscosity reducer, foaming ability, interfacial tension

## INTRODUCTION

With the development of economy, the demand for oil resources is increasing. In the world oil reserves, heavy oil reserves account for more than 70% (Yu, 2001; Zhang et al., 2010). Poor mobility and serious formation heterogeneity are the main reasons for the difficulty of heavy oil development. Thermal recovery is a common method to improve heavy oil recovery. However, due to the energy-intensive emission of a large amount of carbon dioxide, the heavy oil thermal recovery was severely restricted by many countries (De Haan and Van Lookeren, 1969; Hanzlik and Mims, 2003; Ramlal, 2004; Ernandez, 2009). Thus, method of cold recovery of heavy oil has been used in many oil fields. The cold recovery methods of heavy oil mainly include CO<sub>2</sub> huff-n-puff and N<sub>2</sub> huff-n-puff Alvarado

and Manrique, 2010). Carbon dioxide can corrode the pipe networks and tubular columns, and the sources are limited (Dong et al., 2001; Jishun et al., 2015). N<sub>2</sub> can be separated from air, is difficult to dissolve in heavy oil, and has higher miscible pressure than CO<sub>2</sub>. N<sub>2</sub> huff-n-puff recovers oil by increasing power of heavy oil with inject N<sub>2</sub>. Compared to heavy oil thermal recovery, N<sub>2</sub> huff-n-puff is an effective heavy oil recovery method, which has low energy consumption and carbon emission (Clancy and Gilchrist, 1983; Hudgins et al., 1990; Zolghadr et al., 2013). Previous studies have found that N<sub>2</sub> reached low permeability channels during the first cycle of N<sub>2</sub> huff-n-puff and formed foamy oil flow. In the second cycle, the N<sub>2</sub> gradually accumulated in the continuous gas phase. In the third cycle, N<sub>2</sub> was produced mainly in the form of continuous gas phase. The oil recovery is mainly contributed by first cycle (Ma et al., 2015; Lu et al., 2017).

In view of poor dissolved viscosity reduction ability of N<sub>2</sub>, serious gas channeling and low recovery rate may occur after multirounds of N<sub>2</sub> huff-n-puff. In the process of recovery, viscosity reducer and foam agent were usually applied to assist the heavy oil recovery. The active water film formed on the surface of oil by viscosity reducer, which can reduce the oil–water interfacial tension (IFT), and the O/W emulsion was formed in the near-well area, so as to reduce the viscosity of oil (Allenson et al., 2011). Foam can inhibit gas channeling, which is usual produced in the large channel. Foam has many excellent characteristics, such as blocking large channels firstly, water plugging, and oil defoaming. So foam was widely used in plugging water, profile control, and other aspects (Casteel and Djabbarah, 1985; Dalland and Hanssen, 1995; Hirasaki et al., 2005; Xu et al., 2012; Sun et al., 2016a; Li et al., 2019a; Li et al., 2019b). In order to solve the problems of poor mobility of heavy oil and serious gas channeling in N<sub>2</sub> huff-n-puff, a viscosity reduction agent was selected to assist N<sub>2</sub> huff-n-puff, which can not only reduce the viscosity of oil but also plug the larger channels.

In this paper, the oil used in the experiments was collected from ChengBei 15-351 reservoir. The four kinds of viscosity reducer were evaluated, including the viscosity reduction ability, emulsion stability, interfacial performance, and foaming. A viscosity reducer with the optimum comprehensive properties was chosen, which can not only reduce the viscosity of oil effectively, but also has good foaming performance. The N<sub>2</sub> huff-n-puff experiments were performed to investigate flow behaviors of different permeability levels and the effect of viscosity reducer on oil recovery.

## EXPERIMENTAL EQUIPMENT AND METHODS

### Experiment Material

In the N<sub>2</sub> huff-n-puff experiments, the heavy oil was collected from ChengBei 15-351 well (the properties of oil are shown in **Table 1**). The rheological properties of heavy oil were measured by high temperature and high pressure rheometer (model MCR302) in this experiment. The specific viscosity and temperature data were shown in **Figure 1**. Four different viscosity reducers were used in the experiment, labeled as 1#, 2#, 3#, and 4#. Industrial-grade N<sub>2</sub> with a

**TABLE 1** | Properties of oil.

Viscosity at 80°C (mPa·s)	477.63
Density at 80°C (kg/m <sup>3</sup> )	958.3
Saturate content (wt%)	32.12
Aromatic content (wt%)	31.95
Resin content (wt%)	27.82
Asphaltene content (wt%)	6.74
Total acid number (mg KOH/g)	0.54

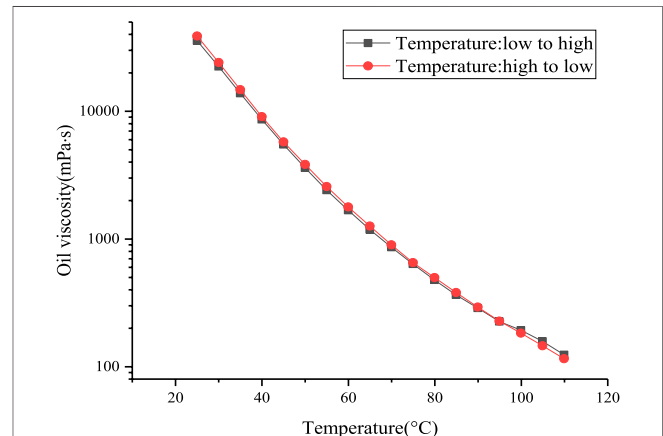


**FIGURE 1** | Viscosity–temperature curve of heavy oil.

purity of 99.99% was used in the experiment. The simulated formation water was composed of a concentration of 10,668 mg/L NaCl and a concentration of 405 mg/L CaCl<sub>2</sub>. And the sizes of silica sand which was used to simulate the dual sandpack models were 180 and 150 μm.

## Physical Properties Evaluation Experiment of Viscosity Reducer

### Viscosity Reduction Effect Evaluation Experiment

Apparatus: DV2TLV digital viscometer (BROOKFIELD, United States, measure range: 1–6,000,000 cP), magnetic stirrer (XiangTian, China, speed range: <2,400 rpm), thermostatic water bath (XiangTian, China, temperature range: <300°C).

Procedure: The temperature of experiment was measured at 50°C. The 1% viscosity reducer and the heavy oil were put into the thermostatic water bath at 50°C. Firstly, the 48 ml viscosity reducer and 112 ml heavy oil were stirred for 3 min by magnetic stirrer at a constant speed (800 rpm); then the emulsion was left to stand for 6 min. Next, the emulsion was stirred at a speed of 400 rpm for 3 min. Finally, the O/W emulsion was obtained. And the DV2TLV digital viscometer was used to measure the viscosity of the emulsion.

### Stability Evaluation Experiment

Apparatus: Magnetic stirrer (XiangTian, China, speed range: <2,400 rpm), thermostatic water bath (XiangTian, China, temperature range: <300°C).



Procedure: In this experiment, the stability evaluation parameter  $S_V$  was measured. The four kinds of prepared heavy oil emulsions were maintained in the thermostatic water bath at 50°C and then the volume of the drained water from emulsion was recorded every 10 min. The water drained rate  $f_v$  was calculated by the following formula:

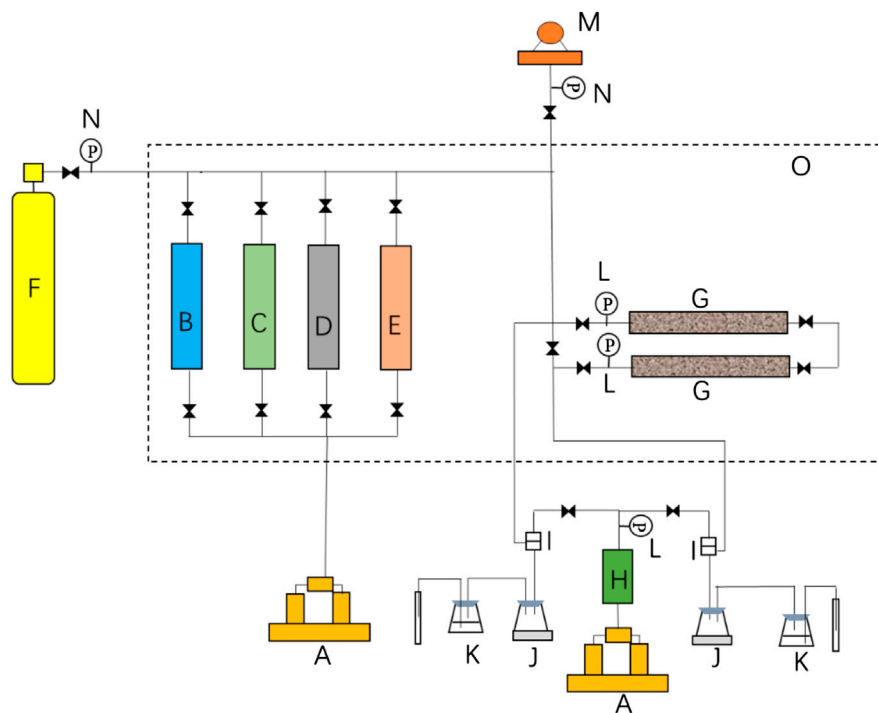
$$f_v = \frac{V_1}{V_2} \times 100\%.$$

In the formula,  $V_1$  and  $V_2$  refer to the volume of the drained water and the total volume of water in the emulsion, respectively,

$V_2 = 48$  ml. Then, the stability  $S_V$  of the emulsion was calculated by the following formula:

$$S_V = \sum K_i [1 - (f_v)_i].$$

In the formula,  $K_i$  refers to the weighted coefficient, and the  $K_i$  was set as 1, 2, 3, 4, 5, and 6 for 10, 20, 30, 40, 50, and 60 min, respectively. With the increase of the  $S_V$ , the stability of the heavy oil emulsion was enhanced.



- |                                       |                            |
|---------------------------------------|----------------------------|
| A. Piston Pump                        | B. N <sub>2</sub> Cylinder |
| C. Simulated Formation Water Cylinder | D. Heavy Oil Cylinder      |
| E. Viscosity Reducer Cylinder         | F. N <sub>2</sub> Cylinder |
| G. Sandpack                           | H. Accumulator Tank        |
| I. Back Pressure Regulator            | J. Electronic Balance      |
| K. Separator                          | L. Pressure Transducer     |
| M. Vacuum Pump                        | N. Pressure Sensor         |
| O. Isothermal Case                    |                            |

**FIGURE 2 |** Schematic diagram of the huff-n-puff apparatus.

### Oil–Water Interfacial Tension Evaluation Experiment

Apparatus: TX-500C rotating IFT apparatus (CNG, Co., United States, speed range: 1,000–10,000 rpm, IFT range:  $10^{-5}$ – $10$  mN/m, accuracy  $<\pm 10^{-6}$  mN/m, temperature range: 20–100°C), thermostatic water bath (XiangTian, China, temperature range:  $<300^{\circ}\text{C}$ ).

Procedure: First of all, the 1% solution of four types of viscosity reducer and two heavy oil samples were prepared. The two heavy oil samples were placed in thermostatic water bath at 50°C and 80°C for 24 h, respectively. Then, the 1% viscosity reducer solution and the heavy oil sample were placed into TX-500C rotating IFT apparatus at a constant speed of 5,000 rpm, and the oil–water IFT at 50 and 80°C was measured.

### Foaming Ability Evaluation Experiment

Apparatus: High temperature and high pressure foam evaluation instrument (FoamEvaluate, Haian Group, China; pressure range  $<32$  MPa and temperature range  $<200^{\circ}\text{C}$ ).

Procedure: The 100 ml 1% viscosity reducer solution was placed in the high temperature and high pressure foam evaluation instrument. The liquid height  $H_0$  was recorded, and high-pressure N<sub>2</sub> was injected until the pressure of the foam evaluation instrument was up to 15 MPa. The temperature was

set at 80°C for 60 min. The foam was manufactured at speed of 1,000 rpm for 1 min. The foaming height  $h_1$  and liquid height  $h_2$  were recorded. Foam half-life  $t_{50}$  was measured which is based on the time required to drain half of the liquid from the foam.

### N<sub>2</sub> Huff-n-Puff Experiment

Apparatus: The apparatus of the huff-n-puff experiment was described in **Figure 2**. According to the different experiment requirements, single sandpack and dual sandpack experiment was carried out. A variety of fluids in the experiment were delivered by ISCO pumps (Model 100DX, Teledyne Technologies, United States, flow accuracy  $<0.25$   $\mu\text{l}/\text{min}$ , pressure accuracy  $<\pm 0.5\%$ ). The sandpack model had a length of 600 mm and a diameter of 25 mm. Pressure gauges (Haian Group, China, measurement range  $<50$  MPa, accuracy  $<0.1\%$  FS), pressure sensors (Model 3210PD, Haian Group, China, measurement range  $<50$  MPa, accuracy  $<0.1\%$  FS), and vacuum gauge (Haian Group, China, measurement range  $<-0.1$  MPa, accuracy  $<0.1\%$  FS) were used to measure pressure. The electronic balances (Model PL 2002, Mettler Toledo, Switzerland, measurement range  $<2,100$  g, accuracy  $<0.01$  g) were used to measure the weight of produced oil.

Single sandpack: The experiment procedures for single sandpack were as follows: 1) Silica sand with the same size

**TABLE 2 |** Sandpack parameters of single sandpack/dual sandpack.

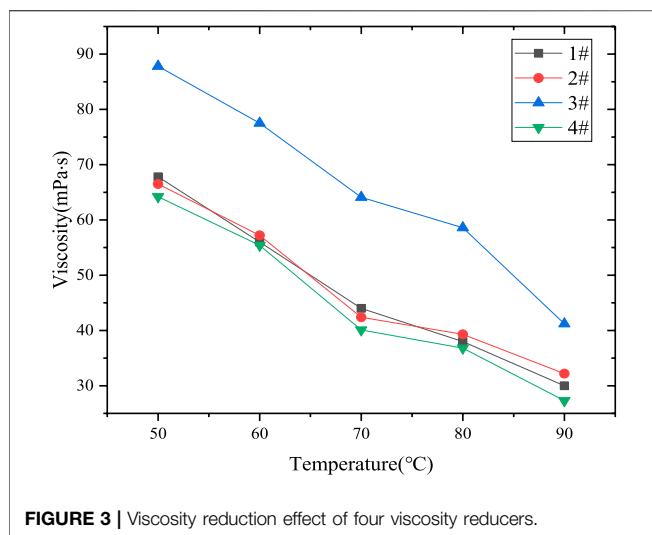
NO.	Type	Particle size ( $\mu\text{m}$ )	Porosity (%)	Permeability (mD)	Original oil saturation (%)
1	Single sandpack	180	0.44	3,018	88.88
2	Single sandpack	180	0.43	3,112	91.24
3	Dual sandpack	180	0.45	3,241	84.63
4		150	0.44	1,123	86.27
5	Dual sandpack	180	0.46	3,439	80.34
6		150	0.44	1,167	86.39

**TABLE 3 |** Experimental data on viscosity reduction effect.

Temperature ( $^{\circ}\text{C}$ )	Initial oil viscosity (mPa-s)	1# (mPa-s)	2# (mPa-s)	3# (mPa-s)	4# (mPa-s)
50	3,610	67.8	66.5	87.8	64.2
60	1,680.4	56	57.2	77.5	55.4
70	862.44	44	42.4	64.1	40.1
80	477.63	38	39.3	58.6	36.8
90	288.14	30	32.2	41.2	27.3

**TABLE 4 |** Experimental data of viscosity reduction rate.

Temperature ( $^{\circ}\text{C}$ )	1# viscosity reduction rate (%)	2# viscosity reduction rate (%)	3# viscosity reduction rate (%)	4# viscosity reduction rate (%)
50	98.12	98.16	97.57	98.22
60	96.67	96.60	95.39	96.70
70	94.90	95.08	92.57	95.35
80	92.04	91.77	87.73	92.30
90	89.59	88.82	85.70	90.53



distribution was used to make sure sandpacks are of similar permeability (2,500–4,000 md). 2) The sandpack was vacuumed for 6 h before being saturated by simulated formation water, and the permeability was measured by the Darcy law. 3) The experimental temperature was maintained at 80°C. The heavy oil was injected into the sandpack with a constant rate of 0.5 ml/min until no water came out at the outlet, and the original oil and water saturations were calculated. 4) The viscosity reducer was

pumped into sandpack; then N<sub>2</sub> was injected into the sandpack to 15 MPa; the huff process stopped. 5) After 12 h of soak time, the puff process started. 6) The sandpack was opened for a puff process, and the pressure gradually reduced at a rate of 0.2 MPa/min, which was controlled with a backpressure regulator and an ISCO pump at the outlet. The volumes of produced oil and gas were measured. 7) After the pressure at the outlet of first cycle was reduced to zero, the second cycle of the huff process was started and so on (Table 2).

**Dual sandpack:** The dual sandpack experiment procedures were as follows: 1) Two sandpacks were vacuumed for 6 h. 2) Under reservoir conditions, one sandpack was saturated with the simulated formation water to obtain its pore volume and the permeability of sandpacks was measured by the Darcy law. 3) The experimental temperature was maintained at 80°C. The original oil and water saturations were determined by pumping the heavy oil into the sandpack until no water came out. 4) The viscosity reducer was pumped into sandpack; then N<sub>2</sub> was injected into the sandpack to 15 MPa; the puff process stopped. 5) Another sandpack was operated in similar ways, that is, 2), 3), and 4). 6) After 12 h of soak time, the puff process started. 7) The sandpack was opened for a puff process, and the depletion rate of 0.2 MPa/min was controlled with two backpressure regulators and an ISCO pump at the outlet. The weight and volume of produced oil and gas were measured. 8) After the pressure of first cycle was reduced to zero, the second cycle of the huff process was started and so on (Table 2).

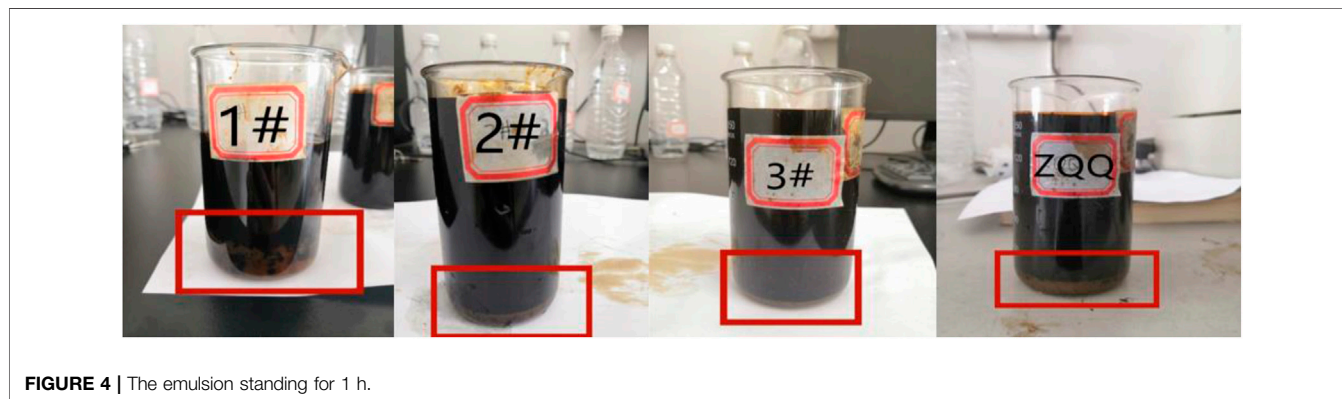
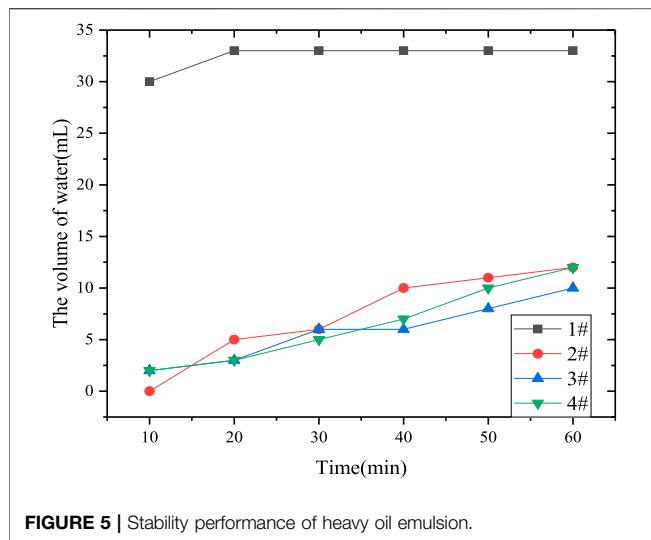


**TABLE 5 |** Experimental results of stability performance of heavy oil emulsion.

Time (min)	1#		2#		3#		4#	
	Water volume (ml)	f <sub>v</sub> (%)	Water volume (ml)	f <sub>v</sub> (%)	Water volume (ml)	f <sub>v</sub> (%)	Water volume (ml)	f <sub>v</sub> (%)
10	24	50	0	0	1	4	1	2
20	25	52	3	6	2	4	2	4
30	25	52	4	8	2	4	3	6
40	26	54	6	13	4	8	5	10
50	26	54	7	15	5	10	5	10
60	26	54	7	15	5	10	6	13
S <sub>v</sub>	9.74		18.52		19.29		19.02	



## EXPERIMENTS, RESULTS, AND DISCUSSION

### Evaluation of Viscosity Reduction Effect

Heavy oil was rich in resin and asphaltene, which results in high density and viscosity of heavy oil. The main reason for the difficulty of heavy oil recovery is poor mobility (Corbett, 1969). Since the viscosity of water was much less than oil, the viscosity of O/W emulsion was less than oil and W/O emulsion. Under the action of viscosity reducer, the mobility of fluid was improved, because the W/O emulsion was transformed into O/W (Kilpatrick, 2012; Liu et al., 2019). According to the experimental procedure and conditions, the experimental results were shown in Tables 3 and 4.

As shown in Table 3, when the temperature was less than 70°C, the viscosity reduction rate of the four viscosity reducers

could be more than 90%. Figure 3 shows the viscosity reduction effect of four viscosity reducers. It is observed that the viscosity decreased almost linearly with temperature. In terms of the viscosity reduction effect, 3# has the worst effect. 1#, 2#, and 4# viscosity reducers showed better performances of viscosity reduction effect as compared 3#.

### Evaluation of Oil-Water Emulsion Stability

Stability was the significant property of heavy oil emulsion, which requires the heavy oil emulsion to remain stable without phase separation and transformation during recovery. The stability of emulsion depends on the strength of oil-water interface. And the viscosity fluctuation of heavy oil O/W emulsion over time depends on its stability (Maneeintr et al., 2013; Yang et al., 2018). The stability of heavy oil emulsion was an important index to evaluate the performance of viscosity reducer. The four kinds of emulsions were prepared and placed in an oven at 50°C. The volume of the drained water was recorded every 10 min (Figure 4). The experimental results were shown in Table 5.

The performance of O/W emulsion stability was measured at 50°C. The stability performance of heavy oil emulsion is shown in Figure 5. The volume of water drained from heavy oil emulsion was increased with time. 2#, 3#, and 4# emulsions have good stability performance, in which the volume of water drained emulsions was similar. 1# emulsion drained out 50% water in 5 min; then, the volume of the drained water has no obvious change. After 60 min (Figure 4), all of emulsion was stable; according to  $S_V$ , 2#, 3#, and 4# showed a better performance of O/W emulsion stability as compared to 1#.

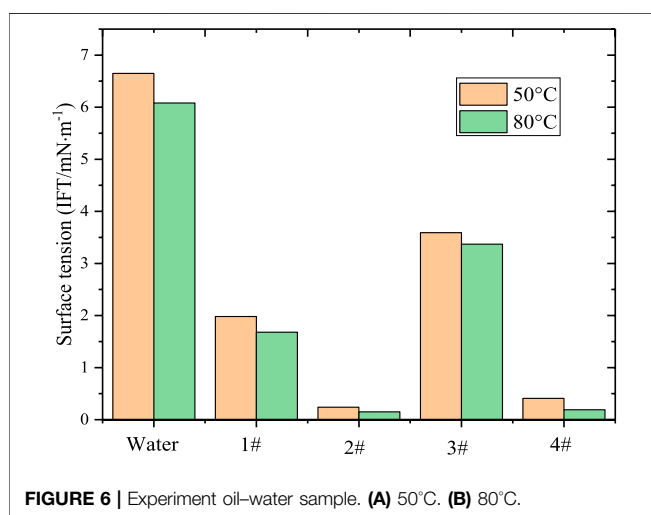
### Evaluation of Oil-Water Interfacial Tension

The oil-water IFT is an important parameter for heavy oil recovery (Sakthivel et al., 2016; Sakthivel et al., 2017). As shown in Figure 6, it is observed that length of oil drop was increased with temperature. Based on the experiment results, shown in Figure 7, the IFT between oil and water was the highest; it reached 6.65 and 6.08 N/m at 50 and 80°C, respectively. Under the action of 4#, the IFT between oil and water decreased to 0.41 and 0.19 IFT/mN·m<sup>-1</sup> at 50 and 80°C, respectively. The 4# viscosity reducer was the best at reducing oil-water IFT.

### Evaluation of Foaming

Foam performance evaluation of viscosity reducer includes foaming ability and drainage half-life (Liu et al., 2010; Sun et al., 2016b). The foaming ability and drainage half-life of four viscosity reducers were measured at 15 MPa and 80°C; the results were shown in Figure 8.

Figure 9 indicated that the foaming volume of 2# viscosity reducer was the largest, 4# viscosity reducer ranks the second, and that of 3# viscosity reducer was the smallest. However, as for the half-life, the 3# has the longest half-life, 4# ranks the second, and the half-life of the 2# and 1# viscosity reducer was shorter. Although 2# viscosity reducer had the largest foaming volume, its half-life was short; similarly 3# viscosity reducer had the longest half-life, but the foaming volume was small. According to the foaming ability and drainage half-life of four kinds of



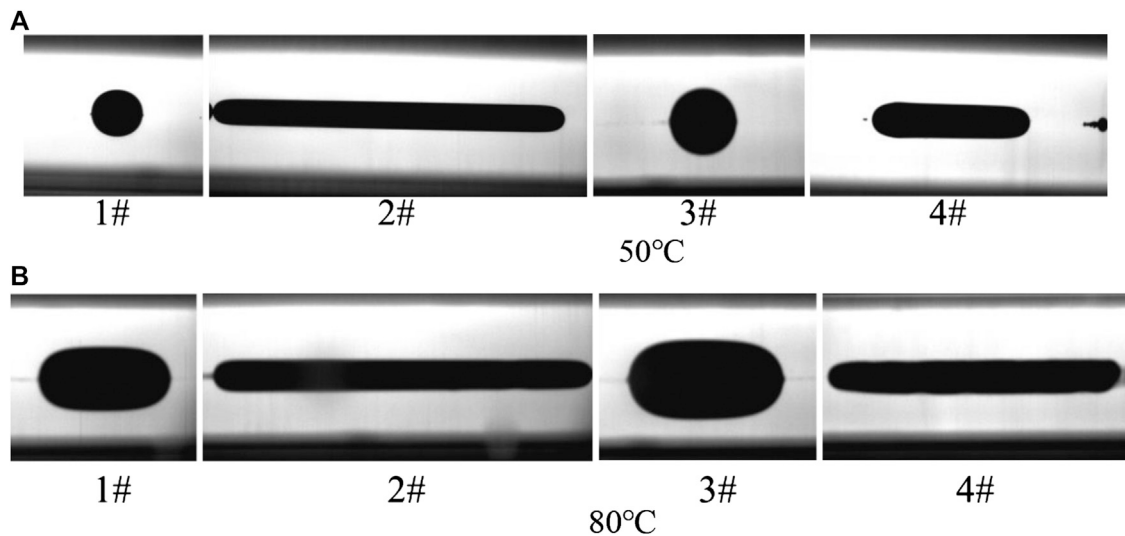


**FIGURE 7 |** Interfacial tension value of heavy oil under the action of viscosity reducer.

viscosity reducers, the foaming performance of 4# viscosity reducer was the best.

By measuring the viscosity reduction ability, emulsion stability, interfacial performance, and foaming ability at different concentrations, the 4# viscosity reducer with best performance was selected to conduct the huff-n-puff experiments.

## Results and Analysis of Huff-n-Puff Experiment

### Analysis of Oil Production

In the huff-n-puff experiment, the N<sub>2</sub> was injected into the sandpack until the pressure increased to 15 MPa, while the soaking time was 12 h. The puff process was started at pressure depletion rate of 0.2 MPa/min. The experimental results are shown in **Table 6**.

The oil recovery of N<sub>2</sub> huff-n-puff process was shown in **Table 6**. It can be seen that the oil recovery was mainly concentrated in the first and second cycles. Among them, the oil recovery in the first and second cycles was 6.86 and 6.85%, respectively. And the oil recovery in the third and fourth cycles was only 2.83 and 0.94%, respectively. Therefore, the total recovery of N<sub>2</sub> huff-n-puff process was 17.5%.

According to **Figure 10B**, in the N<sub>2</sub> huff-n-puff assisted by viscosity reducer experiment, the oil recovery in the first and second cycles was 10.13% and 8.56%, and in the third and fourth cycles was 5.78% and 1.56%, respectively. As shown in **Figures 10A,B**, it is observed that the recovery performance of the first and second cycles was good. However, with the increase of the cycles, the cumulative oil production decreased rapidly. And the recovery performance of N<sub>2</sub> huff-n-puff assisted by viscosity reducer was better than N<sub>2</sub> huff-n-puff in each cycle.

In the N<sub>2</sub> huff-n-puff of dual sandpack process, the total oil recovery of high permeability sandpack was 18.98% and that of the low permeability sandpack was 11.90%. We note that the

permeability of sandpack (NO. 1) and that of sandpack (NO. 3) were similar; however, the oil recovery of sandpack (NO. 3) was increased 1.48%. In the N<sub>2</sub> huff-n-puff assisted by viscosity reducer of dual sandpack process, the total oil recovery of high permeability sandpack was 29.00%, and that of the low permeability sandpack was 17.82% **Figure 11**.

### Analysis of Gas Production

As shown in **Figure 12**, with the increase in the huff-n-puff cycles, the gas production increased rapidly. The oil was produced and the oil position in the sandpack was occupied by N<sub>2</sub> injection in the next huff process, which increased the gas injection volume in each cycle. In the first and second cycles, when the production pressure was in the range of 8–15 MPa, the gas production per unit pressure drop was relatively flat. And when the production pressure was in the range of 0–6 MPa, the gas production increased per unit pressure drop, which was similar to the oil

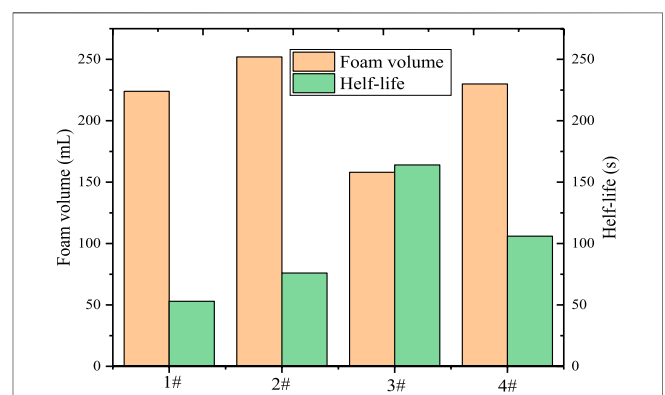
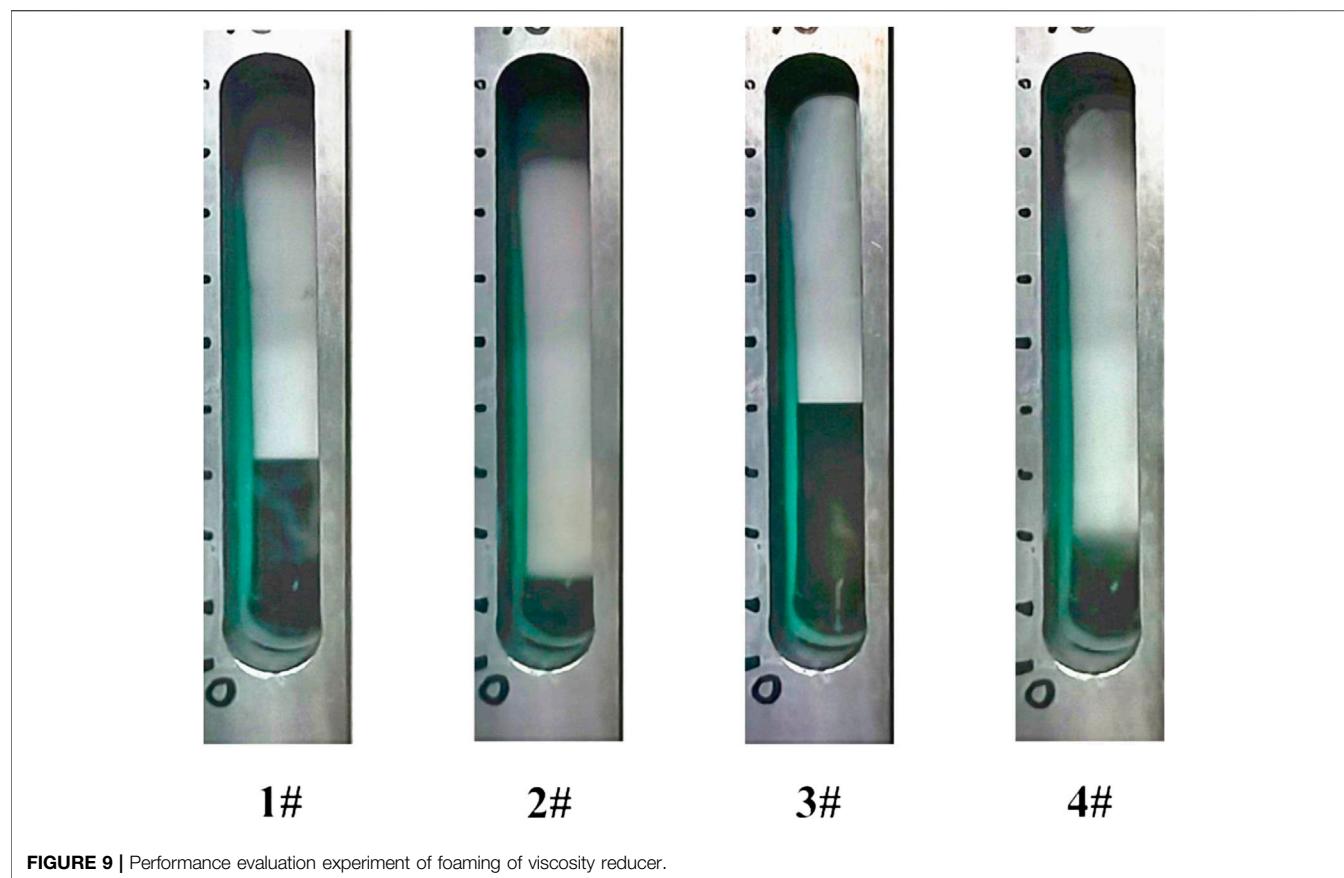


**FIGURE 8 |** Foaming volume and half-life of viscosity reducer.





production. The third and fourth cycle production processes were relatively stable.

As shown in **Figures 13A,B**, the gas production of the high permeability sandpack was higher than that of the low permeability sandpack. This is because the flow resistance of the gas in the high permeability sandpack was less than that in the low permeability sandpack. In the N<sub>2</sub> huff-n-puff experiment, the gas production in the first and second cycles was more than that of the third and fourth cycles. In the first and second cycles, one reason is the higher oil saturation in the low permeability sandpack, and the other reason is the effect of the resistance of N<sub>2</sub> flowing out in the high permeability sandpack less than that in the low permeability sandpack. In the third and fourth cycles, due to the low oil saturation of the low permeability sandpack, the N<sub>2</sub> gas volume was more than the

oil in the channel, and the gas was more likely to flow out from the high permeability sandpack.

As shown in **Figures 13C,D**, in the N<sub>2</sub> huff-n-puff assisted by viscosity reducer experiment, the gas production of low permeability sandpack was increased, especially in the third and fourth cycles. This is because of the foaming pugging effect of 4# viscosity reducer. The foam plugged the large channel, which increased the resistance of N<sub>2</sub> flow in the channel, but did not affect the N<sub>2</sub> displacement of oil (Zhu et al., 1998; Li et al., 2017). Finally, the oil production of low permeability sandpack was improved.

### Analysis of Huff-n-Puff Process

In the process of soaking, N<sub>2</sub> was dispersed in the pores of the sandpack. This is because of the concentration difference of N<sub>2</sub> in

**TABLE 6 |** Results of huff-n-puff experiment.

Sandpack NO.	Type	First cycle oil recovery (%)	Second cycle oil recovery (%)	Third cycle oil recovery (%)	Fourth cycle oil recovery (%)	Total oil production (ml)	Total cycle oil recovery (%)
1	Single sandpack	6.86	6.85	2.83	0.94	20.14	17.5
2	Single sandpack	10.13	8.56	5.78	1.56	30.06	26.03
3	Dual sandpack	6.99	6.99	3.00	2.00	21.28	18.98
4		4.06	4.84	2.33	0.66	13.3	11.9
5	Dual sandpack	9.07	9.36	5.96	4.61	31.55	29.00
6		6.55	6.51	2.38	2.37	19.94	17.82

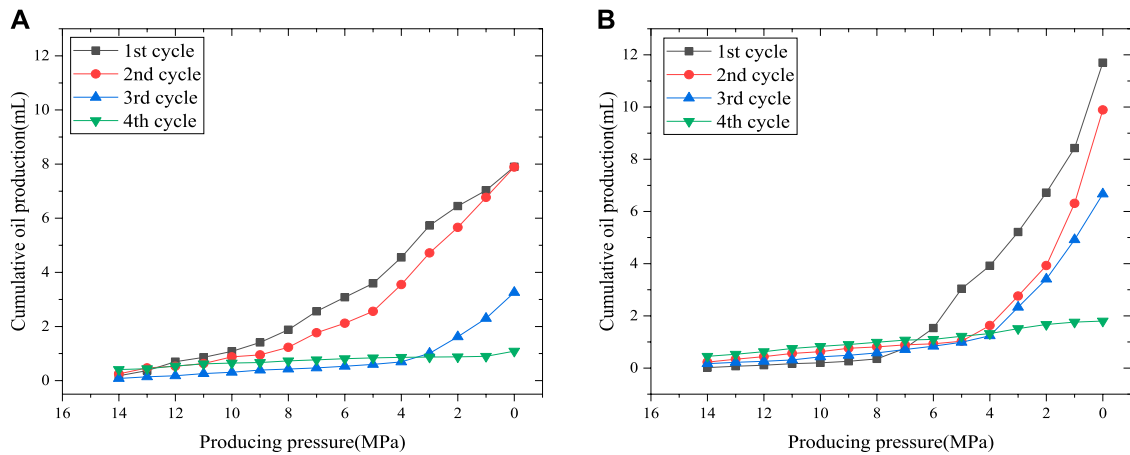


**FIGURE 10 |** Cumulative oil production for each cycle of single sandpack. (A) N<sub>2</sub> huff-n-puff. (B) N<sub>2</sub> huff-n-puff assisted by viscosity reducer.

the sandpack. By this diffusion way, N<sub>2</sub> was almost unaffected by permeability, so N<sub>2</sub> can reach the channel with low permeability (Nguyen et al., 2018). In the first cycle (Figure 14), the N<sub>2</sub> existed

in the sandpack in the form of dispersed small bubbles. In the production process, it was difficult for N<sub>2</sub> to form continuous gas phase, and oil of existence enables the sandpack to maintain a

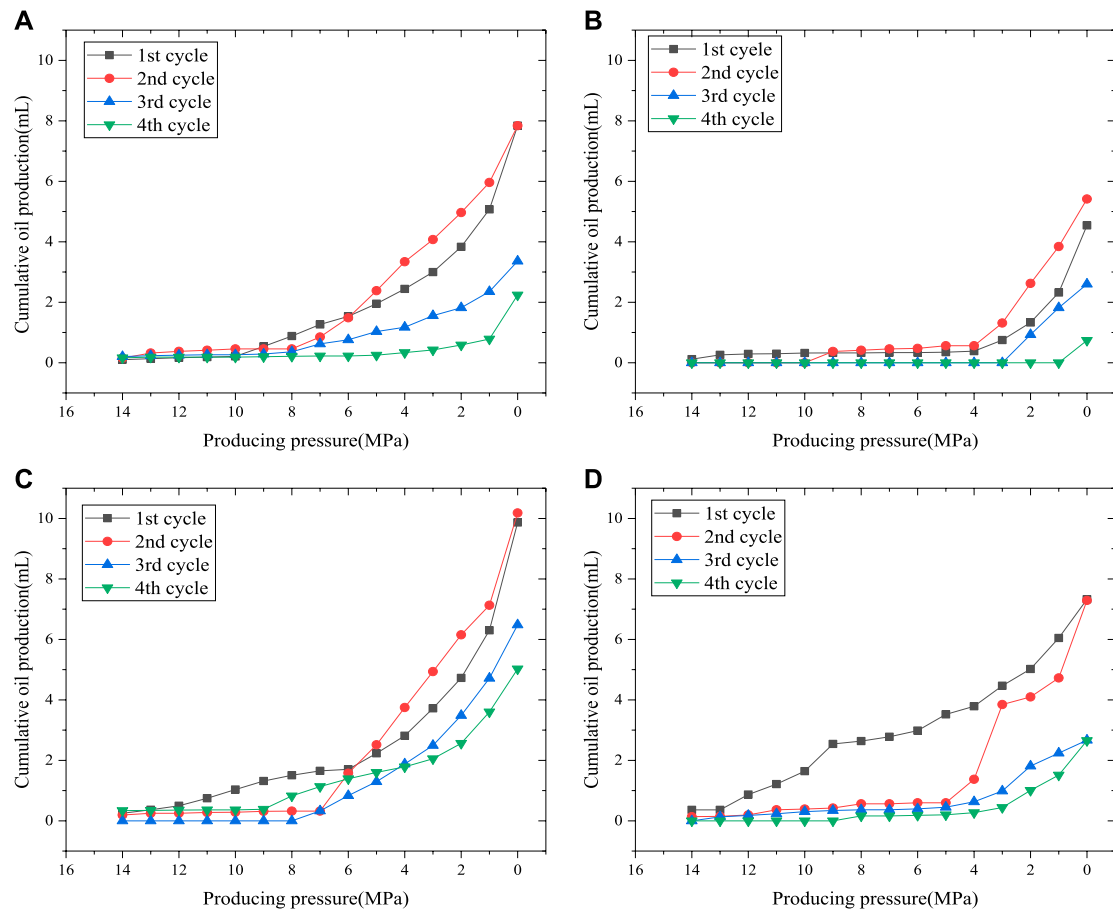


**FIGURE 11 |** Cumulative oil production for each cycle of dual sandpack. (A) High permeability sandpack of N<sub>2</sub> huff-n-puff. (B) Low permeability sandpack of N<sub>2</sub> huff-n-puff. (C) High permeability sandpack of N<sub>2</sub> huff-n-puff assisted by viscosity reducer. (D) Low permeability sandpack of N<sub>2</sub> huff-n-puff assisted by viscosity reducer.

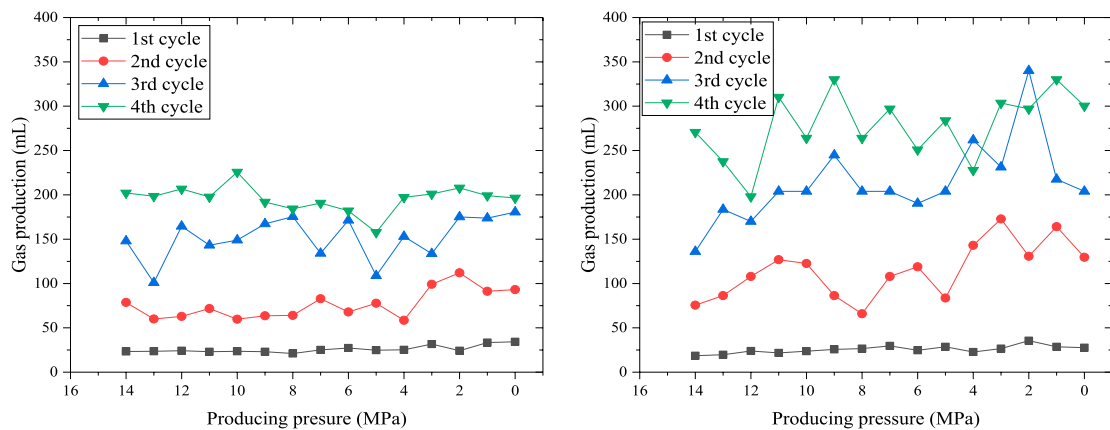


**FIGURE 12 |** Gas production for each cycle of single sandpack. **(A)** N<sub>2</sub> huff-n-puff. **(B)** N<sub>2</sub> huff-n-puff assisted by viscosity reducer.

high relative permeability. In the process of pressure depletion, the bubbles were expanded to increase the elastic energy of oil. In the second cycle, the large channels in the sandpack were increased as the oil was produced, and the amount of N<sub>2</sub> injection increased. The sandpack has continuous gas phase and gas bubbles, the continuous gas phase was usually in the

large channel, and the gas bubbles were in the small channel. This kind of continuous gas contributing to the gas bubbles coalesced in the large channel (Adil and Maini, 2005; Zhang et al., 2018). In the third and fourth cycles, the gas bubbles were coalesced, resulting in channeling. After gas channeling, the gas flowed in the large channel with high permeability in the process of

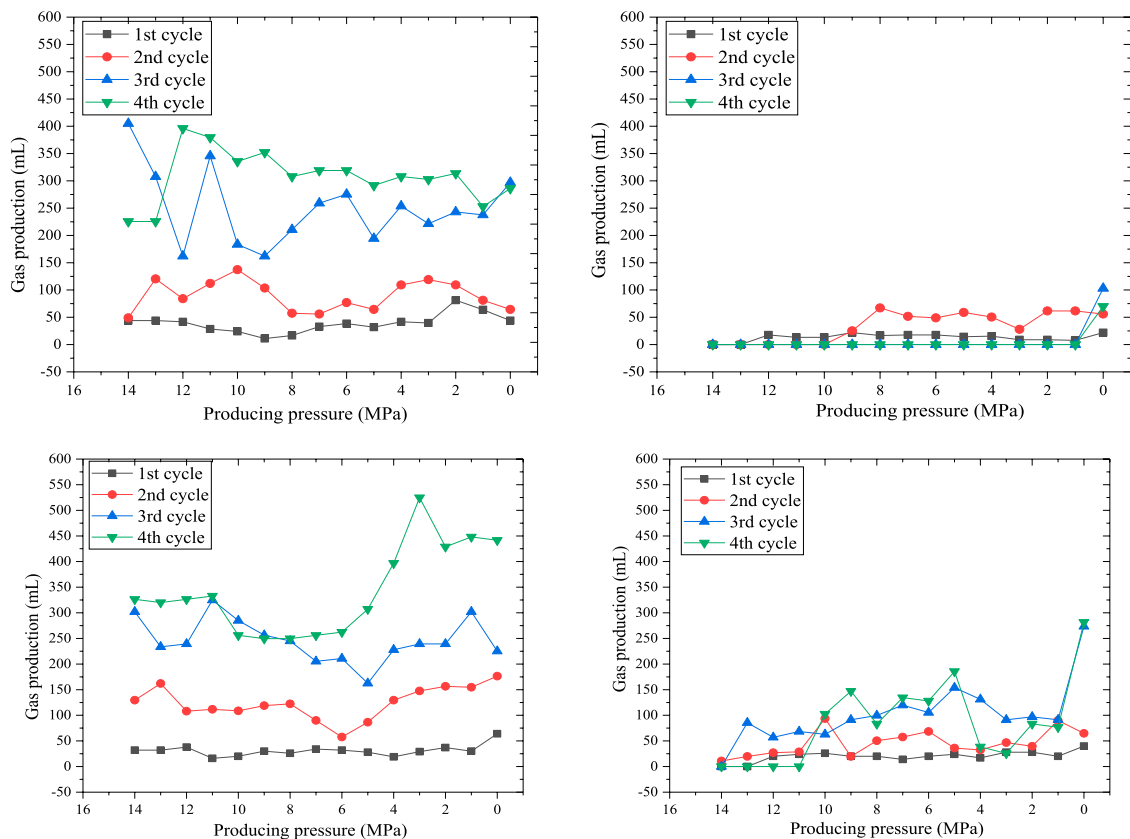
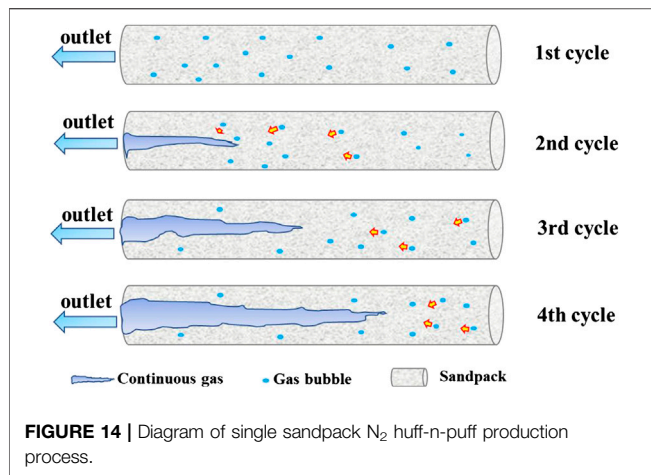


**FIGURE 13 |** Gas production for each cycle of dual sandpack. **(A)** High permeability sandpack of N<sub>2</sub> huff-n-puff. **(B)** Low permeability sandpack of N<sub>2</sub> huff-n-puff. **(C)** High permeability sandpack of N<sub>2</sub> huff-n-puff assisted by viscosity reducer. **(D)** Low permeability sandpack of N<sub>2</sub> huff-n-puff assisted by viscosity reducer.



production, which led to the failure of N<sub>2</sub> to sweep the small channel with high oil saturation and low permeability. The viscous fingering caused by the adverse mobility ratio between the oil and the gas was not a benefit to oil production. When oil was produced, the gas channeling was serious, which was the main reason for low recovery in the third and fourth cycles (Shokri and Babadagli, 2017).

In the dual sandpack N<sub>2</sub> huff-n-puff experiment (Figure 15), the oil production and gas production of the high permeability sandpack (NO. 3) were higher than those of the low permeability sandpack (NO. 4). However, we found that the remaining oil content of the high permeability sand was higher than that of the low permeability (Figure 16). The main reason for this phenomenon was that the flow resistance of oil and N<sub>2</sub> in the high permeability sandpack was lower than that in the low permeability sandpack during the production process. In the process of pressure depletion, the oil and N<sub>2</sub> in the low permeability sandpack near the high permeability sandpack could flow to the high permeability sandpack with low resistance. Although the oil in the high permeability sandpack was produced, it was supplemented by the oil which was in the low permeability sandpack. In this case, the remaining oil content of the high permeability sandpack was higher than that of the low permeability sandpack.

In the first cycle of dual sandpack N<sub>2</sub> huff-n-puff experiment, the oil saturation in the sandpack was high, and the N<sub>2</sub> was dispersed in the high permeability and low permeability sandpack. After pressure depletion, in the low permeability sandpack, the oil was drove by the N<sub>2</sub> to the high permeability sandpack. The produced oil and N<sub>2</sub> in the high permeability sandpack were supplemented by the oil in the low permeability

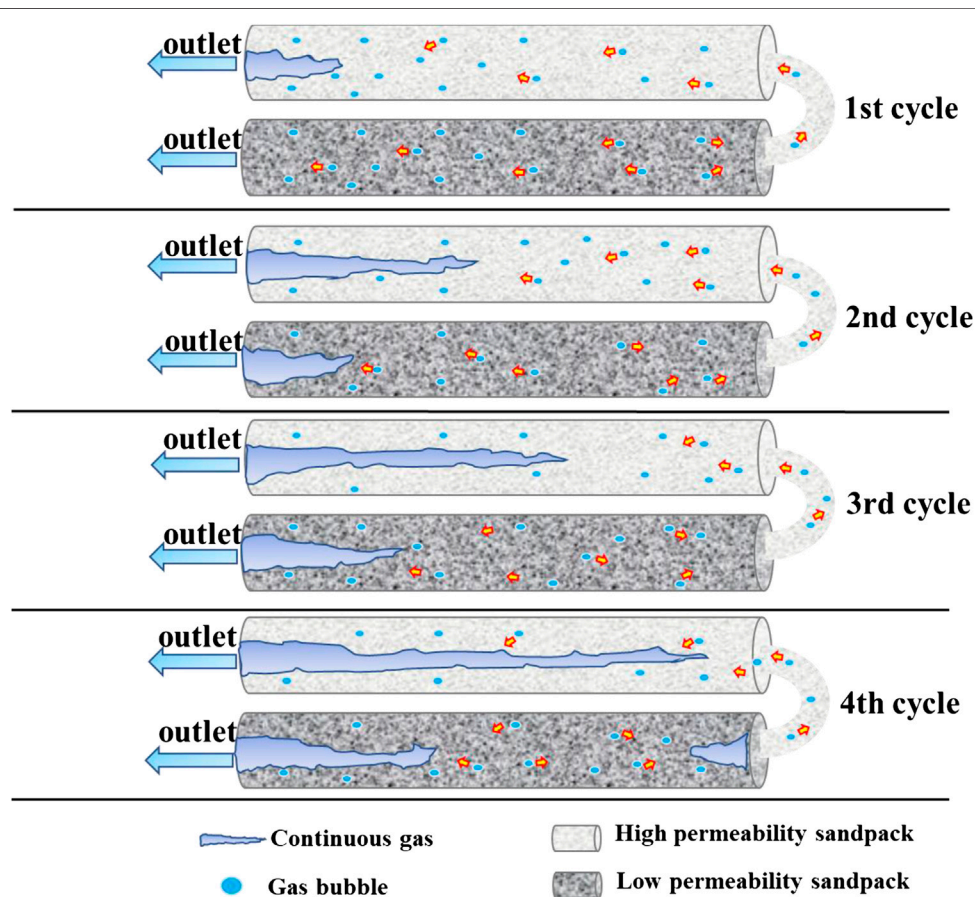






**FIGURE 16 |** Oil sands after huff-n-puff production process.

sandpack. As a result, the gas concentration in the high permeability sandpack was increased, and the relative permeability of gas was increased, resulting in the gas channeling. In the second and third cycles, gas channeling became more and more serious in the high permeability sandpack, and the relative permeability of gas in the low permeability sandpack was increased. In the fourth cycle, the N<sub>2</sub> saturation increased in dual sandpack, the relative permeability of gas increased significantly, and the relative permeability of oil decreased.

From the above analysis, in the single sandpack N<sub>2</sub> huff-n-puff experiment, we can know that the main reason for low oil production was that a large amount of N<sub>2</sub> collects in the high permeability channel to form a continuous gas after the second cycle. Continuous gas flows in large channel with low flow resistance and becomes unable to sweep into low permeability channel with high oil content. In addition, with the relative permeability of gas phase increasing, the relative permeability of oil phase decreases. It is indicated that the oil mobility was

decreased and gas mobility was increased. In dual sandpack N<sub>2</sub> huff-n-puff experiment, the oil and N<sub>2</sub> near the high permeability sandpack in the low permeability sandpack flowed to the high permeability sandpack with low flow resistance. However, there were a large number of channels with high permeability in the high permeability sandpack. In the high permeability sandpack, with the supplement of N<sub>2</sub>, the gas channeling becomes more serious. In order to solve these problems, 4# viscosity reducer with foaming ability was used to assist N<sub>2</sub> huff-n-puff, the large channel was plugged by foam to reduce the collection of N<sub>2</sub>, and the viscosity of oil can be reduced to increase the mobility.

In the process of N<sub>2</sub> huff-n-puff experiment, with the reduction of sandpack pressure, N<sub>2</sub> was collected in the large channel (**Figure 17A**), and the continuous N<sub>2</sub> tended to flow into large channels. And the oil in small channels with low permeability was difficult to drive. At the same time, because the mobility of oil was lower than that of N<sub>2</sub>, and the relative permeability of oil decreased continuously, it was difficult for the oil to flow. In order to reduce the collection of N<sub>2</sub> in the

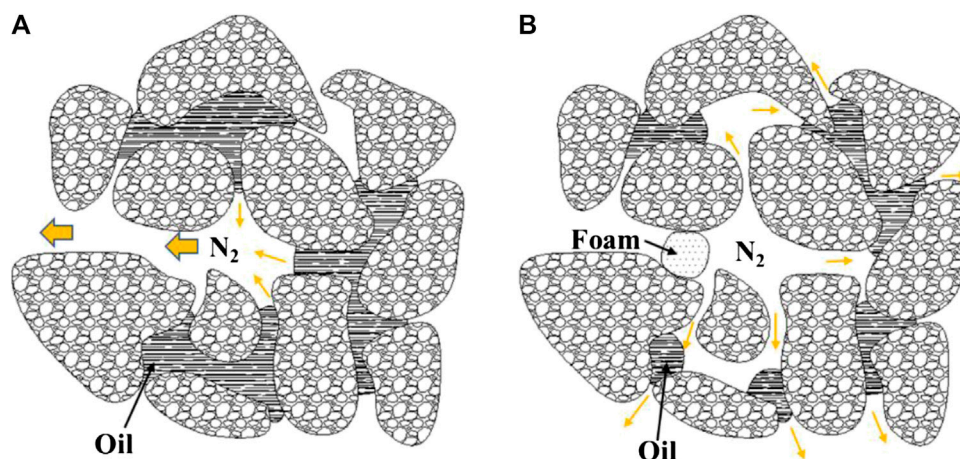


**FIGURE 17 |** Foam plugging process.



production process and improve the mobility of oil, the 4# viscosity reducer was used. In the process of N<sub>2</sub> flow, the 4# viscosity reducer was stirred and foamed, and the foam plugged the large channel (**Figure 17B**). The N<sub>2</sub> was forced to flow to the small channel by gas, and the gas phase relative permeability was reduced.

In the dual sandpack N<sub>2</sub> huff-n-puff assisted by viscosity reducer experiment, the gas production of the low permeability sandpack was obviously increased (**Figure 13D**). It indicated that the 4# viscosity reducer plugged the large channel in the low permeability sandpack and inhibited the flow of N<sub>2</sub> to the high permeability sandpack. The oil production of high permeability sandpack and low permeability sandpack increased by 10.02 and 5.92%, respectively. This is due to the foam of 4# viscosity reducer, which plugged the larger channel, reduced the viscosity of oil, and improved the mobility of oil. The flow of N<sub>2</sub> from the low permeability sandpack to the high permeability sandpack was inhibited by foam, while the flow of oil to the high permeability sandpack was difficult to inhibit. There were a large number of high permeability channels in the high permeability sandpack, and the foam inhibited the gas channeling and improved the oil production of the high permeability sandpack. It is the reason that the oil production of the high permeability sandpack is more than that of the low permeability sandpack.

## CONCLUSION

- (1) The optimized 4# viscosity reducer has good viscosity decreasing effect, which decreases viscosity rate of oil more than 90% at 50–90°C, which can form stable oil emulsion. The oil–water IFT was 0.41 and 0.19 IFT/mN·m<sup>-1</sup> at 50 and 80°C, respectively. What's more, the 4# viscosity reducer has good foaming ability at high temperature and pressure.
- (2) In the single sandpack huff-n-puff experiment, compared with N<sub>2</sub> huff-n-puff, the oil recovery rate of N<sub>2</sub> huff-n-puff assisted by viscosity reducer increased by 8.53%. In the dual sandpack N<sub>2</sub> huff-n-puff experiment, compared with N<sub>2</sub> huff-n-puff, oil production of high permeability sandpack

of N<sub>2</sub> huff-n-puff assisted by viscosity reducer increased by 10.02%, the oil production of low permeability sandpack increased by 5.92%, and total oil production increased by 7.88%.

- (3) After the second cycle of single sandpack N<sub>2</sub> huff-n-puff experiment, the N<sub>2</sub> bubbles coalesced in the large channel, resulting in the gas channeling. In the dual sandpack N<sub>2</sub> huff-n-puff experiment, the oil and N<sub>2</sub> in the low permeability sandpack, near the high permeability sandpack, flowed to the high permeability sandpack, so the oil production of the high permeability sandpack was increased and the remaining oil was higher than the low permeability sandpack.
- (4) The 4# viscosity reducer can reduce the viscosity of oil and plug large channel by foaming. N<sub>2</sub> was forced to flow to small channel, which alleviated the generation of continuous gas phase and increased the oil recovery of small channel. In the dual sandpack huff-n-puff experiment, the foam can effectively inhibit the N<sub>2</sub> flow from the low permeability sandpack to the high permeability sandpack and increase the N<sub>2</sub> displacement efficiency.

## DATA AVAILABILITY STATEMENT

The raw data supporting the conclusions of this article will be made available by the authors, without undue reservation.

## AUTHOR CONTRIBUTIONS

The authors LT and SH have equally contributed to this work.

## FUNDING

This work was supported by the Province Key Scientific and Technological Project for the camellia saponin extraction and CO<sub>2</sub> saponin foam with high mineralization, China (No. KYCX20\_2577).

## REFERENCES

- Adil, I., and Maini, B. B. (2005). "Role of asphaltene in foamy-oil flow," in SPE Latin American and caribbean petroleum engineering conference, Rio de Janeiro, Brazil, 20–23 June (Dallas, TX: Society of Petroleum Engineers). doi:10.2118/94786-MS/10.2118/94786-MS
- Allenson, S. J., Yen, A. T., and Lang, F. (2011). "Application of emulsion viscosity reducers to lower produced fluid viscosity," in OTC Brasil, Rio de Janeiro, Brazil, 4–6 October (Offshore Technology Conference). doi:10.4043/22443-MS
- Alvarado, V., and Manrique, E. (2010). Enhanced oil recovery: an update review. *Energies* 3 (9), 1529–1575. doi:10.3390/en3091529
- Casteel, J., and Djabbarah, N. (1985). "Sweep improvement in carbon dioxide flooding using foaming agents," in Annual SPE technical conference Salt Lake City, UT, May 22–25, Vol. 60. Available at: <https://doi.org/10.2118/11848-MS>
- Clancy, J.P., and Gilchrist, R.E. (1983). "Nitrogen injection applications emerge in the rockies," in SPE rocky mountain regional meeting, Salt Lake City, UT, 22–25 May (Dallas, TX: Society of Petroleum Engineers). doi:10.2118/11848-MS
- Corbett, L. W. (1969). Composition of asphalt based on generic fractionation, using solvent deasphalting, elution-adsorption chromatography, and densimetric characterization. *Anal. Chem.* 41 (4), 576–579. doi:10.1021/ac60273a004
- Dalland, M., and Hanssen, J. E. (1995). Foam barriers for thin oil rims: gas blockage with hydrocarbon foams. *Geol. Soc. Spec. Publ.* 84 (1), 99–109. doi:10.1144/gsl.sp.1995.084.01.11
- De Haan, H. J., and Van Lookeren, J. (1969). Early results of the first large-scale steam soak project in the Tia Juana Field, Western Venezuela. *J. Petrol. Technol.* 21 (1), 101–110. doi:10.2118/1913-pa
- Dong, M., Huang, S., Dyer, S. B., and Mourits, F. M. (2001). A comparison of CO<sub>2</sub> minimum miscibility pressure determinations for Weyburn crude oil. *J. Petrol. Sci. Eng.* 31 (1), 13–22. doi:10.1016/S0920-4105(01)00135-8

- Ernandez, J. (2009). "EOR projects in Venezuela: past and future," in ACI optimising EOR strategy 2009, London, UK, 11–12 March 2009, 11–12.
- Hanzlik, E., and Mims, D. (2003). "Forty years of steam injection in California-The evolution of heat management," in SPE international improved oil recovery conference in Asia pacific, Kuala Lumpur, Malaysia October 20–21, (Dallas, TX: Society of Petroleum Engineers).
- Hirasaki, G. J., Miller, C. A., and Pope, G. A. (2005). *Surfactant based enhanced oil recovery and foam mobility control*. Houston, TX: Rice University.
- Hudgins, D. A., Llave, F. M., and Chung, F. T. H. (1990). Nitrogen miscible displacement of light crude oil: a laboratory study. *SPE Reserv. Eng.* 5 (1), 100–106. doi:10.2118/17372-pa
- Jishun, Q., Haishui, H., and Xiaolei, L. (2015). Application and enlightenment of carbon dioxide flooding in the United States of America. *Petrol. Explor. Dev.* 42 (2), 232–240. doi:10.1016/S1876-3804(15)30010-0
- Kilpatrick, P. K. (2012). Water-in-crude oil emulsion stabilization: review and unanswered questions. *Energy Fuels* 26 (7), 4017–4026. doi:10.1021/ef3003262
- Li, B., Zhang, Q., Li, S., and Li, Z. (2017). Enhanced heavy oil recovery via surfactant-assisted CO<sub>2</sub> huff-n-puff processes. *J. Petrol. Sci. Eng.* 159, 25–34. doi:10.1016/j.petrol.2017.09.029
- Li, S., Wang, Q., and Li, Z. (2019a). Stability and flow properties of oil-based foam generated by CO<sub>2</sub>. *SPE J.* 25 (1), 416–431. doi:10.2118/199339-PA
- Li, S., Wang, Q., Zhang, K., and Li, Z. (2019b). Monitoring of CO<sub>2</sub> and CO<sub>2</sub> oil-based foam flooding processes in fractured low-permeability cores using nuclear magnetic resonance (NMR). *Fuel* 263, 116648. doi:10.1016/j.fuel.2019.116648
- Liu, J., Zhong, L., Yuan, X., Liu, Y., Zou, J., Wang, Q., et al. (2019). Study on the re-emulsification process of water in heavy oil emulsion with addition of water-soluble viscosity reducer solution. *Energy Fuels* 33 (11), 10852–10860. doi:10.1021/acs.energyfuels.9b02733
- Liu, X., Xin, W., Li, G., Zhang, L., Han, Z., and Wang, B. (2010). "Acid-resistant foamer used to control gas Breakthrough for CO<sub>2</sub> drive reservoir," in SPE Asia pacific oil and gas conference and exhibition, Brisbane, Australia, 18–20 October (Dallas, TX: Society of Petroleum Engineers). doi:10.2118/131416-MS
- Lu, T., Li, Z., Li, J., Hou, D., and Zhang, D. (2017). Flow behavior of N<sub>2</sub> huff and puff process for enhanced oil recovery in tight oil reservoirs. *Sci. Rep.* 7 (1), 15695. doi:10.1038/s41598-017-15913-5
- Ma, J., Wang, X., Gao, R., Zeng, F., Huang, C., Tontiwachwuthikul, P., et al. (2015). Enhanced light oil recovery from tight formations through CO<sub>2</sub> huff 'n' puff processes. *Fuel* 154, 35–44. doi:10.1016/j.fuel.2015.03.029
- Maneeintr, K., Sasaki, K., and Sugai, Y. (2013). Investigation of the effects of parameters on viscosities and correlation of heavy oil and stability of its emulsion. *J. Jpn. Inst. Energy* 92 (9), 900–904. doi:10.3775/jie.92.900
- Nguyen, P., Carey, J. W., Viswanathan, H. S., and Porter, M. (2018). Effectiveness of supercritical-CO<sub>2</sub> and N<sub>2</sub> huff-and-puff methods of enhanced oil recovery in shale fracture networks using microfluidic experiments. *Appl. Energy* 230, 160–174. doi:10.1016/j.apenergy.2018.08.098
- Ramlal, V. (2004). "Enhanced oil recovery by steamflooding in a recent steamflood project, cruse 'E' field, trinidad," in SPE/DOE symposium on improved oil recovery, Tulsa, OK, 17–21 April (Dallas, TX: Society of Petroleum Engineers). doi:10.2118/89411-MS
- Sakthivel, S., Gardas, R. L., and Sangwai, J. S. (2016). Effect of alkyl ammonium ionic liquids on the interfacial tension of the crude oil-water system and their use for the enhanced oil recovery using ionic liquid-polymer flooding. *Energy Fuels* 30 (3), 2514–2523. doi:10.1021/acs.energyfuels.5b03014
- Sakthivel, S., Velusamy, S., Nair, V. C., Sharma, T., and Sangwai, J. S. (2017). Interfacial tension of crude oil-water system with imidazolium and lactam-based ionic liquids and their evaluation for enhanced oil recovery under high saline environment. *Fuel* 191, 239–250. doi:10.1016/j.fuel.2016.11.064
- Shokri, A. R., and Babadagli, T. (2017). Feasibility assessment of heavy-oil recovery by CO<sub>2</sub> injection after cold production with sands: lab-to-field scale modeling considering non-equilibrium foamy oil behavior. *Appl. Energy* 205, 615–625. doi:10.1016/j.apenergy.2017.08.029
- Sun, Q., Zhang, N., Li, Z., and Wang, Y. (2016a). Nanoparticle-stabilized foam for effective displacement in porous media and enhanced oil recovery. *Energy Technol.* 4 (9), 1053–1063. doi:10.1002/ente.201600063
- Sun, Q., Zhang, N., Li, Z., and Wang, Y. (2016b). Nanoparticle-stabilized foam for mobility control in enhanced oil recovery. *Energy Technol.* doi:10.1002/ente.201600093
- Xu, H. X., Pu, C. S., Yang, H. B., Man, W. H., and Yang, T. (2012). Study on nitrogen foam flooding in fractured reservoir. *Adv. Mater. Res.* 524–527, 1209–1212. doi:10.4028/www.scientific.net/AMR.524-527.1209
- Yang, F., Chen, Y., Sun, G., Yang, S., Li, C., You, J., et al. (2018). Effects of supercritical CO<sub>2</sub> treatment on the stability of water-in-heavy-oil emulsion and their mechanisms. *Energy Fuels* 32 (2), 1358–1364. doi:10.1021/acs.energyfuels.7b03372
- Yu, L. (2001). Distribution of world heavy oil reserves and its recovery technologies and future. *Spec. Oil Gas Reserv.* 8 (2), 98–10. doi:10.3969/j.issn.1006-6535.2001.02.029
- Zhang, F., Ouyang, J., Wu, M., Wang, G., and Lin, H. (2010). "Enhancing waterflooding effectiveness of the heavy oil reservoir using the viscosity reducer," in SPE Asia pacific oil and gas conference and exhibition, Mishref, Kuwait, 11–14 October (Dallas, TX: Society of Petroleum Engineers). doi:10.2118/175312-MS
- Zhang, N., Wang, Y., Wang, Y., Yan, B., and Sun, Q. (2018). A locally conservative multiscale finite element method for multiphase flow simulation through heterogeneous and fractured porous media. *J. Comput. Appl. Math.* 343, 501–519. doi:10.1016/j.cam.2018.05.005
- Zhu, T., Strycker, A., Raible, C., and Vineyard, K. (1998). "Foams for mobility control and improved sweep efficiency in gas flooding," in SPE/DOE improved oil recovery symposium, Tulsa, OK, 19–22 April (Dallas, TX: Society of Petroleum Engineers). doi:10.2118/39680-MS
- Zolghadr, A., Riazi, M., Escrochi, M., and Ayatollahi, S. (2013). Investigating the effects of temperature, pressure, and paraffin groups on the N<sub>2</sub> miscibility in hydrocarbon liquids using the interfacial tension measurement method. *Ind. Eng. Chem. Res.* 52 (29), 9851–9857. doi:10.1021/ie401283q

**Conflict of Interest:** Author HD was employed by Shandong Ruiheng Xingyu Petroleum Technology Development Co., Ltd.

The remaining authors declare that the research was conducted in the absence of any commercial or financial relationships that could be construed as a potential conflict of interest.

Copyright © 2020 Huang, Tao, Liu, Cheng, Du, Wang, Zhang and Li. This is an open-access article distributed under the terms of the Creative Commons Attribution License (CC BY). The use, distribution or reproduction in other forums is permitted, provided the original author(s) and the copyright owner(s) are credited and that the original publication in this journal is cited, in accordance with accepted academic practice. No use, distribution or reproduction is permitted which does not comply with these terms.



# Effect of Stress-Sensitive Fracture Conductivity on Transient Pressure Behavior for a Multi-Well Pad With Multistage Fractures in a Naturally Fractured Tight Reservoir

Zhan Meng<sup>1,2†</sup>, Honglin Lu<sup>1†</sup>, Xiaohua Tan<sup>1</sup>, Guangfeng Liu<sup>3,4\*</sup>, Lianhe Wang<sup>3</sup> and Daoyong Yang<sup>2\*</sup>

## OPEN ACCESS

### Edited by:

Kaiqiang Zhang,  
Imperial College London,  
United Kingdom

### Reviewed by:

Yu Pang,  
University of Calgary, Canada  
Lu Wang,  
Chengdu University of Technology,  
China  
Qian Wang,  
China University of Petroleum, China

### \*Correspondence:

Guangfeng Liu  
lgfmail@yeah.net  
Daoyong Yang  
Tony.Yang@uregina.ca

<sup>†</sup>These authors have contributed  
equally to this work and share first  
authorship.

### Specialty section:

This article was submitted to  
Advanced Clean Fuel Technologies,  
a section of the journal  
Frontiers in Energy Research

**Received:** 30 August 2020

**Accepted:** 16 October 2020

**Published:** 19 November 2020

### Citation:

Meng Z, Lu H, Tan X, Liu G, Wang L  
and Yang D (2020) Effect of Stress-  
Sensitive Fracture Conductivity on  
Transient Pressure Behavior for a  
Multi-Well Pad With Multistage  
Fractures in a Naturally Fractured  
Tight Reservoir.  
Front. Energy Res. 8:600560.  
doi: 10.3389/fenrg.2020.600560

<sup>1</sup>State Key Laboratory of Oil and Gas Reservoir Geology and Exploitation, Southwest Petroleum University, Chengdu, China, <sup>2</sup>Petroleum Systems Engineering, Faculty of Engineering and Applied Science, University of Regina, Regina, SK, Canada, <sup>3</sup>State Key Laboratory of Petroleum Resources and Prospecting, China University of Petroleum (Beijing), Beijing, China, <sup>4</sup>Engineering Research Center of Gas Resource Development and Utilization of Ministry of Education, China University of Petroleum (Beijing), Beijing, China

This paper presents a semianalytical solution for evaluating transient pressure behavior of a multi-well pad with multistage fractures in a naturally fractured tight reservoir by considering the stress-sensitive effect imposed by both natural and hydraulic fractures. More specifically, the model pertaining to matrix/natural fractures is considered as a dual-porosity continuum, while its analytical flow model can be obtained by use of a slab-source function in the Laplace domain. The hydraulic fracture model is solved by discretizing each fracture into small segments to describe the flow behavior, while stress sensitivity in both the natural fracture (NF) subsystem and hydraulic fracture (HF) subsystem has been taken into account. To validate the newly developed semianalytical model, its solution has been obtained and compared with those of a commercial numerical simulator. By generating the type curves, there may exhibit eight flow regimes: pure wellbore storage, skin effect transition flow, linear flow regime within HFs, early radial flow, biradial flow, transition flow, pseudo-steady diffusion, and the late-time pseudo-radial flow. Furthermore, late-time flow regimes are found to be significantly distorted by the multi-well pressure interference. The smaller the well-rate ratio is, the more distorted the pressure and pressure derivative curves will be. In addition, well spacing and fracture length are found to dominate the flow behavior when multi-well pressure interference occurs. As the well spacing is decreased, the fracture length is increased, and thus occurrence of multi-well pressure interference is initiated earlier. Permeability moduli of NFs and HFs impose no impact on the multi-well pressure interference; however, it can distort flow regimes, leading to a severe distortion of pressure and pressure derivative curves. Similarly, the effect of HF permeability modulus on the flow in a hydraulic fracture, the minimum fracture conductivity is another key factor affecting the “hump” on the pressure curve. As the crossflow coefficient is increased, flow exchange between matrix and NFs is increased. With an increase in the storage ratio, flow exchange lasts longer and the second “dip” on the pressure curve becomes deeper.

**Keywords:** transient pressure analysis, multi-well pad, stress-sensitivity, tight oil reservoir, slab source function

## INTRODUCTION

With the increasing oil and gas consumption, more attentions have recently been directed to exploit the unconventional resources (Schmoker, 2002; Jia, 2017; Yekeen et al., 2018; Gao et al., 2018; Chen et al., 2019). As an important and unconventional clean fossil fuel, tight oil is expected to play an increasingly important role in meeting the energy demand (Song et al., 2015; Yang et al., 2015a; Song and Yang, 2017; Wang M. et al., 2018; Amjed et al., 2019; Jiang et al., 2020a). Owing to the advancement of drilling horizontal wells with multistage hydraulic fractures (HFs), tight oil reservoirs have been exploited commercially though the flow behavior is quite different from those of the conventional reservoirs due to the extremely low permeability (Miller et al., 2008; Meyer and Bazan, 2011; Liu et al., 2018b; Liu et al., 2020a; Liu et al., 2020b, Liu et al., 2020c). To reduce operational costs and mitigate the negative environmental impact, multi-well pad schemes have proven to be more effective for exploiting tight oil/gas reservoirs with and without natural fractures (NFs) (Manchanda and Sharma, 2013; Meng et al., 2017; Xiao et al., 2018; Jiang et al., 2020b; Jiang et al., 2020c); however, multi-well pressure interference under multi-well pad schemes severely distorts the flow patterns. In addition to greatly affecting well production, such a distortion inevitably makes the transient pressure analysis more challenging while the stress-sensitivity effect and contribution of NFs are usually excluded (Liu et al., 2018a). Therefore, it is of fundamental and practical importance to accurately evaluate performance for a multi-well pad with multistage HFs and NFs in a tight formation by taking their stress-sensitive effects into account.

Considering its geological characteristics, fluid flow behavior in a tight formation with both NFs and HFs can be simulated with two main methods: the continuum model and the discrete fracture network (DFN) model. The most classical continuum model is the dual-porosity model proposed by Warren and Root (1963), assuming matrix and NFs as the main storage spaces and flow path. Then, the flow exchange between matrix subsystem and NF subsystem can be quantified (Kazemi 1969; Jalali and Ershaghi, 1987; Hassanzadeh et al., 2009; Wang, L et al., 2018). On the basis of the dual-porosity model, Wu et al. (2004) proposed a triple-porosity model to estimate the flow exchange among matrix, NFs, and HFs, which was subsequently improved with respect to algorithm convergence and computational expenses (Ozkan et al., 2009, 2011; Stalgorova and Mattar, 2012). Due to its simple assumptions and high computational efficiency, the continuum model has been widely used to describe fluid flow in tight oil/shale gas reservoirs.

Using the micro-seismic monitoring and surveillance techniques, it is found that HFs do not occupy the entire formation after being hydraulically fractured. In a DFN model, the HFs are usually described as high permeability channels by means of local grid refinement (Noorishad et al., 1982; Juanes et al., 2002; Rogers et al., 2010). As such, the DFN model is considered to be more rigorously to capture the details of flow behavior in complex fracture network, while it needs to be solved by either numerical difference or dimension reduction. Although the DFN method can be used to accurately describe the fluid flow, its computational expenses are too high (Cipolla et al., 2011).

Combining the advantages of the aforementioned two models, the latest development is to combine the dual-porosity model and the HF model (Zhao et al., 2014; Zhao et al., 2015; Chen et al., 2016; Jia et al., 2016, Jia et al., 2017; Morteza et al., 2018). Such combined models can not only accurately describe fluid flow within the HFs at different angles, but also consider the contribution of the secondary-fracture networks (Ren et al., 2016; Chen et al., 2017b). In practice, either a line-source function or a slab-source function can be used to obtain the semianalytical solution for such complex flow systems under different conditions, though convergence difficulties are encountered and computational expenses are high (Zhang and Yang, 2014; Yang et al., 2015b; Wang et al., 2017; Liu et al., 2018a, Zhang and Yang, 2018). Physically, more practical models together with computational algorithms are desired when the stress-sensitive effect needs to be taken into account (Liu et al., 2015; Chen et al., 2016; Wang et al., 2017). Usually, the stress sensitivities of both NFs and HFs are assumed to be the same while this is found to be not reasonable in reality (Jiang et al., 2019b). In fact, it has been found from laboratory experiments that proppant has a great influence on stress sensitivity of HFs, i.e., the HF permeability modulus is larger than that of NFs (Montgomery and Steanson, 1985; Feng et al., 2017). So far, no attempts have been made to examine the stress sensitivity for NFs and HFs with different contributions in a multi-well pad with consideration of the multi-well pressure interference.

In this paper, a new semianalytical model has been developed and validated to examine the stress-sensitive fracture conductivity on transient pressure response for a multi-well pad in a naturally fractured tight reservoir. More specifically, matrix/NFs is considered as a dual-porosity continuum, which can be solved analytically by use of a slab-source function in the Laplace domain, while HFs can be solved by discretizing each fracture into small segments. Then, the perturbation technique together with superposition principle and the Stehfest algorithm has been employed to solve such a highly nonlinear equation matrix with consideration of different stress-sensitivity for NFs and HFs. In order to validate the semianalytical model, its solution has been compared with that of a commercial simulator. With the assistance of this new approach, not only can flow regimes of multi-well pad with multiple fractures be identified, but also sensitivity analysis has been made to illustrate how key parameters affect the transient pressure responses in such a complex flow system.

## Theoretical Formulations

In this study, two hydraulically fractured horizontal wells are considered as a multi-well pad, producing at two different surface flow rate  $q_{sc1}$  and  $q_{sc2}$  see (Figure 1). It is worthwhile mentioning that this two-well model can be extended to multiple wells, though computational expenses will be correspondingly increased (Appendix B). For convenience, the tight reservoir including matrix subsystem, NF subsystem, and HF subsystem is assumed to be isotropic, while other main assumptions are listed as follows:



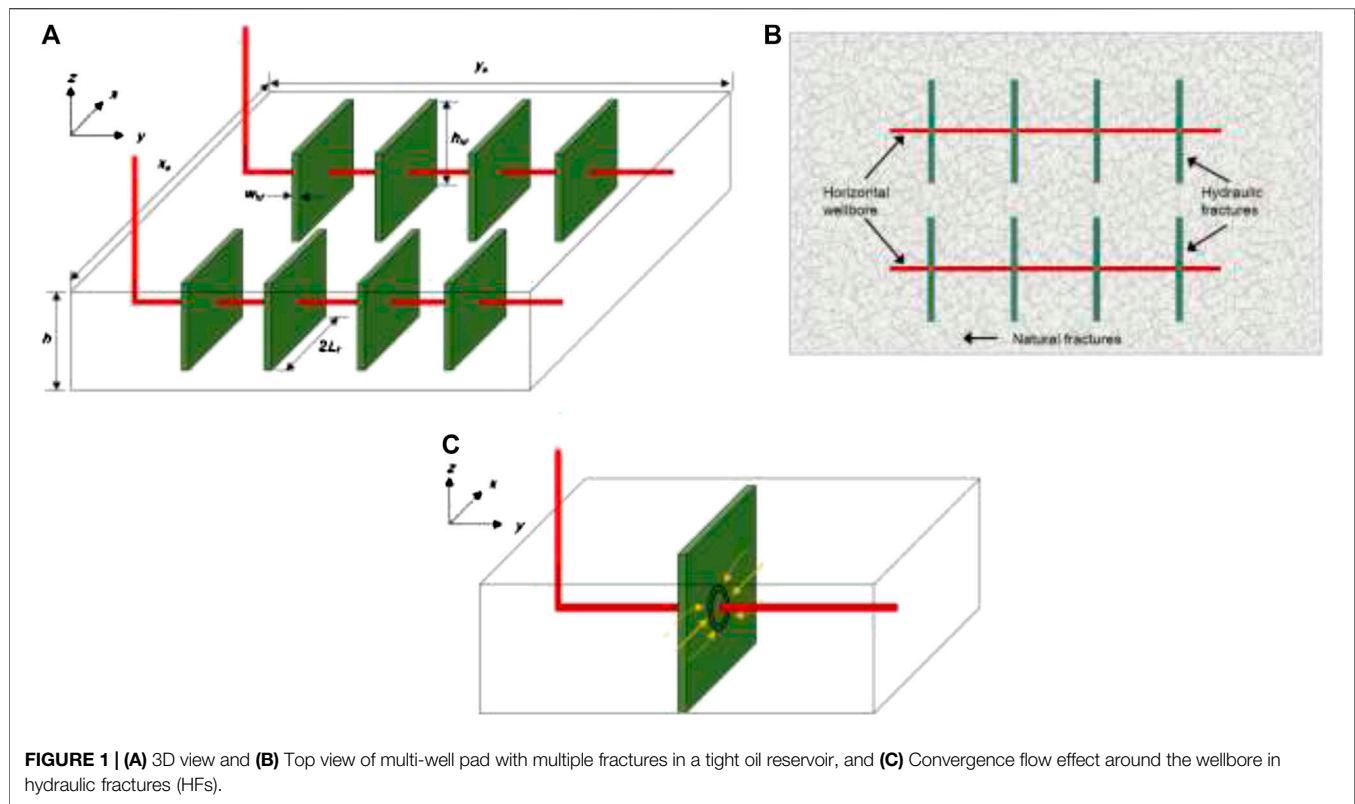


**FIGURE 1 | (A)** 3D view and **(B)** Top view of multi-well pad with multiple fractures in a tight oil reservoir, and **(C)** Convergence flow effect around the wellbore in hydraulic fractures (HFs).

- The reservoir upper and lower boundaries are impermeable and the lateral boundary is infinite.
- Two hydraulic fracturing horizontal wells are parallel to the upper and lower boundaries and penetrate completely, assuming the fractures have finite conductivity.
- Stress-sensitive effects in the NFs and HFs are considered, while their stress sensitivity coefficients are different.
- A pseudo-steady crossflow occurs between the matrix and the NFs, while the HFs are the only pathway for the fluid flow from the NFs to the wellbore.
- Oil flow in the HFs and NFs obeys the Darcy law, and incompressible flow is assumed in the HFs because the fracture volume is negligible compared with that of the NFs (Cinco-Ley and Meng, 1988; Jiang et al., 2019a).
- Single phase and isothermal flow is considered but gravity and capillary effects are neglected.

With the aforementioned assumptions, we first discretize the HFs (**Figure 2**) each of which for Well #1 and Well #2 is respectively divided into  $2 \cdot N_1$  and  $2 \cdot N_2$  segments, assuming the number of HFs for Well #1 and Well #2 is  $M_1$  and  $M_2$ , respectively. The superposition principle can then be used to calculate the pressure responses for these sub-fracture segments. Finally, the dual-porosity flow model and HF flow model are dynamically coupled and solved. In this study, the stress-sensitive effects in the NFs and HFs are considered, while their stress-sensitivity coefficients are different.

The NF permeability modulus,  $\gamma_{nf}$ , is defined as the exponential relationship between NF permeability and its pressure (Chen et al., 2008), i.e.,

$$k_{nf}(p_{nf}) = k_{nfi} \exp[-\gamma_{nf}(p_i - p_{nf})] \quad (1)$$

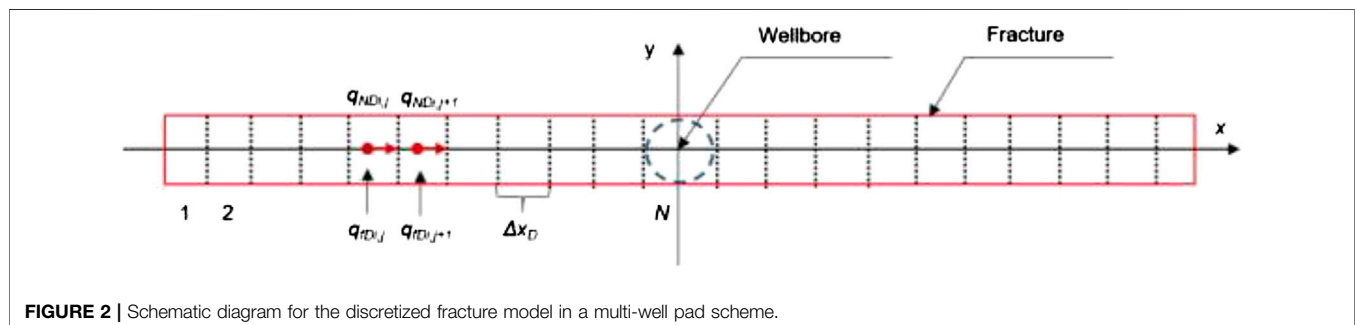


**FIGURE 2 |** Schematic diagram for the discretized fracture model in a multi-well pad scheme.



where  $k_{nf}$  is the NF permeability,  $p_{nf}$  is the NF pressure,  $p_i$  is the initial pressure,  $k_{nfi}$  is the initial NF permeability, and  $\gamma_{nf}$  is the NF permeability modulus.

As for HF, the HF permeability tends to have a minimum value (i.e.,  $k_{hfm}$ ) due to the influence of proppants when the effective stress increases continuously (Weaver et al., 2010). The stress sensitivity of hydraulic fractures can be adjusted by changing the ratio of  $k_{hfm}$  to  $k_{hfi}$ , which is usually obtained by experiments. The larger the ratio of  $k_{hfm}$  to  $k_{hfi}$  is, the weaker the impact of effective stress on HF permeability will be. As such, the relationship between HF permeability and its pressure can be described as follow (Zhang et al., 2014),

$$k_{hf}(p_{hf}) = k_{hfm} + (k_{hfi} - k_{hfm}) \exp[-\gamma_{hf}(p_i - p_{hf})] \quad (2)$$

where  $k_{hf}$  is the HF permeability,  $p_i$  is the initial reservoir pressure,  $p_{hf}$  is the HF pressure,  $k_{hfi}$  is the initial HF permeability,  $\gamma_{hf}$  is the HF permeability modulus, and  $k_{hfm}$  is the minimum HF permeability.

## Governing Equations Matrix Subsystem

Since the matrix permeability of a tight oil reservoir is extremely low, the fluid flow in the matrix can be neglected, and the matrix is considered as evenly distributed sources when the oil in the matrix flows into natural fractures (Li et al., 2017). In this way, the governing equation of the matrix subsystem can be described by:

$$\frac{\partial(\rho\phi_m)}{\partial t} + q_{ex} = 0 \quad (3a)$$

$$q_{ex} = \frac{\alpha k_m \rho}{\mu} (p_m - p_{nf}) \quad (3b)$$

where  $\rho$  is the fluid density,  $\phi_m$  is the matrix porosity,  $k_m$  is the matrix permeability,  $p_m$  is the matrix pressure,  $\mu$  is the fluid viscosity,  $\alpha$  is the shape factor,  $t$  is time, and  $q_{ex}$  is the flow rate between the matrix and NFs.

Because of no flow in the matrix, the initial condition can be described as the following:

$$\frac{\partial p_m}{\partial x} = \frac{\partial p_m}{\partial y} = 0 \quad (4a)$$

$$p_m(x, y, t = 0) = p_i \quad (4b)$$

## Natural Fracture Subsystem

Considering the stress sensitivity of NFs, the governing equation of NFs can be expressed as follows:

$$\begin{aligned} & \frac{\partial}{\partial x} \left[ e^{-\gamma_{nf}(p_i - p_{nf})} \frac{\partial p_{nf}}{\partial x} \right] + \frac{\partial}{\partial y} \left[ e^{-\gamma_{nf}(p_i - p_{nf})} \frac{\partial p_{nf}}{\partial y} \right] + \frac{k_m}{k_{nfi}} \alpha (p_m - p_{nf}) \\ & = \frac{\phi_{nf} \mu c_{tnf}}{k_{nfi}} \frac{\partial p_{nf}}{\partial t} \end{aligned} \quad (5)$$

where  $c_{tnf}$  is the total NF compressibility.

Then, the initial condition and boundary conditions can be expressed as follow:

$$p_{nf}(x, y, t = 0) = p_i \quad (6a)$$

$$\left. \frac{\partial p_{nf}}{\partial x} \right|_{x=0, x_e} = 0, \quad 0 \leq y \leq y_e, \quad \left. \frac{\partial p_{nf}}{\partial y} \right|_{y=0, y_e} = 0, \quad 0 \leq x \leq x_e \quad (6b)$$

## Hydraulic Fracture Subsystem

To date, as for fluid flow in the HF, both compressible and incompressible flows have been extensively studied. Since the reservoir volume is much larger than the hydraulic fracturing volume in a tight oil reservoir (Cinco-Ley and Samaniego, 1981), fluid compressibility is not considered in this study. Considering the stress sensitivity of HF, the governing equation of HF can be written as follows:

$$\frac{k_{hfi}}{\mu} \frac{\partial}{\partial x} \left\{ \left[ \frac{k_{hfm}}{k_{hfi}} + \left( 1 - \frac{k_{hfm}}{k_{hfi}} \right) e^{-\gamma_{hf}(p_i - p_{hf})} \right] \right\} + \frac{q_f}{w_{hf} h_{hf}} = 0 \quad (7)$$

where  $w_{hf}$  and  $h_{hf}$  are the HF width and height, respectively,  $\mu$  is fluid viscosity and  $q_f$  is the flow rate from reservoir into HF.

The initial condition and boundary conditions are expressed as follow:

$$\begin{aligned} & \frac{k_{hfi} h_{hf} w_{hf}}{\mu} \left[ \frac{k_{hfm}}{k_{hfi}} + \left( 1 - \frac{k_{hfm}}{k_{hfi}} \right) e^{-\gamma_{hf}(p_i - p_{hf})} \right] \left. \frac{\partial p_{hf}}{\partial x} \right|_{x=x_w} = q_{Ni,1}, i \\ & = 1, 2, \dots, 2M \end{aligned} \quad (8a)$$

$$\left. \frac{\partial p_{hf}}{\partial x} \right|_{x=x_w+x_{hf}} = 0 \quad (8b)$$

$$p_{hf}(x, t = 0) = p_i \quad (8c)$$

where  $q_{Ni,1}$  is the flow rate from the  $N$  node of the  $i$ th HF to the wellbore and  $M$  is the number of hydraulic fractures.

## Non-Dimensionalization

For the convenience of derivation, analysis, and improving the applicability of the model proposed in this study, dimensionless variables are defined as follows (Chen et al., 2016; Wang et al., 2017; Jiang et al., 2019a; Jiang et al., 2019b):

$$t_D = \frac{k_{nfi} t}{(\phi_m C_{tm} + \phi_{nf} C_{tnf}) \mu x_{hf}^2} \quad (9a)$$

$$p_{hfD} = \frac{2\pi k_{nfi} h (p_i - p_{hf})}{q_{sc} B \mu} \quad (9b)$$

$$p_{mD} = \frac{2\pi k_{nfi} h (p_i - p_m)}{q_{sc} B \mu} \quad (9c)$$

$$p_{nfD} = \frac{2\pi k_{nfi} h (p_i - p_{nf})}{q_{sc} B \mu} \quad (9d)$$

$$C_{fD} = \frac{k_{hf} w_{hf}}{k_{nfi} x_{hf}} \quad (9e)$$

$$q_{fD} = \frac{2q_f x_{hf}}{q_{sc} B} \quad (9f)$$

$$q_{nD} = \frac{q_N x_{hf}}{q_{sc} B} \quad (9g)$$

$$x_D = \frac{x}{x_{hf}} \quad (9h)$$

$$y_D = \frac{y}{y_{hf}} \quad (9i)$$

$$\lambda = \alpha \frac{k_m}{k_{nfi}} x_{hf}^2 \quad (9j)$$

$$w = \frac{\phi_{nf} C_{tnf}}{(\phi_m C_m + \phi_{nf} C_{tnf})} \quad (9k)$$

$$\gamma_{nfd} = \frac{q_{sc} B \mu}{2\pi k_{nfi} h} \gamma_{nf} \quad (9l)$$

$$\gamma_{hfd} = \frac{q_{sc} B \mu}{2\pi k_{nfi} h} \gamma_{hf} \quad (9m)$$

### Matrix Subsystem

According to the aforementioned definitions of dimensionless variables, Eqs 3a–4b can be rewritten as follows:

$$\lambda(p_{mD} - p_{nfd}) + (1 - \omega) \frac{\partial p_{mD}}{\partial t_D} = 0 \quad (10a)$$

$$p_{mD}(x_D, y_D, t_D = 0) = 0 \quad (10b)$$

$$\frac{\partial p_{mD}}{\partial x_D} = \frac{\partial p_{mD}}{\partial y_D} = 0 \quad (10c)$$

### Natural Fracture Subsystem

With the aforementioned definitions, Eqs 5–6b can be rewritten as follows:

$$e^{-\gamma_{nfd} p_{nfd}} \left[ \frac{\partial^2 p_{nfd}}{\partial x_D^2} + \frac{\partial^2 p_{nfd}}{\partial y_D^2} - \gamma_{nfd} \left( \frac{\partial p_{nfd}}{\partial y_D} \right)^2 \right] = \omega \frac{\partial p_{nfd}}{\partial t_D} - \lambda(p_{mD} - p_{nfd}) \quad (11a)$$

$$\left. \frac{\partial p_{nfd}}{\partial x_D} \right|_{x_D=0, x_{eD}} = 0, 0 \leq y_D \leq y_{eD}, \left. \frac{\partial p_{nfd}}{\partial y_D} \right|_{y_D=0, y_{eD}} = 0, 0 \leq x_D \leq x_{eD}, \quad (11b)$$

$$p_{nfd}(x_D, y_D, t_D = 0) = 0 \quad (11c)$$

### Hydraulic Fracture Subsystem

Similarly, Eqs 7–8c can be rewritten as follows:

$$\frac{\partial}{\partial x_D} \left\{ \left[ \frac{C_{fDmin}}{C_{fDi}} + \left( 1 - \frac{C_{fDmin}}{C_{fDi}} \right) e^{-\gamma_{hfd} p_{hfd}} \right] \frac{\partial p_{hfd}}{\partial x_D} \right\} - \frac{\pi q_{fD}}{C_{fDi}} = 0 \quad (12a)$$

$$\left( \delta_s \frac{\partial p_{hfd}}{\partial x_D} \right) \Big|_{x_D=x_{wD}} = -\frac{\pi q_{NDi,1}}{C_{fDi}}, N = 1, 2, \dots, N \quad (12b)$$

$$\left. \frac{\partial p_{hfd}}{\partial x_D} \right|_{x_D=x_{wD}+x_{fD}} = 0 \quad (12c)$$

$$p_{hfd}(x_D, y_D, t_D = 0) = 0 \quad (12d)$$

$$\delta_s = \frac{C_{fDmin}}{C_{fDi}} + \left( 1 - \frac{C_{fDmin}}{C_{fDi}} \right) e^{-\gamma_{hfd} p_{hfd}} \quad (12e)$$

### Solutions for a Multi-Well Pad Matrix/Natural Fractures.

After considering the NF stress sensitivity, it is difficult to obtain analytical solutions for the mathematical models of matrix and NFs. In this paper, we use the perturbation theory (Pedrosa, 1986) to obtain semianalytical solutions of matrix and NFs, i.e.,  $p_{nfd}$  can be rephrased as follows:

$$p_{nfd} = -\frac{1}{\gamma_{nfd}} \ln(1 - \gamma_{nfd} \eta_{nfd}) \quad (13a)$$

According to perturbation theory,  $\eta_{nfd}$  can be rewritten as follow:

$$\eta_{nfd} = \eta_{nfd0} + \gamma_{nfd} \eta_{nfd1} + \gamma_{nfd}^2 \eta_{nfd2} + \dots \quad (13b)$$

$$\frac{1}{1 - \gamma_{nfd} \eta_{nfd}} = 1 + \gamma_{nfd} \eta_{nfd} + \gamma_{nfd}^2 \eta_{nfd}^2 + \dots \quad (13c)$$

Numerous studies have found that the zero-order approximate solution completely meets the solution requirements (Jiang et al., 2019b). Therefore, Eqs 5–b can be rewritten as follows:

$$\lambda(p_{mD} - \eta_{nfd0}) + (1 - \omega) \frac{\partial p_{mD}}{\partial t_D} = 0 \quad (14a)$$

$$\frac{\partial^2 \eta_{nfd0}}{\partial x_D^2} + \frac{\partial^2 \eta_{nfd0}}{\partial y_D^2} = \omega \frac{\partial \eta_{nfd0}}{\partial t_D} + (1 - \omega) \frac{\partial p_{mD}}{\partial t_D} \quad (14b)$$

$$\left. \frac{\partial \eta_{nfd0}}{\partial x_D} \right|_{x_D=0, x_{eD}} = 0, 0 \leq y_D \leq y_{eD}, \left. \frac{\partial \eta_{nfd0}}{\partial y_D} \right|_{y_D=0, y_{eD}} = 0, 0 \leq x_D \leq x_{eD} \quad (14c)$$

And the initial condition can be rewritten as follows:

$$\eta_{nfd0}(x_D, y_D, t_D = 0) = 0 \quad (14d)$$

Then, the equation can be solved in the Laplace domain. In this paper, a slab-source function is derived and presented in Appendix A, while the solution for multi-well pad schemes can be expressed as the follow:

$$\bar{\eta}_{nfd0}(x_D, y_D, s_D, u_D) = \frac{\pi x_{fD}}{x_{eD} y_{fD}} \bar{q}_{fD}(s_D) \left[ \bar{s}_p(y_D, y_{wD}, y_{fD}, u_D) + 2 \sum_{n=1}^{\infty} F_n(x_{fD}/x_{eD}) \cos \frac{n\pi x_{wD}}{x_{eD}} \cos \frac{n\pi x_{fD}}{x_{eD}} \bar{s}_{p(n)}(y_D, y_{wD}, y_{fD}, \alpha_{nD}, u_D) \right] \quad (15a)$$

$$f(s_D) = \frac{\omega(1 - \omega)s_D + \lambda}{(1 - \omega)s_D + \lambda} \quad (15b)$$

$$u_D = s_D \times f(s_D) \quad (15c)$$

### Hydraulic Fractures

Considering the HF stress sensitivity, the corresponding flow equation becomes highly nonlinear and is solved by discretizing each fractures into small segments. According to the dimensionless definitions, Eqs 12e–13a can be rewritten as follows:

$$\delta_s = \frac{C_{fDmin}}{C_{fD}} \exp(\gamma_{nfd} p_{hfd}) + \left( 1 - \frac{C_{fDmin}}{C_{fD}} \right) \exp[-(\gamma_{hfd} - \gamma_{nfd}) p_{hfd}] \quad (16a)$$

$$p_{hfd} = -\frac{1}{\gamma_{nfd}} \ln(1 - \gamma_{nfd} \eta_{hfd}) \quad (16b)$$

Therefore, the governing equation for segments can be rewritten:

$$\frac{\partial^2 \eta_{hFD}}{\partial x_D^2} - \frac{\pi q_{fDi,j}^*}{C_{fDi}} = 0, \quad x_{Di,j} \leq x_D \leq x_{Di,j+1} \quad (17a)$$

with the boundary condition and initial condition:

$$\left( \frac{\partial \eta_{hFD}}{\partial x_D} \right) \Big|_{x_D=x_{Di,j}} = \frac{\pi q_{NDi,j}^*}{C_{fDi}} \quad (17b)$$

$$\left( \frac{\partial \eta_{hFD}}{\partial x_D} \right) \Big|_{x_D=x_{Di,j+1}} = \frac{\pi q_{NDi,j+1}^*}{C_{fDi}} \quad (17c)$$

$$\eta_{hFD}(x_D, t_D = 0) = 0 \quad (17d)$$

where

$$q_{fDi,j}^* = \frac{q_{fDi,j}}{\delta_{Si,j}} \quad (17e)$$

By integrating with the boundary condition, we can obtain

$$\begin{aligned} \bar{p}_{FDi}(x_{Di}) - \bar{p}_{wD} &= \frac{2\pi}{C_{FDj}} \left[ \frac{\Delta x_D}{8} q_{fDi,j}^* + \sum_{j=1}^{i-1} q_{fDi,j}^* \left( \frac{\Delta x_D}{2} + x_{Di} - j\Delta x_D \right) \right. \\ &\quad \left. - x_{Di} \sum_{j=1}^{S_m} q_{fDi,j}^* \right] \quad i \\ &= 1, 2, \dots, 2N \end{aligned} \quad (18a)$$

where

$$\Delta x_D = \frac{L_{FD}}{N}, \quad x_{Di} = \left( i - \frac{1}{2} \right) \Delta x_D \quad (18b)$$

### Coupling Matrix/Natural Fractures and Hydraulic Fractures

The solution of transient flow responses is obtained by coupling the Matrix/NFs and HFs dynamically. According to the previous model description, HFs are discretized into  $2N_1 \times M_1 + 2N_2 \times M_2$  segments, each of which has three variables:  $q_{fDi,j}$ ,  $q_{NDi,j}$ , and  $p_{hFDi,j}$ . In addition, two unknown variables are the flowing bottomhole pressure  $p_{wD1}$  and  $p_{wD2}$ . A closed  $[2(2N_1 \times M_1 + 2N_2 \times M_2) + 2]$ -order matrix from the pressure-continuity condition can be obtained.

Since pressure in NFs and HFs is the same ( $2N_1 \times M_1 + 2N_2 \times M_2$ ) equations can then be obtained,

$$p_{hFDi,j} = p_{hFDi,j} \quad (19)$$

Because it is assumed that fluid in HFs incompressible, inflow and outflow should be conserved according to the conservation of mass,  $(2N_1 \times M_1 + 2N_2 \times M_2)$  equations can be obtained,

$$\bar{q}_{NDi,j} - \bar{q}_{NDi,j+1} - \frac{1}{2} \Delta x_{hFD} \bar{q}_{fDi,j} = 0 \quad (20)$$

Either Well #1 or Well #2 is produced at a constant rate, and ratio of the oil production for these two wells is denoted by  $\epsilon$ . Then, two equations can be obtained,

$$\sum_{i=1}^N \bar{q}_{wD1} = \frac{\epsilon}{2s_D} \quad (21a)$$

$$\sum_{i=1}^N \bar{q}_{wD2} = \frac{1-\epsilon}{2s_D} \quad (21b)$$

Therefore, a closed  $[2(2N_1 \times M_1 + 2N_2 \times M_2) + 2]$ -order matrix is obtained,

$$A \vec{X} = \vec{B} \quad (22)$$

In addition, skin effect and wellbore storage can be introduced into transient-solution directly in the Laplace domain (Cao et al., 2018),

$$\bar{\eta}_{wD} = \frac{s \bar{\eta}_{wDN} + S}{s + C_D s^2 (s \bar{\eta}_{wDN} + S)} \quad (23)$$

### Coupling Solutions

An iterative method proposed by Van Everdingen and Hurst (1949) is applied here to solve the nonlinear matrix, while the detailed flowchart is shown as **Figure 3**. First, the transient-pressure solution (**Eq. 24a**) can be obtained with iterations in the Laplace domain, and then stable solution (**Eq. 24b**) obtained in the real-time domain by using the Stehfest inversion algorithm (Stehfest, 1970). It is worthwhile mentioning that the new semianalytical model can be used to obtain the transient-production solution at a fixed pressure, which can be transformed through **Eq. 24c** in the Laplace domain.

$$\bar{m}_D = -\frac{1}{\gamma_{mD}} \ln(1 - \gamma_{mD} \bar{\eta}_{wD}) \quad (24a)$$

$$\bar{m}_D = -\frac{1}{\gamma_{mD}} \ln \left[ 1 - \frac{\gamma_{mD} \ln 2}{t_D} \sum_{i=1}^N V_i \frac{s_i \bar{\eta}_{wDN} + S}{s_i + C_D s_i^2 (s_i \bar{\eta}_{wDN} + S)} \right] \quad (24b)$$

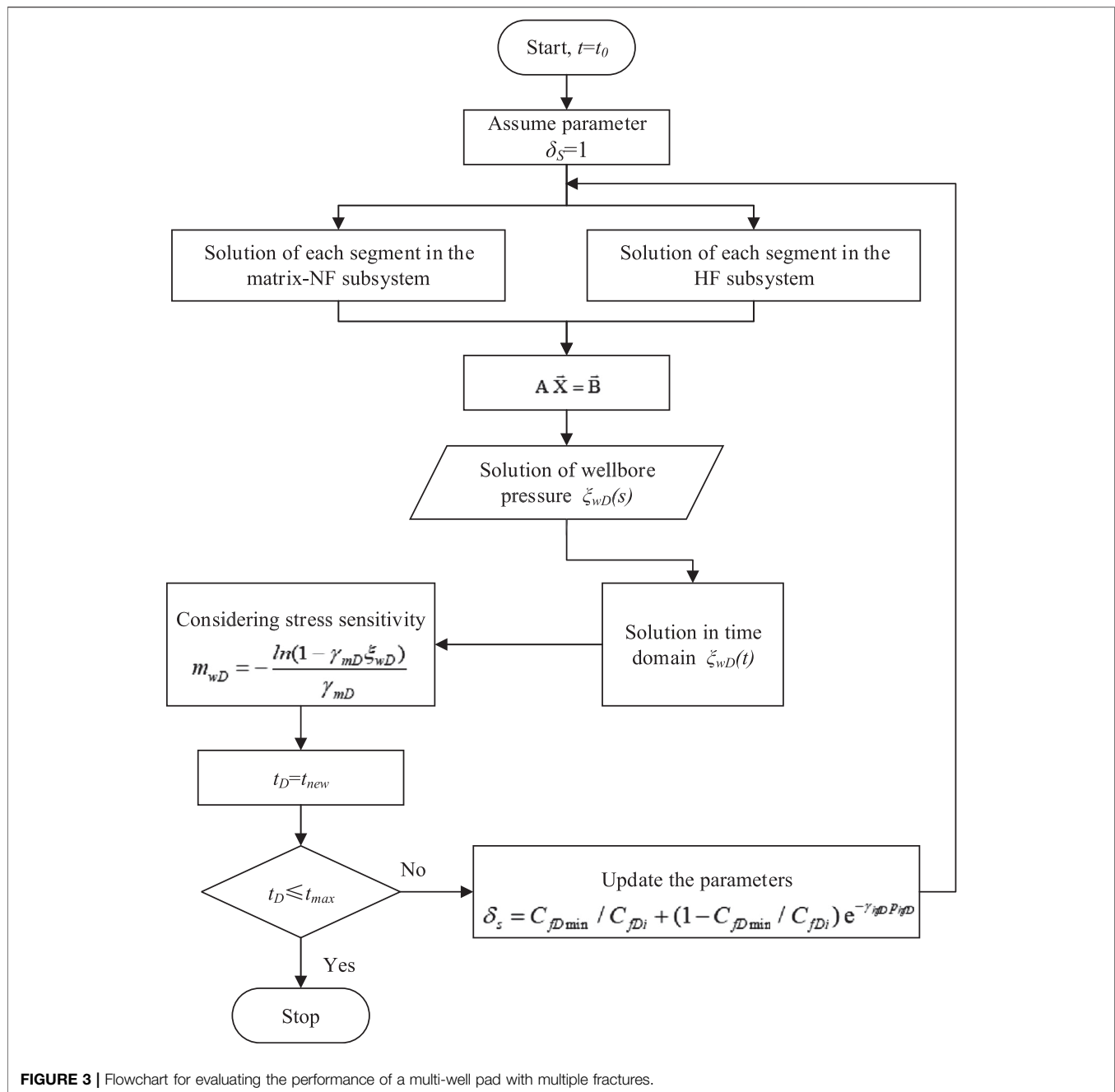
where

$$V_i = (-1)^{\frac{N}{2}+i} \sum_{k=\frac{i-1}{2}}^{\min\left(i, \frac{N}{2}\right)} \frac{k^{\frac{N}{2}} (2k+1)!}{(k+1)! k! \left(\frac{N}{2} - k + 1\right)! (i-k+1)! (2k-i+1)!} \quad (24c)$$

$$\bar{q}_{wD} = \frac{1}{s^2 \bar{m}_{wD}} \quad (24d)$$

### Model Validation

In this section, we used a commercial reservoir simulator (CMG, version 2015) to simulate the performance of a multi-well pad with multiple fractures. In order to simulate the performance of an infinite reservoir, we intentionally enlarged the reservoir scale. The whole grid system is  $300 \times 400 \times 5$ , and the dimension of each grid is  $20 \text{ m} \times 20 \text{ m} \times 2 \text{ m}$ . A “double Klinsenberg permeability, logarithmic spacing and local refined grid (DK-LS-LRG) method” (Cipolla et al., 2010) is used to characterize the HFs. The top view of the multi-well pad with multiple fractures is shown in **Figure 4**, and the physical properties used for model validation are tabulated in **Table 1**. As can be seen in **Figure 5**, there is a good agreement between the numerical simulation and the results



obtained from the newly developed model in this study, confirming that our approach is reliable.

## RESULTS AND DISCUSSION

In this section, type curves of a multi-well pad with multiple fractures are obtained, and the flow regimes are identified. In addition, sensitivity analysis is conducted to examine the effects of some main parameters, including ratio of well rate, hydraulic fracture spacing, hydraulic fracture length, well spacing,

permeability modulus of NFs and HF, minimum fracture conductivity, storage ratio, and crossflow coefficient.

### Identification of Flow Regime

Dimensionless pressure (DP) and the dimensionless pressure derivative (DPD) of a multi-well pad with multiple fractures (MWPMF) are shown in **Figure 6**. The following dimensionless parameters are used to generate the type curves:  $L_{f1D} = L_{f2D} = 75$ ,  $D_{f1} = D_{f2} = 500$ ,  $M_1 = M_2 = 4$ ,  $N_1 = N_2 = 5$ ,  $C_{fDi} = 10$ ,  $C_{fDmin}/C_{fDi} = 0.4$ ,  $\gamma_{mD} = 0.02$ ,  $\gamma_{hfD} = 2$ ,  $\omega = 0.2$ ,  $\lambda = 1 \times 10^{-8}$ ,  $C_D = 10$ , and  $S = 0.1$ . After considering the multi-well pressure interference and stress

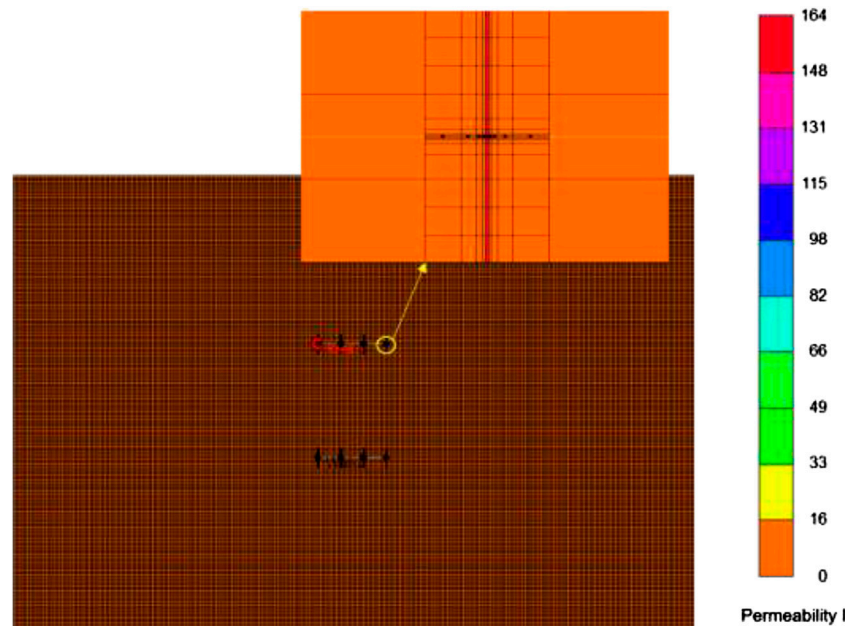


**FIGURE 4 |** Top view of commercial reservoir simulator for the multi-well pad with multiple fractures.

**TABLE 1 |** Physical properties of a multi-well pad with multiple fractures used in the commercial reservoir simulator.

	Parameter	Value	Unit
Reservoir	Reservoir thickness, $h$	10	m
	Reservoir initial pressure, $p_i$	28	MPa
	Matrix porosity, $\phi_m$	0.1	Fraction
	Natural-fracture permeability, $k_f$	$5 \times 10^{-4}$	D
	Matrix permeability, $k_m$	$1 \times 10^{-5}$	D
Horizontal well	Horizontal length for well #1, $L_{H1}$	600	m
	Horizontal length for well #2, $L_{H2}$	600	m
	Wellbore radius, $r_w$	0.1	m
	Well #1 production rate, $q_{sc1}$	5	m <sup>3</sup> /d
	Well #2 production rate, $q_{sc2}$	20	m <sup>3</sup> /d
	Wellbore spacing	1,000	m
Hydraulic fracture	Well #1 fracture number, $M_1$	4	Integer
	Well #2 fracture number, $M_2$	4	Integer
	Well #1 fracture half length, $L_{f1}$	75	m
	Well #2 fracture half length, $L_{f2}$	75	m
	Well #1 fracture conductivity, $C_{FD1}$	10	Dimensionless
	Well #2 fracture conductivity, $C_{FD2}$	10	Dimensionless
	Fracture width, $w_{hf}$	0.001	m
Fluid	Fracture permeability modulus, $\gamma_{hf}$	$2 \times 10^{-8}$	Pa <sup>-1</sup>
	Viscosity, $\mu$	1	cP
	Volume formation factor, $B$	1.1	m <sup>3</sup> /m <sup>3</sup>
	Storage ratio, $\omega$	0.2	Fraction
	Interporosity coefficient, $\lambda$	$1 \times 10^{-8}$	Fraction
	Density, $\rho$	800	kg/m <sup>3</sup>

sensitivity, there are eight flow regimes, which can be detailed as follows:

- (1) The pure wellbore storage period regime: It can be identified by a slope of unity on the log-log plots, when DP curve and
- (2) The skin effect transition flow regime: The most obvious feature of this stage is a “hump” in the pressure derivative curve. This period is mainly dominated by fluid properties (Cao et al., 2018).
- (3) The linear flow regime within HFs: Usually, this period is characterized by a slope of 1/2 on the pressure derivative curve; however, the new model is affected by dynamic conductivity, and the slope of the pressure derivative curve is larger than 1/2. Moreover, the variation rate of the conductivity of two wells is different, which results in that the DP curve and DPD curve of two wells do not overlap at this stage (Yao et al., 2013).
- (4) The early radial flow regime: It is characterized by a slope of 0 on the pressure derivative curve. This period is mainly dominated by hydraulic fracture spacing. This regime will occur only when the hydraulic fracture spacing is appropriate (Chen et al., 2016).
- (5) The biradial flow regime: It is characterized by a slope of 1/3 on the pressure derivative curve. This period is mainly dominated by wellbore length (Zerzar et al., 2004).
- (6) The transition flow regime: This is the transition regime between the biradial flow and pseudo-steady diffusion flow (Cinco-Ley and Meng, 1988).
- (7) The pseudo-steady diffusion regime: The most obvious feature of this regime is a “dip” in the pressure derivative curve. In this period, mass transfer occurs between matrix and NFs (Wang et al., 2017).
- (8) The late-time pseudo-radial flow regime: Under the influence of matrix stress sensitivity, the DPD curve does not show a



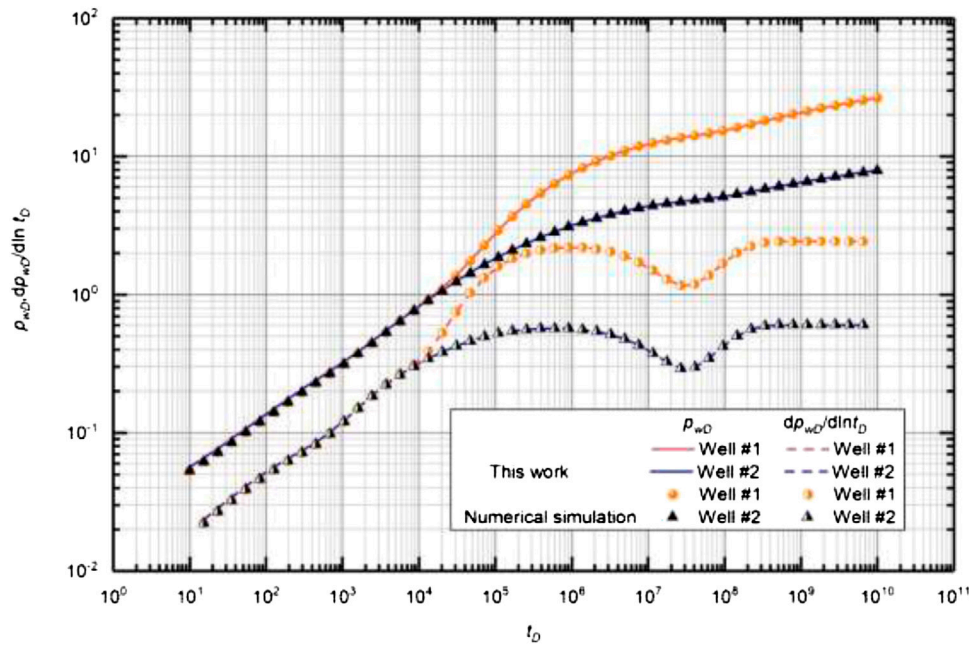


**FIGURE 5** | Comparison between the results obtained from this work and numerical simulation from commercial reservoir simulator.

horizontal line, and its value is greater than 0.5. Because of the existence of multi-well pressure interference, the smaller the oil rate is, the greater the distorted value will be (Liu et al., 2018a).

### Sensitivity Analysis Effect of Well-Rate Ratio

Figure 7 demonstrates the effect of well-rate ratio on type curves of MWPMF. The basic data used to generate the type curves are

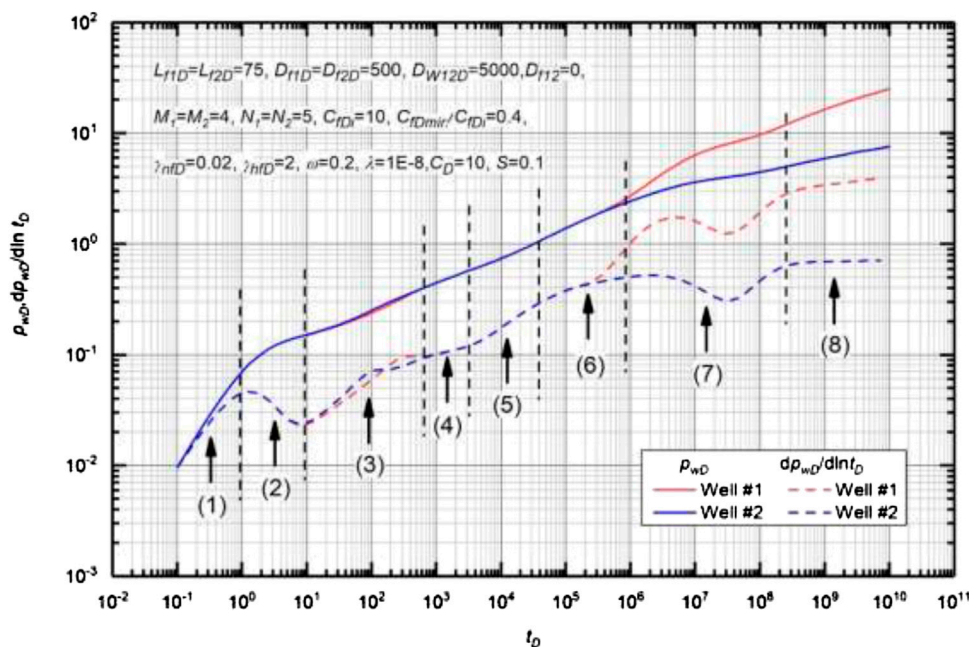


**FIGURE 6** | Flow regimes of a multi-well pad with multiple fractures identified by the type curve.

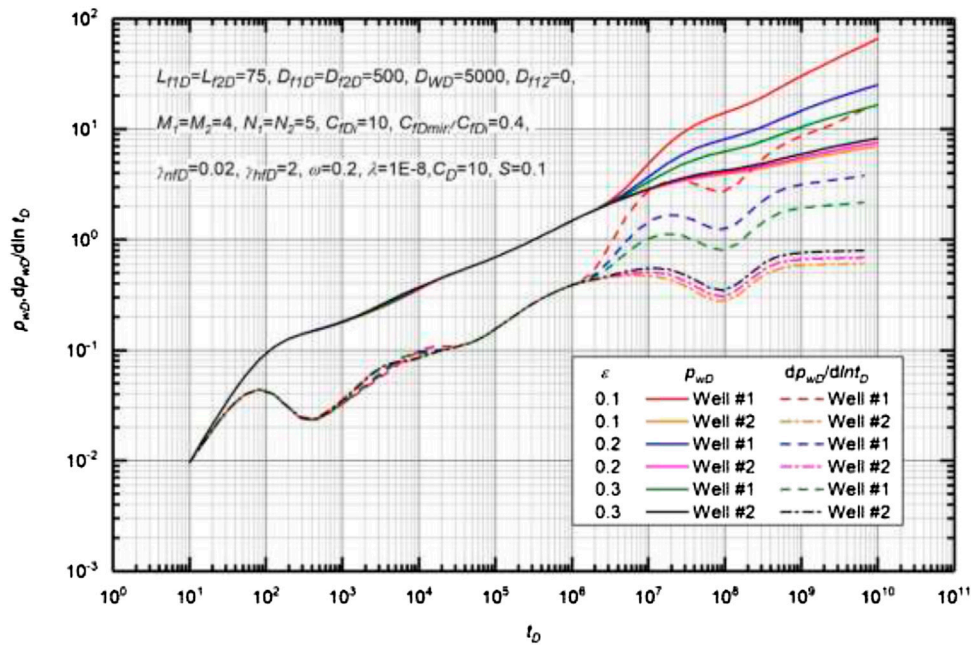


FIGURE 7 | Effect of well rate ratio on the transient pressure for multi-well pad with multiple fractures (MWPMF).

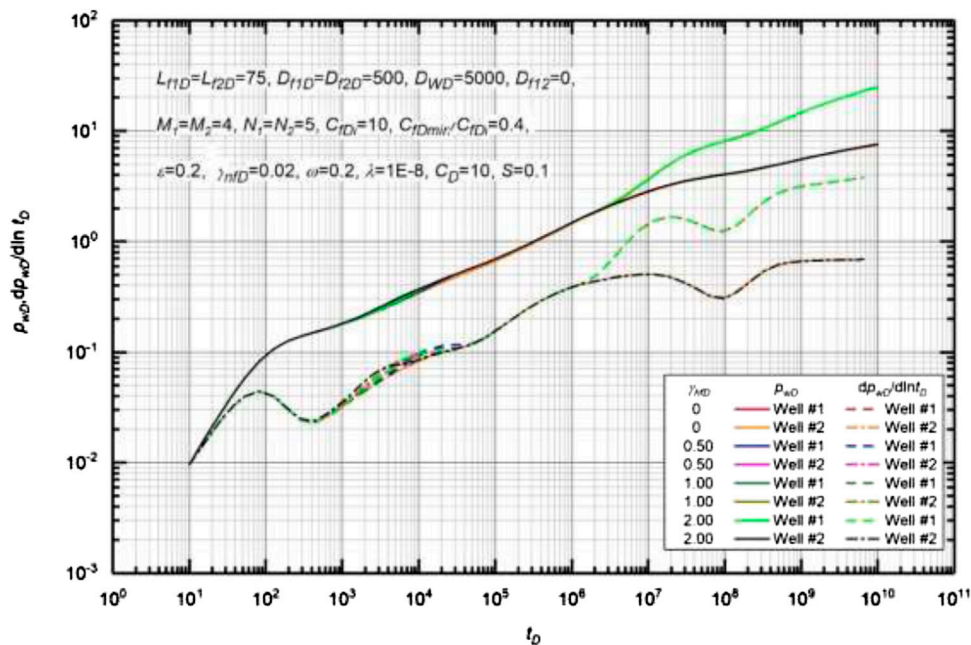


FIGURE 8 | Effect of HF permeability modulus on the transient pressure for MWPMF.

$L_{f1D}=L_{f2D}=75, D_{f1}=D_{f2}=500, M_1=M_2=4, N_1=N_2=5, C_{fD1}=10, C_{fDmin}/C_{fD1}=0.4, \gamma_{mD}=0.02, \gamma_{hD}=2, \omega=0.2, \lambda=1 \times 10^{-8}, C_D=10$ , and  $S=0.1$ . Comparison of different type curves illustrates that a smaller  $\varepsilon$  leads to a larger value of DPD and DPPD after the occurrence of multi-well pressure interference.

In addition, it can be concluded that the well-rate ratio  $\varepsilon$  does not affect the onset time of multi-well pressure interference (Liu et al., 2018a). This is mainly because the onset time of multi-well pressure interference depends on the velocity of pressure wave propagation, which is only related to reservoir properties and well

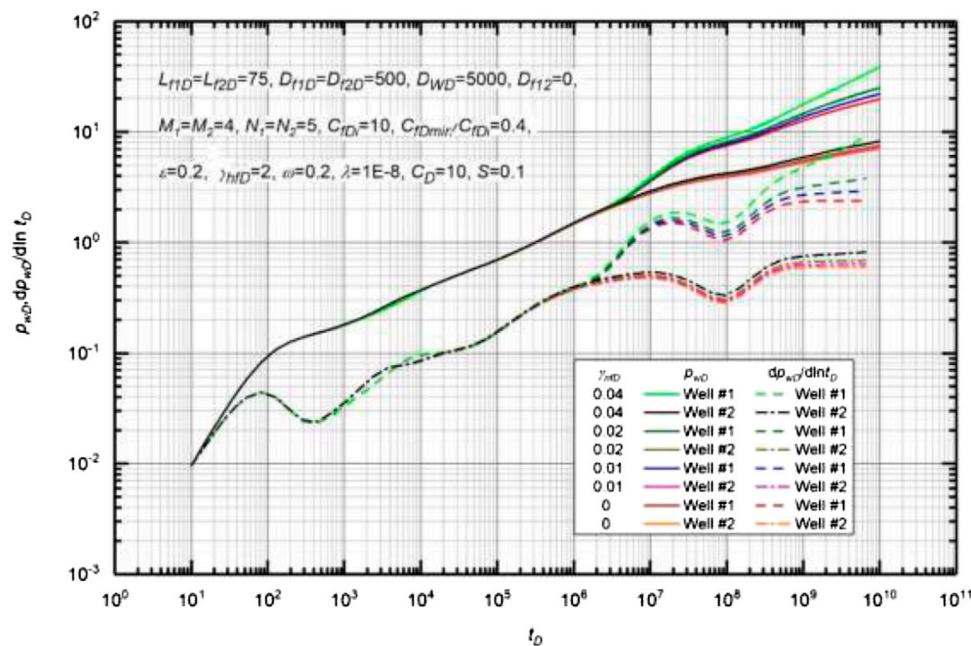


FIGURE 9 | Effect of the natural fracture permeability modulus on the transient pressure for MWPMF.

parameters, mainly including matrix, fracture permeability, fracture half-length, wellbore length, and well spacing, but has nothing to do with the well-rate ratio.

### Effect of Hydraulic Fractures Permeability Modulus

Figure 8 illustrates the effect of HF permeability modulus on type curves of MWPMF. Basic data used to generate the type curves are  $L_{f1D} = L_{f2D} = 75$ ,  $D_{f1D} = D_{f2D} = 500$ ,  $M_1 = M_2 = 4$ ,  $N_1 = N_2 = 5$ ,  $C_{fDi} = 10$ ,  $C_{fDmin}/C_{fDi} = 0.4$ ,  $\gamma_{nFD} = 0.02$ ,  $\omega = 0.2$ ,  $\lambda = 1 \times 10^{-8}$ ,  $\epsilon = 0.2$ ,  $C_D = 10$ , and  $S = 0.1$ . As illustrated in Figure 8, the HF permeability modulus is found to be one of the key factors affecting the “hump,” which only affects the flow in a hydraulic fracture. The slope of the hump becomes larger as the HF permeability modulus is increased (Yao et al., 2013). Certainly, the greater the HF permeability modulus is, the easier it approaches  $C_{fDmin}$ , and it is easier to move to the next regime (i.e., early radial flow regime). For an extreme case  $\gamma_{hFD} = 0$ , the early radial flow regime will be masked by the linear flow regime within HFs. This is because  $C_{fD}$  maintains a constant value and the linear flow lasts longer, and then it is more difficult for the early radial flow to occur.

### Effect of Natural Fracture Permeability Modulus

Figure 9 displays the effect of NF permeability modulus on type curves of MWPMF. Basic data used to generate the type curves are  $L_{f1D} = L_{f2D} = 75$ ,  $D_{f1D} = D_{f2D} = 500$ ,  $M_1 = M_2 = 4$ ,  $N_1 = N_2 = 5$ ,  $C_{fDi} = 10$ ,  $C_{fDmin}/C_{fDi} = 0.4$ ,  $\gamma_{hFD} = 2$ ,  $\omega = 0.2$ ,  $\lambda = 1 \times 10^{-8}$ ,  $\epsilon = 0.2$ ,  $C_D = 10$ , and  $S = 0.1$ . As can be seen in Fig. 9, a larger NF permeability modulus leads to a larger value of DPD and DPPD after the occurrence of multi-well pressure interference (Liu et al., 2018a; Xiao et al., 2018). Besides, the NF permeability modulus

can distort flow regimes, and the distortion of pressure curves become severer as the  $\gamma_{nFD}$  is increased. For the case of  $\gamma_{nFD} = 0$ , the DPPD value in the late-time pseudo-radial flow regime is equal to 0.5. In the early regime of flow, the flow regime is independent of the NF permeability modulus before the multi-well pressure interference occurs.

### Effect of Hydraulic Fracture Spacings

Figure 10 presents the effect of HF spacing on type curves of MWPMF. Basic data used to generate the type curves are  $L_{f1D} = L_{f2D} = 75$ ,  $M_1 = M_2 = 4$ ,  $N_1 = N_2 = 5$ ,  $C_{fDi} = 10$ ,  $C_{fDmin}/C_{fDi} = 0.4$ ,  $\gamma_{nFD} = 0.02$ ,  $\gamma_{hFD} = 2$ ,  $\omega = 0.2$ ,  $\lambda = 1 \times 10^{-8}$ ,  $\epsilon = 0.2$ ,  $C_D = 10$ , and  $S = 0.1$ . Comparison of different type curves illustrates that the HF spacing affects the occurrence time and duration of the biradial flow regime, but has no effect on the distortion of the convection pattern. DPD and DPPD curves only shift from left to right or vice versa (the curve slope remains unchanged) (Liu et al., 2018a). A smaller  $D_{fD}$  leads to the earlier appearance of the biradial flow regime. After the disappearance of this flow regime, the pressure drop and pressure derivative curves overlap again under different well spacings.

### Effect of Hydraulic Fracture Length

Figure 11 plots the effect of HF length on type curves of MWPMF. Basic data used to generate the type curves are  $D_{f1D} = D_{f2D} = 500$ ,  $M_1 = M_2 = 4$ ,  $N_1 = N_2 = 5$ ,  $C_{fDi} = 10$ ,  $C_{fDmin}/C_{fDi} = 0.4$ ,  $\gamma_{nFD} = 0.02$ ,  $\gamma_{hFD} = 2$ ,  $\omega = 0.2$ ,  $\lambda = 1 \times 10^{-8}$ ,  $\epsilon = 0.2$ ,  $C_D = 10$ , and  $S = 0.1$ . It is shown that HF length only affects the early flow regimes, including the skin effect transition flow regime, the linear flow regime within HFs, and the early radial flow regime. As the HF length is decreased, pressure drop and pressure



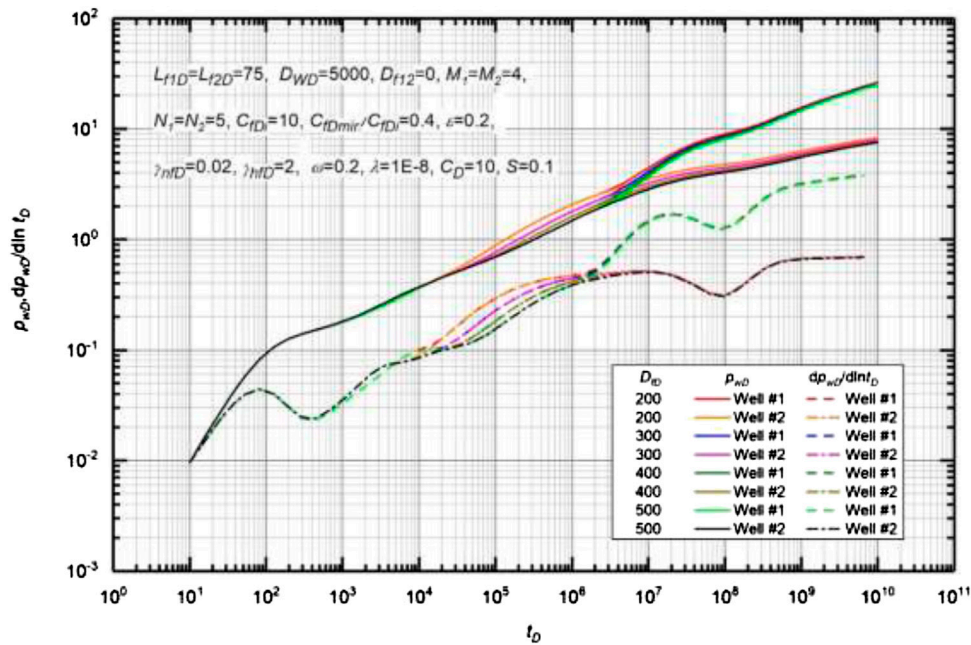


FIGURE 10 | Effect of HF spacing on the transient pressure for MWPMF.

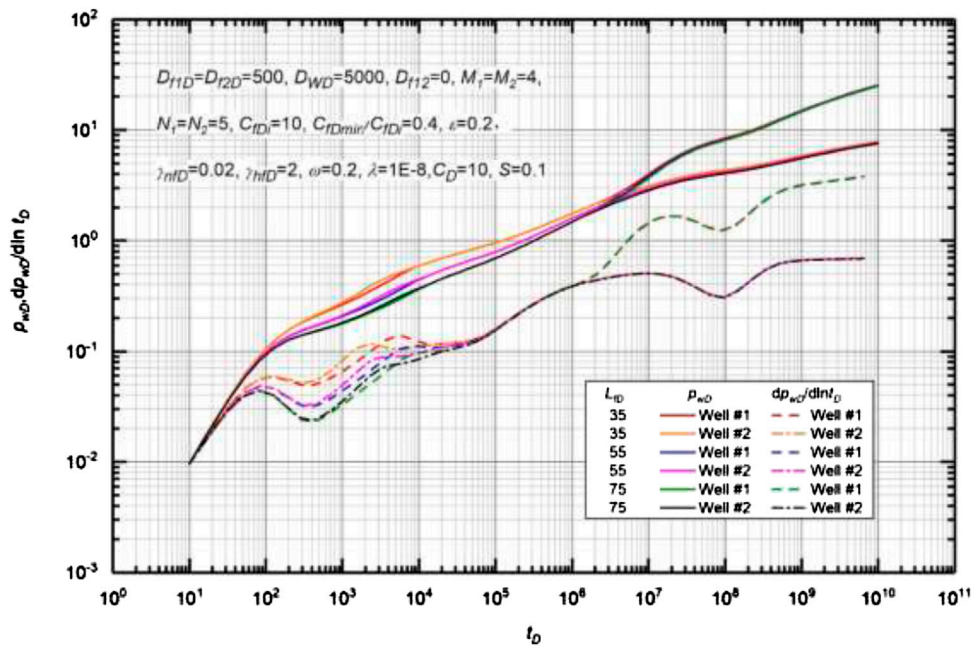


FIGURE 11 | Effect of HF length on the transient pressure for MWPMF.

derivative curves are shifted upwards (Chen et al., 2016; 2Chen et al., 2017a; Cao et al., 2018). With the decrease of HF length, the duration of linear flow regime within HF becomes short. Similar

to the effect of HF spacing, after the completion of the early radial flow regime, the pressure drop and pressure derivative curves overlap again under different HF lengths.

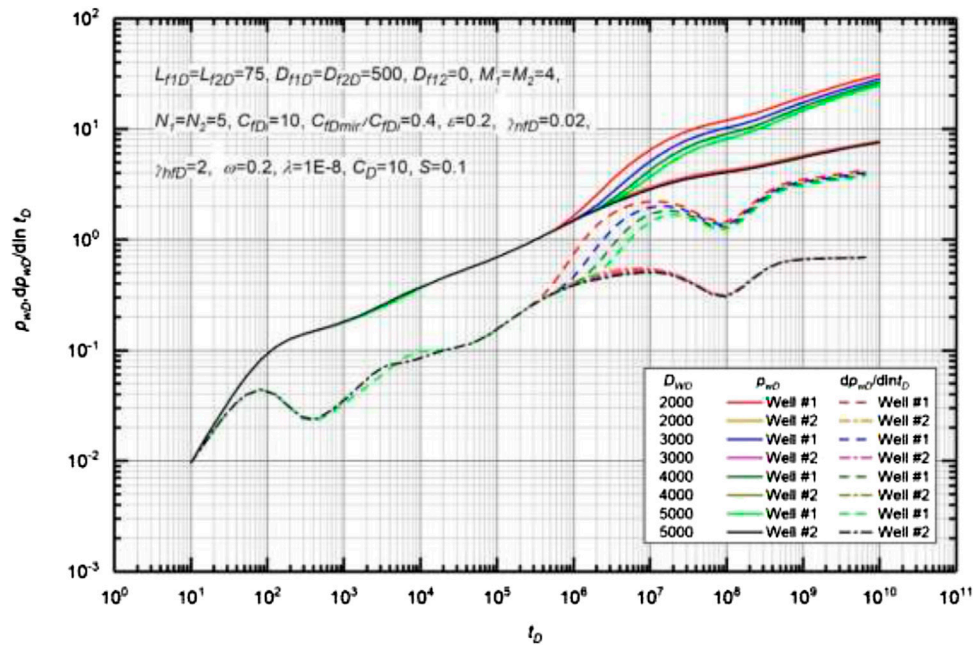


FIGURE 12 | Effect of well spacing on the transient pressure for MWPMF.

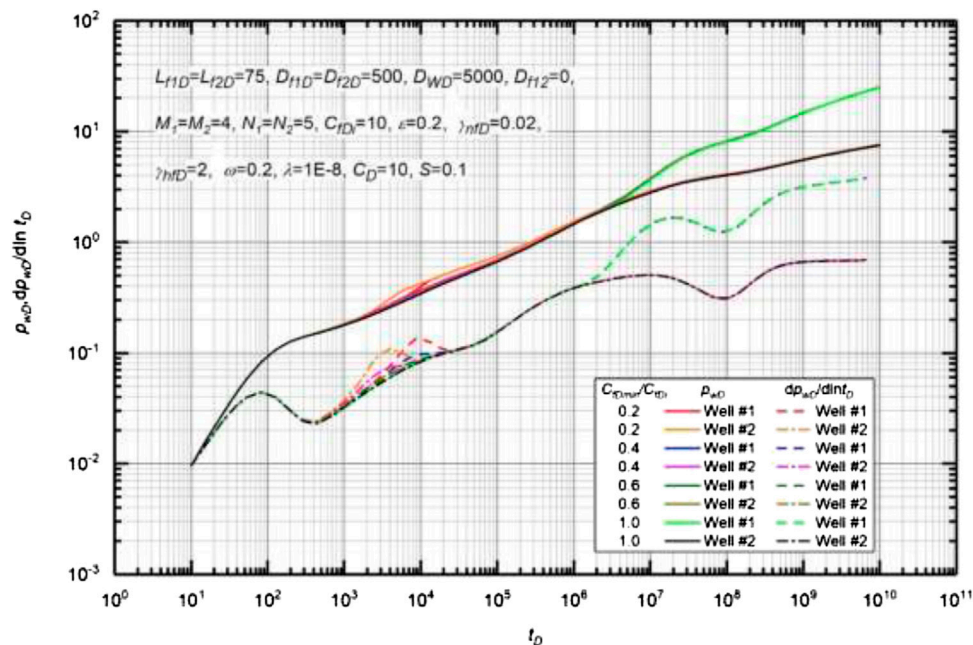


FIGURE 13 | Effect of minimum fracture conductivity on the transient pressure for MWPMF.

### Effect of Well Spacing

Figure 12 depicts the effect of well spacing on type curves of MWPMF. Basic data used to generate the type curves are  $L_{f1D} = L_{f2D} = 75$ ,  $D_{f1D} = D_{f2D} = 500$ ,  $M_1 = M_2 = 4$ ,  $N_1 = N_2 = 5$ ,  $C_{FDi} = 10$ ,  $C_{FDmin}/C_{FDi} = 0.4$ ,  $\gamma_{hFD} = 0.02$ ,  $\gamma_{hFD} = 2$ ,  $\omega = 0.2$ ,  $\lambda = 1 \times 10^{-8}$ ,  $\varepsilon = 0.2$ ,  $C_D = 10$ , and  $S = 0.1$ . By observing whether the pressure derivative curves overlap, we can judge when the multi-well pressure

interference occurs. As shown in Figure 12, well spacing affects flow regimes after multi-well pressure interference starts. Comparison of different type curves illustrates that a smaller  $D_{WD}$  leads to the earlier occurrence of multi-well pressure interference (Liu et al., 2018a; Xiao et al., 2018). It is worthwhile mentioning that well spacing also does not distort the shape of pressure drop and pressure derivative curves, and the



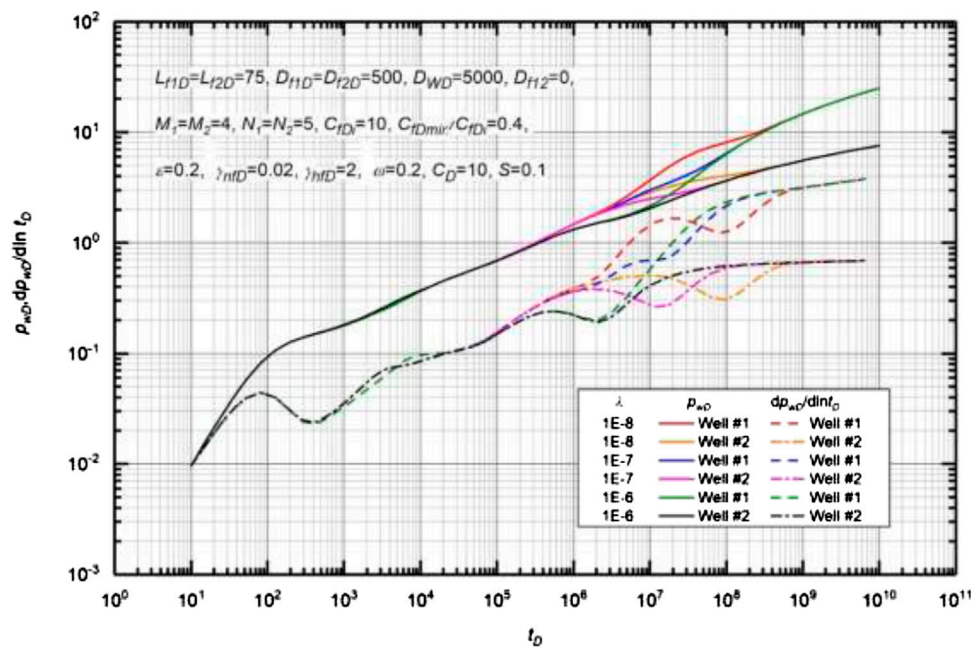


FIGURE 14 | Effect of crossflow coefficient on the transient pressure for MWPMF.

curve is only shifted from left to right or vice versa (i.e., the curve slope remains unchanged).

### Effect of Minimum Fracture Conductivity

Figure 13 illustrates the effect of minimum fracture conductivity on type curves of MWPMF. Basic data used to generate the type curves are  $L_{f1D} = L_{f2D} = 75$ ,  $D_{f1D} = D_{f2D} = 500$ ,  $M_1 = M_2 = 4$ ,  $N_1 = N_2 = 5$ ,  $C_{fDi} = 10$ ,  $\gamma_{nFD} = 0.02$ ,  $\gamma_{hFD} = 2$ ,  $\omega = 0.2$ ,  $\lambda = 1 \times 10^{-8}$ ,  $\varepsilon = 0.2$ ,  $C_D = 10$ , and  $S = 0.1$ . The higher the value of  $C_{fDmin}/C_{fDi}$  is, the stronger the effect of proppant in HF will be, and the higher the fracture conductivity can be maintained when the effective pressure is increased. Similar to the effect of HF permeability modulus on the flow in a hydraulic fracture,  $C_{fDmin}/C_{fDi}$  is another key factor affecting the “hump,” whose slope becomes smaller as the minimum fracture conductivity is decreased. As can be seen in Figure 13, when the value of  $C_{fDmin}/C_{fDi}$  reaches 0.6, the hump basically disappears. This is because a higher  $C_{fDmin}/C_{fDi}$  means that the hydraulic fracture loses a small part of conductivity, and it is difficult to distinguish the difference among type curves.

### Effect of Crossflow Coefficient

Figure 14 reveals the effect of crossflow coefficient on type curves of MWPMF. Basic data used to generate the type curves are  $L_{f1D} = L_{f2D} = 75$ ,  $D_{f1D} = D_{f2D} = 500$ ,  $M_1 = M_2 = 4$ ,  $N_1 = N_2 = 5$ ,  $C_{fDi} = 10$ ,  $C_{fDmin}/C_{fDi} = 0.4$ ,  $\gamma_{nFD} = 0.02$ ,  $\gamma_{hFD} = 2$ ,  $\omega = 0.2$ ,  $\lambda = 1 \times 10^{-8}$ ,  $\varepsilon = 0.2$ ,  $C_D = 10$ , and  $S = 0.1$ . As described by Eq. 14a, with a larger  $\lambda$ , the magnitude of the difference between the NF permeability and the matrix permeability becomes smaller. This means that the ability of NFs to maintain production is weakened. Comparison of different type curves illustrates that the larger the  $\lambda$  is, the flow transfers from the matrix to the NFs easier and the “dip” comes earlier. Especially

for an oil well with low production, it is more unlikely to have crossflow at a smaller  $\lambda$  (Liu et al., 2015; Li et al., 2017).

### Effect of Storage Ratio

Figure 15 shows the effect of storage ratio on type curves of MWPMF. Basic data used to generate the type curves are  $L_{f1D} = L_{f2D} = 75$ ,  $D_{f1D} = D_{f2D} = 500$ ,  $M_1 = M_2 = 4$ ,  $N_1 = N_2 = 5$ ,  $C_{fDi} = 10$ ,  $C_{fDmin}/C_{fDi} = 0.4$ ,  $\gamma_{nFD} = 0.02$ ,  $\gamma_{hFD} = 2$ ,  $\lambda = 1 \times 10^{-8}$ ,  $\varepsilon = 0.2$ ,  $C_D = 10$ , and  $S = 0.1$ . As shown in Figure 15, storage ratio  $\omega$  mainly determinates the duration and the depth of the second “dip” on the pressure derivative curve, while it also has a significant effect on the occurrence of multi-well pressure interference (Li et al., 2017; Jiang et al., 2019a). Comparison of different type curves illustrates that a smaller  $\omega$  results in the earlier occurrence of the multi-well pressure interference with an increase in the duration of flow exchange. The slope of the second dip becomes larger with a decrease in the storage ratio.

## CONCLUSIONS

In this paper, a new semianalytical model has been developed and validated to describe the flow behavior of a multi-well pad with multistage fractures in a naturally fractured reservoir, while various stress-sensitive effects in the NFs and HF are examined. The main conclusions are summarized as follows:

- (1) Type curves of a multi-well pad with multiple fractures are identified, and there may exhibit eight flow regimes: pure wellbore storage, skin effect transition flow, linear flow regime within HF, early radial flow, biradial flow, transition flow, pseudo-steady diffusion, and the late-time pseudo-radial flow.

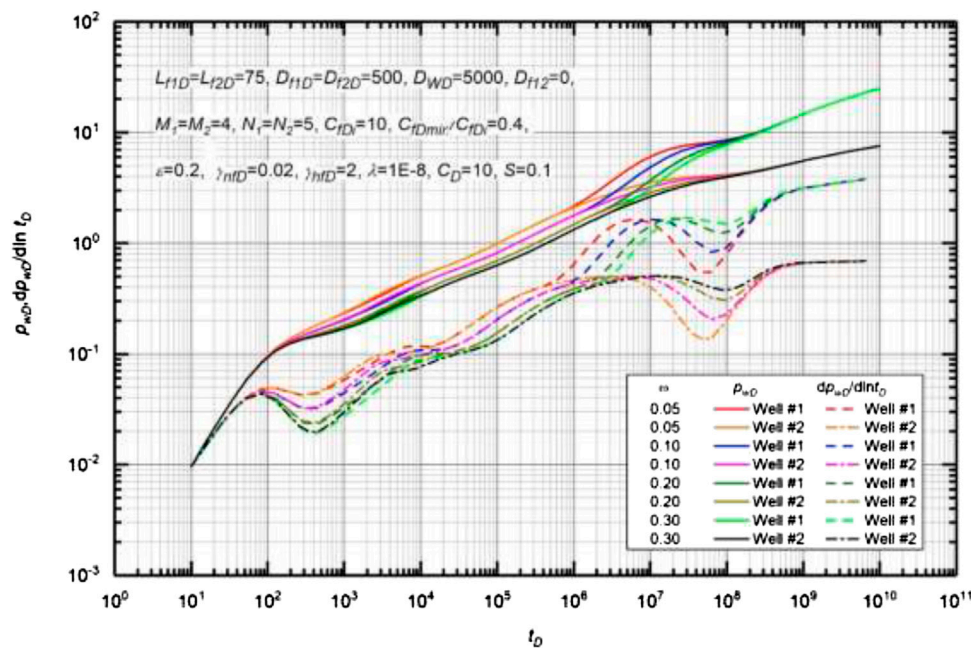


FIGURE 15 | Effect of storage ratio on the transient pressure for MWPMF.

In addition, changing the location of two wells in a multi-well pad may mask some flow regimes.

- (2) Under the multi-well pad schemes, multi-well pressure interference is inevitable and will significantly distort the late-time flow regimes. It is found that the smaller the well-rate ratio is, the more distorted the curve will be. As the well spacing is decreased, the fracture length is increased, and thus the multi-well pressure interference occurs earlier.
- (3) Stress-sensitive effects in the NFs indicate the permeability damage which occurs at intermediate times, resulting in an increasing pressure drop. Stress-sensitive effects in the HF and minimum fracture conductivity only affect the flow regime in hydraulic fractures. The sensitivity analysis shows that the “hump” becomes stronger as the minimum fracture conductivity is decreased.

## DATA AVAILABILITY STATEMENT

The original contributions presented in the study are included in the article/supplementary materials, further inquiries can be directed to the corresponding author/s.

## REFERENCES

- Amjed, H., Mohamed, M., Abdulaziz, A., Mustafa, B., Salaheldin, E., Mohammed, B., et al. (2019). Gas condensate treatment: a critical review of materials, methods, field applications, and new solutions. *J. Petrol. Sci. Eng.* 177, 602–613. doi:10.1016/j.petrol.2019.02.089
- Cao, L., Lu, L., Li, X., Wang, H., He, W., Xu, B., et al. (2018). Transient model analysis of gas flow behavior for a multi-fractured horizontal well incorporating stress-sensitive permeability. *J. Pet. Explor. Prod. Technol.* 9 (2), 855–867. doi:10.1007/s13202-018-0555-z
- Chen, S., Li, H., and Zhang, Q. (2008). A New technique for production prediction in stress-sensitive reservoirs. *J. Can. Petrol. Technol.* 47 (3), 49–54. doi:10.2118/08-03-49
- Chen, Z., Liao, X., Zhao, X., Lv, S., and Zhu, L. (2016). A semianalytical approach for obtaining type curves of multiple-fractured horizontal wells with secondary-fracture networks. *SPE J.* 21 (2), 538–549. doi:10.2118/178913-pa
- Chen, Z., Liao, X., Zhao, X., Lyu, S., and Zhu, L. (2017a). A comprehensive productivity equation for multiple fractured vertical wells with non-linear

## AUTHOR CONTRIBUTIONS

ZM: Conceptualization, Methodology, Formal analysis, Writing - original draft; HL: Methodology, Validation; XT: Revision; GL: Resources, Supervision; LW: Validation, Formal analysis; DY: Conceptualization, Supervision, Funding acquisition, Resources, Writing - review & editing.

## FUNDING

The authors are grateful to the State Key Laboratory of Oil and Gas Reservoir Geology and Exploitation at the Southwest Petroleum University for their support of this work. The authors acknowledge a Natural Science Foundation of China (Grant No.: 51704246 and Grant No.: 51404282) for financial support. Also, the authors acknowledge a Discovery Grant and a Collaborative and Research Development (CRD) Grant awarded to D. Yang from the Natural Sciences and Engineering Research Council (NSERC) of Canada.

- effects under steady-state flow. *J. Petrol. Sci. Eng.* 149, 9–24. doi:10.1016/j.petrol.2016.09.050
- Chen, Z., Liao, X., Zhao, X., Dou, X., Zhu, L., and Sanbo, L. (2017b). A finite-conductivity horizontal-well model for pressure-transient analysis in multiple-fractured horizontal wells. *SPE J.* 22 (4), 1112–1122. doi:10.2118/177230-pa
- Chen, Y., Ma, G., Jin, Y., Wang, H., and Wang, Y. (2019). Productivity evaluation of unconventional reservoir development with three-dimensional fracture networks. *Fuel* 244, 304–313. doi:10.1016/j.fuel.2019.01.188
- Cinco-Ley, H., and Meng, H. (1988). “Pressure transient analysis of wells with finite conductivity vertical fractures in double porosity reservoirs,” in SPE annual technical conference and exhibition, Houston, TX, October 2–5, 1988, Paper SPE-18172-MS.
- Cinco-Ley, H., and Samaniego, -V., F. (1981). Transient pressure analysis for fractured wells. *J. Petrol. Technol.* 33 (9), 1749–1766. doi:10.2118/7490-pa
- Cipolla, C. L., Lolon, E. P., and Erdle, J. C. (2010). Modeling well performance in shale-gas reservoirs. *SPE Reservoir Eval. Eng.* 13 (4), 638–653. doi:10.2118/125530-pa
- Cipolla, C. L., Fitzpatrick, T., Williams, M. J., and Ganguly, U. K. (2011). “Seismic-to-simulation for unconventional reservoir development,” in SPE reservoir characterization and simulation conference and exhibition, Abu Dhabi, UAE, October 9–11, 2011, Paper SPE-146876-MS.
- Feng, Q., Xia, T., Wang, S., and Singh, H. (2017). Pressure transient behavior of horizontal well with time-dependent fracture conductivity in tight oil reservoirs. *Geofluids* 2017, 5279792. doi:10.1155/2017/5279792
- Gao, G., Zhang, W.-W., Ma, G.-F., Chen, G., Li, T., Hu, L.-Z., et al. (2018). Mineral composition and organic geochemistry of the lower cretaceous Xiagou formation source rock from the Qingxi Sag, Jiuquan Basin, Northwest China. *Petrol. Sci.* 15, 51–67. doi:10.1007/s12182-017-0213-y
- Chen, H., Pooladi-Darvish, M., and Atabay, S. (2009). Shape factor in the drawdown solution for well testing of dual-porosity systems. *Adv. Water Resour.* 32 (11), 1652–1663. doi:10.1016/j.advwatres.2009.08.006
- Jalali, Y., and Ershaghi, I. (1987). “Pressure transient analysis of heterogeneous naturally fractured reservoirs,” in SPE California regional meeting, Ventura, CA, April 8–10, 1987, Paper SPE-16341-MS.
- Jia, P., Cheng, L., Huang, S., and Wu, Y. (2016). A semi-analytical model for the flow behavior of naturally fractured formations with multi-scale fracture networks. *J. Hydrol.* 537, 208–220. doi:10.1016/j.jhydrol.2016.03.022
- Jia, P., Cheng, L., Huang, S., Xu, Z., Xue, Y., Cao, R., et al. (2017). A comprehensive model combining Laplace-transform finite-difference and boundary-element method for the flow behavior of a two-zone system with discrete fracture network. *J. Hydrol.* 551, 453–469. doi:10.1016/j.jhydrol.2017.06.022
- Jia, C. (2017). Breakthrough and significance of unconventional oil and gas to classical petroleum geology theory. *Petrol. Explor. Dev.* 44 (1), 1–10. doi:10.1016/s1876-3804(17)30002-2
- Jiang, L., Liu, T., and Yang, D. (2019a). Effect of stress-sensitive fracture conductivity on transient pressure behavior for a horizontal well with multistage fractures. *SPE J.* 24 (3), 1342–1363. doi:10.2118/194509-pa
- Jiang, L., Liu, T., and Yang, D. (2019b). A semianalytical model for predicting transient pressure behavior of a hydraulically fractured horizontal well in a naturally fractured reservoir with non-darcy flow and stress-sensitive permeability effects. *SPE J.* 24 (3), 1322–1341. doi:10.2118/194501-pa
- Jiang, L., Liu, J., Liu, T., and Yang, D. (2020a). A semianalytical model for transient pressure analysis of a horizontal well with non-uniform fracture geometry and shape-dependent conductivity in tight formations. *J. Petrol. Sci. Eng.* 195, 107860.
- Jiang, L., Liu, J., Liu, T., and Yang, D. (2020b). Semi-analytical modeling of transient pressure behaviour for a fractured vertical well with hydraulic/natural fracture networks by considering stress-sensitive effect. *J. Nat. Gas Sci. Eng.* 82, 103477.
- Jiang, L., Liu, J., Liu, T., and Yang, D. (2020c). Semi-analytical modeling of transient rate behaviour of a horizontal well with multistage fractures in tight formations considering stress-sensitivity effect. *J. Nat. Gas Sci. Eng.* 82, 103461.
- Juanes, R., Samper, J., and Molinero, J. (2002). A general and efficient formulation of fractures and boundary conditions in the finite element method. *Int. J. Numer. Methods Eng.* 54, 1751–1774. doi:10.1002/nme.491
- Kazemi, H. (1969). Pressure transient analysis of naturally fractured reservoirs with uniform fracture distribution. *SPE J.* 9 (4), 451–462. doi:10.2118/2156-a
- Li, X., Cao, L., Luo, C., Zhang, B., Zhang, J., and Tan, X. (2017). Characteristics of transient production rate performance of horizontal well in fractured tight gas reservoirs with stress-sensitivity effect. *J. Petrol. Sci. Eng.* 158, 92–106. doi:10.1016/j.petrol.2017.08.041
- Liu, M., Xiao, C., Wang, Y., Li, Z., Zhang, Y., Chen, S., et al. (2015). Sensitivity analysis of geometry for multi-stage fractured horizontal wells with consideration of finite-conductivity fractures in shale gas reservoirs. *J. Nat. Gas Sci. Eng.* 22, 182–195. doi:10.1016/j.jngse.2014.11.027
- Liu, G., Meng, Z., Cui, Y., Wang, L., Liang, C., and Yang, S. (2018a). A semi-analytical methodology for multiwell productivity index of well-industry-production-scheme in tight oil reservoirs. *Energies* 11 (5), 1054. doi:10.3390/en11051054
- Liu, G., Bai, Y., Gu, D., Lu, Y., and Yang, D. (2018b). Determination of static and dynamic characteristics of microscopic pore-throat structure in a tight oil-bearing sandstone formation. *AAPG (Am. Assoc. Pet. Geol.) Bull.* 102(9), 1867–1892. doi:10.1306/0108181613217061
- Liu, G., Meng, Z., Luo, D., Wang, J., Gu, D., and Yang, D. (2020a). Experimental evaluation of interlayer interference during commingled production in a tight sandstone gas reservoir with multi-pressure systems. *Fuel* 262, 116557. doi:10.1016/j.fuel.2019.116557
- Liu, G., Yin, H., Lan, Y., Fei, S., and Yang, D. (2020b). Experimental determination of dynamic pore-throat structure characteristics in a tight gas sandstone formation with consideration of effective stress. *Mar. Petrol. Geol.* 113, 104170. doi:10.1016/j.marpetgeo.2019.104170
- Liu, J., Jiang, L., Liu, T., and Yang, D. (2020c). Modeling tracer flowback behaviour for a fractured vertical well in a tight formation by coupling fluid flow and geomechanical dynamics. *J. Nat. Gas Sci. Eng.* 84, 103656.
- Manchanda, R., and Sharma, M. M. (2013). “Time-delayed fracturing: a new strategy in multi-stage, multi-well pad fracturing,” in the SPE annual technical conference and exhibition, New Orleans, LA, September 30–October 2, 2013, Paper SPE-166489-MS.
- Meng, Z., Yang, S., Wang, L., Zou, J., Jiang, Y., Liang, C., et al. (2017). CO<sub>2</sub> storage capacity for multi-well pads scheme in depleted shale gas reservoirs. *Energies* 10 (11), 1724. doi:10.3390/en10111724
- Meyer, B. R., and Bazan, L. W. (2011). “A discrete fracture network model for hydraulically induced fractures-theory, parametric and case studies,” in SPE hydraulic fracturing technology conference, Woodlands, TX, January 24–26, 2011, Paper SPE-140514-MS.
- Miller, B. A., Paneitz, J. M., Yakeley, S., and Evans, K. A. (2008). “Unlocking tight oil: selective multistage fracturing in the Bakken shale,” in SPE annual technical conference and exhibition, Denver, CA, September 21–24, 2008, Paper SPE-116105-MS.
- Montgomery, C. T., and Steanson, R. E. (1985). Proppant selection: the key to successful fracture stimulation. *J. Petrol. Technol.* 37 (12), 2163–2172. doi:10.2118/12616-pa
- Morteza, D., Hassan, H., and Chen, Z. (2018). Semi-analytical solution for pressure transient analysis of a hydraulically fractured vertical well in a bounded dual-porosity reservoir. *J. Hydrol.* 565, 289–301. doi:10.1016/j.jhydrol.2018.08.020
- Noorishad, J., Ayatollahi, M. S., and Witherspoon, P. A. (1982). A finite-element method for coupled stress and fluid flow analysis in fractured rock masses. *Int. J. Rock Mech. Min. Sci. Geomech. Abstr.* 19, 185–193. doi:10.1016/0148-9062(82)90888-9
- Ozkan, E., Brown, M., Raghavan, R., and Kazemi, H. (2009). “Comparison of fractured horizontal-well performance in conventional and unconventional reservoirs,” in SPE Western regional meeting, San Jose, CA, March 24–26, 2009, Paper SPE-121290-MS.
- Ozkan, E., Brown, M. L., Raghavan, R., and Kazemi, H. (2011). Comparison of fractured-horizontal-well performance in tight sand and shale reservoirs. *SPE Reservoir Eval. Eng.* 14 (2), 248–259. doi:10.2118/121290-pa
- Pedrosa, O. A. (1986). “Pressure transient response in stress-sensitive formations,” in SPE California regional meeting, Oakland, CA, April 2–4, 1986, Paper SPE-15115-MS.
- Ren, Z., Wu, X., W., Liu, D., Rui, R., Wei, G., Chen, Z., et al. (2016). Semi-analytical model of the transient pressure behavior of complex fracture networks in tight oil reservoirs. *J. Nat. Gas Sci. Eng.* 35, 497–508. doi:10.1016/j.jngse.2016.09.006
- Rogers, S., Elmo, D., Dunphy, R., and Bearinger, D. (2010). “Understanding hydraulic fracture geometry and interactions in the horn river basin through DFN and numerical modeling,” in SPE Canadian unconventional

- resources and international Petroleum conference, Calgary, AB, October 19–21, 2010, Paper SPE-137488-MS.
- Schmoker, J. W. (2002). Resource-assessment perspectives for unconventional gas systems. *AAPG (Am. Assoc. Pet. Geol.) Bull.* 86 (11), 1993–1999. doi:10.1306/61EEDDDC-173E-11D7-8645000102C1865D
- Song, C., and Yang, D. (2017). Experimental and numerical evaluation of CO<sub>2</sub> huff-n-puff processes in Bakken formation. *Fuel* 190 (4), 145–162. doi:10.1016/j.fuel.2016.11.041
- Song, Y., Li, Z., Jiang, L., and Hong, F. (2015). The concept and the accumulation characteristics of unconventional hydrocarbon resources. *Petrol. Sci.* 12 (4), 563–572. doi:10.1007/s12182-015-0060-7
- Stalgorova, E., and Mattar, L. (2012). “Analytical model for history matching and forecasting production in multifract composite systems,” in SPE Canadian unconventional resources conference, Calgary, AB, October 30–November 1, 2012, SPE 162516-MS.
- Stehfest, H. (1970). Algorithm 368: numerical inversion of laplace transforms [D5]. *Commun. ACM.* 13 (1), 47–49. doi:10.1145/361953.361969
- Van Everdingen, A. F., and Hurst, W. (1949). The application of the laplace transformation to flow problems in reservoirs. *J. Petrol. Technol.* 1 (12), 305–324. doi:10.2118/949305-g
- Wang, H., Guo, J., and Zhang, L. (2017). A semi-analytical model for multilateral horizontal wells in low-permeability naturally fractured reservoirs. *J. Petrol. Sci. Eng.* 149, 564–578. doi:10.1016/j.petrol.2016.11.002
- Wang, L., Yang, S., Meng, Z., Chen, Y., Qian, K., Han, W., et al. (2018). Time-dependent shape factors for fractured reservoir simulation: effect of stress sensitivity in matrix system. *J. Petrol. Sci. Eng.* 163, 556–569. doi:10.1016/j.petrol.2018.01.020
- Wang, M., Chen, S., and Lin, M. (2018). Enhancing recovery and sensitivity studies in an unconventional tight gas condensate reservoir. *Petrol. Sci.* 15, 305318. doi:10.1007/s12182-018-0220-7
- Warren, J. E., and Root, P. J. The behavior of naturally fractured reservoirs. *SPE J.* (1963). 3(3), 235–255. doi:10.2118/426-pa.
- Weaver, J. D., Rickman, R. D., and Luo, H. (2010). Fracture-conductivity loss caused by geochemical interactions between man-made proppants and formations. *SPE J.* 15 (1), 116–124. doi:10.2118/118174-pa
- Wu, Y., Liu, H., and Bodvarsson, G. S. (2004). A triple-continuum approach for modeling flow and transport processes in fractured rock. *J. Contam. Hydrol.* 73, 145–179. doi:10.1016/j.jconhyd.2004.01.002
- Xiao, C., Dai, Y., Tian, L., Lin, H., Zhang, Y., Yang, Y., et al. (2018). A semianalytical methodology for pressure-transient analysis of multiwell-pad-production scheme in shale gas reservoirs, Part 1: new insights into flow regimes and multiwell interference. *SPE J.* 23 (3), 0885–0905. doi:10.2118/187958-pa
- Yang, D., Song, C., Zhang, J., Zhang, G., Ji, Y., and Gao, J. (2015a). Performance evaluation of injectivity for water-alternating-CO<sub>2</sub> processes in tight oil formations. *Fuel* 139 (1), 292–300. doi:10.1016/j.fuel.2014.08.033
- Yang, D., Zhang, F., Styles, J. A., and Gao, J. (2015b). Performance evaluation of a horizontal well with multiple fractures by use of a slab-source function. *SPE J.* 20 (3), 652–662. doi:10.2118/173184-pa
- Yao, S., Zeng, F., and Liu, H. (2013). “A semi-analytical model for hydraulically fractured wells with stress-sensitive conductivities,” in SPE unconventional resources conference, Calgary, AB, November 57, 2013, Paper SPE-167230-MS.
- Yekeen, N., Padmanabhan, E., and Idris, A. K. (2018). A review of recent advances in foam-based fracturing fluid application in unconventional reservoirs. *J. Ind. Eng. Chem.* 66, 45–71. doi:10.1016/j.jiec.2018.05.039
- Zerzar, A., Tiab, D., and Bettam, Y. (2004). “Interpretation of multiple hydraulically fractured horizontal wells,” in SPE Abu Dhabi international conference and exhibition, Abu Dhabi, UAE, October 10–13, 2004, Paper SPE-88707-MS.
- Zhang, F., and Yang, D. (2014). Determination of fracture conductivity in tight formations with non-Darcy flow behavior. *SPE J.* 19 (1), 34–44. doi:10.2118/162548-pa
- Zhang, F., and Yang, D. (2018). Effects of non-Darcy flow and penetrating ratio on performance of horizontal wells with multiple fractures in a tight formation. *J. Energy Resour. Technol.* 140 (3), 032903. doi:10.1115/1.4037903
- Zhang, Z., He, S., Liu, G., Guo, X., and Mo, S. (2014). Pressure buildup behavior of vertically fractured wells with stress-sensitive conductivity. *J. Petrol. Sci. Eng.* 122, 48–55. doi:10.1016/j.petrol.2014.05.006
- Zhao, Y., Zhang, L., Luo, J., and Zhang, B. (2014). Performance of fractured horizontal well with stimulated reservoir volume in unconventional gas reservoir. *J. Hydrol.* 512, 447–456. doi:10.1016/j.jhydrol.2014.03.026
- Zhao, L., Zhang, L., Liu, Y., Hu, S., and Liu, Q. (2015). Transient pressure analysis of fractured well in bi-zonal gas reservoirs. *J. Hydrol.* 524, 8999. doi:10.1016/j.jhydrol.2015.02.006

**Conflict of Interest:** The authors declare that the research was conducted in the absence of any commercial or financial relationships that could be construed as a potential conflict of interest.

Copyright © 2020 Meng, Lu, Tan, Liu, Wang and Yang. This is an open-access article distributed under the terms of the Creative Commons Attribution License (CC BY). The use, distribution or reproduction in other forums is permitted, provided the original author(s) and the copyright owner(s) are credited and that the original publication in this journal is cited, in accordance with accepted academic practice. No use, distribution or reproduction is permitted which does not comply with these terms.

## GLOSSARY

$B$  = volume formation factor,  $\text{m}^3/\text{m}^3$   
 $C_{FD1}$  = dimensionless Well #1 fracture conductivity, fraction  
 $C_{FD2}$  = dimensionless Well #2 fracture conductivity, fraction  
 $C_{tnf}$  = total compressibility,  $\text{MPa}^{-1}$   
 $h$  = reservoir thickness, m  
 $h_{hf}$  = hydraulic fracture height, m  
 $k_{hf}$  = hydraulic fracture permeability, D  
 $k_{nf}$  = natural fracture permeability, D  
 $k_{nfi}$  = initial natural fracture permeability, D  
 $k_m$  = matrix permeability, D  
 $k_{hfmin}$  = minimum hydraulic fracture permeability, D  
 $L_{H1}$  = horizontal length for Well #1, m  
 $L_{H2}$  = horizontal length for Well #2, m  
 $L_{f1}$  = Well #1 fracture half length, m  
 $L_{f2}$  = Well #2 fracture half length, m  
 $M_1$  = Well #1 fracture number, integer  
 $M_2$  = Well #2 fracture number, integer  
 $N_1$  = Well #1 discrete-fracture segments number, integer  
 $N_2$  = Well #2 discrete-fracture segments number, integer  
 $p_{nf}$  = natural fracture pressure, MPa  
 $p_{hf}$  = hydraulic fracture pressure, MPa  
 $p_m$  = matrix pressure, MPa  
 $p_i$  = reservoir initial pressure, MPa  
 $q_{Ni1}$  = parameter defined in Eq. 8a  
 $q_{sc1}$  = Well #1 production rate,  $\text{m}^3/\text{d}$   
 $q_{sc2}$  = Well #2 production rate,  $\text{m}^3/\text{d}$

$q_f$  = flow-rate strength from reservoir into HFs,  $\text{m}^3/\text{d}$   
 $q_n$  = flow-rate strength within HFs,  $\text{m}^3/\text{d}$   
 $r_w$  = wellbore radius, m  
 $s$  = Laplace transformation variable  
 $t$  = time, hour  
 $w_{hf}$  = HF width, m  
 $x_{hf}$  = reference length, m  
 $x_e$  = reservoir length along  $x$  direction, m  
 $y_e$  = reservoir length along  $y$  direction, m  
 $\alpha$  = shape factor,  $\text{m}^{-2}$   
 $\omega$  = storage ratio, fraction  
 $\lambda$  = interporosity coefficient, fraction  
 $\gamma_{nf}$  = NF permeability modulus,  $\text{MPa}^{-1}$   
 $\gamma_{hf}$  = HF permeability modulus,  $\text{MPa}^{-1}$   
 $\varepsilon$  = well-rate ratio, fraction  
 $\rho$  = fluid density,  $\text{kg}/\text{m}^3$   
 $\mu$  = viscosity, cp  
 $\phi_m$  = matrix porosity, fraction

## Subscripts

$D$  = dimensionless  
 $hf$  = hydraulic fracture  
 $nf$  = natural fracture  
 $m$  = matrix  
 $i$  = initial condition

## Superscript

- = Laplace transform



## APPENDIX A: DERIVATION OF SLAB-SOURCE SOLUTION

A slab-source function can be obtained for the intersection of a slab-source in the  $x$ -direction and the  $y$ -direction (Zhang et al., 2014; Jiang et al., 2019a). Then, the instantaneous source function for a multi-well pad with stress-sensitive effect in both NFs and HF can be expressed as follows,

$$S(x, y, x_w, y_w, x_f, y_f, t) = VII(x, x_w, x_f, t) VII(y, y_w, y_f, t) \quad (A1)$$

Taking the Laplace transform, Eq. A1 can be written as follow,

$$\begin{aligned} \bar{S}(x, y, x_w, y_w, x_f, y_f, s) &= \left[ \frac{h(s_0)}{g'(s_0)} \right]_{(1)} \bar{S}_p(y, y_w, y_f, s) \\ &+ \sum_{n=1}^{\infty} \left[ \frac{h(s_n)}{g'(s_n)} \right]_{(1)} \bar{S}_{p(n)}(y, y_w, y_f, \alpha_n, s) \end{aligned} \quad (A2)$$

where

$$\bar{S}_p(y, y_w, y_f, s) = \frac{2 \sinh(y_f \sqrt{s/\chi}) \cosh[(y_e - y) \sqrt{s/\chi}] \cosh(y_w \sqrt{s/\chi})}{\sqrt{s/\chi} \chi \sqrt{s/\chi} \sinh(y_e \sqrt{s/\chi})} \quad (A3)$$

$$\begin{aligned} \bar{S}_{p(n)}(y, y_w, y_f, \alpha_n, s) &= \frac{2 \sinh(y_f \sqrt{s/\chi + \alpha_n})}{s + \alpha_n \chi} \\ &\frac{\cosh[(y_e - y) \sqrt{s/\chi + \alpha_n}] \cosh(y_w \sqrt{s/\chi + \alpha_n})}{\sinh(y_e \sqrt{s/\chi + \alpha_n})} \end{aligned} \quad (A4)$$

$$\alpha_n = (n\pi/x_e)^2 \quad (A5)$$

where Eq. A2 can be rewritten as follow,

$$\bar{S}(x, y, x_w, y_w, x_f, y_f, s) = \frac{2x_f}{x_e} \left[ \bar{S}_p(y, y_w, y_f, s) \right. \quad (A6)$$

$$\left. + 2 \sum_{n=1}^{\infty} F_n(x_f/x_e) \cos \frac{n\pi x_w}{x_e} \cos \frac{n\pi x}{x_e} \bar{S}_{p(n)}(y, y_w, y_f, \alpha_n, s) \right] \quad (A7)$$

$$F_n(x_f/x_e) = \frac{\sin[(n\pi)(x_f/x_e)]}{(n\pi)(x_f/x_e)}$$

Since the slab source is assumed, the source-shape-dependent rate in terms of withdrawal rate is

$$\bar{q} = \frac{q}{2y_f h} \quad (A8)$$

The pressure-rate-source function in the Laplace domain can be obtained through Eqs A6 and A8,

$$\begin{aligned} \Delta \bar{p}_{hf}(x, y, s) &= \frac{1}{2\phi C_t y_f h} \bar{q}(s) \bar{S}(x, y, x_w, y_w, x_f, y_f, s) \\ &= \frac{\bar{q}(s) x_f}{\phi C_t x_e y_f h} \left[ \bar{S}_p(y, y_w, y_f, s) + 2 \sum_{n=1}^{\infty} F_n(x_f/x_e) \right. \\ &\quad \left. \times \cos \frac{n\pi x_w}{x_e} \cos \frac{n\pi x}{x_e} \bar{S}_{p(n)}(y, y_w, y_f, \alpha_n, s) \right] \end{aligned} \quad (A9)$$

According to the aforementioned definitions of dimensionless variables, Eqs A2–A7 can be rewritten as follows,

$$\bar{p}_{hD}(x_D, y_D, s_D) = \frac{\pi x_{fD}}{x_{eD} y_{fD}} \bar{q}_D(s_D) \left[ \bar{S}_p(y_D, y_{wD}, y_{fD}, s_D) + 2 \sum_{n=1}^{\infty} F_n(x_{fD}/x_{eD}) \cos \frac{n\pi x_{wD}}{x_{eD}} \cos \frac{n\pi x_{fD}}{x_{eD}} \bar{S}_{p(n)}(y_D, y_{wD}, y_{fD}, \alpha_{nD}, s_D) \right] \quad (A10)$$

where

$$\bar{S}_p(y_D, y_{wD}, y_{fD}, s_D) = \frac{2 \sinh(y_{fD} \sqrt{s_D}) \cosh[(y_{eD} - y_{fD})] \cosh(y_{wD} \sqrt{s_D})}{s_D \sinh(y_{eD} \sqrt{s_D})} \quad (A11)$$

$$\bar{S}_{p(n)}(y_D, y_{wD}, y_{fD}, \alpha_{nD}, s_D) = \frac{2 \sinh(y_{fD} \sqrt{s_D + \alpha_{nD}}) \cosh[(y_{eD} - y_{fD})] \cosh(y_{wD} \sqrt{s_D + \alpha_{nD}})}{(s_D + \alpha_{nD}) \sinh(y_{eD} \sqrt{s_D + \alpha_{nD}})} \quad (A12)$$

$$s_D = \frac{S}{L_r^2} \quad (A13)$$

$$\alpha_{nD} = (n\pi/x_{eD})^2 \quad (A14)$$

$$F_n(x_{fD}/x_{eD}) = \frac{\sin[(n\pi)(x_{fD}/x_{eD})]}{(n\pi)(x_{fD}/x_{eD})} \quad (A15)$$

Then, the solution for multi-well pad schemes can be expressed as the follow:

$$\bar{p}_{hD0}(x_D, y_D, s_D, u_D) = \frac{\pi x_{fD}}{x_{eD} y_{fD}} \bar{q}_D(s_D) \left[ \bar{S}_p(y_D, y_{wD}, y_{fD}, u_D) + 2 \sum_{n=1}^{\infty} F_n(x_{fD}/x_{eD}) \cos \frac{n\pi x_{wD}}{x_{eD}} \cos \frac{n\pi x_{fD}}{x_{eD}} \bar{S}_{p(n)}(y_D, y_{wD}, y_{fD}, \alpha_{nD}, u_D) \right] \quad (15a)$$

$$f(s_D) = \frac{\omega(1-\omega)s_D + \lambda}{(1-\omega)s_D + \lambda} \quad (15b)$$

$$u_D = s_D \times f(s_D) \quad (15c)$$

## APPENDIX B: EXTENSION TO MULTIPLE WELLS

A closed  $[2(2N_1 \times M_1 + 2N_2 \times M_2) + 2]$ -order matrix from the pressure-continuity condition can be obtained as,

$$A \vec{X} = \vec{B} \quad (22)$$

where matrix A is a coefficient matrix of dimension  $[2(2N_1 \times M_1 + 2N_2 \times M_2) + 2]$ ,  $\vec{X}$  is the unknown vector, and  $\vec{B}$  is the known vector. The matrix and vectors are further expanded as the submatrix,

$$A = \begin{bmatrix} A_{1,1} \cdot A_{1,mn} \cdot A_{1,2mn} A_{1,2mn+1} A_{1,2mn+2} \\ \vdots \\ A_{v,1} \cdot A_{v,mn} \cdot A_{v,2mn} A_{v,2mn+1} A_{v,2mn+2} \\ \vdots \\ A_{2mn+1,1} \cdot A_{2mn+1,mn} \cdot A_{2mn+1,2mn} A_{2mn+1,2mn+1} A_{2mn+1,2mn+2} \\ A_{2mn+2,1} \cdot A_{2mn+2,mn} \cdot A_{2mn+2,2mn} A_{2mn+2,2mn+1} A_{2mn+2,2mn+2} \end{bmatrix} \quad (B1)$$

where  $mn$  means  $2N_1 \times M_1 + 2N_2 \times M_2$ , and

$$A_{v,w} = \begin{cases} (-1, \dots, -1, \dots, -1)^T & v \leq 2M_1N_1, \quad w = 2mn + 1 \\ (0, \dots, 0, \dots, 0)^T & 2M_1N_1 < v \leq 2M_1N_1 + 2M_2N_2, \quad w = 2mn + 1 \\ (-1, \dots, -1, \dots, -1)^T & 2M_1N_1 < v \leq 2M_1N_1 + 2M_2N_2, \quad w = 2mn + 2 \\ (0, \dots, 0, \dots, 0)^T & v \leq 2M_1N_1, \quad w = 2mn + 2 \\ 1 & v = 2mn + 1, \quad w = N_1, N_1 + 1, 2N_1, 2N_1 + 1 \dots M_1N_1, M_1N_1 + 1 \\ 1 & v = 2mn + 2, \quad w = 2M_1N_1 = N_2, N_2 + 1, 2N_2, 2N_2 + 1 \dots M_2N_2, M_2N_2 + 1 \end{cases} \quad (B2)$$

The submatrix  $A_{v,w}$  can be further written in Eq. B2 if  $v$  and  $w$  do not meet the previously discussed conditions:

$$A_{v,w} = \begin{bmatrix} a_{1,1} \cdot a_{1,j} \cdot a_{1,2mn} \\ \vdots \\ a_{i,1} \cdot a_{i,j} \cdot a_{i,2mn} \\ \vdots \\ a_{2mn,1} \cdot a_{2mn,j} \cdot a_{2mn,2mn} \end{bmatrix} \quad (B3)$$

The element of  $a_{i,j}$  in submatrix  $A_{v,w}$  is given as

$$a_{ij} = \begin{cases} \frac{\pi \Delta x_D}{4C_{FD} \delta_{vj}} & j = i \quad v \leq mn, \quad w \leq mn \\ \frac{2\pi \Delta x_D}{C_{FD} \delta_{vj}} & j < i \quad (k-1)N_1 + 1 \leq v(w) \leq kN_1, \quad (k = 1, 3, 5 \dots mn-1) \\ 0 & j > i \quad (k-1)N_1 + 1 \leq v(w) \leq kN_1, \quad (k = 1, 3, 5 \dots mn-1) \\ \frac{2\pi \Delta x_D}{C_{FD} \delta_{vj}} & j > i \quad (k-1)N_1 + 1 \leq v(w) \leq kN_1, \quad (k = 2, 4, 6 \dots mn) \\ 0 & j < i \quad (k-1)N_1 + 1 \leq v(w) \leq kN_1, \quad (k = 2, 4, 6 \dots mn) \\ 0 & |i-j| > N_1 \end{cases} \quad (B4)$$

$$a_{ij} = S_{v,i}^{w-mn,j} \quad mn < v \leq 2mn, \quad w \leq mn \quad (B5)$$

where  $S_{v,i}^{w-mn,j}$  can be calculated by Eq. 15a,

$$a_{ij} = \begin{cases} -1 & j = i \\ 1 & j = i + 1 \\ 0 & j \neq i, j \neq i + 1 \end{cases} \quad mn < v \leq 2mn, \quad w \leq 2mn \quad (B6)$$

$$a_{ij} = \begin{cases} \Delta x_D / 2 & j = i \\ 0 & j \neq i, j \neq i + 1 \end{cases} \quad mn < v \leq 2mn, \quad mn < w \leq 2mn \quad (B7)$$

The vectors of  $\vec{X}$  and  $\vec{B}$  can be expressed as

$$\vec{X} = (\bar{q}_{NDv,1}, \bar{q}_{NDv,2}, \dots, \bar{q}_{NDv,mn}, \bar{q}_{fDv,1}, \bar{q}_{fDv,2}, \dots, \bar{q}_{fDv,mn}, \bar{p}_{wD1}, \bar{p}_{wD2}) \quad (B8)$$

$$\vec{B} = \left( \underbrace{0, 0, 0 \dots 0}_{2mn}, \frac{\varepsilon}{2s_D}, \frac{1-\varepsilon}{2s_D} \right) \quad (B9)$$

The aforementioned equations show the coupled solution for the nonlinear systems of multi-well pad with two wells. It is

worthwhile mentioning that one of the advantages of the newly developed model is that it can be extended to multiple wells.

Here, three horizontal wells are used as an example to demonstrate such an extension. A closed  $[2(2N_1 \times M_1 + 2N_2 \times M_2 + 2N_3 \times M_3) + 3]$ -order matrix from the pressure-continuity condition can then be obtained,

$$(22) \quad A \vec{X} = \vec{B}$$

where matrix  $A$  is a coefficient matrix of dimension  $[2(2N_1 \times M_1 + 2N_2 \times M_2 + 2N_3 \times M_3) + 3]$ ,  $\vec{X}$  is the unknown vector, and  $\vec{B}$  is the known vector. The matrix and vectors are further expanded as the submatrix,

$$A = \begin{bmatrix} A_{1,1} \cdot A_{1,xy} \cdot A_{1,2xy} A_{1,2xy+1} A_{1,2xy+2} A_{1,2xy+3} \\ \vdots \\ A_{v,1} \cdot A_{v,xy} \cdot A_{v,2xy} A_{v,2xy+1} A_{v,2xy+2} A_{v,2xy+3} \\ \vdots \\ A_{2xy+1,1} \cdot A_{2xy+1,xy} \cdot A_{2xy+1,2xy} A_{2xy+1,2xy+1} A_{2xy+1,2xy+2} A_{2xy+1,2xy+3} \\ A_{2xy+2,1} \cdot A_{2xy+2,xy} \cdot A_{2xy+2,2xy} A_{2xy+2,2xy+1} A_{2xy+2,2xy+2} A_{2xy+2,2xy+3} \\ A_{2xy+3,1} \cdot A_{2xy+3,xy} \cdot A_{2xy+3,2xy} A_{2xy+3,2xy+1} A_{2xy+3,2xy+2} A_{2xy+3,2xy+3} \end{bmatrix} \quad (B10)$$

where  $xy$  means  $2N_1 \times M_1 + 2N_2 \times M_2 + 2N_3 \times M_3$ , and

$$A_{v,w} = \begin{cases} (-1, \dots, -1, \dots, -1)^T & v \leq 2M_1N_1, \quad w = 2xy + 1 \\ (0, \dots, 0, \dots, 0)^T & 2M_1N_1 < v \leq 2M_1N_1 + 2M_2N_2, \quad w = 2xy + 1 \\ (-1, \dots, -1, \dots, -1)^T & 2M_1N_1 < v \leq 2M_1N_1 + 2M_2N_2, \quad w = 2xy + 2 \\ (0, \dots, 0, \dots, 0)^T & v \leq 2M_1N_1, \quad w = 2xy + 2 \\ (0, \dots, 0, \dots, 0)^T & v > 2M_1N_1 + 2M_2N_2, \quad w = 2xy + 2 \\ (-1, \dots, -1, \dots, -1)^T & 2M_1N_1 + 2M_2N_2 < v \leq 2M_1N_1 + 2M_2N_2 + 2M_3N_3, \quad w = 2xy + 3 \\ (0, \dots, 0, \dots, 0)^T & v \leq 2M_1N_1 + 2M_2N_2, \quad w = 2xy + 3 \\ 1 & v = 2mn + 1, \quad w = N_1, N_1 + 1, 2N_1, 2N_1 + 1 \dots M_1N_1, M_1N_1 + 1 \\ 1 & v = 2mn + 2, \quad w = 2M_1N_1 = N_2, N_2 + 1, 2N_2, 2N_2 + 1 \dots M_2N_2, M_2N_2 + 1 \\ 1 & v = 2mn + 3, \quad w = 2M_1N_1 + 2M_2N_2 = N_3, N_3 + 1, 2N_3, 2N_3 + 1 \dots M_3N_3, M_3N_3 + 1 \end{cases} \quad (B11)$$

The submatrix  $A_{v,w}$  can be further written in Eq. B2 if  $v$  and  $w$  do not meet the previously discussed conditions:

$$A_{v,w} = \begin{bmatrix} a_{1,1} \cdot a_{1,j} \cdot a_{1,2xy} \\ \vdots \\ a_{i,1} \cdot a_{i,j} \cdot a_{i,2xy} \\ \vdots \\ a_{2xy,1} \cdot a_{2xy,j} \cdot a_{2xy,2xy} \end{bmatrix} \quad (B12)$$

The element of  $a_{i,j}$  in submatrix  $A_{v,w}$  is given as

$$a_{ij} = \begin{cases} \frac{\pi \Delta x_D}{4C_{FD} \delta_{vj}} & j = i \quad v \leq xy, \quad w \leq xy \\ \frac{2\pi \Delta x_D}{C_{FD} \delta_{vj}} & j < i \quad (k-1)N_1 + 1 \leq v(w) \leq kN_1, \quad (k = 1, 3, 5 \dots xy-1) \\ 0 & j > i \quad (k-1)N_1 + 1 \leq v(w) \leq kN_1, \quad (k = 1, 3, 5 \dots xy-1) \\ \frac{2\pi \Delta x_D}{C_{FD} \delta_{vj}} & j > i \quad (k-1)N_1 + 1 \leq v(w) \leq kN_1, \quad (k = 2, 4, 6 \dots xy) \\ 0 & j < i \quad (k-1)N_1 + 1 \leq v(w) \leq kN_1, \quad (k = 2, 4, 6 \dots xy) \\ 0 & |i-j| > N_1 \end{cases} \quad (B13)$$

$$a_{ij} = S_{v,i}^{w-xy,j} \quad xy < v \leq 2xy, \quad w \leq xy \quad (B14)$$

where  $S_{v,i}^{w-xy,j}$  can be calculated by Eq. 15a,

$$a_{i,j} = \begin{cases} -1 & j = i \\ 1 & j = i + 1 \\ 0 & j \neq i, j \neq i + 1 \end{cases} \quad xy < v \leq 2xy, w \leq 2xy \quad (\text{B15})$$

$$a_{i,j} = \begin{cases} \Delta x_D/2 & j = i \\ 0 & j \neq i, j \neq i + 1 \end{cases} \quad xy < v \leq 2xy, xy < w \leq 2xy \quad (\text{B16})$$

The vectors of  $\vec{X}$  and  $\vec{B}$  can be expressed as

$$\vec{X} = (\bar{q}_{NDv,1}, \bar{q}_{NDv,2}, \dots, \bar{q}_{NDv,xy}, \bar{q}_{fDv,1}, \bar{q}_{fDv,2}, \dots, \bar{q}_{fDv,xy}, \bar{q}_{wD1}, \bar{p}_{wD2}, \bar{p}_{wD3}) \quad (\text{B17})$$

$$\vec{B} = \left( \underbrace{0, 0, 0, \dots, 0}_{2xy}, \frac{\varepsilon_1}{2s_D}, \frac{\varepsilon_2}{2s_D}, \frac{1 - \varepsilon_1 - \varepsilon_2}{2s_D} \right) \quad (\text{B18})$$



# Investigation of Clay Type on Low Salinity Water Flooding Using a Glass Micromodel

Xuemei Wei<sup>1,2\*</sup>, Wenchao Jiang<sup>1,2</sup>, Yanyu Zhang<sup>1,2\*</sup>, Zhao Wang<sup>1,2</sup>, Xiaojun Li<sup>3</sup> and Feipeng Wu<sup>1,2</sup>

<sup>1</sup>Key Laboratory of Unconventional Oil and Gas Development, China University of Petroleum East China, Ministry of Education, Qingdao, China, <sup>2</sup>School of Petroleum Engineering, China University of Petroleum (East China), Qingdao, China, <sup>3</sup>Dongxin Oil Production Plant, Shengli Oilfield, Dongying, Shandong, China

## OPEN ACCESS

### Edited by:

Kaiqiang Zhang,  
Imperial College London,  
United Kingdom

### Reviewed by:

Pat Brady,  
Sandia National Laboratories,  
United States  
Fajian Nie,  
Zhengzhou Zoo, China

### \*Correspondence:

Yanyu Zhang  
yyzhang@upc.edu.cn  
Xuemei Wei  
307725687@qq.com

### Specialty section:

This article was submitted to  
Advanced Clean Fuel Technologies,  
a section of the journal  
Frontiers in Energy Research

**Received:** 30 August 2020

**Accepted:** 26 October 2020

**Published:** 20 November 2020

### Citation:

Wei X, Jiang W, Zhang Y, Wang Z, Li X  
and Wu F (2020) Investigation of Clay  
Type on Low Salinity Water Flooding  
Using a Glass Micromodel.  
Front. Energy Res. 8:600448.  
doi: 10.3389/fenrg.2020.600448

Clay minerals are usually regarded as an important factor affecting the results of low salinity water (LSW) flooding. However, experiments on clay minerals are mainly in qualitative stage, the mechanism of clay minerals has not been studied completely. In this paper, Zeta potential of four kinds of clay minerals (montmorillonite; chlorite; illite; kaolinite) in different brine was measured, microscopic models of these clay minerals were made to measured wetting angle in different brine, and montmorillonite and kaolinite were chosen to conduct microscopic displacement experiments through customized micro-glass etching models. From experiment results, the following conclusions can be get: 1). With the decrease of salinity of injected water, the negative zeta potential of clay minerals increases and the wetting angle decreases. 2). Clay minerals are more sensitive to monovalent Na<sup>+</sup> than bivalent Ca<sup>2+</sup>. 3). The results of microscopic experiments show that LSW can effectively improve oil recovery, whether kaolinite or montmorillonite. The recovery of montmorillonite is better with a relatively high salinity of LSW and kaolinite is better with a relatively low salinity of LSW. The mechanism of LSW improves kaolinite recovery factor is the change of wettability while that of montmorillonite is the increase of water phase wettability. However, a lot of droplet-like residual oil cannot be displaced in the montmorillonite throat. In filed production, both kaolinite-rich and montmorillonite-rich reservoirs are suitable for LSW flooding to improve oil recovery. However, for kaolinite reservoirs, a lower salinity of injected water would produce a better result, while for montmorillonite reservoirs, residual oil droplets in the throat are noteworthy.

**Key words:** low salinity water flooding, clay minerals, wettability, zeta potential, micro displacement

## INTRODUCTION

With the exploitation of oil and gas resources, the development of oilfield becomes more and more difficult. It requires new and effective enhanced oil recovery (EOR) methods. As an emerging oil recovery technology, the popularity of low salinity water (LSW) is mainly caused by its low cost, environmental-friendly and easy operation, all of which being economic benefits compared with chemical EOR methods (Lager et al., 2008; Al Shalabi et al., 2014; Nasralla and Nasr-El-Din, 2014a; Reed and McDonald, 2015). LSW flooding can increase oil recovery by 8–12% and up to 40% on secondary recovery (Lager et al., 2008).

**TABLE 1 |** Composition of Na<sup>+</sup> and Ca<sup>2+</sup> Solutions (mg/L).

No	Na <sup>+</sup>	Ca <sup>2+</sup>	K <sup>+</sup>	Mg <sup>2+</sup>	Cl <sup>-</sup>	SO <sub>4</sub> <sup>2-</sup>
1	500	0	50	50	550	50
2	1,000	0	100	100	1,100	100
3	5,000	0	500	500	5,500	500
4	10,000	0	1,000	10,000	11,000	1,000
5	20,000	0	2000	2000	22,000	2000
6	0	500	50	50	1,050	50
7	0	1,000	100	100	2,100	100
8	0	5,000	500	500	10,500	500
9	0	10,000	1,000	1,000	21,000	1,000
10	0	20,000	2000	2000	42,000	2000

LSW flooding can alter physical and chemical properties of reservoir by injecting water with a low concentration of soluble ions. It can reduce the saturation of residual oil and improve oil recovery. The EOR mechanism of LSW flooding is pretty complex. Meanwhile, it is generally believed that clay minerals in reservoir rocks are important factors that would affect the result of LSW flooding (Tang and Morrow, 1999; Zhang et al., 2007; Loahardjo et al., 2010; Tina et al., 2018; Zhang et al., 2018). Lots of studies on the influence mechanisms of clay minerals in LSW flooding were conducted (Barnaji et al., 2016; Al-Saedi et al., 2018).

The main mechanism of LSW flooding on enhancing oil recovery includes the migration of particles (Tang and Morrow, 1999) and changes in wettability (Zhang et al., 2007; Demir et al., 2016; Al-Saedi and Flori, 2018; Zhang et al., 2018). Tang and Morrow, (1999) first discovered that the migration of clay mineral particles is an important factor for the flooding of residual oil adsorbed on the pore wall. Kim and Lee, (2017) studied the influence of clay type on relative permeability changes in LSW flooding, results show that the difference of relative permeability curve between conventional water flooding and LSW flooding is related to the type of clay minerals. The moving range of the relative permeability curve in kaolinite was proportional to clay contents. Although the moving range in illite showed similar characteristics, it was not as obvious as that in kaolinite. As a result, they thought the existence of kaolinite has a positive effect on oil recovery in LSW flooding and the influence of illite was negligible. Fogden et al., (2011) designed sandstone core displacement experiments, which illustrated that the principle of enhancing recovery by LSW is the migration of clay particles.

As for changes in wettability, Zhang et al., (2007), Zhang et al., (2018) measured contact angle on core slices and Zeta potential of rock particles, their results showed that the impact of clay minerals on oil recovery under LSW is the reduction of contact angle. Lager et al., (2008) proposed that the cation exchange from LSW to rock surface was the main reason for the change of wettability and improved recovery. LSW can absorb organic compounds and organic metal

**TABLE 2 |** Physical properties and components of crude oil.

The oil samples	GD2-23X602	
Components/wt%	Saturated hydrocarbons	36.12
	Aromatics	31.13
	Resin	22.42
Viscosity/(mPa-s)	Asphaltene	10.33
	50°C	5,080
	60°C	2,530
	70°C	1,290
	80°C	690

complexes on clay surface and replace them with simple cations to increase the hydrophilicity of the rock surface. Hilner et al. (2015) believed the diffusion of the double-electron layer played an important role in the change of wettability. With the decrease of the salinity of injected fluids, the expansion of the double-electron layer reduced the attraction of organic molecules to the rock surface and changed the wettability of rock.

Yousef et al. (2011) thought the key to improve recovery with LSW is the change of wettability of rock surface by core displacement experiments. Tammy and Manouchehr (2018) indicated that the exchange of cation from LSW to rock surface has a significant effect on the change of wettability. Stanislav et al., (2018) found that the surface charge of clay minerals is a key factor in LSW flooding experiments. Results from *in situ* ATR-FITR experiments emphasized that the exchange of cation between formation water and LSW is an important step in changing reservoir wettability, and the build of cation bridges between organic compounds and clay mineral surface that decrease repulsive forces between negative solutes and negative reservoir surfaces is essential for LSW flooding EOR.

Under different conditions, study results differ from each other greatly due to the influence of the occurrence mode of clay minerals and fluid properties. Meanwhile, the EOR mechanism varies a lot among different clay minerals and is rarely studied. Therefore, four kinds of clay minerals (montmorillonite, illite, kaolinite, chlorite), which are primary clay minerals in sandstone reservoirs, are selected in this paper. Through the measurement of Zeta potential, diffusion mechanism of the double-electron layer is analyzed from the angle of van der Waals force and electrostatic force. Besides, to analyze the mechanism behind the change of wettability, wetting angle measurement of clay mineral foil is carried out systematically. At the same time, micro-seepage characteristics of LSW flooding under customized mineral surface were studied by using two different kinds of clay minerals, kaolinite and montmorillonite. EOR mechanisms of LSW flooding with different clay minerals are characterized by morphological changes and dynamic distribution rules of crude oil, water and residual oil in the pore channel during water flooding, and further suggestions are made for field production.



**TABLE 3** | Characterization of different clay minerals.

Specification	Montmorillonite	Kaolinite	Illite	Chlorite
Chloride (Cl)/mass%	<0.025	<0.025	<0.02	<0.03
Sulfate (SO <sub>4</sub> )/mass%	<0.1	<0.1	<0.1	<0.1
Heavy metals/mass%	<0.005	<0.005	<0.005	<0.005
Loss on drying/mass%	<0.2	<0.15	<0.1	<0.15
CEC (meq/100g)	95	4.3	32	20
Average particle size/μm	3.4	3	2.9	3.2

## EXPERIMENT

### Material Low Salinity Water

To determine the influence of ion type and concentration of low salinity water on clay minerals, we used distilled water without any ionic to prepare NaCl and CaCl<sub>2</sub> solutions with the Na<sup>+</sup> and Ca<sup>2+</sup> concentrations of 500 mg L<sup>-1</sup>, 1,000 mg L<sup>-1</sup>, 5,000 mg L<sup>-1</sup>, 10,000 mg L<sup>-1</sup>, and 20,000 mg L<sup>-1</sup>, respectively. And the detailed composition of these solutions are shown in **Table 1**.

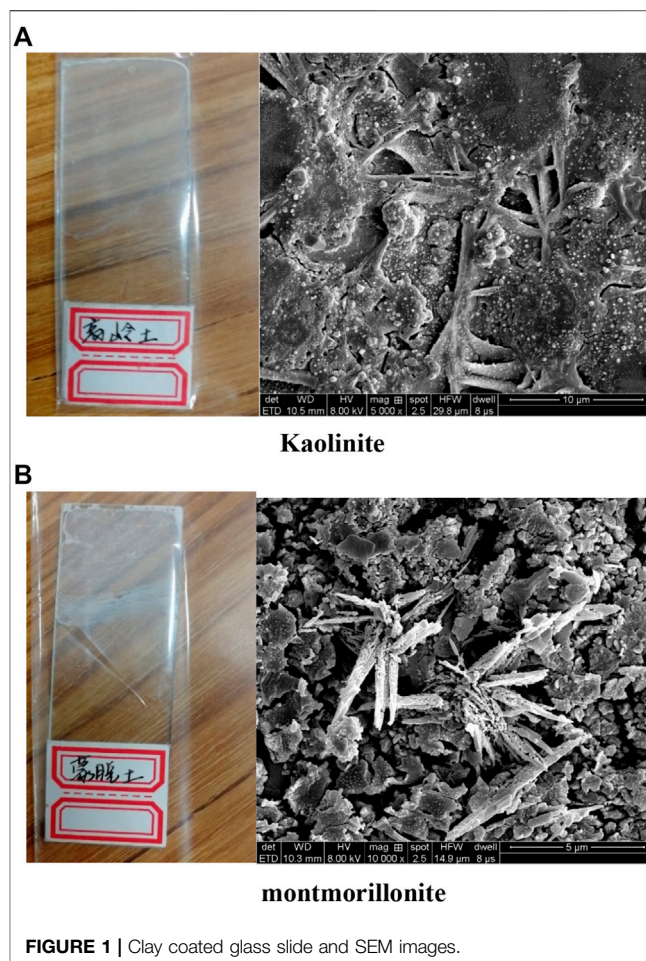
### Crude Oil

Oil used in this experiment is crude oil from Shengli Oilfield. Composition and basic physical properties of the oil can be seen in **Table 2**. Its viscosity, colloid and asphaltene are pretty high, which makes it belong to the heavy oil.

### Clay Minerals

Clay minerals used in experiments were from Shendeng Chemistry company. X-ray diffraction (XRD) was conducted to characterize their mineral compositions. Also, CEC of them were measured through the methylene blue test. Specifications of them are presented in **Table 3**. From this table we can see that the montmorillonite has the highest CEC value, indicating its highest swelling potential among these minerals. A higher CEC value of the clay mineral means its surface can carry more electric charges, and the surface electronegativity will be stronger after dissociation. Montmorillonite carries permanent negative charge mainly through lattice substitution, and its cation exchange capacity is largest among these clay minerals. Although illite is similar to montmorillonite in structure, which is charged by lattice substitution, there are ionic bonds and molecular bonds between crystal layers and cations are not easily replaced by strong electrostatic force. As a result, negative charge of illite is less than that of montmorillonite. Charge between crystal layers of kaolinite has reached equilibrium, so it is not easy for the occurrence of lattice substitution. Compared with montmorillonite and illite, kaolinite has a lesser negative charge. As for chlorite, it has the lowest negative, so its cation exchange capacity is the worst.

To determine the effects of different clay minerals, quartz-sand with a granularity of 200 mesh, which is the largest mesh can float in solution, and four clay minerals (montmorillonite, kaolinite, chlorite and illite) were selected for the Zeta potential measurement experiments. Quartz-sand with a granularity of 1,250 mesh, which is well attached to the micromodel, and four clay minerals (montmorillonite,

**FIGURE 1** | Clay coated glass slide and SEM images.

kaolinite, chlorite and illite) were selected for the wetting angle measurement and microscopic displacement experiments.

To coat micromodel with clay minerals, a slurry made of clay particles and high salinity water (HSW), whose Na<sup>+</sup> concentration is 20,000 mg L<sup>-1</sup>, was injected into the micromodel. And optimized concentration of clay in the suspension is 20 wt%. Before injection, to obtain a homogeneous solution, the mixture was stirred for 20 min, followed by sonication for 0.5 h, to prevent flocculation from occurring. To avoid the settlement and clog of clay and ensure a quasi-homogeneous distribution of clay in the micromodel, a syringe pump with a rate of 20 m/day was used for slurries with different pore volumes in the injection process.

In most reported work, after slurry injection, micromodels would be heated in ovens for 72 h under 80°C (Bondino et al., 2013). However, heat-dried clay minerals will lead to irreversible clay coating, which means that clay particles would be left on the surface and they would be immobile and unresponsive to any changes that happened in the displacement experiment. To avoid this issue, models were placed on an 80°C plate and were hot-air-dried for 2 h (Amirian et al., 2017). Interfacial tension between air and water phases would dislodge blocked throats and the moderate temperature of the hot plate would assist with the drying process.

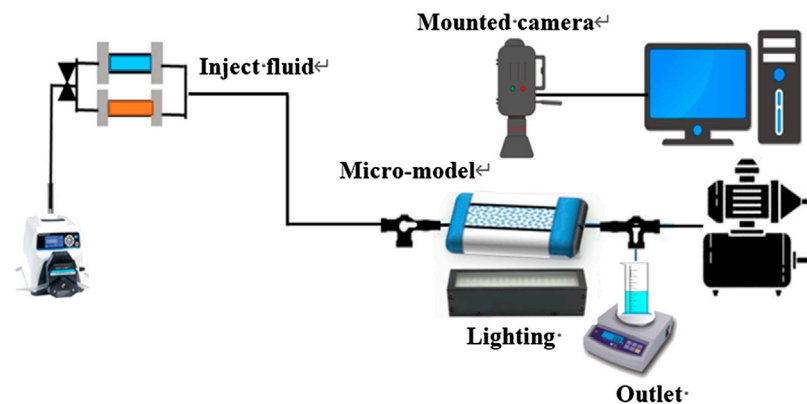


FIGURE 2 | Microscopic visual model displacement experimental device.

## Zeta Potential Determination

Nano Brook 90Plus Pals Zeta potential and granularity analyzer was used in Zeta potential determination experiments. We weighed accurately 1 g purified 200-mesh quartz-sand, montmorillonite, kaolinite, chlorite and illite, dispersed them into 200 ml NaCl and CaCl<sub>2</sub> solutions with Na<sup>+</sup> and Ca<sup>2+</sup> ionic concentrations of 500 mg L<sup>-1</sup>, 1,000 mg L<sup>-1</sup>, 5,000 mg L<sup>-1</sup>, 10,000 mg L<sup>-1</sup> and 20,000 mg L<sup>-1</sup>, respectively, then used a magnetic stirring to stir under 30°C for 15 h and let stand for 24 h. After that, we measured the Zeta potential value of quartz-sand and clay-salt water under room temperature.

## Measurement of Wetting Angles

Experiments were carried out using the SL200KS wetting angle and interface tensiometer. Micromodel mentioned in *Clay Minerals* was used to measure the wetting angles. Besides, a JSM-IT200 scanning electron microscope was used to scan micromodels at a scale of 10 μm. Completed models and scanned figures are shown in Fig 1. Vacuumed the pressed clay flakes, saturated crude oil, then aged for 24 h as the standby. Above solutions were taken separately in the injection pump, and different kinds of saline water droplets were dropped onto the surface of clay models with a high-precision injection pump. Then, the wetting angles were measured after 2 h of stabilization. The measurement aimed to study the influence of brine salinity and clay minerals on rock-wettability alteration.

## Experiment of Microscopic Displacement

In order to study the seepage characteristics of LSW flooding at the micro-model scale and verify the mechanism of LSW flooding, the influence of clay type on seepage characteristics of LSW was studied by two-dimensional glass micro-model and pore-scale visualization method.

Montmorillonite and kaolinite were selected as representatives of swelling clay and non-swelling clay to carry out the microscopic displacement experiments, and experiments were carried out using the experimental instrument showed in Fig 2. A mixture of clay minerals and brine with a salinity of 20,000 mg L<sup>-1</sup> NaCl was injected into the micromodel.

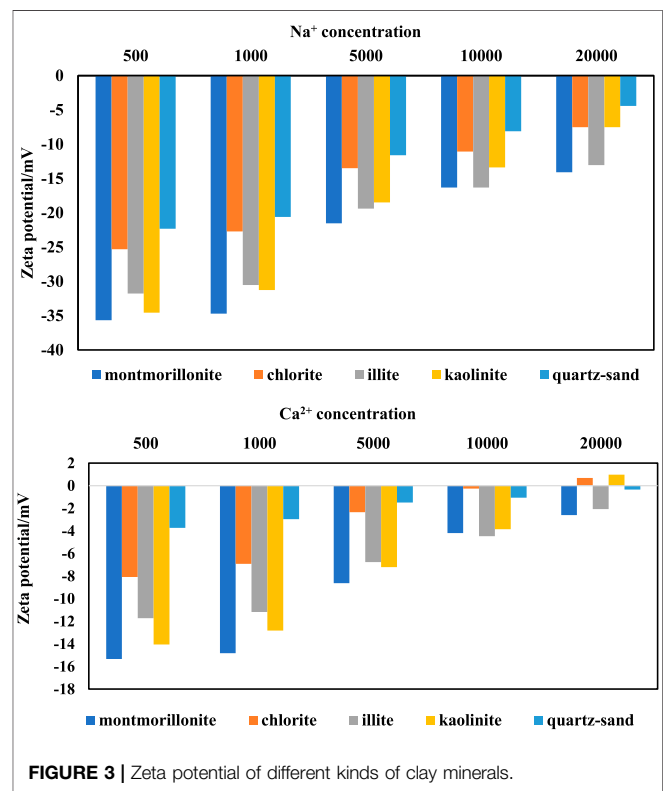


FIGURE 3 | Zeta potential of different kinds of clay minerals.

Afterward, the micromodel was hot-air dried and clay-coated model was saturated first with HSW (20,000 mg L<sup>-1</sup> NaCl) and then crude oil. Then, put the micromodel for 1 week under 80°C for aging purpose.

After the aging process, HSW was injected at a rate of 0.2 ml min<sup>-1</sup> as designed. When there is no crude oil in the produced fluid, HSW was injected at a rate of 0.2 ml min<sup>-1</sup> until there is no increase in water saturation, then, injected the LSW at a rate of 0.2 ml min<sup>-1</sup>. The pH value of the brine used in the experiment was 7. A microscope was used to observe and record changes in the oil and water interface in the pore space. The

microscope provides visual evidence for migration characteristic changes.

## RESULTS AND DISCUSSION

### Results and Discussion of Zeta Potential Measurement

Zeta potential is the potential on the boundary sliding surface of the electric double layer, and it is positively correlated with the electrostatic repulsion force. Therefore, Zeta potential is used to represent the surface potential of clay particles (Kaya et al., 2006). Results of Zeta potential measurement are shown in Fig 3.

With the increase of the concentration of  $\text{Na}^+$  and  $\text{Ca}^{2+}$ , the negative values of Zeta potential of quartz sand-brine interface and clay mineral-brine interface gradually decrease. This is because clay particles are negatively charged and have an adsorption effect on cations. When the concentration of cation increases, more cations enter into the tight layer through the diffusion layer, and the ability to neutralize the negative charge on clay surface is enhanced. As a result, the absolute value of Zeta potential on the surface of quartz sand and clay mineral particles gradually decrease (Kaya et al., 2006). In addition, Zeta potential values of different kinds of clay minerals in the same brine are different, and the negative Zeta potential values of clay minerals-brine interface are almost larger than those of quartz sand-brine, and the negative values of Zeta potential of quartz sand and clay minerals from large to small are: montmorillonite > kaolinite > illite > chlorite. Different ions have different effects on Zeta potential. For quartz sand and clay minerals in solutions with the same concentration of  $\text{Na}^+$  and  $\text{Ca}^{2+}$ , the negative value of Zeta potential in NaCl solution is larger than that in  $\text{CaCl}_2$  solution, and the variation magnitude of Zeta potential shows the same relationship. This is because the divalent  $\text{Ca}^{2+}$  ions can compress the diffusion layer on the surface of quartz sand and clay mineral particles more easily than the monovalent  $\text{Na}^+$  ions in a brine solution with the same ion concentration, and the thickness of the diffusion layer decreases as a result. The  $\text{Ca}^{2+}$  ions enter into the adsorption layer from the diffusion layer, which neutralizes more negative charges on the surface of particles, resulting in a decrease of the negative Zeta potential. At the same time, the potential reversal of kaolinite and chlorite happens in the environment of high  $\text{Ca}^{2+}$  concentration. The reason is that kaolinite and chlorite carry less negative charge because of their lattice structure and charging characteristics. With the increase of the concentration of  $\text{Ca}^{2+}$  ions, the concentration of counter ion  $\text{Ca}^{2+}$  around the particle surface increases continuously, which compresses the diffusion layer and pushes more  $\text{Ca}^{2+}$  into the slipping plane and makes the negative value of Zeta potential on the particle surface decrease continuously, and finally makes the Zeta potential positive.

Through the Zeta potential measurement experiment, it can be inferred that the injection of LSW will increase the negative value of Zeta potential and increase the thickness of the diffusion layer in the double electron layer on the surface of clay minerals, which

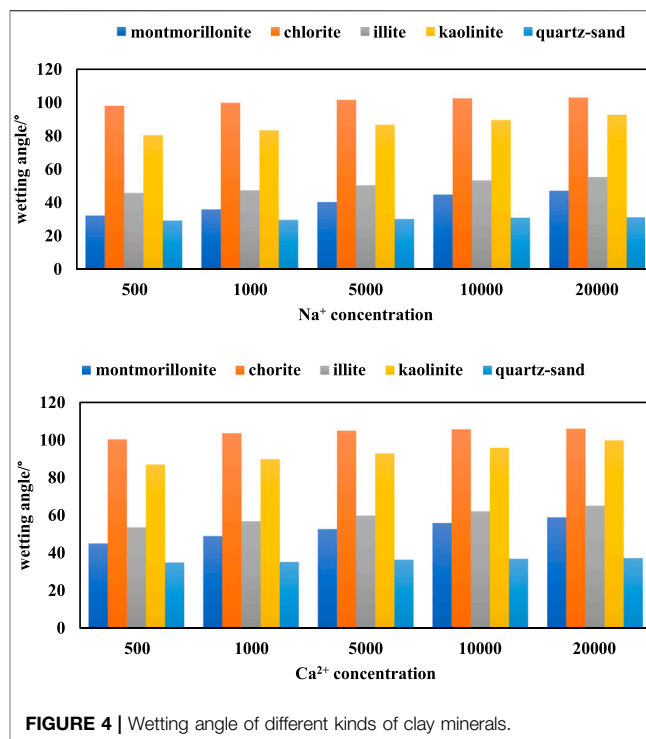


FIGURE 4 | Wetting angle of different kinds of clay minerals.

makes the oil with negative electricity easily desorb from the rock surface attached with clay minerals. Therefore, double electron layer diffusion is the main mechanism of the LSW flooding effect.

### Results and Discussion of Wetting Angle Measurement

Wetting angle between the oil-water-mineral was measured in the experiment. The wettability of reservoir rock depends on the stability of the thin brine film that wets its surface. The stability of the film is influenced by interactions between its brine-rock and oil-rock interfaces which are described by classical DLVO theory (Myint and Firoozabadi, 2015).

Wetting angles of quartz sand – brine interface are shown in Fig 4. From this figure, we can see that the LSW can effectively reduce the wetting angle of minerals. The wetting angle is a function of decomposition pressure which is composed of the expansion force of the double electron layer, Van Der Waals force and structural force (Hirasaki, 1991). The decrease of the ion concentration makes Zeta potential of clay-brine interface strongly negative (Nasralla and Nasr-El-Din, 2014b), forming a thick double electron layer, increasing the electrostatic repulsion force on the surface of simulated oil and clay (Xie et al., 2016), reducing the wetting angle and increasing the hydrophilicity.

Wetting angle of droplets on the surface of quartz sand and different types of clay flakes varies with the change of droplet salinity. With the increase of droplet salinity, the wetting angle of quartz sand and different types of clay flakes gradually increased, as a result, water wettability decreased and oil wettability increased. As shown by the results, the change of wetting



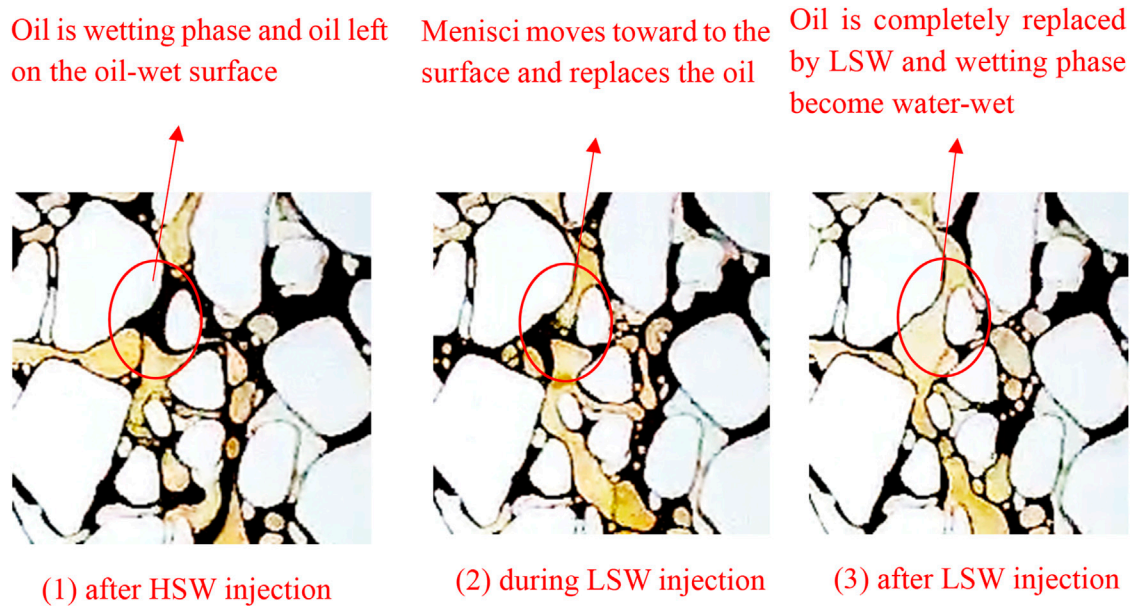


**FIGURE 5 |** Kaolinite coated micromodel during displacement.

angle is caused by the different amounts of negative charge in HSW and LSW. HSW produced weak charges at the oil-water and rock-water interfaces, which lead to the weak repulsive force between the oil and rock system and resulted in a stable water film and a less water-wet system. On the contrary, LSW increased the magnitude of the negative charges. An increase in the magnitude of the negative charge at oil-water and rock-water interfaces resulted in a higher repulsive force between oil and rock, which expanded the double layer and produced a more water-wet system.

Comparing the wetting angles of quartz sand and clay minerals in NaCl and CaCl<sub>2</sub> solutions, it can be found that the wetting angles of quartz sand and clay minerals of CaCl<sub>2</sub> solution droplets are larger than that of NaCl solution droplets under the same ion concentration. This indicates that the ionic valence state adsorbed by clay minerals in aqueous solution affects the thickness of hydration film, when the ionic valence state is lower, the hydration film will be thicker and the water wettability will be stronger. Since the valence of Ca<sup>2+</sup> is larger than that of Na<sup>+</sup>, Ca<sup>2+</sup> will carry more positive charges than Na<sup>+</sup> under the same solution concentration, which can neutralize more negative charges on the surface of quartz sand, clay sheet and simulated oil surface. The negative value of the Zeta potential is smaller. Consequently, the diffusion layer in the double electron layer is compressed to a greater extent, showing a weaker negative charge, and the electrostatic repulsion force is smaller. The ability of the oil to fall from the surface of quartz sand and clay minerals is weaker. As a result, the wettability of CaCl<sub>2</sub> solution on the surface of quartz sand and clay minerals is weaker than that of NaCl solution, the oil wettability is stronger and the wetting contact is larger.

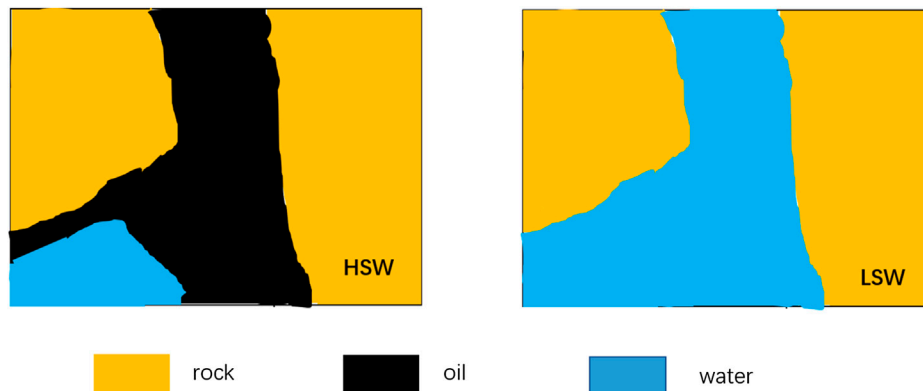
## Results and Discussion of Micro Displacement

### Low Salinity Water Flooding in Kaolinite

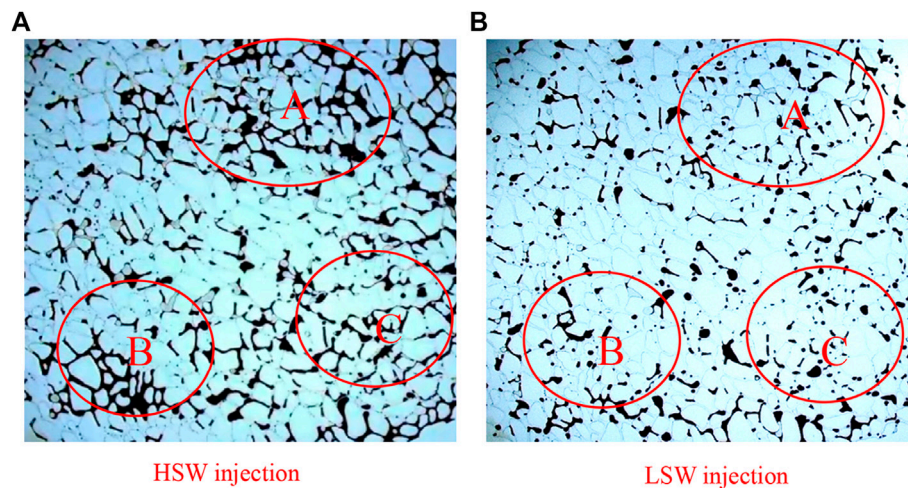
The clay-coated model was first saturated with LSW (20,000 mg L<sup>-1</sup> NaCl) and then crude oil. Before saturated with crude oil, the porous medium was completely water-wet since kaolinite is highly hydrophilic and the presence of salt enhances the water wettability considerably. When the clay-coated model with kaolinite was saturated by crude oil under formation water environment, surface charges of kaolinite and crude oil were neutralized by the oppositely charged ion in the formation water, the electrostatic repulsion between the rock-oil interfaces decreased and the brine film was destabilized. Then the polar components of crude oil adhered to the surface of clay particles, making the surface of clay particles more oil-wetting.

As illustrated in Fig 5, dynamics of two-phase flow were visualized. In the oil-wet porous medium, during the injection of LSW, the moving mechanism was observed and the oil-water interface moved through narrow throats to large pores, displacing the wetting phase (oil phase).

After the injection of HSW, as shown in Fig 5. 1), the whole system was oil-wet and the oil phase cannot flow from the rock surface, which resulted in the low oil recovery efficiency. During the injection of LSW, as shown in Fig 5. 2), wetting properties of pores changed from oil-wet to mixed wetting. The meniscus was continuously advanced, leaving the oil film attached near the wall of the lipophilic hole. However, on the hydrophilic surface, the interface moved toward the surface of kaolinite particles, replacing the oil film, so the amount of oil in pores was reduced significantly. After the injection of LSW, as shown in Fig 5. 3), the water-oil menisci displaced oil in many small pores.



**FIGURE 6** | Wetting properties of kaolinite model during high salinity water (HSW) and low salinity water (LSW).



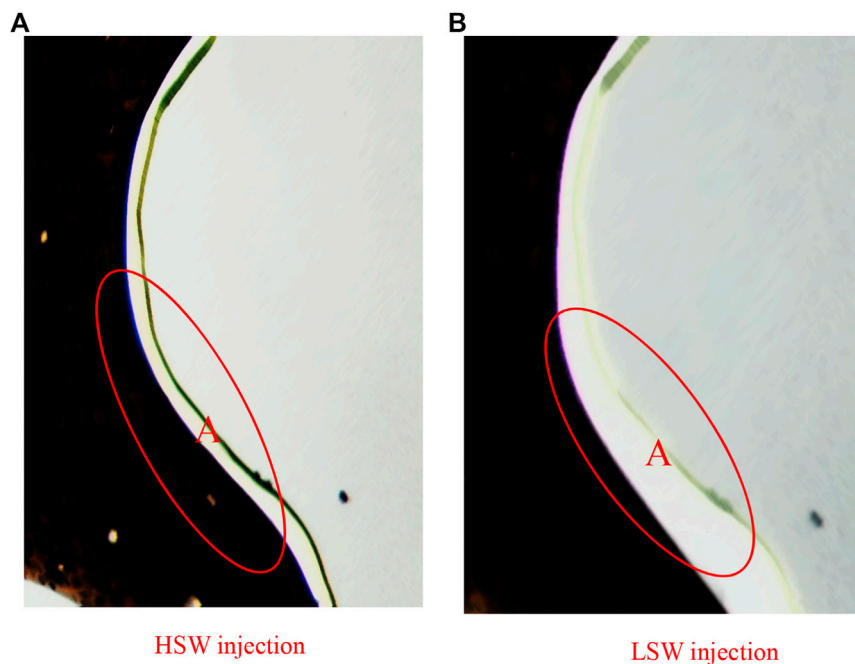
**FIGURE 7** | Result of macro-displacement of kaolinite micromodel under (A) HSW injection and (B) LSW injection.

Fig 6. shows the wetting properties of the kaolinite model in HSW and LSW. Difference in the change of surface wetting properties of the model attached with kaolinite under two types of displacement modes can be explained by the diffusion of the double electric layer. In HSW flooding, negatively charged kaolinite and crude oil would be neutralized by cations, the electric double layer between kaolinite and crude oil would become thinner, offsetting the exclusion between oil and clay. Then, the bridge of cations in HSW keeps the crude oil connected with the clay surface, forming a lipophilic porous medium. After LSW flooding, highly mineralized formation water is gradually replaced. The reduction of the strength of ion bridge leads to the diffusion of electric double layer between clay and crude oil, which weakens the bridge of cations in formation water, thus increasing the electrostatic repulsion between clay and crude oil, destroying the adsorption state of crude oil on the surface of clay particles, and transforming wetting properties to a more hydrophilic state. When the electrostatic repulsion is high

enough, oil droplets are released from the surface of clay particles and replaced by low salinity water.

Result of the macro-displacement of kaolinite is shown in Fig 7, and oil recovery of A, B, C region in the figure increases greatly. For micromodel attached with kaolinite, in the process of HSW flooding, since pore surface is oil-wetting and oil film stranded on pore is thick, it is not easy to replace the oil. Besides, injected water cannot enter into small throats easily, as a result, a large amount of crude oil was bypassed, resulting in low oil recovery efficiency. In the process of LSW flooding, due to the diffusion of electric double layer and other mechanisms which can lead to the change of wetting properties, the Van der Waals force between clay particles and crude oil was weakened, static repulsion force was enhanced, pore surface changed from oil-wetting into mixed wetting, oil droplets detached from the pore of hydrophilia surface, and crude oil in small throats was displaced, so the recovery rate was significantly improved.





**FIGURE 8** | Wetting properties of montmorillonite micromodels during (A) HSW injection and (B) LSW injection.

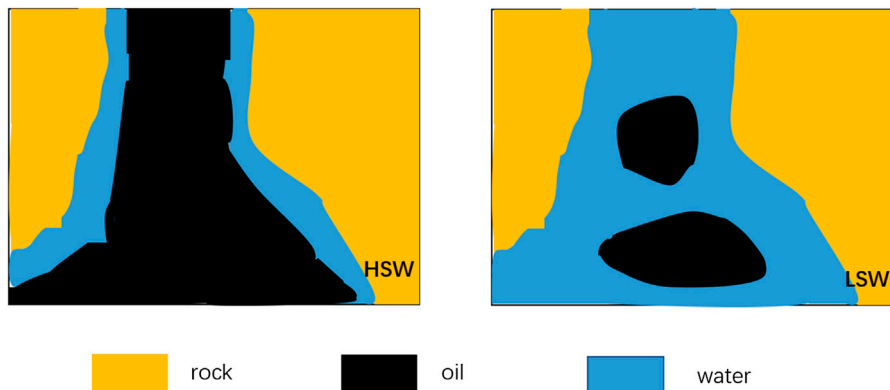


**FIGURE 9** | Schematic of oil distribution in HSW and LSW flooding.

### Low Salinity Water Flooding in Montmorillonite

Procedure of the montmorillonite experiment was similar to that of kaolinite and montmorillonite had obvious water-wet due to its weak crystal lattice and cations on the surface.

Micromodel attached with montmorillonite is shown in Fig 8. In the process of HSW flooding, the surface of the pore wall is water wetting, the surface of the water film is thin, and the adsorption capacity of crude oil is strong. In the process of LSW flooding, it can be seen from the figure that the thickness of the water film in the A area increases, the ability to absorb crude oil is weakened, and residual oil in the hole throat becomes more fluid. This difference is caused by the

lattice structure of montmorillonite. When low salinity water is injected, low valence cations replace high valence cations between structural unit layers and electric double layer on the clay surface diffuses, causing the increase of the electrostatic repulsion between clay and crude oil and being more hydrophilic.

Although there was no evidence of wettability alteration and the whole system remained water-wet, it had been suggested that polar components of crude oil contacted with a brine phase and became highly elastic under LSW condition. Increased viscoelasticity of water-oil interface hinders the snap-off of the oil into small droplets that would disperse in brine, this

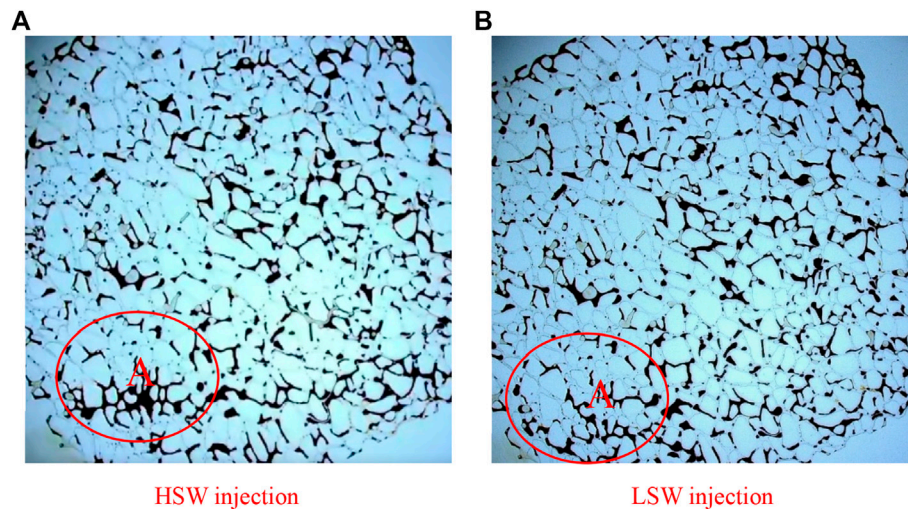


**FIGURE 10 |** Result of macro-displacement of montmorillonite micromodel under (A) HSW flooding and (B) LSW flooding.

phenomenon is shown in **Fig 9**. As a result, oil in LSW is more continuous and mobile than that in HSW. Therefore, the viscoelastic characteristic of the water-oil interface may make a critical contribution to the EOR of LSW flooding.

Characteristics of residual oil migration of the micromodel attached with montmorillonite are shown in **Fig 9**. We can see that in the process of HSW flooding, injected water moves along the pore throat and easy to get stuck. Due to the capillary force, there is a large amount of residual oil in the middle of the hole channel that is illiquid. And we can see that there is a large amount of residual oil in positions A, B, and C in the figure. In the process of LSW flooding, residual oil in positions A, B, and C is reduced, and it changes from block to beaded, drop-shaped. Capillary force in the whole system no longer dominates, and oil is less stuck in the narrower hole throat. During this process, water is kept at the waterflood front, while only oil phase is moving in front of the waterflood front.

Result of the macro-displacement of montmorillonite micromodel is shown in **Fig 10**. In this figure, recovery degree is greatly improved only in the A region and it is not obvious enough in other remaining areas. For micromodel attached with montmorillonite, in the HSW flooding process, its result is slightly better than the result of micromodel attached with kaolinite under the same flooding condition since the surface of the montmorillonite pore is water-wetting. In the LSW flooding process, the water-wet characteristic of montmorillonite is enhanced, water film thickens and adsorption capacity of crude oil is reduced, while residual oil has undergone a shift from snap-and-replace to piston-like displacement. However, there is still droplet-like residual oil in the throat.

As for pH values of input and output. The pH of input brine was 7, and the pH of output after HSW flooding is nearly 9 and is around 7 after LSW flooding. The downward shift in effluent pH difference between HSW and LSW is traditionally ascribed to the

exchange of  $H^+$  and positive ion on clay surface (Li et al., 2020a; Li et al., 2020b).

## CONCLUSIONS

Through the experiment of micro-seepage characteristics of low salinity water, the surface mechanism of LSW flooding EOR is verified from a microscopic point, and the following conclusions are concluded:

- (1) Diffusion happens in double electron layer, ion exchange and wettability changes occur between clay minerals and LSW interfaces, are main mechanisms of LSW flooding EOR and these mechanisms are correlated to each other. Clay minerals undergo ion exchange under the action of low salinity water, which causes the diffusion of the double electron layer, resulting in the change of potential, and the wetting angle changes as a result.
- (2) For micromodel attached with kaolinite, in the process of HSW flooding, residual oil is attached to the surface in a membrane-like way, and the oil membrane is thick, so it is not easy to be replaced. In the process of LSW flooding, the membranous residual oil is thin and easy to be replaced. The mechanism of LSW to improve recovery rate is the change of surface wettability, so the residual oil can be replaced easily. There is no wetting transition from lipophilicity to hydrophilicity for micromodels attached to montmorillonite. The montmorillonite is still water phase wetting. The mechanism of LSW to improve the recovery rate is the further enhancement of water phase wetting and a thicker water membrane. The adsorption state of residual oil in the large hole channel is not obvious, and residual oil in the small hole is changed from columnar form to beaded and drop-shaped form.

- (3) In field production, LSW is suitable for reservoirs containing clay minerals. But for reservoirs rich in kaolinite, the lower the mineralization of the water, the better. For reservoirs rich in montmorillonite, there are lots of drop-shaped residual oil left in throat when using LSW flooding, and new methods are needed to recover the remaining oil.

## DATA AVAILABILITY STATEMENT

The original contributions presented in the study are included in the article/supplementary materials, further inquiries can be directed to the corresponding author.

## REFERENCES

- Al Shalabi, E. W., Sepehrnoori, K., and Delshad, M. (2014). Mechanisms behind low salinity water injection in carbonate reservoirs. *Fuel* 121, 11–19. doi:10.1016/j.fuel.2013.12.045
- Al-Saedi, H. N., Brady, P. V., Flori, R., and Heidari, P. (2018). “Novel insights into low salinity water flooding enhanced oil recovery in sandstone: the clay role study,” in SPE Improved Oil Recovery Conference, Tulsa, OKLA, April 14–18. doi:10.2118/190215-MS
- Al-Saedi, H. N., and Flori, R. E. (2018). Enhanced oil recovery of low salinity water flooding in sandstone and the role of clay. *Petrol. Explorat. Develop.* 45, 927–931. doi:10.1016/S1876-3804(18)30096-X
- Amirian, T., Haghighi, M., and Mostaghimi, P. (2017). Pore scale visualization of low salinity water flooding as an enhanced oil recovery method. *Energy Fuels*. 31, 13133–13143. doi:10.1021/acs.energyfuels.7b01702
- Barnaji, M. J., Pourafshary, P., and Rasaie, M. R. (2016). Visual investigation of the effects of clay minerals on enhancement of oil recovery by low salinity water flooding. *Fuel* 184, 826–835. doi:10.1016/j.fuel.2016.07.076
- Bondino, I., Doorwar, S., Ellouz, R., and Hamon, G. (2013). “Visual microscopic investigations about the role of pH Salinity and clay on oil clay on oil adhesion and recovery,” in International Symposium of the Society of Core Analysts, Napa Valley, CA, September 16–19.
- Demir, A. B., Bilgesu, H. I., and Hascakir, B. (2016). “The effect of clay and salinity on asphaltene stability,” SPE Western Regional Meeting, Anchorage, AK, May 23–26. doi:10.2118/180425-MS
- Fogden, A., Kumar, M., Morrow, N. R., and Buckley, J. S. (2011). Mobilization of fine particles during flooding of sandstones and possible relations to enhanced oil recovery. *Energy Fuels*. 25, 237–242. doi:10.1021/ef101572n
- Hilner, E., Andersson, M. P., Hassenkam, T., Matthiesen, J., Salino, P. A., and Stipp, S. L. S. (2015). The effect of ionic strength on oil adhesion in sandstone – the search for the low salinity mechanism. *Entific Reports*. 5, 9933. doi:10.1038/srep09933
- Hirasaki, G. J. (1991). Wettability: fundamentals and surface forces. *SPE Form. Eval.* 6 (2), 217–226. doi:10.2118/17367-PA
- Kaya, A., Ren, A. H., and Yükselen, Y. (2006). Settling of kaolinite in different aqueous environment. *Mar. Georesour. Geotechnol.* 24 (3), 203–218. doi:10.1080/10641190600788429
- Kim, C., and Lee, J. (2017). Experimental study on the variation of relative permeability due to clay minerals in low salinity water-flooding. *J. Petrol. Sci. Eng.* 151, 292–304. doi:10.1016/j.petrol.2017.01.014
- Lager, A., Webb, K. J., Black, C. J. J., Singleton, M., and Sorbie, K. S. (2008). Low salinity oil recovery - an experimental investigation. *Petrophysics* 49 (1), 28–35. <https://www.researchgate.net/publication/241783001>
- Lager, A., Webb, K. J., Collins, I. R., and Richmond, D. M. (2008). “LoSal enhanced oil recovery: evidence of enhanced oil recovery at the reservoir scale,” in SPE symposium on improved oil recovery, Tulsa, OKLA, April 20–23. doi:10.2118/113976-MS

## AUTHOR CONTRIBUTIONS

XW: Conceptualization, Methodology, Validation, Formal analysis, Writing - Original Draft, Supervision, Project administration, unding acquisition. YZ: Validation, Project administration. WJ: Methodology, Validation, Formal analysis, Writing - Original Draft. ZW: Experimental running. XL: Investigation, Resources. FW: Methodology.

## ACKNOWLEDGMENTS

This study was supported by the Natural Science Foundation of China (Project Number: 51874339)

- Li, S., Wang, Q., and Li, Z. (2020a). Stability and flow properties of oil-based foam generated by CO<sub>2</sub>. *SPE J.* 25 (1), 416–431. doi:10.2118/199339-PA
- Li, S., Wang, Q., Zhang, K., and Li, Z. (2020b). Monitoring of CO<sub>2</sub> and CO<sub>2</sub> oil-based foam flooding processes in fractured low-permeability cores using nuclear magnetic resonance (NMR). *Fuel* 263–116648. doi:10.1016/j.fuel.2019.116648
- Loahardjo, N., Xie, X., and Morrow, N. R. (2010). Oil recovery by sequential waterflooding of mixed-wet sandstone and limestone. *Energy & Fuels*. 24, 5073–5080. doi:10.1021/ef100729b
- Myint, P. C., and Firoozabadi, A. (2015). Thin liquid films in improved oil recovery from low-salinity brine. *Current Opinion in Colloid & Interface ence.* 20 (2), 105–114. doi:10.1016/j.cocis.2015.03.002
- Nasralla, R. A., and Nasr-El-Din, H. A. (2014a). Double-layer expansion: is it a primary mechanism of improved oil recovery by low-salinity waterflooding? *SPE Reservoir Eval. Eng.* 17 (1), 49–59. doi:10.2118/154334-MS
- Nasralla, R. A., and Nasr-El-Din, H. A. (2014b). Impact of cation type and concentration in injected brine on oil recovery in sandstone reservoirs. *J. Petrol. Engineer.* 122, 384–395. doi:10.1016/j.petrol.2014.07.038
- Reed, J., and Mcdonald, A. (2015). “Influence of clay content and type on oil recovery under low salinity waterflooding on north sea reservoirs,” in SPE Offshore Europe Conference and Exhibition, Aberdeen, Scotland, September 8–11. doi:10.2118/175506-MS
- Stanislav, J., Susan, S., and Nicolas, B. (2018). Adsorption of organic ligands on low surface charge clay minerals: the composition in the aqueous interface region. *Phys. Chem. Chem. Phys.* 20, 17226–17233. doi:10.1039/C8CP01189C
- Tammy, A., and Manouchehr, H. (2018). Impact of clay type and water composition on low salinity water injection – visualisation approach. *APPEA J.* 58 (1), 51–59. doi:10.1071/AJ17076
- Tang, G. Q., and Morrow, N. R. (1999). Influence of brine composition and fines migration on crude oil/brine/rock interactions and oil recovery. *J. Petrol. Engineer.* 24 (2), 99–111. doi:10.1016/S0920-4105(99)00034-0
- Tina, P., Aleksandr, M., Zahra, A., Oline, F. G., Marie, M. G., Skule, S., et al. (2018). Role of kaolinite clay minerals in enhanced oil recovery by low salinity water injection. *Energy Fuels*. 32 (7), 7374–7382. doi:10.1021/acs.energyfuels.8b00790
- Xie, Q., Saedi, A., Pooryousefy, E., and Liu, Y. (2016). Extended DLVO-based estimates of surface force in low salinity water flooding. *J. Mol. Liq.* 221, 658–665. doi:10.1016/j.molliq.2016.06.004
- Yousef, A. A., Al-Saleh, S., Al-Kaabi, A., and Al-Jawfi, M., (2011). Laboratory investigation of the impact of injection-water salinity and ionic content on oil recovery from carbonate reservoirs. *SPE Reservoir Eval. Eng.* 14 (5), 578–593. doi:10.2118/137634-PA
- Zhang, L., Zhang, J., Wang, Y., Yang, R., Zhang, Y., Gu, J., et al. (2018). Experimental investigation of low salinity water flooding in a low-permeability oil reservoir. *Energy Fuels*. 32 (3), 3108–3118. doi:10.1021/acs.energyfuels.7b03704
- Zhang, Y., Xie, X., and Morrow, N. (2007). “Waterflood performance by injection of brine with different salinity for reservoir cores,” in SPE

Annual Technical Conference and Exhibition, Anaheim, CA, November 11–14. doi:10.2118/109849-MS

**Conflict of Interest:** The authors declare that the research was conducted in the absence of any commercial or financial relationships that could be construed as a potential conflict of interest.

*Copyright © 2020 Wei, Zhang, Jiang, Wang, Li and Wu. This is an open-access article distributed under the terms of the Creative Commons Attribution License (CC BY). The use, distribution or reproduction in other forums is permitted, provided the original author(s) and the copyright owner(s) are credited and that the original publication in this journal is cited, in accordance with accepted academic practice. No use, distribution or reproduction is permitted which does not comply with these terms.*



# Numerical Simulation of a Horizontal Well With Multi-Stage Oval Hydraulic Fractures in Tight Oil Reservoir Based on an Embedded Discrete Fracture Model

Zhi-dong Yang<sup>1,2\*</sup>, Yong Wang<sup>2</sup>, Xu-yang Zhang<sup>2</sup>, Ming Qin<sup>3</sup>, Shao-wen Su<sup>2</sup>, Zhen-hua Yao<sup>3</sup> and Lingfu Liu<sup>1\*</sup>

<sup>1</sup>State Key Laboratory of Oil and Gas Reservoir Geology and Exploitation, Southwest Petroleum University, Chengdu, China, <sup>2</sup>Baikouquan Oil Production Plant, PetroChina Xinjiang Oilfield Company, Karamay, China, <sup>3</sup>Exploration and Development Research Institute of Petro China Xinjiang Oilfield Company, Karamay, China

## OPEN ACCESS

### Edited by:

Kaiqiang Zhang,  
Imperial College London,  
United Kingdom

### Reviewed by:

Salam Al-Rbeawi,  
Middle East Technical University,  
Turkey  
Freddy Humberto Escobar,  
South Colombian University,  
Colombia  
Xu Jianchun,  
China University of Petroleum, China

### \*Correspondence:

Lingfu Liu  
lingfu.liu@outlook.com  
Zhi-dong Yang  
Yangzd688@petrochina.com.cn

### Specialty section:

This article was submitted to  
Advanced Clean Fuel Technologies,  
a section of the journal  
Frontiers in Energy Research

**Received:** 31 August 2020

**Accepted:** 20 October 2020

**Published:** 23 November 2020

### Citation:

Yang Z, Wang Y, Zhang X, Qin M, Su S,  
Yao Z and Liu L (2020) Numerical  
Simulation of a Horizontal Well With  
Multi-Stage Oval Hydraulic Fractures in  
Tight Oil Reservoir Based on an  
Embedded Discrete Fracture Model.  
Front. Energy Res. 7:601107.  
doi: 10.3389/fenrg.2020.601107

Tight oil is a kind of unconventional oil and gas resource with great development potential. Due to the unconventional characteristics of low porosity and low permeability in tight oil reservoirs, single wells generally have no natural productivity, and industrial development is usually conducted in combination with horizontal wells and hydraulic fracturing techniques. To capture the flow behavior affected by fractures with complex geometry and interaction, we adopted embedded discrete fracture models (EDFMs) to simulate the development of fractured reservoirs. Compared with the traditional discrete fracture models (DFMs), the embedded discrete fracture models (EDFMs) can not only accurately represent the fracture geometry but also do not generate a large number of refine grids around fractures and intersections of fractures, which shows the high computational efficiency. To be more consistent with the real characteristic of the reservoir and reflect the advantage of EDFMs on modeling complex fractures, in this work, the hydraulic fractures are set as oval shape, and we adopted 3-dimensional oil–gas two-phase model considering capillary forces and gravity effects. We developed an EDFM simulator, which is verified by using the fine grid method (FGM). Finally, we simulated and studied the development of tight oil without and with random natural fractures (NFs). In our simulation, the pressure varies widely from the beginning to the end of the development. In real situation, tight oil reservoirs have high initial pressure and adopt step-down bottom hole pressure development strategy where the bottom hole pressure of the last stage is below the bubble point pressure and the free gas appears in the reservoir. Modeling studies indicate that the geometry of fracture has a great influence on the pressure and saturation profiles in the area near the fractures, and dissolved gas flooding contributes to the development of tight oil, and NFs can significantly improve production, while the effect of the stress sensitivity coefficient of NFs on production is more significant in the later stage of production with lower reservoir pressure.

**Keywords:** numerical simulation, flow in porous media, tight oil reservoirs, embedded discrete fracture model, Multi-stage fractured horizontal well



## INTRODUCTION

Along with the increasing social and economic development of world, the demand for energy is getting larger and larger. In China, conventional oil and gas resources only account for about 20% of the total resources, while the proportion of unconventional oil and gas resources is as high as 80% (Zou et al., 2012). Therefore, the abundant unconventional oil and gas resource is a major source of short- and long-term energy in China. As a kind of important unconventional oil and gas resource, tight oil is accumulated in tight clastic or carbonate reservoirs that is interbedded with or adjacent to oil-generating strata, which has not been migrated over large distances. Tight oil wells usually have no natural production capacity, or the natural production capacity is lower than the minimum industrial production capacity. To obtain economic development of tight oil, horizontal wells and hydraulic fracturing techniques are often used to stimulate the tight rock. It is important to accurately characterize and simulate the production of wells and variation of pressure in reservoirs for choosing the best stimulation and development strategy. However, compared with low-permeability matrices, fractures have high conductivity and complex geometry, which makes the numerical simulation of fluid flow very challenging. There are two major classes of models proposed to model the fractured system: dual continuum models and discrete fracture models (DFMs).

Dual continuum models are widely used in the industry. The concept of the dual porosity (DP) model was first proposed by Barenblatt et al. (1960). Later, Warren and Root (1963) developed the DP model, known as the sugar cube model. In Warren and Root's model, reservoirs are divided into two systems: matrix system and fracture system. Fluid exchange between the two systems is described by interporosity flow. Warren and Root's model is also called DP single permeability (DPSK or DPSP) because fluid stores in two systems, while fluid flow only occurs in the fracture system. The dual continuum model, in addition to DP single permeability, also includes the DP dual permeability (DPDK or DPDP) model and the multiple interacting continuum (MINC) model. DPDK was proposed by Blaskovich et al. (1983). In DPDK, both the fracture and the matrix systems are not only storage space but also flow channels of fluid. Multiple interacting continuum (Pruess and Narasimhan, 1982; Wu and Pruess, 1988) creates a series of "nested" matrix control volumes in fracture control volumes, which makes it successful to model nonisothermal and multi-phase flow and effectively reduces the subgridding cells compared to explicit discretization. Continuum models are widely used in analytical and semi-analytical solutions to research the fractured unconventional reservoirs (Zhao et al., 2013; Al-Rbeawi, 2017a; Al-Rbeawi, 2017b; Zhang et al., 2018; Kou and Wang, 2020). However, dual continuum models are only suitable for the reservoir with a large number of highly connected and small fractures (Karimi-Fard and Firoozabadi, 2003). Moreover, they may have difficulties representing highly localized anisotropy in reservoirs (Moinfar et al., 2013).

To overcome these limitations, DFMs were developed. DFMs can explicitly represent the real geometry of fractures. Each fracture has its own size, shape, orientation, and permeability. Scholars used many methods for simulation with DFMs, such as finite element methods (Kim and Deo, 2000; Karimi-Fard and Firoozabadi, 2003; Zhang et al., 2016), mixed finite element methods (Hoteit and Firoozabadi, 2006), control volume finite element methods (Bastian et al., 2000), and hybrid finite element/finite volume methods (Fu et al., 2005). Most of above methods rely on unstructured grids, which provide flexibility to model more realistic fracture geometries. However, the quality of the generated unstructured grids relies much on the mathematical algorithms applied, which could be very complicated for certain scenarios (Jiang et al., 2014). Besides, DFMs will generate a large number of refined grids around the position where fractures intersect or are densely distributed, which results in low computational efficiency.

Therefore, there is still a demand for improvement in the DFM. Lee et al. (2001) and Li and Lee (2008) proposed embedded DFMs (EDFMs). Compared to DFMs, embedded DFMs have simpler mathematical algorithms for generating grids and will not generate many refined grids when fractures have complex geometric features. Based on such advantages, many scholars used embedded DFMs to simulate and research the flow phenomenon in the fractured tight reservoir.

However, most scholars modeled the hydraulic fractures (HFs) as rectangle plates, which cannot reflect the complex geometry of HFs and the characteristic of fluid flow in the fractured reservoir. Besides, recent studies ignore the feature of abnormal high pressure in tight oil reservoirs. Owing to the stress sensitivity, the permeability of the matrix and fractures will gradually decrease as the pressure of reservoir drops down caused by development of the reservoir. Therefore, if the initial pressure of the reservoir is not high enough, the permeability of the matrix and fractures will only decrease a little from the beginning to the end of development. Consequently, some simulation results may seem overly optimistic because of the relatively high permeability. Furthermore, in the late stage of actual tight oil development, bottom hole pressure (BHP) will drop below the bubble point pressure, and two-phase flow of oil and gas occurs in the reservoir. Nevertheless, recent studies about tight oil hardly consider the fact of oil-gas two-phase flow and the energy of dissolved gas.

In this study, we used embedded DFMs to simulate the development of fractured reservoirs. Then, we verified our EDFM simulator and demonstrated EDFMs' advantages for modeling complex fractures by a scenario setting HFs as oval shape in 3D reservoir models. In order to reflect the actual development of tight reservoir, reservoirs have high initial pressure, and multistage fractured wells adopt the step-down BHP production strategy. Moreover, an oil-gas two-phase flow model is applied to capture the phenomenon of dissolved gas drive. At last, we generate nature fractures in reservoirs to study the influence of nature fractures in the tight reservoir.

## METHODOLOGY

### Embedded Discrete Fracture Models

Lee et al. (2001) and Li and Lee (2008) developed embedded DFMs. Embedded DFMs use orthogonal structured grids to represent the matrix. In this model, each fracture passes through many matrix grids and is divided into a series of segments by matrix cell boundaries. These fracture segments are fracture cells, which are “embedded” into matrix cells, so this model is called embedded DFMs. In embedded DFMs, fluid flows in both matrix and fracture systems, and interporosity flow also occurs between two systems.

**Figure 1** shows a 2D scenario of the EDFM. In this scenario, two fractures are divided into four fracture cells, and one fracture cell (f3) connects to the wellbore. As you can see, there are many kinds of connection relationship between cells, such as two adjacent matrix cells, fracture cell, and its embedded matrix cell, two adjacent fracture cells inside the same fracture, and two intersecting fracture cells in two different fractures, and fracture cell and its connecting well cells. To describe and record these connection relationship, non-neighboring connection concept (Moinfar et al., 2013; Xu, 2015) and connection list method (Jiang et al., 2014; Zhao et al., 2019) are usually used, which is also helpful for assembling computational matrices.

The mass exchange between these connections can be calculated by the following unified form:

$$q = T\Delta\Phi \quad (1)$$

$$T = Gf_s f_p, \quad (2)$$

where  $q$  (in  $\text{m}^3/\text{day}$ ) represents the flow rate,  $T$  represents the transmissibility,  $\Delta\Phi$  (in kPa) represents the potential difference,  $G$  represents the transmissibility geometric factor,  $f_s$  represents a strongly nonlinear transmissibility term related to saturation, and  $f_p$  represents a weakly nonlinear transmissibility term related to pressure.

The main difference among these connections is the calculation method of the transmissibility geometric factor, which is described as below. It is noted that, in this study, fluid cannot directly flow from the matrix to the wellbore, which fits the fact of hydraulic fracturing. Therefore, there is no connection between the matrix and wellbore.

(1) Two adjacent matrix cells, such as m1–m2 in **Figure 1**

$$G_{mm} = \frac{2G_{m1}G_{m2}}{G_{m1} + G_{m2}}, G_{m1} = \beta_c \left( \frac{k_{m1}A_{mm}}{d_{m1}} \right), G_{m2} = \beta_c \left( \frac{k_{m2}A_{mm}}{d_{m2}} \right), \quad (3)$$

where  $k_{m1}$  and  $k_{m2}$  (in D) represent the permeability of two matrix cells, respectively,  $A_{mm}$  (in  $\text{m}^2$ ) represents the contact area of two matrix cells,  $d_{m1}$  and  $d_{m2}$  (in m) represent mean distance from the common surface of two matrix cells to their centers, respectively, and  $\beta_c$  ( $= 86.4 \times 10^{-6}$ ) represents the transmissibility constant.

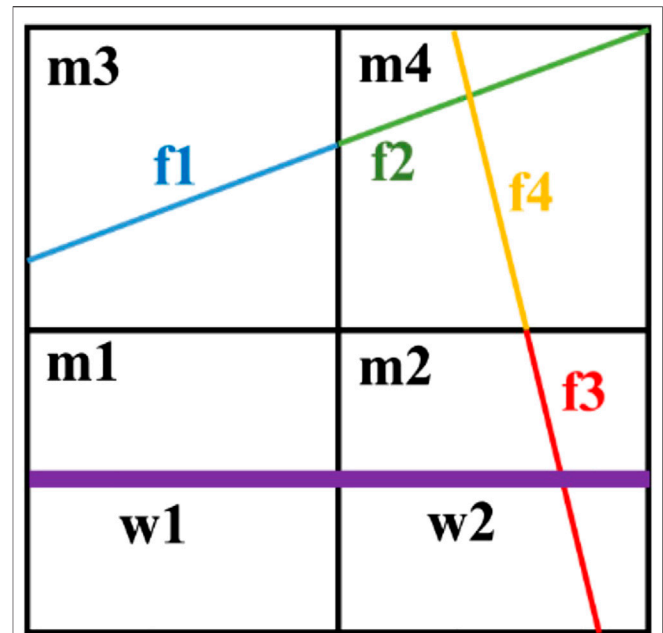


**FIGURE 1** | EDFM with one horizontal wellbore and two fractures.

(2) Fracture cell and its embedded matrix cell, such as m3–f1 in **Figure 1** (Li and Lee, 2008)

$$G_{mf} = \beta_c \frac{k_{mf}A_{mf}}{d_{mf}}, \quad (4)$$

where  $k_{mf}$  (in D) represents the permeability of this connection, which is approximately equal to matrix permeability, since this interporosity flow is mainly determined by the matrix with low permeability;  $A_{mf}$  (in  $\text{m}^2$ ) represents the contact area between the fracture cells and its imbedded matrix cell, which is equal to twice the area of one side of the fracture plane ( $2A_f$ ), since both sides of the fracture are connected to the matrix; and  $d_{mf}$  (in m) represents the average normal distance, which can be obtained by calculating the integral value of average vertical distance between all points in the matrix cell and the fracture.

(3) Two adjacent fracture cells inside the same fracture, such as f1–f2 in **Figure 1** (Xu, 2015)

$$G_f = \frac{G_{f1}G_{f2}}{G_{f1} + G_{f2}}, G_{f1} = \beta_c \frac{k_{f1}A_f}{d_{f1}}, G_{f2} = \beta_c \frac{k_{f2}A_f}{d_{f2}}, \quad (5)$$

where  $k_{f1}$  and  $k_{f2}$  (in D) represent the permeability of two fracture cells,  $A_f$  (in  $\text{m}^2$ ) represents the contact area of two fracture cells, and  $d_{f1}$  and  $d_{f2}$  (in m) represent mean distance from all points in fracture cells to the common surface of two cells, respectively.

(4) Two intersecting fracture cells inside same matrix cell, such as f2–f4 in **Figure 1** (Moinfar et al., 2014)

$$G_{ff} = \frac{G_{ff1} G_{ff2}}{G_{ff1} + G_{ff2}}, G_{ff1} = \beta_c \frac{k_{f1} \omega_{f1} L_{int}}{d_{f1}}, G_{ff2} = \beta_c \frac{k_{f2} \omega_{f2} L_{int}}{d_{f2}}, \quad (6)$$

where  $k_{f1}$  and  $k_{f2}$  (in D) represent the permeability of two fracture cells, respectively,  $\omega_{f1}$  and  $\omega_{f2}$  (in m) represent the aperture of two fracture cells, respectively,  $G_{wff} = \beta_c \frac{\Delta\theta \cdot k_f \omega_f}{\ln(\frac{r_e}{r_w})}$ ,  $r_e = 0.14 \sqrt{L_f^2 + h_f^2}$  (in m) represents the length of intersecting lines of two cells, and  $d_{f1}$  and  $d_{f2}$  (in m) represent the mean distance from all points in fracture cell to the common surface of the two cells, respectively.

(5) fracture cell and its connecting wellbore, such as f3-w2 in **Figure 1** (Moinfar et al., 2013)

$$G_{wf} = \frac{\Delta\theta \cdot k_f \omega_f}{\ln(\frac{r_e}{r_w})}, r_e = 0.14 \sqrt{L_f^2 + h_f^2}, \quad (7)$$

where  $k_f$  (in D) represents the fracture permeability,  $\omega_f$  (in m) represents the fracture aperture,  $L_f$  (in m) represents the length of the fracture cell,  $h_f$  (in m) represents the height of the fracture cell,  $r_e$  (in m) represents the equivalent well grid radius,  $r_w$  (in m) represents the wellbore radius, and  $\Delta\theta$  (in rad) represents the central angle of the well within the fracture, which is, in general, equal to  $2\pi$ , since the wellbore passes through one fracture cell.

## Model Assumptions and Boundary Conditions

The basic assumptions for this research are as follows. 1) The flow obeys Darcy flow in both the fracture and matrix. 2) Ignore changes in temperature in the reservoir. 3) The reservoir is rectangular. 4) The shapes of fractures are parallel plates of equal thickness. 5) Only fluid from the HF flows into the wellbore, and no fluid from the matrix flows into the wellbore. 6) Ignore capillary force in fractures.

The boundary conditions of the reservoir and fractures are as follows. 1) The reservoir has closed boundaries. 2) There is fluid exchange between the matrix and the fracture. 3) In order to conform to the actual hydraulic fracturing technology, only the fluid in HFs flows into wellbore directly, while fluid in the matrix do not flows into wellbore directly.

## Governing Equations

The mass conservation equations of two-phase oil-gas flow are

$$\nabla \cdot \left[ \frac{kk_{ro}}{\mu_o B_o} (\nabla p_o + \rho_o g \nabla Z_o) \right] + q_{osc} = \frac{\partial}{\partial t} \left( \frac{\phi s_o}{B_o} \right) \quad (8)$$

$$\begin{aligned} \nabla \cdot \left[ \frac{kk_{rg}}{\mu_g B_g} (\nabla p_g + \rho_g g \nabla Z_g) + \frac{kk_{ro} R_s}{\mu_o B_o} (\nabla p_o + \rho_o g \nabla Z_o) \right] + q_{gsc} \\ = \frac{\partial}{\partial t} \left[ \frac{\phi s_g}{B_g} + \frac{\phi R_s s_o}{B_o} \right], \end{aligned} \quad (9)$$

where subscripts o and g represent oil and gas, respectively;  $k$  (in D) represents absolute permeability;  $k_r$  (dimensionless) represents relative permeability;  $\mu$  (in Pa·s) represents viscosity;  $B$  (dimensionless) represents volume factor;  $p$  (in kPa) represents pressure;  $\rho$  (in kg/m<sup>3</sup>) represents density;  $Z$  (in

m) represents height;  $g$  ( $=9.8066$  m/s<sup>2</sup>) represents the acceleration of gravity;  $q$  (in m<sup>3</sup>/day) represents source/sink term;  $\phi$  (dimensionless) represents porosity;  $s$  (dimensionless) represents saturation; and  $R_s$  (dimensionless) represents solution gas/oil ratio.

In EDFMs, the interporosity flow is represented in the source sink term  $q$ . Owing to kinds of cell connection in the EDFM, the mass conservation equation (Eqs. 8 and 9) can be transformed into the following discrete form: the left side of the equation is expressed as the sum of the flow into the cell by different connections, while the right side of the equation still maintains the form of net cumulative fluid.

Combined with the relationship of saturation,

$$s_o + s_g = 1 \quad (10)$$

the equations of the matrix cells can be transformed as follows:

$$\sum q_{omm} + \sum q_{omf} = \frac{V_b}{\alpha_c \Delta t} \Delta t \left[ \frac{(1 - s_g) \phi_m}{B_{om}} \right] \quad (11)$$

$$\sum q_{gmm} + \sum q_{gmf} = \frac{V_b}{\alpha_c \Delta t} \Delta t \left[ \frac{s_g \phi_m}{B_{gm}} + \frac{(1 - s_g) R_s \phi_m}{B_{om}} \right] \quad (12)$$

and the equations of fracture cells can be transformed as follows:

$$\sum q_{of} + q_{ofm} + \sum q_{off} + q_{ofw} = \frac{V_b}{\alpha_c \Delta t} \Delta t \left[ \frac{(1 - s_g) \phi_f}{B_{of}} \right] \quad (13)$$

$$\sum q_{gf} + q_{gfm} + \sum q_{gff} + q_{gfw} = \frac{V_b}{\alpha_c \Delta t} \Delta t \left[ \frac{s_g \phi_f}{B_{gf}} + \frac{(1 - s_g) R_s \phi_f}{B_{of}} \right], \quad (14)$$

where  $V_b$  (in m<sup>3</sup>) represents the volume of the matrix grid block,  $\alpha_c$  ( $=1$ ) the volume conversion constant,  $\Delta t$  (in day) represents time step, subscript m and f represent the matrix and fracture cell, respectively,  $\phi_m$  (dimensionless) represents the ratio of the pore volume in the matrix cell to the volume of the matrix cell block,  $\phi_f$  (dimensionless) represents the ratio of the pore volume in the fracture grid to the volume of the matrix grid block where the fracture is embedded,  $\sum q_{mm}$  (in m<sup>3</sup>/day) represents the rate of flow from all adjacent matrix grids to the matrix grid,  $\sum q_{mf}$  (in m<sup>3</sup>/day) represents the rate of flow from all fracture grids to the matrix grid where all these fracture grids are embedded,  $\sum q_f$  (in m<sup>3</sup>/day) represents the rate of flow from all adjacent fracture grids to the fracture grid (all fracture grids are in the same fracture plate),  $q_{fm}$  (in m<sup>3</sup>/day) represents the rate of flow from the matrix cell, in which the fracture cell is embedded, to the fracture cell,  $\sum q_{ff}$  (in m<sup>3</sup>/day) represents the total rate of flow from all the other intersecting fracture cells to the fracture cell (all fracture cells are embedded in the same matrix cell), and  $q_{fw}$  (in m<sup>3</sup>/day) represents the rate of flow from the well to its connected fractured grid, whose value will be negative when the well is a production well.

## Stress Sensitivity in Tight Reservoirs

In order to highlight the flow mechanism of tight reservoirs, the stress sensitivity of tight reservoirs is considered to study stress

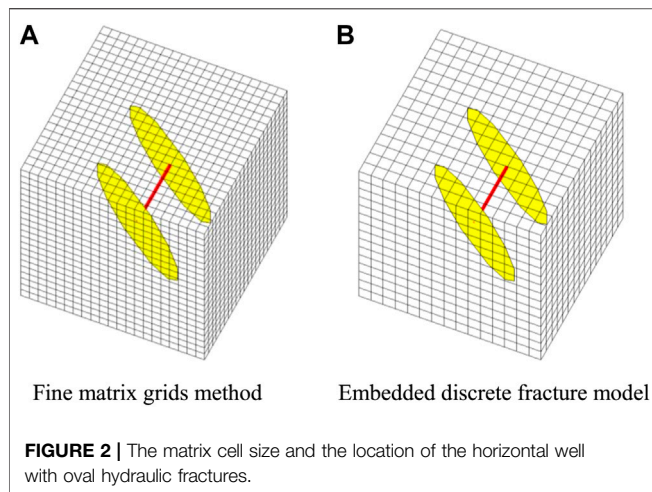


**TABLE 1 |** Simulation parameters for verification.

Parameter	Value	Unit
Matrix permeability $K_x = K_y = K_z$	$0.1 \times 10^{-3}$	D
Reservoir porosity	0.1	Dimensionless
Major axis of oval fractures	40	m
Minor axis of oval fractures	20	m
Horizontal wellbore length	40	m
Fracture aperture	0.005	m
Fracture permeability	25	D
Well radius	0.1	m
Rock compressibility	$1 \times 10^{-4}$	$\text{MPa}^{-1}$
Simulation time per production stage	50	day
Simulation time in total	100	day

sensitivity effects of matrix and fracture permeability. There are kinds of types of stress-sensitive models, including binomial, logarithmic, power law, and exponential relationship (Jones, 1975; David et al., 1994; Zhao et al., 2011; Xiao et al., 2016).

In this study, a widely used exponential relationship model is adopted for both matrix permeability and fracture permeability:

$$k = k_0 \cdot e^{-\alpha(p_0 - p)}, \quad (15)$$

where  $\alpha$  (in  $\text{MPa}^{-1}$ ) represents the stress sensitivity coefficient,  $p_0$  (in MPa) represents reference pressure, and  $k_0$  (in D) represents permeability under reference pressure.

## MODEL VERIFICATION

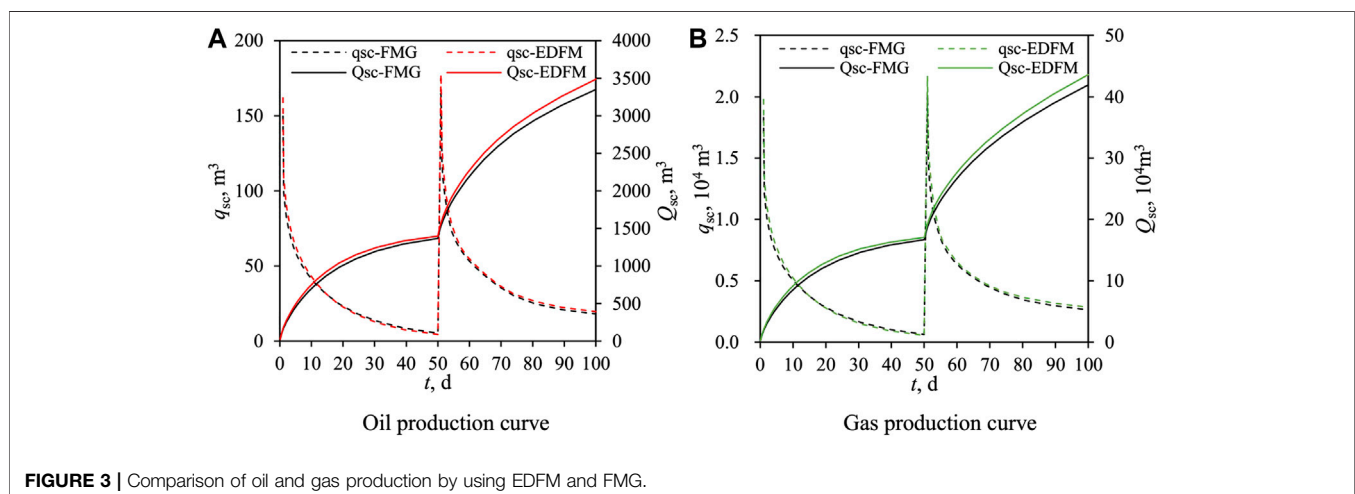
EDFMs have the flexibility to handle fractures with complex shapes and in any orientation. In our model, the HF's are considered as oval shape in 3D reservoirs, and fractures are allowed to be not perpendicular to the border of reservoir, so it is complex to generate 3D unstructured cells by DFMs. Therefore, we used fine matrix grid (FMG) method to verify accuracy of our simulator developed by using embedded DFMs.

In the FMG method, the reservoirs are divided into a large number of FMGs, and the effect of high permeability of fracture is considered into the matrix cells. When a matrix grid passes through fracture, to maintain fracture conductivity, the permeability of this matrix cell will increase as below.

$$k_{f\_eff} = \frac{k_f \times w_f}{w_{f\_eff}}, \quad (16)$$

where  $k_f$  (in D) is the permeability of fracture,  $w_f$  (in m) is the aperture of fracture, and  $w_{f\_eff}$  (in m) is the effective aperture of fracture, which is equal to the grid size in this verification.

In this verification, we modeled the development of the tight oil reservoir. The size of the reservoir is  $100 \text{ m} \times 100 \text{ m} \times 100 \text{ m}$ . There is a horizontal well with two HF's of oval shape. The angle between the fracture plane and horizontal well is  $55^\circ$ , as shown in **Figure 2**. The reservoir's initial pressure is 30 MPa. The development process of the reservoir consists of two stages of production with two constant BHP, 20 and 10 MPa, respectively. Because the bubble point pressure is





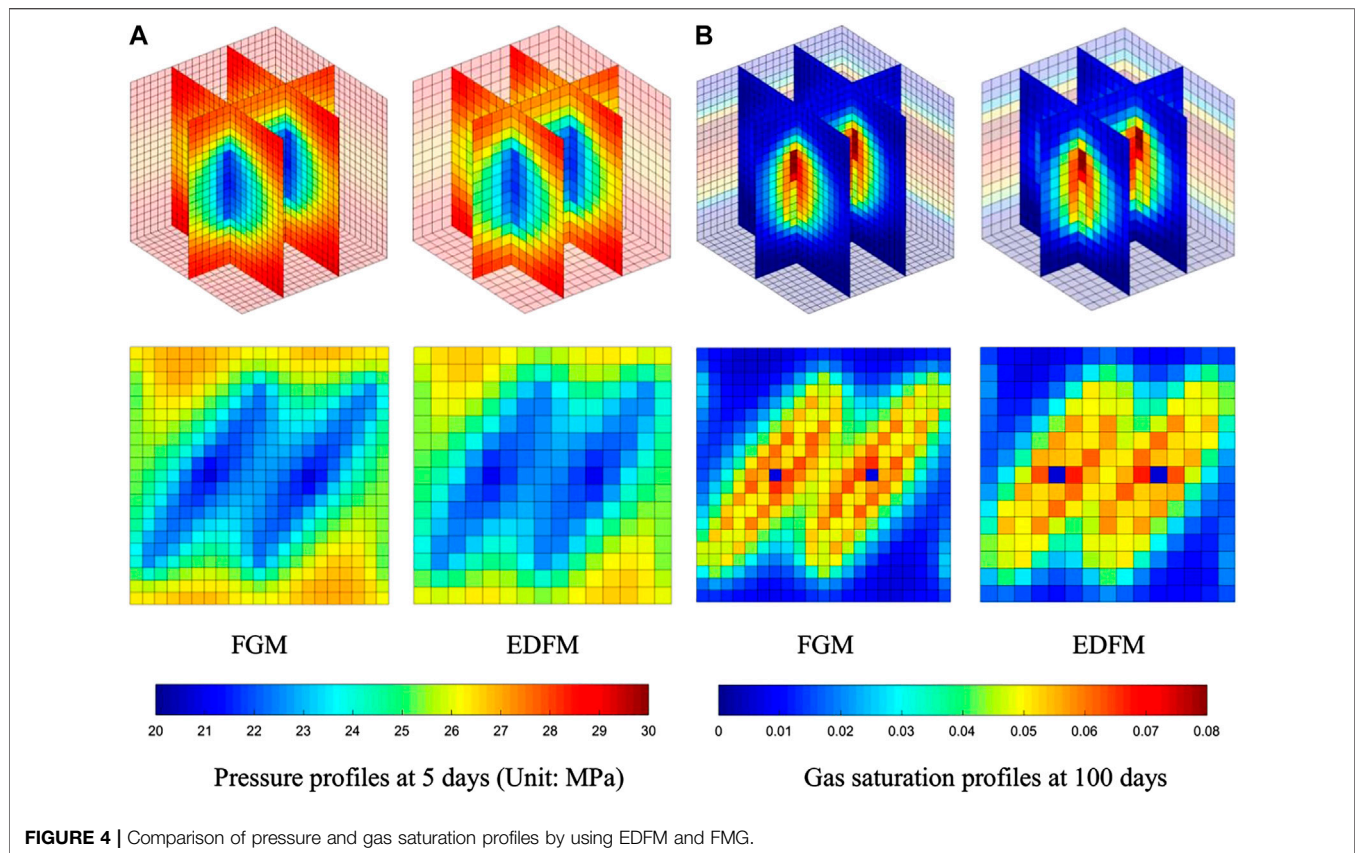


**FIGURE 4 |** Comparison of pressure and gas saturation profiles by using EDFM and FMG.

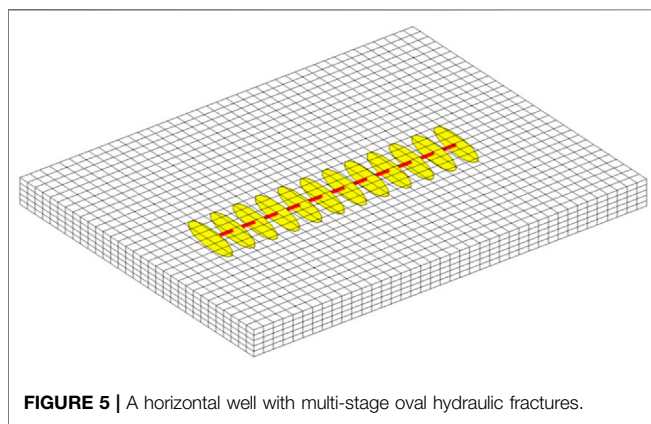


**FIGURE 5 |** A horizontal well with multi-stage oval hydraulic fractures.

12 MPa, the first production stage is a single-phase (oil) flow, and the second production stage is a two-phase (oil-gas) flow. We also considered the influence of gravity and capillary effect in the matrix in two-phase flow, while the capillary effect in fracture is ignored. The PVT property of oil and gas is shown in **Appendix**, and other reservoir properties and some simulation parameters are shown in **Table 1**. The oil and gas relative permeability relationship and gas–oil capillary force of matrix are shown in **Appendix**. We ignore the capillary force in fractures. The oil and gas relative

permeability of fracture cells is equal to the oil and gas saturation of fracture cells.

In the FMG method, the number of matrix cells is 9,261 ( $21 \times 21 \times 21$ ), while the number of matrix cells is only 3,375 ( $15 \times 15 \times 15$ ) in the embedded DFM. Adding the number of fracture cells 198, the total number of cells in EDFM is 3,573. The matrix cell and the location of the fractured horizontal well are shown in **Figure 2**.

We simulated this scenario with the EDFM and FMG. The oil and gas production curve is shown in **Figure 3**, where the dotted lines represent daily production and the solid lines represent cumulative production. **Figure 4** compares the pressure profiles after 5 days of production and the gas saturation profiles after 100 days of production of the EDFM and FMG. In **Figure 4**, the two-dimensional figures represent the pressure and saturation profiles on the horizontal surface where the horizontal well is located. Although the total cell number of the EDFM is about one-third of that of FMGs, all figures (**Figures 3 and 4**) indicate that our EDFM simulator can reach similar accuracy as the FMG simulator. Moreover, as shown in **Figure 4**, in the region containing free gas around fractures, the gas saturation at higher place is higher than that at lower place, confirming our simulator can reflect the effect of density and gravity. Besides, the daily production declines more slowly and cumulative production is larger in the second stage, reflecting the effect of dissolved gas flooding on production, which is consistent with qualitative knowledge.



**TABLE 2** | Simulation parameters.

Parameter	Value	Unit
Reservoir dimensions (x, y, z)	800, 620, 50	m, m, m
Grid block size (x, y, z)	20, 20, 10	m, m, m
Initial matrix permeability $k_x = k_y = k_z$	$0.1 \times 10^{-3}$	D
Initial matrix porosity	0.1	Dimensionless
Initial reservoir pressure	50	MPa
Rock compressibility	$1 \times 10^{-4}$	MPa <sup>-1</sup>
Stress sensitivity coefficient of matrix	0.001	MPa <sup>-1</sup>
Major axis of oval fractures	60	m
Minor axis of oval fractures	20	m
Horizontal wellbore length	500	m
Number of hydraulic fracture	12	—
Hydraulic fracture aperture	0.005	m
Hydraulic fracture permeability	25	D
Stress sensitivity coefficient of natural fractures	0.02	MPa <sup>-1</sup>
Well radius	0.1	m
Simulation time per production stage	200	day
Simulation time in total	800	day

From this verification, it seems that FMGs are similar to EDFMs and EDFMs do not show much advantage. However, if there are more fractures with more complex interaction relationship and we still want to get enough simulation accuracy, such as **Figure 9**, there will be much more fine cells in FMGs to achieve satisfying accuracy, resulting in very low efficiency for model calculation.

## EXAMPLE SIMULATION

### A Multi-Stage Horizontal Well With Oval Hydraulic Fractures

First, we simulated the development of a horizontal well with multi-stage oval HFs, as shown in **Figure 5**. In order to reflect the actual development of the tight reservoir, reservoirs have high initial pressure, and multi-stage fractured wells adopt the step-down BHP production strategy. At the last step-down BHP

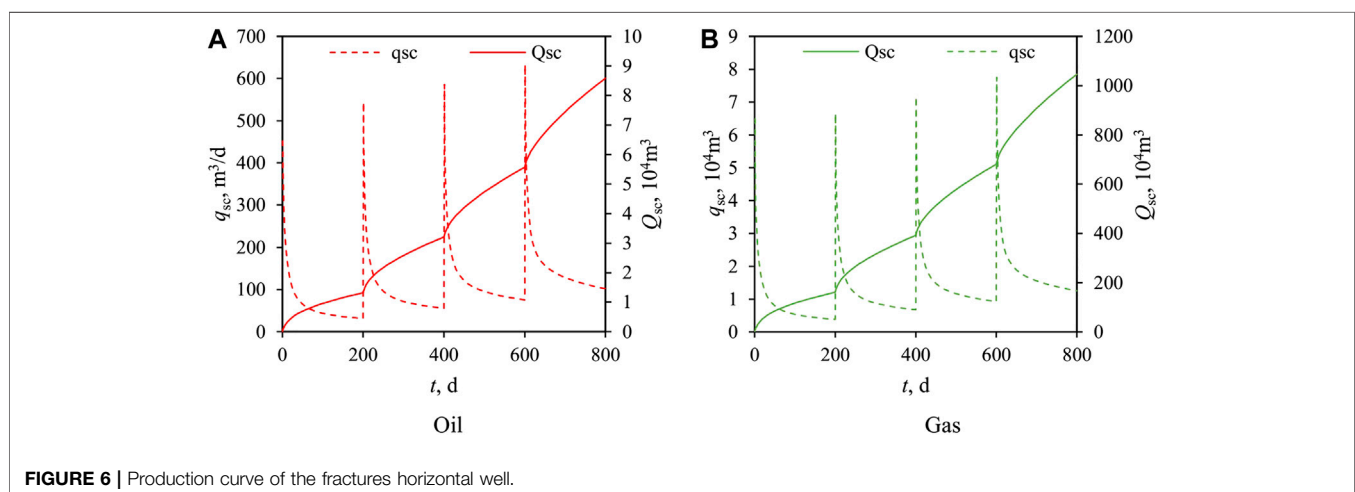
production stage, the BHP is lower than bubble point pressure of oil, resulting in oil–gas two-phase fluid flow in the reservoir.

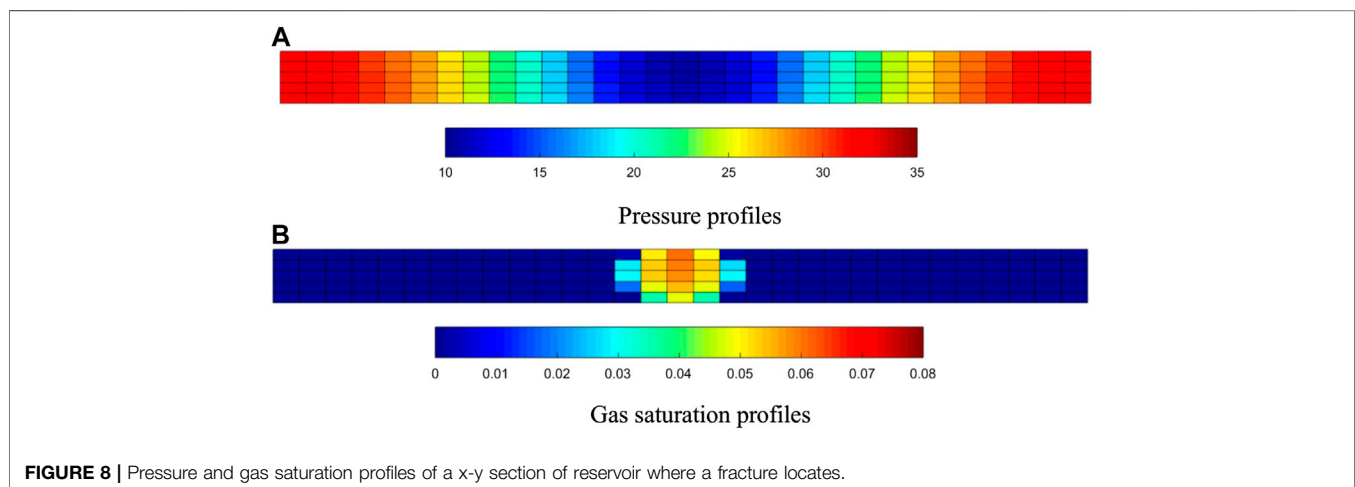
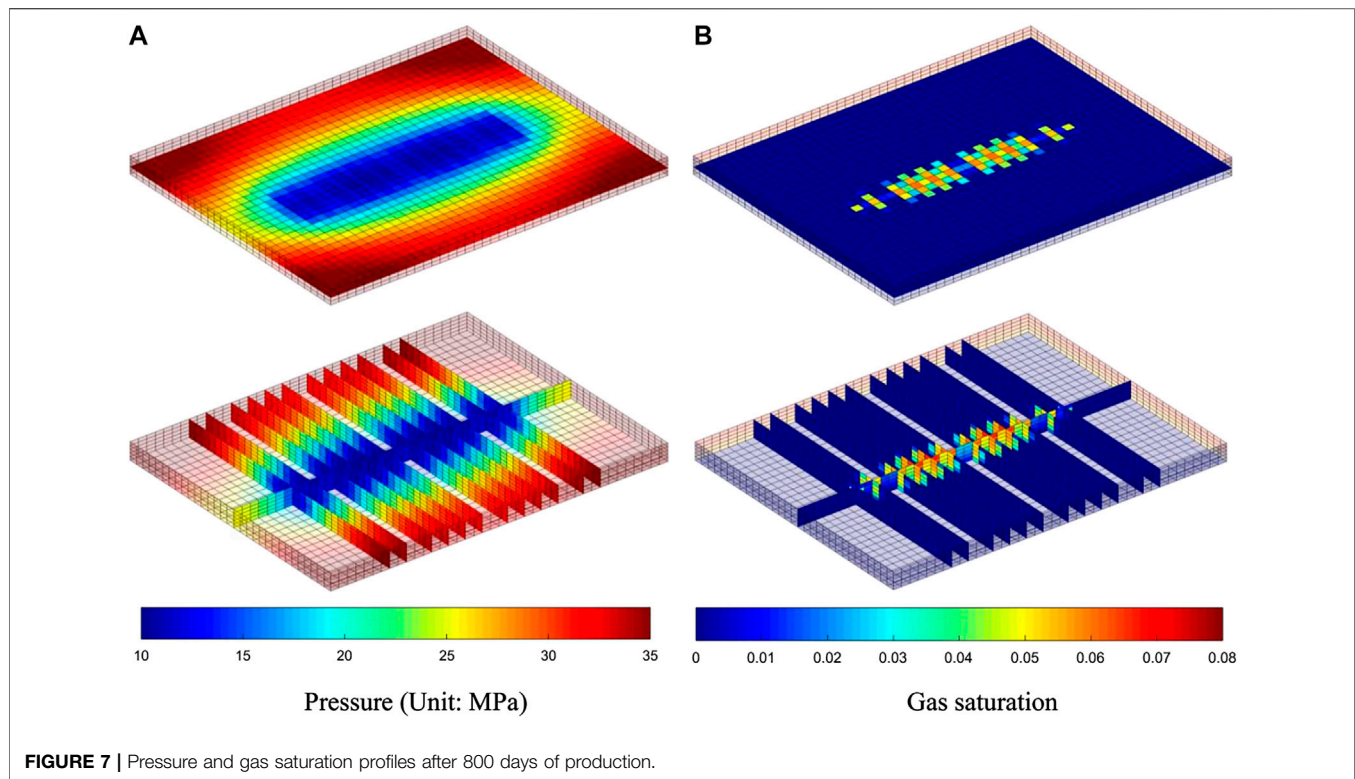
We set the initial reservoir pressure at 50 MPa. There are four stages of production (200 days per stage). The BHP of four stages is set as 40, 30, 20, 10 MPa. Because the bubble point pressure is 12 MPa, the last stage of production is oil–gas two-phase flow in the reservoir. Other simulation parameters are listed in **Table 2**. The PVT property of oil and gas is shown in **Appendix**. **Appendix** shows the oil and gas relative permeability relationship and gas–oil capillary force of the matrix. For fractures, we ignore the capillary force in fractures, and the oil and gas relative permeability of fracture cells is equal to the oil and gas saturation of fracture cells.

We simulated this scenario. The results of daily and accumulative production of oil and gas are shown in **Figure 6**. The simulation results show that in each production stage, the early production decreases rapidly, followed by a slow rate of production decline. **Figure 7** shows the pressure and gas saturation at the end of simulation. The free gas dissolved from oil in formation occurs only in the near-well area because the region of pressure below the bubble point is relatively small, which is only around the well. Moreover, due to the good seepage condition in the near-well area, the free gas is quickly produced by the fractured well, which keeps the gas saturation in the near-well area low and does not significantly affect the oil phase permeability. **Figure 8** presents the pressure and gas saturation profiles of a vertical y-z section of reservoir where the fracture in the middle of horizontal well locates. **Figure 8** clearly exhibits the effect of fracture shape, gravity, and fluid density on pressure and saturation profiles.

### Influence of Stress Sensitivity of Natural Fractures

Because of the absence of proppant, natural fractures (NFs) are generally more stress-sensitive than HFs, resulting in NFs to be nearly closed at late period of production and causing a significant

**FIGURE 6** | Production curve of the fractures horizontal well.



impact on well production. In our work, we generated 70 random NFs (as shown in **Figure 9**). The parameters of NFs are listed in **Table 3**. Then, we studied the effect of stress sensitivity of NFs by varying the stress sensitivity coefficient of NFs (0.03, 0.05, and 0.08 MPa<sup>-1</sup>), while the stress sensitivity coefficient of HF and the matrix are smaller, 0.02 and 0.001 MPa<sup>-1</sup>, respectively. **Figure 10** represents the relationship between permeability of fractures and pressure, including HF and NFs.

**Figure 11** shows the relationship between production and the stress sensitivity coefficient of NFs, where the dotted lines represent the production without NFs. Simulation results demonstrate the remarkable effect of increasing production

of NFs. According to **Figure 11**, in the first stage of production (0–200 days), the difference of production among three stress sensitivity coefficients is small. As time goes on, the difference of production among three stress sensitivity coefficients become larger, and the effect of NFs

**TABLE 3** | Parameters of natural fractures.

Parameter	Value	Parameter	Value
Length of natural fractures, m	80	Height of natural fractures, m	10
Aperture of natural fractures, m	0.003	Permeability of natural fractures, D	20

on production decreases with the increase in the stress sensitivity coefficient. At the last stage, NFs with  $0.08 \text{ MPa}^{-1}$  stress sensitivity coefficient have little effect on production compared the scenario without NFs.

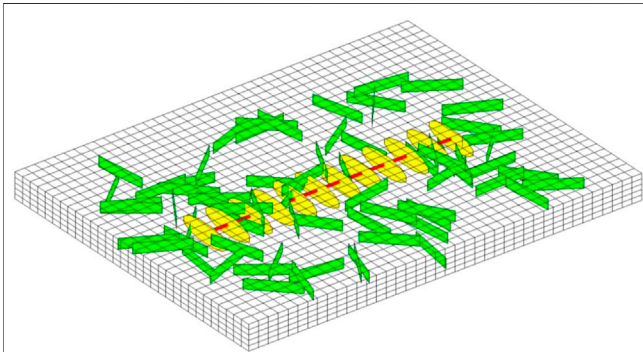


**FIGURE 9** | Distribution of the multi-stage fractured horizontal well and natural fractures.

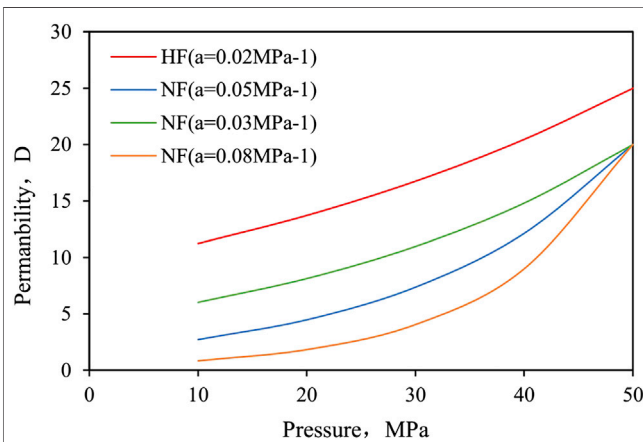


**FIGURE 10** | The relationship between permeability of fractures and pressure.

**Figure 12** presents the pressure profiles after 200 and 800 days of production. In **Figure 12A**, pressure profiles under different stress sensitivity coefficients are almost the same, and the distribution of pressure is also affected by fractures obviously. However, in **Figure 12B**, pressure profiles differ from each other, which is reflected in the smoothness of the shape of isopiestic lines affected by NFs. In **Figure 12B**, on the condition that the stress sensitivity coefficient is  $0.08 \text{ MPa}^{-1}$ , the pressure profile is almost the same as if there were no NFs (**Figure 7A**). Besides, at the first stage of production, the permeability of NFs in three scenarios is quite different (**Figure 11**), but the production of three scenarios is almost equal (**Figure 11**), which may be due to the fact that the production/development of the tight reservoir with fractures is determined only by the matrix when the permeability difference between matrix and fracture is extremely great. Because the permeability of the tight reservoir matrix is very small, the fluid transport capacity from the matrix to the fracture is much smaller than the capacity in fractures. Therefore, when the permeability of fractures is high enough, the overall flow in the formation is mainly determined by the matrix with smaller permeability. As the fracture permeability decreases, production becomes more sensitive to the permeability of fractures.

## CONCLUSION

In our work, an EDFM simulator is developed to study the development of multi-stage horizontal wells in tight reservoirs. To capture the complex shape of HF, the HF is considered as oval shape. In our simulations, reservoirs have high initial pressure, and wells adopt the step-down BHP production strategy conforming to the character of the actual tight reservoir and its development strategy. Moreover, the phenomenon of solution gas drive is also captured by applying an oil-gas two-phase flow model. Our EDFM simulator is verified by using the fine matrix cell method, which also demonstrates the advantages of the EDFM for modeling fractures with complex shape. Finally, we generate random nature fractures in

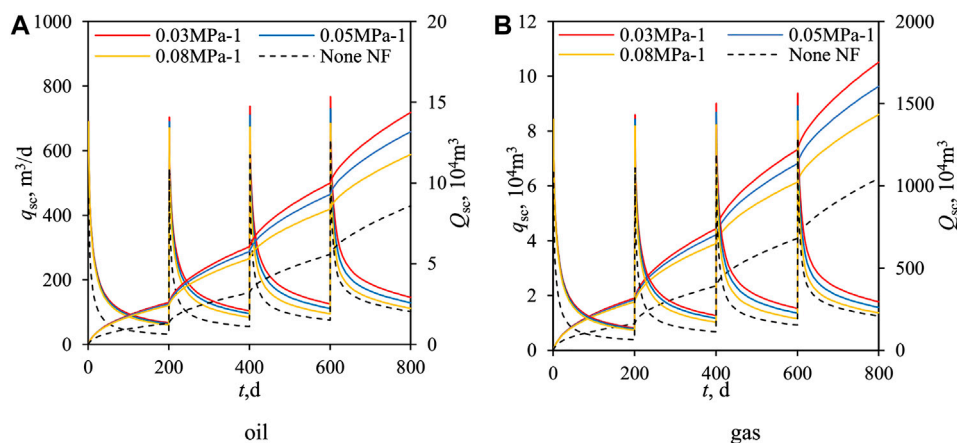


**FIGURE 11** | Oil and gas production curve under different stress sensitivity coefficient of natural fractures.

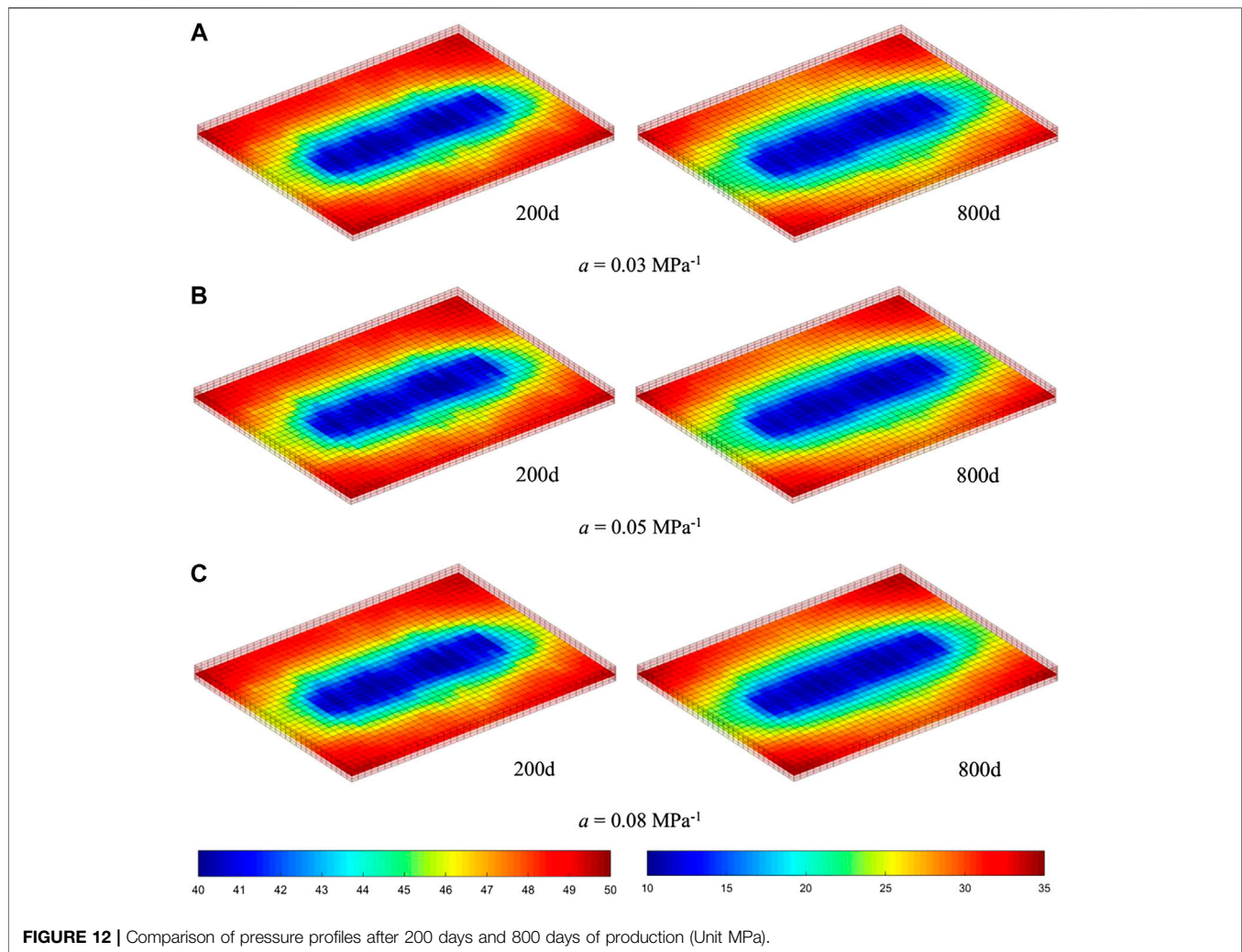


**FIGURE 12 |** Comparison of pressure profiles after 200 days and 800 days of production (Unit MPa).

reservoirs to study the influence of nature fractures and their stress sensitivity in tight reservoirs. From simulations, we could obtain following conclusions from simulation results:

- (1) The geometry of fracture has a great influence on the pressure and saturation profiles in the area near the fractures, but the influence distance is limited.
- (2) Dissolved gas drive contributes to the development of tight oil. Free gas first appears in the near-wellbore fractured zone with low pressure and quickly flows out of the reservoir because of the good seepage condition in the near-wellbore fractured zone, which does not harm the oil permeability around wells significantly.
- (3) As high-permeability channels in the reservoir, NFs can greatly improve production and affect the shape of the oval-like low-pressure zone formed by multi-stage fractured horizontal wells. However, with the development of production, the stress-sensitive effect of NF permeability gradually weakens the positive effect of NFs on production, and the effect of stress sensitivity coefficient on production is

more significant in the late stage of production with low reservoir pressure.

## DATA AVAILABILITY STATEMENT

The raw data supporting the conclusions of this article will be made available by the authors, without undue reservation.

## AUTHOR CONTRIBUTIONS

Z-dY participates in most work in this research. YW participates in developing simulator and derive formulas. XZ participates in developing simulator and derive formulas. MQ participates in derive formulas and dealing with results and data. ZY participates in derive formulas and dealing with results and data. LL participates in most work in this research. Z-hY took part in the revision of our manuscript and made valuable comments and contribution to our revision.



## REFERENCES

- Al-Rbeawi, S. (2017a). Analysis of pressure behaviors and flow regimes of naturally and hydraulically fractured unconventional gas reservoirs using multi-linear flow regimes approach. *J. Nat. Gas Sci. Eng.* 45, 637–658. doi:10.1016/j.jngse.2017.06.026
- Al-Rbeawi, S. (2017b). How much stimulated reservoir volume and induced matrix permeability could enhance unconventional reservoir performance. *J. Nat. Gas Sci. Eng.* 46, 764–781. doi:10.1016/j.jngse.2017.08.017
- Barenblatt, G. I., Zheltov, I. P., and Kochina, I. N. (1960). Basic concepts in the theory of seepage of homogeneous liquids in fissured rocks [strata]. *J. Appl. Math. Mech.* 24 (5), 1286–1303. doi:10.1016/0021-8928(60)90107-6
- Bastian, P., Chen, Z., Ewing, R., Helmig, R., Jakobs, H., and Reichenberger, V. (2000). *Numerical simulation of multiphase flow in fractured porous media. Numerical treatment of multiphase flows in porous media*. Berlin, Heidelberg: Springer, 50–68.
- Blaskovich, F., Cain, G., Sonier, F., Waldren, D., and Webb, S. J. (1983). “A multicomponent isothermal system for efficient reservoir simulation,” in Middle East oil technical conference and exhibition, Manama, Bahrain, 14–17 March.
- David, C., Wong, T.-F., Zhu, W., and Zhang, J. (1994). Laboratory measurement of compaction-induced permeability change in porous rocks: implications for the generation and maintenance of pore pressure excess in the crust. *Pure Appl. Geophys.* 143, 425–456. doi:10.1007/bf00874337
- Fu, Y., Yang, Y., and Deo, M. (2005). “Three-dimensional, three-phase discrete-fracture reservoir simulator based on control volume finite element (CVFE) formulation,” SPE reservoir simulation symposium, The Woodlands, TX, 31 January–2 February (Dallas, TX: Society of Petroleum Engineers).
- Hoteit, H., and Firoozabadi, A. (2006). Compositional modeling of discrete-fractured media without transfer functions by the discontinuous galerkin and mixed methods. *SPE J.* 11 (3), 341–352. doi:10.2118/90277-pa
- Jiang, J., Shao, Y., and Younis, R. (2014). “Development of a multi-continuum multi-component model for enhanced gas recovery and CO<sub>2</sub> storage in fractured shale gas reservoirs,” in SPE improved oil recovery symposium, Tulsa, OK, 12–16 April (Dallas, TX: Society of Petroleum Engineers).
- Jones, F. O. (1975). A laboratory study of effects of confining pressure on fracture flow and storage capacity in carbonate rocks. *J. Petrol. Technol.* 27 (1), 21–27. doi:10.2118/4569-pa
- Karimi-Fard, M., and Firoozabadi, A. (2003). Numerical simulation of water injection in fractured media using the discrete-fractured model and the galerkin method. *SPE Res. Eval. Eng.* 6 (2), 117–126. doi:10.2118/83633-pa
- Kim, J.-G., and Deo, M. D. (2000). Finite element, discrete-fracture model for multiphase flow in porous media. *AIChE J.* 46 (6), 1120–1130. doi:10.1002/aic.690460604
- Kou, Z., and Wang, H. (2020). Transient pressure analysis of a multiple fractured well in a stress-sensitive coal seam gas reservoir. *Energies* 13 (15), 3849. doi:10.3390/en13153849
- Lee, S. H., Lough, M. F., and Jensen, C. L. (2001). Hierarchical modeling of flow in naturally fractured formations with multiple length scales. *Water Resour. Res.* 37 (3), 443–455. doi:10.1029/2000wr900340
- Li, L., and Lee, S. H. (2008). Efficient field-scale simulation of black oil in a naturally fractured reservoir through discrete fracture networks and homogenized media. *SPE Reservoir Eval. Eng.* 11 (4), 750–758. doi:10.2118/103901-pa
- Moinfar, A., Varavei, A., Sepehrnoori, K., and Johns, R. T. (2013). “Development of a coupled dual continuum and discrete fracture model for the simulation of unconventional reservoirs,” in SPE reservoir simulation symposium, The Woodlands, TX, 18–20 February (Dallas, TX: Society of Petroleum Engineers).
- Moinfar, A., Varavei, A., Sepehrnoori, K., and Johns, R. T. (2014). Development of an efficient embedded discrete fracture model for 3D compositional reservoir simulation in fractured reservoirs. *SPE J.* 19 (2), 289–303. doi:10.2118/154246-pa
- Pruess, K., and Narasimhan, T. (1982). A practical method for modeling fluid and heat flow in fractured porous media. *SPE J.* 25 (1), 14–26. doi:10.2118/10509-PA
- Warren, J. E., and Root, P. J. (1963). The behavior of naturally fractured reservoirs. *Soc. Petrol. Eng. J.* 3 (3), 245–255. doi:10.2118/426-pa
- Wu, Y.-S., and Pruess, K. (1988). A multiple-porosity method for simulation of naturally fractured petroleum reservoirs. *SPE Reservoir Eng.* 3 (1), 327–336. doi:10.2118/15129-pa
- Xiao, W., Li, T., Li, M., Zhao, J., Zheng, L., and Li, L. (2016). Evaluation of the stress sensitivity in tight reservoirs. *Petrol. Explor. Dev.* 43 (1), 107–114. doi:10.1016/s1876-3804(16)30013-1
- Xu, Y. (2015). *Implementation and application of the embedded discrete fracture model (EDFM) for reservoir simulation in fractured reservoirs*. Austin, TX: The University of Texas at Austin.
- Zhang, L., Kou, Z., Wang, H., Zhao, Y., Dejam, M., Guo, J., et al. (2018). Performance analysis for a model of a multi-wing hydraulically fractured vertical well in a coalbed methane gas reservoir. *J. Petrol. Sci. Eng.* 166, 104–120. doi:10.1016/j.petrol.2018.03.038
- Zhang, R. H., Zhang, L. H., Wang, R. H., Zhao, Y. L., and Huang, R. (2016). Simulation of a multistage fractured horizontal well with finite conductivity in composite shale gas reservoir through finite-element method. *Energy & Fuels*. 30 (30), 9036–9046.
- Zhao, J., Xiao, W., Li, M., Xiang, Z., Li, L., and Wang, J. (2011). The effective pressure law for permeability of clay-rich sandstones. *Pet. Sci.* 8 (2), 194–199. doi:10.1007/s12182-011-0134-0
- Zhao, Y.-L., Zhang, L.-h., Zhao, J.-z., Luo, J.-x., and Zhang, B.-n. (2013). “Triple porosity” modeling of transient well test and rate decline analysis for multi-fractured horizontal well in shale gas reservoirs. *J. Petrol. Sci. Eng.* 110, 253–262. doi:10.1016/j.petrol.2013.09.006
- Zhao, Y. L., Liu, L. F., Zhang, L.-h., Zhang, X. Y., and Li, B. (2019). Simulation of a multistage fractured horizontal well in a tight oil reservoir using an embedded discrete fracture model. *Energy Sci. Eng.* 7 (5), 1485–1503. doi:10.1002/ese3.379
- Zou, C., Zhu, R., Wu, S., Yang, Z., Tao, S., Yuan, X., et al. (2012). Types, characteristics, genesis and prospects of conventional and unconventional hydrocarbon accumulations: taking tight oil and tight gas in China as an instance. *Acta Pet. Sin.* 33 (2), 173–187. doi:10.7623/syxb201202001

**Conflict of Interest:** Authors Z-dY, YW, XZ and SS were employed by PetroChina Xinjiang Oilfield Company. Authors MQ and Z-hY were employed by Exploration and Development Research Institute of PetroChina Xinjiang Oilfield Company.

The remaining author declares that the research was conducted in the absence of any commercial or financial relationships that could be construed as a potential conflict of interest.

Copyright © 2020 Yang, Wang, Zhang, Qin, Yao and Liu. This is an open-access article distributed under the terms of the Creative Commons Attribution License (CC BY). The use, distribution or reproduction in other forums is permitted, provided the original author(s) and the copyright owner(s) are credited and that the original publication in this journal is cited, in accordance with accepted academic practice. No use, distribution or reproduction is permitted which does not comply with these terms.



## APPENDIX

**TABLE A1** | Property of oil and gas.

Pressure kPa	Oil				Gas		
	density, m <sup>3</sup> / kg	Viscosity cP	volumetric coefficient Dimensionless	SolutionGas-oil ratio Dimensionless	density, m <sup>3</sup> / kg	Viscosity cP	volumetric coefficient Dimensionless
3,000	660.13	1.17	1.1806	45.93	25.9351	0.012654	0.035502
4,500	652.26	0.97	1.2104	57.63	38.6406	0.01315	0.023019
6,000	644.92	0.85	1.2397	69.43	51.8383	0.013675	0.016821
7,500	637.83	0.76	1.2698	81.65	65.6071	0.014254	0.013138
9,000	630.87	0.69	1.3010	94.44	79.956	0.014907	0.010714
10,500	623.96	0.64	1.3338	107.92	94.848	0.015649	0.009012
12,000	617.07	0.58	1.3734	122.18	110.212	0.016493	0.007762
13,500	617.83	0.58	1.3697	122.18	—	—	—
15,000	619.82	0.60	1.3653	122.18	—	—	—
16,500	621.74	0.61	1.3611	122.18	—	—	—
18,000	623.58	0.63	1.3571	122.18	—	—	—
19,500	625.34	0.64	1.3533	122.18	—	—	—
21,000	627.04	0.66	1.3496	122.18	—	—	—
22,500	628.68	0.68	1.3461	122.18	—	—	—
24,000	630.26	0.69	1.3427	122.18	—	—	—
25,500	631.78	0.71	1.3395	122.18	—	—	—
27,000	633.26	0.73	1.3364	122.18	—	—	—
28,500	634.81	0.74	1.3331	122.18	—	—	—
30,000	636.33	0.76	1.3298	122.18	—	—	—
31,500	637.86	0.78	1.3266	122.18	—	—	—
33,000	639.39	0.79	1.3233	122.18	—	—	—
34,500	640.91	0.81	1.3201	122.18	—	—	—
36,000	642.44	0.83	1.3168	122.18	—	—	—
37,500	643.96	0.84	1.3136	122.18	—	—	—
39,000	645.49	0.86	1.3104	122.18	—	—	—
40,500	647.02	0.88	1.3071	122.18	—	—	—
42,000	648.54	0.89	1.3039	122.18	—	—	—
43,500	650.07	0.91	1.3006	122.18	—	—	—
45,000	651.59	0.93	1.2974	122.18	—	—	—
46,500	653.12	0.94	1.2941	122.18	—	—	—
48,000	654.64	0.96	1.2909	122.18	—	—	—
49,500	656.17	0.98	1.2877	122.18	—	—	—
51,000	657.69	0.99	1.2844	122.18	—	—	—
52,500	659.22	1.01	1.2812	122.18	—	—	—
54,000	660.74	1.03	1.2779	122.18	—	—	—
55,500	662.27	1.04	1.2747	122.18	—	—	—

**TABLE A2** | Oil and gas relative permeability relationship of matrix.

$S_g$	$k_{rg}$	$k_{ro}$	$S_g$	$k_{rg}$	$k_{ro}$
0.04	0	1	0.44	0.27725	0.07938
0.08	0.01103	0.70778	0.48	0.31683	0.05912
0.12	0.02912	0.55844	0.52	0.35788	0.04319
0.16	0.05138	0.4454	0.56	0.40031	0.03084
0.20	0.07687	0.35562	0.60	0.44408	0.02143
0.24	0.10506	0.28302	0.64	0.48911	0.01442
0.28	0.13561	0.22392	0.68	0.53536	0.00933
0.32	0.16827	0.17574	0.72	0.58279	0.00574
0.36	0.20286	0.13656	0.76	0.63134	0.00332
0.40	0.23923	0.10485	0.79	0.67989	0.0009

**TABLE A3** | Oil–gas capillary force of matrix.

$S_g$	$p_{cgo}$ , kPa
0.04	0
0.24	270
0.34	510
0.49	1,040
0.59	1,490
0.69	2,220
0.74	2,940
0.79	4,760



# Experimental Study on the Cyclic Steam Stimulation Assisted by Flue Gas Under Shallow Heavy-Oil Reservoir Conditions: Optimization of the Steam-Flue Gas Ratio

Songyan Li<sup>1,2\*</sup>, Zhoujie Wang<sup>2</sup>, Rui Han<sup>2</sup>, Lei Wang<sup>2</sup> and Zukang Hu<sup>2</sup>

<sup>1</sup>Key Laboratory of Unconventional Oil & Gas Development (China University of Petroleum (East China)), Ministry of Education, Qingdao, China, <sup>2</sup>School of Petroleum Engineering, China University of Petroleum (East China), Qingdao, China

## OPEN ACCESS

### Edited by:

Kalpiti V. Shah,  
RMIT University, Australia

### Reviewed by:

Ahmet Arsoy,  
Istanbul Technical University, Turkey  
Hari Vuthaluru,  
Curtin University, Australia  
Alireza Bahadori,  
Oil and Gas Center, China

### \*Correspondence:

Songyan Li  
lsyupc@163.com

### Specialty section:

This article was submitted to  
Advanced Clean Fuel Technologies,  
a section of the journal  
Frontiers in Energy Research

**Received:** 27 August 2020

**Accepted:** 27 October 2020

**Published:** 30 November 2020

### Citation:

Li S, Wang Z, Han R, Wang L and Hu Z  
(2020) Experimental Study on the  
Cyclic Steam Stimulation Assisted by  
Flue Gas Under Shallow Heavy-Oil  
Reservoir Conditions: Optimization of  
the Steam-Flue Gas Ratio.  
Front. Energy Res. 8:599370.  
doi: 10.3389/fenrg.2020.599370

Normally, the recovery effect of a heavy-oil reservoir gradually deteriorates after multiple rounds of cyclic steam stimulation (CSS). However, the injection of flue gas can effectively increase the utilization degree of steam heat energy, which improves the recovery effect. In this paper, an experimental method for CSS using an energy storage container was established. Based on this method, a one-dimensional core physical simulation experiment for CSS under different flue gas ratios was performed. During the experiment, the changes in temperature field, oil production rate, increase in backpressure, and oil recovery factors were tested. In addition, differences in these data under different injection steam-flue gas ratios were compared. The results show that the flue gas provides a channel of fluids in porous media for steam, which is conducive to the heat transfer of steam to the deeper part of the sandpack. The sandpack has a higher temperature in each cycle than the CSS. The core temperature of each round of flue-gas-assisted CSS is higher than that of the CSS. The final oil recovery factors of flue-gas-assisted CSS using different steam-flue gas ratios are 22.2, 26.7, 30.8, 24.4, and 21.6%, while that of CSS is only 17.2%. According to the experiment, it is concluded that the best steam-flue gas ratio to optimize the flue-gas-assisted CSS is 1:10. With the combined effect of three factors (the temperature field of the sandpack, energizing effect of the flue gas, and degree of oil during recovery), the flue-gas-assisted CSS using the steam-flue gas ratio of 1:10 maximizes the steam heat transfer, increases the energy of return discharge, replenishes formation energy, and improves the oil recovery factor. Through the experiment, the research results provide theoretical guidance for improving the effectiveness of the CSS of heavy-oil reservoirs.

**Keywords:** flue gas, cyclic steam stimulation, heat transfer, oil recovery factor, physical simulation

## INTRODUCTION

With the decreasing reserves of conventional oil reservoirs around the world and increasing oil demand, unconventional oil resources are beginning to attract increasing attention (Nguyen et al., 2018). As one of the unconventional oil reservoirs, heavy oil is extremely rich in reserves. It is estimated that there are approximately 940 billion tons of geological reserves of heavy-oil resources worldwide, which account for 20 percent of the total hydrocarbon resources (Wang et al., 2013; Xu et al., 2013; Zhao et al., 2019). Therefore, the effective development of heavy-oil resources is of great significance to satisfy future energy demands.

Among the technologies to extract heavy-oil reservoirs, the thermal recovery technology is the main development method. Mainly based on steam flooding, cyclic steam stimulation (CSS), and steam-assisted gravity drainage (SAGD), the thermal recovery technology uses technological measures to increase the temperature of the oil layer, reduce the viscosity of heavy oil, and make the heavy oil easily flow to recover the heavy oil (Burkill and Rondon, 1990; Wang et al., 2018a; Li et al., 2019; Chen et al., 2020).

Steam flooding is a technique that continuously injects high-quality steam into the oil layer through an injection well. The oil layer is continuously heated by steam, so that the viscosity of the crude oil in the formation is greatly reduced. In the progress, the injected steam becomes a hot fluid in the formation, which drives the crude oil around the production well and is extracted to the surface (Li et al., 2018; Zhang et al., 2020). The main mechanisms of steam flooding include reducing the viscosity of crude oil, steam distillation, thermal expansion of crude oil, and steam drive (Fan et al., 2019). Currently, steam flooding is a large-scale industrial application of thermal recovery technology, which is an effective method to increase the oil recovery factor after CSS with achieved results (Dong et al., 2019; Du et al., 2019; Wang et al., 2019).

The SAGD technology was first proposed by Butler et al., in 1994. It uses steam as a heat source to realize the convection between steam, oil and water with heat conduction, and it relies on the gravity of crude oil and condensate to extract the heavy oil (Su et al., 2012; Shi et al., 2019; Wang et al., 2019). SAGD can be achieved by two methods: to drill a pair of horizontal wells near the bottom of the reservoir and to drill a horizontal well at the bottom of the reservoir with multiple vertical wells above it. Steam is injected into the oil layer from the upper injection well and moves upward and sideways. Hence, the heated crude oil flows to the production well under the action of gravity. CSS, which injects a certain amount of steam into a heavy-oil production well and subsequently closes its inlet, is an important part in the thermal recovery technology of heavy oil. The closed period is determined by the actual exploitation of heavy oil. After the steam heat has been fully diffused, the wellhead of the production well is opened for heavy-oil production (Tong et al., 2015; Mohsenzadeh et al., 2016; Li et al., 2017).

CSS is mainly a method to increase the production of heavy oil by periodically injecting steam into the oil well to introduce a

large amount of heat into the oil layer. The injected heat greatly reduces the viscosity of the crude oil, which improves the fluidity of the crude oil in the oil well and increases production. CSS is a relatively simple and mature steam injection technology for heavy-oil exploitation. It is currently widely used in the United States, Venezuela, and Canada (Huang et al., 2013; Xi et al., 2013; Sun et al., 2015; Li et al., 2020c). With a wide range of reservoir adaptability and fast oil recovery factor, it mainly uses the natural energy of the reservoir for development. Although CSS has achieved good development results in this oilfield block, the heat loss of steam along its injection process is large, the formation pressure rapidly increases, and the bottom hole steam injection pressure is close to or higher than the critical pressure (Song and Yang, 2017; Wei et al., 2017; Wei et al., 2019; Li et al., 2020b; Wan et al., 2020). Moreover, the limited range of steam increases the water cut in the near-wellbore zone, which reduces the heat utilization rate after repeated CSS. Therefore, conventional CSS is not sufficiently ideal to satisfy the efficient economic development of oilfields, so solutions to improve the development effect of CSS are urgently required (Sheng, 2015; Meng and Sheng, 2016; Shilov et al., 2019).

With the development of heavy-oil thermal recovery technology in recent years, increasingly many noncondensable gases such as  $N_2$ ,  $CO_2$  and flue gas have been mixed into the conventional CSS process to improve the effectiveness of thermal recovery by steam injection in heavy-oil reservoirs (Ma et al., 2013; Jie et al., 2016; Hu et al., 2017). Under such background, flue-gas-assisted CSS can significantly improve the development effect of CSS, where the flue gas helps to solve the problems in this block. Injecting flue gas in CSS can replenish the formation energy that is lost in the later stage of the CSS on a large scale without significantly reducing the formation temperature (Li and Li, 2016; Chen and Gu, 2017). Simultaneously, the heat-carrying capacity of steam can be enhanced, the direction of steam can be controlled, and the heat exchange process between steam and crude oil in the deep formation can be strengthened to improve the thermal recovery. Therefore, this flooding technology, which utilizes the synergistic effect of  $N_2$  and  $CO_2$  in the flue gas and steam, can be used as a replacement development method in the later stage of CSS and an independent development method to exploit low- and ultra-low-permeability reservoirs (Bardon et al., 1994; Sahin et al., 2012; Sisakht et al., 2020). Flue gas can increase the formation pressure, dissolve crude oil to expand, reduce the viscosity of heavy oil, reduce the interfacial tension, expand the swept volume, speed up drainage and oil recovery, and expand the heating range; thus, it is conducive to increasing crude oil production and oil layer recovery, reducing exhaust gas emissions, and benefitting environmental protection (Li et al., 2012).

The Junin 4 block in the Orinoco heavy-oil belt in Venezuela was studied in this paper. The viscosity of the heavy oil is approximately 19,000 mPa s at 50°C. The formation water has a pH of 6.71 at 22.4°C, a conductivity of 6.05, a total salinity of 4930.86 mg/L, a  $Cl^-$  content of 856 mg/L, and an  $Na^+$  and  $K^+$  content of 1,597 mg/L; the water type is  $NaHCO_3$ . The average depth of the formation is 345 m, the average porosity is 45.40%, the average permeability is 3,200 mD, the average temperature of

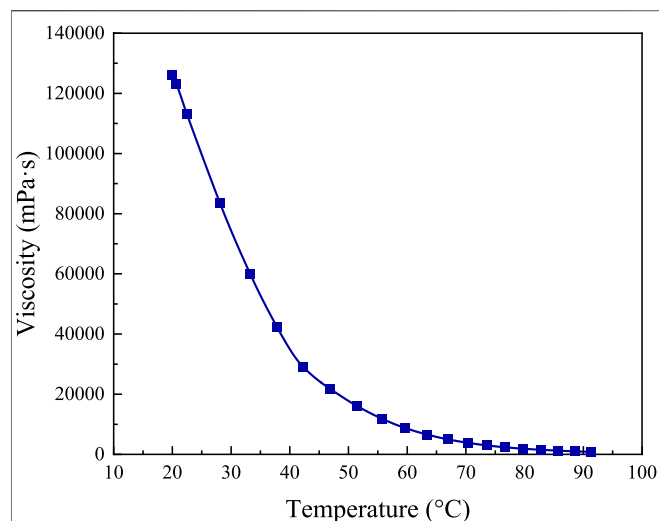


FIGURE 1 | Viscosity-temperature curve for heavy oil in the experiment.

the formation is 43°C, and the formation pressure in the middle of the reservoir is 3.4 MPa. The oil reservoir of this block, which has high viscosity, shallow burial depth, and low formation temperature, is difficult for fluid to flow. In addition, there are other problems such as fast heat loss of steam, low steam heat utilization efficiency, low formation pressure, serious formation deficit, insufficient energy in the production process, uneven steam absorption, high oil-water mobility, large differences in degree of spread, and low recovery efficiency (Nnabuihe et al., 2007; Riveros and Barrios, 2011; Ramirez et al., 2018). Therefore, the flue-gas-assisted oil recovery technology was studied for this block in Venezuela to help the flue gas oil recovery technology become gradually matured and perfected to form flue gas oil recovery technology, which effectively improves the recovery rate. This is of great practical significance for delaying the decline in oil field production and promoting the overall coordinated development of oil regions (Wu et al., 2018).

Since flue-gas-assisted CSS is widely used in heavy-oil thermal recovery currently, research on the optimization of the ratio of injected flue gas into steam becomes particularly important (Li and Elsworth, 2019; Xu et al., 2019). However, there are relatively few studies on this aspect, and the relevant mechanism remains unclear. Therefore, it is necessary to conduct research in related fields to find the optimal flue-gas-assisted CSS technology method. In this paper, an experimental method for CSS using an energy storage container was established. On this basis, a one-dimensional core physical simulation experiment of CSS under different flue gas ratio conditions was performed. During the experiment, the temperature field, oil production rate, increase in backpressure, oil recovery factor, etc., were tested to study the characteristics of the production mode and change law of the produced fluid. Furthermore, the production effect of flue-gas-assisted CSS under different steam-flue gas ratios was compared and analyzed to optimize the steam-flue gas ratios and improve the efficiency of heavy-oil production.

## EXPERIMENTAL SECTION

### Materials

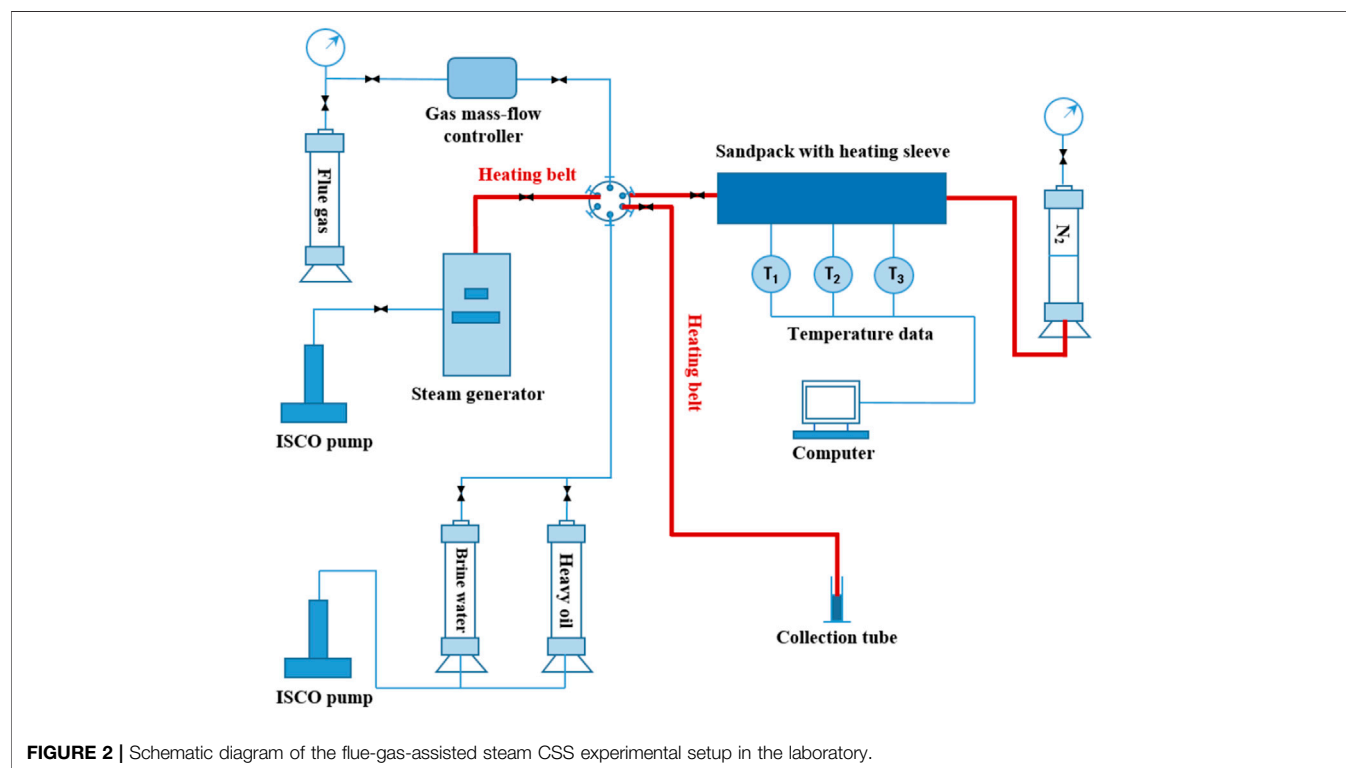
The oil in the experiment was crude oil from the Junin 4 block in the Orinoco heavy-oil belt in Venezuela. The viscosity of crude oil after dehydration was tested by a rheometer (Model MCR 302, Anton Paar, Austria) to be 19,243 mPa s at 50.0°C and ambient pressure, and the viscosity-temperature curve for the heavy oil in the experiment is shown in **Figure 1**. In the experiment, both N<sub>2</sub> and CO<sub>2</sub> had purities of 99.9 mol%, which were provided by Tianyuan, Inc., China. The flue gas in the experiment was obtained by mixing N<sub>2</sub> and CO<sub>2</sub> at a molar ratio of 0.8701:0.1299. The flue gas composition was simplified in the indoor experiments by considering it a mixture of N<sub>2</sub> and CO<sub>2</sub>. During the process of flue gas configuration, the partial pressure of N<sub>2</sub> and CO<sub>2</sub> in a certain amount of flue gas was calculated according to Dalton's law of partial pressure. After calculating the partial pressure, N<sub>2</sub> and CO<sub>2</sub> were injected into two gas storage tanks of identical volume. After the injection was completed, the pressure of the gas storage tank was the calculated partial pressure. Then, all CO<sub>2</sub> in the gas storage tank was transferred to the N<sub>2</sub> gas storage tank for mixing to obtain a certain proportion of flue gas. In the experiment, water for making steam was homemade distilled water with a resistivity of 15 MΩ cm. The water for the saturated sandpack was a simulated brine prepared concerning the salinity of the Junin 4 formation water in the Venezuelan target block. The total salinity was 4930.86 mg/L, where the Cl<sup>-</sup> content was 856 mg/L, and Na<sup>+</sup> and K<sup>+</sup> were 1,597 mg/L. KCl and NaCl, which were required to prepare the simulated brine, were made with purities of 99.5%, which were provided by Sinopharm Chemical Reagent Co., Ltd. In the experiment, steam was produced by distilled water in a steam generator. The injection temperature of steam was 300°C at the outlet temperature of the on-site steam boiler, and the steam quality was 75%. The sandpack in the experimental model was made of 80 and 120 mesh sand mixed at a ratio of 1:1. The parameters of the sandpacks for the CSS experiments are listed in **Table 1**, which had almost identical physical parameters and were maintained according to the reservoir conditions. The porosity of these sandpacks is approximately 44.72%, the permeability is approximately 3,133.2 mD, and the original oil saturation is approximately 88.9%.

### Apparatus

The schematic diagram of the flue-gas-assisted CSS experimental setup in the laboratory is shown in **Figure 2**. The flue gas at a specific flow rate was injected into the experimental models by a gas flow controller (model Sla5861, Brooks, United States; flow rate range: 0–350 ml/min under standard conditions; flow accuracy: ±0.5%). Distilled water, which was boosted by a high-precision syringe pump (model 100DX, Teledyne ISCO Company, Teledyne Co., Ltd., USA; flow accuracy: ±0.25 μl/min; pressure accuracy: ±0.5%) was heated into steam by a steam generator (model GL-1, Haian Petroleum Equipment Company; temperature range: 100–350°C; pressure range: 0.1–25 MPa). The flue gas and steam were mixed in the six-way valve and subsequently injected into the sandpack with

**TABLE 1** | Sandpack parameters for the CSS experiment.

Test no	Length/cm	Diameter/cm	Porosity/%	Permeability/mD	Initial oil saturation/%	Flue gas injection rate/ml min <sup>-1</sup>
#1	60	2.5	44.34	3184.5	88.9	0
#2	60	2.5	44.91	3159.8	89.3	3
#3	60	2.5	44.82	3023.1	87.9	10
#4	60	2.5	44.95	3086.4	88.4	30
#5	60	2.5	44.19	3242.4	89.2	100
#6	60	2.5	45.08	3102.7	89.7	300

**FIGURE 2** | Schematic diagram of the flue-gas-assisted steam CSS experimental setup in the laboratory.

thermal insulation material (model 304, Nantong Scientific Research Instrument Co., Ltd.; temperature range: 0–300°C; pressure range: 0–40 MPa). By setting the temperature of the heating and insulating jacket (model A1, Nantong Scientific Research Instrument Co., Ltd.; thermal conductivity at room temperature: 0.035 W/M·K – 0.045 W/M·K ± 0.005; heating range: 0–200°C; temperature accuracy: ±0.5°C), the preset oil reservoir temperature required by the sandpack was provided. The temperature was tested by three thermocouples (model K, Nantong Scientific Research Instrument Co., Ltd.; temperature accuracy: ±0.1°C). Then, the temperature data were transmitted to the computer via the thermocouples. The backpressure control device consists of an intermediate container filled with N<sub>2</sub> to 2 MPa on the upper part of the piston. During the steam stimulation experiment, the fluid in the sandpack flowed to the lower part of the piston of the intermediate container and was stored in it. When the fluid flowed into the intermediate container, the indication of the pressure gauge increased. When

the well was opened, the fluid in the intermediate container flowed back due to the pressure difference. Therefore, the intermediate container plays a role in energy storage.

## Experimental Procedures

- (1) The airtightness of the sandpack was tested; then, the sandpack was filled with the prepared mixed sand, and the dry weight of the sandpack was measured;
- (2) The sandpack was placed in vacuum for 4 h and subsequently saturated with brine. The weight of the sandpack was tested, and the pore volume was calculated based on the weight difference. The permeability of the sandpack was measured by water flooding according to Darcy equation;
- (3) The sandpack was placed in a heating jacket with a preset reservoir temperature of 40°C for 4 h. When a stable temperature was reached, crude oil was injected into the sandpack at a flow rate of 0.5 ml/min for oil saturation. The volume of saturated oil was measured; then, the original oil



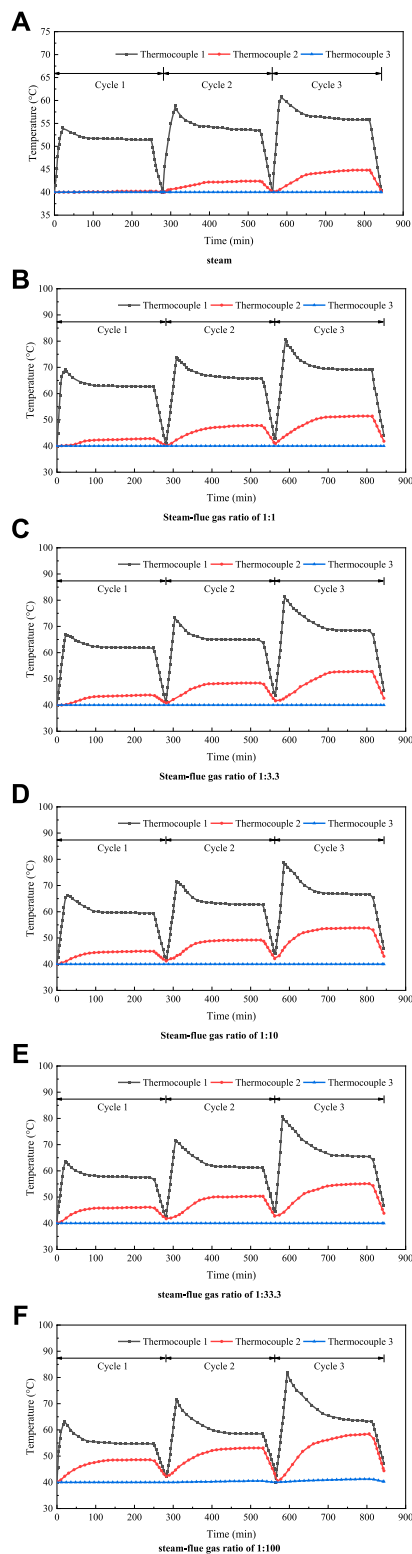


**FIGURE 3** | Changes in sandpack temperature for three thermocouples with different steam-flue gas ratios. **(A)** Pure steam. **(B)** Steam-flue gas ratio of 1:1. **(C)** Steam-flue gas ratio of 1:3.3. **(D)** Steam-flue gas ratio of 1:10. **(E)** Steam-flue gas ratio of 1:33.3. **(F)** Steam-flue gas ratio of 1:100.

saturation in the sandpack was calculated using the volume method;

- (4) The experimental equipment was installed according to the schematic diagram, and the backpressure was set to 2 MPa. The steam generator was turned on at a temperature of 250°C to preheat. When the temperatures of the sandpack and steam generator became stabilized, the experiment began. According to the experimental design, the steam injection rate was set to 3 ml/min, and the flue gas injection rate-setting parameters are shown in **Table 1**. The injection time was set to 10 min. The steam injection flow rate was set with the equivalent condensation water, and the gas was set under standard conditions. During the injection process, the fluid in the sandpack flowed to the lower part of the intermediate container piston and was stored in it. After the steam injection was stopped, all valves were closed. The inlet valve was opened after 4 h of simmering the well. The fluid in the intermediate container flowed back, and oil and gas were spit out from the valve until the pressure in the sandpack dropped to the set backpressure, and no fluid flowed out;
- (5) During the experiment, the temperature distributed at each temperature measurement point of the sandpack was recorded in real time. The oil production, water production, liquid production, and pressure gauge data were recorded;
- (6) We repeated steps (4) and (5) to perform the throughput experiment of the next cycle. When the cumulative recovery rate in the cycle was less than 2%, the experiment was stopped;
- (7) The CSS experiment with steam-flue gas ratio of 1:10 was carried out for three times to investigate the repeatability of the results. This minimizes the uncertainty of the experimental observation.

## RESULTS AND DISCUSSION

### Heat Transfer Properties

Since the viscosity of heavy oil is greatly affected by temperature, i.e., an increase in temperature can significantly decrease the viscosity of crude oil, it is extremely important to study the temperature changes during the CSS process for heavy-oil production. Under identical conditions, three cycles of flue-gas-assisted CSS experiments were performed for five different steam-flue gas ratios (1:1, 1:3.3, 1:10, 1:33.3, 1:100), and a set of CSS experiment was performed as a control group. The changes in sandpack temperature for three thermocouples with different steam-flue gas ratios are shown in **Figure 3**. Thermocouple 1 is 15 cm from the injection end, thermocouple 2 is 30 cm from the injection end, and temperature point 3 is 45 cm from the injection end.

It can be seen from the law of heat transfer that the heat transfer requires the existence of temperature difference as the premise. In other words, in the heat transfer process, the internal energy of a substance determines the temperature of the

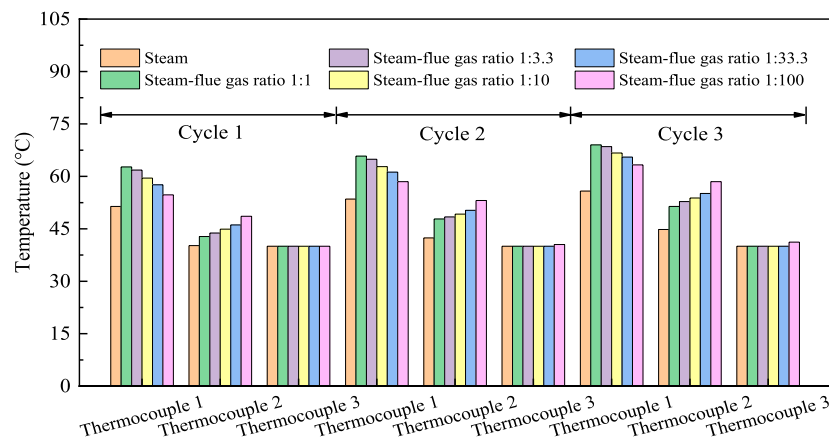


**FIGURE 4 |** Comparison of well-opening temperatures at different steam-flue gas ratios at each cycle for the three thermocouples.

substance, and the change of internal energy leads to the change of temperature, which can be expressed by Eq. 1.

$$Q = C \cdot M \cdot \Delta t \quad (1)$$

where  $Q$  is heat energy, J;  $C$  is the heat capacity, J/(kg·°C);  $M$  is the mass, kg;  $\Delta T$  is the temperature change, °C.

In the process of heat transfer, heat is always transferred by heat conduction, heat convection and thermal radiation. Moreover, two or three heat transfer methods usually occur for transmission, rather than a single one.

**Figure 3** shows that the temperature field curves obtained by CSS under different conditions are generally consistent. The temperature of thermocouples 1 and 2 in the first 20 min of each cycle under different steam-flue gas ratio conditions increases with time because the injection of steam increases the temperature of the sandpack. After approximately 20 min, since the heat of the steam continues to be transferred to the far side of the sandpack, the temperature of thermocouple 1 decreases, and that of 2 increases. After the well has been simmered for 4 h, the temperature of each thermocouple tends to be stable. The steam and crude oil have fully exchanged heat, the heat of the steam is fully utilized, and the heat utilization rate is maximal at this time. When the production time increases after the well is opened, the heat carried by the fluid is produced with the production end. Therefore, the overall temperature of the sandpack decreases. At this time, the temperature of the thermocouple gradually decreases and tends to the preset reservoir temperature. However, the temperature of the thermocouples does not completely reduce to 40°C but has a small increase at the end of exploitation, and it increases accordingly with increasing cycle. The reason is that the steam retains some heat in the sandpack after the end of the cycle (Sun et al., 2016; Wang et al., 2018b; Li et al., 2019), which also results in a higher overall temperature in the sandpack after the next cycle of steam injection compared to the previous cycle. The temperature increase of thermocouple 2 is obvious after the end of the simmering well, but it is lower than that of thermocouple 1.

The location of thermocouple 3 is not affected because of the limited amount of steam injection, so the temperature has been maintained at the preset reservoir temperature. Thus, the sandpack can simulate the entire reservoir of CSS.

To further analyze the temperature field of flue-gas-assisted CSS under different steam-flue gas ratio conditions, the opening temperatures of three thermocouples in each cycle of different steam-flue gas ratios are compared and shown in **Figure 4**. The well-opening temperature under different steam-flue gas ratios in the first cycle is observed. For thermocouple 1, the temperature during CSS is the lowest at 51.4°C. After the addition of flue gas of five steam-flue gas ratios, the temperature of thermocouple 1 is 62.7, 61.8, 59.5, 57.6, 54.7°C, i.e., 21.2, 20.2, 15.8, 12.1, 6.4% increases compared to CSS, respectively. The temperature of thermocouple 2 in the first cycle is the lowest (40.2°C) under pure steam conditions. The temperature of thermocouple 2 after the addition of the flue gas of five steam-flue gas ratios is 42.8, 43.8, 44.9, 46.1, and 48.6°C, with temperature increases of 6.5, 9.0, 11.7, 14.7, and 20.9%, respectively. The temperature of thermocouple 3 is basically 40°C with a slight increase under five steam-flue gas ratio conditions.

First, the overall temperature of thermocouple 2 is lower than that of thermocouple 1, and thermocouple 3 has the lowest temperature. Since steam does not completely spread to thermocouple 2, the thermocouple 2 has a lower overall temperature than thermocouple 1 after the completion of the simmering well. The location of temperature measurement point 3 is not affected by steam and flue gas, so the temperature has been maintained at the preset reservoir temperature. With the increase in number of cycles, the temperatures of thermocouples 1 and 2 increase to varying degrees, while thermocouple 3 remains at the preset reservoir temperature. Only when the steam-flue gas ratio is 1:100, the flue-gas-assisted CSS has a small temperature increase at thermocouple 3 in the second and third cycles. The principle is that after the previous round of CSS, some of the heat carried by the steam remains in the sandpack, so the temperature increases when the next round of

throughput is performed (Li et al., 2017; Dong et al., 2020; Zhao, 2020). Second, when the cycle increases, more gas is trapped in the sandpack, which forms a gas channel. With the increase in number of cycles, the gas channel grows, and the steam flows further in porous media (Zhang et al., 2006; Li et al., 2011; Zhu et al., 2020). Therefore, the internal temperature of the sandpack increases with increasing cycles. During the third cycle, the temperature of thermocouple 1 increases to 69.0, 68.5, 66.7, 65.5, and 63.3°C under five steam-flue gas ratios, and the temperature of CSS also increases to 55.8°C.

In addition, the temperature and heating range of the oil layer after the flue gas mixing are much higher than those of the conventional CSS. Compared with CSS, the temperatures of thermocouples 1 and 2 increase after flue gas was added. The reason is that the flue gas has a strong flow ability, which can open up channels for the steam, reduce the resistance to steam flow in porous media, facilitate heat transfer to the deeper regions and increase the temperature of the sandpack compared to CSS. What's more, the flue gas forms a gas film on the surface of the well wall, which can inhibit the heat transfer of steam condensation, so that the heat transferred to the rock near the well is reduced. The reduced heat loss enables more heat transfer deeper into the core. The flue gas has a strong heat-carrying and diffusing effect, which effectively increases the heat sweep volume of the steam in the formation (Abedini and Torabi, 2014; Xu et al., 2020). Further observation shows that the temperature increase of thermocouple 1 shows a decreasing trend after flue gas was added, while thermocouple 2 shows an increasing trend. When the steam-flue gas ratio is 1:1–1:100, the well opening temperature at thermocouple 1 in the first cycle gradually decreases, while thermocouple 2 gradually increases. When the steam-flue gas ratio reaches 1:100, the temperatures of thermocouples 1 and 2 were minimal and maximal, respectively. At this time, the temperature field is evenly distributed, and the situation is best.

The principle is that when the proportion of flue gas increases, it is more conducive to the heat transfer of steam to deeper regions (Haskin and Alston, 1989). On one hand, the flue gas forms a gas film on the surface of the well wall, which can inhibit the heat transfer of steam condensation, so that the heat transferred to the rock near the well is reduced. The reduced heat loss enables more heat transfer deeper into the core. On the other hand, the flue gas opens up a channel for the steam, which reduces the resistance of steam flow in porous media and makes it easier for the steam to advance along the gas channel to the core in the next cycle. The heat-carrying capacity of the steam is enhanced, the direction of the steam is controlled, the heat exchange between steam and crude oil is strengthened, and the steam heat is fully utilized (Ma et al., 2015; Xiao et al., 2016; Song and Yang, 2017; Li et al., 2020a; Pang et al., 2020). Therefore, under the combined action of these two aspects, the flue gas can more quickly carry steam at the injection end to the deep part of the model. The steam heat energy is fully utilized, the heat loss along the way is reduced, and the temperature of the deep part of the seepage is increased. When the steam-flue gas ratio is 1:1, although the temperature of the sandpack increases compared to CSS in the presence of flue gas, most of the heat remained trapped at the injection end. Therefore, the temperature

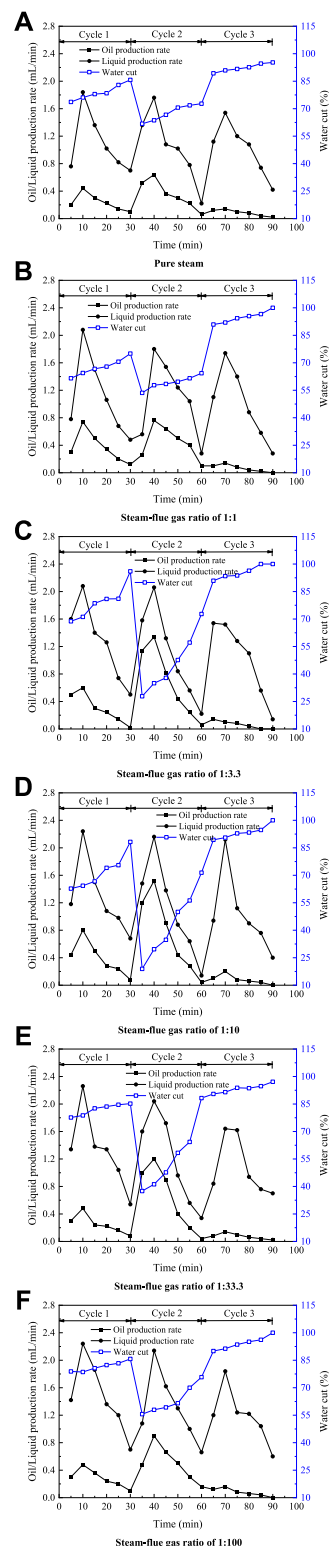


**FIGURE 5 |** Changes in oil production rate, liquid production rate and water cut with time. (A) Pure steam. (B) Steam-flue gas ratio of 1:1. (C) Steam-flue gas ratio of 1:3.3. (D) Steam-flue gas ratio of 1:10. (E) Steam-flue gas ratio of 1:33.3. (F) Steam-flue gas ratio of 1:100.

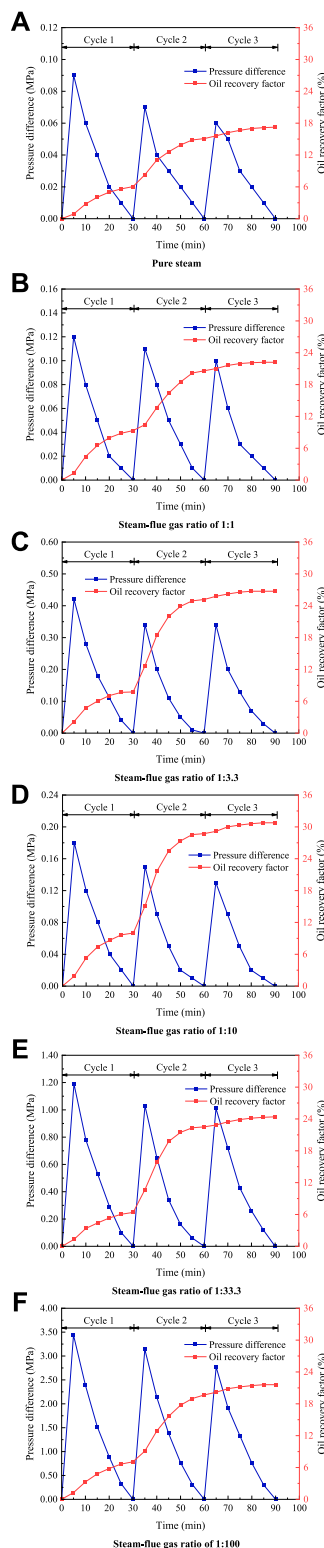


**FIGURE 6 |** Changes in backpressure and oil recovery factor with time. (A) Pure steam. (B) Steam-flue gas ratio of 1:1. (C) Steam-flue gas ratio of 1:3.3. (D) Steam-flue gas ratio of 1:10. (E) Steam-flue gas ratio of 1:33.3. (F) Steam-flue gas ratio of 1:100.

at thermocouple 1 is higher than at other steam-flue gas ratios. At this time, the steam heat energy is not fully utilized. In summary, when the steam-flue gas ratio is 1:100, the flue-gas-assisted steam stimulation has the best effect. The reason is that the heat-carrying capacity of the steam can be enhanced when the flue-gas-assisted CSS is performed at this steam-flue gas ratio, and the heat exchange process between steam and crude oil in the depth of the sandpack can be strengthened. Hence, the steam heat energy is maximized.

## Oil Production Properties

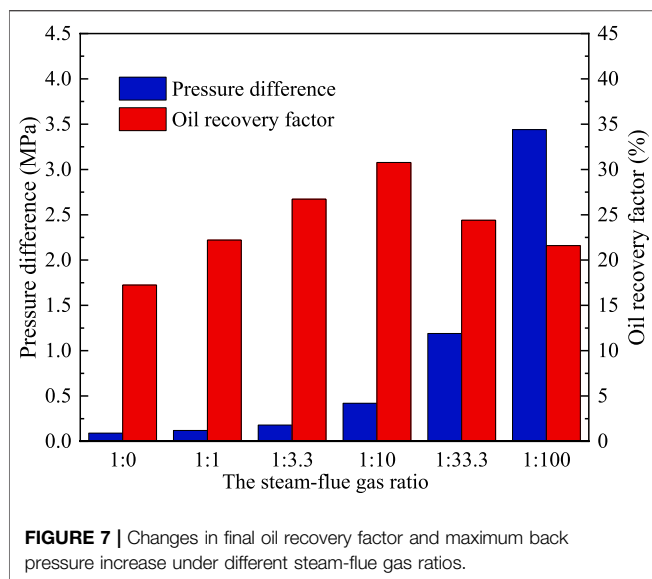
Figure 5 depicts the changes in oil production rate, liquid production rate, and water cut with time. With the increase in exploitation time in the same cycle, the oil production rate and liquid production rate first increase and subsequently gradually decrease, while the water cut shows an increasing trend during the collection process. Thus, the early stage of each cycle is the main area of oil production. At this time, the liquid production is large, but the oil content is high. When the exploitation time increases, the oil production efficiency decreases, the water cut increases, and the oil recovery effect decreases. When the cycle increases, the maximum fluid production rate decreases. Due to the lower formation energy caused by greater extraction than injection at the end of the previous cycle, the fluid production rate in the next cycle is lower. The oil production rate curve shows that the second cycle has a greater oil production rate than the other cycles. Thus, the main oil production cycle is in the second cycle. In the third cycle, the oil production rate is extremely low, and the water cut of the produced fluid is extremely high. The cumulative recovery rate during this period is less than 2%. The exploitation limit was attained under indoor experimental conditions, and the experiment should be terminated.

Oil recovery factor is an important index to measure the level of oilfield development. It refers to the ratio of the amount of oil extracted from the reservoir to the geological reserves within a certain economic limit under modern technological conditions. The formula for oil recovery factor in reservoir development is as the following.

$$\eta = \frac{N_p}{N} \quad (2)$$

$N_p$  is recoverable reserves;  $N$  is the original geological reserves.

Figure 6 depicts the changes in backpressure and oil recovery factor with time. The CSS experiment with steam-flue gas ratio of 1:10 was carried out for three times, and the oil recovery factor of the three times was 29.2, 30.8, and 32.1% respectively, with an error range of  $\pm 2\%$ . Then, the appropriate one was selected among them. This demonstrates the reproducibility of the experimental results, and minimizes the uncertainty of the experimental observation. This also shows that the experiment follows a certain law of necessity, rather than happens by chance. Thus, the experimental conclusion that follows the objective law must also be reliable and scientific. The curve of the oil recovery factor shows an increasing trend in each cycle. The highest increase in oil recovery factor is observed in the second cycle with a slow increase in the third cycle. The increase in



backpressure decreases with the increase in exploitation time in each cycle, and the increase in backpressure decreases to 0 MPa at the end of exploitation. The reason is that the back pressure is increased due to the injection of steam or flue gas into the sandpack at the end of the simmering well. As exploitation progresses, oil and water are produced, and the increase in backpressure decreases. Since the extracted amount during the cycle is greater than the injected amount, the maximum increase in backpressure decreases when the cycle increases. The backpressure increase and oil recovery factor of CSS and flue-gas-assisted CSS generally have similar trends.

By comparing the injection of pure steam with different proportions of flue gas, we found that the average liquid production rate of CSS was 1.05 ml/min, while it was 1.06, 1.13, 1.14, 1.20, and 1.32 ml/min for different steam-flue gas ratios. The average liquid production rate increases after the addition of flue gas and increases with the increase in proportion of flue gas. It is minimal when the steam-flue gas ratio is 1:1 and maximal when the steam-flue gas ratio is 1:100. The back pressure increase curve shows that the maximum backpressure increase of CSS in the first cycle is 0.09 MPa, while it is 0.12, 0.18, 0.42, 1.19, and 3.44 MPa for different steam-flue gas ratios.

After flue gas was added, the increase in backpressure increases to different degrees. Moreover, the increase in back pressure increases when the proportion of flue gas increases. The principle of this phenomenon is that the flue gas has a large compression coefficient and good expansion, which can maintain the pressure within the corresponding value. It can effectively supplement the reservoir pressure and provide energy for oil and water production (Grogan and Pinczewski, 1987). Therefore, the average liquid production rate and increase in back pressure will increase. The oil production rate curve shows that the average oil production rate under different steam-flue gas ratios is 0.29, 0.34, 0.40, 0.31, 0.28 ml/min. The average oil production rate of CSS is only 0.22 ml/min. The final oil recovery factor and maximum increase in backpressure are observed for different steam-flue gas

ratios in **Figure 7**. The final oil recovery factor is 17.2% when the CSS experiment is performed. When the flue-gas-assisted CSS is performed under different water-to-gas ratios, the final recovery rate is 22.2, 26.7, 30.8, 24.4, and 21.6%, i.e., it increases by 5.0, 9.5, 13.6, 7.2, 4.4, respectively. The addition of flue gas is shown to increase the oil recovery factor. With the increasing proportion of flue gas, the expansion of the flue gas dissolved in the crude oil and low thermal conductivity of the flue gas can increase the heatwave range of the steam. The addition of flue gas effectively reduces the oil-water interfacial tension and improves the microscopic oil washing efficiency during a steam injection (Renner, 1988; Riazi, 1996).

**Figure 7** shows that the final oil recovery factor increases with the increase in proportion of flue gas in the injection mixture. When the steam-flue gas ratio is 1:10, both quantities reach the maximum value. Afterward, the final oil recovery factor begins to decrease with the increase in flue gas ratio. In other words, a steam-flue gas ratio of 1:10 is most suitable for flue-gas-assisted CSS under the formation conditions.

Thus, there is a threshold amount of effective flue gas injection for the development of flue-gas-assisted CSS, i.e., it is best exploited when the injected steam-flue gas ratio is approximately 1:10.

When the steam-flue gas ratio is 1:1–1:10, oil production is mainly based on the temperature field distribution and pressure energization effects. At this time, when the proportion of flue gas increases, the temperature field is more evenly distributed, and the energy gain due to the effect of the backpressure is larger. Therefore, the final oil recovery factor increases with the increase in flue gas ratio. When the steam-flue gas ratio is 1:10–1:100, oil production is mainly based on the control of mobility during recovery. Heavy oil is produced under the joint action of water and gas. When the proportion of flue gas continues to increase, the overall mobility of water and gas decreases, the oil displacement efficiency decreases, the final oil recovery factor decreases, and the production effect worsens. Under the joint influence of the temperature field, energy increase of backpressure, water and air flow during recovery, the final result is that when the steam-flue gas ratio is 1:10, the flue-gas-assisted CSS has the highest final recovery rate.

## CONCLUSION

- (1) By establishing an experimental method of CSS with an energy storage container, a one-dimensional core physical simulation experiment is performed. It is found that the temperature field gradually improves with the increase in flue gas ratio. When the steam-flue gas ratio is 1:100, the flue gas can maximize the heat-carrying capacity of steam, inhibit the condensation heat transfer of steam, open a channel and reduce the resistance for the steam to flow in porous media, which is more conducive to the heat transfer of steam to the deep area and improves the steam heating range.
- (2) When the flue-gas-assisted CSS experiment is performed under different steam-flue gas ratios, the maximum



increase in backpressure is 0.12, 0.18, 0.42, 1.19, and 3.44 MPa, while the CSS is only 0.09 MPa. After flue gas has been added, the increase in backpressure significantly increases with the increase of flue gas proportion. Thus, flue gas can well replenish the formation of energy and enhance the recovery factor.

- (3) The final oil recovery of flue-gas-assisted CSS experiments with different steam-flue gas ratios is 22.2, 26.7, 30.8, 24.4, and 21.6%, while that of CSS is only 17.2%. The oil recovery factor greatly increases with the addition of flue gas. When the steam-flue gas ratio is 1:10, the oil recovery factor is the highest, and the effect of CSS is the best under the joint action of the temperature field, energy increasing effect and mobility during recovery.

## DATA AVAILABILITY STATEMENT

The raw data supporting the conclusion of this article will be made available by the authors, without undue reservation.

## REFERENCES

- Abedini, A., and Torabi, F. (2014). On the CO<sub>2</sub> storage potential of cyclic CO<sub>2</sub> injection process for enhanced oil recovery. *Fuel* 124, 14–27. doi:10.1016/j.fuel.2014.01.084
- Bardon, C., Corlay, P., Longeron, D., and Miller, B. (1994). CO<sub>2</sub> Huff 'n' puff revives shallow light-oil-depleted reservoirs. *SPE Reservoir Eng.* 9, 92–100. doi:10.2118/22650-pa
- Burkill, G. C. C., and Rondon, L. A. (1990). Steam stimulation pilot project in the Orinoco belt, Zuata Area, Venezuela, in SPE Latin America Petroleum Engineering Conference, LAPEC, October 14–19, 1990. Rio de Janeiro, Brazil: Society of Petroleum Engineers. doi:10.2118/21090-ms
- Chen, C., and Gu, M. (2017). Investigation of cyclic CO<sub>2</sub> huff-and-puff recovery in shale oil reservoirs using reservoir simulation and sensitivity analysis. *Fuel* 188, 102–111. doi:10.1016/j.fuel.2016.10.006
- Chen, H., Wang, Z., Wang, K., Li, Z., and Li, S. (2020). Investigation of EOR mechanism for flue gas assisted SAGD. *J. Petrol. Sci. Eng.* 193, 107420. doi:10.1016/j.petrol.2020.107420
- Dong, X., Liu, H., Chen, Z., Wu, K., Lu, N., and Zhang, Q. (2019). Enhanced oil recovery techniques for heavy oil and oilsands reservoirs after steam injection. *Appl. Energy* 239, 1190–1211. doi:10.1016/j.apenergy.2019.01.244
- Dong, X., Shen, L. W., Golsanami, N., Liu, X., Sun, Y., Wang, F., et al. (2020). How N<sub>2</sub> injection improves the hydrocarbon recovery of CO<sub>2</sub> HnP: an NMR study on the fluid displacement mechanisms. *Fuel* 278, 118286. doi:10.1016/j.fuel.2020.118286
- Du, Q., Liu, H., Wu, G., Hou, J., Zhou, K., and Liu, Y. (2019). Application of flue-gas foam in thermal-chemical flooding for medium-depth heavy oil reservoirs. *Energy Sci. Eng.* 7, 2936–2949. doi:10.1002/ese3.471
- Fan, J., Jin, B., Yang, J., and Fan, X. (2019). The flue gas-solvent assisted steam assisted gravity drainage studies: experiments and numerical simulation in extra-heavy oil reservoirs,” in *Energy sources part a-recovery utilization and environmental effects*. Philadelphia, PA: Taylor & Francis Inc. doi:10.1080/15567036.2019.1686552
- Grogan, A. T., and Pinczewski, W. V. (1987). The role of molecular diffusion processes in tertiary CO<sub>2</sub> flooding. *J. Petrol. Technol.* 39 (05), 591–602. doi:10.2118/12706-pa
- Haskin, H. K., and Alston, R. B. (1989). An evaluation of CO<sub>2</sub> huff 'n' puff tests in Texas. *J. Petrol. Technol.* 41, 177–184. doi:10.2118/15502-pa

## AUTHOR CONTRIBUTIONS

SL: Conceptualization, Methodology, Supervision, Funding acquisition. ZW: Investigation, Writing-Original Draft. RH: Investigation.

## FUNDING

This project was financially supported by the National Natural Science Foundation of China (No. 51774306 and No. 51974346), National Key Scientific and Technological Project for the Oil & Gas Field and Coalbed Methane of China (2016ZX05031002-004-002), and the Youth Innovation of University in Shandong Province under (No. 2019KJH002).

## ACKNOWLEDGMENTS

We are grateful to the Shandong Engineering Research Center for Foam Application in Oil and Gas Field Development and UPC—COSL Joint Laboratory on Heavy Oil Recovery for their assistance with the experimental research.

- Hu, R., Crawshaw, J. P., Trusler, J. P. M., and Boek, E. S. (2017). Rheology and phase behavior of carbon dioxide and crude oil mixtures. *Energy Fuels* 31, 5776–5784. doi:10.1021/acs.energyfuels.6b01858
- Huang, Y., Liu, D., and Luo, Y. (2013). Research on multiple thermal fluid stimulation for offshore heavy oil production. *Spec. Oil Gas Reservoirs* 20, 84–86. (in Chinese)
- Jie, F., Xiangfang, L., and Weiwei, Z. (2016). Prediction of the productivity of steam assisted gravity drainage using gray relational analysis and BP artificial neural network. *J. Comput. Theor. Nanosci.* 13, 2838–2842. doi:10.1166/jctn.2016.4626
- Li, Z., and Elsworth, D. (2019). Controls of CO<sub>2</sub>-N<sub>2</sub> gas flood ratios on enhanced shale gas recovery and ultimate CO<sub>2</sub> sequestration. *J. Petrol. Sci. Eng.* 179, 1037–1045. doi:10.1016/j.petrol.2019.04.098
- Li, S., and Li, Z. (2016). Effect of temperature on the gas/oil relative permeability of Orinoco belt foamy oil. *SPE-199339-PA* 21, 170–179. doi:10.2118/174089-pa
- Li, G., Moridis, G. J., Zhang, K., and Li, X. (2011). The use of huff and puff method in a single horizontal well in gas production from marine gas hydrate deposits in the Shenhu Area of South China Sea. *J. Petrol. Sci. Eng.* 77, 49–68. doi:10.1016/j.petrol.2011.02.009
- Li, S., Li, B., Zhang, Q., Li, Z., and Yang, D. (2018). Effect of CO<sub>2</sub> on heavy oil recovery and physical properties in huff-n-puff processes under reservoir conditions. *J. Energy Res. Technol. Trans. ASME* 140. doi:10.1115/1.4039325
- Li, S., Li, Z., and Sun, X. (2017a). Effect of flue gas and n-hexane on heavy oil properties in steam flooding process. *Fuel* 187, 84–93. doi:10.1016/j.fuel.2016.09.050
- Li, S., Lu, C., Wu, M., Hu, Z., Li, Z., and Wang, Z. (2020a). New insight into CO<sub>2</sub> huff-n-puff process for extraheavy oil recovery via viscosity reducer agents: an experimental study. *J. CO<sub>2</sub> Utili.* 42, 101312. doi:10.1016/j.jcou.2020.101312
- Li, L., Su, Y., Hao, Y., Zhan, S., Lv, Y., Zhao, Q., and Wang, H. (2019). A comparative study of CO<sub>2</sub> and N<sub>2</sub> huff-n-puff EOR performance in shale oil production. *J. Petrol. Sci. Eng.* 181, 106174. doi:10.1016/j.petrol.2019.06.038
- Li, X., Wang, Y., Duan, L., Li, G., Zhang, Y., Huang, N., and Chen, D. (2012). Experimental investigation into methane hydrate production during three-dimensional thermal huff and puff. *Appl. Energy* 94, 48–57. doi:10.1016/j.apenergy.2012.01.024
- Li, S., Wang, Q., and Li, Z. (2020b). Stability and flow properties of oil-based foam generated by CO<sub>2</sub>. *SPE J.* 25(01), 416–431. doi:10.2118/199339-pa
- Li, S., Wang, Q., Zhang, K., and Li, Z. (2020c). Monitoring of CO<sub>2</sub> and CO<sub>2</sub> oil-based foam flooding processes in fractured low-permeability cores using

- nuclear magnetic resonance (NMR). *Fuel* 263, 116648. doi:10.1016/j.fuel.2019.116648
- Li, S., Yu, T., Li, Z., and Zhang, K. (2019). Experimental investigation of nitrogen-assisted SAGD in heavy-oil reservoirs: a two-dimensional visual analysis. *Fuel* 257, 1–16. doi:10.1016/j.fuel.2019.116013
- Li, B., Zhang, Q., Li, S., and Li, Z. (2017b). Enhanced heavy oil recovery via surfactant-assisted CO<sub>2</sub> huff-n-puff processes. *J. Petrol. Sci. Eng.* 159, 25–34. doi:10.1016/j.petrol.2017.09.029
- Ma, C., Liu, Y., Lian, P., Wang, C., and Li, J. (2013). Study on steam huff and puff injection parameters of herringbone well in shallow and thin heavy oil reservoir. *Open Petrol. Eng. J.* 6, 69–75. doi:10.2174/1874834101306010069
- Ma, J., Wang, X., Gao, R., Zeng, F., Huang, C., Tontiwachwuthikul, P., and Liang, Z. (2015). Enhanced light oil recovery from tight formations through CO<sub>2</sub> huff 'n' puff processes. *Fuel* 154, 35–44. doi:10.1016/j.fuel.2015.03.029
- Meng, X., and Sheng, J. J. (2016). Optimization of huff-n-puff gas injection in a shale gas condensate reservoir. *J. Unconventional Oil Gas Resources* 16, 34–44. doi:10.1016/j.juogr.2016.09.003
- Mohsenzadeh, A., Escrochi, M., Afraz, M. V., Karimi, G., Al-Wahaibi, Y., and Ayatollahi, S. (2016). Non-hydrocarbon gas injection followed by steam-gas co-injection for heavy oil recovery enhancement from fractured carbonate reservoirs. *J. Petrol. Sci. Eng.* 144, 121–130. doi:10.1016/j.petrol.2016.03.003
- Nguyen, P., Carey, J. W., Viswanathan, H. S., and Porter, M. (2018). Effectiveness of supercritical-CO<sub>2</sub> and N<sub>2</sub> huff-and-puff methods of enhanced oil recovery in shale fracture networks using microfluidic experiments. *Appl. Energy* 230, 160–174. doi:10.1016/j.apenergy.2018.08.098
- Nnabuihe, L., Couzigou, E., Chan, A., and Solana, A. (2007). Technology based formation damage control mitigation measures in the SINCOR Zuata field Venezuela, in Nigeria annual international conference and exhibition 2007, NAICE, August 6–8, 2007. Abuja (Nigeria): Society of Petroleum Engineers. doi:10.2118/111887-ms
- Pang, Z., Jiang, Y., Wang, B., Cheng, G., and Yu, X. (2020). Experiments and analysis on development methods for horizontal well cyclic steam stimulation in heavy oil reservoir with edge water. *J. Petrol. Sci. Eng.* 188, 13. doi:10.1016/j.petrol.2020.106948
- Ramirez, A. E., Quevedo, L. D., Ulacio, I. M., and Vasquez, E. M. (2018). Integral analysis of production behavior of horizontal wells associated to the first polymerized water injection pilot project in unconventional reservoir: Zuata principal field, Venezuela, in SPE international heavy oil conference and exhibition 2018, HOCE, December 10–12, 2018. Kuwait City (Kuwait): Society of Petroleum Engineers.
- Renner, T. A. (1988). Measurement and correlation of diffusion coefficients for CO<sub>2</sub> and rich-gas applications. *SPE Reservoir Eng.* 3 (02), 517–523. doi:10.2118/15391-pa
- Riazi, M. R. (1996). A new method for experimental measurement of diffusion coefficients in reservoir fluids. *J. Petrol. Sci. Eng.* 14 (3–4), 235–250. doi:10.1016/0920-4105(95)00035-6
- Riveros, G. V., and Barrios, H. (2011). Steam injection experiences in heavy and extra-heavy oil fields Venezuela, SPE international heavy oil conference and exhibition 2011, HOCE 2011, December 12–14, 2011. Kuwait City (Kuwait): Society of Petroleum Engineers, 265–279.
- Sahin, S., Kalfa, U., and Celebioglu, D. (2012). Unique CO<sub>2</sub>-injection experience in the Bati Raman field may lead to a proposal of EOR/sequestration CO<sub>2</sub> network in the Middle East. *SPE-139616-PA* 4, 42–50. doi:10.2118/139616-pa
- Sheng, J. J. (2015). Increase liquid oil production by huff-n-puff of produced gas in shale gas condensate reservoirs. *J. Unconventional Oil Gas Resources* 11, 19–26. doi:10.1016/j.juogr.2015.04.004
- Shi, X., Jiang, X., Chen, F., Lu, S., He, N., and Liu, L. (2019). Reservoir selection evaluation and application of flue gas-assisted gravity drainage technique. *Petrol. Geol. Recovery Efficiency* 26, 93–98.
- Shilov, E., Cheremisin, A., Maksakov, K., and Kharlanov, S. (2019). Huff-n-puff operational studies of CO<sub>2</sub> with heavy oil. *Energies* 12. doi:10.3390/en1224308
- Sisakht, N. N., Rouzbahani, M. M., Karbasi, A., Zarinabadi, S., and Sabzalipour, S. (2020). CO<sub>2</sub> chemical absorption from fluid catalytic cracking unit flue gases of Abadan Oil Refinery in Iran, using diethanolamine solvent. *Environ. Sci. Pollut. Control Ser.* 27, 25312–25326. doi:10.1007/s11356-020-08708-1
- Song, C., and Yang, D. (2017). Experimental and numerical evaluation of CO<sub>2</sub> huff-n-puff processes in Bakken formation. *Fuel* 190, 145–162. doi:10.1016/j.fuel.2016.11.041
- Su, Z., Moridis, G. J., Zhang, K., and Wu, N. (2012). A huff-and-puff production of gas hydrate deposits in Shenhu area of South China Sea through a vertical well. *J. Petrol. Sci. Eng.* 86–87, 54–61. doi:10.1016/j.petrol.2012.03.020
- Sun, J., Zou, A., Sotelo, E., and Schechter, D. (2016). Numerical simulation of CO<sub>2</sub> huff-n-puff in complex fracture networks of unconventional liquid reservoirs. *J. Nat. Gas Sci. Eng.* 31, 481–492. doi:10.1016/j.jngse.2016.03.032
- Sun, X., Li, Z., Li, S., and Yang, Y. (2015). Performance of reducing surface tension by adding flue gas and solvent in SAGD process. *J. Central South Univ. Sci. Technol.* 46, 324–331. (in Chinese)
- Tong, L., Zhang, G., and Kang, A. (2015). Experiment of steam stimulation effect improved by different assisted methods and its numerical simulation. *Petrol. Geol. Recovery Efficiency* 22, 93–97. (in Chinese)
- Wan, T., Wang, X., Jing, Z., and Gao, Y. (2020). Gas injection assisted steam huff-n-puff process for oil recovery from deep heavy oil reservoirs with low-permeability. *J. Petrol. Sci. Eng.* 185, 106613. doi:10.1016/j.petrol.2019.106613
- Wang, X., Wang, J., and Qiao, M. (2013). Horizontal well, nitrogen and viscosity reducer assisted steam huff and puff technology: taking super heavy oil in shallow and thin beds, Chunfeng Oilfield, Junggar Basin, NW China, as an example. *Petrol. Explor. Dev.* 40, 104–110. doi:10.1016/s1876-3804(13)60010-5
- Wang, Y., Hou, J., Song, Z., Yuan, D., Zhang, J., and Zhao, T. (2018a). A case study on simulation of in-situ CO<sub>2</sub> huff- 'n'-puff process. *SPE-176327-PA* 21, 109–121. doi:10.2118/176327-pa
- Wang, Y., Ren, S., Zhang, L., Peng, X., Pei, S., Cui, G., and Liu, Y. (2018b). Numerical study of air assisted cyclic steam stimulation process for heavy oil reservoirs: recovery performance and energy efficiency analysis. *Fuel* 211, 471–483. doi:10.1016/j.fuel.2017.09.079
- Wang, Y., Ren, S., Zhang, L., Deng, J., Gong, Z., and Hu, C. (2019a). Experimental investigation and field pilot testing of air assisted cyclic steam stimulation technique for enhanced heavy oil recovery. *Int. J. Oil Gas Coal Technol.* 21, 407–434. doi:10.1504/ijogct.2019.101471
- Wang, Z., Li, Z., Sarma, H. K., Xu, Y., Wu, P., Yang, J., Wang, H., and Lu, T. (2019b). A visualization experimental study on gas penetration through interlayer to improve SAGD performance. *J. Petrol. Sci. Eng.* 177, 959–970. doi:10.1016/j.petrol.2019.03.001
- Wei, B., Pang, S., Pu, W., Lu, L., Wang, C., and Kong, L. (2017). "Mechanisms of N<sub>2</sub> and CO<sub>2</sub> assisted steam huff-n-puff process in enhancing heavy oil recovery: a case study using experimental and numerical simulation," in SPE Middle East oil and gas show and conference 2017, March 6–9, 2017. Manama (Bahrain): Society of Petroleum Engineers (SPE), 1597–1608.
- Wei, B., Zhang, X., Wu, R., Zou, P., Gao, K., Xu, X., Pu, W., and Wood, C. (2019). Pore-scale monitoring of CO<sub>2</sub> and N<sub>2</sub> flooding processes in a tight formation under reservoir conditions using nuclear magnetic resonance (NMR): a case study. *Fuel* 246, 34–41. doi:10.1016/j.fuel.2019.02.103
- Wu, Z., Liu, H., Zhang, Z., and Wang, X. (2018). A novel model and sensitive analysis for productivity estimate of nitrogen assisted cyclic steam stimulation in a vertical well. *Int. J. Heat Mass Tran.* 126, 391–400. doi:10.1016/j.ijheatmasstransfer.2018.05.025
- Xi, C., Guan, W., Jiang, Y., Liang, J., Zhou, Y., Wu, J., et al. (2013). Numerical simulation of fire flooding for heavy oil reservoirs after steam injection: a case study on Block H1 of Xinjiang Oilfield, NW China. *Petrol. Explor. Dev.* 40, 766–773. doi:10.1016/s1876-3804(13)60102-0
- Xiao, P., Yang, Z., Wang, X., Xiao, H., and Wang, X. (2016). Experimental investigation on CO<sub>2</sub> injection in the Daqing extra/ultra-low permeability reservoir. *J. Petrol. Sci. Eng.* 149, 765–771. doi:10.1016/j.petrol.2016.11.020
- Xu, A., Mu, L., Fan, Z., Wu, X., Zhao, L., Bo, B., and Xu, T. (2013). Mechanism of heavy oil recovery by cyclic superheated steam stimulation. *J. Petrol. Sci. Eng.* 111, 197–207. doi:10.1016/j.petrol.2013.09.007
- Xu, Z., Li, B., Zhao, H., He, L., Liu, Z., Chen, D., et al. (2020). Investigation of the effect of nanoparticle-stabilized foam on EOR: nitrogen foam and methane foam. *ACS Omega* 5, 19092–19103. doi:10.1021/acsomega.0c02434
- Xu, Z., Li, Z., Jing, A., Meng, F., Dang, F., and Lu, T. (2019). Synthesis of magnetic graphene oxide (MGO) and auxiliary microwaves to enhance oil recovery. *Energy Fuels* 33 (10), 9585–9595. doi:10.1021/acs.energyfuels.9b01841

- Zhang, H., Liu, Y., Ta, Y., and Zou, F. (2020). Physical simulation experiment of flue gas-assisted SAGD in super heavy oil reservoir. *Fault-Block Oil Gas Field* 27, 244–247. (in Chinese)
- Zhang, Y. P., Sayegh, S. G., Huang, S., and Dong, M. (2006). Laboratory investigation of enhanced light-oil recovery by CO<sub>2</sub>/flue gas huff-n-puff process. *PETSOC*- 45, 24–32. (in Chinese)
- Zhao, Q., Li, Z., Wang, S., Lai, F., and Li, H. (2019). Phase behavior measurements and modeling for N<sub>2</sub>/CO<sub>2</sub>/extra heavy oil mixtures at elevated temperatures. *Ind. Eng. Chem. Res.* 58, 428–439. doi:10.1021/acs.iecr.8b03945
- Zhao, Y. (2020). Laboratory experiment and field application of high pressure and high quality steam flooding. *J. Petrol. Sci. Eng.*, 189. doi:10.1016/j.petrol.2020.107016
- Zhu, Y., Huang, S., Zhao, L., Yang, M., and Wu, T. (2020). A new model for discriminating the source of produced water from cyclic steam stimulation wells in edge-bottom water reservoirs. *Energies* 13 (11), 15. doi:10.3390/en13112683
- Conflict of Interest:** The authors declare that the research was conducted in the absence of any commercial or financial relationships that could be construed as a potential conflict of interest.
- Copyright © 2020 Li, Wang, Han, Wang and Hu. This is an open-access article distributed under the terms of the Creative Commons Attribution License (CC BY). The use, distribution or reproduction in other forums is permitted, provided the original author(s) and the copyright owner(s) are credited and that the original publication in this journal is cited, in accordance with accepted academic practice. No use, distribution or reproduction is permitted which does not comply with these terms.



# Effects of Dissociation Water Retention on Pore Structure Disintegration in Hydrate Sediments

Liu Yang<sup>1\*</sup>, Shuo Wang<sup>1</sup>, Hongfeng Lu<sup>2\*</sup>, Ling Liu<sup>2</sup> and Rina Sa<sup>2</sup>

<sup>1</sup>State Key Laboratory for Geomechanics and Deep Underground Engineering, China University of Mining and Technology (Beijing), Beijing, China, <sup>2</sup>Guangzhou Marine Geological Survey, China Geological Survey, Guangzhou, China

## OPEN ACCESS

### Edited by:

Songyan Li,  
China University of Petroleum  
(Huadong), China

### Reviewed by:

Yongge Liu,  
China University of Petroleum  
(Huadong), China  
Bo Jiang,  
Nanjing University of Science and  
Technology, China

### \*Correspondence:

Liu Yang  
shidayangliu@126.com  
Hongfeng Lu  
gmgsllhf@126.com

### Specialty section:

This article was submitted to  
Advanced Clean Fuel Technologies,  
a section of the journal  
Frontiers in Energy Research

**Received:** 27 August 2020

**Accepted:** 06 November 2020

**Published:** 01 December 2020

### Citation:

Yang L, Wang S, Lu H, Liu L and Sa R  
(2020) Effects of Dissociation Water  
Retention on Pore Structure  
Disintegration in Hydrate Sediments.  
Front. Energy Res. 8:599542.  
doi: 10.3389/fenrg.2020.599542

During the depressurization process, natural gas hydrates (NGHs) decompose and release methane gas and water. Field experience shows that only 1% of the dissociation water is recovered, hindering the continuous pressure decline and further NGHs decomposition. The retention effect of the dissociation water on the pore structure is still unclear in NGHs sediments. In this paper, the hydrate sediment samples were tested for porosity, permeability, pore structure and clay minerals content, etc. The ions concentration change of solution was continuously measured using a conductivity meter to evaluate the disintegration mechanism of sediments. The results show that the pore structure of sediments tend to disintegrate under the action of dissociation water, leading to an increase in the ions concentration of dissociation water. According to the ions concentration curve, the sediment disintegration is divided into two stages. The rapid disintegration stage is mainly related to clay minerals. The slow disintegration stage is mainly related to the dissolution of soluble salt minerals. The initial water content is the main factor affecting the disintegration of the sediment skeleton. Under the condition of low initial water content, the sediment skeleton disintegrates instantaneously in dissociation water. When the initial water content exceeds 30.6–37.9%, the pore structure of sediments tends to be stable in dissociation water. Studying the effect of dissociation water on the sediment pore structure is helpful to understand the mechanism of low water production and to optimize the exploitation regime of gas hydrate.

**Keywords:** gas hydrate, pore structure, disintegration, ions diffusion, dissociation water

## 1 INTRODUCTION

Natural gas hydrates (NGHs) are ice-like crystalline materials that exist under coexistence conditions of high pressure and low temperature (less than 300 K) (Cai et al., 2020b). The natural gas molecule is confined within the hydrogen bond molecule, and the molecular structure resembles a cage structure (Pandey et al., 2019). NGHs are mainly distributed in deep seas below 300 m and in permafrost zones. As one of the new energy sources, the total energy of an NGH is about two times larger than that of conventional oil and gas resources (Cai et al., 2020a). It is regarded as an energy source and has broad prospects for development. According to the molecular structure of hydrate, 1 cubic meter of NGHs can decompose and release about 164 cubic meters of methane gas and 0.8 cubic meters of water. However, less than 1% of the dissociation water can be produced, and a large amount of water is retained in the NGHs sediments (Yang et al., 2020). It has a significant impact on the pore structure

and water-gas flow (Omelchenko and Makogon, 2013; Linga and Clarke, 2017; Shen et al., 2019). It involves the physical and chemical processes, which has not been well studied yet (Radich et al., 2009; Kang et al., 2016).

Water retention refers to the water content in the sediment under a certain capillary force (Mahabadi et al., 2016). As an important parameter, capillary force is usually integrated into the water retention function (Moridis and Sloan, 2007). In the initial stage of dissociation, the capillary force between hydrate particles promotes the combination of dissociated water and undecomposed hydrate into large particles, which hinders the subsequent separation of hydrate (Chen et al., 2014). Many researchers have established mathematical equations to quantitatively analyze water retention. The most commonly used model is the Van Genuchten model. Water retention has an important influence on the dissociation of hydrates (Van Genuchten, 1980; Mahabadi et al., 2016; Moridis and Sloan, 2007; Moridis and Reagan, 2007; Gamwo and Liu, 2010; Anderson et al., 2011). The hydrate dissociation can change the relative permeability of water and gas as a function of hydrate saturation (Mahabadi et al., 2016). Numerous researchers have conducted extensive research on the dissociation process of hydrates and the flow of dissociation water. Zhong et al. (Zhong et al., 2019) used *in-situ* Raman spectroscopy to study the effects of gas composition and temperature on the structure transformation of hydrate dissociation. Mahabadi et al. (Mahabadi et al., 2019) proposed that the permeability of hydrate sediment directly affected the dissociation of hydrates and the production of methane gas. He established the relationship model between permeability and hydrate saturation. The dissociation water hinders the production of methane gas from hydrate-bearing sediments. Jin et al. (Jin et al., 2019) established a new dissociation model to identify the hydrodynamic mechanism, and reproduced the process of dissociation water into ice. Shagapov and Tazetdinov (Shagapov and Tazetdinov, 2014) simulated the hydrate dissociation process by MRI and found that the liquid water produced by the dissociation hindered the release of methane gas.

Hydrate sediments are argillaceous siltstone, so high water retention may cause disintegration of the sediment structure. At present, a large number of studies have focused on the disintegration of terrestrial rocks in water. Luo et al. (Luo et al., 2020) studied the decomposition of pyrite in carbonaceous rocks. Its decomposition changed the pH value of the aqueous solution, leading to the collapse of the porous media structure. By changing the pH of the solution, Huang et al. (Huang et al., 2017) found that argillaceous shale is more prone to disintegration under acidic solution conditions. Yan's research (Yan et al., 2018) pointed out that temperature can accelerate the interaction of water and red-bed soft rock and increase the rate of soft rock disintegration. Zhang et al. (Zhang et al., 2018) performs 11 wet and dry cycles on mudstone. He found that the dry-wet cycle in the early stage had a greater impact on the disintegration of mudstone. Yang et al. (Yang et al., 2020) has quantitatively studied the dispersion time of hydrate sediments. When the

moisture absorption time exceeds the dispersion time, the sediments will disintegrate.

A large number of studies have proved that water retention can cause the structure of porous media to collapse. However, the characteristics of the sediments structure caused by water retention have not been clearly studied. The basic characteristics are studied by a series of tests, such as porosity, permeability, pore structure and clay minerals content. The conductivity meter is used to measure the ions concentration change of solution, which can be used as an evaluation method for pore structure disintegration.

## 2 MATERIALS AND METHODS

The experiments are divided into three groups. The first experimental group is conducted on eight samples of three sediments under normal pressure and temperature. The conductivity curves are used to characterize the disintegration process of hydrate sediment. The basic information of sediment samples is shown in **Tables 1** and **2**. The second group of experiments is to determine the effects of initial water content on disintegration process. The basic information of sediment samples is presented in **Table 3**. In the third group of experiments, the effects of different temperature on disintegration are studied and the basic information of sediment samples is presented in **Table 4**.

### 2.1 Samples Characterization

**Figure 1** presents the experimental samples of different sediments. The surfaces of the samples are not smooth, and they contain a great amount of cracks and large pores. In addition, the samples have different colors, which may be related to initial water content. The larger the water content is, the darker the color is. The samples with higher water content are black, and the dry samples are gray.

The basic information of different sediments is shown in **Table 1**. The permeability of three sediments is about 0.324–7.805 mD, and the average permeability is about 3.6 mD. The sediments present low permeability characteristics. The porosity of three sediments is about 21.47–35.39%, and the average porosity is about 30.74%. The sediments present high porosity characteristics. The specific surface area is about 6.4512–13.84 m<sup>2</sup>/g, and the average value is about 11.0822 m<sup>2</sup>/g. The permeability, porosity and specific surface area help understand the basic properties of three sediments and study the influencing factors of pore structure disintegration.

According to the mineral composition analysis, the main minerals are quartz and clay. The quartz minerals account for nearly half of the total mineral content (**Table 2**). The mineral composition data of some hydrate sediments comes from Yang et al., 2020. The clay mineral content is about 26.1%–30.7%. The other mineral content is not more than 10%, such as feldspar, calcite, and dolomite. The clay mineral contents of ZN, LK and HT are 28.7%, 28.6% and 27.9%. The



**TABLE 1 |** The basic information of different sediments.

Sample	Quality, g	Permeability, mD	Porosity, %	Specific surface area, m <sup>2</sup> /g	Ion diffusion rate D, (μS/cm)/t <sup>0.5</sup>
ZN1-1	1.125	7.805	32.54	11.309	5.367
ZN1-2	1.135	2.047	32.39	11.780	7.806
ZN1-3	1.136	0.973	21.47	10.769	6.885
ZN1-4	1.152	3.904	32.68	10.499	7.765
ZN1-5	1.143	6.647	31.39	13.84	3.978
LK1-1	1.166	5.114	35.39	6.451	4.855
LK1-2	1.150	0.324	29.51	12.525	5.358
HT1-1	1.150	1.929	30.56	11.484	9.084

**TABLE 2 |** Mineral composition analysis.

Label	Mineral composition (%)						Relative abundance (%)			
	Quartz	Feldspar	Calcite	Dolomite	Pyrite	Clay	I/S <sup>a</sup>	Illite	Kaolinite	Chlorite
ZN1-1	36.7	8.7	13.7	3.5	7.6	29.8	41	36	9	14
ZN1-2	42.0	6.8	18.0	3.6	3.5	26.1	42	33	9	16
ZN1-3	36.0	5.9	23.0	3.6	2.3	29.2	43	32	9	16
ZN1-4	43.1	9.5	10.5	4.7	0.5	30.7	35	38	11	16
ZN1-5	45.7	10.4	12.6	3.0	0.5	27.8	33	38	10	19
LK1-1	47.9	8.7	10.8	4.6	1.1	26.9	34	37	11	18
LK1-2	44.3	7.8	12.4	4.1	1.1	30.3	31	38	13	18
HT1-1	40.7	8.5	12.5	5.2	3.1	27.9	52	29	6	13

<sup>a</sup>I/S is Illite/Smectite mixed-layer.

**TABLE 3 |** The sample information for water content test.

Label	Initial mass, g	Dry mass, g	Drying time, h	Water content, %
ZN1-6	1.115	0.924	1	9.13
ZN1-7	1.110	0.983	8	3.60
ZN1-8	1.114	0.891	48	0
LK1-3	1.116	1.038	1	4.70
LK1-4	1.117	0.998	8	0.79
LK1-5	1.115	0.991	48	0
HT1-2	1.154	1.075	0.1	44.90
HT1-3	1.156	1.023	0.2	37.90
HT1-4	1.157	0.969	0.4	30.56
HT1-5	1.153	0.912	0.8	22.95
HT1-6	1.156	0.742	48	0

**TABLE 4 |** The sample information for temperature effects analysis.

Label	Quality, g	Temperature, °C	Observations
ZN1-9	1.1457	27.5	Slow disintegration is observed, and cracks appear one after another
ZN1-10	1.1317	40	Fast disintegration is observed, and the sample is dispersed into fine sand
ZN1-11	1.1527	60	Due to fast disintegration, the sample is dispersed into fine sand. The solution color is slightly yellow

three sediments have nearly equal clay minerals content, but the relative abundance of clay minerals is quite different. The Illite/Smectite mixed-layer (I/S) and illite minerals are main clay minerals. The I/S minerals have strong water

sensitiveness, which can result in expansion and pore structure disintegration. According to the mineral composition, the average I/S minerals contents of ZN, LK and HT are 11.1%, 9.2% and 14.5%, respectively.

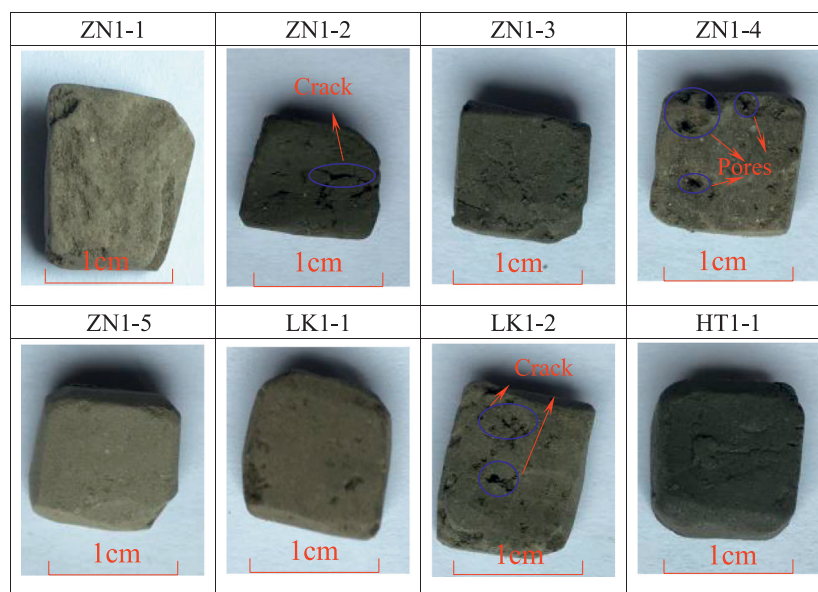


**FIGURE 1 |** The experimental samples of different sediments.

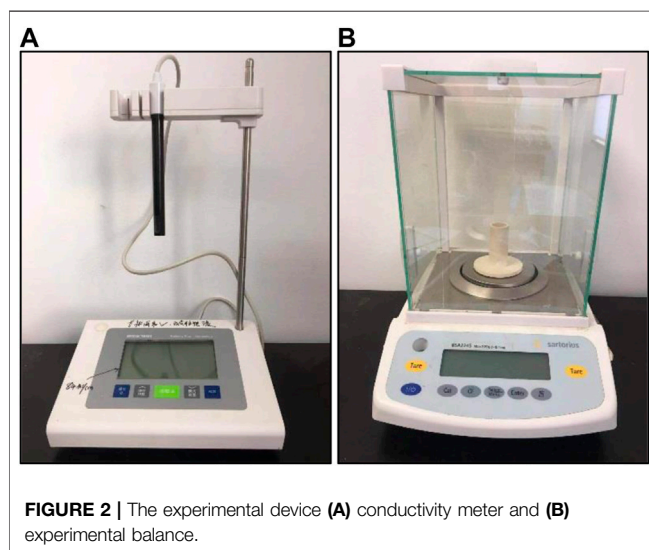


**FIGURE 2 |** The experimental device (A) conductivity meter and (B) experimental balance.

## 2.2 Experimental Procedures

The conductivity meter (Mettler Toledo SevenExcellence) is used to determine the ions concentration change of solution (Figure 2A). The range of conductivity is 0.01~500 uS/cm, and that of the total dissolved solids is 0.01 mg/L~300 g/L. The measurement temperature is  $-5^{\circ}\sim 105^{\circ}\text{C}$ . The conductivity meter is composed of an electrode, movable bracket and host. The ions are dissolved in the dissociation water, causing the concentration of the solution to rise. The ions form a conductive loop with the conductivity meter, thereby measuring the conductivity change. The experimental balance (Mettler Toledo ME204E) is used to measure the sample mass

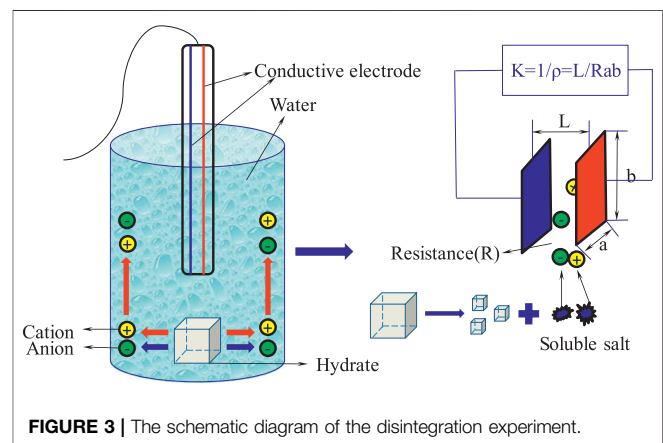


**FIGURE 3 |** The schematic diagram of the disintegration experiment.

(Figure 2B). The measurement accuracy is 0.1 mg, and the range is 0~220 mg.

Experimental materials include 250 ml beaker, 100 ml measuring cylinder, plastic wrap, rubber band, conductivity meter, electronic balance, tweezers, vernier caliper, drying box, measuring test paper, knife, and thermometer. The schematic diagram of disintegration experiment is presented in Figure 3.

The experimental procedures of first group are as follows.

- (1) Cut the sample into prisms with a knife, measure the size of the sample with a vernier caliper, and weigh the sample with an electronic balance.
- (2) Pour 200 ml distilled water into the beakers and place the samples in the water

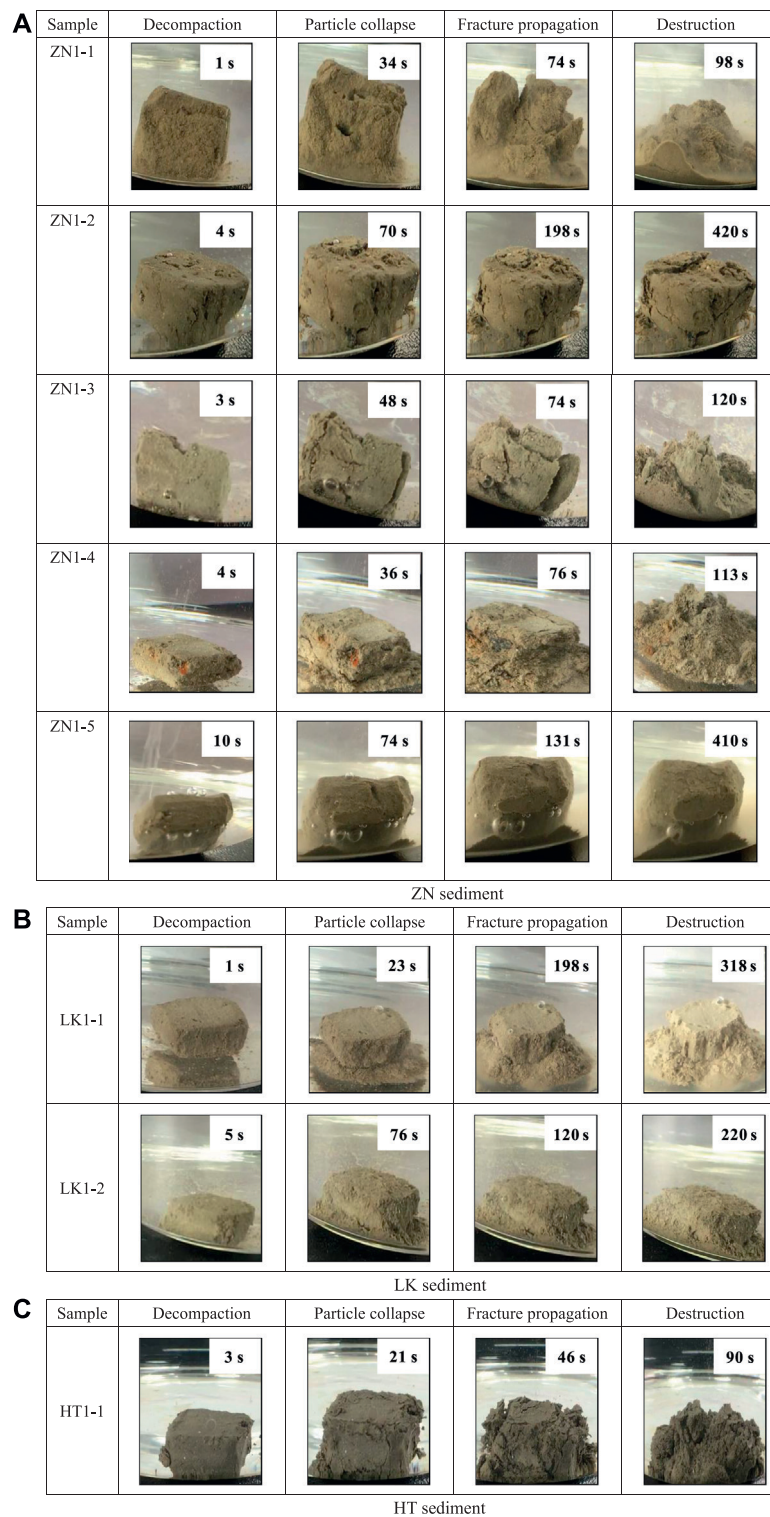
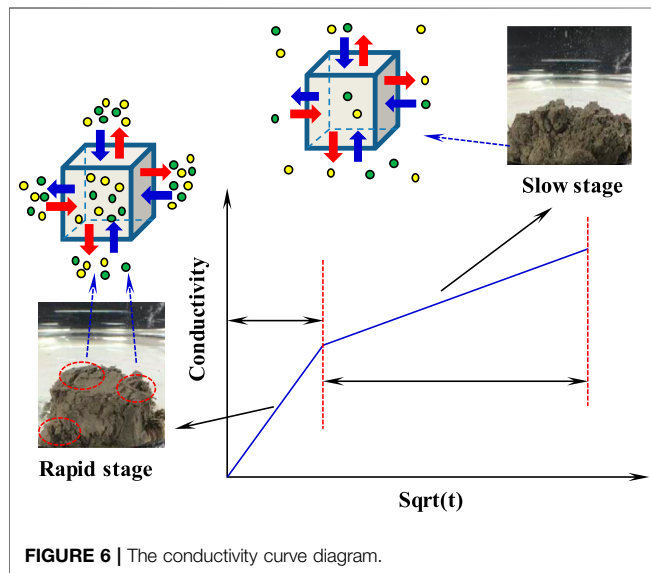
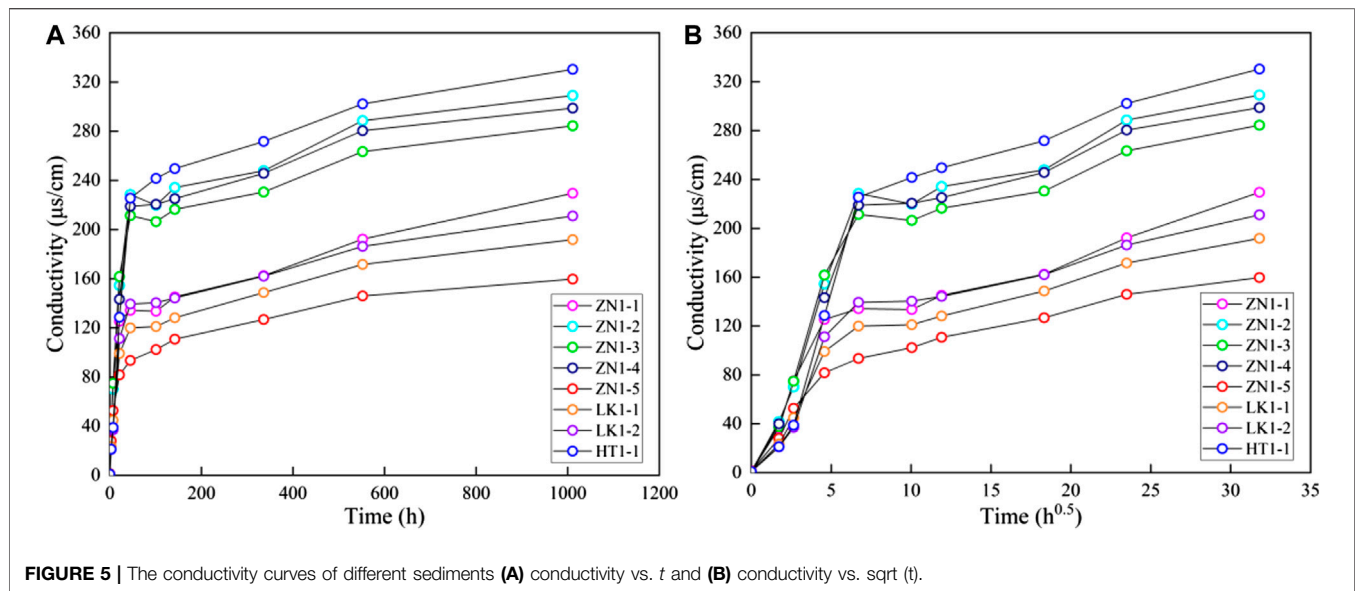


**FIGURE 4 |** The diagram of disintegration process **(A)** ZN sediment, **(B)** LK sediment and **(C)** HT sediment.



- (3) Immerse the conductive electrode in the water to measure the conductivity. After testing, the beakers are sealed with plastic wrap and a rubber band.
- (4) Repeat the step 3 to determine the conductivity change over soaking time.

The experimental procedures of second group are as below.

- (1) The different water content can be established by drying the sample. Dry the samples in the oven for 1, 8 and 48 h. After the drying process of 48 h, the mass of samples do not change any more, and the water content is 0. The water content  $S_w$  is defined as

$$S_w = \frac{m_w - m_d}{m_d} \times 100\%$$

where  $m_w$  is the mass of sample containing water, and  $m_d$  is the mass of dried sample.

- (2) Conduct the disintegration experiments according to the procedures of first group.

The experimental procedures of third group are as follows.

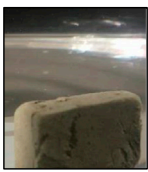



- (1) Heat distilled water to 27.5°C, 40°C and 60°C. Keep the temperature constant during the experiment.
- (2) Conduct the disintegration experiments according to the procedures of the first group, and study the effects of temperature.

## 3 RESULTS AND DISCUSSION

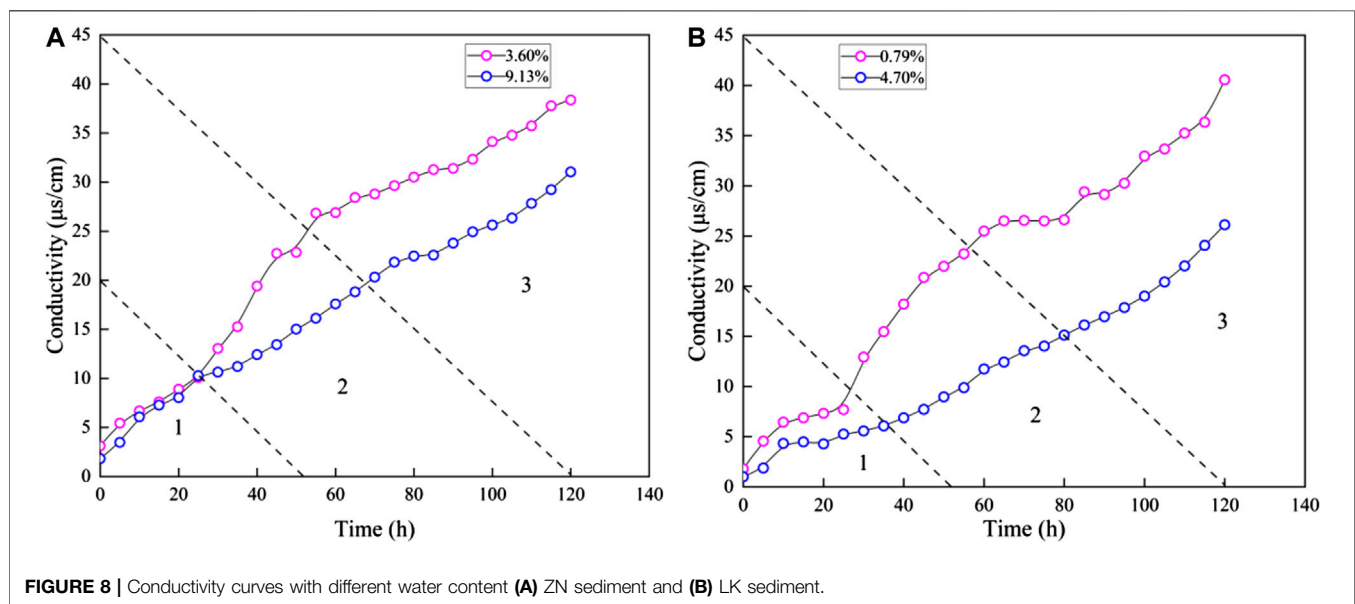
### 3.1 Observations During Disintegration Experiments

Figure 4 presents the observations during disintegration experiments. The whole process can be divided into four stages: decompaction stage, particle collapse stage, fracture propagation stage and structure destruction stage. The water enters into the pores, resulting in the pore structure decompaction. After a certain period, the particles begin to scatter. Some fractures appear to form fracture networks. At the final stage, the skeleton structure of samples tends to be destroyed completely. It suggests that the retention of dissociation water can destroy pore structure in hydrate sediments.

It should be noted that different sediments present different disintegration characteristics. In terms of pore

Water content	44.9%	37.9%	30.6%	22.9%
HT sediment				

**FIGURE 7** | Disintegration diagram of samples with different water content.



**FIGURE 8** | Conductivity curves with different water content (A) ZN sediment and (B) LK sediment.

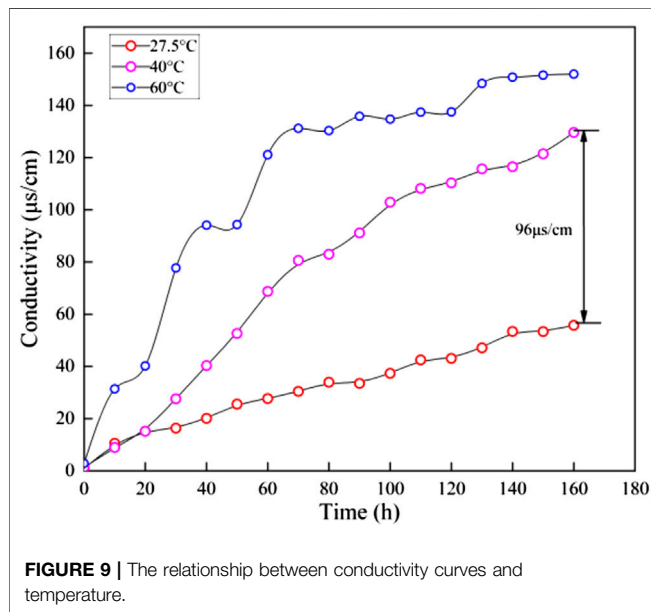
structure, the particle diameter of ZN and LK sediments is much smaller than that of HT sediments. The dissociation water leads to more destruction on pore structure in ZN and LK sediments. However, the pore structure of ZN1-2 and ZN1-5 is relatively complete after disintegration experiments. Maybe the samples of ZN1-2 and ZN1-5 have much larger cementing strength. In terms of disintegration time, large disintegration time suggest low disintegration rate. Except for the ZN1-2 and ZN1-5 sample, the disintegration time of ZN and LK sediment samples is about 90–113 s. The disintegration time of LK sediment is about 220–318 s. The ZN and LK sediments have a smaller disintegration rate than LK sediment. In terms of disintegration process, the fractures propagate rapidly in the samples with fast disintegration. No buffering occurs, and they finally become fine sands. For the samples with slow disintegration, fractures propagation is slow in the disintegration process. Many bubbles appear on the surface of sample ZN1-5 and no obvious cracks occur. The skeleton structure softens gradually and homogeneously, preventing rapid gas discharge (Cui et al., 2018).

### 3.2 Characteristics of Ions Diffusion in Disintegration Experiments

The conductivity tests are used to analyze the solution concentration during the disintegration experiments. **Figure 5A** presents the solution conductivity curves corresponding to eight samples. The overall trends of conductivity curves are similar in spite of different characteristics in three sediments. At the initial stage, the conductivity increases significantly. When the soaking time exceeds about 25 h, the rate of conductivity rise slows down. From 600 to 1,000 h, the conductivity curve basically does not increase with time.

**Figure 5B** presents the relationship between solution conductivity and the square root of time. The bilinear characteristics are observed in conductivity curves of three samples. In other words, the disintegration process can be divided into two stages: a rapid disintegration stage and a slow disintegration stage (**Figure 6**). In the rapid disintegration stage, the expansion deformation occurs due to clay minerals expansion and the dissociation water rapidly destroys the pore skeleton. The soluble salt in the





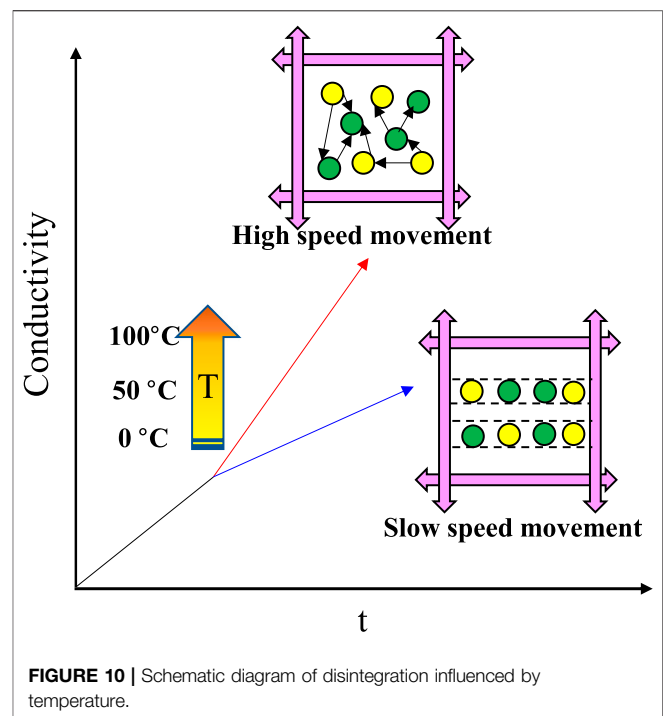
pores is rapidly released, resulting in the fast conductivity rise. The bond ability of particles is diminished, thereby accelerating ions diffusion. In the slow disintegration stage, the conductivity rise is mainly related to the dissolution of soluble salt minerals. A large amount of salt minerals dissolve and diffuse into the dissociation water, causing the sediment skeleton to further disperse and eventually become powdery. In general, the change of solution conductivity can well reflect the disintegration process of different sediments. The slope of conductivity curves represents the ions diffusion rate, which can be considered as the characteristic parameter of the disintegration rate. In the following paragraphs, the sediments characteristics are studied, such as water content, temperature, clay minerals, pore structure, porosity, and permeability. The effects of dissociation water retention on pore structure are clarified.

### 3.3 Influencing Factors of Pore Structure Disintegration

#### 3.3.1 Effects of Initial Water Content

The disintegration experiments are conducted on HT sediments to study the effects of initial water content. It helps clarify the relationship between the disintegration state of hydrate sediments and water content under the effects of dissociation water. The water content of HT1-2, HT1-3, HT1-4 and HT1-5 are 44.9%, 37.9%, 30.6% and 22.9%, respectively. The disintegration observations of four samples are presented in **Figure 7**. The sample with high initial water content does not cause disintegration, but a low initial water content is liable to cause disintegration. A critical value (30.6% to 37.9%) exists. When the initial water content exceeds 30.6%–37.9%, the pore structure of sediments tends to be stable in dissociation water.

The ZN sediments samples (ZN1-6 and ZN1-7) and LK sediments samples (LK1-3 and LK1-4) are used to establish



the relationship between initial water content and electrical conductivity. It helps to analyze the effect of dissociation water on pore structure. **Figure 8** presents the conductivity change over soaking time. As for the same sediment, the conductivity rise rate of samples with higher water content is faster than that of samples with lower water content. However, the conductivity difference between samples with higher water content and samples with lower water content changes over soaking time. According to the conductivity difference, the disintegration process can be divided into three stages. In the first stage, the rate of conductivity rise is the same and the conductivity is approximately equal. In the second stage, the rise rate of samples with lower water content is accelerated, and the conductivity difference increases with time. In the third stage, the conductivity difference does not change with time. The final conductivity difference of ZN sediment is about 8 uS/cm, and that of LK sediment is about 13 uS/cm.

By comparing the disintegration characteristics of samples with different water content, the particles adhesion capacity of samples in the environment of high water content is greater than that in the environment of low water content (Zhao et al., 2015). In the case of dissociation water, samples with higher water content are more resistant to destruction. The higher the water content, the less likely it is to disintegrate. In other words, the water existence can increase the cementing strength of sediments, and contribute to pore structure stability during the NGH depressurization process.

#### 3.3.2 Effects of Temperature

Gas hydrate can exist stably in a real environment that corresponds to certain temperature and pressure.

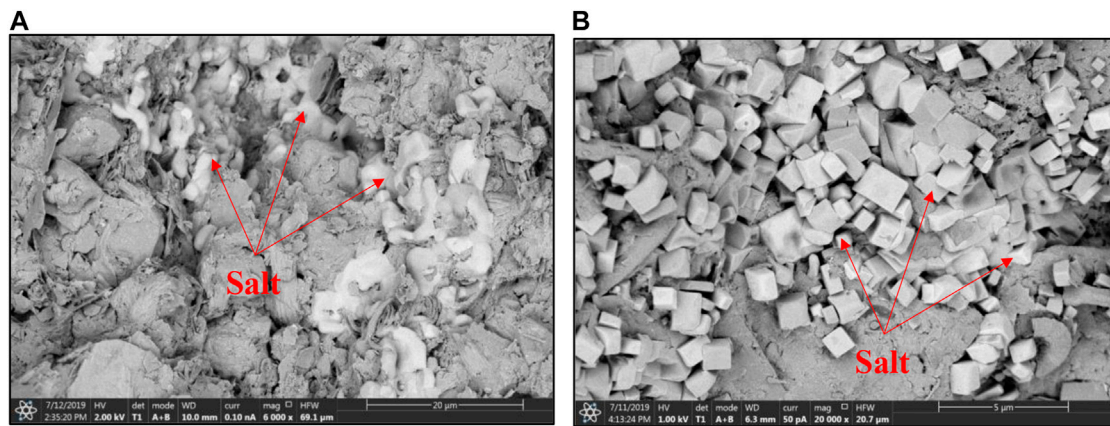


**FIGURE 11** | SEM pictures (A) ZN1-1 and (B) ZN1-2.

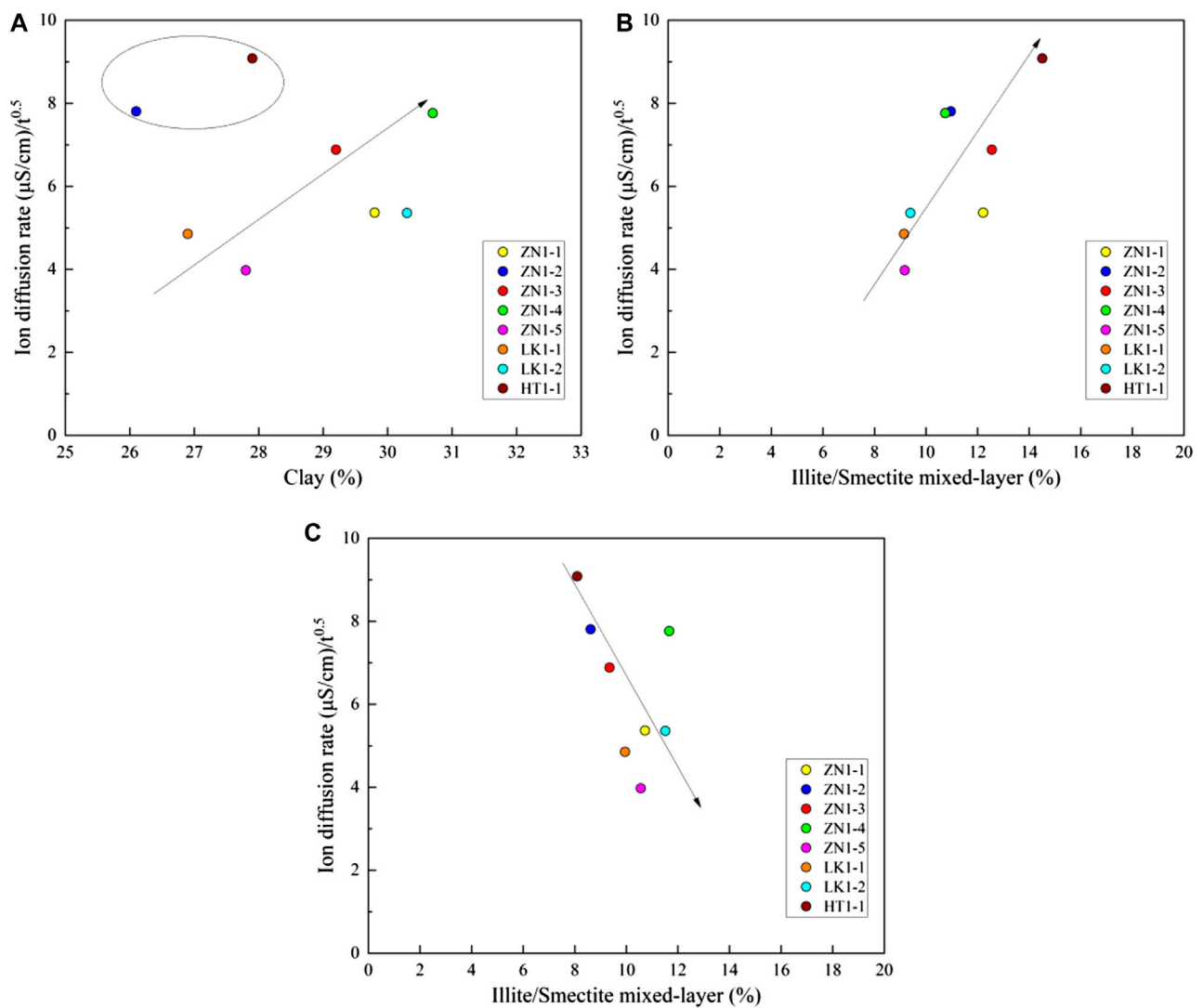
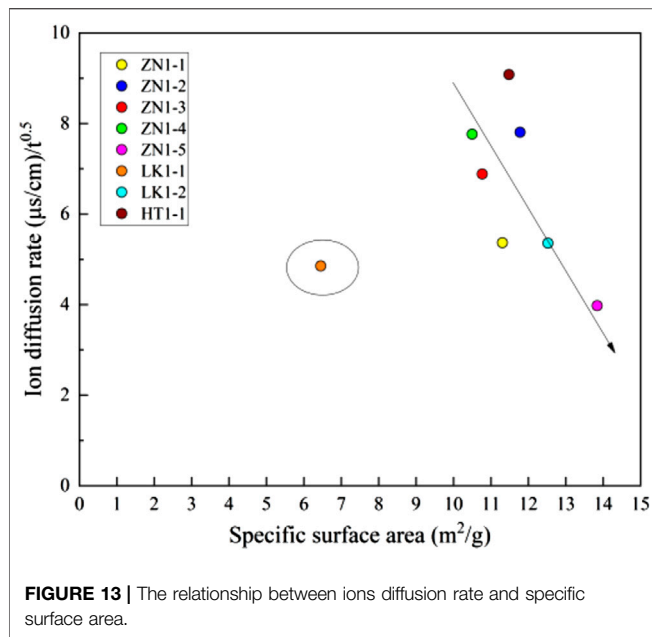


**FIGURE 12** | The effects of clay minerals on ions diffusion rate (A) the total clay minerals, (B) the I/S minerals and (C) the illite minerals.



Therefore, the sediment disintegration should involve the temperature effects. **Figure 9** presents the relationship between conductivity curves and temperature. It suggests that the conductivity of ZN sediments samples increases with temperature. At the slow disintegration stage, the pore structure of sediments is completely destroyed, and its temperature environment had little effect on disintegration process. Therefore, only the temperature tests are carried out to study the disintegration characteristics at the fast disintegration stage. At 170 min, the conductivity value at 60°C is about 3 times as large as the conductivity value at 27.5°C. According to the conductivity difference at different temperatures, the conductivity curve is divided into two stages. The first stage corresponds to the disintegration process before 20 min. In spite of the different temperatures, the rate at which the conductivity rises is basically the same. The second stage corresponds to the disintegration process after 20 min. The higher the temperature, the faster the rate of conductivity rises.

It should be noted that the conductivity rise rate is unstable at a temperature of 60°C. The high temperature result in the intense and disordered ions diffusion and complex disintegration process (**Figure 9**). The high temperature contributes to accelerating the

disintegration process of the hydrate sediment. High temperatures make molecules move faster, and ion migration is more efficient (**Figure 10**). During the gas hydrate exploitation, temperature rise is an effective to intensify hydrate decomposition, resulting in more dissociation water. The residual heat may accelerate the process of microscopic pore structure destruction.

### 3.3.3 Effects of Clay Minerals

The mineral composition has important effects on disintegration, especially clay minerals and salt minerals. The total amount of clay minerals and the relative content of each mineral are obtained by X-ray diffraction analysis, as shown in **Table 2**. The salt minerals are too limited to measure accurately. The scanning electron microscopy (SEM) can help analyze the distribution characteristics of salt minerals (**Figure 11**). The soluble salts and clay minerals are present in the ZN sediment.

**Figure 12A** presents the effects of clay minerals on ions diffusion rate. The ions diffusion rate is positively related to total clay mineral content. The larger the amount of total clay minerals, the faster the ions diffusion rate. The content of total clay mineral is about 25%–30%, and the ions diffusion rate varies from 3 to 10 (uS/cm)/h<sup>0.5</sup>. Most of the clay minerals have a large expansion and deformation capacity after water absorption. The expansion force can instantaneously and significantly destroy the pore structure. Therefore, it plays a dominant role in the rapid disintegration stage. It should be noted that samples ZN1-1 and ZN1-2 have large ions diffusion rate despite of low clay minerals content. A great amount of salt minerals is observed in SEM pictures of sample ZN1-1 and ZN1-2. The salt minerals existence can enhance the ions diffusion rate.

The ions diffusion rate also depends on the clay minerals type. The I/S and illite minerals are important water-sensitive minerals, which should be paid more attention. The content of the I/S minerals is about 5%–15%. **Figure 12B** presents the ions diffusion rate increase with the I/S minerals content. The higher the content of I/S minerals, the faster the ions diffusion rate. In other words, more I/S minerals can result in pore structure expansion and destruction. **Figure 12C** shows the relationship between ions diffusion rate and illite minerals content. The illite content is about 5%–15%. The ions diffusion rate decreases with illite minerals content. The reason is that illite minerals are in the form of a film. The “films” are arranged around the inner pores and other mineral particles. They are arranged neatly,

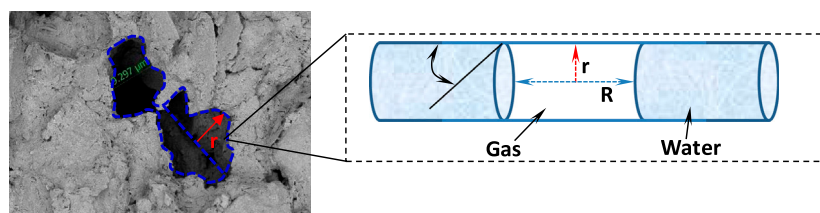
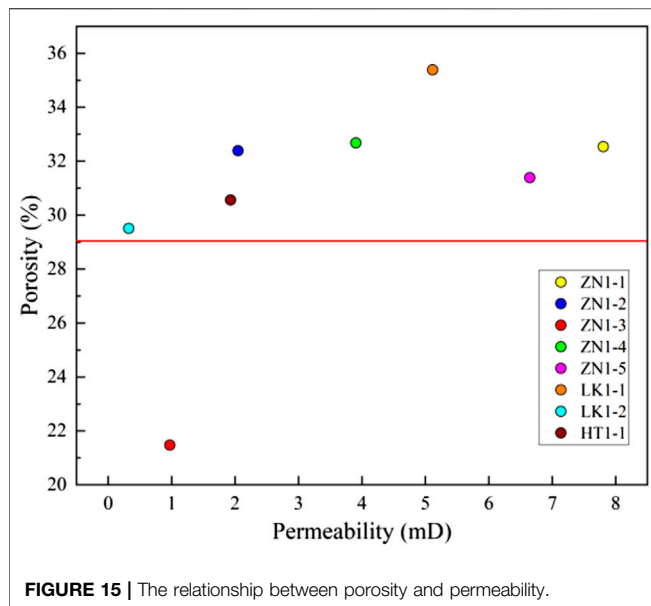


**FIGURE 14 |** Schematic diagram of pore pressure due to capillary force.



which makes the internal pore size smaller and hinders ions exchange.

### 3.3.4 Effects of Pore Structure

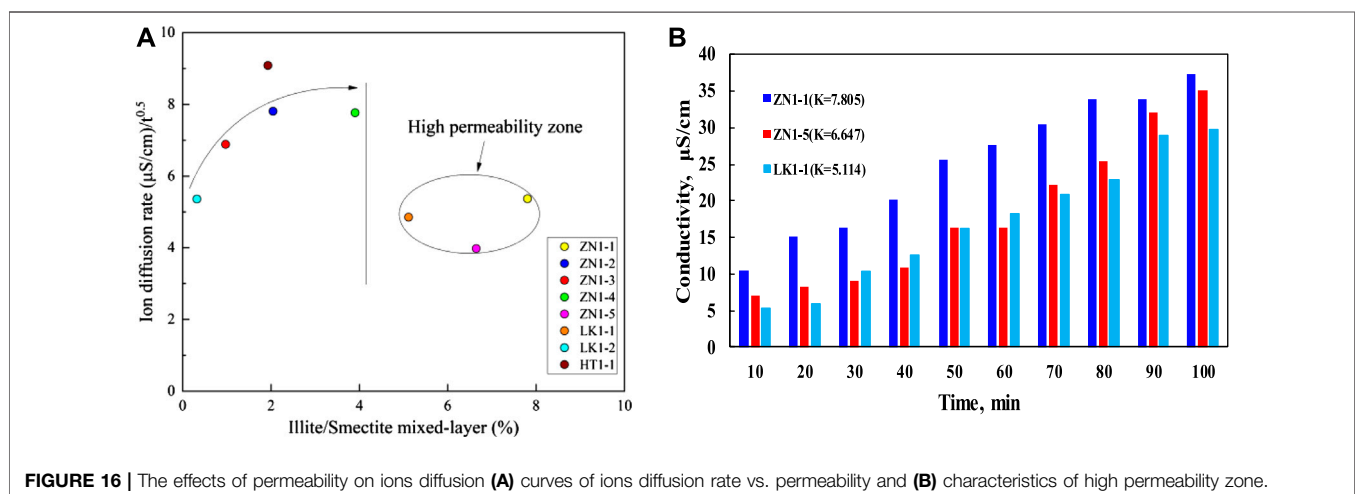
The specific surface area is an important parameter of pore structure, and reflects the pore size. The smaller the pore size, the larger the specific surface area. The specific surface area is obtained by a nitrogen adsorption test. **Figure 13** shows the relationship between ions diffusion rate and specific surface area. The specific surface area of the sediments varies from 6.4512 to 13.84 m<sup>2</sup>/g, which is nearly equal to that of gas shale (Ripmeester et al., 2010). It can be assumed that the pores are at the micro-nano level, and the pressure force can reach 5.3–19 MPa (Jin et al., 2019; Mahabadi et al., 2019). In **Figure 13**, the specific surface area has a negative correlation with ions diffusion rate. In other words, the smaller the pore size, the smaller the ions diffusion rate. According to capillary

force theory, the pore size is negatively related to capillary force (Lal, 1999). The dissociation water enters into the matrix pores, but part of the gas cannot be discharged completely. A great amount of gas is trapped in the matrix pores, increasing the pore pressure (**Figure 14**). The pore pressure is nearly equal to capillary pressure, which is about 5.3–19 MPa. The disintegration and fragmentation can be motivated when the high internal pore pressure gets higher than the tensile strength of the sediments. Under the effects of dissociation water retention, the pore structure corresponding to high specific surface area is very easy to destroy.

### 3.3.5 Effects of Permeability and Porosity

Studying the relationship between permeability and porosity contributes to understanding the effects of permeability and porosity on ions diffusion. **Figure 15** shows the relationship between porosity and permeability, and a positive correlation is observed. In terms of low permeability sediments (<4 mD), the porosity increases significantly with the rise in permeability. As for high permeability sediments (>4 mD), the porosity approximately keeps constant, and basically does not change with permeability rise.

Considering the positive correlation between permeability and porosity, it is only necessary to study the effects of permeability. The disintegration is a rapid process, leading to the change of pore structure (Li and Hou, 2019). Therefore, the permeability effects mainly happen in the initial disintegration stage. In the late disintegration stage, the samples are dispersed into broken particles, and the permeability no longer affects sediment disintegration (Sun et al., 2018). **Figure 16A** presents the effects of permeability on ions diffusion rate. It can also be divided into two zones. At the low permeability zone (<4 mD), the ions diffusion rate increases significantly with permeability rise. The larger permeability contributes to the water flow, and enhances the interactions between dissociation water and pore skeleton. At the high permeability zone (>4 mD), There is no obvious correlation between permeability and ions diffusion rate. The samples ZN1-1, ZN1-5 and LK1-1 correspond to high permeability zone. **Figure 16B** presents shows the effects of



permeability on conductivity change. According to the conductivity data before 20 min and after 70 min, the positive correlations between permeability and conductivity rise are observed. No obvious correlation between them is found in the curves from 20 to 70 min. In general, the permeability and porosity positively promote the disintegration of sediments.

## 4 CONCLUSIONS

In this paper, a series of characteristics are measured in sediments, such as porosity, permeability, pore structure and clay minerals content. The disintegration mechanism of sediments is evaluated by quantitative analysis of the conductivity experiment. Because the dissociation process of hydrate is very complicated, the current experiment has certain limitations. The conclusions are as follows.

- (1) The dissociation water can lead to the disintegration of the pore structure of sediments. The ions concentration of dissociation water can act as an important parameter to evaluate the disintegration process.
- (2) The sediment disintegration is divided into two stages: a rapid disintegration stage and a slow disintegration stage. The rapid disintegration stage is mainly related to clay minerals. The slow disintegration stage is mainly related to the dissolution of soluble salt minerals.
- (3) The initial water content is the main factor affecting the disintegration of the sediment skeleton. Under the condition

of low initial water content, the sediment skeleton disintegrates instantaneously in dissociation water. When the initial water content exceeds 30.6%–37.9%, the pore structure of sediments tends to be stable in dissociation water.

## DATA AVAILABILITY STATEMENT

The original contributions presented in the study are included in the article/supplementary material, further inquiries can be directed to the corresponding authors.

## AUTHOR CONTRIBUTIONS

The idea of the article comes from LY. The paper was written by SW. HL is responsible for reviewing the papers. LL and RS added to the article.

## FUNDING

The research was funded by National Natural Science Foundation of China (No. 11702296), the China Geological Survey (No. DD20190232), by the Fundamental Research Funds for the Central Universities (No. 2462019YJRC011), and by Natural Science Foundation of China (41941018).

## REFERENCES

- Anderson, B. J., Kurihara, M., White, M. D., Moridis, G. J., Wilson, S. J., Pooladi-Darvish, M., et al. (2011). "Regional long-term production modeling from a single well test," mount elbert gas hydrate stratigraphic test well, Alaska north slope. *Mar. Petrol. Geol.* 28 (2), 493–501. doi:10.1016/j.marpetgeo.2010.01.015
- Cai, J., Xia, Y., Lu, C., Bian, H., and Zou, S. (2020a). Creeping microstructure and fractal permeability model of natural gas hydrate reservoir. *Mar. Petrol. Geol.* 115, 104282. doi:10.1016/j.marpetgeo.2020.104282
- Cai, J., Xia, Y., Xu, S., and Tian, H. (2020b). Advances in multiphase seepage characteristics of natural gas hydrate sediments. *Chin. J. Theor. Appl. Mech.* 52, 208–223. doi:10.6052/0459-1879-19-362
- Chen, J., Liu, J., Chen, G.-J., Sun, C.-Y., Jia, M.-L., Liu, B., et al. (2014). Insights into methane hydrate formation, agglomeration, and dissociation in water+diesel oil dispersed system. *Energy Convers. Manag.* 86, 886–891. doi:10.1016/j.enconman.2014.06.056
- Cui, Y., Lu, C., Wu, M., Peng, Y., Yao, Y., and Luo, W. (2018). Review of exploration and production technology of natural gas hydrate. *Adv. Geo-Energy Res.* 2, 3–62. doi:10.26804/ager.2018.01.05
- Gamwo, I. K., and Liu, Y. (2010). Mathematical modeling and numerical simulation of methane production in a hydrate reservoir. *Ind. Eng. Chem. Res.* 49, 5231–5245. doi:10.1021/ie901452v
- Huang, M., Xu, C.-S., and Zhan, J. (2017). Assessments of the disintegrating behaviour of clay shale considering the effect of pH condition. *Eur. J. Environ. Civil Eng.* 24, 97–109. doi:10.1080/19648189.2017.1366952
- Jin, Y. R., Yang, D. Y., Li, S. X., and Pang, W. X. (2019). Hydrate dissociation conditioned to depressurization below the quadruplepoint and salinity addition. *Fuel* 255, 1157–1158. doi:10.1016/j.fuel.2019.115758
- Kang, D. H., Yun, T. S., and Kim, K. Y. (2016). Effect of hydrate nucleation mechanisms and capillarity on permeability reduction in granular media. *Geophys. Res. Lett.* 43, 9018–9025. doi:10.1002/2016gl070511
- Lal, M. (1999). "Shale stability: drilling fluid interaction and shale strength," in SPE Asia Pacific oil and gas conference and exhibition, Jakarta, Indonesia, April 20–22, 1999 (Dallas, TX: Society of Petroleum Engineers), 10.
- Li, S., and Hou, S. (2019). A brief review of the correlation between electrical properties and wetting behaviour in porous media. *Capillarity* 2, 53–56. doi:10.26804/capi.2019.03.02
- Linga, P., and Clarke, M. (2017). A review of reactor designs and materials employed for increasing the rate of gas hydrate formation. *Energy Fuel* 31, 1–13. doi:10.1021/acs.energyfuels.6b02304
- Luo, J., Wu, Y., Mi, D., Ye, Q., Huang, H., Chang, Z., et al. (2020). Analysis of the distribution and microscopic characteristics and disintegration characteristics of carbonaceous rocks: a case study of the middle devonian luofu formation in western guangxi of China. *Adv. Civ. Eng.* 2020, 1–15. doi:10.1155/2020/8810648
- Mahabadi, N., Dai, S., Seol, Y., and Jang, J. (2019). Impact of hydrate saturation on water permeability in hydrate-bearing sediments. *J. Petrol. Sci. Eng.* 174, 696–703. doi:10.1016/j.petrol.2018.11.084
- Mahabadi, N., Zheng, X. L., and Jang, J. (2016). The effect of hydrate saturation on water retention curves in hydrate-bearing sediments. *Geophys. Res. Lett.* 43, 4279–4287. doi:10.1002/2016gl068656
- Moridis, G. J., and Reagan, M. T. (2007). "Strategies for gas production from oceanic Class 3 hydrate accumulations," in Offshore technology conference, Houston, TX, April 30–May 3, 2007 (Houston, TX: Offshore Technology Conference), 29.
- Moridis, G. J., and Sloan, E. D. (2007). Gas production potential of disperse low-saturation hydrate accumulations in oceanic sediments. *Energy Convers. Manag.* 48 (6), 1834–1849. doi:10.1016/j.enconman.2007.01.023



- Omelchenko, R. Y., and Makogon, Y. F. (2013). Commercial gas production from Messoyakha deposit in hydrate conditions. *J. Nat. Gas Sci. Eng.* 11, 1–6. doi:10.1016/j.jngse.2012.08.002
- Pandey, J. S., Daas, Y. J., and Solms, N. V. (2019). Insights into kinetics of methane hydrate formation in the presence of surfactants. *Processes* 7, 598. doi:10.3390/pr7090598
- Radich, J., Rogers, R. E., French, W. T., and Zhang, G. (2009). Biochemical reaction and diffusion in seafloor gas hydrate capillaries: implications for gas hydrate stability. *Chem. Eng. Sci.* 64, 4278–4285. doi:10.1016/j.ces.2009.06.073
- Ripmeester, J. A., Alireza, S., Hosseini, B., Englezos, P., and Alavi, S. (2010). “Fundamentals of methane hydrate decomposition,” in Canadian unconventional resources and international petroleum conference, Calgary, Alberta, Canada, October 19–21, 2010 (Dallas, TX: Society of Petroleum Engineers), 7.
- Shagapov, V., and Tazetdinov, B. I. (2014). Formation and dissociation of gas hydrate inclusions during migration in water. *Thermophys. Aeromechanics* 21, 337–345. doi:10.1134/s086986431403007x
- Shen, W. J., Song, F. Q., Hu, X., Zhu, G. M., and Zhu, W. Y. (2019). Experimental study on flow characteristics of gas transport in micro- and nanoscale pores. *Sci. Rep.* 9, 10196. doi:10.1038/s41598-019-46430-2
- Sun, Y., Lu, H., Lu, C., Li, S., and Lv, X. (2018). Hydrate dissociation induced by gas diffusion from pore water to drilling fluid in a cold wellbore. *Adv. Geo-Energy Res.* 2, 410–417. doi:10.26804/ager.2018.04.06
- Van Genuchten, M. T. (1980). A closed-form equation for predicting the hydraulic conductivity of unsaturated soils. *Soil Sci. Soc. Am. J.* 44, 892–898. doi:10.2136/sssaj1980.03615995004400050002x
- Yan, L., Liu, P., Peng, H., Kašanin-Grubin, M., and Lin, K. (2018). Laboratory study of the effect of temperature difference on the disintegration of redbed softrock. *Phys. Geogr.* 40, 149–163. doi:10.1080/02723646.2018.1559418
- Yang, L., Zhang, C., Cai, J., and Lu, H. (2020). Experimental investigation of spontaneous imbibition of water into hydrate sediments using nuclear magnetic resonance method. *Energies* 13. doi:10.3390/en13020445
- Yang, L., Zhang, C., Lu, H., Zheng, Y., and Liu, Y. (2020). Experimental Investigation on the Imbibition Capacity and Its Influencing Factors in Hydrate Sediments. *ACS OMEGA* 5. doi:10.1021/acsomega.0c01269
- Zhang, Z., Liu, W., Cui, Q., Han, L., and Yao, H. (2018). Disintegration characteristics of moderately weathered mudstone in drawdown area of Three Gorges Reservoir, China. *Arab. J. Geosci.* 11, 405. doi:10.1007/s12517-018-3751-8
- Zhao, J. F., Zhu, Z. H., Song, Y. C., Liu, W. G., Zhang, Y., and Wang, D. Y. (2015). Analyzing the process of gas production for natural gas hydrate using depressurization. *Appl. Energy* 142, 125–134. doi:10.1016/j.apenergy.2014.12.071
- Zhong, J. R., Sun, Y. F., Li, W. Z., Xie, Y., Chen, G.-J., Sun, C.-Y., et al. (2019). Structural transition range of methane-ethane gas hydrates during decomposition below ice point. *Appl. Energy* 250, 873–881. doi:10.1016/j.apenergy.2019.05.092

**Conflict of Interest:** The authors declare that the research was conducted in the absence of any commercial or financial relationships that could be construed as a potential conflict of interest.

Copyright © 2020 Yang, Wang, Lu, Liu and Sa. This is an open-access article distributed under the terms of the Creative Commons Attribution License (CC BY). The use, distribution or reproduction in other forums is permitted, provided the original author(s) and the copyright owner(s) are credited and that the original publication in this journal is cited, in accordance with accepted academic practice. No use, distribution or reproduction is permitted which does not comply with these terms.



# Transient Pressure Analysis of Inclined Well in Continuous Triple-Porosity Reservoirs With Dual-Permeability Behavior

Sheng-Zhi Qi<sup>1,2,3\*</sup>, Xiao-Hua Tan<sup>1,3\*</sup>, Xiao-Ping Li<sup>1,3</sup>, Zhan Meng<sup>1,3</sup>, You-Jie Xu<sup>1,3</sup> and Daming Tang<sup>4</sup>

<sup>1</sup>State Key Laboratory of Oil and Gas Reservoir Geology and Exploitation, Southwest Petroleum University, Chengdu, China, <sup>2</sup>Energy Engineering College, Longdong University, Qingyang, China, <sup>3</sup>Key Laboratory of Seepage and Rock Mechanics of Oil and Gas Wells in Shanxi Province, Xian, China, <sup>4</sup>Shuguang Oil Production Plant of Liaohe Oilfield, Panjin, China

## OPEN ACCESS

### Edited by:

Kaiqiang Zhang,  
Imperial College London, United  
Kingdom

### Reviewed by:

Fanhua Zeng,  
University of Regina, Canada  
Fuping Li,  
Curtin University, Australia

### \*Correspondence:

Sheng-Zhi Qi  
ctfy742@163.com  
Xiao-Hua Tan  
xiaohua-tan@163.com

### Specialty section:

This article was submitted to  
Advanced Clean Fuel Technologies,  
a section of the journal  
Frontiers in Energy Research

**Received:** 31 August 2020

**Accepted:** 02 October 2020

**Published:** 01 December 2020

### Citation:

Qi S-Z, Tan X-H, Li X-P, Meng Z, Xu Y-J and Tang D (2020) Transient Pressure Analysis of Inclined Well in Continuous Triple-Porosity Reservoirs With Dual-Permeability Behavior. *Front. Energy Res.* 8:601082. doi: 10.3389/fenrg.2020.601082

Inclined wells has recently been adopted to develop fractured-vuggy carbonate hydrocarbon reservoirs (FVCHRs) composed by matrix, fracture and vug system. Therefore, it is significant for us to describe pressure transient of inclined well for FVCHRs. In this paper, it is assumed that vug and fracture system connect with wellbore, and inter-porosity flow from vug to fracture system appears. Therefore, the pressure transient responses model of inclined well with triple-porosity dual-permeability behavior was built. The model is solved by employing Laplace integral transform and finite cosine Fourier transform. Real-domain solution of the model is obtained by Stehfest inversion algorithm. On the basis model of the published paper, the solution of the simplified model of this paper was validated with horizontal and vertical well of FVCHRs with triple-porosity dual-permeability behavior, and results reach a good agreement. Type curve, according to pressure derivative curve characteristic, can be divided into eight flow regimes, which includes wellbore storage, skin reflect, early vertical radial flow, top and bottom boundary reflection, linear flow, inter-porosity flow from vug to fracture, inter-porosity from matrix to vug and fracture and pseudo-radial flow regimes. The influence of some vital parameters (inclination angle, inter-porosity flow coefficient, well length and permeability ratio etc.) on dimensionless pressure and its derivative curves are discussed in detail. The presented model can be used to understand pressure transient response characteristic of inclined wells in FVCHRs with dual-permeability behavior.

**Keywords:** inclined well, fractured-vuggy carbonate hydrocarbon reservoirs, triple-porosity dual-permeability, inter-porosity flow, pressure transient

## INTRODUCTION

Since the 1960s, numerous scholars mainly studied the flow characteristic of the fluid in naturally fractured reservoirs by the method of the pressure transient analysis (Warren and Root, 1963; Pruess and Narasimhan, 1985; Kuchuk and Biryukov, 2014; Kui et al., 2017; Tan et al., 2018; Yin, 2018; Song et al., 2019; Pang et al., 2020; Tontiwachwuthikul et al., 2020; Wang et al., 2020). Since a large number of the fractured-vuggy carbonate hydrocarbon reservoirs (FVCHRs) were found around the world, most of scholars have focused on studies of FVCHRs to understand flow characteristic of the fluid in the FVCHRs (Abadassah and Ershaghi, 1986; Liu et al., 2003; Sun et al., 2018). Compared with

naturally fractured reservoirs, the complex structures of the FVCHRs posed significant research challenges towards scholars and scientists about pressure transient response of the FVCHRs. Therefore, the mathematic model describing flow process of the fluid in FVCHRs is established to evaluate the properties and pressure transient characteristics of this type reservoirs.

During the last 20 years, pressure transient analysis is used widely to obtain some vital parameters of reservoirs. With the help of these parameters, reservoir engineers can evaluate oil and gas reservoirs effectively and develop a reasonable development plan for the FVCHRs. The source function method plays a vital role in the process of well test model solution. Gringarten and Ramey (1973) first put forward the real-domain point source analytical solution under the conditions of the different outer boundary. On the basis of the real-domain point source solution, Ozkan and Raghavan (1991; 2004) applied Green's function theory to expand the point source to the Laplace domain and the corresponding calculation method is given.

Most of the world's giant oil and gas produce from naturally fractured and vuggy carbonate reservoirs with complex pore system. Vug porosity is common pore system in FVCHRs, and the size of the vug have an important influence on pressure and production performance. The FVCHRs can be subdivided into triple-continuum medium model and discontinuous medium according to the size of the vug. For the research of the pressure and production of triple-continuum medium model, Abadassah and Ershaghi (1986) first presented triple-porosity single-permeability well-test mathematical model for vertical well, and semi-log and log-log curves were drawn to analysis flow characteristic of the triple-continuum medium. Camacho-Velázquez et al. (2005) established and solved mathematical model of triple-porosity dual-permeability of the vertical well, which assumed that fluid of the natural fracture and vuggy porosity flow into wellbore directly, and the characteristic of pressure transient and decline curve are analyzed. Wu et al. (2004; 2011) solved a triple-continuum pressure transient model of the multi-phase fluid by employing analytical and numerical method. Corbett et al. (2010) studied on fractured carbonate rocks by adopting the numerical well test, and summarized that numerical well testing has its limitations. Guo et al. (2012) established a triple-porosity single-permeability flow mathematical model of the horizontal well in a triple-continuum FVCHRs under different boundary condition, and standard pressure and its derivative log-log curves were drawn. Nie et al. (2012) presented pressure response mathematical model of the horizontal well in coal seam. Pressure and its derivative response curves are drawn in log-log plot, and influence of some vital parameters on type curves were analyzed. Jia et al. (2013) studied on flow issues of a porous-vuggy carbonate reservoir without fracture system. It is assumed that vug system is spherical and pressure distribute symmetrically. Corresponding mathematical model was established and solved by employing Laplace transform. Wang et al. (2018) developed a pressure transient mathematical model of acid fracturing wells in FVCHRs. Therefore, a composite system is considered, the inner region is made up with finite number of

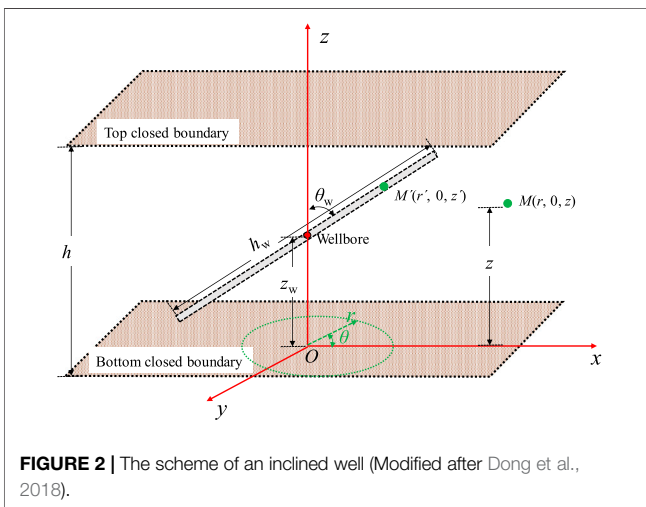
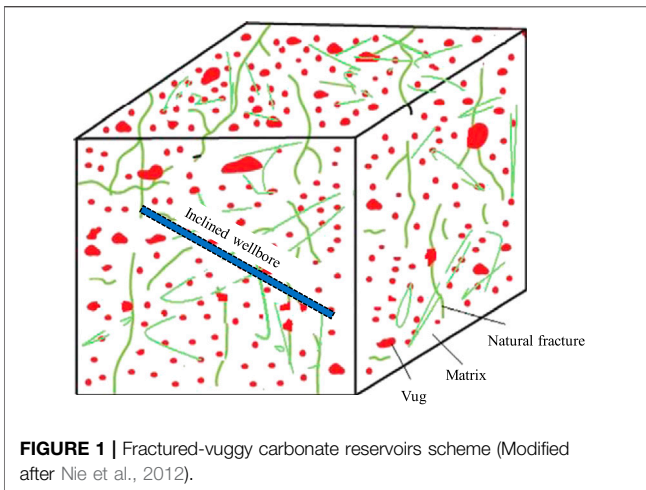
artificial fractures and wormholes, and the outer region is made up triple-porosity medium. Wang et al. (2014) derived well test mathematical model of hydraulic fractured well in FVCHRs by point sink integral method. This model assumed that fluid of matrix and natural fractures system flow into wormholes directly. The existence of large-scale cavities will have a noticeable influence on the transient pressure behavior. For the research of the pressure and production of discontinuous medium model, Gao et al. (2016) and Xing et al. (2018) presented a flow mathematical model, it is assumed that well is drilled through large-scale cavities and fluid flow into a filled cavity. Wellbore storage and skin factor were considered in their model. Du et al. (2019) presented an analytical well test model of fractured vuggy carbonate reservoirs. Pressure difference between the wellbore and large vug was considered in their model.

Because the reservoir geological condition becomes more and more complex, the technology of inclined wells has recently been adopted to solve the problem of onshore oil and gas reservoirs extraction. To estimate pressure transient behavior of inclined well, many scholars established pressure response mathematical model of inclined well. Cinco-Ley et al. (1975; 2007) presented an analytical solution of inclined well in real domain and shown the existence of the pseudo-radial flow period at large time values. Yildiz and Ozkan (Yildiz and Ozkan, 1999; Ozkan et al., 1999; Ozkan and Raghavan, 2000) studied transient pressure behavior and rate distributions of slanted well and perforated wells. Corresponding calculation method of slanted and perforated wells was shown to improve the computational efficiency and increase the accuracy. Feng and Liu (2015) established a well test mathematical model of inclined well with an impermeable fault by employing point source theory. Dong et al. (2018) presented a skin factor model of partially penetrated directionally-drilled wells in anisotropic reservoirs to study the stimulation effect of slanted.

This paper summarizes the published literature about well test model of the FVCHRs and slanted well, absorbs their highlights and studies on pressure transient behavior of the inclined well in FVCHRs. Therefore, the objective of this paper is to establish and solve well test mathematical model of inclined well in FVCHRs with triple-porosity dual-permeability behavior by employing Laplace transform and finite cosine Fourier transform. The fluid of natural fractures and vug system can flow into wellbore directly. Inter-porosity flows from matrix system to both natural fracture and vug system, and inter-porosity flow from vug system to a natural fracture system were also considered in this paper. Pressure and its derivative type curves under condition of constant production by adopting the Stehfest numerical inversion are drawn. Influence of some vital parameters on type curves are discussed in detail.

## PHYSICAL MODELING AND ASSUMPTIONS

The fractured-vuggy carbonate reservoirs in Tahe oilfield of China is an example, reservoir is composed of vug, natural fracture and matrix systems (**Figure 1**). The fluid of the



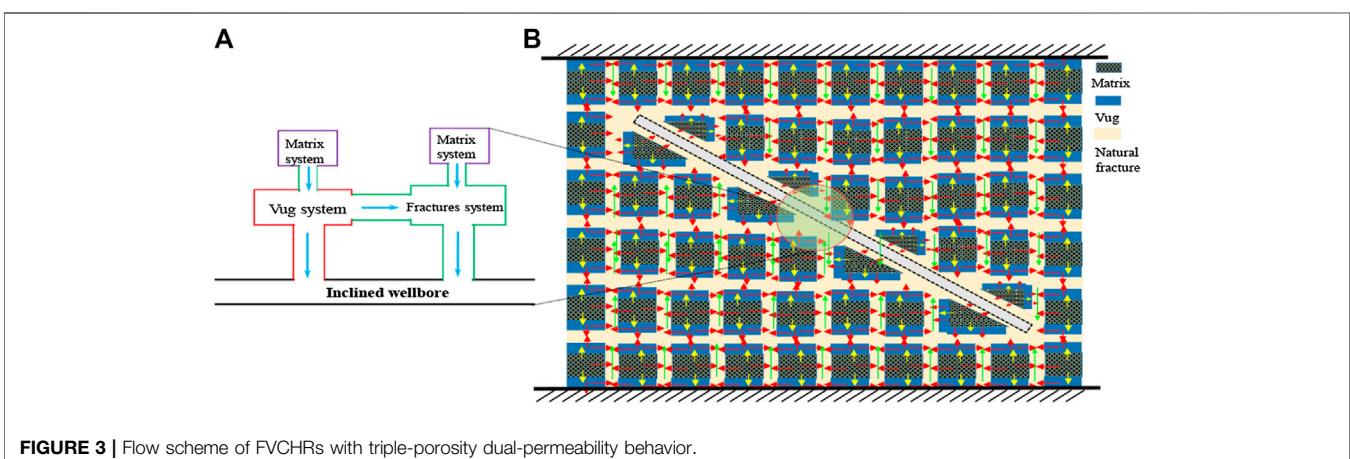
fractures and vug system flow into the inclined wellbore directly. There is an inclined well in top and bottom closed boundary in FVCHRs. The length of the well is denoted by  $h_w$ , inclination

angle of the well is denoted by  $\theta_w$ , and height of reservoirs is denoted by  $h$ , the coordinates of point source in the reservoir is  $M(r, 0, z)$ , the coordinates of any point on the well is  $M'(r', 0, z')$  (Figure 2). The end view of an inclined well opened practically in FVCHRs is shown in Figure 3. The fluid of the fracture and vug systems flow into the inclined wellbore directly, Inter-porosity flows from matrix system to both natural fracture and vug systems, and inter-porosity flow from vug system to natural fracture system were considered. This process is named triple-porosity dual-permeable flow behavior. In order to better establish mathematical model of an inclined well in FVCHRs, the other assumptions are as follows:

- (1) The production of the inclined well is denoted by  $q_{sc}$  in FVCHRs of closed the top and bottom boundaries.
- (2) The rock and fluid are slightly compressible, and the fluid flowing in the fractures and reservoirs is isothermal seepage.
- (3) The inclined well is assumed to be penetrated fully or partially, and formation thickness and well length meet the relationships:  $|(z_D - z_{wD})\cos\psi'| \leq h_{wD}, \psi' = \tan^{-1}(\sqrt{k_{fv}/k_{fh}} \tan\theta_w)$ .
- (4) The fluid in the natural fracture and vug system can flow into the inclined well and inter-porosity flow from vug system to a natural fracture system were considered. The fluid in the matrix system flow into inclined wellbore through vug and fracture system (see Figure 3A).
- (5) The permeability of the matrix system is  $k_m$ , the permeability of the natural fracture is  $k_f$ , the permeability of the vug is  $k_v$ , and the permeability anisotropy of the horizontal and vertical directions is considered in FVCHRs.
- (6) The original formation pressure of the matrix, fracture and vug system is equal to initial pressure  $p_e$ .

## MATHEMATICAL MODELING

Based on the scheme of an inclined well as shown in Figure 2, the mathematical model of the inclined well is established in FVCHRs. In order to help reader to understand coordinate



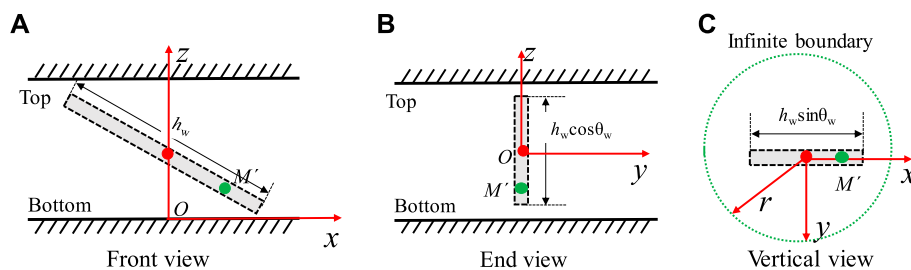


**FIGURE 4** | Three different view in **Figure 2** (Modified after Nie et al., 2012). **(A)** Comparison with Guo et al.' result. **(B)** Comparison with Camacho-Velázquez et al. result.

system as shown in **Figure 2**, three different views of an inclined well in top and bottom closed boundary are given in **Figure 4**.

According to the state equation, the motion equation and the continuity equation, the differential equation of matrix, vug and natural fracture systems is established in FVCHRs (Camacho-Velázquez et al., 2005). Inclined well could be regarded as a line source in 3D space. Therefore, to obtain solutions for inclined well, we must establish a 3D point source model. Then we can get a surface source solution through point source integral method.

- (1) The two-dimensional seepage differential equation of natural fracture system can be described as:

$$\begin{aligned} \frac{1}{r} \frac{k_{fh}}{\mu} \frac{\partial}{\partial r} \left( r \frac{\partial p_f}{\partial r} \right) + \frac{k_{fv}}{\mu} \frac{\partial}{\partial z} \left( \frac{\partial p_f}{\partial z} \right) + \frac{\alpha_m k_{mh}}{\mu} (p_m - p_f) \\ + \frac{\alpha_v k_{vh}}{\mu} (p_v - p_f) \\ = (\phi C_t)_f \frac{\partial p_f}{\partial t} \end{aligned} \quad (1)$$

- (2) The two-dimensional seepage differential equation of vug system can be described as:

$$\begin{aligned} \frac{1}{r} \frac{k_{vh}}{\mu} \frac{\partial}{\partial r} \left( r \frac{\partial p_v}{\partial r} \right) + \frac{k_{vv}}{\mu} \frac{\partial}{\partial z} \left( \frac{\partial p_v}{\partial z} \right) + \frac{\alpha_m k_{mh}}{\mu} (p_m - p_v) \\ - \frac{\alpha_v k_{vh}}{\mu} (p_f - p_v) \\ = (\phi C_t)_v \frac{\partial p_v}{\partial t} \end{aligned} \quad (2)$$

- (3) The seepage differential equation of matrix system can be described as:

$$\frac{\alpha_m k_{mh}}{\mu} (p_m - p_v) - \frac{\alpha_m k_{mh}}{\mu} (p_m - p_f) = (\phi C_t)_m \frac{\partial p_m}{\partial t} \quad (3)$$

- (4) Initial condition can be described as:

$$p_m(r, 0) = p_f(r, 0) = p_v(r, 0) = p_e \quad (4)$$

- (5) Inner condition boundary can be described as:

$$\lim_{\varepsilon \rightarrow 0} \int_{z-\varepsilon/2}^{z+\varepsilon/2} \left[ \lim_{\delta \rightarrow 0} 2\pi \frac{r}{\mu} \left( k_{fh} \frac{\partial p_f}{\partial r} + k_{vh} \frac{\partial p_v}{\partial r} \right) \right]_{r=\varepsilon} dz = \tilde{q}(t) \quad (5)$$

- (6) Outer condition boundary can be described as:

$$\frac{\partial p_f(r, z, 0, t)}{\partial z} = \frac{\partial p_m(r, z, 0, t)}{\partial z} = \frac{\partial p_v(r, z, 0, t)}{\partial z} = 0 \quad (6)$$

$$\frac{\partial p_m(r, z, h, t)}{\partial z} = \frac{\partial p_f(r, z, h, t)}{\partial z} = \frac{\partial p_v(r, z, h, t)}{\partial z} = 0 \quad (7)$$

$$p_f(r \rightarrow \infty, z, t) = p_m(r \rightarrow \infty, z, t) = p_v(r \rightarrow \infty, z, t) = 0 \quad (8)$$

where:  $p_v$  is pressure of vug system, MPa;  $p_f$  is pressure of natural fracture system, MPa;  $p_m$  is pressure of matrix system, MPa;  $p_e$  is initial reservoirs pressure, MPa;  $k_{fh}$  is horizontal permeability of natural fracture system, mD;  $k_{fv}$  is vertical permeability of natural fracture system, mD;  $k_{mh}$  is horizontal permeability of matrix system, mD;  $k_{vh}$  is horizontal permeability of vuggy system, mD;  $C_{tf}$  is total compressibility factor of natural fracture system,  $\text{MPa}^{-1}$ ;  $C_{mf}$  is total compressibility factor of matrix system,  $\text{MPa}^{-1}$ ;  $C_{vf}$  is total compressibility factor of vuggy system,  $\text{MPa}^{-1}$ ;  $\phi_f$  is porosity of natural fracture system, dimensionless;  $\phi_m$  is porosity of matrix system, dimensionless;  $\phi_v$  is porosity of vuggy system, dimensionless;  $t$  is production time, s;  $\mu$  is fluid viscosity, cp;  $\tilde{q}$  is strength of continuous point source of reservoirs,  $\text{m}^2/\text{s}$ ;  $\alpha$  is shape factor;  $x, y, z$  is Descartes coordinates, m;  $\varepsilon, \delta$  is infinitesimal distance, m;  $q_{sc}$  is production rate,  $\text{m}^3/\text{s}$ ;  $r_w$  is wellbore radial, m.

For convenience of derivation, the relevant dimensionless variables are defined in **Table 1**: Laplace transformation with respect to  $t_D$  is then adopted to invert the above seepage model into Laplace domain (Van Everdingen and Hurst, 1949).

$$L[p_{jD}(r_D, t_D)] = \bar{p}_{jD}(r_D, s) = \int_0^\infty p_{jD}(r_D, t_D) e^{-st_D} dt_D, \quad (j = m, f, v) \quad (9)$$

where:  $\bar{p}_{jD}$  is dimensionless pressure in Laplace domain;



**TABLE 1** | Dimensionless variables definition.

Dimensionless pressure	$p_D = \frac{2\pi(k_{fh}+k_{fv})h}{q_{sc}\mu} (p_e - p_j), (j = m, f, v)$	Dimensionless well storage	$C_D = \frac{C}{2\pi h\phi C_1 L_{ref}^2}$
Dimensionless time	$t_D = \frac{(k_{fh}+k_{fv})t}{\mu(\phi C_1)_{f+m+v} r_w^2}$	Dimensionless instantaneous rate	$\tilde{q}_D = \frac{\tilde{q}}{q_{sc}}$
Dimensionless reservoirs height	$h_D = \frac{h}{r_w} \sqrt{\frac{k_{fv}}{\kappa}}, k_{fv} = \frac{k_{fv}}{k_{fh}}$	Inter-porosity flow coefficient	$\lambda_{vf} = \frac{\alpha_{vf} k_{fh}}{k_{fh}+k_{fv}} r_w^2, (j = f, v)$
Dimensionless radial distance	$r_D = \frac{r}{r_w}$	Inter-porosity flow coefficient	$\lambda_{mv} = \frac{\alpha_{mv} k_{fv}}{k_{fh}+k_{fv}} r_w^2, (j = f, v)$
Dimensionless coordinate	$x_D = \frac{x}{L_{ref}}, y_D = \frac{y}{L_{ref}}, z_D = \frac{z}{r_w} \sqrt{\frac{k_{fv}}{\kappa}}$	Storativity ratio	$\omega_j = \frac{(\phi C_1)_{j+m+v}}{(\phi C_1)_{f+m+v}}, (j = m, f, v)$
Dimensionless infinitesimal distance	$\varepsilon_D = \frac{\varepsilon}{L_{ref}}, \delta_D = \frac{\delta}{L_{ref}}$	Permeability ratio	$\kappa = \frac{k_{fv}}{k_{fh}+k_{fv}}$
Permeability ratio of vug and fracture	$k_D = \frac{k_{fv}}{k_{fh}}$	Dimensionless well length	$h_{wD} = \frac{h_w}{r_w} \sqrt{\frac{k_{fv}}{k_{fh}}} \cos^2 \theta_w + \sin^2 \theta_w$

According to the dimensionless definition, the dimensionless forms of the differential equation and boundary conditions can be given by:

$$\left\{ \begin{aligned} & \kappa \frac{1}{r_D} \frac{\partial}{\partial r_D} \left( r_D \frac{\partial \bar{p}_{fD}}{\partial r_D} \right) + \frac{\partial}{\partial z_D} \left( \frac{\partial \bar{p}_{fD}}{\partial z_D} \right) + \lambda_{mf} (\bar{p}_{mD} - \bar{p}_{fD}) \\ & + \lambda_{vf} (\bar{p}_{vD} - \bar{p}_{fD}) = \omega_f s \bar{p}_{fD} (1 - \kappa) \frac{1}{r_D} \frac{\partial}{\partial r_D} \left( r_D \frac{\partial \bar{p}_{vD}}{\partial r_D} \right) \\ & + k_D \frac{\partial}{\partial z_D} \left( \frac{\partial \bar{p}_{vD}}{\partial z_D} \right) + \lambda_{mv} (\bar{p}_{mD} - \bar{p}_{vD}) - \lambda_{vf} (\bar{p}_{vD} - \bar{p}_{fD}) \\ & = \omega_v s \bar{p}_{vD} - \lambda_{mv} (\bar{p}_{mD} - \bar{p}_{vD}) - \lambda_{mf} (\bar{p}_{mD} - \bar{p}_{fD}) \\ & = \omega_m s \bar{p}_{mD} \\ & \bar{p}_{mD}(r_D, 0) = \bar{p}_{fD}(r_D, 0) = \bar{p}_{vD}(r_D, 0) \\ & = 0 \lim_{\varepsilon_D \rightarrow 0} \int_{z_{wD}-\varepsilon_D/2}^{z_{wD}+\varepsilon_D/2} \left[ \lim_{\delta_D \rightarrow 0} \left( \kappa r_D \frac{\partial \bar{p}_{fD}}{\partial r_D} + (1 - \kappa) r_D \frac{\partial \bar{p}_{vD}}{\partial r_D} \right) \right]_{r_D=\varepsilon_D} dz_D \\ & = -\tilde{q}_D \bar{p}_{fD}(r_D, z_D = 0, t_D) \\ & = \frac{\partial \bar{p}_{mD}(r_D, z_D = 0, t_D)}{\partial z_D} = \frac{\partial \bar{p}_{vD}(r_D, z_D = 0, t_D)}{\partial z_D} \\ & = 0 \frac{\partial \bar{p}_{fD}(r_D, z_D = h_D, t_D)}{\partial z_D} = \frac{\partial \bar{p}_{mD}(r_D, z_D = h_D, t_D)}{\partial z_D} \\ & = \frac{\partial \bar{p}_{vD}(r_D, z_D = h_D, t_D)}{\partial z_D} = 0 \bar{p}_{fD}(r_D \rightarrow \infty, z_D, t_D) \\ & = \bar{p}_{mD}(r_D \rightarrow \infty, z_D, t_D) = \bar{p}_{vD}(r_D \rightarrow \infty, z_D, t_D) = 0 \end{aligned} \right. \quad (10)$$

where:  $k_D$  is permeability ratio between vug and fracture, dimensionless;  $\kappa$  is permeability ratio, dimensionless;  $\lambda_{mf}$  is

inter-porosity flow coefficient from matrix to fracture, dimensionless;  $\lambda_{mv}$  is inter-porosity flow coefficient from matrix to vuggy, dimensionless;  $\lambda_{vf}$  is inter-porosity flow coefficient from vuggy to fracture, dimensionless;  $\omega_f$  is fracture storativity ratio, dimensionless;  $\omega_m$  is matrix storativity ratio, dimensionless;  $\omega_v$  is vuggy storativity ratio, dimensionless;  $s$  is Laplace variables; subscripts D is dimensionless variables; superscripts - is variables in the Laplace domain;

By employing the finite cosine Fourier transform with respect to  $z_D$  in Eq. 10, and expressing dimensionless pressures of natural fracture and vug systems by dimensionless matrix system pressure in Laplace domain after the finite cosine Fourier transform, Eq. 10 can be described as:

$$\left\{ \begin{aligned} & \kappa \frac{1}{r_D} \frac{\partial}{\partial r_D} \left( r_D \frac{\partial \hat{\bar{p}}_{fD}}{\partial r_D} \right) + m_{1n} \hat{\bar{p}}_{fD} + \lambda \hat{\bar{p}}_{vD} = 0 \\ & (1 - \kappa) \frac{1}{r_D} \frac{\partial}{\partial r_D} \left( r_D \frac{\partial \hat{\bar{p}}_{vD}}{\partial r_D} \right) + \lambda \hat{\bar{p}}_{fD} + m_{2n} \hat{\bar{p}}_{vD} \\ & = 0 \lim_{\varepsilon_D \rightarrow 0} \left( \kappa r_D \frac{\partial \hat{\bar{p}}_{fD}}{\partial r_D} + (1 - \kappa) r_D \frac{\partial \hat{\bar{p}}_{vD}}{\partial r_D} \right)_{r_D=\varepsilon_D} \\ & = -h_D \cos \left( \frac{n\pi z'_D}{h_D} \right) \tilde{q}_D \\ & \hat{\bar{p}}_{fD}(r_D \rightarrow \infty, n, s) = \hat{\bar{p}}_{vD}(r_D \rightarrow \infty, n, s) \\ & = \hat{\bar{p}}_{mD}(r_D \rightarrow \infty, n, s) = 0 \end{aligned} \right. \quad (11)$$

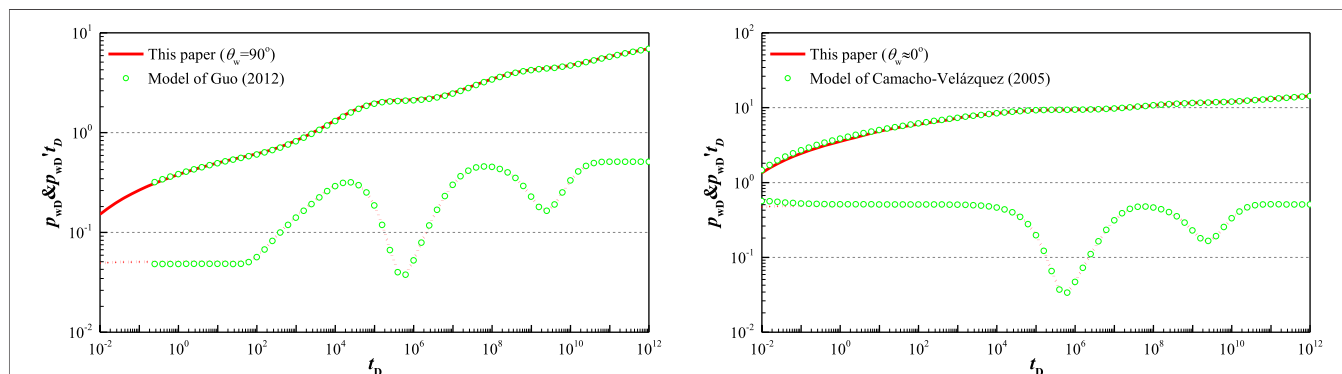


**FIGURE 5** | Comparison with Guo et al. (2012) and Camacho-Velázquez et al. (2005) models ( $h = 100, h_w = 100.4, r_w = 0.1, k_{fv} = 1, k_D = 1, \kappa = 0.7, \omega_f = 0.001, \omega_v = 0.1, \lambda_{mf} = 10^{-12}, \lambda_{mv} = 10^{-10}, \lambda_{vf} = 10^{-8}$ )

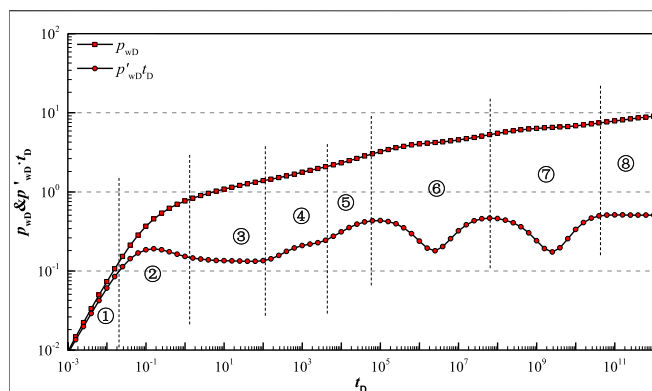


**FIGURE 6** | Pressure transient type curve of inclined well in FVCHRs with triple-porosity dual-permeability behavior ( $C_D = 0.1$ ,  $S = 0.1$ ,  $h = 100$ ,  $h_w = h/\cos(\psi)$ ,  $r_w = 0.1$ ,  $\theta_w = 75^\circ$ ,  $k_{fV} = 1$ ,  $k_D = 1$ ,  $\kappa = 0.7$ ,  $\omega_f = 0.01$ ,  $\omega_V = 0.1$ ,  $\lambda_{mf} = 10^{-12}$ ,  $\lambda_{mV} = 10^{-10}$ ,  $\lambda_{Vf} = 10^{-8}$ )

where:  $m_{1n} = \frac{\lambda_{mf}^2}{\lambda_{mf} + \lambda_{mV} + S\omega_m} - \lambda_{mf} - \lambda_{Vf} - \left( S\omega_f + \frac{n^2\pi^2}{h_D^2} \right)$ ;  $\lambda = \frac{\lambda_{mf}\lambda_{mV}}{\lambda_{mf} + \lambda_{mV} + S\omega_f} + \lambda_{Vf}$ ;

subscripted variable ( $n=0, 1, 2, \dots, n$ ).

By solving Eq. 10, the general point source solution for the top and bottom closed boundary, constant production and infinite lateral boundary FVCHRs with triple-porosity dual-permeability behavior can be obtained through Laplace transform and Fourier transform methods (Liu et al., 2019; Wang et al., 2019; Xue et al., 2019):

$$\bar{p}_D = \bar{q}_D \left[ \sum_{i=1}^2 C_{i0} K_0(\sigma_{i0} r_D) + 2 \sum_{n=1}^{\infty} \sum_{i=1}^2 C_{in} K_0(\sigma_{in} r_D) \cos\left(\frac{n\pi z_D}{h_D}\right) \cos\left(\frac{n\pi z'_D}{h_D}\right) \right] \quad (12)$$

where:  $C_{1n} = \frac{(1-a_2)}{[\kappa + (1-\kappa)a_1](1-a_2) - (1-a_1)[\kappa + (1-\kappa)a_2]}$ , ( $n = 0, 1, 2, \dots, n$ );  $C_{2n} = \frac{(1-a_1)}{[\kappa + (1-\kappa)a_2](1-a_1) - (1-a_2)[\kappa + (1-\kappa)a_1]}$ ;

$$r_D = \sqrt{(x_D - x'_D)^2 + (y_D - y'_D)^2}$$

It is useful to express the Eq. 12 in polar coordinates, let the polar coordinates of the points  $(x_D, y_D)$  and  $(x'_D, y'_D)$  be given by  $(r_D, \theta)$  and  $(r'_D, \theta')$  respectively according to Raghavan and Ozkan

(2017). We can do integration to the point source solution along inclined well in polar coordinates system as shown in Figure 4C. Therefore, the solution of the inclined well is obtain as following.

$$\bar{p}_{wD \text{ incline}} = \frac{1}{sh_{wD} \sin \psi'} \int_{-(h_{wD}/2) \sin \psi'}^{(h_{wD}/2) \sin \psi'} \left[ \sum_{i=1}^2 C_{i0} K_0(\sigma_{i0} R_D) + 2 \sum_{n=1}^{\infty} \sum_{i=1}^2 C_{in} K_0(\sigma_{in} R_D) \cos\left(\frac{n\pi z_D}{h_D}\right) \cos\left(\frac{n\pi z'_D}{h_D}\right) \right] dr'_D \quad (13)$$

where:  $K_0(x)$  is the second kind modified Bessel function;

$$R_D = \sqrt{(r_D \cos \theta - r'_D)^2 + (r_D \sin \theta)^2}; z'_D = z_{wD} + r'_D \cot \psi'.$$

Although Gringarten et al. (1974) pointed out that the wellbore pressure of horizontal well and infinite conductivity hydraulic fractured well can be calculate by an equivalent-pressure point  $x_D = 0.732$ , there is difference between horizontal well and inclined well. Fortunately, Cinco-Ley et al. (1975) given the equivalent-pressure point of inclined well in the polar coordinates. As following:

$$r_D = \sqrt{1 + (0.3h_{wD} \sin \psi')^2}; \theta = \cos^{-1} \left( \frac{0.3h_{wD} \sin \psi'}{r_D} \right); z_D = z_{wD} \pm 0.3h_{wD} \cos \psi';$$

In order to enhance calculation speed of the inclined well, Ozkan and Raghavan (2000) provides an efficient algorithm to compute transient pressure responses of inclined wells in Laplace domain. The principle of convolution can be used to obtain solution with the effects of wellbore storage and skin factor, which could be given by

$$\bar{p}_{wD} = \frac{s\bar{p}_{wD \text{ incline}} + S}{s + C_D s^2 (s\bar{p}_{wD \text{ incline}} + S)} \quad (14)$$

where:  $p_{wD}$  is dimensionless wellbore pressure with wellbore storage and skin;  $p_{wD \text{ incline}}$  is dimensionless wellbore pressure without wellbore storage and skin;  $C_D$  is dimensionless wellbore storage;  $S$  is skin factor.

The solution of inclined well in real domain for FVCHRs with triple-porosity dual-permeability behavior is obtained by employing Stehfest (1970) numerical inversion algorithm. Dimensionless pressure and its derivative type curves are drawn analyzed.

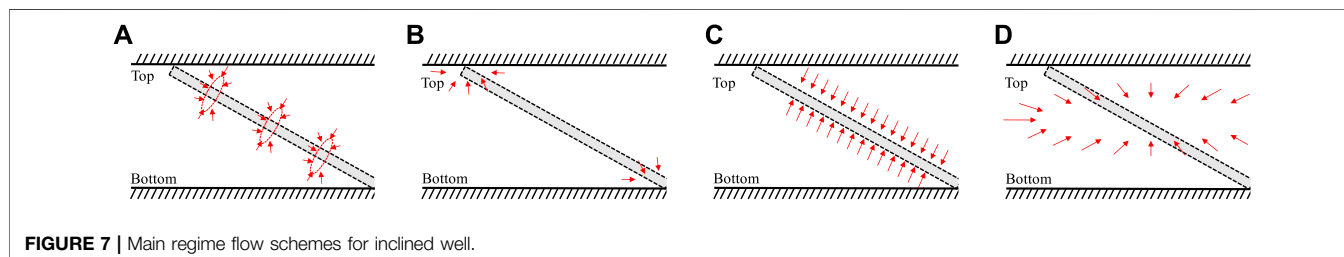


**FIGURE 7** | Main regime flow schemes for inclined well.

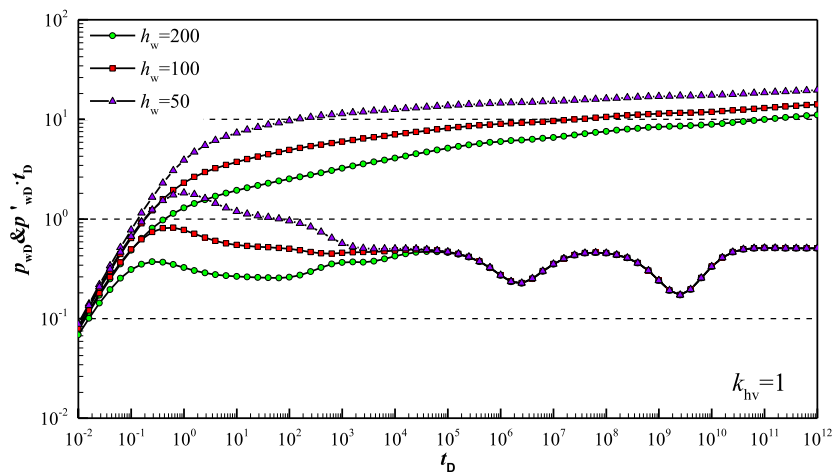


**FIGURE 8 |** Type curve affected by length of inclined well ( $C_D = 0.1, S = 0.1, h = 100, r_w = 0.1, \theta_w = 60^\circ, k_{hv} = 1, k_D = 1, \kappa = 0.7, \omega_f = 0.01, \omega_v = 0.1, \lambda_{mf} = 10^{-12}, \lambda_{mv} = 10^{-10}, \lambda_{vf} = 10^{-8}$ )

## MODEL VERIFICATION

Compared with vertical wells and horizontal wells, wellbore pressure solution of the inclined well is more universal, so our work expands analytical solution of vertical well and horizontal well in FVCHRs with triple-porosity dual-permeability behavior. However, in order to verify the correctness of our model and solution, the simplified model of this paper is compared with analytical solution of horizontal well for FVCHRs with triple-porosity dual-permeability behavior (Guo et al., 2012) and vertical well for FVCHRs with triple-porosity dual-permeability behavior (Camacho-Velázquez et al., 2005).

Guo et al. (2012) established the mathematical model of the horizontal well under condition of different outer boundary in FVCHRs with triple-porosity dual-permeability behavior. What is different with our model is that they assumed that fluid of the naturally fractured and the matrix system are directly flow into the wellbore, inter-porosity flow from matrix to fracture and inter-porosity flow from vug to matrix and fracture is considered. In order to make verification result reliable, if parameters

$\lambda_{vf}, \lambda_{vm}, \lambda_{mf}$  of the Guo' model are replaced by parameters  $\lambda_{mf}, \lambda_{mv}, \lambda_{vf}$  of this paper correspondingly and corresponding value of these parameters is same. On the basis of replacement, we can prove that our model is same with Guo' model. If  $\theta_w$  is  $90^\circ$  in our paper, and  $h_w = 1,000$  of our paper, inclined well of this paper will become horizontal well, which is similar to the Guo et al.' model with horizontal well length is 500. Other common parameters are same and their values are:  $h = 100, r_w = 0.1, k_{hv} = 1, k_D = 1, \kappa = 0.7, \omega_f = 0.001, \omega_v = 0.1, \lambda_{mf} = 10^{-12}, \lambda_{mv} = 10^{-10}, \lambda_{vf} = 10^{-8}$ . As shown in Figure 5A, result reaches a good agreement.

Camacho-Velázquez et al. (2005) established the mathematical model of the vertical well in FVCHRs with triple-porosity dual-permeability behavior. It is assumed that fluid of the fracture and the vug system are directly flow into the wellbore. Inter-porosity flow from vug to fracture and inter-porosity flow from matrix to vug and fracture is considered, which is same with our assumption. If inclination angle of wellbore is less than  $5^\circ$  and well is penetrated fully, we can think that our model is equal to vertical well. Other common

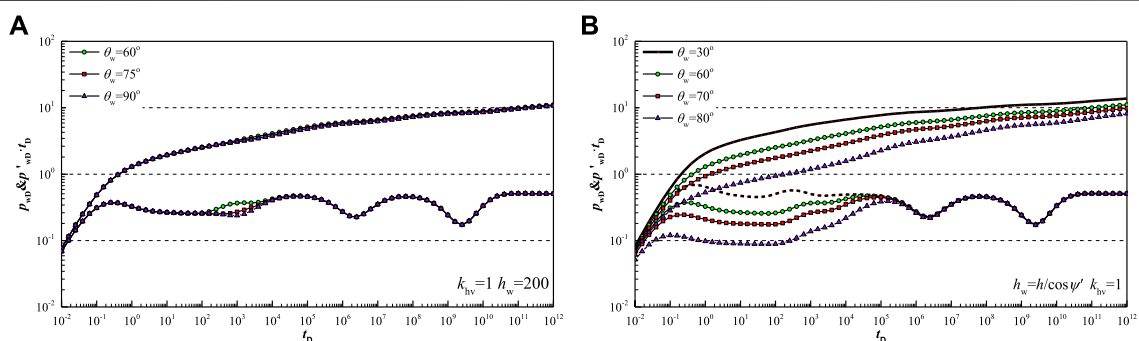


**FIGURE 9 |** Type curve affected by inclination angle of well ( $C_D = 0.1, S = 0.1, h = 100, h_w = h/\cos(\psi'), r_w = 0.1, k_{hv} = 1, k_D = 1, \kappa = 0.7, \omega_f = 0.01, \omega_v = 0.1, \lambda_{mf} = 10^{-12}, \lambda_{mv} = 10^{-10}, \lambda_{vf} = 10^{-8}$ )

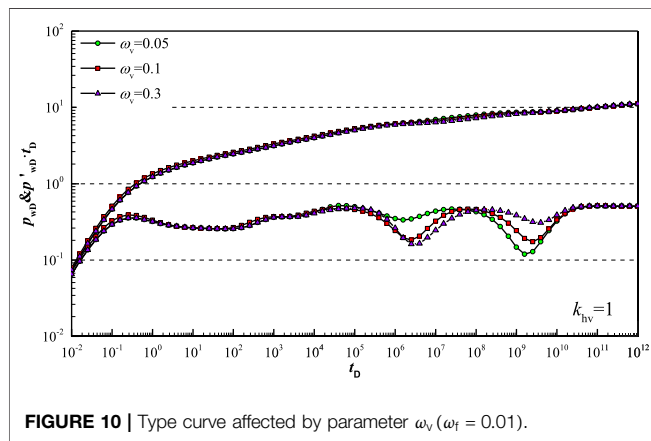


FIGURE 10 | Type curve affected by parameter  $\omega_v$  ( $\omega_f = 0.01$ ).

parameters are same and their values are:  $h = 100$ ,  $r_w = 0.1$ ,  $k_{hv} = 1$ ,  $k_D = 1$ ,  $\kappa = 0.7$ ,  $\omega_f = 0.001$ ,  $\omega_v = 0.1$ ,  $\lambda_{mf} = 10^{-12}$ ,  $\lambda_{mv} = 10^{-10}$ ,  $\lambda_{vf} = 10^{-8}$ . As shown in **Figure 5A**, result reaches a good agreement.

By comparing with horizontal and vertical well in FVCHRs with triple-porosity dual-permeability behavior, the results reached a good agreement, which verifies the correctness of our model and solution.

## TYPE CURVE AND SENSITIVITY OF PARAMETERS

### Type Curve

**Figure 6** shows type curves of dimensionless pressure and its derivative of inclined well with dual-permeability behavior. According to the characteristic of the dimensionless pressure derivative curve, the type curve of inclined well can be divided into eight flow regimes for FVCHRs with triple-porosity dual-permeability behavior, which mainly includes well storage regime, skin effect regime, early vertical radial flow regime (**Figure 7A**), top and bottom boundary reflection (**Figure 7B**), linear flow regime (**Figure 7C**), inter-porosity flow and pseudo-radial flow regime (**Figure 7D**).

**Regime①:** Wellbore storage regime. During the pure wellbore storage, pressure and its derivative curves coincide and is a unit-slope straight line.

**Regime②:** Skin effect regime. Due to consideration of skin, pressure derivative curve looks like a “hump.”

**Regime③:** Early vertical radial flow regime. Pressure derivative curve is a constant value horizontal line in log-log plot (**Figure 7A**).

**Regime④:** Top and bottom boundary reflection regime. Pressure derivative curve take on a small step in log-log plot. However, this stage may disappear because of change of the length of wellbore and inclination angle of wellbore (**Figure 7B**).

**Regime⑤:** Linear flow regime. Pressure derivative curve is 1/2-slope straight line in log-log plot. Shorter well length lead to disappearance of 1/2-slope straight line (**Figure 7C**).

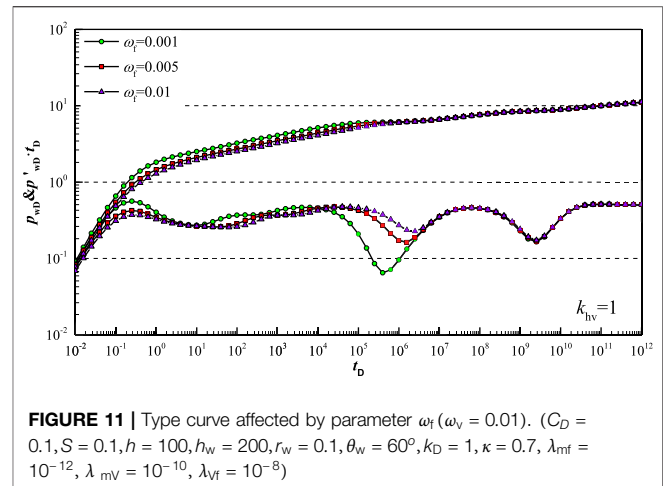


FIGURE 11 | Type curve affected by parameter  $\omega_f$  ( $\omega_v = 0.01$ ). ( $C_D = 0.1$ ,  $S = 0.1$ ,  $h = 100$ ,  $h_w = 200$ ,  $r_w = 0.1$ ,  $\theta_w = 60^\circ$ ,  $k_D = 1$ ,  $\kappa = 0.7$ ,  $\lambda_{mf} = 10^{-12}$ ,  $\lambda_{mv} = 10^{-10}$ ,  $\lambda_{vf} = 10^{-8}$ )

**Regime⑥:** Inter-porosity flow from vug to fracture. Because vug permeability is better than matrix permeability, inter-porosity flow from vug to fracture appear firstly. The curve of pressure derivative is V-shaped.

**Regime⑦:** Inter-porosity flow from matrix to vug and fracture. The curve of pressure derivative is V-shaped, which is controlled by parameters  $\omega_m$  and  $\omega_v$ .

**Regime⑧:** Pseudo-radial flow regime. Inter-porosity flows have already finished and the curve of pressure derivative is a 0.5-value horizontal line in log-log plot (**Figure 7D**).

### Sensitivity of Parameters

**Figure 8** shows type curve affected by length of inclined well in FVCHRs with triple-porosity dual-permeability behavior. Because short inclined well length can decrease contract area between reservoirs and wellbore, the short inclined well length can increase pressure loss that fluid flows into wellbore. Therefore, short inclined well length can lead to high position of pressure curve in the whole flow regime in log-log plot and make top and bottom boundary reflection regime disappear and spherical flow characteristic more obvious in pressure derivative curve.

**Figure 9** shows type curve affected by inclination angle in FVCHRs with triple-porosity dual-permeability behavior. It is assumed that length of inclined well keep constant when inclination angle changes. The large inclination angle change can only lead to disappearance of the top and bottom boundary reflection regime of pressure derivative curve without consideration of anisotropy (**Figure 9A**). However, if the inclined well is penetrated fully, inclination angle has a more effect on pressure and its derivative curves than inclined well penetrated partly. With the increasing of inclination angle length of inclined well become length, which leads to low position of pressure curve in whole regime and low position of pressure derivative curve during early vertical radial flow regime (**Figure 9B**).

**Figure 10** shows type curve affected by vug storativity ratio in FVCHRs with triple-porosity dual-permeability behavior.

According the flow model shown **Figure 3A**, fluid of the vug system do not flow into fracture, but also flow into wellbore directly. Therefore, as shown in **Figure 10**, small vug storativity ratio can make the second V-shaped of the pressure derivative curve become more and more deep while the first V-shaped become more and more shallow.

**Figure 11** shows type curve affected by fracture storativity ratio in FVCHRs with triple-porosity dual-permeability behavior. According the flow model shown **Figure 3A**, fluid of fracture system only flow into wellbore directly. Therefore, as is shown in **Figure 11**, fracture storativity ratio has an influence on the first V-shaped. The first V-shaped become more and more deeply with the decrease of fracture storativity ratio. The position of pressure curve become higher during vertical radial flow regime and top and bottom boundary reflection regime.

**Figure 12** shows type curve affected by inter-porosity flow coefficient  $\lambda_{vf}$  in FVCHRs with triple-porosity dual-permeability behavior. According the flow model shown **Figure 3A**, fluid of fracture system only flow into wellbore directly. Therefore, as shown in **Figure 12**, inter-porosity flow coefficient  $\lambda_{vf}$  has an influence on the first V-shaped. As  $\lambda_{vf}$  increase, starting time of inter-porosity flow from vug system to fracture system become earlier, which makes the first V-shaped of pressure derivative move towards left in log-log plot.

**Figure 13** shows type curve affected by inter-porosity flow coefficient  $\lambda_{mv}$  in FVCHRs with triple-porosity dual-permeability behavior. As shown in **Figure 13**, inter-porosity flow coefficient  $\lambda_{mv}$  has an influence on the second V-shaped. As  $\lambda_{mv}$  increase, starting time of inter-porosity flow from matrix system to vug system become earlier, which makes the second V-shaped of pressure derivative move towards left in log-log plot. Of course, with the flow coefficient  $\lambda_{mv}$  keep increasing, first V-shaped may be covered and first V-shaped become more deeply.

**Figure 14** shows type curve affected by inter-porosity flow coefficient  $\lambda_{mf}$  in FVCHRs with triple-porosity dual-permeability behavior. As shown in **Figure 14**, inter-porosity flow coefficient  $\lambda_{mf}$  has an influence on the second V-shaped. As  $\lambda_{mf}$  increase, starting time of inter-porosity flow from matrix system to fracture system become earlier, which makes the second V-shaped of pressure derivative move towards left in log-log plot. Of course,

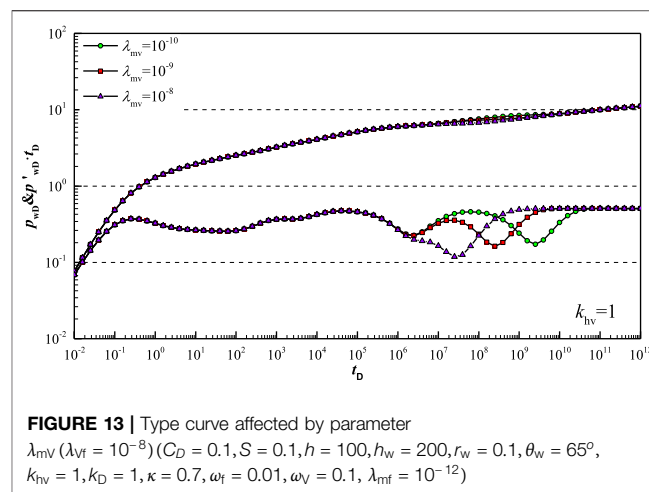


**FIGURE 13 |** Type curve affected by parameter  $\lambda_{mv}$  ( $\lambda_{vf} = 10^{-8}$ ) ( $C_D = 0.1, S = 0.1, h = 100, h_w = 200, r_w = 0.1, \theta_w = 65^\circ, k_{hv} = 1, k_D = 1, \kappa = 0.7, \omega_f = 0.01, \omega_v = 0.1, \lambda_{mf} = 10^{-12}$ )

because some of fluid of fracture system come from supplement of vug system, but also others come from supplement of matrix system. Therefore, when inter-porosity flow coefficient  $\lambda_{mf} < \lambda_{vf}$ , the change of inter-porosity flow coefficient  $\lambda_{mf}$  has an influence on pressure derivative curve slightly.

**Figure 15** shows type curve affected by permeability ratio  $\kappa$  in FVCHRs with triple-porosity dual-permeability behavior. The large permeability ratio indicates that permeability of fracture system is higher than vug system, and vug storativity capacity is lower than fracture storativity capacity. Therefore, the first V-shaped of pressure derivative curve becomes more and more deeply with the increase of permeability ratio.

**Figure 16** shows type curve affected by permeability ratio  $k_{hv}$  between horizontal permeability and vertical permeability in FVCHRs with triple-porosity dual-permeability behavior. The large  $k_{hv}$  indicates that permeability of horizontal permeability is higher than vertical permeability. Because inclination angle of wellbore is considered in vertical direction, difference between vertical and horizontal flow is shown obviously during early vertical radial flow regime. The greater the value of  $k_{hv}$ , the greater the loss of wellbore flow pressure in the vertical direction.

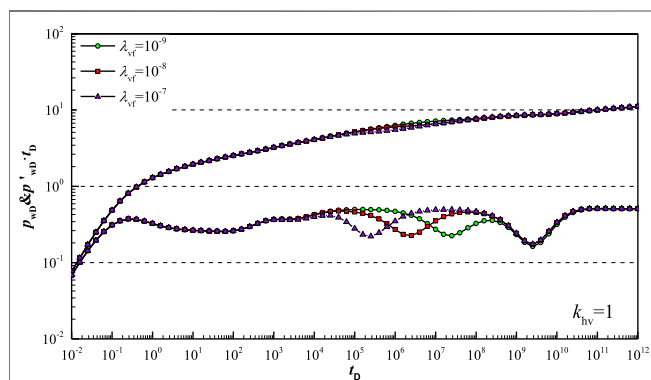


**FIGURE 12 |** Type curve affected by parameter  $\lambda_{vf}$  ( $\lambda_{mv} = 10^{-10}$ )

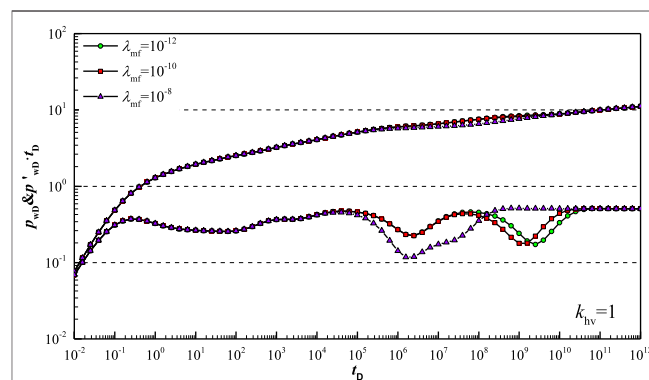


**FIGURE 14 |** Type curve affected by parameter  $\lambda_{mf}$  ( $\kappa = 0.7$ )



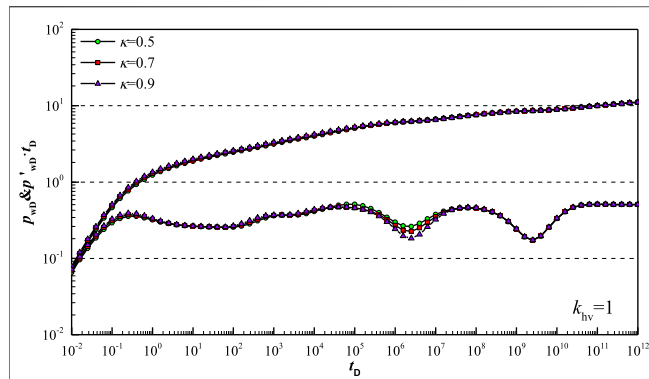


**FIGURE 15 |** Type curve affected by parameter  $\kappa$  ( $\lambda_{mf} = 10^{-12}$ ) ( $C_D = 0.1$ ,  $S = 0.1$ ,  $h = 100$ ,  $h_w = 200$ ,  $r_w = 0.1$ ,  $\theta_w = 60^\circ$ ,  $k_{fV} = 1$ ,  $k_D = 1$ ,  $\omega_f = 0.01$ ,  $\omega_v = 0.1$ ,  $\lambda_{mV} = 10^{-12}$ ,  $\lambda_{vF} = 10^{-8}$ )

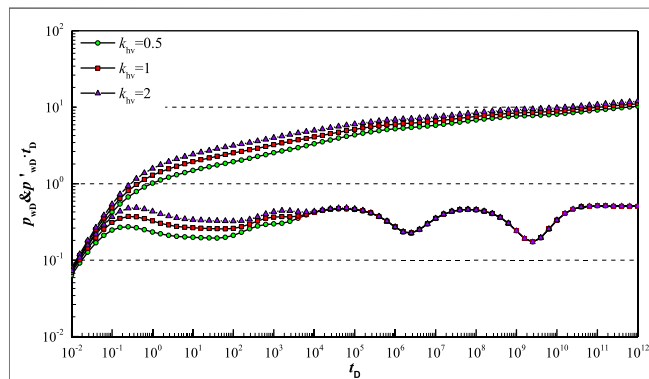


**FIGURE 16 |** Type curve affected by parameter  $k_{hv}$  ( $C_D = 0.1$ ,  $S = 0.1$ ,  $h = 100$ ,  $h_w = 200$ ,  $r_w = 0.1$ ,  $\theta_w = 60^\circ$ ,  $k_D = 1$ ,  $\kappa = 0.7$ ,  $\omega_f = 0.01$ ,  $\omega_v = 0.1$ ,  $\lambda_{mV} = 10^{-12}$ ,  $\lambda_{vF} = 10^{-8}$ )

Therefore, large  $k_{hv}$  will lead to higher position of pressure and its derivative curve in early flow regime.

## CONCLUSION

It is assumed that fluid of vug system and fracture system flows into incline wellbore directly, and inter-porosity flow from vug

## REFERENCES

- Abadassah, D., and Ershaghi, I. (1986). Triple-porosity systems for representing naturally fractured reservoirs. *SPE Form. Eval.* 1 (2), 113–127. doi:10.2118/13409-pa
- Camacho-Velázquez, R., Vásquez-Cruz, M., Castrejón-Aivar, R., and Arana-Ortiz, V. (2005). Pressure-transient and decline-curve behavior in naturally fractured vuggy carbonate reservoirs. *SPE Reservoir Eval. Eng.* 8 (2), 95–111. doi:10.2118/77689-pa
- Cinco-Ley, H., Miller, F. G., and Ramey, H. J. (1975). Unsteady-State pressure distribution created by a directionally drilled well. *J. Petrol. Technol.* 27, 1392–1400. doi:10.2118/5131-PA

system to fracture system and inter-porosity flow from matrix system to vug and fracture system is considered. Pressure transient mathematical model of inclined well is established and solved by employing Laplace transform and finite cosine Fourier transform for FVCHRs with triple-porosity dual-permeability behavior. The following conclusions can be drawn:

- (1) A new analytical model was established to analysis pressure transient behavior of inclined well in FVCHRs with triple-porosity dual-permeability behavior.
- (2) The model was validated by comparing our simplified model with model of horizontal well and vertical well of FVCHRs with triple-porosity dual-permeability behavior. Result reach a good agreement.
- (3) Eight flow regimes, according to the characteristic of pressure derivative curve, can be recognized, and flow characteristic of each flow regime was described in detail.
- (4) The effect of some vital parameters (such as well length, well inclination angle and permeability ratio, etc.) on pressure and its derivative curves are analyzed.

## DATA AVAILABILITY STATEMENT

The raw data supporting the conclusions of this article will be made available by the authors, without undue reservation.

## AUTHOR CONTRIBUTIONS

XL and ZM designed the research; SQ and XT built the model; SQ and YX analyzed and simulated experimental data; ZM, TD and SQ were in charge of revision and writing.

## FUNDING

This article was supported by the National Natural Science Foundation of China (51704246) and Sichuan Science and Technology Project (18SYXHZ0090).

- Cinco-Ley, H., Ramey, H. J., and Miller, F. (2007). "Pseudo-skin factors for partially-penetrating directionally-drilled wells," in Fall meeting of the society of petroleum engineers of AIME, Dallas, TX, 28 September–1 October. doi:10.2523/5589-ms
- Corbett, P. W.M., Geiger, S., Borges, L., Garayev, M., Gonzalez, J. G., and Valdez, C. (2010). "Limitations in numerical well rest modelling of fractured carbonate rocks." in 72nd European association of geoscientists and engineers conference and exhibition 2010: a new Spring for geoscience, Barcelona, Spain, 14–17 June, 1135–1145. doi:10.2523/130252-ms
- Dong, W., Wang, X., and Wang, J. (2018). A new skin factor model for partially penetrated directionally-drilled wells in anisotropic reservoirs. *J. Petrol. Sci. Eng.* 161, 334–348. doi:10.1016/j.petrol.2017.11.062

- Du, X., Lu, Z., Li, D., Xu, Y., Li, P., and Lu, D. (2019). A novel analytical well test model for fractured vuggy carbonate reservoirs considering the coupling between oil flow and wave propagation. *J. Petrol. Sci. Eng.* 173, 447–461. doi:10.1016/j.petrol.2018.09.077
- Feng, G. Q., and Liu, Q.-G. (2015). Pressure transient behavior of a slanted well with an impermeable fault. *J. Hydrodyn.* 26 (6), 980–985. doi:10.1016/S1001-6058(14)60108-6
- Gao, B., Huang, X., Yao, J., Lv, X., and Wu, Y. (2016). Pressure transient analysis of a well penetrating a filled cavity in naturally fractured carbonate reservoirs. *J. Petrol. Sci. Eng.* 145, 392–403. doi:10.1016/j.petrol.2016.05.037
- Gringarten, A. C., and Ramey, H. J. (1973). Use of source and green's functions in solving unsteady-flow problems in reservoirs. *Soc. Pet. Eng. AIME J.* 13 (5), 285–296. doi:10.2118/3818-PA
- Gringarten, A. C., Ramey, H. J., and Raghavan, R. (1974). Unsteady-state pressure distributions created by a well with a single infinite-conductivity vertical fracture. *Soc. Pet. Eng. AIME J.* 14 (4), 347–360. doi:10.2118/4051-pa
- Guo, J. C., Nie, R. S., and Jia, Y. L. (2012). Dual permeability flow behavior for modeling horizontal well production in fractured-vuggy carbonate reservoirs. *J. Hydrol.* 464–465, 281–293. doi:10.1016/j.jhydrol.2012.07.021
- Jia, Y. L., Fan, X. Y., Nie, R. S., Huang, Q. H., and Jia, Y. L. (2013). Flow modeling of well test analysis for porous-vuggy carbonate reservoirs. *Transp. Porous Media* 97 (2), 253–279. doi:10.1007/s11242-012-0121-y
- Kuchuk, F., and Biryukov, D. (2014). Pressure-transient behavior of continuously and discretely fractured reservoirs. *SPE Reservoir Eval. Eng.* 17 (1), 82–97. doi:10.2118/158096-PA
- Kui, M. Q., Tan, X. H., Li, X. P., and Cai, J. (2017). Analysis on unsteady flow for power-law fluids in dual fractal media. *J. Porous Media* 20 (12), 1071–1086. doi:10.1615/JPorMedia.v20.i12.20
- Liu, J., Bodvarsson, G. S., and Wu, Y. S. (2003). Analysis of flow behavior in fractured lithophysal reservoirs. *J. Contam. Hydrol.* 62–63, 189–211. doi:10.1016/S0169-7722(02)00169-9
- Liu, Q., Xu, Y., Peng, X., Liu, Y., and Qi, S. (2019). Pressure transient analysis for multi-wing fractured wells in dual-permeability hydrocarbon reservoirs. *J. Petrol. Sci. Eng.* 180, 278–288. doi:10.1016/j.petrol.2019.05.013
- Nie, R. S., Meng, Y. F., Guo, J. C., and Jia, Y. L. (2012). Modeling transient flow behavior of a horizontal well in a coal seam. *Int. J. Coal Geol.* 92, 54–68. doi:10.1016/j.coal.2011.12.005
- Ozkan, E., and Raghavan, R. (1991). New solutions for well-test-analysis problems. Part 2. Computational considerations and applications. *SPE Form. Eval.* 6 (3), 369–378. doi:10.2118/18616-PA
- Ozkan, E., and Raghavan, R. (2000). A computationally efficient, transient-pressure solution for inclined wells. *SPE Reservoir Eval. Eng.* 3 (5), 414–425. doi:10.2118/66206-PA
- Ozkan, E., and Raghavan, R. (2004). New solutions for well-test-analysis problems: Part 1-Analytical Considerations (includes associated papers 28666 and 29213). *SPE Form. Evaluation.* 6 (03), 359–368. doi:10.2118/18615-PA
- Ozkan, E., Yildiz, T., and Raghavan, R. (1999). "Pressure-transient analysis of perforated slant and horizontal wells," in SPE Annual Technical Conference and Exhibition, Houston, TX, October 3–6, 1999.
- Pang, Y., Hu, X., Wang, S., Chen, S., Soliman, M. Y., and Deng, H. (2020). Characterization of adsorption isotherm and density profile in cylindrical nanopores: modeling and measurement. *Chem. Eng. J.* 396, 125212. doi:10.1016/j.cej.2020.125212
- Pruess, K., and Narasimhan, T. N. (1985). Practical method for modeling fluid and heat flow in fractured porous media. *Soc. Petrol. Eng. J.* 25 (1), 14–26. doi:10.2118/10509-pa
- Raghavan, R., and Ozkan, E. (2017). *A method for computing unsteady flows in porous media*. Oxon, UK: Routledge. doi:10.1201/9781315136387
- Song, F., Bo, L., Zhang, S., and Sun, Y. (2019). Nonlinear flow in low permeability reservoirs: modelling and experimental verification. *Adv. Geo-Energy Res.* 3, 76–81. doi:10.26804/ager.2019.01.06
- Stehfest, H. (1970). Algorithm 368: numerical inversion of Laplace transforms [D5]. *Commun. ACM* 13 (1), 47–49.
- Sun, Q., Zhang, N., Mohamed, F., and Wang, Y. (2018). Structural regeneration of fracture-vug network in naturally fractured vuggy reservoirs. *J. Petrol. Sci. Eng.* 165, 28–41. doi:10.1016/j.petrol.2017.11.030
- Tan, X. H., Jiang, L., Li, X. P., Zhang, B. J., and Li, X. C. (2018). Flow model of a multi-stage hydraulic fractured horizontal well based on tree-shaped fractal fracture networks. *J. Petrol. Sci. Eng.* 169, 494–503. doi:10.1016/j.petrol.2018.06.008
- Tontiwachwuthikul, P., Chan, C. W., Zeng, F., Liang, Z., Sema, T., and Chao, M. (Forthcoming 2020). Recent progress and new developments of applications of artificial intelligence (AI), knowledge-based systems (KBS), and machine learning (ML) in the petroleum industry. *Petroleum*. doi:10.1016/j.petlm.2020.08.001
- Van Everdingen, A. F., and Hurst, W. (1949). The application of the Laplace transformation to flow problems in reservoirs. *J. Petrol. Technol.* 1 (12), 305–324. doi:10.2118/949305-g
- Wang, L., Cheng, D., Xiang, L., Chen, X., and Xia, Z. (2019). Pressure transient analysis for asymmetrically fractured wells in dual-permeability organic compound reservoir of hydrogen and carbon. *Int. J. Hydrog. Energy* 44 (11), 5254–5261. doi:10.1016/j.ijhydene.2018.08.082
- Wang, L., Wang, X., Luo, E., and Wang, J. (2014). Analytical modeling of flow behavior for wormholes in naturally fractured-vuggy porous media. *Transp. Porous Media* 105 (3), 539–558. doi:10.1007/s11242-014-0383-7
- Wang, M., Fan, Z., Dong, X., Song, H., Zhao, W., and Xu, G. (2018). Analysis of flow behavior for acid fracturing wells in fractured-vuggy carbonate reservoirs. *Math. Probl. Eng.* 2018 (PT. 3), 6431910. doi:10.1155/2018/6431910
- Wang, Q., Yang, S., Glover, P. W. J., Lorinczi, P., Qian, K., and Wang, L. (2020). Effect of pore-throat microstructures on formation damage during miscible CO<sub>2</sub> flooding of tight sandstone reservoirs. *Energy Fuels* 34 (4), 4338–4352. doi:10.1021/acs.energyfuels.0c00158
- Warren, J. E., and Root, P. J. (1963). The behavior of naturally fractured reservoirs. *Soc. Petrol. Eng. J.* 3 (3), 245–255. doi:10.2118/426-pa
- Wu, Y. S., Liu, H. H., and Bodvarsson, G. S. (2004). A triple-continuum approach for modeling flow and transport processes in fractured rock. *J. Contam. Hydrol.* 73 (1–4), 145–179. doi:10.1016/j.jconhyd.2004.01.002
- Wu, Y. S., Yuan, D., Kang, Z., and Fakcharoenphol, P. (2011). A multiple-continuum model for simulating single-phase and multiphase flow in naturally fractured vuggy reservoirs. *J. Petrol. Sci. Eng.* 78 (1), 13–22. doi:10.1016/j.petrol.2011.05.004
- Xing, C., Yin, H., Liu, K., Li, X., and Fu, J. (2018). Well test analysis for fractured and vuggy carbonate reservoirs of well drilling in large scale cave. *Energies* 11 (1), 1–15. doi:10.3390/en11010080
- Xue, L., Chen, X., and Wang, L. (2019). Pressure transient analysis for fluid flow through horizontal fractures in shallow organic compound reservoir of hydrogen and carbon. *Int. J. Hydrog. Energy* 44 (11), 5245–5253. doi:10.1016/j.ijhydene.2018.08.084
- Yildiz, T., and Ozkan, E. (1999). Pressure-transient analysis for perforated wells. *SPE J.* 4. doi:10.2118/56878-PA
- Yin, C. (2018). Test and analysis on the permeability of induced fractures in shale reservoirs. *Nat. Gas. Ind. B* 5 (5), 513–522. doi:10.1016/j.ngib.2018.03.006

**Conflict of Interest:** The authors declare that the research was conducted in the absence of any commercial or financial relationships that could be construed as a potential conflict of interest.

Copyright © 2020 Qi, Tan, Li, Meng, Xu and Tang. This is an open-access article distributed under the terms of the Creative Commons Attribution License (CC BY). The use, distribution or reproduction in other forums is permitted, provided the original author(s) and the copyright owner(s) are credited and that the original publication in this journal is cited, in accordance with accepted academic practice. No use, distribution or reproduction is permitted which does not comply with these terms.



# Implementation of Ion Exchange Processes for Carbon Dioxide Mineralization Using Industrial Waste Streams

## OPEN ACCESS

### Edited by:

Kaiqiang Zhang,  
Imperial College London,  
United Kingdom

### Reviewed by:

Ziqing Pan,  
Imperial College London,  
United Kingdom  
Adam Hughmanick Berger,  
Electric Power Research Institute  
(EPRI), United States

### \*Correspondence:

Dante A. Simonetti  
dasimonetti@ucla.edu

### <sup>†</sup>Present address:

Abdulaziz Alturki,  
Department of Chemical Engineering,  
King Abdulaziz University, Rabigh,  
Saudi Arabia

### <sup>‡</sup>Present address:

Erika Callagon La Plante,  
Department of Materials Science and  
Engineering, University of Texas,  
Arlington, TX, United States

### Specialty section:

This article was submitted to  
Advanced Clean Fuel Technologies,  
a section of the journal  
Frontiers in Energy Research

**Received:** 25 September 2020

**Accepted:** 18 November 2020

**Published:** 10 December 2020

### Citation:

Bustillos S, Alturki A, Prentice D, La  
Plante EC, Rogers M, Keller M,  
Ragipani R, Wang B, Sant G and  
Simonetti DA (2020) Implementation of  
Ion Exchange Processes for Carbon  
Dioxide Mineralization Using  
Industrial Waste Streams.  
Front. Energy Res. 8:610392.  
doi: 10.3389/fenrg.2020.610392

Steven Bustillos<sup>1,2</sup>, Abdulaziz Alturki<sup>1†</sup>, Dale Prentice<sup>2,3,4</sup>, Erika Callagon La Plante<sup>2,3‡</sup>, Mitchell Rogers<sup>1</sup>, Mark Keller<sup>1</sup>, Raghavendra Ragipani<sup>5</sup>, Bu Wang<sup>5</sup>, Gaurav Sant<sup>2,3,4,6,7</sup> and Dante A. Simonetti<sup>1,3\*</sup>

<sup>1</sup> Department of Chemical and Biomolecular Engineering, University of California Los Angeles, Los Angeles, CA, United States,

<sup>2</sup> Department of Civil and Environmental Engineering, Laboratory for the Chemistry of Construction Materials (LC2), University of California Los Angeles, Los Angeles, CA, United States, <sup>3</sup> Institute for Carbon Management, University of California, Los Angeles, Los Angeles, CA, United States, <sup>4</sup> Department of Civil and Environmental Engineering, University of California, Los Angeles, Los Angeles, CA, United States, <sup>5</sup> Department of Civil and Environmental Engineering, University of Wisconsin, Madison, WI, United States, <sup>6</sup> Department of Materials Science and Engineering, University of California, Los Angeles, Los Angeles, CA, United States, <sup>7</sup> California NanoSystems Institute, University of California, Los Angeles, Los Angeles, CA, United States

Sequestration of CO<sub>2</sub> within stable mineral carbonates (e.g., CaCO<sub>3</sub>) represents an attractive emission reduction strategy because it offers a leakage-free alternative to geological storage of CO<sub>2</sub> in an environmentally benign form. However, the pH of aqueous streams equilibrated with gaseous streams containing CO<sub>2</sub> (pH < 4) are typically lower than that which is required for carbonate precipitation (pH > 8). Traditionally, alkalinity is provided by a stoichiometric reagent (e.g., NaOH) which renders these processes environmentally hazardous and economically unfeasible. This work investigates the use of regenerable ion-exchange materials to induce alkalinity in CO<sub>2</sub>-saturated aqueous solutions such that the pH shift required for mineralization occurs without the need for stoichiometric reagents. Na<sup>+</sup>-H<sup>+</sup> exchange isotherms (at [H<sup>+</sup>] = 10<sup>-8</sup>–10<sup>-1</sup> M) and rates were measured for 13X and 4A zeolites and TP-207 and TP-260 organic exchange resins in batch equilibrium and fixed-bed exchange experiments, respectively. At solutions equilibrated with CO<sub>2</sub> at 1.0 atm (pH = 3.9), H<sup>+</sup> exchange capacities for the materials were similar (1.7–2.4 mmol H<sup>+</sup>/g material) and resulted in pH increases from 3.9 to greater than 8.0. Multi-component mixtures using Ca<sup>2+</sup> and Mg<sup>2+</sup> cations (at 10<sup>-3</sup>–10<sup>-1</sup> M) in CO<sub>2</sub>-saturated water were used to probe competitive ion exchange. The presence of divalent cations in solution inhibited H<sup>+</sup> exchange, reducing capacities to as low as 0.2 mmol H<sup>+</sup>/g for both resins and zeolites. Dynamic H<sup>+</sup> exchange capacities in fixed-bed ion exchange columns were similar to equilibrium values for resins (~1.5 mmol/g) and zeolites (~0.8 mmol/g) using inlet solutions that were equilibrated with gaseous streams of CO<sub>2</sub> at 1.0 atm. However, exchange kinetics were limited by intraparticle diffusion as indicated by the increased rate parameters with increasing inlet flow rates (20–160 cm<sup>3</sup> min<sup>-1</sup>). Experimental calcite precipitation from mixing the alkaline CO<sub>3</sub><sup>2-</sup>-rich water solution obtained from the ion-exchange column with a simulated liquid waste stream solution achieved thermodynamic maximum yields. The

results from these studies indicate that ion exchange processes can be used as an alternative to the addition of stoichiometric bases to induce alkalinity for the precipitation of CaCO<sub>3</sub>, thereby opening a pathway toward sustainable and economic mineralization processes.

**Keywords:** carbon dioxide, mineralization, sustainable manufacturing, calcium carbonate, ion exchange

## INTRODUCTION

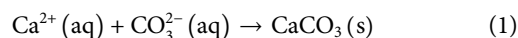
From 1975 to 2018, atmospheric CO<sub>2</sub> levels have dramatically increased from 250 to 410 ppm. The International Energy Outlook reported that world energy carbon dioxide (CO<sub>2</sub>) emissions would reach 35 gigatons CO<sub>2</sub> equivalent (Gt CO<sub>2</sub>e) by 2020 (IEA, 2020b). Of these emissions, thirty-two percent (17.8 Gt CO<sub>2</sub>e) have been generated during primary energy consumption of oil and gas in the transportation and industrial sectors (IEA, 2019; IEA, 2020a). In the United States, transportation emissions (totaling 1.9 Gt CO<sub>2</sub>e in 2018 Nyquist and Ruys, 2009; IEA, 2019) are generated via distributed sources and must be mitigated via direct air capture technology, industrial power generation [1.0 Gt CO<sub>2</sub>e in 2018 from direct combustion of fossil fuels for energy (Nyquist and Ruys, 2009; IEA, 2019)] can be considered as point sources of CO<sub>2</sub>. In addition to non-electric power generation, oil and gas production operations (i.e., refineries, onshore oil and natural gas production, and natural gas processing) contribute greater than 10% [0.34 Gt CO<sub>2</sub>e per year (Sofia Plagakis, 2013; Allen, 2016; U.S. Department of Energy, 2019)] of emissions associated with the oil and gas sector.

Post-combustion capture of CO<sub>2</sub> [e.g., from power plants using amine-based processes (Kim et al., 2016; El Hadri et al., 2017; Kar et al., 2019)] and storage in geological formations (CCS) is the current state-of-the-art for CO<sub>2</sub> emissions mitigation. Decades of process optimization (Cohen et al., 2012; Mores et al., 2014; Bui et al., 2014) and large theoretical storage capacities in the United States (Drage et al., 2012; Armstrong and Styring, 2015; Zhang et al., 2016) make amine-based CCS processes particularly effective for large point source emitters [e.g., fossil fuel fired power plants (Manzolini et al., 2015; Dutcher et al., 2015; Rao and Rubin, 2020)]. However, large energy demands [>0.36 MWh per ton CO<sub>2</sub> captured for streams with less than 12% CO<sub>2</sub> (Dutcher et al., 2015; Liu et al., 2019)], high capital costs of large amine plants (Dutcher et al., 2015; Oh et al., 2018; Baseline Survey, 2019), and high operating expenses (e.g., for pipeline transportation and for storage site monitoring) are barriers for the use of amine-based processes in the oil and gas sector where emissions are more dilute and/or distributed [e.g., less than 3% CO<sub>2</sub> in flare gases from refineries, petrochemical plants, and natural gas wells (Chaikittisilp et al., 2011; Choi et al., 2011a; Choi et al., 2011b)]. Thus, the low carbon future envisioned to combat climate change will require new technologies for CO<sub>2</sub> emissions mitigation from primary energy users and during oil and gas recovery.

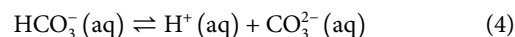
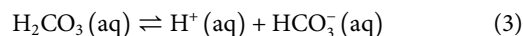
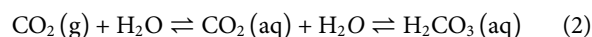
Sequestration of CO<sub>2</sub> as a solid carbonate (i.e., mineralization) is an alternative emission mitigation strategy opposed to post-

combustion capture of CO<sub>2</sub>. CO<sub>2</sub> is captured as a stable carbonate solid (usually in the form of calcium or magnesium carbonates) via chemical reaction with Ca/Mg ions in alkaline aqueous solutions (Seifritz, 1990; Azdarpour et al., 2014). Mineralization-based CO<sub>2</sub> capture and storage involve inherently lower energy processes because the CO<sub>2</sub> capture and storage occur without requiring a separate removal/concentration step (i.e., absorption from a vapor phase). These processes also exploit the favorable thermodynamics of carbonate precipitation reactions ( $\Delta G = -1129.1$  kJ/mol for calcite precipitation). By avoiding the CO<sub>2</sub> capture steps, mineralization-based approaches can be applied across a wide range of CO<sub>2</sub> concentrations (i.e., atmospheric concentrations to 100 vol. % CO<sub>2</sub>) and temperatures (i.e., ambient to ~90 °C) without increasing energy requirements [i.e., associated with large heat duties for thermal swing amine-based processes (Zhang et al., 2016)]. These processes are also insensitive to the impurities in CO<sub>2</sub>-containing streams (e.g., hydrocarbons and H<sub>2</sub>S). Thus, mineralization approaches represent an attractive alternative to CCS for CO<sub>2</sub> emission mitigation in the oil and gas sector because reduced process complexity and broad operating conditions enable modularity with few unit operations (i.e., process intensification) and flexibility in fulfilling carbon management goals across diverse locations and settings without the need for transport infrastructure (e.g., pipelines, compression stations, etc.).

CO<sub>2</sub> mineralization (e.g., as calcium carbonate) occurs via the following reaction



The speciation reactions that describe the CO<sub>2</sub>-H<sub>2</sub>O system are written as:

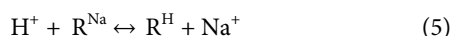


In general, the concentration of CO<sub>3</sub><sup>2-</sup> anions (and thus, the extent of carbonate precipitation) depends on pH (e.g., in water, CO<sub>3</sub><sup>2-</sup> is the dominant carbon species at pH > 10.33 (King and Farlow, 2000; Cerozi and Fitzsimmons, 2016), so the mineralization strategy described above requires sources of Ca/Mg ions and alkalinity. Approximately 22 billion barrels of liquid-waste water, known as produced water (PW), is produced during oil and gas extraction yearly (Guerra et al., 2011; Roach et al., 2013; Dastgheib et al., 2014; Scanlon et al., 2020;). The vast majority of PW is injected for disposal, resulting in only 0.6% of PW utilized for beneficial reuse (Guerra et al., 2011; Dastgheib et al., 2014; Scanlon et al., 2020). After separation of organic



components, PW is rich in primarily Na<sup>+</sup>, Ca<sup>2+</sup>, Mg<sup>2+</sup> and Cl<sup>-</sup> ions (0.050–3.0 M) (Blondes et al., 2018). These high cation concentrations make PW viable sources of cations for mineralization processes. However, these streams are typically produced at 4 < pH < 7 (with bicarbonate, HCO<sub>3</sub><sup>-</sup>, as the predominant species) (Blondes et al., 2018). The addition of caustic soda (NaOH) to increase the pH of these streams would render mineralization processes uneconomical because of the costs and hazards of using NaOH. Previous studies have explored the use of alkaline solid wastes (i.e., combustion fly ashes and slags) (Teir et al., 2007; Said et al., 2013; Chang et al., 2017; Humbert and Castro-Gomes, 2019), however, this still involves the use of a stoichiometric reagent whose production occurs in much lower abundance (130 million tons per year) (Federal Highway Administration, 2016; Humbert and Castro-Gomes, 2019) compared to CO<sub>2</sub> emissions from oil and gas processes (2.9 billion tons per year).

In this work, we investigate the use of ion exchange (IEX) processes as an alternative method to induce alkalinity for the precipitation of CaCO<sub>3</sub> using wastewater streams. Exposing CO<sub>2</sub>-saturated solutions (pH = 3.9) to regenerable IEX materials can shift the pH to >10.0, thereby creating favorable conditions for CO<sub>2</sub>-mineralization reactions. Ion exchange occurs between an electrolyte solution and similarly charged ions immobilized in an IEX material through a stoichiometric, reversible IEX reaction. Previous research has shown the reversible exchange of H<sup>+</sup> and Na<sup>+</sup> ions in a solution using clay minerals (Avena and De Pauli, 1998; Klein et al., 2010; Robin et al., 2015). H<sup>+</sup>-Na<sup>+</sup> ion exchange is described by:



where R<sup>Na/H</sup> is the IEX material in either sodium or proton form and H<sup>+</sup> and Na<sup>+</sup> are ions in solution. Protons in solution are introduced by dissolving CO<sub>2</sub> (pCO<sub>2</sub> = 1.0 atm; pH 3.9) into water according to Eqs. 2–4. As protons are removed from the solution via ion exchange, the equilibria of reactions 2–4 shifts toward the formation of CO<sub>3</sub><sup>2-</sup> ions. (Druckenmiller and Maroto-Valer, 2005) The resulting solution after IEX is an alkaline, CO<sub>3</sub><sup>2-</sup>-rich solution that can be used for CaCO<sub>3</sub> precipitation without the addition of caustic soda. The regeneration energy requirement for CO<sub>2</sub> capture using solid IEX materials is significantly lower than that of dry solid adsorbent and aqueous amine-based processes due to the absence of heat requirement since the process uses a concentrated sodium chloride waste stream to regenerate the materials (as described in this work) (Rao and Rubin, 2020).

IEX technology is commonly used to purify solutions by removing the dissolved ions by electrostatic sorption into IEX materials of various physical forms (Harland, 1994; Nasef, 2008). All zeolites can serve as IEX materials because of their specific structural features. However, for practical applications, high-alumina zeolites, or zeolites with Si/Al ratios in the range of 1–5 (Flanigen et al., 2010), are preferred for IEX applications because of the large number of acid sites (Inglezakis, 2005). IEX and selectivity in zeolites are mainly affected by the properties of the exchangeable cations, the concentration of the solution, the

presence of other cations and the characteristics of the zeolite such as channels and Si/Al ratios (Kirov and Filizova, 2012). Type A and Type X zeolites have high affinities for proton exchange in solutions of pH 3.9–7 because of their small Si/Al ratios (Munthali et al., 2014), making them suitable materials for a pH swing process. IEX resins contain functionalized ionizable groups placed along their polymer-backbone chains and are classified depending on the functional group into weakly (WAC) and strongly (SAC) acidic materials. The high H<sup>+</sup> affinity of WAC resins makes it advantageous to use instead of SAC resins because they can be regenerated using weakly acidic feeds. The pKa of the functional groups on WAC resins are generally greater than 2, whereas SAC resins generally require concentrated acids (pH < 2) because of the functional group's smaller pKa values (Kunin and Vassiliou, 1963; Leaković et al., 2000; Guo et al., 2013; Maul et al., 2014; Víctor-Ortega et al., 2017).

This work aims to identify commercially available IEX materials capable of shifting the pH of CO<sub>2</sub>-saturated solutions for subsequent precipitation as carbonates. Commercially available WAC resins (TP-207, TP-260) and synthetic zeolites (Type 4A, Type 13X) were selected to quantify exchange capacities and kinetic exchange parameters. These resins and synthetic zeolites were selected because of their weakly acidic functional groups and small Si/Al ratios (1.0 for Type 4A and 1.24 for Type 13X), respectively. IEX was studied across a range of H<sup>+</sup> concentrations from HCl and CO<sub>2</sub> batch solutions to determine the effect of proton and anion concentrations on the exchange capacities of these materials. Equilibrium IEX isotherms were developed for materials and compared with competitive ions to determine the process design and configuration. IEX kinetic constants and capacities are quantified using simple linear driving force (LDF) models for dynamic IEX experiments performed by column exchange. Materials were regenerated to quantify working capacities and kinetics. Furthermore, CO<sub>2</sub> mineralization was performed using simulated PW streams as the source for calcium ions (Otton and Kharaka, 2003; Roach et al., 2013; Dastgheib et al., 2014; Blondes et al., 2018) and the effluent solution compositions from the IEX columns. Geochemical modeling to rapidly estimate the propensity of formation of minerals in solution (e.g., CaCO<sub>3</sub>) was performed using Gibbs Energy Minimization (GEM) software (Kulik et al., 2012; Wagner et al., 2012). The work presented herein demonstrates these processes by identifying suitable materials and process parameters and by presenting possible strategies for integration with various processes related to the oil and gas sector.

## MATERIALS AND METHODS

### Materials

Sodium chloride (NaCl, >99.0%), calcium chloride dihydrate (CaCl<sub>2</sub>·2 H<sub>2</sub>O, >99.0%), calcium sulfate dihydrate (CaSO<sub>4</sub>·2 H<sub>2</sub>O, >99.0%), ferric chloride hexahydrate (FeCl<sub>3</sub>·6 H<sub>2</sub>O, >99.0%), potassium chloride (KCl, >99.0%) and magnesium chloride hexahydrate (MgCl<sub>2</sub>·6 H<sub>2</sub>O, >99.0%) were all purchased from Fisher Chemicals. 70% (w/w) nitric acid (HNO<sub>3</sub>) and 12.5% (w/w)



hydrochloric acid (HCl) solutions were purchased from Sigma Aldrich. High purity carbon dioxide (CO<sub>2</sub>, 99.99%, Airgas) cylinders were used as the source for the preparation of CO<sub>2</sub>-saturated solutions. All chemicals were used as received unless otherwise stated. Commercially available synthetic zeolites (4A and 13X; 8–12 mesh; Fisher Chemicals) and sodium-form chelating cation exchange resins (Lewatit TP 207 (iminodiacetate functional groups) and Lewatit TP 260 (aminomethyl phosphonate functional groups); Sigma Aldrich) were used for IEX experiments. Cation exchange resins were preconditioned using 2 N HCl (Sigma Aldrich), 1 N NaOH (Sigma Aldrich), and washed with ultra-pure water (Milli-Q, resistance of 18.2 MΩ cm<sup>-1</sup>) to remove any contaminants and ensure resins are Na<sup>+</sup>-form at saturation (Seggiani et al., 2006).

Chemical analysis of ion-exchange materials (**Supplementary Table S1**) was performed by electron dispersion spectroscopy (EDS; Nova 230 model) with a 10 kV accelerating voltage and a working distance of 5 mm. Brunauer-Emmett-Teller (BET) surface areas were calculated from N<sub>2</sub> adsorption-desorption isotherms, measured at 77 K with a Micrometrics ASAP 2020 Plus I system. Before measurements, samples were degassed at 1 × 10<sup>-3</sup> Torr, and 573 K. Pore size distributions were calculated from the adsorption branches of the isotherms using the Barrett-Joyner-Halenda (BJH) model. Bulk porosities and densities were measured using helium pycnometry (AccuPyc II 1340, Micrometrics) after drying the materials at 65°C for 3 h. Additionally, particle size distributions were measured using static light scattering (SLS; LS13-320, Beckman Coulter Static Light Scattering) with water and sonication being used to ensure particle dispersion. A summary of material properties is shown in **Supplementary Table S2**.

## Batch Equilibrium Ion-Exchange Experiments

Single component IEX experiments using HCl and CO<sub>2</sub>-saturated solutions (pCO<sub>2</sub> = 1.0 atm, pH = 3.9) were performed to determine Na<sup>+</sup>-H<sup>+</sup> exchange isotherms. Aqueous solutions with 0.001, 0.010, 0.1, 0.25, and 0.5 M of HCl were prepared by diluting 12.5% (w/w) HCl with ultra-pure water (18.2 MΩ cm<sup>-1</sup>). CO<sub>2</sub>-saturated solutions were prepared by bubbling CO<sub>2</sub> into ultra-pure water at 25°C, where [CO<sub>2</sub>] = 0.0334 M according to Henry's law (KH = 30 L atm mol<sup>-1</sup>), resulting in a saturation pH of 3.9 (Bhaduri et al.). CO<sub>2</sub> was bubbled until a stable pH of 3.9 was read using a pH electrode (Thermo Scientific Orion Versa Star). Exchange capacities for divalent cations were measured using 0.001, 0.010, 0.1, 0.25, 0.5, and 1 M of CaCl<sub>2</sub> and MgCl<sub>2</sub> separately, prepared in ultra-pure water. All experiments were performed using a solid/liquid ratio of 0.003 g/ml and at 25°C unless otherwise stated. All batch equilibrium experiments were performed using tightly sealed conical centrifuge tubes of equal dimensions and shaken continuously using a Corning LSE orbital shaker for four days. Solutions from all batch equilibrium experiments were sampled at 5, 10, 30, 60, 100, 180, and 240 min, and every 24 h afterward for cation concentration analysis by inductively coupled plasma-optical emission spectroscopy (ICP-OES; Avio 200 ICP Optical Emission Spectrometer, Perkin Elmer) to ensure

equilibrium was achieved. Samples were filtered through a 0.2-micron Corning filter and diluted in 5% (w/w) HNO<sub>3</sub> (prepared by diluting 70% HNO<sub>3</sub> in ultra-pure water).

Equilibrium was established when cation concentrations in solution were invariant with time. Equilibrium exchange capacities (EC; mmol/g) were calculated by

$$EC = \frac{(C_0 - C_f) \cdot V}{W} \quad (6)$$

where  $C_f$  and  $C_0$  are final and initial cation concentrations in solution, respectively,  $V$  is the solution volume, and  $W$  is the mass of solid.

Competitive IEX was performed using the following solutions (summarized in **Supplementary Tables S3–S6**) containing Na-Ca, Na-Mg, Mg-Ca, HCl-NaCl and CO<sub>2</sub>-NaCl (saturated CO<sub>2</sub> in solution at pCO<sub>2</sub> = 1.0 atm). Binary Na-Ca and Na-Mg solutions contained a fixed concentration of 1 M NaCl with CaCl<sub>2</sub> and MgCl<sub>2</sub> concentrations varying from 0.001 to 1 M. Binary Ca-Mg solutions contained equimolar concentrations of each cation varying from 0.001 to 1 M. Binary HCl-NaCl experiments consisted of a fixed concentration of 1 M HCl (pH = 0.2) for resin experiments and 0.1 M HCl (pH = 1.0) for zeolite experiments with varying NaCl concentrations from 0.001 to 1 M. Ternary IEX experiments (summarized in **Supplementary Table S7**) were performed in solutions composed of CO<sub>2</sub>-NaCl-CaCl<sub>2</sub> to further quantify competitive exchange between H<sup>+</sup>, Na<sup>+</sup>, and Ca<sup>2+</sup>. Solutions were equilibrated with CO<sub>2</sub> at 1.0 atm with CaCl<sub>2</sub> concentrations varied from 0.001 to 1 M and NaCl concentrations at 0.1, 0.5 and 1.0 M.

## Fixed Bed Ion-Exchange Experiments

An IEX column apparatus was constructed to study the dynamic ion exchange performance for the IEX materials. A schematic of the apparatus is shown in **Supplementary Figure S1**. Liquid feed was introduced into a glass tube (3.5 cm inner diameter) using a BioLogic LP peristaltic pump. Fixed beds of IEX material (performed using bed volumes of 134.7 cm<sup>3</sup> [14 cm height] unless otherwise stated) were held in place using quartz wool. Flow-rate studies using an inlet CO<sub>2</sub>-saturated solution (pCO<sub>2</sub> = 1.0 atm, pH 3.9) were performed at 20, 40, 60, 120 and 160 cm<sup>3</sup> min<sup>-1</sup> (ccm) until the effluent pH (or cation concentration) was equivalent to that of the inlet. Effluent samples were collected at intervals of 5 min during the first hour and 30 min thereafter. Collected effluent samples were analyzed using a pH meter and ICP-OES. The breakthrough curves developed are presented as the normalized effluent H<sup>+</sup> concentration (**Eq. 7**) as a function of the number of normalized bed volumes (NBV) processed (**Eq. 8**). NBV is defined as liquid flowrate,  $Q$  (ml/min) divided by IEX material bed volume (BV; cm<sup>3</sup>) multiplied by time,  $t$  (min).

$$\text{Normalized Effluent Concentration} = \frac{C_{\text{effluent}}}{C_{\text{inlet}}} \quad (7)$$

$$NBV = \frac{Q \cdot t}{BV} \quad (8)$$

The effect of inlet CO<sub>2</sub> concentrations on the H<sup>+</sup> exchange was performed using TP-207 (134.7 cm<sup>3</sup>; 14 cm height; 40 ccm) at the following CO<sub>2</sub> inlet concentrations: 1.0 atm/pH 3.9, 0.5 atm/pH

4.1, 0.25 atm/pH 4.2 and 0.10 atm/pH 4.4. Samples were collected at the same intervals described previously and analyzed using a pH meter and ICP-OES.

## Regeneration Experiments

Regeneration of IEX materials was performed using 0.001, 0.010, 0.10, and 1 M NaCl solutions. Regeneration efficiency (RE) of IEX materials is defined by:

$$RE = \left( 1 - \frac{EC_H - EC_{Na}}{EC_H} \right) \times 100 \quad (9)$$

where  $EC_H$  and  $EC_{Na}$  are the exchange capacities of  $H^+$  and  $Na^+$ , respectively, determined from single component exchange experiments. Fixed-bed IEX regeneration experiments (12.4 cm<sup>3</sup>; 1.5 cm inner diameter and 7 cm bed length; 40 ccm) were performed using an inlet CO<sub>2</sub>-saturated solution ( $pCO_2 = 1.0$  atm, pH 3.9) to exhaust the column to the saturation limit and subsequently regenerated using an inlet solution composed of 0.7 M NaCl at pH 9.9 (representative of the solution composition following mineralization in this process). Three cycles were performed for each IEX material used in this study.

## Analytical Models for Dynamic Ion-Exchange Processes

Mathematical models that relate the properties of the material and the experimental conditions to the concentration-time profiles in the effluent of a fixed bed (i.e., a breakthrough curve) were used to quantify the rate and maximum exchange capacity from dynamic IEX experiments. Combining the partial differential equation that arises from the mass balance on the cation in a fixed bed with an ordinary differential equation that represents a linear exchange rate leads to a simple, two parameter equation [the exchange rate parameter ( $kK$ ) and the maximum exchange capacity ( $q_s$ )] that describes the breakthrough curve (see the SI for the detailed derivation). These parameters can be regressed from breakthrough curve data using nonlinear least squares fitting (Chowdhury et al., 2014).

The rate parameter ( $kK$ ) reflects resistance to exchange at three length scales: 1) diffusion of cations in the bulk liquid phase to the solid surface, 2) diffusion within solid phase pores, and 3) ion exchange at the anionic site. Diffusion resistances can be determined from known engineering correlations [see SI (IEA, 2019; IEA, 2020a)], and these resistances can be summed in series (similar to electrical resistances) according to Eq. 10 (Ruthven, 1984):

$$\frac{1}{kK} = \frac{R_p}{3k_f} + \frac{R_p^2}{15\epsilon_p D_p} + \frac{1}{k_{ex}} \quad (10)$$

where  $R_p$  is the radius of the ion exchanger particles,  $D_p$  is the effective diffusivity of the incoming cation inside the pores of the solids,  $k_f$  is the mass transfer coefficient for fluid film mass,  $k_{ex}$  rate of exchange at the anionic site, and  $\epsilon_p$  is the porosity of the solid particles. The distribution parameter ( $K$ ) is the ratio of the concentration of the cation in the solid phase to that in the fluid phase at equilibrium.

## Carbon Dioxide Mineralization Using Simulated Produced Water and Ion Exchange Solutions

CO<sub>2</sub> mineralization experiments were performed using the effluents collected from dynamic IEX experiments described in *Fixed Bed Ion-Exchange Experiments*. Simulated produced water samples (see **Supplementary Table S9** for compositions) were mixed with IEX effluents at varying volume ratios within a 1 L beaker, and solid precipitates were collected after 6 h. Volume ratios,  $V_R$ , are defined as:

$$V_R = V_{PW} / (V_{PW} + V_{IEX}) \quad (11)$$

where  $V_{IEX}$  represents the volume of IEX solution of the effluent stream from the IEX column and  $V_{PW}$  represents the volume of simulated PW.

The IEX effluent and produced water solutions were continuously stirred for 4 h to ensure the CO<sub>2</sub> mineralization reaction had occurred. After precipitation, two separate samples of the supernatant were analyzed via ICP-OES and pH measurements. Both samples were filtered through a 0.2-micron Corning filter and the ICP-OES sample was diluted in 5% (w/w) HNO<sub>3</sub> (prepared by diluting 70% HNO<sub>3</sub> in ultra-pure water). The solid was collected from the solution via vacuum filtration and dried at 60 °C for 24 h prior to analysis. Powder X-ray diffraction (XRD) patterns of the precipitated phases were obtained on an X-Ray diffractometer (Panalytical X'Pert Pro X-ray Powder Diffractometer) using Cu K $\alpha$  radiation of 1.5410 Å to identify the phases in the precipitated solids. Scanning electron microscopy (SEM; Nova 230; 5 kV accelerating voltage and a working distance of 5 mm) and EDS was used to quantify elemental composition at the surface of the solids.

## Thermodynamic Modeling of Precipitation Products

The activities and speciation of aqueous components were calculated using GEMSelektor, version 3.4, which includes a native GEM (Gibbs energy minimization) solver (Kulik et al., 2012; Wagner et al., 2012), a built-in NAGRA-PSI "Kernel", and the *slop98.dat* and *Cemdata18* thermodynamic databases (Johnson et al., 1992; Hummel et al., 2002; Thoenen et al., 2007; Lothenbach et al., 2019). Thermodynamic data for the solid phases are shown in **Supplementary Table S10**, and thermodynamic data for aqueous species/complexes and gases are shown in **Supplementary Tables S11, S12**, respectively. Thermodynamic data for nesquehonite (MgCO<sub>3</sub>·3H<sub>2</sub>O) (Robie and Hemingway, 1995), hydromagnesite (Mg<sub>5</sub>(CO<sub>3</sub>)<sub>4</sub>(OH)<sub>2</sub>·4H<sub>2</sub>O) (Galvez-Martos et al., 2018), dolomite ((Ca<sub>0.5</sub>Mg<sub>0.5</sub>)CO<sub>3</sub>) (Galvez-Martos et al., 2018), monohydrocalcite (CaCO<sub>3</sub>·H<sub>2</sub>O) (Robie and Hemingway, 1995), and an iron-calcium carbonate solid-solution model ((Ca,Fe)CO<sub>3</sub>) (Di Lorenzo et al., 2017) were included in the simulations. Thermodynamic data for metastable nesquehonite and hydromagnesite were included as potential magnesium carbonate phases, opposed to "natural" mineral thermodynamic data to represent the short-term precipitation time. The dolomite phase was chosen to represent

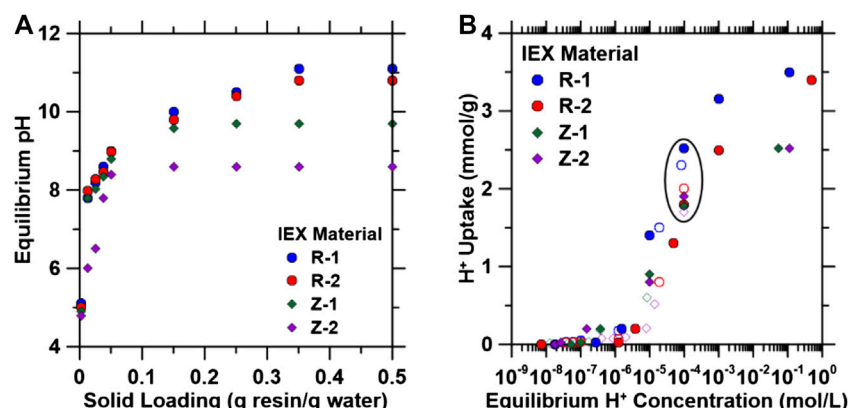


**FIGURE 1 | (A)** Changes in the pH of saturated carbon dioxide (CO<sub>2</sub>) solutions (pCO<sub>2</sub> = 1.0 atm; initial pH = 3.9) using various amounts of ion exchange (IEX) materials (i.e., 0.010–10 g of IEX material were added to 20 ml of the CO<sub>2</sub>-saturated solution). **(B)** H<sup>+</sup> exchange isotherms for organic IEX resins and zeolites in DI water. Batch exchange experiments were conducted using HCl (closed symbols) and CO<sub>2</sub> (open symbols) as a source of H<sup>+</sup> ions. HCl isotherms were developed by varying HCl concentrations from 0.001 to 1 M. CO<sub>2</sub> isotherms were developed by varying mass load at fixed volume of carbonated water at initial pCO<sub>2</sub> = 1.0 atm. Circled area represents the equilibrium H<sup>+</sup> capacities at 10<sup>-4</sup> M H<sup>+</sup> (pH ~ 3.9, similar to CO<sub>2</sub> saturated water).

partial calcium replacement by magnesium within CaCO<sub>3</sub>. The (Ca,Fe)CO<sub>3</sub> non-ideal solution model was developed in a CaO-MgO-FeOOH-CO<sub>2</sub> system to represent iron (II) replacement within the CaCO<sub>3</sub> structure in the presence of magnesium (Di Lorenzo et al., 2017).

The activity of any relevant ion species is described within GEMS using the Truesdell-Jones modification of the extended Debye-Hückel equation that is applicable for ionic strengths (*I*, mol/L) less than 2 mol/L (see Eq. 12) (Helgeson et al., 1981):

$$\log \gamma_i = \frac{-Az_i^2\sqrt{I}}{1 + \bar{a}B\sqrt{I}} + b_\gamma I + \log \frac{X_{jw}}{X_w} \quad (12)$$

where,  $\gamma_i$  and  $z_i$  are the activity coefficient and charge of the  $i^{\text{th}}$  aqueous species respectively,  $A$  and  $B$  are temperature- and pressure-dependent coefficients,  $I$  is the molar ionic strength,  $X_{jw}$  is the molar quantity of water, and  $X_w$  is the total molar amount of the aqueous phase. A common ion size parameter,  $\bar{a}$  (3.72 Å) and short-range interaction parameter,  $b_\gamma$  (0.064 kg mol<sup>-1</sup>), are used as constants for the NaCl background electrolyte (Helgeson et al., 1981). NaCl was selected as the dominant electrolyte throughout this study to simulate the IEX product solution compositions and pH shown in **Supplementary Table S8** because of constantly larger NaCl concentration in solution. Solution compositions in the simulations used the  $V_R$  ratios as described by Eq. 11 using the solutions shown in **Supplementary Tables S8–S9**.

## RESULTS AND DISCUSSION

### Non-competitive H<sup>+</sup> and Na<sup>+</sup> Uptake from DI Water

To demonstrate the feasibility of pH shift using TP-207 (R-1), TP-260 (R-2), 4A (Z-1), and 13X (Z-2), increasing amounts of these materials were added to 20 ml of CO<sub>2</sub>-saturated DI water (pCO<sub>2</sub> = 1.0 atm; pH = 3.9). 13X and 4A exhibited maximum pH

increases to 8.8 and 9.8, respectively, at solid loading ratios of 0.15 g/g, while the two organic resins increased the solution pH to ~11 at ratios of 0.35 (**Figure 1A**) within 48 h (**Supplementary Figure S2**). To further quantify the maximum H<sup>+</sup> exchange (i.e., non-competitive) at equilibrium pH values similar to those for a CO<sub>2</sub>-saturated solution (pH ~ 4), H<sup>+</sup>-Na<sup>+</sup> exchange isotherms (**Figure 1B**) were collected for the resins and zeolites in DI water. Exchange isotherms were the same using HCl and CO<sub>2</sub>-saturated solutions, indicating that there is negligible counter ion (i.e., Cl<sup>-</sup>, HCO<sub>3</sub><sup>-</sup> or CO<sub>3</sub><sup>2-</sup>) effect. H<sup>+</sup> exchange capacities at solution equilibrium concentrations of 10<sup>-4</sup> M H<sup>+</sup> (pH ~ 3.9, similar to CO<sub>2</sub>-saturated water) range from 1.7 to 2.4 mmol H<sup>+</sup> (g material)<sup>-1</sup> (circled in **Figure 1B**), with the organic resins exhibiting higher uptake capacities than the zeolites under more acidic solutions (pH < 4; [H<sup>+</sup>] > 10<sup>-4</sup> M). These data demonstrate the ability of these ion exchange materials to sufficiently shift the pH of aqueous solutions to conditions that favor carbonate precipitation (i.e., pH from 3.9 to >10) via compact flow processes (i.e., 50 g of material required to increase the pH of 1 L of water from 4 to 10; described in more detail in *Dynamic Ion Exchange*).

Na<sup>+</sup> exchange experiments were subsequently performed on the materials tested in **Figure 1** using 0.001–1 M NaCl solutions to probe the reversibility (i.e., regeneration) of this exchange. Na<sup>+</sup> exchange isotherms (**Figure 2A**) exhibit similar forms as H<sup>+</sup> exchange isotherms, with maximum regeneration capacity achieved at Na<sup>+</sup> concentrations greater than 0.1 M. To quantify the extent of regeneration, materials at the 10<sup>-4</sup> M concentration point on the isotherms in **Figure 1B** were subsequently exposed to 1 M NaCl solutions [i.e., the typical minimum concentration in produced and waste water streams (Blondes et al., 2018)], and the H<sup>+</sup> and Na<sup>+</sup> exchange capacities of these materials are shown in **Figure 2B**, indicating near complete reversibility of the exchange. Regeneration efficiencies were calculated from these values (using Eq. 9), and for all exchange materials, >95% regeneration was achieved. Multi-

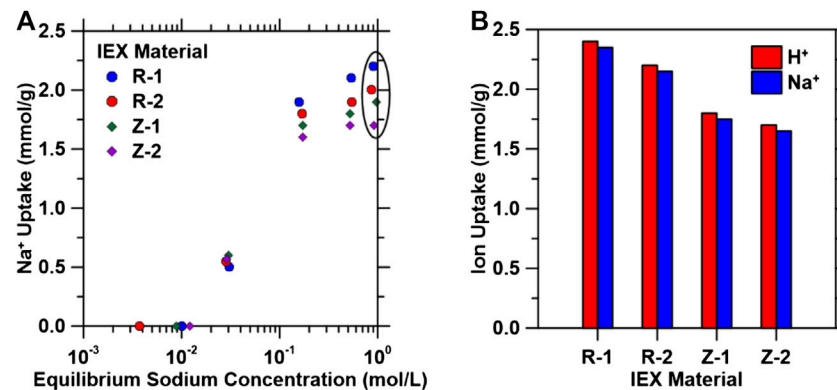


**FIGURE 2 | (A)** Regeneration isotherms of ion exchange materials using initial  $[H^+]$  of  $10^{-4}$  M at varying equilibrium NaCl concentrations within the range  $0.001 < [NaCl] < 1$  M. **(B)** Ion exchange capacities for  $H^+$  (in equilibrium with  $10^{-4}$  M  $H^+$  in solution) and  $Na^+$  (in equilibrium with 1 M NaCl in solution) ions for the four ion exchange materials used in this study. Circled area in **(A)** represents the equilibrium  $Na^+$  capacities at 1 M  $Na^+$ , where maximum uptake was observed.

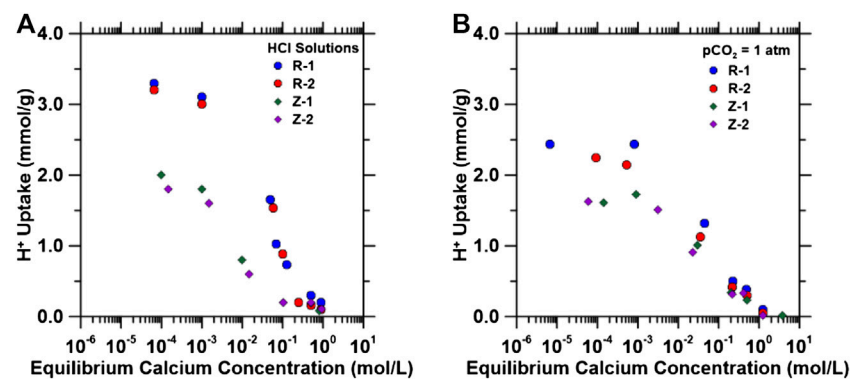


**FIGURE 3 |**  $H^+$  capacity as a function of equilibrium calcium concentrations (0.001–1.0 M  $CaCl_2$ ) in solution in **(A)** 1 mol/L HCl for resins, 0.1 mol/L HCl for zeolites, and **(B)** aqueous solutions equilibrated with  $pCO_2 = 1.0$  atm (initial pH = 3.9) using a solid/liquid ratio of 0.003 g/ml.

cycle experiments under flowing conditions (described in *Regeneration Experiments*) were conducted to further quantify the regenerability and stability of these IEX materials. Thus, the results indicate that these IEX materials are promising candidates for the regenerable pH shift process presented herein and that they can be regenerated using industrial wastewater streams (e.g., produced water).

## Competitive Ion Exchange

### Competitive Exchange Between $H^+$ and $Ca^{2+}$

Industrial produced water typically contains a variety of ions [in particular, Ca and Mg at 0.1 and 0.05 M respectively (Blondes et al., 2018)]. The organic cation exchange resins used in this study have a high affinity for divalent cations because of the chelating-like functional groups, as they are commonly used for water hardness removal (i.e., removal of Ca and Mg ions from water) (Dinu and Dragan, 2008). Similarly, the zeolites used in this study readily exchange cationic species (e.g., exchange of  $Na^+$  with  $Ca^{2+}$  leads to the formation of zeolite Type 5A from 4A)

(Breck, 1974). Thus, these affinities for divalent cations may hinder  $Na^+$  and  $H^+$  uptake when using a produced water feed for the pH shift process, so binary component IEX isotherms were generated (**Figures 3A,B**) using 0.01–1 M  $CaCl_2$  solutions with fixed initial HCl (1 M for resins, 0.1 M for zeolites to avoid dissolution) or CO<sub>2</sub> (equilibration with  $pCO_2 = 1.0$  atm, pH = 3.9) concentrations to quantify the effect of  $Ca^{2+}$  exchange on  $H^+$  uptake capacity. As shown in **Figures 3A,B**,  $H^+$  uptake decreased (and final pH decreased; **Supplementary Figure S3**) with increasing equilibrium calcium concentrations for all materials. These results indicate that a pH swing process using the materials studied herein requires pH shift of a Ca/Mg depleted stream with subsequent mixing with PW in a separate precipitation reactor (as described subsequently in *Carbon Dioxide Mineralization of Simulated Produced Water and Ion Exchange Solutions*).

### Competitive Exchange Between $Na^+$ and $Ca^{2+}$ or $Mg^{2+}$

Selectivity of IEX materials for divalent cations over monovalent cations during the regeneration step was further probed using a



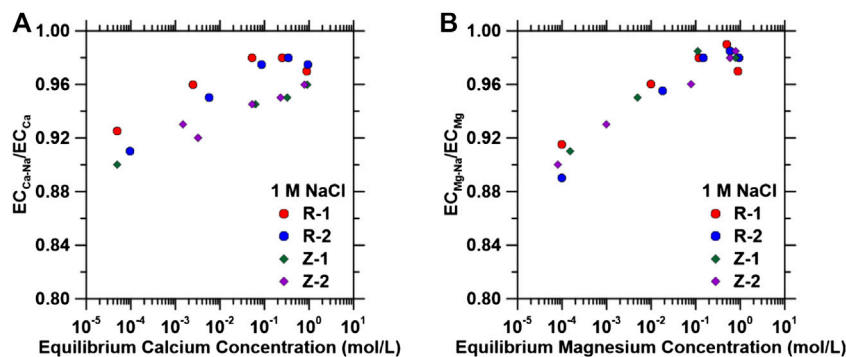


**FIGURE 4 |** Effect of 1 M NaCl on (A) calcium and (B) magnesium normalized exchange capacities of ion exchange materials as a function of equilibrium concentrations.

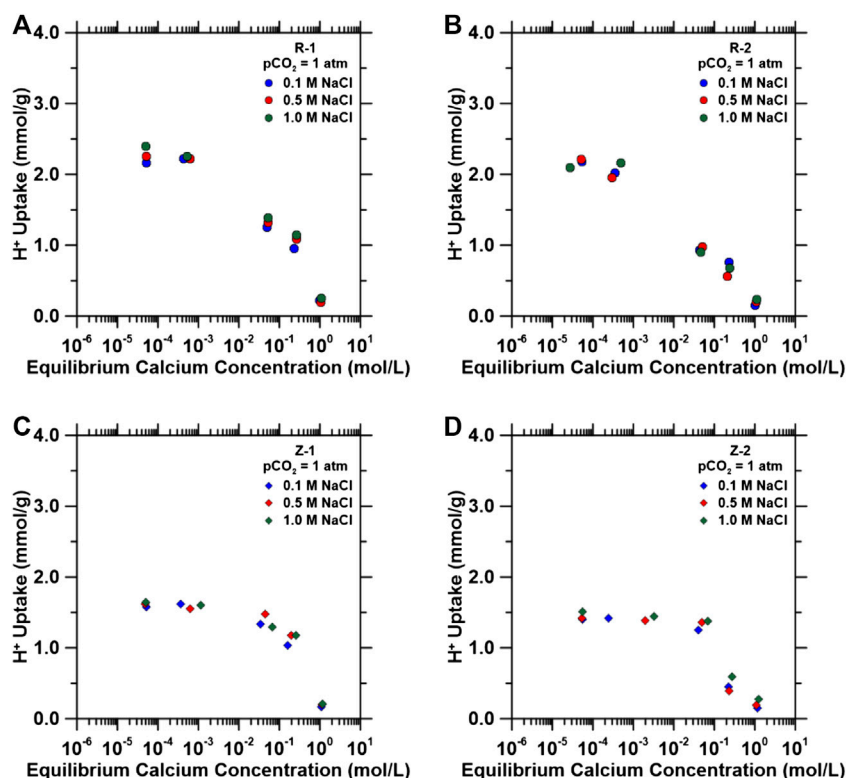
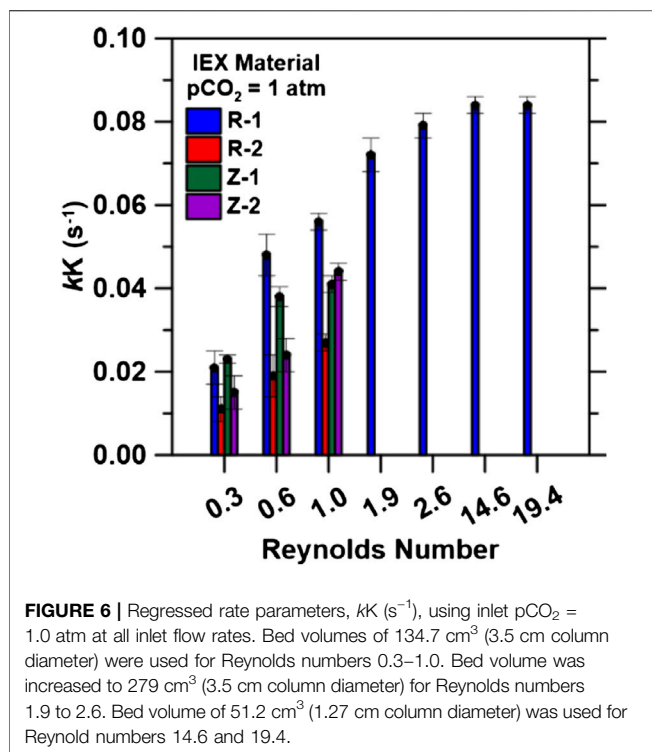


**FIGURE 5 |** H<sup>+</sup> inhibition in ternary systems composed of fixed pCO<sub>2</sub> = 1.0 atm and variable NaCl concentration as a function of equilibrium calcium concentration in solution for (A) R-1, (B) R-2, (C) Z-1 and (D) Z-2. H<sup>+</sup> uptake capacities were quantified using varying CaCl<sub>2</sub> solutions (0.01–1 M), fixed pCO<sub>2</sub> = 1.0 atm, and varying background NaCl solutions (0.1–1 M). Background NaCl concentrations remained the same in solution before and after H<sup>+</sup> exchange.

binary mixture of NaCl-CaCl<sub>2</sub> and NaCl-MgCl<sub>2</sub>. These solutions contained a fixed concentration of 1 M NaCl and CaCl<sub>2</sub> or MgCl<sub>2</sub> concentrations in a range from 0.001 to 1 M. **Supplementary Figures S4A,B** show the single component calcium and magnesium isotherms, respectively. **Figures 4A,B** shows the ratio of the exchange capacity (Eq. 6) for Ca and Mg in the presence of 1 M NaCl ( $EC_{Ca-Na}$  and  $EC_{Mg-Na}$ ) to that for single component Ca and Mg exchange ( $EC_{Ca}$  and  $EC_{Mg}$ ). These exchange capacity ratios are >0.9 across the entire experimentally tested range

and approach 1.0 for concentrations of Mg and Ca found in typical PW. At ambient temperature and low concentrations of cations, the extent of exchange is a function of ion's valence, radius, and activity. However, at a higher concentration of the incoming cation, the effect of valence in ion exchange is weakened, and ions with lower valence have higher exchange potential (Wachinski, 2017). As shown in **Figure 4**, IEX material regeneration must be accomplished with PW that is deficient of divalent cations due to the larger divalent cation uptake.





### H<sup>+</sup> Exchange in the Presence of Na<sup>+</sup> and Ca<sup>2+</sup>

The effect on H<sup>+</sup> uptake capacity in a ternary system composed of CO<sub>2</sub>-NaCl-CaCl<sub>2</sub> was quantified to examine the effect of high NaCl concentrations on the H<sup>+</sup> capacities. In systems containing large NaCl concentrations and small CaCl<sub>2</sub> concentrations (i.e., typical produced waters), Ca<sup>2+</sup> cation uptake may be inhibited because of the larger concentration gradient of the monovalent cations present (Galvez-Martos et al., 2018). Figure 5 shows the effect of Ca<sup>2+</sup> on H<sup>+</sup> capacities.

For each material and consistent with the results shown in *Competitive Exchange Between H<sup>+</sup> and Ca<sup>2+</sup>*, increasing equilibrium calcium concentrations decreases H<sup>+</sup> uptake despite the additional presence of background Na<sup>+</sup> cations in solution. Both types of materials exhibited similar divalent cation uptake, and, in this regard, there is no clear advantage to choose one material over another.

These results confirm the requirement of removal of divalent cations from PW prior to the pH shift step. In the overall process (as later described in *Process Design*), produced water streams will be mixed with basic (pH > 10), CO<sub>2</sub>-saturated effluents from the IEX columns to induce precipitation of CaCO<sub>3</sub>. The residual liquid after precipitation, which is rich in Na and Mg but depleted of Ca, will be processed via nanofiltration and reverse osmosis to remove Mg and produce a Na-rich stream for IEX column regeneration. The Na-depleted stream from the effluent of regeneration can then be saturated with CO<sub>2</sub> for the pH swing process to produce alkaline solutions for precipitation. Thus, this configuration ensures utilization of the entire PW stream while minimizing the need for fresh DI water streams.

### Dynamic Ion Exchange

Fixed bed exchange experiments were conducted to determine the impact of transport phenomena on exchange capacities and to quantify exchange rates so that IEX columns can be sized for various process conditions (e.g., column contact times and feed pH). The performance of the fixed-bed columns (i.e., determination of parameters  $kK$  and  $q_s$ ) were quantified using the LDF models described in *Fixed Bed Ion-Exchange Experiments* (and in the SI). The breakthrough curves (Supplementary Figures S4–S6; Figure 6) are presented as the normalized effluent H<sup>+</sup> concentration as a function of the number of NBV as defined in *Fixed Bed Ion-Exchange Experiments* (Eq. 8).

### Effects of Flowrate on H<sup>+</sup> Uptake Capacities and Rates

Flowrate is an important parameter to evaluate the efficiency of ion exchange materials in a continuous process because contact time and column hydrodynamics [i.e., Reynolds number (Re)] can impact IEX capacities and rates (Cooper, 1965; Barros et al., 2004; Borba et al., 2006; Chatterjee et al., 2018). The effect of varying flow rate on H<sup>+</sup> saturation capacities and ion exchange rate parameters were probed using saturated CO<sub>2</sub> (1.0 atm CO<sub>2</sub>; pH = 3.9) feed solutions at flow rates ranging from 20–160 ccm (Re 0.3–19.4). Experimental saturation capacities were quantified when the outlet H<sup>+</sup> concentration was equivalent to 95% of the inlet H<sup>+</sup> concentration. The second order LDF model (Supplementary Equation S2) was used to quantify the rate parameter ( $kK$  in Eq. 10). (Bohart and Adams, 1920) IEX resins had larger capacities compared to zeolites, which is consistent with the exchange isotherms described previously. However, shown in Supplementary Figure S6, saturation capacities (mmol H<sup>+</sup>/g) achieved in the flow experiments (1.45 for R-1, 1.44 mmol/g for R-2, 0.91 mmol/g for Z-1 and 0.75 mmol/g for Z-2 at BV = 134.7 cm<sup>3</sup>) were lower compared to the equilibrium values determined from the isotherms (Figure 1B) and decreased with increasing inlet flow rate. It has previously been reported that increasing flow rates reduces contact times with the IEX solid resulting in decrease in saturation capacities (and smaller values compared to equilibrium capacities) because of insufficient diffusion of solute into the pores of the IEX solid, consequently limiting the number of active sites or ionic groups in contact with the solute for ion exchange (Baker et al., 1954; Aksu and Gönen, 2004; Han et al., 2006; El-Kamash, 2008; El-Kamash, 2008; Mondal, 2009; Guo et al., 2013; Bhaumik et al., 2013; Jang and Lee, 2016; Malik et al., 2018).

Additional breakthrough tests (Supplementary Figure S5E,F) using bed volumes of 279 cm<sup>3</sup> (height 29 cm, diameter 3.5 cm), 51.2 cm<sup>3</sup> (height 29 cm, diameter 1.27 cm) and inlet flow rates of 120 and 160 ccm for R-1 were conducted to probe the IEX process at higher Re (>1.0). Re = 1.0 (~1.35) and Re = 1.9 (~1.75). Increasing bed volume (from 134.7 to 279 cm<sup>3</sup> for Re = 1.9 and 2.6) increased H<sup>+</sup> capacities to 1.71 mmol/g (Supplementary Figure S6), closer to its equilibrium capacity (2.4 mmol/g). This increase in saturation capacity can be explained by the increase in contact time and the expansion of the mass transfer zone due to the increase in ion exchange sites available along the larger bed length (Golie and Upadhyayula, 2016; Mazur et al.,

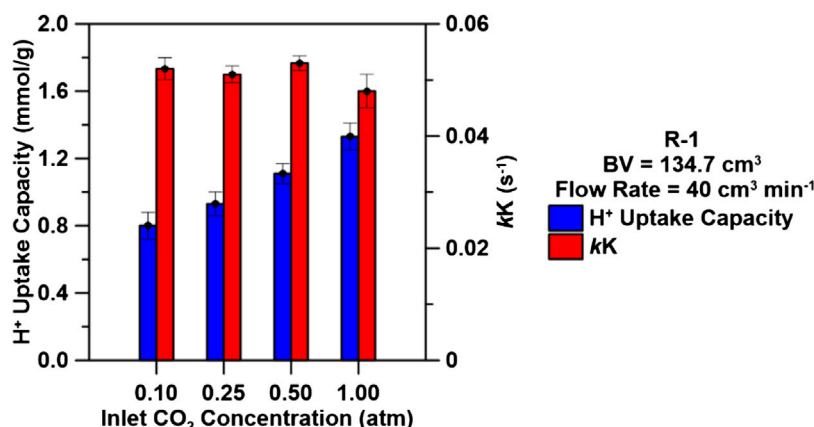


**FIGURE 7** | H<sup>+</sup> uptake capacities (mmol/g) and regressed rate parameter,  $kK$ , (s<sup>-1</sup>) for R-1 at varying carbon dioxide inlet concentrations using a bed volume of 134.7 cm<sup>3</sup> and an inlet flow rate of 40 cm<sup>3</sup> min<sup>-1</sup>.

2016; Chatterjee et al., 2018; Jin et al., 2018). Furthermore, as shown in **Figure 7**, increasing flowrate led to an increase in  $kK$  for all materials. The regressed rate parameter increased significantly with an increase in flow rate (20–60 ccm) from 0.021 to 0.056 s<sup>-1</sup> for R-1, from 0.011 to 0.027 s<sup>-1</sup> for R-2, 0.023 to 0.041 s<sup>-1</sup> for Z-1 and 0.015 to 0.044 s<sup>-1</sup> for Z-2, demonstrating the overall system kinetics is dominated by external mass transfer in the column (Aksu and Gönen, 2004; Ostroski et al., 2011; Bhaumik et al., 2013; Puerta-Falla et al., 2017; Gouran-Orimi et al., 2018). Under convective mixing, the ion-exchange rate increases as the mixing speed increases (in this case the flow rate), and the resistance of the boundary layer that surrounds the ion exchange materials weakens (Dyer and Gettins, 1970). When diffusion is the rate-controlling step, then the rate-controlling diffusion process may not be within the micropores themselves but, instead, limited by the transport via a near-static boundary layer that is inserted between the external solution and the crystalline surface (Townsend, 1991). This process is described as a film or boundary-layer diffusion. However, increasing flow rates up to 160 ccm, from 60 ccm, for R-1 using pCO<sub>2</sub> = 1.0 atm displayed minimal changes to the rate parameter  $kK$  (~0.075 s<sup>-1</sup>), indicating decreased influence of film diffusion limitations. Additionally, increasing Re by reducing the column diameter at 120 and 160 ccm (Re 14.6 and 19.4, respectively) showed no changes in the rate parameter (0.084 s<sup>-1</sup>). At this point,  $k$  represents intraparticle diffusion rates that will define the kinetics of the IEX process and can be used to design the process at the appropriate flow rates as discussed in *Process Design*.

### Effect of Inlet Concentration on H<sup>+</sup> Uptake Capacities

CO<sub>2</sub> concentrations by volume from point sources are about 3% for natural gas-fired power plants, 12% for coal-fired power plants and iron and steel mills, 20% for cement plants, and >90% from ammonia, ethanol, and hydrogen plants (Florin et al., 2010). An increase in inlet concentrations for IEX processes lead to higher uptake capacities and faster breakthrough time because of the large concentration gradient produced (Chowdhury et al., 2014). Therefore, breakthrough

curves at varying inlet CO<sub>2</sub> concentrations (0.10, 0.25, 0.50, and 1.0 atm CO<sub>2</sub>) were collected for R-1 IEX resin (the IEX material with the highest H<sup>+</sup> uptake capacity) to probe this effect under flowing conditions.

Breakthrough curves were collected for R-1 at CO<sub>2</sub> concentrations from 0.10 to 1.0 atm (10–100%) to quantify its effect on saturation capacities and breakthrough time using an inlet flow rate of 40 ccm and a bed volume of 134.7 cm<sup>3</sup>. The breakthrough time decreased as CO<sub>2</sub> influent concentration increased from 0.10 to 1.0 atm and H<sup>+</sup> uptake capacities decreased with decreasing inlet CO<sub>2</sub> concentrations, as shown in **Supplementary Figure S7**; **Figure 8**. The maximum uptake capacity was achieved using an initial CO<sub>2</sub> concentration of 1.0 atm at 1.33 mmol/g with minimal changes to the kinetic rate parameter  $kK$  (~0.050 s<sup>-1</sup>). The driving force for ion exchange is the concentration difference between the solute on the sorbent and the solute in the solution (Aksu and Gönen, 2004; El-Kamash, 2008; Bhaumik et al., 2013). A high concentration difference provides a high driving force for the ion exchange process, which may explain why higher H<sup>+</sup> uptake capacities were obtained using larger CO<sub>2</sub> inlet concentrations. Additionally, at larger inlet CO<sub>2</sub> concentrations, binding sites are rapidly filled with sorbate H<sup>+</sup> which results in a decrease in breakthrough time. Maximizing H<sup>+</sup> uptake capacities across all concentrations can be performed by increasing bed-depth as discussed in *Effects of Flowrate on H<sup>+</sup> Uptake Capacities and Rates*.

### Regeneration and Cycling of Ion Exchange Materials

Cycle-to-cycle stability of IEX materials were studied via successive H<sup>+</sup>-Na<sup>+</sup> exchange cycles, as shown in **Figure 6** (at BV of 12.4 cm<sup>3</sup>, flow rate of 40 ccm, H<sup>+</sup> exchange pH = 3.9, and Na<sup>+</sup> + exchange inlet concentrations of 0.7 M NaCl/pH 9.9). Regeneration for all IEX materials was achieved within 100 normalized bed volumes for each cycle, when the effluent pH was equivalent to the inlet pH, as shown in **Supplementary Figure S8**. Breakthrough curves for all three cycles for each IEX material are shown in **Figure 6** with their respective exchange parameters shown in **Supplementary Table S13**. The

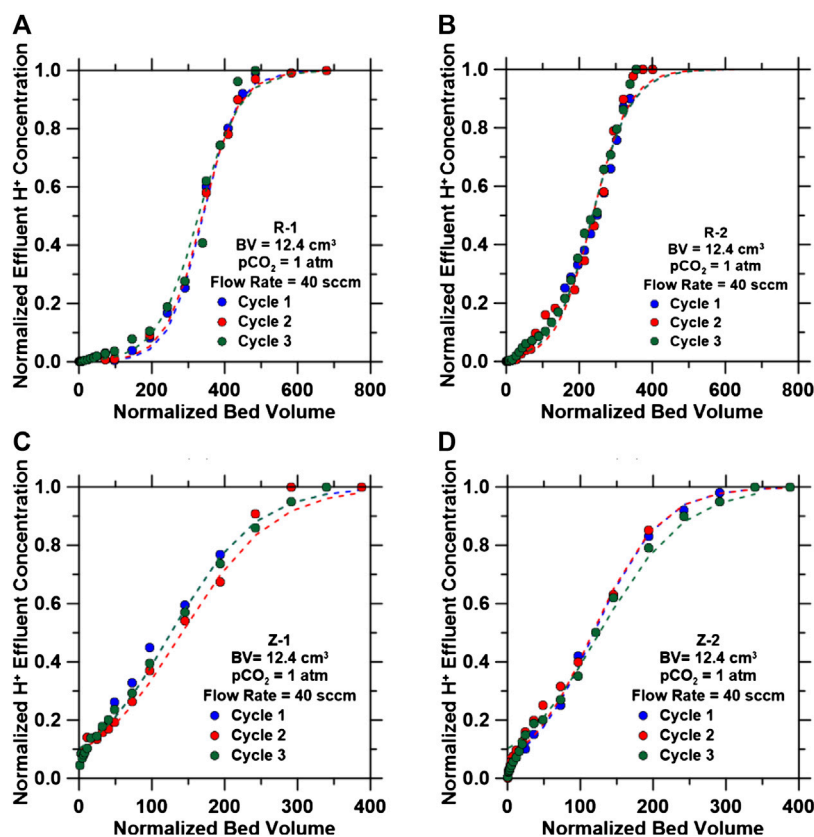


**FIGURE 8 |** Breakthrough curves for the H<sup>+</sup> exchange reaction for three cycles after regenerating with an inlet composition of 0.7 M NaCl at a pH 9.9. Breakthrough curves developed using inlet flow rates of 40 ccm and pCO<sub>2</sub> = 1.0 atm for (A) R-1, (B) R-2, (C) Z-1 and (D) Z-2. Dashed lines represent Bohart-Adams model predictions for breakthrough curves.

breakthrough time for each material was almost constant for each of their respective cycles, resulting in identical H<sup>+</sup> uptake capacities and rate parameter  $kK$  values (Supplementary Table S13).

The four IEX materials studied displayed similar H<sup>+</sup> uptake capacities after three cycles using a regenerant feed composed of 0.7 M NaCl at a pH 9.9, which is representative of the solution following the mineralization step of this process (discussed in *Carbon Dioxide Mineralization of Simulated Produced Water and Ion Exchange Solutions*). Regeneration time for the IEX resins can be reduced using higher pH solutions as is done industrially with caustic soda (Kunin and Vassiliou, 1963; Maul et al., 2014; Víctor-Ortega et al., 2017). More cycles will be necessary to identify the point at which the IEX materials begin to reduce in H<sup>+</sup> uptake capacities.

## Carbon Dioxide Mineralization of Simulated Produced Water and Ion Exchange Solutions

Simulated CO<sub>3</sub><sup>2-</sup>-rich water with the same Na<sup>+</sup> and CO<sub>3</sub><sup>2-</sup> concentrations as the IEX columns was mixed with simulated produced water solutions at varying volumetric ratios,  $V_R$  (Eq. 11). As shown in Supplementary Table S8, R-1 displayed a larger

pH swing, with a final solution pH 11.1, compared to the other IEX materials. Therefore, thermodynamic simulations were performed to predict phase formation and calcite yield using R-1 compositions as a function of different volume fractions ( $V_R$ ), shown in Figure 9A.

As shown in Figure 9A, CaCO<sub>3</sub> formation changes with varying volume ratio due to increasing [Ca]:[CO<sub>2</sub>] ratio in solution. CaCO<sub>3</sub> formation is maximized when the [Ca]:[CO<sub>2</sub>] ratio was 1:1, which occurs at a  $V_R$  of 0.23. R-1 solutions produce the largest quantities of CaCO<sub>3</sub> and highest purities of calcite as shown in Figures 9B,C, respectively, because of the higher initial pH.

For zeolitic solutions, aragonite formation is dominant between volume ratios of 0.2–0.6 because large [Ca]/[Fe] ratios are required to favor calcite formation (Di Lorenzo et al., 2017), with goethite as the primary contaminant. The reduction of the initial pH reduces goethite formation which decreases the [Ca]/[Fe] in solution to a point where it enters the miscibility gap of the (Fe,Ca)CO<sub>3</sub> solid solution model used (Di Lorenzo et al., 2017). The FeCO<sub>3</sub> end-member forms preferentially but at low quantities which causes aragonite to form in place of calcite. CaCO<sub>3</sub> precipitation decreases at  $V_R > 0.25$  for ion exchange materials because of the lower initial pH and reduction of aqueous CO<sub>2</sub>, reducing the activity of CO<sub>3</sub><sup>2-</sup> in solution.

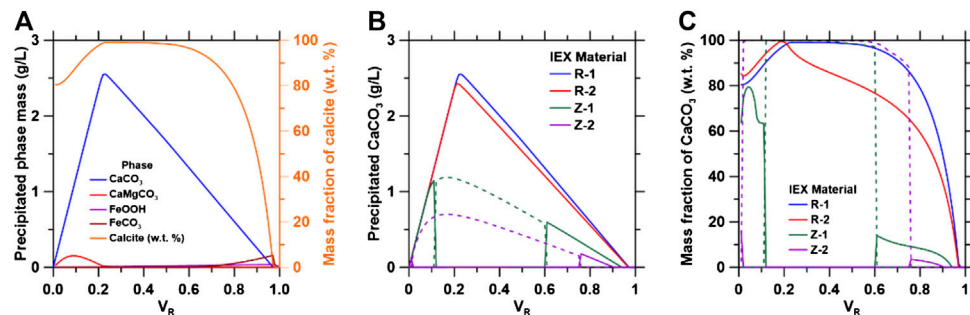


**FIGURE 9 | (A)** Simulated phase formation and purity of calcite in alkaline conditions; **(B)** CaCO<sub>3</sub> formation and **(C)** purity of calcite formed as a function of varying volume fractions for the four ion exchange solutions studied. The dashed lines for zeolitic materials represent aragonite phase formation.

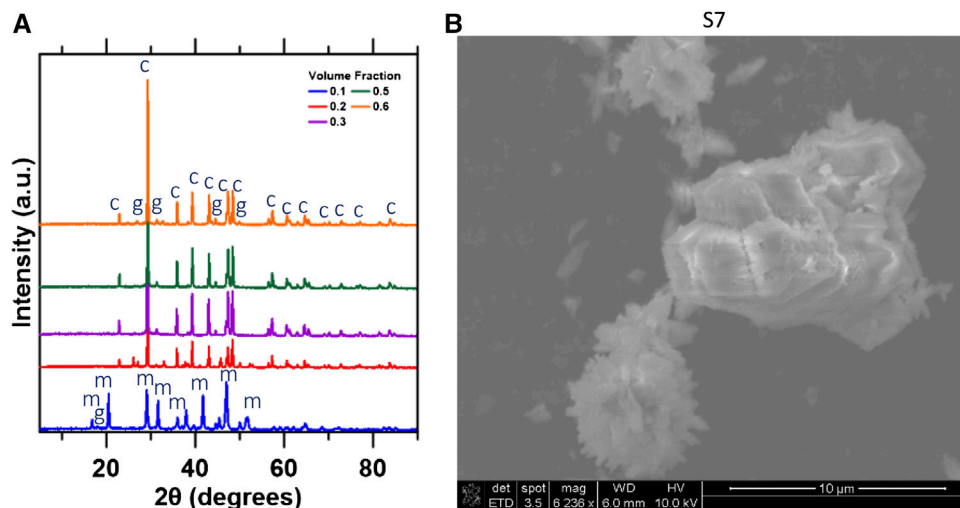


**FIGURE 10 | (A)** XRD diffraction patterns identifying present phases over varying volume ratios. c, calcite, g, goethite and m, monohydrocalcite; **(B)** SEM image of calcite synthesizes at a volume fraction of 0.7.

To validate the thermodynamic simulations, experiments were performed using R-1 solutions because of the larger predicted mass and purity of CaCO<sub>3</sub> precipitated. The dominant phase formed from volume fractions 0.2–0.6 was calcite with goethite as the primary contaminant as shown in the XRD patterns (**Figure 10A**). At  $V_R = 0.1$ , monohydrocalcite (MHC) was the primary phase that formed during mineralization (**Supplementary Figure S9A**) as it requires a solution containing  $[Mg]/[Ca] > 0.2$  and  $[CO_2]/[Ca] > 1$  to form (Nishiyama et al., 2013; Rodriguez-Blanco et al., 2014; Blue et al., 2017). When  $V_R = 0.1$ , the  $[Mg]/[Ca]$  and  $[CO_2]/[Ca]$  were 0.44 and 2.54, respectively, which are within the parameters required for MHC formation. At  $V_R > 0.18$ , the  $[CO_2]/[Ca] < 1.0$  thus, MHC did not form after this point.

The SEM image (**Figure 10B**) of calcite precipitated at  $V_R = 0.3$  displays the stable rhombohedral structure expected of calcite formation (Kralj et al., 2004). The rhombohedral

structure was observed for  $V_R$  values of 0.2–0.6. At  $V_R = 0.1$ , the stable rod-like structure for MHC was dominant, as shown in **Supplementary Figure S9B**. EDS analysis at the surface was performed to quantify CaCO<sub>3</sub> purity. As shown in **Supplementary Table S14**, experimental results are consistent with thermodynamic simulations performed for across the volume fractions studied.

The experimental data and simulated mass balances showed good agreement. Simulated goethite was within 0.3 mass % of the experimental values throughout. Within the range  $0.2 < V_R < 0.6$ , simulated calcite was within 2 mass % of the experimental values. Significant CaCO<sub>3</sub> differences was observed for  $V_R = 0.1$  because simulations predicted 9.9 mass% of potential CaMgCO<sub>3</sub> phase formation. CaMgCO<sub>3</sub> phases were not detected in XRD patterns across all volume ratios leading to differences in the mass of magnesium detected and simulated, implying either the small magnesium content is not detectable by XRD or the magnesium is adsorbed at the surface of the solid.



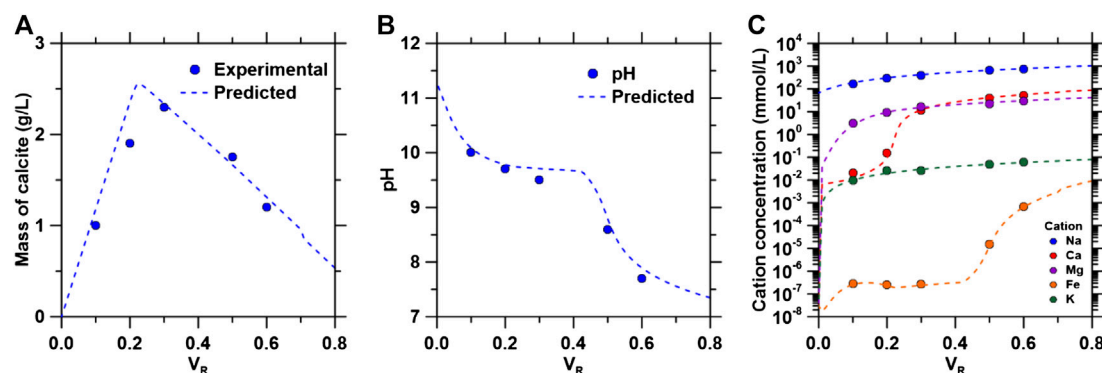


**FIGURE 11 | (A)** Yield of precipitated calcite, **(B)** final pH of solution after precipitation and **(C)** cation concentrations in solution following precipitation as a function of volume ratios. The “filled” circle represent experimental data and the dotted lines represent simulation results.

The precipitated mass of calcite increased and decreased, shown in **Figure 11A**, following the molar ratios of  $[\text{Ca}]:[\text{CO}_3^{2-}]$ , where <5% difference between simulated and experimental values were observed. The pH was observed to decrease as the  $V_R$  increased as shown in **Figure 11B**, because of the increasing dilution of the alkaline IEX solution by produced water. The pH buffering effect of carbonate ions is observed up to  $V_R = 0.43$ , where  $\text{pH} = 9.6$ . A significant drop in pH may be the result of increased goethite formation in the system, consuming additional  $[\text{OH}^-]$  provided by the IEX column. Additionally, simulated pH values were in good agreement with the experimental results as they were within 0.1–0.3 pH units. Concentrations of cations increased as the PW ratio increased, shown in **Figure 11C**. However, calcium concentrations observed a postponed rise due to calcite formation. Iron concentrations do not increase significantly until  $V_R = 0.46$ . The available iron at  $V_R < 0.46$  was converted into goethite resulting in  $[\text{Fe}] < 2.3 \times 10^{-6}$  mmol/L. When  $V_R > 0.46$ , the iron concentration rose rapidly due to decreasing  $[\text{OH}^-]$  as the alkalinity provided by the IEX solution decreased. The accurate thermodynamic predictions shown from the experimental results and simulations are significant as they can further be used to predict phase formations and  $\text{CaCO}_3$  yields for the IEX process using different compositions of PW or of other brine compositions (e.g., desalination brine discharge).  $\text{CaCO}_3$  yields will be significantly affected by total  $\text{Ca}^{2+}$  concentrations, whereas purities will significantly be affected by total  $\text{Mg}^{2+}$  and  $\text{Fe}^{2+/3+}$  concentrations as the results have shown.

## Process Design

The results from these studies indicate that ion exchange processes can be used as an alternative to the addition of stoichiometric bases to induce alkalinity for the precipitation of  $\text{CaCO}_3$ . A process flow diagram for the industrial scale setup is shown in **Figure 12**.  $\text{CO}_2$  from flue gas ( $\text{pCO}_2 = 0.12$  atm) is combined with fresh water to provide  $\text{H}^+$  in solution ( $\text{pH} 4.4$ ) that is used as the inlet solution for the IEX columns. Minor acidic impurities in the flue gas (e.g., sulfur) are not expected to substantially impact the process performance (e.g.,  $\text{H}^+$  exchange

capacities). The carbonate-rich effluent of the columns ( $\text{pH} > 10$ ) is mixed with the calcium-rich produced water in a precipitation reaction to produce  $\text{CaCO}_3$ . Following separation of the solids, the remaining solution undergoes a nanofiltration step for the removal of the remaining divalent cations in solution that would inhibit regeneration of the IEX columns (e.g.,  $\text{Ca}^{2+}$ ,  $\text{Mg}^{2+}$  and  $\text{Fe}^{2+/3+}$  cations preferably exchanging at the exchanging sites instead of  $\text{Na}^+$  cations). Performance studies of nanofiltration membranes are required to quantify the compositions of these cations following this step as they may decrease IEX performance (e.g., regeneration capacities and cycles). A reverse osmosis step is implemented for the continuous production of fresh water that is used in the first step of the IEX process and for simultaneous concentration of sodium cations in solution used for regeneration of IEX columns. The pH in both retentate and permeate streams of the reverse-osmosis step would have to be monitored as this can effect regeneration time and  $\text{CO}_2$  absorption. The retentate is transferred to the IEX columns for regeneration, where a larger pH would result in a faster regeneration time. The permeate is utilized for the initial carbonation step, where a larger pH would result in larger  $\text{CO}_2$  absorption, inducing a change in  $V_R$  where  $\text{CaCO}_3$  yields are maximized. High calcium carbonate yields (1-ton  $\text{CO}_2/\text{day}$ ) can be achieved by utilizing a  $\text{CO}_2$  mass flow rate = 69.2 kg/min, a produced water flow rate = 57.8 L/min and a total bed volume = 0.05 m<sup>3</sup>. The cycling and regeneration efficiency of these IEX materials discussed earlier make this a viable alternative process for  $\text{CO}_2$  mineralization at standard temperature and pressure.

## CONCLUSION

Our initial discoveries show that the ion exchange process can be used to induce alkalinity through the system to a degree where precipitation is favored. The results from these studies indicate that ion exchange processes can be used as an alternative to the addition of stoichiometric inorganic bases (e.g., sodium hydroxide) to induce alkalinity for the consequent precipitation of  $\text{CaCO}_3$ . Batch equilibrium isotherms showed



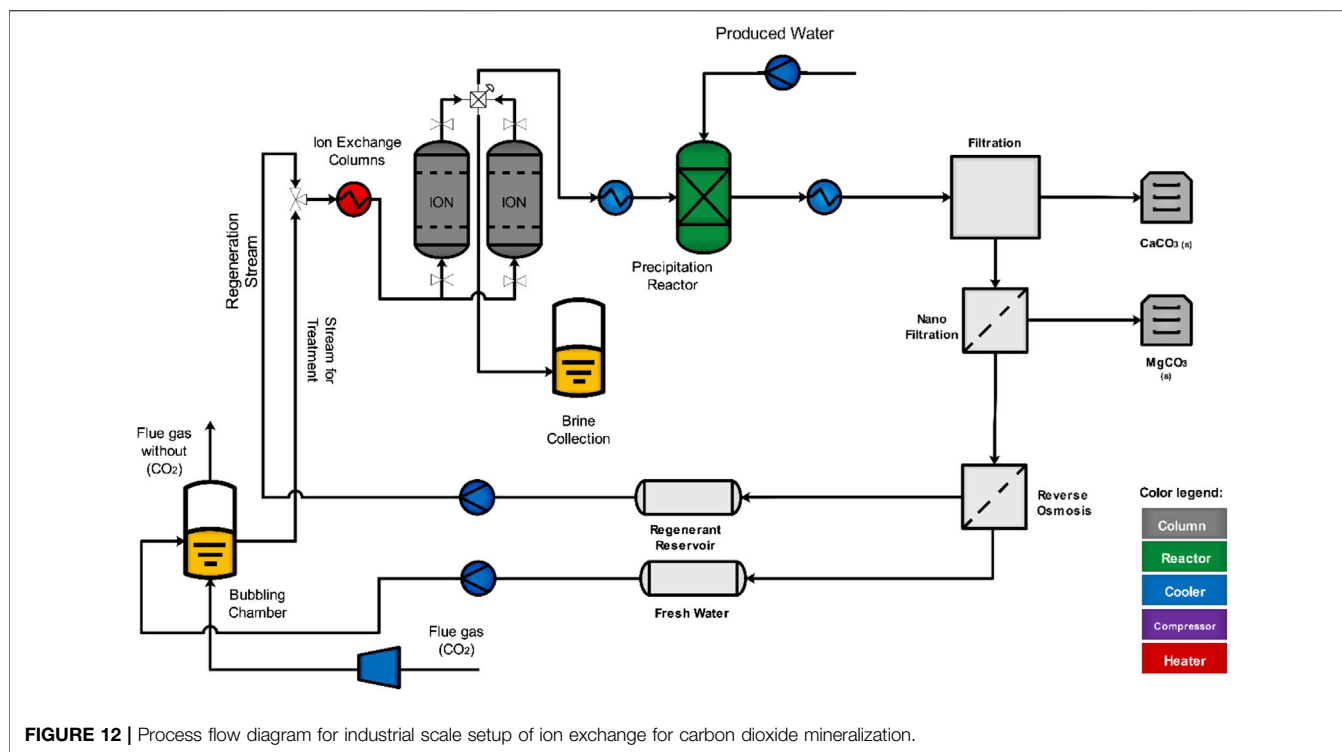


**FIGURE 12 |** Process flow diagram for industrial scale setup of ion exchange for carbon dioxide mineralization.

larger H<sup>+</sup> uptake capacities for IEX resins compared to zeolites. For all materials in all conditions, H<sup>+</sup> uptake increased with a decrease in divalent cation concentrations in solution. Inhibition of H<sup>+</sup> exchange is likely the result of the larger field strength of divalent cations. Results identified that an inlet stream for the IEX process must be absent of divalent cations in solution. Dynamic IEX experiments showed changes in uptake capacities due to contact time and changes in kinetic bulk parameters due to changes in flow rate implying external diffusion limitations. Capacities for zeolites were smaller than those for IEX resins; H<sup>+</sup> uptake may be hindered by the porous structure of zeolites. IEX materials were shown to be regenerable using simulated produced water feeds following mineralization.

CO<sub>2</sub> mineralization experiments followed thermodynamic predictions with regards to phase formations and concentrations of cations in solutions. Experimental calcite yields were 2.3 g/L for cation exchange resins with the formation of goethite (an iron-hydroxide phase, FeOOH) as the primary contaminant phase (99% calcite, 1% goethite). Yields calculated via simulations were 2.6 g/L for the resin, indicating that the experimental process was able to achieve thermodynamic maximum production of calcite. Calcite was the dominant phase for volume ratios 0.2–0.6, with goethite as the primary contaminant phase. These results indicate high purity of calcite formation and volume ratios required to achieve these purities. The high calcium carbonate yields (1 ton CO<sub>2</sub>/day utilizing a produced water flow rate = 57.8 L/min and a total bed volume = 0.05 m<sup>3</sup>) obtained for the materials examined and the successful operation at standard temperature

and pressure conditions support their potential for industrial implementation.

## DATA AVAILABILITY STATEMENT

The raw data supporting the conclusions of this article will be made available by the authors, without undue reservation.

## AUTHOR CONTRIBUTIONS

SB, AA, and DP conducted experiments and analyzed data. SB, DP, and DS wrote and edited the manuscript. BW and RR edited the manuscript. DS, ELP, GS, and BW conceived the technological concept and directed the research.

## FUNDING

This work was supported by the United States Department of Energy under Award Number DE-FE0031705.

## SUPPLEMENTARY MATERIAL

The Supplementary Material for this article can be found online at: <https://www.frontiersin.org/articles/10.3389/fenrg.2020.610392/full#supplementary-material>.

## REFERENCES

- Allen, D. T. (2016). Emissions from oil and gas operations in the United States and their air quality implications. *J. Air Waste Manag. Assoc.* 66 (6), 549–575. doi:10.1080/10962247.2016.1171263
- Aksu, Z., and Gönen, F. (2004). Biosorption of phenol by immobilized activated sludge in a continuous packed bed: prediction of breakthrough curves. *Process Biochem.* 39 (5), 599–613. doi:10.1016/S0032-9592(03)00132-8
- Armstrong, K., and Styring, P. (2015). Assessing the potential of utilization and storage strategies for post-combustion CO<sub>2</sub> emissions reduction. *Front. Energy Res.* 3, 1–8. doi:10.3389/fenrg.2015.00008
- Avena, M. J., and De Pauli, C. P. (1998). Proton adsorption and electrokinetics of an argentinean montmorillonite. *J. Colloid Interface Sci.* 202 (1), 195–204. doi:10.1006/jcis.1998.5402
- Azadpour, A., Asadullah, M., Junin, R., Manan, M., Hamidi, H., and Daud, A. R. M. (2014). Carbon dioxide mineral carbonation through PH-swing process: a review. *Energy Procedia* 61, 2783–2786. doi:10.1016/j.egypro.2014.12.311
- Baker, J. M., Gehrke, C. W., Affsprung, H. E. (1954). An ion-exchange resin-contact time method for the study of inorganic equilibria in milk. *J. Dairy Sci.* 37 (12), 1409–1415. doi:10.3168/jds.S0022-0302(54)91425-3
- Barros, M. A. S. D., Silva, E. A., Arroyo, P. A., Tavares, C. R. G., Schneider, R. M., Suszek, M., et al. (2004). Removal of Cr(III) in the fixed bed column and batch reactors using as adsorbent zeolite NaX. *Chem. Eng. Sci.* 59 (24), 5959–5966. doi:10.1016/j.ces.2004.07.040
- Baseline Survey (2019). Baseline studies overview. Available at: <https://netl.doe.gov/node/7512> (Accessed November 4, 2020).
- Bhaduri, G. A., Alamir, M. A. H., and Šiller, L. (2015). Nickel nanoparticles for enhancing carbon capture. *J. Nanomater.* 2015, 1–13. doi:10.1155/2015/581785
- Bhaumik, M., Setshedi, K., Maity, A., and Onyango, M. S. (2013). Chromium(VI) removal from water using fixed bed column of polypyrrole/Fe<sub>3</sub>O<sub>4</sub> nanocomposite. *Separ. Purif. Technol.* 110, 11–19. doi:10.1016/j.seppur.2013.02.037
- Blondes, M., Engle, M., Kharaka, Y., Reidy, M., Saraswathula, V., Thordsen, J., et al. (2018). *Geological survey national produced waters geochemical database (ver. 2.3, January 2018)*. Reston, VI: U.S. Geological Survey Data Release.
- Blue, C. R., Giuffrè, A., Mergelsberg, S., Han, N., De Yoreo, J. J., and Dove, P. M. (2017). Chemical and physical controls on the transformation of amorphous calcium carbonate into crystalline CaCO<sub>3</sub> polymorphs. *Geochem. Cosmochim. Acta* 196, 179–196. doi:10.1016/j.gca.2016.09.004
- Bohart, G. S., and Adams, E. Q. (1920). Some aspects OF the behavior OF charcoal with respect to CHLORINE. *J. Am. Chem. Soc.* 42 (3), 523–544. doi:10.1021/ja01448a018
- Borba, C. E., Guirardello, R., Silva, E. A., Veit, M. T., and Tavares, C. R. G. (2006). Removal of nickel(II) ions from aqueous solution by biosorption in a fixed bed column: experimental and theoretical breakthrough curves. *Biochem. Eng. J.* 30 (2), 184–191. doi:10.1016/j.bej.2006.04.001
- Breck, D. (1974). *Zeolite molecular sieves: structure, chemistry and use*. New York, NY: John Wiley & Sons Inc.
- Bui, M., Gunawan, I., Verheyen, V., Feron, P., Meuleman, E., and Adeloju, S. (2014). Dynamic modelling and optimisation of flexible operation in post-combustion CO<sub>2</sub> capture plants—a review. *Comput. Chem. Eng.* 61, 245–265. doi:10.1016/j.compchemeng.2013.11.015
- Cerozi, B. D. S., and Fitzsimmons, K. (2016). The effect of PH on phosphorus availability and speciation in an aquaponics nutrient solution. *Bioresour. Technol.* 219, 778–781. doi:10.1016/j.biortech.2016.08.079
- Chaikittisilp, W., Kim, H.-J., and Jones, C. W. (2011). Mesoporous alumina-supported amines as potential steam-stable Adsorbents for capturing CO<sub>2</sub> from simulated flue gas and ambient air. *Energy Fuels* 25 (11), 5528–5537. doi:10.1021/ef201224v
- Chang, R., Kim, S., Lee, S., Choi, S., Kim, M., and Park, Y. (2017). Calcium carbonate precipitation for CO<sub>2</sub> storage and utilization: a review of the carbonate crystallization and polymorphism. *Front. Energy Res.* 5, 2–12. doi:10.3389/fenrg.2017.00017
- Chatterjee, S., Mondal, S., and De, S. (2018). Design and scaling up of fixed bed adsorption columns for lead removal by treated laterite. *J. Clean. Prod.* 177, 760–774. doi:10.1016/j.jclepro.2017.12.249
- Choi, S., Drese, J. H., Eisenberger, P. M., and Jones, C. W. (2011a). Application of amine-tethered solid sorbents for direct CO<sub>2</sub> capture from the ambient air. *Environ. Sci. Technol.* 45 (6), 2420–2427. doi:10.1021/es102797w
- Choi, S., Gray, M. L., and Jones, C. W. (2011b). Amine-tethered solid adsorbents coupling high adsorption capacity and regenerability for CO<sub>2</sub> capture from ambient air. *ChemSusChem* 4 (5), 628–635. doi:10.1002/cssc.201000355
- Chowdhury, Z. Z., Hamid, S. B. A., and Zain, S. M. (2014). Evaluating design parameters for breakthrough curve analysis and kinetics of fixed bed columns for Cu(II) cations using lignocellulosic wastes. *BioResources* 10 (1), 732–749. doi:10.15376/biores.10.1.732-749
- Cohen, S. M., Rochelle, G. T., and Webber, M. E. (2012). Optimizing post-combustion CO<sub>2</sub> capture in response to volatile electricity prices. *Inter. J. Greenhouse Gas Contr.* 8, 180–195. doi:10.1016/j.ijggc.2012.02.011
- Cooper, R. S. (1965). Slow particle diffusion in ion exchange columns. *Ind. Eng. Chem. Fund.* 4 (3), 308–313. doi:10.1021/i160015a012
- Dastgheib, S. A., Knutson, C., and Yang, Y. (2014). Produced water from CO<sub>2</sub>-EOR in the Illinois basin. *Energy Procedia* 63, 6878–6886. doi:10.1016/j.egypro.2014.11.722
- Di Lorenzo, F., Burgos-Cara, A., Ruiz-Agudo, E., Putnis, C. V., and Prieto, M. (2017). Effect of ferrous iron on the nucleation and growth of CaCO<sub>3</sub> in slightly basic aqueous solutions. *CrystEngComm* 19 (3), 447–460. doi:10.1039/C6CE02290A
- Dinu, M. V., and Dragan, E. S. (2008). Heavy metals adsorption on some iminodiacetate chelating resins as a function of the adsorption parameters. *React. Funct. Polym.* 68 (9), 1346–1354. doi:10.1016/j.reactfunctpolym.2008.06.011
- Drage, T. C., Snape, C. E., Stevens, L. A., et al. (2012). Materials challenges for the development of solid sorbents for post-combustion carbon capture. *J. Mater. Chem.* 22 (7), 2815–2823. doi:10.1039/C2JM12592G
- Druckenmiller, M. L., and Maroto-Valer, M. M. (2005). Carbon sequestration using brine of adjusted PH to form mineral carbonates. *Fuel Process. Technol.* 86 (14), 1599–1614. doi:10.1016/j.fuproc.2005.01.007
- Dutcher, B., Fan, M., and Russell, A. G. (2015). Amine-based CO<sub>2</sub> capture technology development from the beginning of 2013—a review. *ACS Appl. Mater. Interfaces* 7 (4), 2137–2148. doi:10.1021/am507465f
- Dyer, A., and Gettings, R. B. (1970). The mobility of cations in synthetic zeolites with the faujasite framework — III: self-diffusion of cations into X and Y zeolites from non-aqueous solutions. *J. Inorg. Nucl. Chem.* 32 (7), 2401–2410. doi:10.1016/0022-1902(70)80523-1
- El Hadri, N., Quang, D. V., Goetheer, E. L. V., and Abu Zahra, M. R. M. (2017). Aqueous amine solution characterization for post-combustion CO<sub>2</sub> capture process. *Appl. Energy* 185, 1433–1449. doi:10.1016/j.apenergy.2016.03.043
- El-Kamash, A. M. (2008). Evaluation of zeolite A for the sorptive removal of Cs<sup>+</sup> and Sr<sup>2+</sup> ions from aqueous solutions using batch and fixed bed column operations. *J. Hazard Mater.* 151 (2), 432–445. doi:10.1016/j.jhazmat.2007.06.009
- Federal Highway Administration (2016). Blast furnace slag - material description - user guidelines for waste and Byproduct materials in pavement construction - FHWA-RD-97-148. Available at: <https://www.fhwa.dot.gov/publications/research/infrastructure/structures/97148/bfs1.cfm#:~:text=It%20is%20estimated%20that%20approximately,annually%20in%20the%20United%20States.&text=Almost%20all%20of%20the%20blast,of%20this%20slag%20is%20ACBFS> (Accessed August 4, 2020).
- Flanigen, E. M., Broach, R. W., and Wilson, S. T. (2010). *Zeolites in industrial separation and catalysis*. Hoboken, NJ: John Wiley & Sons, 1–26. doi:10.1002/9783527629565.ch1
- Florin, N. H., Blamey, J., and Fennell, P. S. (2010). Synthetic CaO-based sorbent for CO<sub>2</sub> capture from large-point sources. *Energy Fuel.* 24 (8), 4598–4604. doi:10.1021/ef100447c
- Galvez-Martos, J.-L., Elhoweris, A., Morrison, J., and Al-horri, Y. (2018). Conceptual design of a CO<sub>2</sub> capture and utilisation process based on calcium and magnesium rich brines. *J. CO<sub>2</sub> Utilizat.* 27, 161–169. doi:10.1016/j.jcou.2018.07.011
- Golie, W. M., and Upadhyayula, S. (2016). Continuous fixed-bed column study for the removal of nitrate from water using chitosan/alumina composite. *J. Water Process Engin.* 12, 58–65. doi:10.1016/j.jwpe.2016.06.007
- Gouran-Orimi, R., Mirzayi, B., Nematollahzadeh, A., and Tardast, A. (2018). Competitive adsorption of nitrate in fixed-bed column packed with

- bio-inspired polydopamine coated zeolite. *J. Environ. Chem. Engin.* 6 (2), 2232–2240. doi:10.1016/j.jece.2018.01.049
- Guerra, K., Dahm, K., and Dundorf, S. (2011). Oil and gas produced water management and beneficial use in the western United States. *Reclamation Managing Water in the West* 157, 1–113.
- Guo, H., Ren, Y., Sun, X., Xu, Y., Li, X., Zhang, T., et al. (2013). Removal of Pb<sup>2+</sup> from aqueous solutions by a high-efficiency resin. *Appl. Surf. Sci.* 283, 660–667. doi:10.1016/j.apsusc.2013.06.161
- Han, R., Zou, W., Li, H., Li, Y., and Shi, J. (2006). Copper(II) and lead(II) removal from aqueous solution in fixed-bed columns by manganese oxide coated zeolite. *J. Hazard Mater.* 137 (2), 934–942. doi:10.1016/j.jhazmat.2006.03.016
- Harland, C. E. (1994). *Ion exchange*. Cambridge, UK: Royal Society of Chemistry. doi:10.1039/9781847551184
- Helgeson, H. C., Kirkham, D. H., and Flowers, G. C. (1981). Theoretical prediction of the thermodynamic behavior of aqueous electrolytes by high pressures and temperatures; IV, calculation of activity coefficients, osmotic coefficients, and apparent molal and standard and relative partial molal properties to 600 degrees C and 5kb. *Am. J. Sci.* 281 (10), 1249–1516. doi:10.2475/ajs.281.10.1249
- Humbert, P. S., and Castro-Gomes, J. (2019). CO<sub>2</sub> activated steel slag-based materials: a review. *J. Clean. Prod.* 208, 448–457. doi:10.1016/j.jclepro.2018.10.058
- Hummel, W., Berner, U., Curti, E., Pearson, F., and Thoenen, T. (2002). *Nagra/PSI chemical thermodynamic data base 01/01*. doi:10.1524/ract.2002.90.9-11\_2002.805
- IEA (2019). Global energy and CO<sub>2</sub> status report 2019–analysis. Available at: <https://www.iea.org/reports/global-energy-co2-status-report-2019> (Accessed August 12, 2020).
- IEA (2020a). Global CO<sub>2</sub> emissions in 2019–analysis in 2019. Available at: <https://www.iea.org/articles/global-co2-emissions-in-2019> (Accessed August 12, 2020).
- IEA (2020b). Global energy and CO<sub>2</sub> emissions in 2020–global energy review 2020–analysis. Available at: <https://www.iea.org/reports/global-energy-review-2020/global-energy-and-co2-emissions-in-2020> (Accessed August 12, 2020).
- Inglezakis, V. J. (2005). The concept of “capacity” in zeolite ion-exchange systems. *J. Colloid Interface Sci.* 281 (1), 68–79. doi:10.1016/j.jcis.2004.08.082
- Jang, J., and Lee, D. S. (2016). Enhanced adsorption of cesium on PVA-alginate encapsulated prussian blue-graphene oxide hydrogel beads in a fixed-bed column system. *Bioresour. Technol.* 218, 294–300. doi:10.1016/j.biortech.2016.06.100
- Jin, Y., Teng, C., Yu, S., Song, T., Dong, L., Liang, J., et al. (2018). Batch and fixed-bed biosorption of Cd(II) from aqueous solution using immobilized pleurotus ostreatus spent substrate. *Chemosphere* 191, 799–808. doi:10.1016/j.chemosphere.2017.08.154
- Johnson, J. W., Oelkers, E. H., and Helgeson, H. C. (1992). SUPCRT92: a software package for calculating the standard molal thermodynamic properties of minerals, gases, aqueous species, and reactions from 1 to 5000 bar and 0 to 1000°C. *Comput. Geosci.* 18 (7), 899–947. doi:10.1016/0098-3004(92)90029-Q
- Kar, S., Goeppert, A., and Prakash, G. K. S. (2019). Integrated CO<sub>2</sub> capture and conversion to formate and methanol: connecting two threads. *Acc. Chem. Res.* 52 (10), 2892–2903. doi:10.1021/acs.accounts.9b00324
- Kim, S., Shi, H., and Lee, J. Y. (2016). CO<sub>2</sub> absorption mechanism in amine solvents and enhancement of CO<sub>2</sub> capture capability in blended amine solvent. *Inte. J. Greenhouse Gas Contr.* 45, 181–188. doi:10.1016/j.ijggc.2015.12.024
- King, D. W., and Farlow, R. (2000). Role of carbonate speciation on the oxidation of Fe(II) by H<sub>2</sub>O<sub>2</sub>. *Mar. Chem.* 70 (1), 201–209. doi:10.1016/S0304-4203(00)00026-8
- Kirov, G., and Filizova, L. (2012). Cationic hydration impact on zeolite formation and properties: a review and discussion. *Geokhim., Mineral. Petrol* 49, 65–82.
- Klein, A. R., Baldwin, D. S., Singh, B., and Silvester, E. (2010). Salinity-induced acidification in a wetland sediment through the displacement of clay-bound iron (II). *Environ. Chem.* 7, 413–421. doi:10.1071/EN10057
- Kralj, D., Kontrec, J., Brecević, L., Falini, G., and Nöthig-Laslo, V. (2004). Effect of inorganic anions on the morphology and structure of magnesium calcite. *Chem. Eur J.* 10 (7), 1647–1656. doi:10.1002/chem.200305313
- Kulik, D. A., Wagner, T., Dmytrieva, S. V., Kosakowski, G., Hingerl, F. F., Chudnenko, K. V. et al. (2012). *GEM-selektor geochemical modeling package: revised algorithm and GEMS3K numerical kernel for coupled simulation codes*. Berlin, Germany: Springer. doi:10.1007/s10596-012-9310-6
- Kunin, R., and Vassiliou, B. (1963). Regeneration of carboxylic cation exchange resins with carbon dioxide. *Ind. Eng. Chem. Prod. Res. Dev.* 2 (1), 1–3. doi:10.1021/i360005a001
- Leaković, S., Mijatović, I., Cerjan-Stefanović, Š., and Hodžić, E. (2000). Nitrogen removal from fertilizer wastewater by ion exchange. *Water Res.* 34 (1), 185–190. doi:10.1016/S0043-1354(99)00122-0
- Liu, S., Gao, H., He, C., and Liang, Z. (2019). Experimental evaluation of highly efficient primary and secondary amines with lower energy by a novel method for post-combustion CO<sub>2</sub> capture. *Appl. Energy* 233–234, 443–452. doi:10.1016/j.apenergy.2018.10.031
- Lothenbach, B., Kulik, D. A., Matschei, T., Balonis, M., Baquerizo, L., Dilnesa, B., et al. (2019). Cemdata18: a chemical thermodynamic database for hydrated portland cements and alkali-activated materials. *Cement Concr Res.* 115, 472–506. doi:10.1016/j.cemconres.2018.04.018
- Malik, D. S., Jain, C. K., and Yadav, A. K. (2018). Heavy metal removal by fixed-bed column – a review. *ChemBioEng Rev.* 5 (3), 173–179. doi:10.1002/cben.201700018
- Manzolini, G., Sanchez Fernandez, E., Rezvani, S., Macchi, E., Goetheer, E. L. V., and Vlucht, T. J. H. (2015). Economic assessment of novel amine based CO<sub>2</sub> capture technologies integrated in power plants based on European benchmarking task force methodology. *Appl. Energy* 138, 546–558. doi:10.1016/j.apenergy.2014.04.066
- Maul, G. A., Kim, Y., Amini, A., Zhang, Q., and Boyer, T. H. (2014). Efficiency and life cycle environmental impacts of ion-exchange regeneration using sodium, potassium, chloride, and bicarbonate salts. *Chem. Eng. J.* 254, 198–209. doi:10.1016/j.cej.2014.05.086
- Mazur, L. P., Pozdniakova, T. A., Mayer, D. A., Boaventura, R. A., and Vilar, V. J. (2016). Design of a fixed-bed ion-exchange process for the treatment of rinse waters generated in the galvanization process using laminaria hyperborea as natural cation exchanger. *Water Res.* 90, 354–368. doi:10.1016/j.watres.2015.12.027
- Mondal, M. K. (2009). Removal of Pb(II) ions from aqueous solution using activated tea waste: adsorption on a fixed-bed column. *J. Environ. Manag.* 90 (11), 3266–3271. doi:10.1016/j.jenvman.2009.05.025
- Mores, P. L., Godoy, E., Mussati, S. F., and Scenna, N. J. (2014). A NGCC power plant with a CO<sub>2</sub> post-combustion capture option. Optimal economics for different generation/capture goals. *Chem. Eng. Res. Des.* 92 (7), 1329–1353. doi:10.1016/j.cherd.2013.11.013
- Munthali, M., Elsheikh, M., Johan, E., and Matsue, N. (2014). Proton adsorption selectivity of zeolites in aqueous media: effect of Si/Al ratio of zeolites. *Molecules* 19 (12), 20468–20481. doi:10.3390/molecules191220468
- Nasef, M. (2008). *Polymer grafting and crosslinking*. Hoboken, NJ: John Wiley & Sons, 233–272. doi:10.1002/9780470414811.ch10
- Nishiyama, R., Munemoto, T., and Fukushi, K. (2013). Formation condition of monohydrocalcite from CaCl<sub>2</sub>–MgCl<sub>2</sub>–Na<sub>2</sub>CO<sub>3</sub> solutions. *Geochem. Cosmochim. Acta* 100, 217–231. doi:10.1016/j.gca.2012.09.002
- Nyquist, S., and Ruys, J. (2009). *CO<sub>2</sub> abatement: exploring options for oil and natural gas companies*. New York, NY: McKinsey & Company.
- Oh, S.-Y., Yun, S., and Kim, J.-K. (2018). Process integration and design for maximizing energy efficiency of a coal-fired power plant integrated with amine-based CO<sub>2</sub> capture process. *Appl. Energy* 216, 311–322. doi:10.1016/j.apenergy.2018.02.100
- Ostroski, I. C., Borba, C. E., Silva, E. A., Arroyo, P. A., Guirardello, R., and Barros, M. A. S. D. (2011). Mass transfer mechanism of ion exchange in fixed bed columns. *J. Chem. Eng. Data* 56 (3), 375–382. doi:10.1021/je100568n
- Otton, J. K., and Kharaka, Y. K. (2003). *Environmental impacts of Petroleum production: initial results from the osage-skiatook petroleum environmental research sites*, Osage County, OK: Diane Publishing. doi:10.3133/wri034260
- Puerta-Falla, G., Balonis, M., Falzone, G., Bauchy, M., Neithalath, N., and Sant, G. (2017). Monovalent ion exchange kinetics of hydrated calcium-alumino layered double hydroxides. *Ind. Eng. Chem. Res.* 56 (1), 63–74. doi:10.1021/acs.iecr.6b03474
- Rao, A. B., and Rubin, E. S. (2020). A technical, economic, and environmental assessment of amine-based CO<sub>2</sub> capture technology for power plant Greenhouse gas control. *Environ. Sci. Technol.* 44 (5), 330. doi:10.1021/es0158861
- Roach, R. W., Carr, R. S., Howard, C. L., and Cain, B. W. (1993). AN assessment OF produced water impacts IN the galveston bay system, 38.

- Robie, R., and Hemingway, B. (1995). *Thermodynamic properties of minerals and related substances at 298.15 K and 1 bar (105 pascals) pressure and at higher temperatures*. San Bernardino County, CA: U.S Geological Survey Bulletin. doi:10.3133/b1452
- Robin, V., Tertre, E., Beaufort, D., Regnault, O., Sardini, P., and Descostes, M. (2015). Ion exchange reactions of major inorganic cations (H<sup>+</sup>, Na<sup>+</sup>, Ca<sup>2+</sup>, Mg<sup>2+</sup> and K<sup>+</sup>) on beidellite: experimental results and new thermodynamic database. Toward a better prediction of contaminant mobility in natural environments. *Appl. Geochem.* 59, 74–84. doi:10.1016/j.apgeochem.2015.03.016
- Rodriguez-Blanco, J. D., Shaw, S., Bots, P., Roncal-Herrero, T., and Benning, L. G. (2014). The role of Mg in the crystallization of monohydrocalcite. *Geochem. Cosmochim. Acta* 127, 204–220. doi:10.1016/j.gca.2013.11.034
- Ruthven, D. M. (1984). *Principles of adsorption and adsorption processes*. Hoboken, NJ: Wiley. Available at: <https://www.wiley.com/en-us/Principles+of+Adsorption+and+Adsorption+Processes-p-9780471866060> (Accessed August 12, 2020).
- Said, A., Mattila, H.-P., Järvinen, M., and Zevenhoven, R. (2013). Production of precipitated calcium carbonate (PCC) from steelmaking slag for fixation of CO<sub>2</sub>. *Appl. Energy* 112, 765–771. doi:10.1016/j.apenergy.2012.12.042
- Scanlon, B. R., Reedy, R. C., Xu, P., Engle, M., Nicot, J. P., Yoxtheimer, D., et al. (2020). Can we beneficially reuse produced water from oil and gas extraction in the U.S.? *Sci. Total Environ.* 717, 137085. doi:10.1016/j.scitotenv.2020.137085
- Seggiani, M., Vitolo, S., and D'Antone, S. (2006). Recovery of nickel from orimulsion fly ash by iminodiacetic acid chelating resin. *Hydrometallurgy* 81 (1), 9–14. doi:10.1016/j.hydromet.2005.09.005
- Seifritz, W. (1990). CO<sub>2</sub> disposal by means of silicates. *Nature* 345 (6275), 486. doi:10.1038/345486b0
- Sofia Plagakis (2013). *ource of Greenhouse gas emissions, EPA data reveals*. Washington, DC: Center for Effective Government. Available at: <https://www.foreffectivegov.org/oil-and-gas-production-major-source-of-greenhouse-gas-emissions-epa-data-reveals> (Accessed August 4, 2020).
- Teir, S., Eloneva, S., Fogelholm, C.-J., and Zevenhoven, R. (2007). Dissolution of steelmaking slags in acetic acid for precipitated calcium carbonate production. *Energy* 32 (4), 528–539. doi:10.1016/j.energy.2006.06.023
- Thoenen, T., Hummel, W., Berner, U., and Curti, E. (2007). *The PSI/nagra chemical thermodynamic database 12/07; villigen PSI*. Villigen, Switzerland: Paul Scherrer Institut.
- Townsend, R. P. (1991). "Chapter 10 ion exchange in zeolites," in *Studies in surface science and catalysis. Introduction to zeolite science and practice*. Editors H. van Bekkum, E. M. Flanigen, and J. C. Jansen (Amsterdam, Netherlands: Elsevier), Vol. 58, 359–390. doi:10.1016/S0167-2991(08)63608-3
- U.S. Department of Energy (2019). *Natural gas flaring and venting: state and federal regulatory Overview. Trends, and impacts*.
- Víctor-Ortega, M. D., Ochando-Pulido, J. M., and Martínez-Ferez, A. (2017). Impacts of main parameters on the regeneration process efficiency of several ion exchange resins after final purification of olive mill effluent. *Separ. Purif. Technol.* 173, 1–8. doi:10.1016/j.seppur.2016.08.037
- Wachinski, A. M. (2017). *Environmental ion exchange: principles and design*. 2nd Edn. Boca Raton, London, New York: CRC Press, Taylor & Francis Group.
- Wagner, T., Kulik, D. A., Hingerl, F. F., and Dmytrieva, S. V. (2012). Gem-selektor geochemical modeling package: TSolMod library and data interface for multicomponent phase models. *Cancer Mineral.* 50 (5), 1173–1195. doi:10.3749/canmin.50.5.1173
- Zhang, W., Liu, H., Sun, Y., Cakstins, J., Sun, C., and Snape, C. E. (2016). Parametric study on the regeneration heat requirement of an amine-based solid adsorbent process for post-combustion carbon capture. *Appl. Energy* 168, 394–405 doi:10.1016/j.apenergy.2016.01.049

**Conflict of Interest:** The authors declare that the research was conducted in the absence of any commercial or financial relationships that could be construed as a potential conflict of interest.

Copyright © 2020 Bustillos, Alturki, Prentice, La Plante, Rogers, Keller, Ragipani, Wang, Sant and Simonetti. This is an open-access article distributed under the terms of the Creative Commons Attribution License (CC BY). The use, distribution or reproduction in other forums is permitted, provided the original author(s) and the copyright owner(s) are credited and that the original publication in this journal is cited, in accordance with accepted academic practice. No use, distribution or reproduction is permitted which does not comply with these terms.





# Evaluating the Effect of Oil-Displacing Agents Using Computer Graphics and Visualization Glass Plate Model Experiments

Xiangyu Sun<sup>1</sup>, Jijiang Ge<sup>1\*</sup>, Shang Ren<sup>1</sup> and An Zhao<sup>2</sup>

<sup>1</sup>School of Petroleum Engineering, China University of Petroleum (East China), Qingdao, Shandong, China, <sup>2</sup>Research Institute of Exploration and Development, Tarim Oilfield Company, PetroChina, Korla, China

## OPEN ACCESS

### Edited by:

Wei Yu,  
University of Texas at Austin,  
United States

### Reviewed by:

Bo Jiang,  
Nanjing University of Science and  
Technology, China  
Bing Wei,  
Southwest Petroleum University,  
China

### \*Correspondence:

Jijiang Ge  
gejijiang@163.com

### Specialty section:

This article was submitted to  
Advanced Clean Fuel Technologies,  
a section of the journal  
Frontiers in Energy Research

**Received:** 31 August 2020

**Accepted:** 25 November 2020

**Published:** 21 January 2021

### Citation:

Sun X, Ge J, Ren S and Zhao A (2021)  
Evaluating the Effect of Oil-Displacing  
Agents Using Computer Graphics and  
Visualization Glass Plate  
Model Experiments.  
Front. Energy Res. 8:601158.  
doi: 10.3389/fenrg.2020.601158

The results of visualization experiments primarily provide descriptions of local features or a general conclusion because, to obtain accurate numerical results, it is necessary to count each small point in the visual image and calculate the remaining oil based on the color. There is currently no method that can automatically and accurately calculate the recovery factor based on a visualized image. Computer graphics can be used to solve this problem, and Matlab software with its powerful image calculation functions was used to analyze and calculate images of visualization experiment processes. This article first summarizes the development and respective characteristics of the visual experiment evaluation of oil displacement agents. Then, the corresponding relationship between the actual oil displacement recovery parameters and the image parameters is introduced in detail, and a calculation formula for the visual image recovery factor is summarized. Finally, using the quantitative visual experimental results from different oil displacement agent injection methods as an example, we compared the different oil displacement processes and their recovery. The different characteristics of the two injection methods were evaluated, and the feasibility of the calculation method was verified. This method provides data support for interpreting visual experimental processes and a description of the experimental results. This provides a clear and unified calculation method for the recovery factors of oil displacement processes, which often involve many difficult-to-compare processes.

**Keywords:** visualization experiment, computer graphics, MATLAB software, glass plate model, recovery factor

## INTRODUCTION

At present, most oil fields in China have entered the tertiary oil recovery period, and it is necessary to inject oil-displacing agents into oil and gas formations to improve oil recovery; therefore, the evaluation of oil-displacing agents is particularly important and is usually divided into two stages (Pei et al., 2017; Li et al., 2018; Wu et al., 2018). The first is the phase state test of the oil-displacing agent itself. This stage mainly analyzes the properties and parameters to indirectly evaluate the oil-displacing effect of the oil-displacing agent and formulate injection plans. The second stage is directly evaluating the performance of the oil-displacing agent to enhance the recovery factor by simulating the exploitation of a formation. According to the injection plan, the oil-displacing agent is tested, and the results are compared with previous estimates to improve the performance of the oil-displacing agent (Sun et al., 2019).



The two most commonly used methods for complete and systematic process simulation evaluation of oil-displacing agent enhanced oil recovery are numerical simulation experiments and core displacement experiments. Traditional core displacement experiments provide the oil displacement efficiency, but it is impossible to observe the oil-displacing process in the formation of crude oil. It also does not reflect the different influences of different variables (such as injection mode, injection speed, concentration, dose, etc.) on the internal reservoir, and therefore it is impossible to improve the oil-displacing agent system according to the differences between experimental phenomena during displacement (Wang et al., 2019). For the mathematical model evaluation experiments, although the oil displacement process can be observed, it is a simulation process calculated based on geological characteristics and oil displacement agent parameters using discovered laws. However, the seepage laws of many low-permeability pores have not been fully clarified, making it difficult to simulate the real underground fluid flow process (Artun and Kulga, 2020; Liu et al., 2020a; Miah et al., 2018; Sabet et al., 2020; Shi et al., 2019; Wu et al., 2019; Zhang et al., 2020a). At the same time, the evaluation results obtained by this method are too modular and difficult to verify.

In addition to the two conventional methods of core displacement evaluation and mathematical simulation evaluation, visualization model evaluation methods have also been used, such as microfluidics and micromodels (Priest et al., 2011). In fact, as early as 1954, Charles et al. studied gas-liquid displacement and liquid-liquid displacement in capillary tubes (Templeton, 1954). In 1959, Chatenever et al. first used a plane model filled with glass beads to roughly study the solution gas flooding behavior and developed a model from a thin tube to a plane model (Chatenever et al., 1959). In 1971, Donaldson and others tested the oil displacement in a lipophilic system and a hydrophilic system by filling sand in a glass plate. The resulting visualization model was used to develop a sand-filling model (Donaldson and Thomas, 1971). In 1982, Wang et al. used a microscopic visualization glass bead filling model to study the CO<sub>2</sub> flooding process, which further reduced the visualization plane model (Wang, 1982). In 1986, Trygstad et al. developed a visualization model for etching microscopic rock pores on a glass plate, which changed the pores of the microscopic model from homogeneous to heterogeneous (Trygstad et al., 1986). In 2007, Clerke et al. fitted the displacement efficiency calculated by a mathematical model with a microscopic visualization model and established a connection between the visualization model and the digital model (Clerke, 2007). In 2011, based on a visualization model, Shabani et al. used a refinement algorithm to show the color contrast of the displacement channels and applied image-processing technology to the visualization displacement model (Afrapoli et al., 2011). In the following ten years, micro-visualization model technology developed rapidly, resulting in a variety of visualization models and test methods. The magnification of the observation lens continuously increased, making it easier to observe phenomena (Neel et al., 2018; Zhang et al., 2020b).

Visualization model experiments require only short test times and provide easy observations, explanations, and understanding, and convenient methods for improving oil-displacing agents, but their further development is limited by their ability to calculate experimental results (Chen et al., 2019). Visualization evaluation methods are mostly used to observe subtle phenomena of fluids in porous media. The analysis of overall oil displacement results is relatively vague and general and cannot provide accurate oil recovery values to support further trend analysis and rule induction of experimental data. The main reason why the experimental results cannot be accurately analyzed is that the visualization model is small and the output fluid of the experiment is difficult to measure. Secondly, because the color of crude oil or formation water is similar to some injections, it is not easy to distinguish the mixed or overlapping parts based on experimental images. To solve the above problems and increase the accuracy of the visualization simulations, an evaluation method using a visualization glass plate model to evaluate oil-displacing agents and writing an analysis program in Matlab for visual image analysis and data calculation is proposed.

There are many types of visualization models, which can be divided by their size (macro models and micro models), the simulated stratigraphic structure (homogeneous models and heterogeneous models), and the production method (etching models and filling models). Etching models are based on the stratum structure or a specific shape using an etching machine to engrave hollow pore channels on a transparent plastic or glass plate. In recent years, the development of microfluidics using micro-etching methods has made breakthroughs in many fields. In the petroleum industry, microfluidic models are mostly used to observe changes in the fluid structure and droplet flow. For example, Kang et al. observed the morphology and stability of sodium polyacrylate emulsions in a 5 × 5 cm glass microetching model (Wang et al., 2020). The advantage of this etching model is that the image is clear and easy to compare and analyze. The disadvantage is that the model structure cannot be changed, and its flexibility is insufficient. The filling model involved digging out a regular-shaped groove of a specified size between two transparent plates and then filling the groove with specific sand to simulate a formation. This model generally simulates a homogeneous layer or a fractured formation. For example, Pei et al. observed the influence of plugging agent injection on the remaining oil distribution in an 18 × 18 cm sand filling model (Pei et al., 2018). The advantage of this model is that the permeability of the simulated formation can be adjusted according to the formation conditions. The disadvantage is that it cannot simulate heterogeneous formations, the sand filling process is cumbersome, and the experimental efficiency is low.

Comparison and screening showed that the visual glass plate model developed by Ren in 2003 is suitable for simulating oil displacement experiments for different formation pore structures (Fu et al., 2016; Liu et al., 2020b). A transparent glass plate experiment was observed through a lens that provided 20-times magnification and allowed the experiment process video to be recorded. This method could show the increased production effect of oil displacement agent flooding compared with water

flooding, and also show some of the subsequent effects of the oil displacement system on the formation. It is also possible to more intuitively observe the state when oil droplets are trapped and carried out of the simulated formation during the crude oil viscosity reduction process. In addition, visual glass plate model experiments can show the oil production and production increase process of the oil field by recording the whole experiment, which is easier for field technicians to understand. The phenomenon occurring during displacement can also explain the phenomena of fluid mechanics, reservoir physics, and other disciplines, and helps understand the dynamics of underground fluids. At the same time, it also complements and validates traditional core displacement experiments and numerical simulation experiments (Guo et al., 2018; Mask et al., 2019; Zhang et al., 2019).

The advantage of the glass plate model compared with other visualization models is that it has an independent device for simulating formations. This model is not etched or filled with sand on a visualization glass plate but is micro-etched on two independent hard plastic films and then filled with fine particles. After the two plastic films are processed into a simulated formation, the back of the hard plastic film is glued to the center of the two glass plates. Then, the glass plates are aligned and compacted according to the corresponding positions of the plastic film etching structure, and the model is completed. This method of simulating stratum with an independent hard plastic film is convenient for changing the structure of the stratum and making strata with different homogeneities. According to the reservoir conditions or requirements, a variety of infrared etching designs that simulate the formation structure can be carried out on the plastic film. The permeability difference between the heterogeneous layers can be adjusted by changing the size of the fill gravel, which makes it easy to distinguish between high-permeability and low-permeability regions during the experiment. After the experiment, the plastic film used to simulate the formation can be gently scraped off with a knife, and a new stratum-simulating thin plate can be immediately attached to the glass plate for the next set of experiments, which greatly improves the experimental efficiency.

However, the current limitation of this visualization glass plate model method is that it can only perform test experiments at room temperature and low pressures. Under high pressures, the rubber plugged around the plastic film that simulates a formation can leak fluid and cause the experiment to fail. The maximum pressure that the experiment can withstand is only about 3 MPa; therefore, this model cannot be used to test strong plugging agents. At present, the problem that needs to be solved in high-temperature experiments is the observation and recording problem during constant-temperature heating.

## EXPERIMENTAL IMAGE ANALYSIS TECHNIQUES

A typical computer graphics research tool is Matlab (Matrix and Laboratory) software, which is an advanced computing environment that mainly involves scientific computing,

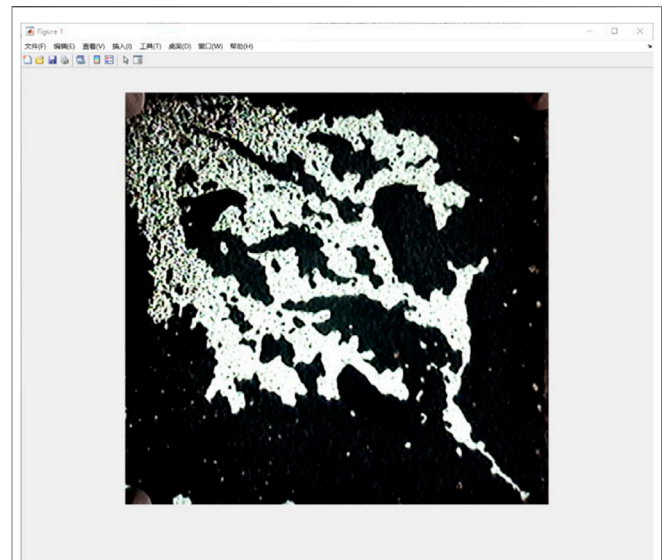


**FIGURE 1 |** Oil displacement outline of the visualization glass plate experiment.

visualization, and interactive programming. It is widely used for data visualization and results prediction, by converting data into images. In contrast, image processing (image digitization) is also its main function, but this function has relatively few applications in oilfield development. The study found that many image processing functions of Matlab are similar to the principle of the image analysis method sought by the visual model test. It must be able to divide and highlight the indistinguishable area of the image color and also obtain an accurate value through analysis.

This paper is based on the visualization of a glass plate model, according to the graphics processing function of Matlab, using image processing technology to analyze a visual displacement experiment. After programming as required, the following analysis is performed on the visual displacement picture.

- (1) Edge detection: the edge detection will display the displacement range and residual oil in the range;
- (2) Contour extraction: based on (1), the displacement range, i.e., the sweep coefficient (the ratio between the reservoir volume swept by the displacement agent and the entire oil-containing volume), was extracted and determined. The calculation method is shown in Eq. 1;
- (3) Generate a gray-scale histogram: Based on (2), the gray-scale histogram generated from the image can be used to calculate the corresponding oil washing efficiency according to the proportion of the vertical axis (the ratio of the amount of oil produced by the oil layer affected by the oil displacing agent to the reserves of this part of the oil layer). The calculation method is shown in Eq. 2;
- (4) Generate a three-dimensional grayscale image based on (2), which can be rotated, and the grayscale size of each point can be observed. The displacement model that clearly shows the oil content is used to compare the displacement effect of each

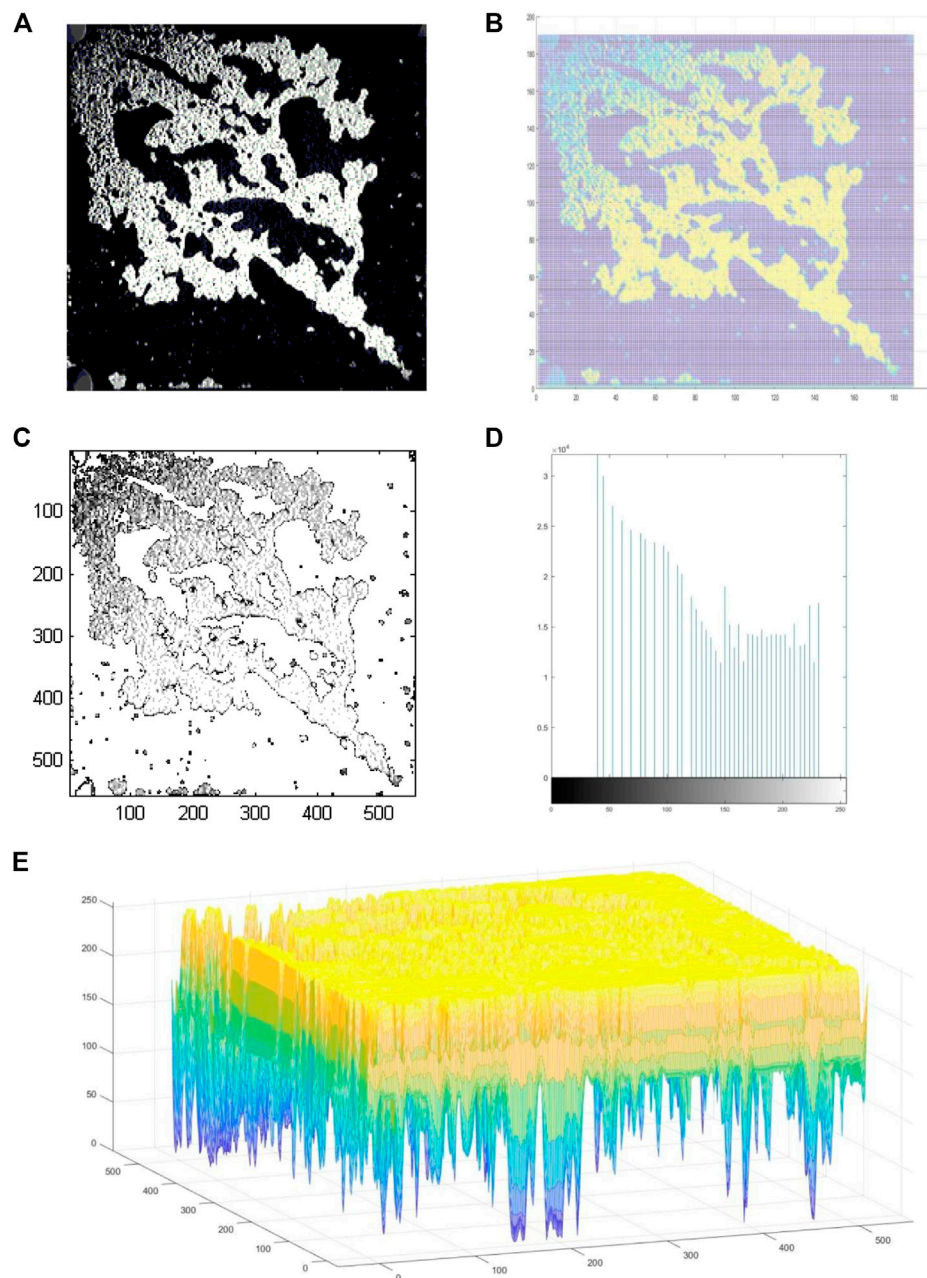


**FIGURE 2 |** The visualization displacement experiment analyzed by Matlab software. **(A)** Grayscale image, **(B)** Pixelated grid image, **(C)** Edge detection and contour extraction image, **(D)** Grayscale histogram and **(E)** Three-dimensional graph.

position throughout the whole experiment, and it is easy to identify deficiencies in the oil displacement agent, making it easy to identify areas for improvement.

The calculation principle of the experimental recovery factor is based on the empirical formula of the recovery degree of geological reserves proposed by Sipachv and Nazarov. The oil recovery factor is equal to the product of the swept efficiency of water flooding and the oil washing efficiency (Eq. 3). **Figure 1** is used as an example to explain in detail how to use computer

graphics to obtain relevant parameters for calculating the displacement recovery factor.

$$R_o = E_D \times E_V, \quad (1)$$

$$E_D = \frac{S_{oi} - S_{or}}{S_{oi}}, \quad (2)$$

$$E_V = \frac{N_p}{N_{om}}, \quad (3)$$

$R_o$ —Oil recovery factor;  $E_D$ —Oil washing efficiency;  $E_V$ —Swept efficiency of water flooding;  $S_{oi}$ —Original oil saturation;



$S_{or}$ —Residual oil saturation;  $N_p$ —Cumulative oil production;  $N_{om}$ —Available reserves.

## Analysis of Sweep Efficiency

First, the selected picture is converted into a gray-scale image by removing the color of the injection or oil with dye (**Figure 2A**). Authors also generates a pixelated grid on the picture to facilitate subsequent understanding and analysis, as shown in **Figure 2B**. Based on this, edge detection and contour extraction are performed on the image (**Figure 2C**). Compared with the original image, the image after contour extraction is divided into three parts: the outer part of the contour, the inner part of the contour, and the coordinate axis. The color of the untouched crude oil outside the displacement channel (the part outside the contour) is inverted to white. The displacement channel (the inner part of the contour) retains the original grayscale. The pixelated grid axis of the contour extraction map is used to calculate the area within the contour range and its percentage in the entire picture. The calculation formula used for the above process is as follows:

$$E_V = 100\% - \frac{S}{x_{\max} \times y_{\max}}, \quad (4)$$

$E_V$ —Swept efficiency of water flooding;  $S$ —The area of crude oil that has not been driven (inverted to white);  $x_{\max}$ —Maximum value of abscissa;  $y_{\max}$ —Maximum value of ordinate.

The above-mentioned parameters calculated by the program are compared with the actual values obtained from the visual model simulation flooding experiment. The visualization model is used to simulate the entire oil layer, which is described numerically as the product of the horizontal and vertical coordinates. The displacement channel is the sweep range of the oil-displacing agent, that is, the area within the contour range in **Figure 2C**. Then, the percentage of the area within the outline to the area of the entire picture is the sweep efficiency of the oil-displacing agent.

## Analysis of Oil Washing Efficiency

A grayscale histogram is generated for **Figure 2C**, where the horizontal axis of the generated grayscale histogram is pixels (grayscale), and the vertical axis represents the number of pixels (the number of grayscales), see **Figure 2D**. The grayscale gradually increases from left to right on the horizontal axis (the color changes from black to white). The grayscale in the program is divided into 255 pieces, where each piece represents a grayscale color. The grayscale at 0 on the horizontal axis is the smallest, which represents the crude oil that has not been displaced in the experiment. The maximum gray value of the horizontal axis is 255 in the original image, which represents the point where the crude oil in the displacement channel has been completely displaced during the experiment. The height of each blue histogram represents the total number of points in this grayscale.

Combined with the definition of oil washing efficiency and oil-displacement recovery rate, the value of 255 on the horizontal axis represents a 100% oil washing efficiency; therefore, the oil

washing efficiency of each point is obtained by subtracting each value representing the grayscale on the horizontal axis from 255 and then dividing by 255. The sum of all the points of a certain gray level forms a blue bar on the vertical axis, as shown in **Figure 2D**. The sum of all the blue bars is the area affected by the entire displacement. The generated three-dimensional graph is more conducive to understanding the above process from the scope of the entire experiment (**Figure 2E**). That is, the ratio of the cumulative value of the oil washing efficiency of each point to the sum of the numbers of all points is the oil washing efficiency in the affected range. The calculation formula is as follows:

$$E_D = \frac{\sum_{n=0}^{255} ((255 - x_n/255) \times y_n)}{\sum_{n=0}^{255} y_n}, \quad (5)$$

$E_D$ —Oil washing efficiency, %;  $n$ —One of 255 gray scales;  $x_n$ —Abscissa value when the gray level is  $n$ ;  $y_n$ —The  $y$  value of the abscissa at  $x_n$ .

Matlab's image processing feature was used to analyze visualization experiments by combining the experimental process of the visual physical model experiment with the specific numerical results calculated through mathematical model analysis. This provides a clear and unified calculation method for a large number of difficult-to-compare oil displacement processes. It can conveniently compare the different effects of various quantitative experiments and promote the development of evaluation techniques using visual models.

This paper uses Chenzhuang oil and Yong eight oil as specific examples and uses the above analysis method to screen the oil-displacement agent PA-5 and OH-3 systems. The influence of different injection methods on the oil displacement effect of the oil-displacement agent was also evaluated.

## MATERIALS AND METHODS

### Materials

Chenzhuang oil and Yong eight oil were provided by Shengli Oilfield Petroleum Exploration and Development Institute, and their basic characteristics are shown in **Table 1**. The two oil-displacing agent systems, PA-5 and OH-3, were obtained from the Shengli Oilfield site, and their composition is shown in **Table 2**.

### Apparatuses

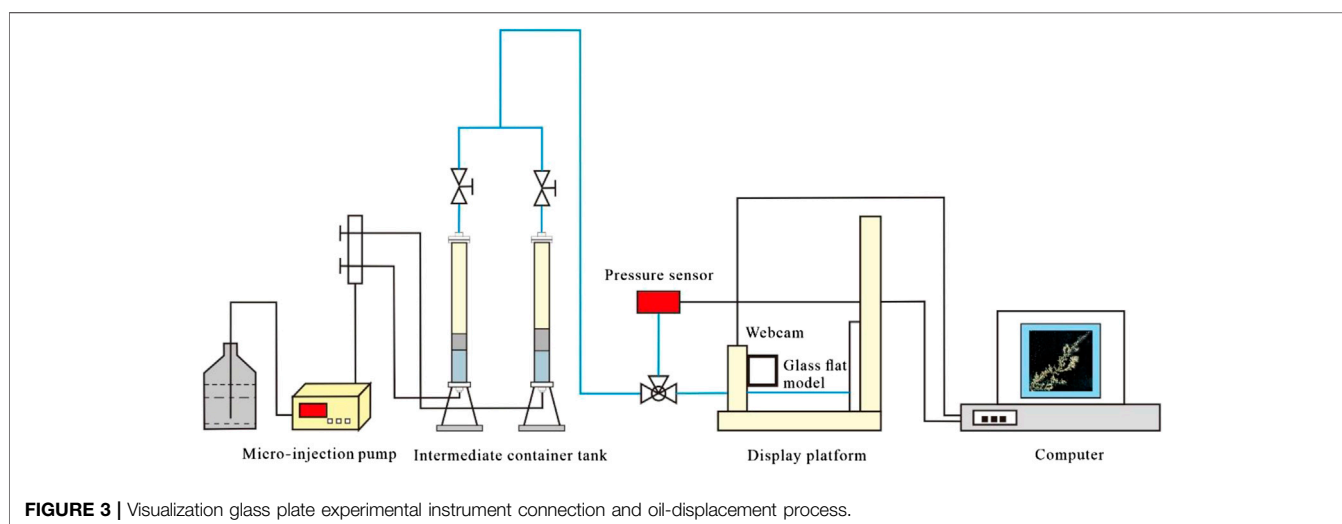
The two visualization glass plate models were designed according to the stratigraphic structure and parameters of the reservoir. The permeability of the homogeneous formation is about 80–1,000 mD, the low permeability zone of the heterogeneous formation is about 300–400 mD, and the high permeability zone is about 800–1,000 mD. The above formation porosity is about 20%. A GK-8000A projector of Hangzhou Gaoke Industry and Trade Co., Ltd. was used to observe the oil displacement process. A 100DX Teledyne ISCO micro-syringe pump was used to inject the oil displacement agent, and a Haian Petroleum Scientific

**TABLE 1** | Basic properties of crude oil.

Type of oil	Content of four components/%				Density/(g/cm <sup>3</sup> )	Viscosity/mPa.s (26 °C)
	Saturated hydrocarbon	Aromatic hydrocarbons	Colloid	Asphaltene		
Chenzhuang oil	25	36	21	18	0.874	460
Yong 8 oil	27	29	30	14	0.923	670

**TABLE 2** | Composition of the oil-displacing agent system.

Oil-displacing agent system	Betaine (0.02 wt%)		Type of polymer (0.1 wt%)
	Type	Molecular formula	
PA-5	Palmitic acid amidopropyl dimethyl betaine	$C_{16}H_{33} - \begin{array}{c} CH_3 \\   \\ N \\   \\ CH_3 \end{array} - CH_2CH_2CH_2 - COOH$	Hydrophobically associating polymer, APM5
OH-3	Oleic acid amidopropyl dimethyl betaine	$C_{17}H_{33} - \begin{array}{c} CH_3 \\   \\ N \\   \\ CH_3 \end{array} - CH_2CH_2CH_2 - COOH$	Hydrophobically associating polymer, HPM3



Research Instrument Co., Ltd. pressure acquisition system was used to control the injection pressure. The instruments that were connected together are shown in **Figure 3**.

## METHODS

### Visualization Glass Plate Model Production

First, the quartz sand and conglomerate particles were sieved into two sizes of 100 and 50 mesh, respectively, and then the same size quartz sand and conglomerate particles were mixed in a mass ratio of 3:1.50 mesh mixed particles were used to make high-

permeability formations, and 100 mesh mixed particles were used to make low-permeability areas. A special glue-containing clay was used to adhere closely-accumulated particles to two square rigid plastic templates (length: 16 cm). As shown in **Figure 4**, the hard plastic template formation model was pasted on the middle positions of two 0.5 cm thick and 18 cm long square glass plates. The corresponding positions of the simulated formation structure were aligned between the two glass plates, and the four sides of the simulated formation plate were sealed with a rubber cord with a diameter of 0.3 cm. The four sides of the glass plate were clamped with clamps dedicated to the model. Then, the visualization glass plate model was ready for experimental tests.



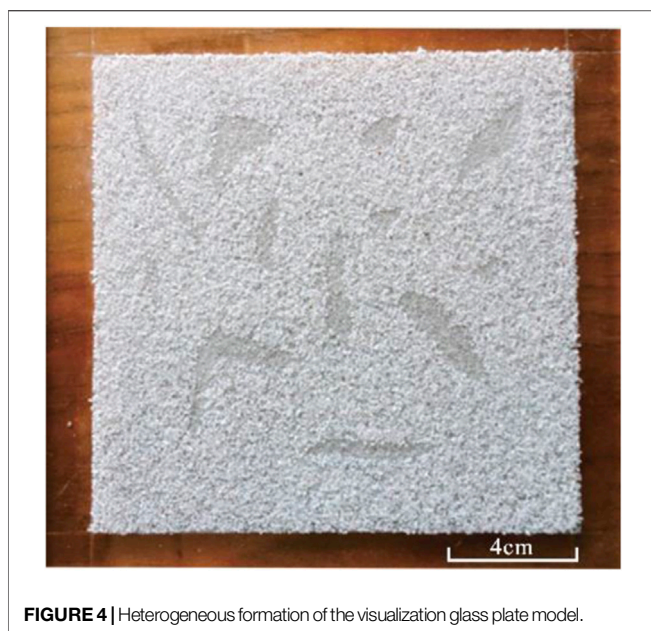


**FIGURE 4** | Heterogeneous formation of the visualization glass plate model.

## EXPERIMENTAL RESULTS AND ANALYSIS

### Homogeneous Model Experiment

The homogeneous visualization glass plate model was used to observe and measure the effectiveness of the oil-displacing agent on enhancing oil recovery and the distribution of remaining oil at different times, as shown in **Figure 5**.

After the homogeneous formation was displaced by water, the Yong eight oil-water displacement channel was diagonal, and the initially produced tributaries no longer flowed with the water displacement. This is due to the phenomenon of fingering in the main flow channel, in which the crude oil flows out of the production well from this channel first, causing the pressure of the branch channel to decrease. The diagonal main channel of the Chenzhuang oil-water drive channel is narrow, and most oil flows out of the wellhead along the upper and lower tributaries (**Figure 5**, yellow arrows). This phenomenon differs from the commonly known rule of diagonal main channels, so accurate numerical simulations cannot be performed.

These two different phenomena are mainly related to the viscosity of crude oil. When low-viscosity Chenzhuang oil is

**TABLE 3** | Visual glass plate model of the oil displacement experiment scheme.

Type of oil	Type of model	Oil-displacing agent system	Injection method of oil-displacing agent
Chenzhuang oil	Homogeneous model	PA-5	Single slug
		OH-3	Single slug
			Double slug
Yong 8 oil	Homogeneous model	PA-5	Single slug
		OH-3	Single slug
			Double slug
	Heterogeneous model	OH-3	Single slug
			Double slug

### Visualization Oil-Displacement Experimental Procedures

In this experiment, two kinds of visual glass plate oil displacement experiments with homogeneous and heterogeneous simulated formations were designed, as shown in **Table 3**. Each group of experiments was repeated 3 times to reduce experimental error, and the reported result is the average of the three replicates. The experiment process is as follows (the experiment was carried out at 26 °C and atmospheric pressure, and the displacement rate was 0.3 ml/min):

After the glass plate model was filled with oil, water flooding was conducted until the produced fluid contained 95% water. The subsequent oil-displacing agent injection methods are divided into single-slug and double-slug. The single-slug involves a one-time injection of 0.5 PV oil displacing agent, and the double-slug involves injecting 0.3 PV oil-displacing agent first, then 0.3 PV water, and then injecting 0.3 PV of the oil-displacing agent for a second time. After the oil-displacing agent is injected, water flooding is resumed until the water production rate reaches 98%.

displaced by water, the flow pressure in the diagonal channel gradually increased due to the accumulation of crude oil and is greater than the respective pressures of the two branch channels; thus, the upper and lower branches will flow out of the production well first. At this time, the pressure of the production well decreases, the pressure gradient between the diagonal channel and the production well rises, and the fingering phenomenon intensifies, which narrows the diagonal channel. For high-viscosity oil, the pressure difference between the flow channels is not sufficient to drive the tributaries to flow out of the production well quickly, so the diagonal flow rule is still obeyed. Image analysis of the first water displacement of the four tests was used to calculate the oil recovery rate of the water flooding, as shown in **Figure 6**. Although all the recovery rates of water displacement are in the range of 13–15%, the water displacement processes of the two oils in the formation were different. This precisely achieves the purpose of using visual model experiments to distinguish different experimental processes.

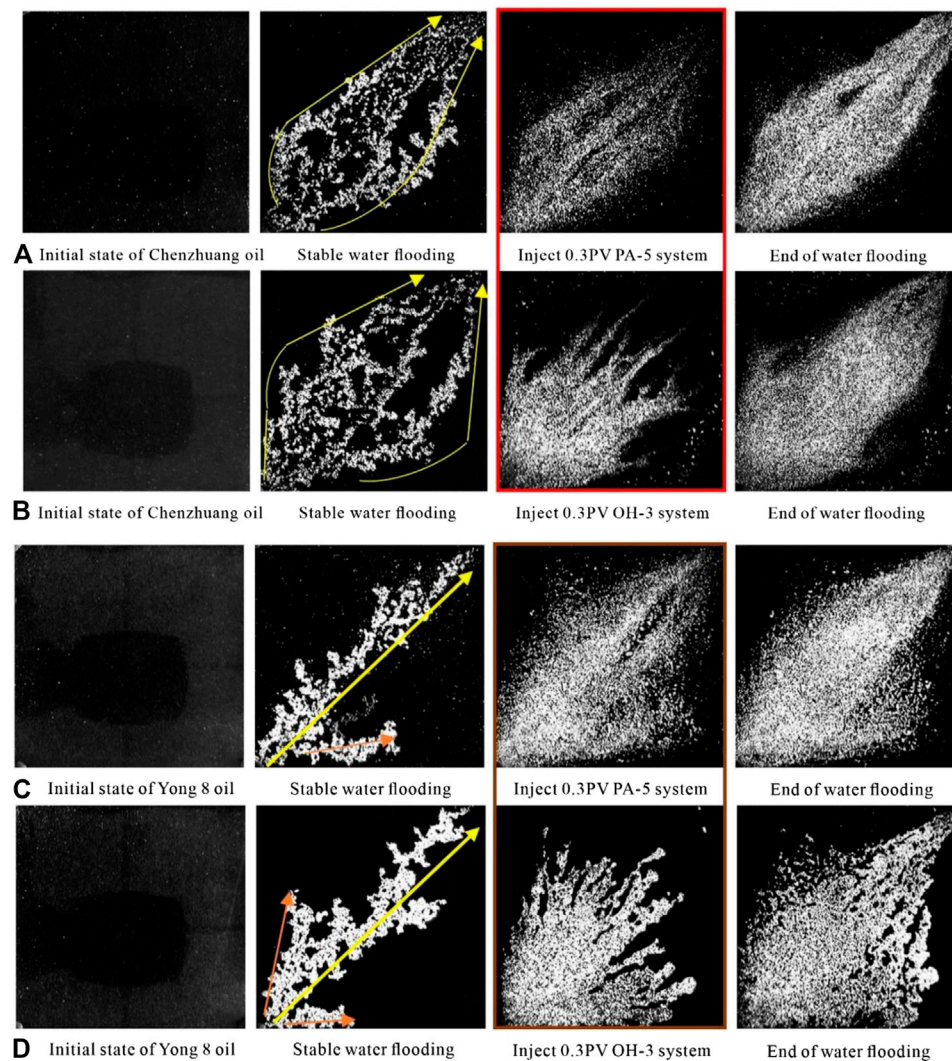


**FIGURE 5 |** Experimental process of the visualization glass plate homogeneous model. \*The yellow arrow is the main channel, the orange is the tributary, the red box is the effect of PA-5 and OH-3 on Chenzhuang oil, and the brown box is the effect of PA-5 and OH-3 on Yong eight oil.

In the experiment, the OH-3 oil-displacing system was better than the PA-5 system after being injected into the formation, and the oil-displacement effect on Yong eight oil was better than that on Chenzhuang oil, as shown in the boxed diagram in **Figures 5, 6**. Continuing water displacement after agent injection will cause the oil displacing agent to flow forward and carry the crude oil along the road to the wellhead after reducing the viscosity of the oil. After that, continued water injection does not greatly improve the recovery factor. In the four groups of experiments, the highest last water displacement recovery factor was improved by 3%, which was obtained by using PA-5 oil displacement agent to displace Chenzhuang oil.

The oil-displacing agent did not significantly increase the oil recovery as expected due to the high concentration of the oil-displacing agent, which formed a film on the surface of the crude oil. This phenomenon is particularly obvious near the injection well. Thus, a high oil-displacing agent concentration does not

always result in a better oil-displacing effect. The effect of the oil-displacing agent is directly related to its injection rate and concentration. To further exploit the remaining oil near the oil well, it is necessary to adjust the application method of oil-displacing agents. Subtle differences before and after the last water displacement can only be compared and analyzed using image analysis to obtain accurate data, which reflects the advantages of this automatic calculation method.

The results of the image analysis after the experiment showed that although the displacement has a wide range and the sweep efficiency is about 60%, the oil washing efficiency was not high, and the overall recovery rate is still about 25%; therefore, the key to enhancing oil recovery in homogeneous oil reservoirs to improve the oil washing efficiency.

The OH-3 oil-displacing agent system was tested using the double-slug injection method, and the recovery factor of the two oils was calculated by the Matlab image analysis method



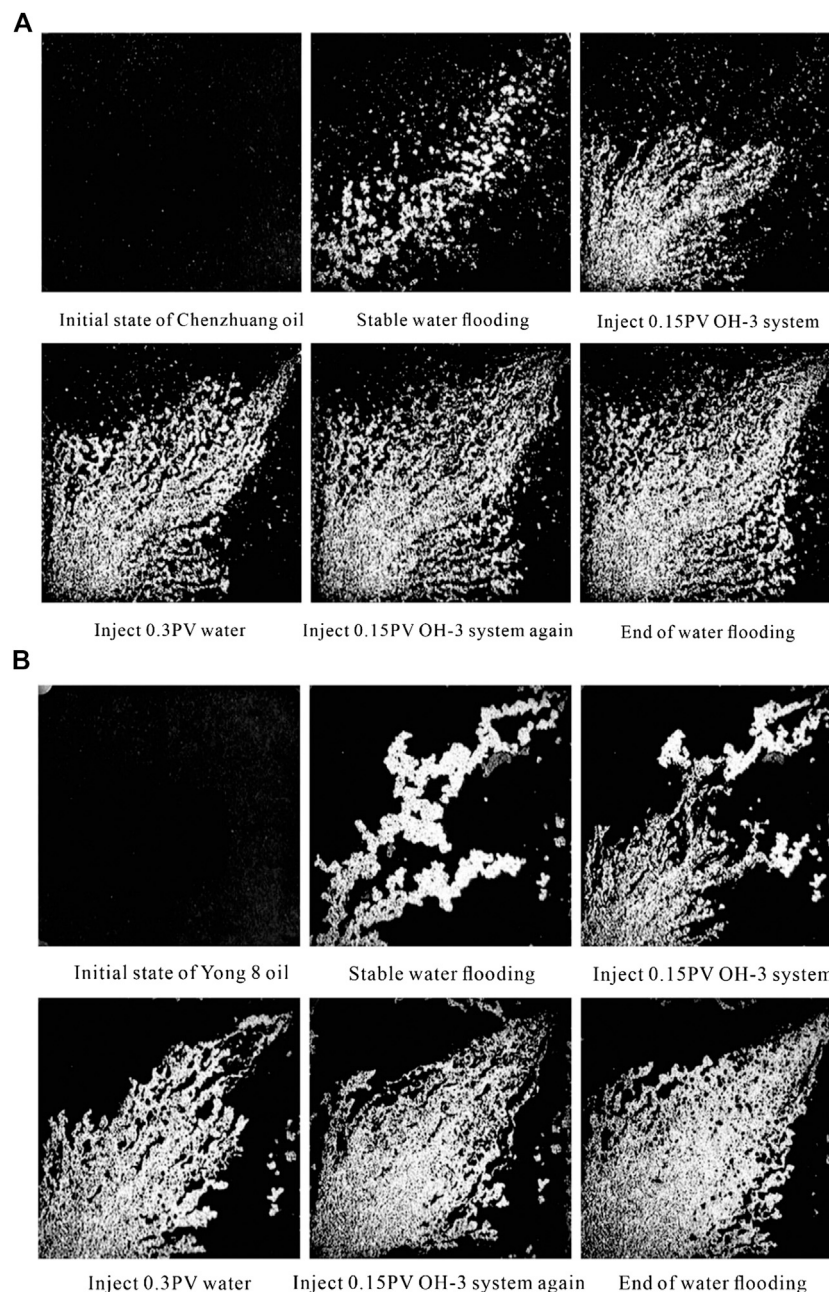


**FIGURE 6 |** Comparison of the recovery factor between single slug (0–1 water displacement, 1–4 oil-displacing agent injection, 4–5 the last water displacement) and double slug (0–1 water displacement, 1–2 first oil-displacing agent injection, 2–3 water injection, 3–4 secondary oil-displacing agent injection, 4–5 the last water displacement) injection methods.

(Figures 6, 7). The two-stage oil-displacing agent and the water in the middle stage gradually expanded the outer edge of the original water-flooding channel, which increased the spread to 70%, but the oil washing efficiency was improved to only 40%; therefore, the improvement of oil displacement recovery rate was still small.

For homogeneous formations, the double-slug injection method only slightly improves the oil recovery efficiency. The final water displacement after injection of the agent has little effect on enhancing the oil recovery, which is an urgent problem

that needs to be solved for subsequent enhancement of oil recovery after injecting an oil-displacing agent.

## Heterogeneous Model Experiment

A heterogeneous model experiment was used to test the effect of single-slug injection of the OH-3 oil displacement agent system for enhancing the oil recovery of Yong eight oil, as shown in Figure 8A. During water displacement, the oil in the high-permeability area was driven out, and the oil in the

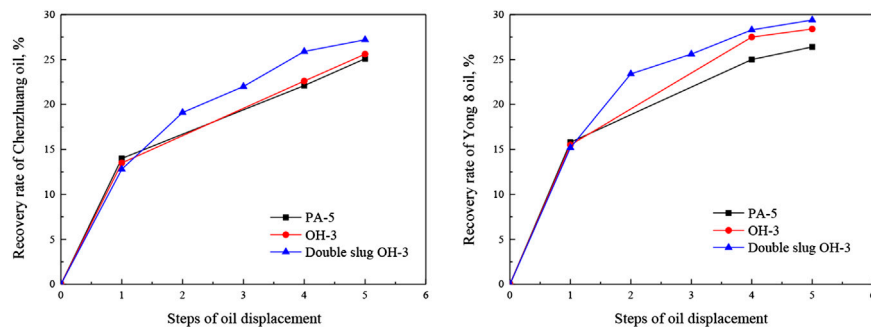


**FIGURE 7 |** Double slug experiment of the homogeneous formation of the visualization glass plate model.

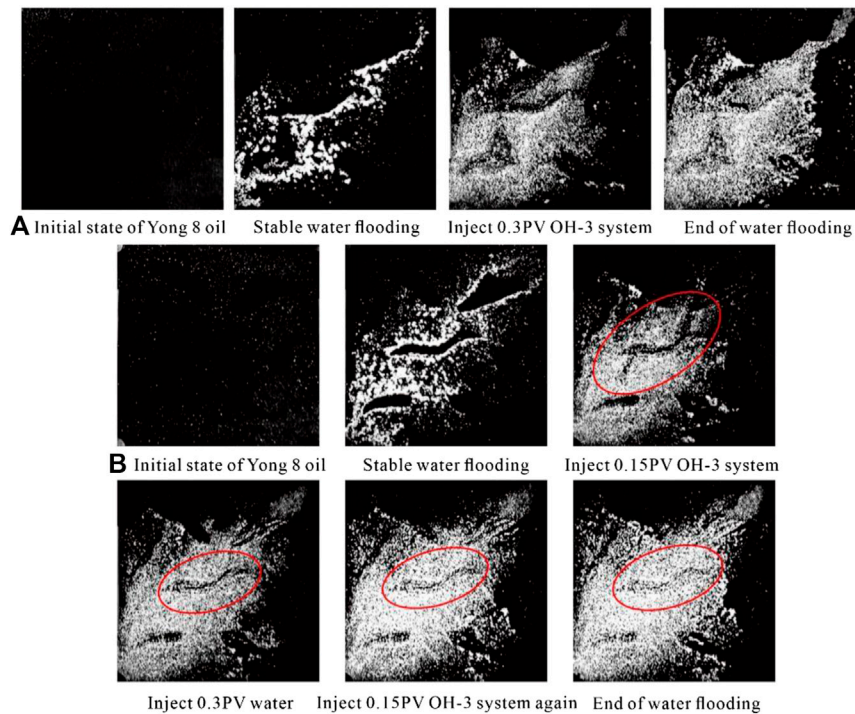
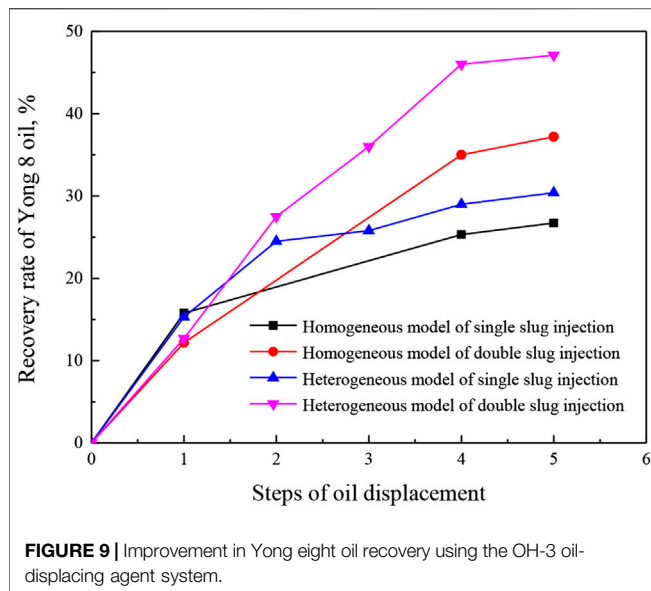


**FIGURE 8 |** Heterogeneous formation experiment for the visualization glass plate model. **(A)** Single-slug injection, **(B)** Dual-slug injection.

low-permeability area was retained. The OH-3 oil-displacing agent system reduces the viscosity of the crude oil at the edge of the tight block under shear and gradually peels off the peripheral oil, which drives the oil-displacing agent into tight formations. The oil-displacing agent slowly penetrates into tight blocks, reducing the viscosity of the remaining oil in the tight block and allowing it to flow into the high-permeability zone, which gradually increases the oil washing efficiency to 55%. So, the total recovery factor is 8% higher than that of the homogeneous layer, which is mainly due to the improved oil washing efficiency.

The oil displacement effect of the OH-3 system using the dual-slug injection method was further tested, as shown in **Figure 8B**. Results analysis showed that the oil washing efficiency in the tight

block was higher. Only the water injection stage between the two oil-displacing agent slugs increased the oil recovery of the tight block by about 3%. This is because the water injected between the two injections of the OH-3 oil-displacing agent slug also acted as an “oil-displacing agent,” which generated a peeling oil effect. The water between the slugs of the two oil-displacing agents has a predetermined isolation effect and also adjusts the concentration of the injected OH-3 oil-displacing agent system. This prolongs the action time of the oil-displacing agent and gives full play to the viscosity-reducing effect of the oil-displacing agent. The final water displacement can slightly improve the oil washing efficiency at the edge of tight reservoirs, but it has little effect on the internal oil displacement of tight blocks. The total recovery



factor of this method was 47%, which is 18% higher than that of the double-slug injection method in the homogeneous layer (Figure 9). Therefore, high concentrations of oil-displacing agents are more suitable for heterogeneous reservoirs, and the injection rate should be as slow as possible to ensure maximum viscosity reduction of crude oil in tight areas to achieve a higher oil washing efficiency.

## SUMMARY AND CONCLUSION

- (1) In this paper, the image processing function of Matlab software was used to combine the oilfield oil displacement recovery factor calculation formula, which linked experimental images with the parameters in the formula and summed a set of evaluation methods based on computer graphics for visualization plate model displacement experiments.

## REFERENCES

- Artun, E., and Kulga, B. (2020). Selection of candidate wells for re-fracturing in tight gas sand reservoirs using fuzzy inference. *Petrol. Explor. Dev.* 47 (2), 413–420. doi:10.1016/S1876-3804(20)60058-1
- Chatenever, A., Indra, M. K., Kyte, J. R., and Alme, M. (1959). *Microscopic observations of solution gas-drive behavior*. Tokyo, Japan: SPEJ.
- Chen, L., Suzuki, T., Nonomura, T., and Asai, K. (2019). Characterization of luminescent mini-tufts in quantitative flow visualization experiments: surface flow analysis and modelization. *Exp. Therm. Fluid Sci.* 103, 406–417. doi:10.1016/j.expthermflusc.2019.02.002
- Clerke, E. A. (2007). *Permeability and microscopic displacement efficiency of M-1 bimodal pore systems in arab-D limestone*. Manama, Bahrain: SPE.
- Donaldson, E. C., and Thomas, R. D. (1971). *Microscopic observations of oil displacement in water-wet and oil-wet systems*. Orleans, LA: SPE.

- (2) Matlab software image processing technology was used to digitized visualization experimental results by combining physical model experiments with digital model analysis technology. This provided a convincing comparison of oil displacement efficiency and perfected the visualization simulation technology.
- (3) The evaluation of an oil-displacing agent was used as an example by visualizing a glass plate model experiment and Matlab image processing. The improvement effects of two different injection methods on the oil recovery rate were compared, and it was found that OH-3 oil-displacing agent using a dual-slug injection method was more suitable for heterogeneous reservoirs.

## DATA AVAILABILITY STATEMENT

The raw data supporting the conclusion of this article will be made available by the authors, without undue reservation.

## AUTHOR CONTRIBUTIONS

XS developed the original structure of the draft. JG revised the manuscript by substantially restructuring it and adding up critical insights. SR and AZ did some experiments and assisted in processing related data. JG is the corresponding author who communicate on behalf of all authors.

## FUNDING

This study was conducted using funds from the National Natural Science Foundation of China (No. 51574266), the Major Scientific and Technological Projects of CNPC under Grant (ZD2019-183-007), National Key R&D Program of China (2018YFA0702400) and Postgraduate Innovation Funding Project of China University of Petroleum (East China) (YCX2020024).

- Fu, L., Zhang, G., Ge, J., Liao, K., Pei, H., Jiang, P., et al. (2016). Study on organic alkali-surfactant-polymer flooding for enhanced ordinary heavy oil recovery. *Colloids Surf. A*. 508, 230–239. doi:10.1016/j.colsurfa.2016.08.042
- Guo, J., Yang, Y., Zhang, D., Wu, W., Yang, Z., and He, L. (2018). A general model for predicting apparent viscosity of crude oil or emulsion in laminar pipeline at high pressures. *J. Petrol. Sci. Eng.* 160, 12–23. doi:10.1016/j.petrol.2017.10.034
- Li, X., Shi, L., Li, H., Liu, P., Luo, J., and Yuan, Z. (2018). Experimental study on viscosity reducers for SAGD in developing extra-heavy oil reservoirs. *J. Petrol. Sci. Eng.* 166, 25–32. doi:10.1016/j.petrol.2018.03.022
- Liu, H., Yang, F., Yang, Z., and Duan, Y. (2020a). Modeling the viscosity of hydrofluorocarbons, hydrofluoroolefins and their binary mixtures using residual entropy scaling and cubic-plus-association equation of state. *J. Mol. Liq.* 308, 113027. doi:10.1016/j.molliq.2020.113027
- Liu, Z., Wu, G., and Wei, C. (2020b). Physical experiments and numerical simulations of viscosity reducer flooding for ordinary heavy oil. *J. Petrol. Sci. Eng.* 192, 107194. doi:10.1016/j.petrol.2020.107194



- Mask, G., Wu, X., and Ling, K. (2019). An improved model for gas-liquid flow pattern prediction based on machine learning. *J. Petrol. Sci. Eng.* 183, 106370. doi:10.1016/j.petrol.2019.106370
- Miah, M. I., Elhaj, M. A., Ahmed, S., and Hossain, M. E. (2018). Modeling of temperature distribution and oil displacement during thermal recovery in porous media: a critical review. *Fuel*. 226, 423–440. doi:10.1016/j.fuel.2018.04.018
- Neel, G., Debashis, D., and Brijes, M. (2018). “Analysis of crack propagation in shale using microscopic imaging techniques.” in 52nd U.S. Rock Mechanics/Geomechanics Symposium, Seattle, WA, June, 2018. ARMA.
- Pei, H., Shu, Z., Zhang, G., Ge, J., Jiang, P., Qin, Y., et al. (2018). Experimental study of nanoparticle and surfactant stabilized emulsion flooding to enhance heavy oil recovery. *J. Petrol. Sci. Eng.* 163, 476–483. doi:10.1016/j.petrol.2018.01.025
- Pei, H., Zhang, G., Ge, J., Jiang, P., Zhang, J., and Zhong, Y. (2017). Study of polymer-enhanced emulsion flooding to improve viscous oil recovery in waterflooded heavy oil reservoirs. *Colloids Surf. A*. 529, 409–416. doi:10.1016/j.colsurfa.2017.06.039
- Priest, C., Reid, M. D., and Whitby, C. P. (2011). Formation and stability of nanoparticle-stabilised oil-in-water emulsions in a microfluidic chip. *J. Colloid Interface Sci.* 363 (1), 301–306. doi:10.1016/j.jcis.2011.07.060
- Sabet, N., Mohammadi, M., Zirahi, A., Zirrahi, M., Hassanzadeh, H., and Abedi, J. (2020). Numerical modeling of viscous fingering during miscible displacement of oil by a paraffinic solvent in the presence of asphaltene precipitation and deposition. *Int. J. Heat Mass Tran.* 154, 119688. doi:10.1016/j.ijheatmasstransfer.2020.119688
- Shabani Afrapoli, M., Nikooee, E., and Alipour, S. (2011). *Experimental and analytical study of microscopic displacement mechanisms of MIOR in porous media*. Houston, TX: SPE.
- Shi, L., Ma, D., Liu, P., Li, X., Xi, C., and Wang, C. (2019). Experimental and numerical simulation studies on effects of viscosity reducers for steam assisted gravity drainage performances in extra-heavy oil reservoirs. *J. Petrol. Sci. Eng.* 173, 146–157. doi:10.1016/j.petrol.2018.10.008
- Sun, Z., Wu, X., Kang, X., Lu, X., Li, Q., Jiang, W., et al. (2019). Comparison of oil displacement mechanisms and performances between continuous and dispersed phase flooding agents. *Petrol. Explor. Dev.* 46 (1), 121–129. doi:10.1016/S1876-3804(19)30011-4
- Templeton, C. C. (1954). A study of displacements in microscopic capillaries. *J. Pet. Technol.* 6, 7. doi:10.2118/307-G
- Trygstad, J. C., Ehrlich, R., and Wardlaw, N. C. (1986). *Physical modeling of microscopic rock-pore heterogeneities*. Tulsa, OK: SPE.
- Wang, F., Yang, H., Li, M., Kang, X., Zhang, X., Zhang, H., et al. (2020). Study on stabilization of emulsion formed by the supramolecular system of amphiphilic polymer and sodium polyacrylic acid. *J. Mol. Liq.* 314, 113644. doi:10.1016/j.molliq.2020.113644
- Wang, G. C. (1982). *Microscopic Investigation of CO<sub>2</sub> flooding process*. Birmingham, AL: SPE.
- Wang, Y., Hou, J., Tang, Y., and Song, Z. (2019). Effect of vug filling on oil displacement efficiency in carbonate fractured-vuggy reservoir by natural bottom-water drive: a conceptual model experiment. *J. Petrol. Sci. Eng.* 174, 1113–1126. doi:10.1016/j.petrol.2018.12.014
- Wu, M., Ding, M., Yao, J., Li, C., Li, X., and Zhu, J. (2019). Development of a multi-continuum quadruple porosity model to estimate CO<sub>2</sub> storage capacity and CO<sub>2</sub> enhanced shale gas recovery. *J. Petrol. Sci. Eng.* 178, 964–974. doi:10.1016/j.petrol.2019.03.077
- Wu, Z., Liu, H., Wang, X., and Zhang, Z. (2018). Emulsification and improved oil recovery with viscosity reducer during steam injection process for heavy oil. *J. Ind. Eng. Chem.* 61, 348–355. doi:10.1016/j.jiec.2017.12.033
- Zhang, A., Yang, Z., Li, X., Xia, D., Zhang, Y., Luo, Y., et al. (2020a). An evaluation method of volume fracturing effects for vertical wells in low permeability reservoirs. *Petrol. Explor. Dev.* 47 (2), 441–448. doi:10.1016/S1876-3804(20)60061-1
- Zhang, N., Wei, M., Fan, J., Aldhaferi, M., Zhang, Y., and Bai, B. (2019). Development of a hybrid scoring system for EOR screening by combining conventional screening guidelines and random forest algorithm. *Fuel*. 256, 115915. doi:10.1016/j.fuel.2019.115915
- Zhang, Y., Khorshidian, H., Mohammadi, M., Sanati-Nezhad, A., and Hejazi, S. H. (2020b). Functionalized multiscale visual models to unravel flow and transport physics in porous structures. *Water Res.* 175, 115676. doi:10.1016/j.watres.2020.115676

**Conflict of Interest:** Author AZ was employed by company Tarim Oilfield, PetroChina.

The remaining authors declare that the research was conducted in the absence of any commercial or financial relationships that could be construed as a potential conflict of interest.

Copyright © 2021 Sun, Ge, Ren, and Zhao. This is an open-access article distributed under the terms of the Creative Commons Attribution License (CC BY). The use, distribution or reproduction in other forums is permitted, provided the original author(s) and the copyright owner(s) are credited and that the original publication in this journal is cited, in accordance with accepted academic practice. No use, distribution or reproduction is permitted which does not comply with these terms.



# Study of Rheological Property and Flow Behavior for Nanoparticles Enhanced VES System in Porous Media

Zhaoxia Liu\*, Qiang Wang, Ming Gao, Wenli Luo and Hongyan Cai

State Key Laboratory of EOR, RIPED, Beijing, China

In this paper, a composite sample (VES and SiO<sub>2</sub> nanoparticle) was used to overcome the deficiencies of polymer. The rheological character of the VES/nanoparticles hybrid and flow behavior in porous media were examined. It was found that SiO<sub>2</sub> nanoparticles exhibited viscosifying action and improved the oil tolerance. In addition, the VES solution without nanoparticles showed a lower capacity to recover oil, which might be attributed to the fact that wormlike micelles would be destroyed in crude oil. On the contrary, an enhanced oil recovery of 9.68% was achieved in the composited experiment for the VES sample with nanoparticles which is relatively stable with oil.

## OPEN ACCESS

### Edited by:

Songyan Li,  
China University of Petroleum  
(Huadong), China

### Reviewed by:

Hairong Wu,  
China University of Petroleum, China  
Mingwei Zhao,  
China University of Petroleum  
(Huadong), China

### \*Correspondence:

Zhaoxia Liu  
zhaoxliu@163.com

### Specialty section:

This article was submitted to  
Advanced Clean Fuel Technologies,  
a section of the journal  
Frontiers in Energy Research

**Received:** 24 August 2020

**Accepted:** 08 January 2021

**Published:** 23 February 2021

### Citation:

Liu Z, Wang Q, Gao M, Luo W and  
Cai H (2021) Study of Rheological  
Property and Flow Behavior for  
Nanoparticles Enhanced VES System  
in Porous Media.  
Front. Energy Res. 9:598177.  
doi: 10.3389/fenrg.2021.598177

**Keywords:** worm-like, nano-SiO<sub>2</sub>, rheology, enhanced oil recovery, viscoelastic surfactant, worm

## INTRODUCTION

Viscoelastic surfactant (VES) fluids, generally formed by wormlike micelles, have been utilized as completion or stimulation agents in the oil and gas industry (Jeffrey Giacomini et al., 2008). Durga P. Acharya discussed the formation of wormlike micelles and the evolution of rheological properties in different mixed surfactant systems (Zhang, et al., 2018; Chu, et al., 2010). Lstvan Lakatos evaluated the VES fluid as a mobility control agent. It shows that a slug-type injection protocol is more efficient than the continuous injection of any single displacement fluids (Lakatos, et al., 2007). Michael Golombok carried out experiments on inert glass cores in the range of 45–2,200mD. By analogy they considered their observations to correspond to permeability thickening, although it was understood that the permeability was fixed and the apparent viscosity increased. For the range of permeabilities that are applicable to oil reservoirs, the apparent viscosities observed at high permeabilities are around 10 times that of the low permeabilities (Golombok and van der Wijst, 2013).

Recent work has shown the advantageous use of nanoparticles in VES fluid systems, which included significantly increased thermal stability and fluid loss control properties in the fluid system (Huang and Crews, 2007; Qin, et al., 2017). It shows that when selected nanoparticles are added to a VES solution, they will associate or “pseudo-crosslink” the VES micelles together through charge attraction and surface adsorption (Huang, 2007). Ranjini Bandyopadhyay and A.K. Sood studied the effects of the addition of submicrometer-sized colloidal silica spheres on the linear and nonlinear rheology of semidilute solutions of a viscoelastic gel (Bandyopadhyay and Sood, 2005). The oscillatory rheological measurements for nanoparticles in viscoelastic surfactant fluids noted that the nanoparticles apparently strengthened the micelle-micelle interactions. Lab proppant settling tests demonstrated that the nanoparticle induced VES micelle network structures that dramatically increased the capacity of the surfactant fluid to suspend and transport proppant in well treatments

(Huang et al., 2008; Huang and Crews, 2007; Huang and Crews, 2008; Crews and Huang, 2008; Crews and Ahmed, 2012; Gurluk, et al., 2013). M.F. Fakoya thinks the nanofluids could be used for hydraulic fracturing (Fan et al., 2011; Fakoya and Shah, 2013; Fakoya and Shah, 2014). They also investigated the pyroelectric barium titanate ( $\text{BaTiO}_3$ ) nanoparticle and found the viscosity of the MES micelle solution increased with the temperature within a certain range because of the pyroelectric effect of the nanoparticles (Luo, et al., 2012; Helgeson, et al., 2010).

For the majority of oil reservoirs, large amounts of oil are still left unrecovered after extensive water flooding. Chemical EOR technology is the most promising tertiary recovery technique to both improve sweep and displacement efficiency. The well-known process to improve sweep efficiency consists in injecting polymer solution. This process known as polymer flooding has been widely used at large scale especially at Daqing field in China (Morvan, et al., 2009). For conventional polymer flooding, the injection of concentrated polymer solutions raises injectivity issues and requires higher injection pressure with the risk of exceeding the formation fracturing pressure. Micelles behave like polymer chains. In particular, at high concentrations, they form a network of topological entanglements and, as a result, the solution acquires viscoelastic properties. However, compared to polymers, the micellar chains of surfactants can reversibly break and recover. However, unlike polymers in solutions, wormlike micelles undergo breaking and recombination (Chu et al., 2010). Mikel Morvan studied the viscoelastic behavior, thermal stability, and adsorption on sandstone. They suspected that WLMs could increase the 29% of oil recovery vs. water flooding (Morvan, et al., 2012a; Degre, et al., 2012; Morvan, et al., 2012b). Joris van Santvoort studied the retardation ratio of VES in the different permeability core. Flow resistance in a high permeability core was shown to be significantly higher than in a low permeability core. Increasing the concentration of surfactant and co-solute led to an enhanced resistance factor (Zhu et al., 2013; Joris van and Golombok, 2015).

Herein, a novel hybrid sample (VES and  $\text{SiO}_2$  nanoparticle) has been studied to overcome the deficiencies of HPAM. We investigated the effects of nano- $\text{SiO}_2$  on the rheology of VES solutions and the influencing parameters, including surfactant concentrations, nanoparticle concentrations, particle diameters, and NaCl concentrations. We also compared the ability of the VES system in enhancing oil recovery in the presence and absence of nanoparticles. Our investigation may provide a new idea for the development of an oil recovery agent.

## EXPERIMENTAL

### Materials

The VES solutions used during the experiments are composed of sodium dodecyl sulfate (chemical pure) and lauroylamidopropyl betaine (industrial product) purchased from Sinopharm.  $\text{SiO}_2$  nanoparticles with different particle diameters including 7 nm, 12 nm, and 22 nm are those of Ludox SM, HS, and TM, were received as a gift from W. R. Grace. Sodium chloride (NaCl) was

purchased from the Xilong Scientific Company. Deionized water with an electrical resistivity of  $18.2 \text{ M}\Omega\cdot\text{cm}$  was used to prepare the solutions. Crude oil was obtained from the Shengli Oilfield in China, with a density and viscosity of  $0.89 \text{ g/cm}^3$  and  $80.1 \text{ mPa}\cdot\text{s}$ , respectively, at  $50^\circ\text{C}$ . Component analysis results show that this oil is composed of 70.66 wt% saturated hydrocarbons, 20.92 wt% aromatic hydrocarbons, 5.83 wt% resins, and 2.59 wt% asphaltene.

### Rheology Test

Rheological experiments were performed using an Anton Paar MCR301 rotational rheometer. The sample temperature was adjusted using a Peltier thermostat (Chen, et al., 2012). The viscosity of the samples was measured at different temperatures and various shear rates. During the angular frequency scan, elastic and storage moduli were determined at  $50^\circ\text{C}$  with the same rheometer (Zhu et al., 2013).

### Interfacial Tension Measurements

The dynamic IFT values were measured using a Texas-500 spinning drop tensiometer (Temco, United States) (Jiang, et al., 2014). The instrument was equipped with an image-acquisition module and the IFT value could be automatically calculated according to the length and the width of the oil droplet. The temperature for all the measurements was maintained at  $50^\circ\text{C}$  using a semiconductor thermostat.

### Sandpack Flooding Experiment

Flooding experiments were performed at  $50^\circ\text{C}$ . A steel cylinder of 10 inches in height and 1 inch in inner diameter was filled with quartz sands of different sizes. The porosity of the porous sandpack was about 35.8%. The sandpack was initially saturated with synthetic brine, and then displaced by dehydrated crude oil. Water flooding was performed until the water proportion of the output fluid was higher than 98%. Afterward, the composite VES solution was injected. The difference between water flooding recovery and total recovery was calculated as the tertiary recovery increased by nanoparticle/surfactant composite flooding. The injection rate was maintained at  $0.5 \text{ ml/min}$  (Zhu et al., 2013).

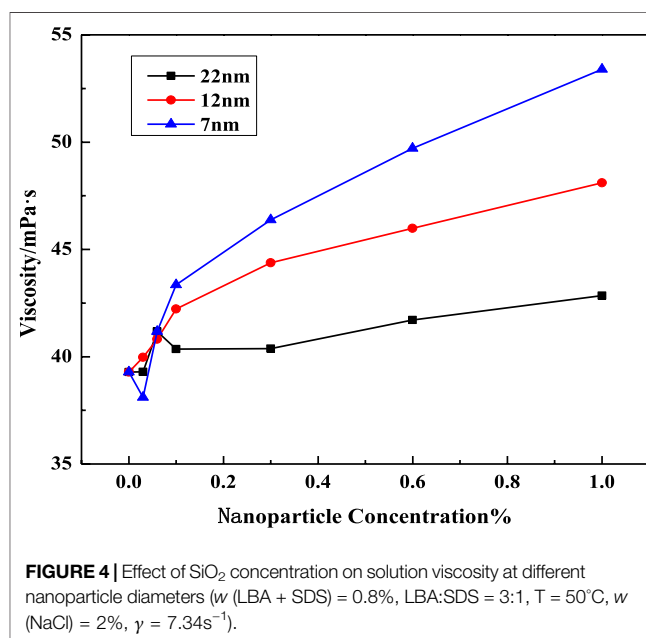
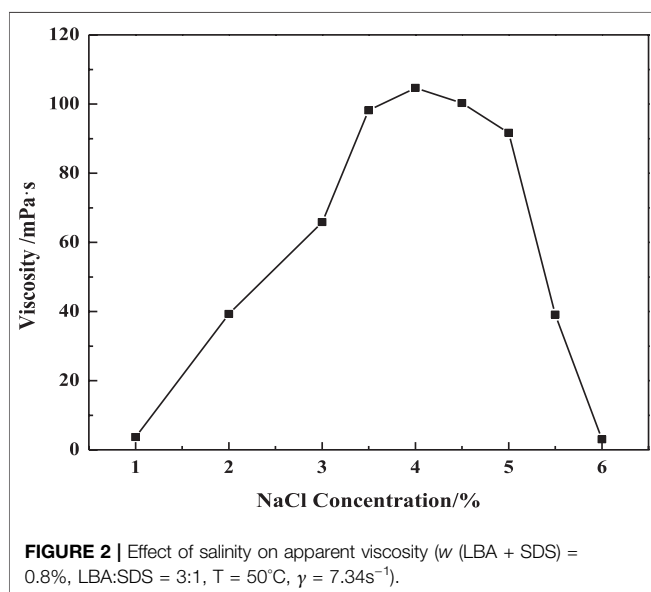
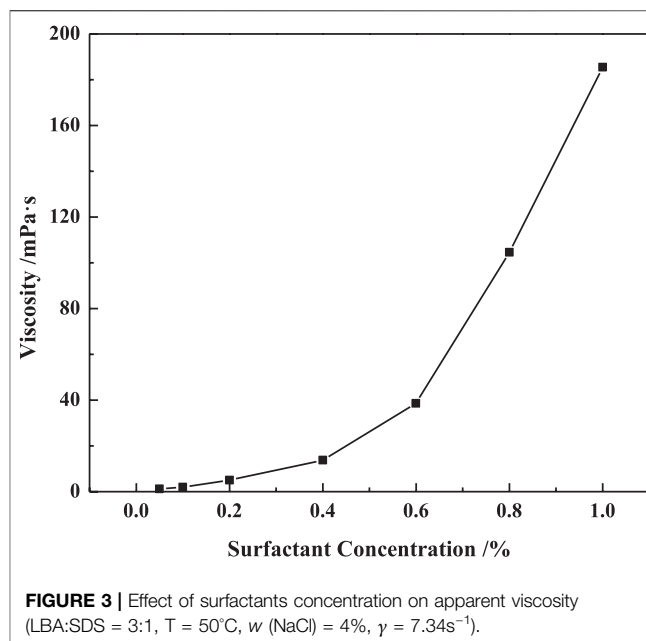
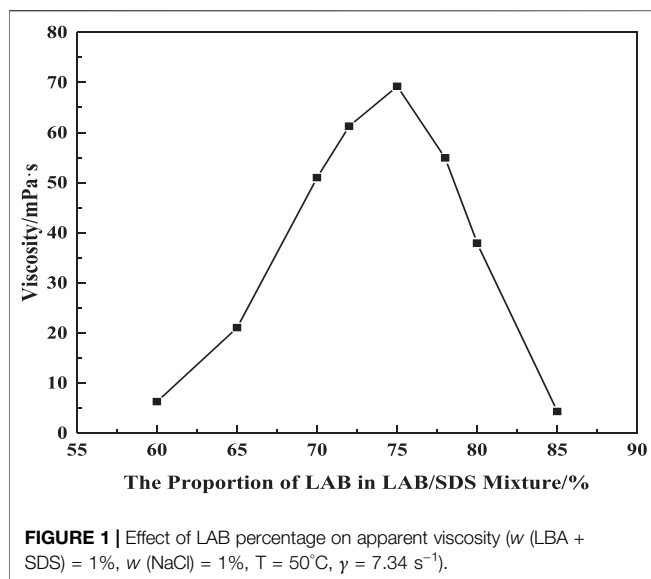
## RESULTS AND DISCUSSION

### Rheological Properties of VES

The viscosity of injected solutions plays a significant role in displacing crude oil during oilfield development. Consequently, it is necessary to clarify the rheological behaviors of nanoparticle/surfactant solutions (Zhu et al., 2013).

**Figure 1** shows the viscosities of VES at the shear rate of  $7.34 \text{ s}^{-1}$  against the percentage of LAB in the LAB/SDS mixture. The viscosity increases with the increasing LAB percentage on composite surfactants until the mass ratio of LAB/SDS is 3:1, after which the viscosity begins to drop. Therefore, this proportion is used in the following experiments.

**Figure 2** shows that the viscosity of VES is significantly affected by salinities. The VES viscosity increases with a

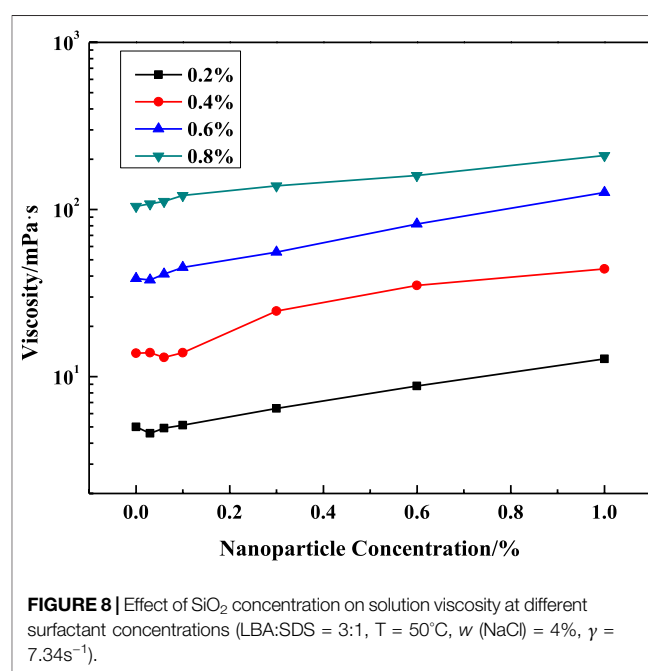
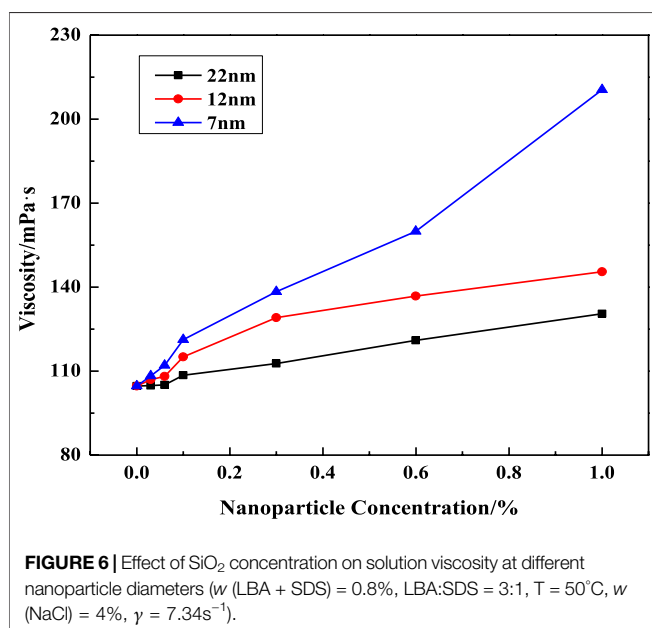
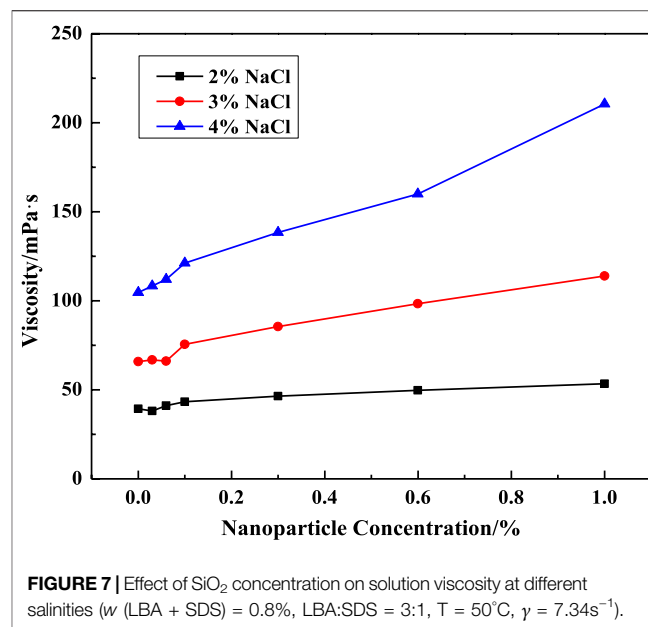
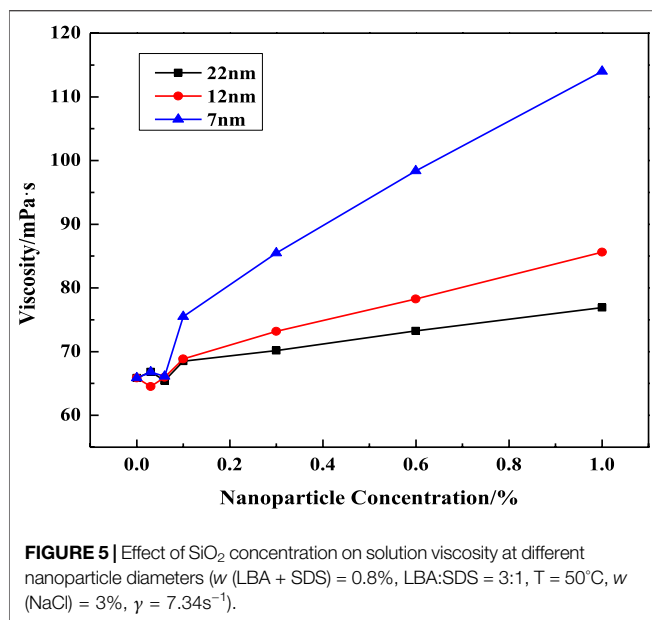


salinity until 4%, before which the NaCl could compress the diffuse electric double-layer of the surfactants. And it causes more surfactant molecules to go into the micelle promoting the growth of entangled wormlike micelles. But if the salinity is more than 4%, the diffuse electric double layer would be over compressed. The surface charge of the micelle is too low, making the micelles coil and decreases the fluid dynamics radius.

The viscosity variation of the VES solution against surfactant concentration is shown in Figure 3. The solution viscosity increases as the concentration rises especially when the surfactant concentration is more than 0.4%. The viscosity increases from 13.79 mPa·s to 185.49 mPa·s as the concentration increases from 0.4% to 1%, at which concentration the micelles could form a large space structure with higher viscosity.

## Rheological Behaviors of VES Samples With $\text{SiO}_2$ Nanoparticles

The curves of VES viscosity against the nanoparticle concentration at different salinities is shown in Figures 4–6. It shows that the viscosity of the VES solution at the same surfactant concentration could be apparently improved. These results can be interpreted in terms of the growth of entangled wormlike micelles, followed by the formation of bilayers due to the adsorption of the headgroups on  $\text{SiO}_2$  surfaces (Bandyopadhyay and Sood, 2005). It also shows that the  $\text{SiO}_2$  nanoparticles with a smaller diameter have a higher viscosifying



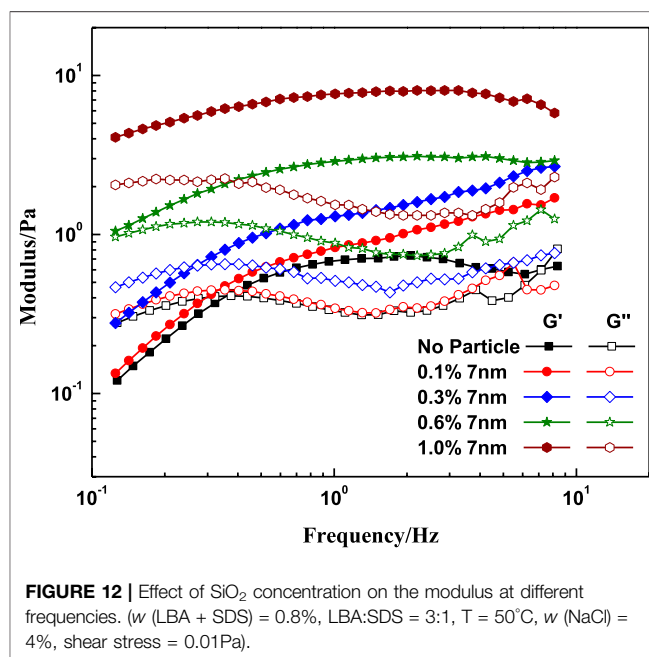
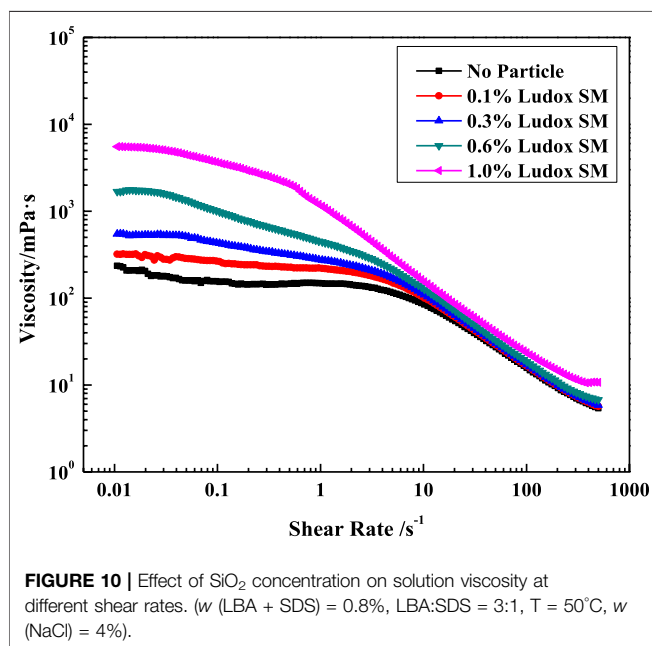
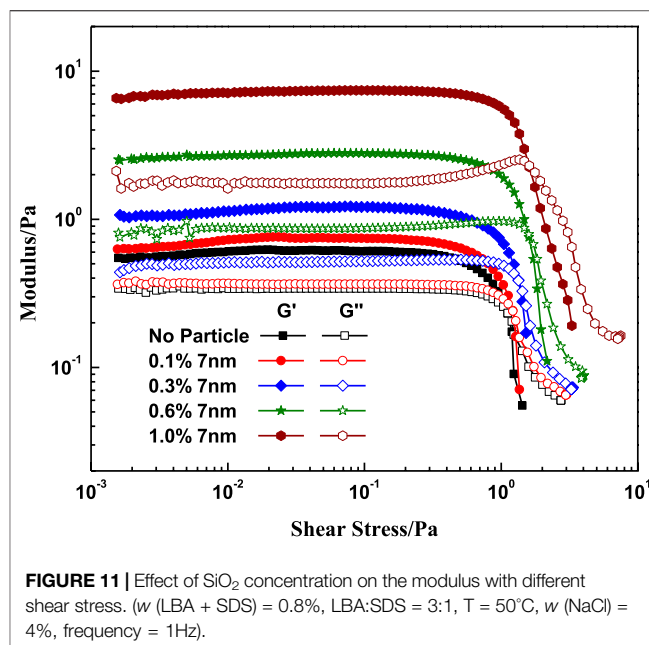
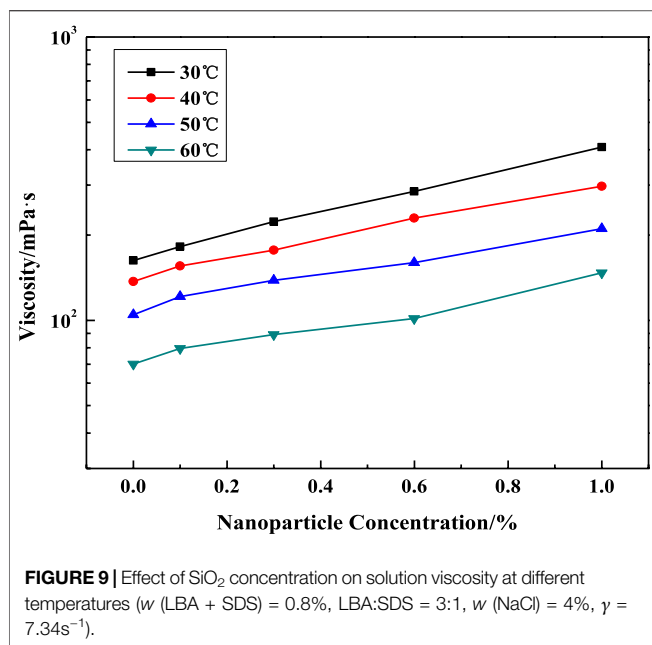
ability. This could be attributed to the fact that smaller nanoparticles have a higher specific surface area and higher amounts at a certain concentration, which may provide more crosslinking points. Therefore, 7nm SiO<sub>2</sub> nanoparticles were used in the following experiments.

The influence of silica particle concentration, salinity, surfactant concentration, and temperature on VES viscosity is shown in **Figures 7–9**. In **Figure 7**, the solution viscosity increases with the rise of SiO<sub>2</sub> concentration and salinity. Especially, the test sample containing 4% NaCl presents a wide range of viscosity increase with the nanoparticle addition compared with the low salinity solution, which means that nanoparticles enhanced the viscosity of VES

solutions by increasing the entanglements of wormlike micelles. As expected, the viscosity of the VES solution continuously decreases at increasing temperatures, which is similar to that of the system without particles.

Rheological evaluation of the viscoelastic nature of the surfactant fluids with and without nanoparticles was carried out. **Figure 10** shows the dependence of viscosity of the VES solution against the silica particle concentration on shear rate. At low shear rates, the viscosity of the VES solution without particles remains unchanged (Newtonian viscosity); then, its value

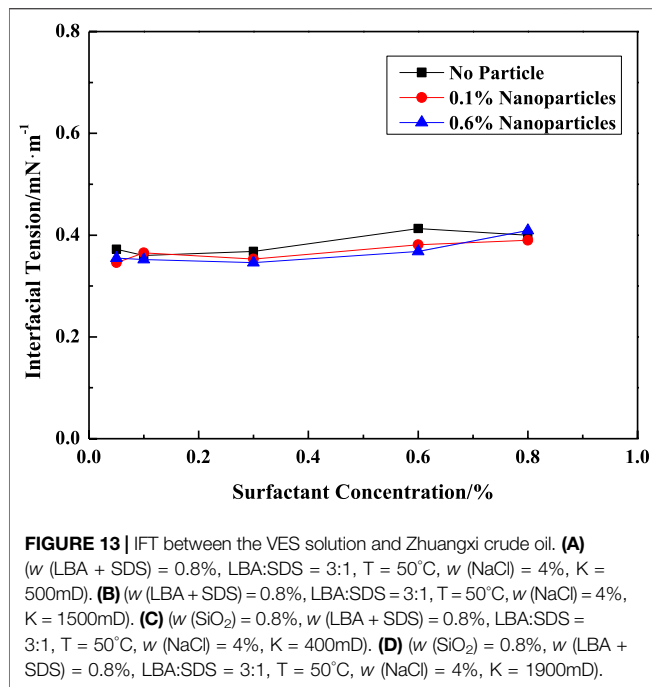




decreases as the shear rate grows above  $2\text{s}^{-1}$ , which is associated with the orientation of micellar chains along the flow direction and possibly with their partial break. And adding particles has a significant effect on the viscosity of VES solutions especially at low shear rates. Note that 1% nanoparticles increased the viscosity of the VES fluid by more than 23 times at the shear rate of  $0.1\text{s}^{-1}$ , which may be caused by the influence of particles on the network structure of micelles. But at high shear rates, the effect of the nanoparticles is weakened.

The  $G'$  and  $G''$  viscous-elastic behavior between the VES fluids with and without nanoparticles at different shear stress and

frequency are shown in **Figures 11, 12**. **Figure 11** shows that  $G'$  and  $G''$  of the VES solution with or without particles were constant at low shear stress and significantly decreased at high shear stress above 0.8Pa. Within the plateau area, the system shows strong elastic properties. And in the range of high shear stress, the loss modulus exceeds the value of the storage modulus. Meanwhile, adding nanoparticles increases both  $G'$  and  $G''$ , which indicated that the addition of small amounts of nanoparticles to the VES solution resulted in the strengthening of the micelle-micelle associations and elongated micelle structures in the fluids. The intersection point of the  $G'$  and



$G''$  right shifts with the increase of the nanoparticle concentration, which indicates that the SiO<sub>2</sub> has a greater contribution to  $G'$ .

Figure 12 shows that at low frequency the loss modulus exceeds the value of storage modulus, and the elastic properties dominate at high frequency. Meanwhile, adding nanoparticles increases both  $G'$  and  $G''$ , and the intersection point of the  $G'$  and  $G''$  left shift with the increases of the nanoparticles concentration indicates that the SiO<sub>2</sub> has a greater contribution to  $G'$  which is similar to the results of Figure 11.

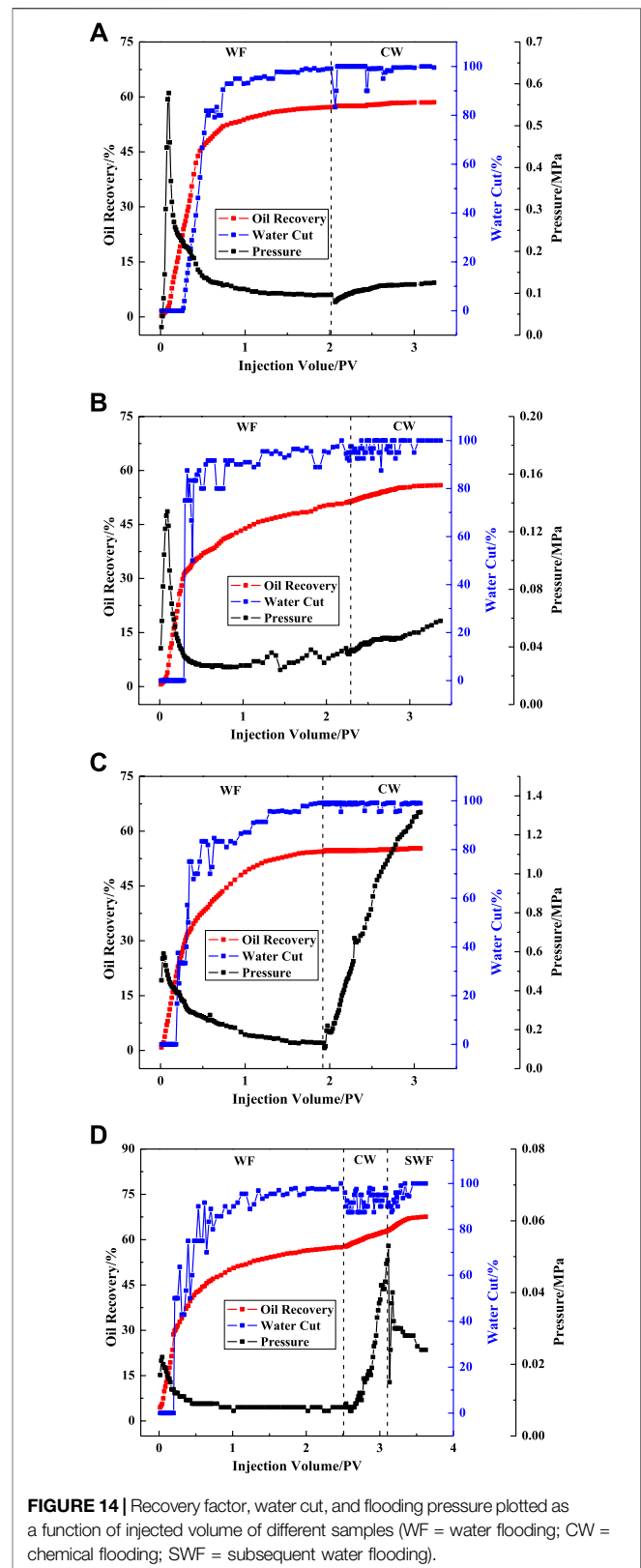
## Interfacial Tension Between VES Solution and Oil

Figure 13 shows the interfacial tensions between Zhuangxi crude oil and surfactant/silica solutions of various concentrations at 50°C. The interfacial tension is about 0.38mN/m within a wide range of surfactant concentrations. And adding SiO<sub>2</sub> has less effect on the IFT.

## Oil Displacement Test

Variations of recovery factors, water contents, and displacement pressures with injected volumes are plotted in Figure 14 of the VES solutions with and without nanoparticles in different permeability media. Sandpack parameters, flooding processes, and the oil recovery results are summarized in Table 1.

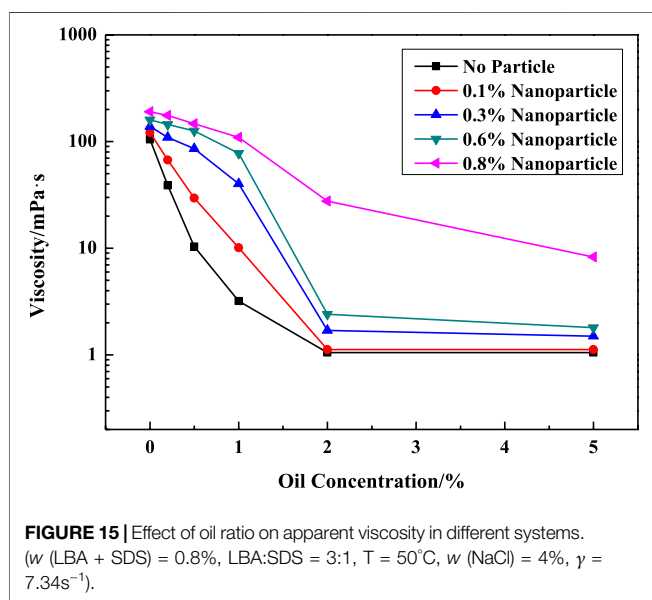
Less than 5% oil recovery was achieved by the VES solution without particles (Figures 14A,4B). As shown in Figures 14C, 4D, the oil recovery factor of the hybrid sample (VES solution with silica particles) was 9.68% in the high permeability zone, which was larger than that in low permeability media. In order to find the reason why VES has no effect on oil recovery, the apparent viscosity of VES with different oil ratios was measured, as shown in Figure 15.



It shows that oil has great influence on the apparent viscosity of the VES solution. Note that only 1% oil decreased the viscosity of the VES solution without nanoparticles by more than 97%

**TABLE 1** | Sandpack parameters, displacement process, and the results of these oil displacement tests.

	0.8% (LAB:SDS = 3:1) + 4% NaCl		0.8% (LAB:SDS = 3:1) + 4% NaCl + 0.8% 7nm SiO <sub>2</sub>	
Permeability/mD	500	1,500	400	1900
Initial oil saturation S <sub>o</sub> /%	88.56	88.16	89.90	88.45
Primary recovery efficiency R <sub>p</sub> /%	57.36	51.37	51.64	57.89
Secondary recovery factor R <sub>o</sub> /%	1.14	4.52	0.25	9.68
Overall recovery efficiency R <sub>o</sub> /%	58.50	55.89	51.89	67.57



which indicates the oil break of the structure of WLMs. But the presence of particles could weaken the influence of oil. The viscosity of the system with 0.8% SiO<sub>2</sub> only decreased about 43% when mixed with 1% crude oil.

The poor oil recovery efficiency of the VES solution without particles may be attributed to the fact that VES micelles could be easily destructed while in residual crude oil. On the contrary, the structure of VES in the presence of nanoparticles could be significantly enhanced, and thus the water/oil mobility ratio could be improved, resulting in a higher oil recovery (Zhu et al. 2013). The main reason for the invalidity of the hybrid samples in low permeability sandpicks can be ascribed to the bridging of nanoparticles at the inlet, a consequence of the continuously increasing injection pressures.

## CONCLUSION

The rheological behaviors of the VES/SiO<sub>2</sub> nanoparticle hybrid and sandpick flooding experiments were examined. It was found

that the SiO<sub>2</sub> nanoparticle exhibited viscosifying action and improved oil tolerance. In addition, the poor oil recovery efficiency of the solution without nanoparticles may be attributed to the destruction of the VES micelles upon contacting the residual oil. On the contrary, 9.68% of oil recovery was achieved from the VES and nanoparticle samples in the high permeability sandpick flooding test for the VES sample with nanoparticles which is relatively stable with oil in order to produce more oil. However, the nanoparticles bridging off the sandpick inlet restrict its use in a low permeability reservoir.

## DATA AVAILABILITY STATEMENT

The original contributions presented in the study are included in the article/Supplementary Material, further inquiries can be directed to the corresponding author.

## AUTHOR CONTRIBUTIONS

ZL, QW, and HC contributed to the conception and design of the work; QW, MG, and WL contributed to the acquisition and analysis of data for the work; QW, MG, and WL drafted the work; ZL and HC revise the work critically; All the five authors made the final approval of the version to be published; All the five authors made the agreement to be accountable for all aspects of the work in ensuring that questions related to the accuracy or integrity of any part of the work are appropriately investigated and resolved.

## ACKNOWLEDGMENTS

We acknowledge the Natural Science Foundation of China (51474234 and 51574266), the Natural Science Foundation of Shandong Province, China (ZR2014EZ002 and ZR2015EQ013), and the Fok Ying Tung Education Foundation (151049) for supporting this work.

## REFERENCES

- Bandyopadhyay, R., and Sood, A. K. (2005). Effect of silica colloids on the rheology of viscoelastic gels formed by the surfactant cetyl trimethylammonium tosylate. *J. Colloid. Interface. Sci.* 283 (2), 585–591. doi:10.1016/j.jcis.2004.09.038
- Chen, Q., Wang, Y., Lu, Z., and Feng, Y. (2012). Thermoviscosifying polymer used for enhanced oil recovery: rheological behaviors and core flooding test. *Polymer Bulletin*. 70, 391–401. doi:10.1007/s00289-012-0798-7
- Chu, Z., Feng, Y., Su, X., and Han, Y. (2010). Wormlike micelles and solution properties of a C22-tailed amidosulfobetaine surfactant. *Langmuir* 26, 7783–7791. doi:10.1021/la904582w
- Crews, J. B., and Ahmed, M. G. (2012). “Nanoparticle-associated surfactant micellar fluids: an alternative to crosslinked polymer systems,” in SPE 157055 was prepared for presentation at the SPE international oilfield nanotechnology conference held in Noordwijk, Noordwijk, Netherlands, June 12–14, 2012.
- Crews, J. B., and Huang, T. (2008). “Performance enhancements of Viscoelastic surfactant stimulation fluids with nanoparticles,” in SPE 113533 was prepared for presentation at the 2008 SPE Europec/EAGE annual conference and exhibition held in Rome, Rome, Italy, June 9–12, 2008.
- Degre, G., Morvan, M., and Beaumont, J. (2012). “Viscosifying surfactant technology for chemical EOR: a reservoir case,” in SPE 154675 was prepared for presentation at the spe EOR conference at oil and gas west asia held in Muscat, Muscat, Oman, April 16, 2012, 16–18.
- Fakoya, M. F., and Shah, S. N. (2013). “Rheological properties of surfactant-based and polymeric nano-fluids,” in SPE 163921 was prepared for presentation at the SPE/ICoTA coiled tubing & well intervention conference & exhibition held in the Woodlands, Woodlands, TX, United States, March 26–27, 2013.
- Fakoya, M. F., and Shah, S. N. “Enhancement of filtration properties in surfactant-based and polymeric fluids by nanoparticles,” in SPE-171029-MS was prepared for presentation at the SPE Eastern Regional Meeting held Charleston, Charleston, WV, United States, October 21–23, 2014.
- Fan, H., Luo, M., Jia, Z., and Hou, T. (2011). Effect of Nano-SiO<sub>2</sub> on the rheology of anionic viscoelastic solutions formed by the biodegradable surfactant fatty acid methyl ester sulfonate. *Materials Sci. Forum*. 694, 64–67. doi:10.4028/www.scientific.net/msf.694.64
- Golombok, M., and van der Wijst, R. (2013). Permeability thickening fluids for improved secondary oil recovery. *J. Petrol. Sci. Engineer.* 110, 22–26. doi:10.1016/j.petrol.2013.08.040
- Gurluk, M. R., Nasr-El-Dina, H. A., and Crews, J. B. (2013). “Enhancing the performance of viscoelastic surfactant fluids using nanoparticles,” in SPE 164900 was prepared for presentation at the EAGE Annual Conference & Exhibition incorporation SPE Europec held in London, London, United Kingdom, June 10–13, 2013. doi:10.2118/164900-MS
- Helgeson, M. E., Hodgdon, T. K., Kaler, E. W., Wagner, N. J., and Vethamuthu, K. P. A. (2010). Formation and rheology of viscoelastic “double networks” in wormlike micelle–nanoparticle mixtures. *Langmuir* 26 (11), 8049–8060. doi:10.1021/la100026d
- Huang, T., and Crews, J. B. (2007). “Nanotechnology applications in viscoelastic surfactant stimulation fluids,” in SPE 107728 presented at the 2007 SPE European formation damage conference held in Scheveningen, Scheveningen, Netherlands, May 30, 2007.
- Huang, T., and Crews, J. B. (2008). “Do viscoelastic-surfactant diverting fluids for acid treatments need internal breakers,” in SPE 112484 was prepared for presentation at the 2008 SPE International Symposium and Exhibition on Formation Damage Control held in Lafayette, Lafayette, LA, United States, February 13–15, 2008.
- Huang, T., Crews, J. B., and Willingham, J. R. (2008). “Nanoparticles for foam formation fines fixation and improving performance of surfactant structure fluids,” in IPTC 12414 prepared for presentation at the international petroleum technology conference held in Kuala Lumpur, Kuala Lumpur, Malaysia, December 3–5, 2008. doi:10.2523/IPTC-12414-MS
- Huang, T. (2007). “Nanotechnology applications in viscoelastic surfactant stimulation fluids,” in Proceedings of European formation damage conference EFDC, Scheveningen, Netherlands, May 30, 2007.
- Jeffrey Giacomini, A., Albert, C., Gary, L. L., and Ralph, H. C. (2008). Nanoparticle associated surfactant micellar fluids. *AIP Conf. Proc.* 1027, 857. doi:10.1063/1.2964872
- Jiang, P., Li, N., Ge, J., Zhang, G., Wang, Y., Chen, L., et al. (2014). Efficiency of a sulfobetaine-type surfactant on lowering IFT at crude oil–formation water interface. *Colloid. Sur. A: Physicochem. Engineer. Aspects*. 443, 141–148. doi:10.1016/j.colsurfa.2013.10.061
- Joris van, S., and Golombok, M. (2015). Viscoelastic surfactants for diversion control in oil recovery. *J. Petrol. Sci. Engineer.* 135, 671–677. doi:10.1016/j.petrol.2015.10.030
- Lakatos, L., Toth, J., Bodi, T., Lakatos-Szabo, J., Berger, P. D., and Lee, C. (2007). “Application of viscoelastic surfactants as mobility-control agents in low-tension surfactant floods” in SPE 106005 was prepared for presentation at the 2007 SPE international symposium on oilfield chemistry held in Houston, Texas, United States, February 28, 2007.
- Luo, M., Jia, Z., Sun, H., Lejun, L., and Qingzhi, W. (2012). Rheological behavior and microstructure of an anionic surfactant micelle solution with pyroelectric nanoparticle. *Colloids and Surfaces A: Physicochem.* 395, 267–275. doi:10.1016/j.colsurfa.2011.12.052
- Morvan, M., Degre, G., Leng, J., Masselon, J., Bouillot, A. Z., and Moreau, P. (2009). “New viscoelastic fluid for chemical EOR,” in SPE 121675 was prepared for presentation at the 2009 SPE international symposium on oilfield chemistry held in the Woodlands, Woodlands, TX, United States, April 20–22, 2009.
- Morvan, M., Degre, G., Beaumont, J., Dupuis, G., Zaitoun, A., and Al-Maamari, R. S. (2012a). “Optimization of viscosifying surfactant technology for chemical EOR,” in SPE 154053 was prepared for presentation at the eighteenth SPE improved oil recovery symposium held in Tulsa, Tulsa, OK, United States, April 14–18, 2012.
- Morvan, M., Degre, G., Beaumont, J., Colin, A., Dupuis, G., Zaitoun, A., et al. (2012b). “Viscosifying surfactant technology for heavy oil reservoirs,” in SPE 157729 was prepared for presentation at the SPE Heavy Oil Conference Canada held in Calgary, Calgary, AB, Canada, June 12–14, 2012.
- Qin, W., Yue, L., Liang, G., Jiang, G., Jiang, Y., and Liu, Y. (2017). Effect of multi-walled carbon nanotubes on linear viscoelastic behavior and microstructure of zwitterionic wormlike micelle at high temperature. *Chem. Engineer. Res. Design*. 123, 12–23. doi:10.1016/j.cherd.2017.04.027
- Zhang, Y., Dai, C., Yao, Q., Xiqun, F., Jianfeng, J., Yining, W., et al. (2018). Rheological properties and formation dynamic filtration damage evaluation of a novel nanoparticle-enhanced VES fracturing system constructed with wormlike micelles. *Colloids Surfaces A: Physicochem. Engineer. Aspects*. 553, 244–252. doi:10.1016/j.colsurfa.2018.05.065
- Zhu, D., Zhang, J., Han, Y., Wang, H., and Feng, Y. (2013). Laboratory study on the potential EOR use of HPAM/VES hybrid in high-temperature and HighSalinity oil reservoirs. *J. Chem.* 2013, 927519. doi:10.1155/2013/927519

**Conflict of Interest:** The authors declare that the research was conducted in the absence of any commercial or financial relationships that could be construed as a potential conflict of interest.

Copyright © 2021 Liu, Wang, Gao, Luo and Cai. This is an open-access article distributed under the terms of the Creative Commons Attribution License (CC BY). The use, distribution or reproduction in other forums is permitted, provided the original author(s) and the copyright owner(s) are credited and that the original publication in this journal is cited, in accordance with accepted academic practice. No use, distribution or reproduction is permitted which does not comply with these terms.



# Emulsion Characterization of the Heavy Oil-Alkaline Water System in Alkaline Flooding Mechanism Investigation Using a Combination of Modified Bottle Test and Sandpack Flooding

Zhiyu Xi, Na Jia\* and Ezeddin Shirif

Program of Petroleum Systems Engineering, Faculty of Engineering and Applied Science, University of Regina, Regina, SK, Canada

## OPEN ACCESS

### Edited by:

Wei Yu,  
University of Texas at Austin,  
United States

### Reviewed by:

Xiaohu Dong,  
China University of Petroleum, China  
Zengbao Wang,  
China University of Petroleum  
(Huadong), China

### \*Correspondence:

Na Jia  
Na.Jia@uregina.ca;  
jia\_na76@hotmail.com

### Specialty section:

This article was submitted to  
Advanced Clean Fuel Technologies,  
a section of the journal  
Frontiers in Energy Research

**Received:** 30 August 2020

**Accepted:** 26 February 2021

**Published:** 18 March 2021

### Citation:

Xi Z, Jia N and Shirif E (2021)  
Emulsion Characterization of the  
Heavy Oil-Alkaline Water System  
in Alkaline Flooding Mechanism  
Investigation Using a Combination  
of Modified Bottle Test and Sandpack  
Flooding.  
Front. Energy Res. 9:600676.  
doi: 10.3389/fenrg.2021.600676

Due to the diversity of alkali categories and reservoir conditions, the varied oil recovery driving mechanism of alkaline flooding is subjected to different types of emulsion generation. In this study, a modified bottle test method that assesses major emulsion type formation for preliminary prediction of alkaline flooding performance in oil recovery is introduced. The modified method considers the necessary energy input required for mixing immiscible bulk phases at low interfacial tension (IFT) regions to improve the representativity of emulsion formation in the bottle test to that of in porous media. To accurately evaluate the emulsion type and phase volume distribution from the bottle test, each emulsion phase after aging in the test bottle was sampled and its water content was measured through Karl Fischer titration. Afterward, material balance calculations other than pure volume observation were applied to quantify the emulsion volume and determine the major emulsion type formation. It is found that the majority of emulsion effluent type from the sandpack flooding test were in agreement with the bottle test forecast which proved the feasibility of the modified bottle test method. The statistically optimized experimental designs were implemented due to the simplicity of the new bottle test method and it considerably cut the time expense regarding the alkaline flooding performance prediction. The high versatility of the modified bottle test ensures that the alkali usage is not limited to the inorganic alkalis mentioned in this study; other type of alkaline solutions can also be used for further expanding the scope of its application.

**Keywords:** heavy oil, alkaline flooding, emulsion characterization, *in situ* surfactant, sandpack flooding, bottle test

## INTRODUCTION

The heavy oil recovery process in field mainly undergoes three stages. Initially, the primary production utilizes pressure depletion owing to formation rock expansion and solution gas drive to make oil produced spontaneously (Kokal and Abdulaziz, 2010). However, the primary recovery is not long-lasting in the heavy oil reservoir due to the rapid reservoir pressure depletion and



high viscous nature of the heavy oil. Water flooding as a secondary recovery method is conducted afterward to maintain the reservoir pressure and mobilize the initially unmovable oil. Nonetheless, the low viscous water that displaces fluid results in an unfavorable mobility ratio. Severe viscous fingering contributes to early water breakthrough and high residual oil saturation ( $S_{or}$ ) (Homsy, 1987; Bryan and Kantzas, 2007). In order to recover more oil, enhanced oil recovery (EOR) is implemented following water flooding. Most of the EOR processes focus on scaling down the mobility ratio to further diminish the  $S_{or}$ . These goals can be achieved by incorporating the solvent injection, thermal treatment, and chemical injection to efficiently recover an additional 10% original oil in place (OOIP) or more from the reservoir (Kokal and Abdulaziz, 2010).

As one of the chemical EOR processes, alkaline flooding has numerous merits which are mainly represented by its low cost (Ding et al., 2010) and high versatility. Different from in surfactant flooding, the alkaline solution reacts with the acidic groups of residual oil through neutralization reactions and generates *in situ* surfactants spontaneously (Rivas et al., 1997; Sun et al., 2008; Ashrafizadeh et al., 2012). Thus, the total acid number (TAN) of oil becomes an important index that implies the feasibility of alkaline flooding in a specific reservoir. Acevedo et al. (1992) have concluded that the majority of carboxylic acid groups in the heavy oil is made up of asphaltenes, phenols, or resins. In addition, the natural polarity of asphaltenes is capable of fortifying the emulsion stability (Dehghan et al., 2013). These advantages make the unconventional heavy oil recovery in Canada a good candidate for the implementation of alkaline flooding (Acevedo et al., 2001; Bryan and Kantzas, 2007; Ashrafizadeh et al., 2012).

In past decades, many chemical EOR studies, either experimental or numerical, have been performed considering the synergy features of alkaline, surfactant, and polymer; however, little research has focused only on the pure alkaline injection for heavy oil reservoirs. Although a series of sandpack and microfluidics flooding tests were conducted to examine the alkaline flooding performance and mechanisms (Dong et al., 2012), the screening methods which were used for determining

the operating alkaline concentration, salinity, and temperature of heavy oil alkaline flooding are relatively rough. These preliminary screening methods mainly include bottle test and dynamic IFT measurement (Acevedo et al., 2001; Dehghan et al., 2013; Sun et al., 2017) while both tests have their limitations. The spinning drop IFT test is a convenient way to quantify the emulsification process because the IFT is directly proportional to the amount of surfactants adhering to the fluids' contact. However, this method is not able to provide visualized evidence to predict the type of emulsion generation (Bryan and Kantzas, 2007). As Bryan and Kantzas (2007) studied, the evolution process of emulsion generation is controlled by conditions of shear according to fluid velocity. Former researchers usually conducted the bottle test through mingling the alkaline solution and oil at certain volume ratios by shaking the bottle manually (Nelson et al., 1984) or through a tube shaker (Aminzadeh et al., 2016). Some other researchers used a blender or agitator to accomplish the task (Ding et al., 2010; Wang et al., 2010). Nevertheless, when it comes to high viscous heavy oil, these mixing processes cannot effectively provide an agitation environment with shear as sufficient as that in the porous media to overcome the Gibbs's free energy and additional energy expressed by Young-Laplace equation for emulsification (Isaacs and Chow, 1992). In addition, the quality of the final mixture is affected by operating conditions and oil properties. Among the series of heavy oil alkaline flooding performance studies, oils with viscosities lower than 3,000 cp were frequently studied (Ashrafizadeh et al., 2012; Dehghan et al., 2013; Aminzadeh et al., 2016), albeit the heavy oil viscosity in Canada can be as high as 10,000 cp (Bryan and Kantzas, 2007; Ashrafizadeh et al., 2012; Dong et al., 2012). For high viscous oil samples, bottle tests at temperature lower than 50°C are tougher to manage and the poor fluidity of high viscous heavy oil reduces the chance of mixing with aqueous phase. This phenomenon has been reported by Dong et al. (2012), who noted that the oil either sticks on the bottle wall or remains intact as a solely bulk phase through bottle shaking. Thus, W/O emulsion is hard to form. On the other hand, as a visualization method, the bottle test result is demonstrated by distribution of the emulsion phases based on density difference. A preceding phase distribution analysis was usually done through direct observation (Nelson et al., 1984; Bryan and Kantzas, 2007; Panthi and Mohanty, 2013; Aminzadeh et al., 2016; Baek et al., 2018). It is achieved by reading the volume scale marked on the container to determine the individual phase volume changes. However, a significant difference exists between the alkaline solution bottle test and the surfactant involved solution test owing to the neutralization reaction. The emulsification process in the alkaline solution case takes longer compared to the surfactant solution case, and multiple *in situ* surfactants may appear that induce different emulsion types. Therefore, oil-external and water-external emulsion emerge simultaneously in most alkaline water-heavy oil cases. Nevertheless, the IFT reduction mainly occurs on the surface of the dispersed droplets where the *in situ* surfactants are adhering to Ashrafizadeh et al. (2012) rather than the contact of bulk oil and water emulsions inside the bottle. It makes it difficult to accurately measure the phase volume because of the meniscus at the oil-external and water-external emulsions contact. Using

**Abbreviation:** IFT, Interfacial tension;  $S_{or}$ , Residual oil saturation; OOIP, Original oil in place; TAN, Total acid number, g KOH/g oil; W/O emulsion, Water in oil emulsion; O/W emulsion, Oil in water emulsion;  $m_{ao}$ , Bottle mass with oil and water, g;  $m_{sa}$ , Bottle mass with water, g;  $m_t$ , Total mass of introduced oil and water, g;  $\rho_{OT}$ , Oil density at test temperature and ambient pressure, g/cm<sup>3</sup>;  $\rho_w$ , Water density at test temperature and ambient pressure, default, g/cm<sup>3</sup>;  $\rho_{avgO}$ , Density of W/O emulsion phase after emulsification and 24 h aging at test temperature and ambient pressure, g/cm<sup>3</sup>;  $\rho_{avgW}$ , Density of bottom O/W emulsion phase after emulsification and 24 h aging at test temperature and ambient pressure, g/cm<sup>3</sup>;  $\rho_{avgm}$ , Density of middle O/W emulsion phase after emulsification and 24 h aging at test temperature and ambient pressure, g/cm<sup>3</sup>; MBE%, Percentage of material balance error; W%, Water weight fraction in each emulsion phase; V%, Water volume fraction in each emulsion phase;  $V_{oi}$ , Initial introduced oil volume, cm<sup>3</sup>;  $V_{wi}$ , Initial introduced water volume, cm<sup>3</sup>;  $V_o$ , Measured W/O emulsion volume after emulsification and 24 h aging, cm<sup>3</sup>;  $V_w$ , Measured O/W emulsion volume after emulsification and 24 h aging, cm<sup>3</sup>;  $V_{mcal1}$ , Calculated emulsion phase volume by volume balance, cm<sup>3</sup>;  $V_{mcal2}$ , Calculated emulsion phase volume by mass balance, cm<sup>3</sup>;  $V_d\%$ , Volume fraction of total water and oil phase dispersion;  $V_{dw}$ , Volume of water phase dispersion into oil phase, cm<sup>3</sup>;  $V_{do}$ , Volume of oil phase dispersion into water phase, cm<sup>3</sup>;  $K_n$ , Summation of nth level of  $V_d\%$ ;  $k_n$ , Average of nth level of  $K_n$ ; PV, Pore volume.

a wide mouth bottle in test can mitigate the meniscus effect on volume measurement (Ding et al., 2010) when large volumes of oil and alkaline solution are required. Some researchers used fused-end ultra slim pipettes as the container, but their slender shape also aggravates the difficulty of mixing oil and water (Panthi and Mohanty, 2013; Baek et al., 2018). In general, previous bottle test methods are not handy for the system which involves high viscous heavy oil and alkaline solution. Conducting a conventional bottle test method disregarding its drawbacks may result in inaccurate prediction and misleading conclusions.

In this paper, a modified bottle test method is developed for preliminary alkaline flooding performance prediction on heavy oil recovery through meticulous emulsion phase distribution analysis. Different from the early studies, a high-shear homogenizer—which is capable of providing sufficient shear rate in promoting droplet breakup (Isaacs and Chow, 1992)—was used when mixing the oil and alkaline solution. During the homogenization step, the bulk heavy oil and alkaline solution are forced into the extremely narrow annulus between the rotating shaft and the inner wall of the probe under pressure. Then, the fluids exit through the hole on the shaft before the next mixing circle starts (Dhankhar, 2014). The surface area of viscous oil, which is hard to be stretched by hand shaking or stirring, can be easily extended through the homogenizer. It provides a better mixing quality of the two bulk phases and thus facilitates the neutralization reaction. In addition, each sample bottle is treated by homogenizer in a fixed time and rotation rate; hence, the uniformity of energy introduction can be assured. Furthermore, each emulsion phase at equilibrium of a sample bottle was sampled and its water content was measured by Karl Fischer titration to enhance the accurate emulsion volume measurement. A new material balance method using emulsion's water volume fraction data will be introduced to show how the visually observed phase volume is fortified.

The paper was organized as follows: In section “Modified Bottle Test and Phase Distribution Study,” two commonly used inorganic alkalis ( $\text{NaOH}$  and  $\text{Na}_2\text{CO}_3$ ) were selected to implement the modified bottle test through orthogonal experimental design to reduce the total experimental efforts and obtain the phase distribution pattern through varying control factors. In section “Sandpack Flooding Test,” the accuracy of emulsion type prediction by using the new bottle test method was verified through the sandpack flooding test. Then in section “Modified Bottle Test Trend Study,” the modified bottle test trend studies were conducted to further ensure the correctness of the phase distribution pattern derived and a persistent agreement was found with the previous orthogonal test results.

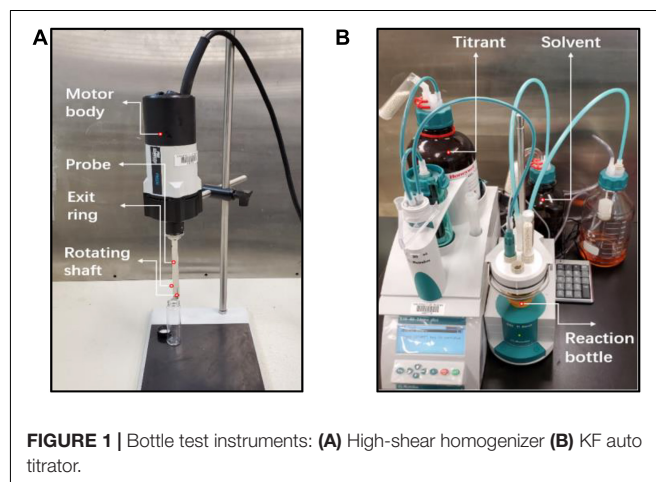
## MODIFIED BOTTLE TEST AND PHASE DISTRIBUTION STUDY

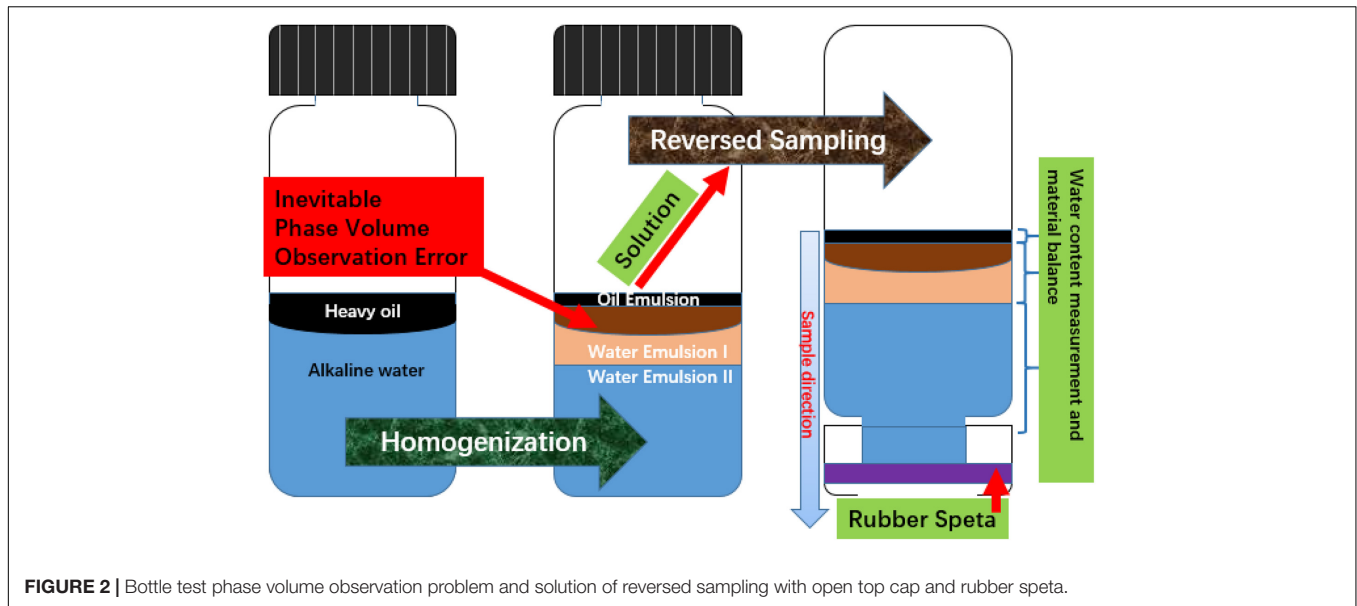
The bottle test was conducted using a specified alkaline water-oil volume ratio of 2:1 in 15 cm<sup>3</sup> glass bottles. The alkaline solution and heavy oil were preheated to test the temperature separately in the oven, and 2 cm<sup>3</sup> oil was transferred through a syringe to the bottle which contains 4 cm<sup>3</sup> of the alkaline

solution. The deviation of total injected oil volume was controlled to minimize the influence of alkaline water:oil ratio on the emulsification performance. It is worth noting that water:oil volume ratio has a big influence on the emulsion type generation. As studied, when water:oil ratio is lower than 1:9, phase inversion occurred and only water in oil emulsion will be formed (Sun et al., 2017). In this study, there is no intention in preparation of specific type of emulsion. So, water:oil ratio is set to be 2:1 considering the volume capacity of the test bottle in order to facilitate both water and oil dispersion into other phases. Then, the bottle was sent to the homogenizer to mix the oil and the solution at 6,000 round per minute (rpm) for 30 s. The PRO 250 homogenizer from PRO Scientific used in the experiment is shown in **Figure 1A**.

Afterward, the bottle was settled in the oven at a pre-set temperature overnight to accomplish the emulsification and phase redistribution. The volume of each phase was measured after 24 h settlement by observing the phase-to-phase contact through calibrated scale. A long settling time is necessary because both oil- and water-based emulsions were generated with various stabilities. Aging the mixture can mitigate the unstable emulsion impact and favor the determination of the dominant emulsion type (Bryan and Kantzas, 2007; Xu et al., 2013).

Due to the external phase discrepancy of the multi-emulsion system, the meniscus phenomenon shown in the middle bottle of **Figure 2** significantly affects the volume observation and emulsion sampling since the top phase is partially covered by the middle phase. Conventional methods of sampling emulsion phases from top to bottom with a syringe is also not applicable because the W/O emulsion phase has a high possibility to contaminate the needle and cause further interruption to the following emulsion layers. Thus, the bottle test emulsion sampling started from the O/W emulsion with less oil dispersion at the bottom. This procedure was achieved by flipping the bottle upside-down and leaving it to stand for another 6 h after volume measurement. An open top cap with thin rubber septa was equipped on each bottle for needle penetration (**Figure 2**). Sampling the complete bulk





phase is unnecessary because a trace volume ( $\leq 10 \mu\text{L}$ ) is required in Karl Fischer titration and the water content of each emulsion phase was assumed to be constant. Only the most stable emulsion in each phase was taken while any sample close to the boundary of different emulsion types were discarded. Afterward, the titration process was operated through Metrohm 870 KF Titrino plus automatic titrator, shown in **Figure 1B**.

For the purpose of enhancing the phase volume determination, the material balance equation was used to correct the visualization error from the observed interface of W/O emulsion and middle O/W emulsion (**Figure 2**). For the three-emulsion phase (type A) system, the first step is direct volume balancing by subtracting the volumes of top and bottom phases at equilibrium from initial total volume to calculate the middle emulsion volume.

It can be explained by the following equations:

$$V_{oi} = (m_{sa0} - m_{sa}) / \rho_{oT}$$

$$V_{mcalc1} = V_{oi} + V_{wi} - V_o - V_w$$

Here,  $m_{a0}$  is the bottle mass including oil and water and  $m_{sa}$  is the bottle mass with water only.  $\rho_{oT}$  stands for the oil density at test temperature.  $V_{oi}$  and  $V_{wi}$  denote the initial introduced oil volume and water volume, respectively, while  $V_o$  and  $V_w$  are the measured oil volume and water volume. The calculated emulsion phase volume by volume balance is represented by  $V_{mcalc1}$ .

Then, the water content data of each sampled phase can be used to derive the emulsion density at equilibrium state by using the mixing rule for immiscible fluids (Chhabra and Richardson, 2008; Zhang et al., 2018), which is:

$$\rho_{avg} = V\% * 1 + (1 - V\%) * \rho_{oT}$$

$$V\% = 1 / (1 + (\rho_w / \rho_{oT}) * (1 / W\% - 1))$$

where  $\rho_{avg}$  denotes the density of emulsion phase after emulsification and 24 h aging.  $\rho_w$  is water density,  $W\%$  is water weight fraction, and  $V\%$  is water volume fraction.

As the original oil and alkaline solution volumes are known, the middle emulsion weight at equilibrium can also be derived by deducting the top and bottom emulsions' mass from the total mass,  $m_t$ . Therefore, the volume of middle emulsion can be

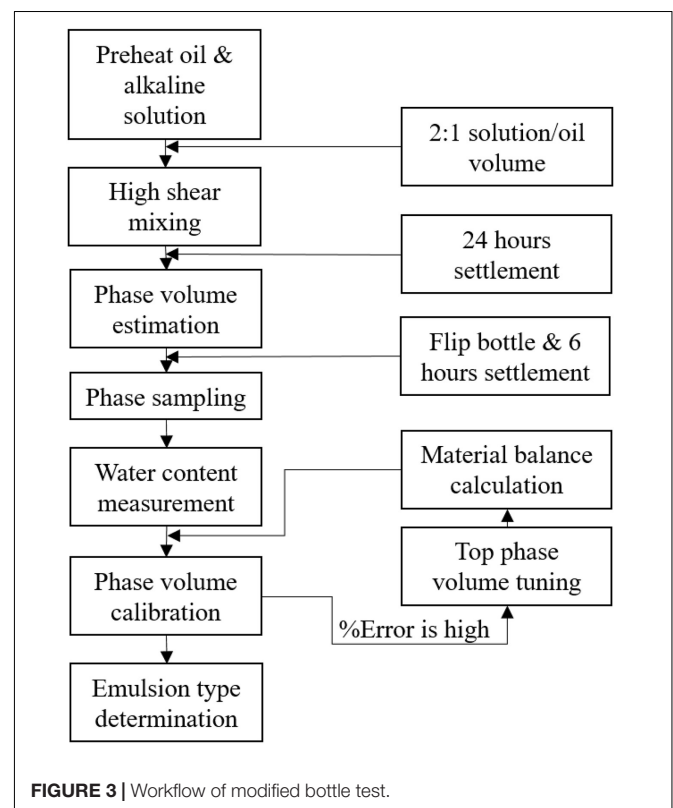


**TABLE 1** | NaOH orthogonal test phase migration volume fraction of 3-phase distribution cases.

Type A	Temp., °C	Salinity, ppm	Aconc., mol/L	V <sub>w</sub> , cm <sup>3</sup>	V <sub>o</sub> , cm <sup>3</sup>	V <sub>mcalc1</sub> , cm <sup>3</sup>	V <sub>mcalc2</sub> , cm <sup>3</sup>	MBE, %	Vd, %
A-1	50	0	0.01	3.460	1.943	0.666	0.666	0.062	20.550
A-2	50	1,000	0.01	3.503	2.000	0.601	0.597	0.654	20.548
A-3	50	5,000	0.05	2.791	2.657	0.402	0.402	0.184	27.469
A-4	50	8,000	0.02	3.483	2.251	0.123	0.128	3.927	9.505
A-5	60	0	0.02	2.294	2.343	1.342	1.342	0.004	40.363
A-6	60	1,000	0.01	2.314	2.886	0.918	0.918	0.002	30.023
A-7	60	3,000	0.005	2.723	2.546	0.780	0.780	0.008	23.853
A-8	70	0	0.05	3.366	1.743	0.771	0.779	0.952	25.781
A-9	70	1,000	0.02	2.186	1.857	1.936	1.935	0.058	43.283
A-10	70	3,000	0.01	1.611	2.629	1.705	1.704	0.026	44.452

**TABLE 2** | NaOH orthogonal test phase migration volume fraction of 2-phase distribution cases.

Type B	Temp., °C	Salinity, ppm	Aconc., mol/L	V <sub>w</sub> , cm <sup>3</sup>	V <sub>o</sub> , cm <sup>3</sup>	Vd, %
B-1	40	0	0.005	3.114	2.845	16.455
B-2	40	1,000	0.000	3.626	2.232	8.408
B-3	40	3,000	0.050	3.789	2.051	5.598
B-4	40	5,000	0.020	3.483	2.378	10.635
B-5	40	8,000	0.010	3.363	2.479	12.661
B-6	50	3,000	0.000	3.663	2.131	15.664
B-7	60	5,000	0.000	3.977	2.213	0.990
B-8	60	8,000	0.050	2.623	3.352	24.385
B-9	70	5,000	0.005	3.074	2.879	17.123
B-10	70	8,000	0.000	3.934	1.874	3.086

calculated according to the middle emulsion density,  $\rho_{avgm}$ . The calculation can be conveyed by the following equations:

$$m_t = V_{oi} * \rho_{oi} + V_{wi} * \rho_w$$

$$V_{mcalc2} = (m_t - V_o * \rho_{avgw} - V_w * \rho_{avgw}) / \rho_{avgm}$$

Here  $V_{mcalc2}$  stands for the calculated emulsion phase volume by mass balance and  $\rho_{avgw}$  is the density of bottom O/W emulsion phase after emulsification and 24 h aging.

Theoretically, the two calculated middle emulsion volumes should be the same; however, the improper oil-external emulsion volume observation results in material balance (MBE) error:

$$MBE\% = \frac{V_{mcalc2} - V_{mcalc1}}{V_{mcalc2}} * 100\%$$

Thus, W/O emulsion volume can be corrected by tuning  $V_o$  and less error indicates the  $V_o$  value is getting closer to the true volume.

If the middle emulsion generation is only of a trace amount or does not exist, the middle emulsion volume will be merged into the bottom water phase or ignored and the two-emulsion phase (type B) system will be considered. Therefore, the following simplified equation can be used to balance the bottom water volume through tuning the top W/O emulsion volume. In this case, material balance error is not considered.

$$V_{oi} + V_{wi} - V_o = (m_t - V_o * \rho_{avgw}) / \rho_{avgw}$$

where  $\rho_{avgw}$  is the density of bottom O/W emulsion phase after emulsification and 24 h aging.

The above calculations always use gram as the mass unit and cm<sup>3</sup> as volume unit unless otherwise specified.

On account of the involvement of *in situ* surfactants, the original glass bottle wettability will be adjusted to partial oil-wetting after agitation. Small volumes of W/O emulsion may remain on the bottle wall, thus it is not included in the

**TABLE 3** | Na<sub>2</sub>CO<sub>3</sub> orthogonal test phase migration volume fraction of 3-phase distribution cases.

Type A	Temp., °C	Salinity, ppm	Aconc., mol/L	V <sub>w</sub> , cm <sup>3</sup>	V <sub>o</sub> , cm <sup>3</sup>	V <sub>mcalc1</sub> , cm <sup>3</sup>	V <sub>mcalc2</sub> , cm <sup>3</sup>	MBE, %	Vd, %
A-1	50	1,000	0.005	2.680	0.263	3.147	3.105	1.358	58.278
A-2	40	0	0.005	2.551	0.389	2.625	2.618	0.242	59.093
A-3	50	0	0.010	2.166	1.331	2.578	2.571	0.292	52.731
A-4	70	1,000	0.025	3.537	0.749	1.760	1.722	2.172	41.096
A-5	70	3,000	0.010	2.960	1.389	1.575	1.559	1.040	35.735
A-6	70	5,000	0.005	3.957	0.831	1.225	1.211	1.153	38.641
A-7	60	0	0.025	3.629	1.514	0.672	0.666	0.802	25.119
A-8	70	0	0.040	4.114	1.143	0.637	0.632	0.890	26.197
A-9	60	1,000	0.010	3.111	2.366	0.583	0.609	4.226	29.719
A-10	40	3,000	0.040	4.040	1.346	0.460	0.455	1.131	16.878
A-11	60	3,000	0.005	3.591	2.163	0.351	0.365	4.010	16.290



phase volume observation. On the other hand, using material balance in calculating emulsion phase distribution by water content data surpasses the pure volume observation as it eliminates the inevitable experimental error from volume loss. The material balance calculation majorly focuses on the water content of emulsion phases and each phase distribution is balanced according to the known original oil and water volume introduction. The observed O/W and W/O emulsion volumes are only used as references to reduce the balance calculation trials, but they do not have significant influence on the final result of emulsion phase distribution. **Figure 3** provides the

**TABLE 4** | Na<sub>2</sub>CO<sub>3</sub> orthogonal test phase migration volume fraction of 2-phase distribution cases.

Type B	Temp., °C	Salinity, ppm	Aconc., mol/L	V <sub>w</sub> , cm <sup>3</sup>	V <sub>o</sub> , cm <sup>3</sup>	V <sub>d</sub> , %
B-1	40	1,000	0.000	4.091	1.42	2.845
B-2	60	5,000	0.000	3.997	1.720	3.396
B-3	70	8,000	0.000	4.031	1.574	3.102
B-4	50	3,000	0.000	4.166	1.714	6.738
B-5	40	5,000	0.040	4.269	1.457	12.493
B-6	60	8,000	0.025	4.129	1.600	16.343
B-7	50	5,000	0.010	3.817	1.957	7.270
B-8	40	8,000	0.025	4.117	1.683	5.731
B-9	50	8,000	0.040	3.891	2.137	8.356

**TABLE 5** | NaOH V<sub>d</sub>% orthogonal data processing.

V <sub>d</sub> %	Temp.	Salinity	Aconc.
K1	0.000	103.149	28.148
K2	53.756	102.262	77.979
K3	93.735	89.566	107.686
K4	119.614	56.216	103.786
K5	133.725	49.637	83.232
k1	0.000	20.630	5.630
k2	10.751	20.452	15.596
k3	18.747	17.913	21.537
k4	23.923	11.243	20.757
k5	26.745	9.927	16.646
Range	26.745	10.702	15.908

**TABLE 6** | Na<sub>2</sub>CO<sub>3</sub> V<sub>d</sub>% orthogonal data processing.

V <sub>d</sub> %	Temp.	Salinity	Aconc.
K1	0.000	163.140	16.081
K2	97.039	131.938	172.301
K3	133.373	75.641	125.456
K4	137.868	61.800	88.290
K5	144.771	33.532	63.923
k1	0.000	32.628	3.216
k2	19.408	26.388	34.460
k3	26.675	15.128	25.091
k4	18.174	12.360	17.658
k5	28.954	6.706	12.785
Range	28.954	25.922	31.244

workflow of the modified bottle test method to summarize the aforementioned procedures.

Based on this methodology, a series of modified bottle tests for two inorganic alkalis (NaOH and Na<sub>2</sub>CO<sub>3</sub>) with heavy oil under various temperatures, salinities (NaCl), and alkaline concentrations were conducted. The TAN of the heavy oil sample is 2.1 mg KOH/g oil, and the heavy oil viscosity is 20,300 cp at 20°C. The heavy oil density at 20°C is measured to be 983.3 kg/m<sup>3</sup> and its molecular weight is 512 g/mol.

Three main control factors, alkaline concentration, brine salinity, and temperature, were studied for each alkali whose alkaline concentration ranged from 0 to 0.5 mol/L, salinity was within the upper limit of 8,000 ppm, and reached a highest temperature of 70°C. The orthogonal experimental design was conducted to evaluate the importance of each factor to alkaline water performance in emulsification with heavy oil sample. 25 combinations of the three control factors at certain levels for NaOH and Na<sub>2</sub>CO<sub>3</sub> were plugged in a refined L25(5<sup>3</sup>) orthogonal table to conduct the bottle test (Fan and Chen, 1996).

During the emulsification process, oil and water tend to disperse into each other's phase at low IFT due to the existence of *in situ* surfactants. So, the quantity of water and oil dispersion at equilibrium plays an important role in determining the emulsion stability as well as the emulsion type formation. Therefore, the total volume fraction of dispersed water and oil, V<sub>d</sub>%, which can be used to represent the quantity of phase migration, was selected as the ranking index of the orthogonal bottle experiment to evaluate the emulsification performance of different alkaline solutions under various operating conditions. The dispersed water and oil phase volumes were calculated based on the water content data of the emulsions. It should be noted that five bottle tests running at 20°C failed in the agitation stage due to the heavy oil's high viscous nature. However, the calculation of V<sub>d</sub>% still took these five tests in consideration and the dispersed phase volume were assigned 0 cm<sup>3</sup> to represent the temperature effect on bottle test emulsion preparation.

The calibrated orthogonal bottle test phase distribution results of the two alkalis are provided in **Tables 1–4**, where the experimental conditions, water and oil emulsions volume distribution at equilibrium, and the dispersed water and oil phase volume fraction are provided. As was mentioned, Type A and Type B systems co-existed among the 20 bottle tests of each alkali. They were provided, respectively, in separate tables and the material balance error was given for Type A bottle test cases.

The orthogonal experiment data for both alkaline solutions were processed by Analysis of Variances (ANOVA) (Athreya and Venkatesh, 2012) using V<sub>d</sub>% as index; the results are shown in **Tables 5, 6**. In the calculation, K<sub>n</sub> of a factor represents the summation of indices among 25 bottle tests at nth level and k<sub>n</sub> is the corresponding average. The “range” of a factor is calculated by subtracting the lowest k-value from the highest k-value within five levels. The range magnitude of a factor indicates its influence on alkaline solution performance during emulsification. Therefore, some emulsification tendencies of each alkali referring to the control factors can be derived through orthogonal data processing.



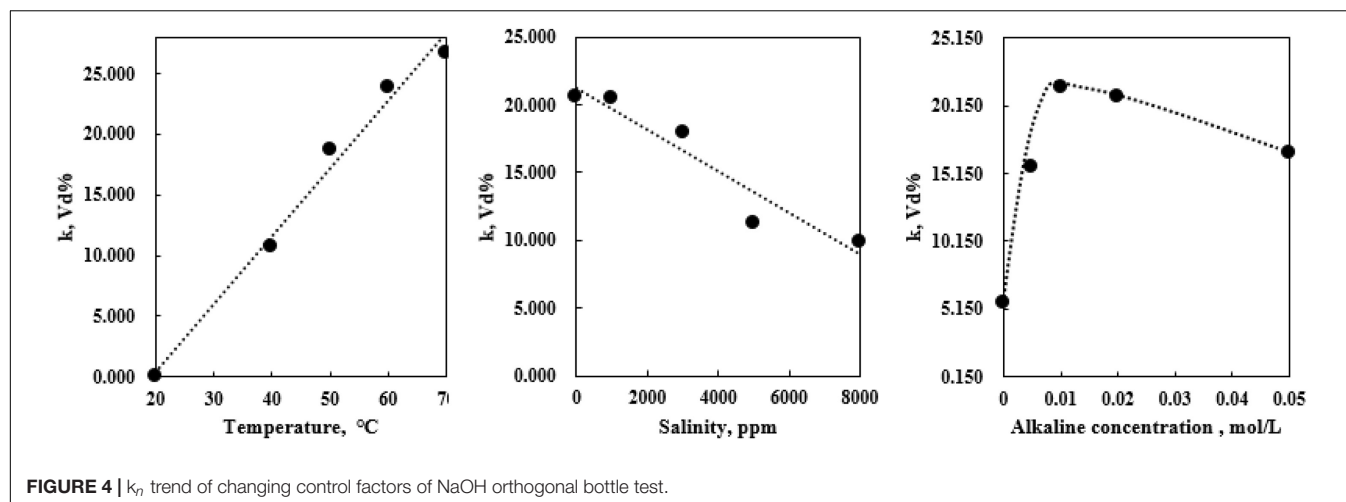


FIGURE 4 |  $k_n$  trend of changing control factors of NaOH orthogonal bottle test.

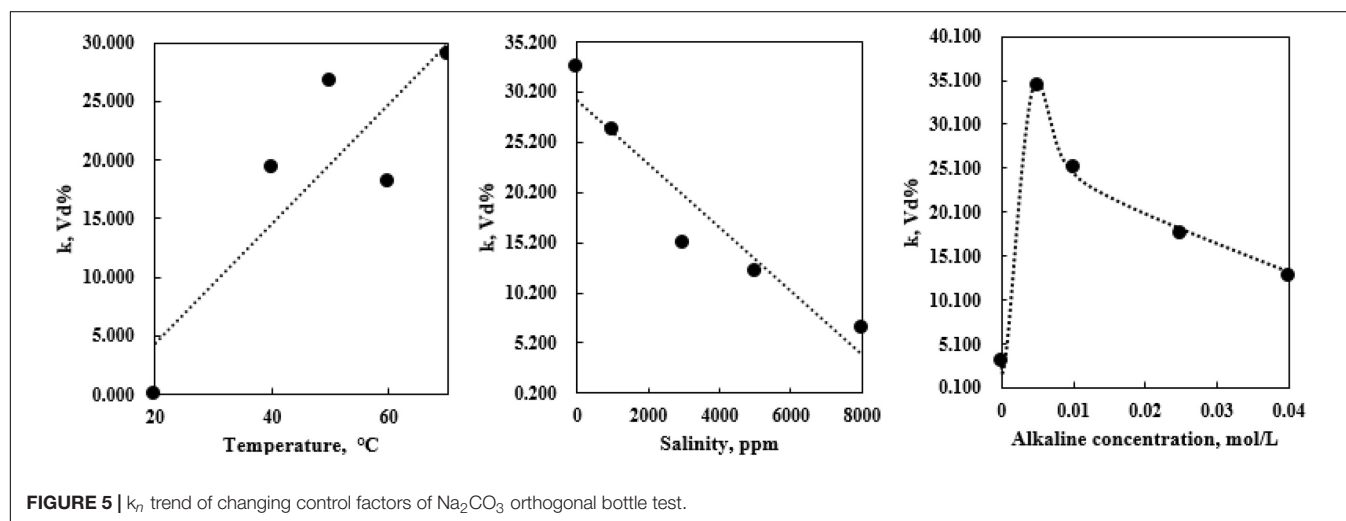


FIGURE 5 |  $k_n$  trend of changing control factors of  $\text{Na}_2\text{CO}_3$  orthogonal bottle test.

As Table 5 shows, the most important factor that affects the total phase dispersion for NaOH bottle test is temperature, with the range of 26.745%. The other two factor ranges are

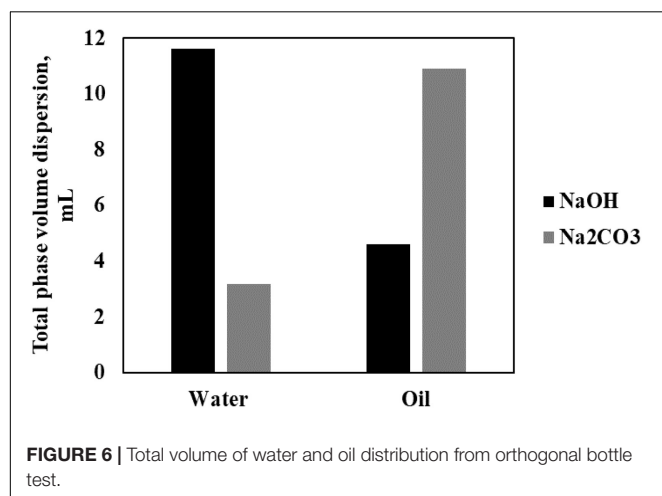


FIGURE 6 | Total volume of water and oil distribution from orthogonal bottle test.

inferiorly lower than the temperature affected range. Thus, NaOH concentration has a medium influence on phase dispersion while the salinity has the least impact. On the other hand, as shown in Table 6, the  $\text{Na}_2\text{CO}_3$  orthogonal bottle test has factor ranges with similar values, which indicated that temperature, salinity, and  $\text{Na}_2\text{CO}_3$  concentration all play significant roles during the emulsification process. The  $\text{Na}_2\text{CO}_3$  concentration is the most influencing factor, followed by temperature and salinity.

Besides, the change of  $k_n$  for each factor follows a certain pattern that depicted the overall phase dispersion ability under various conditions. Figures 4, 5 plot the relationship of  $k_n$  at each level of a factor for NaOH and  $\text{Na}_2\text{CO}_3$  cases and some findings can be drawn.

In general, the temperature increase has a positive effect on phase dispersion; this is mainly due to the viscosity reduction of the heavy oil sample. At 70°C, the heavy oil viscosity is lower than 150 cp. This phenomenon increases the contact possibility of the oil and alkaline solution and further promotes the neutralization reaction to generate extra amounts of *in situ* surfactants. Thus, the difficulty in mixing oil and water phases can be considerably overcome. On the other hand, the salinity increment tends to

hinder phase dispersion for both alkali cases. When it comes to the alkaline concentration effect, the optimum concentration can be clearly seen from both alkalis. The quantity of phase dispersion experiences a sudden boost with the involvement of alkalis while additional alkaline concentration restrains the phase dispersion. This variation tendency is especially featured in the  $\text{Na}_2\text{CO}_3$  case, while additional NaOH concentration has a milder influence on the phase dispersion once the optimum concentration is reached. The results of  $k_n$  analysis have shown the general effects of the control factors on emulsification; however, a detailed study regarding specific phase dispersion is required as dispersion exists in both water and oil phases. Therefore, the total volume of water and oil dispersion into each other phases of the 25 bottle test for each alkali case was calculated according to the phase volume distribution and measured water content data. It is found that 11.6 mL water went into the oil phase and 4.6 mL of oil dispersed into the water phase for the NaOH case. Nevertheless, the phase volume dispersion reversed for the  $\text{Na}_2\text{CO}_3$  case with 3.2 mL water and 10.9 mL oil dispersion into the other phase. These data have clearly proposed the tendency of dominant emulsion type generation for different alkalis within the given control factor range. According to **Figure 6**, the water tends to disperse into oil phase for the NaOH system while oil is more likely to disperse into the water phase in the  $\text{Na}_2\text{CO}_3$  system. Hence, the W/O emulsion is the major emulsion generated for NaOH bottle tests and O/W emulsion is dominant for the  $\text{Na}_2\text{CO}_3$  case.

**Tables 7, 8** collected and processed the oil and water absolute volume dispersion data from the NaOH and  $\text{Na}_2\text{CO}_3$  orthogonal bottle test, respectively, according to the dominant emulsion formation for different alkalis.

Correspondingly,  $k_n$  analysis has been conducted to further study the control factor effects on dominant emulsion generation. It is shown in **Figures 7, 8** that the temperature effect basically follows the same pattern determined from the total dispersed phase volume fraction trend study shown in **Figures 4, 5**.

Nonetheless, only the changes of salinity and alkaline concentration from the  $\text{Na}_2\text{CO}_3$  case shown in **Figure 8** keep the same trend as that of in **Figure 5**, while these two curves showed different patterns for the NaOH cases. It can be seen from **Figure 7** that salinity change does not significantly influence the W/O emulsion generation. Similarly, additional

NaOH concentration also has the least effect on water dispersion volume in oil phase as long as optimum NaOH concentration has been achieved.

Consequently, it can be concluded that the influences of salinity and alkaline concentration on the emulsification process were majorly embodied by the oil dispersion into the water phase. According to Cooke et al. (1974), surfactant tends to soar in elevation to upper phases when aqueous phase salinity grows. For alkali types like NaOH, which facilitates W/O emulsion formation at the first stage, the volume of oil dispersion in water phase is limited. Thus, salinity or alkaline concentration impact is low. For the  $\text{Na}_2\text{CO}_3$  case in which O/W emulsion is dominant in the system, the effect from salinity and  $\text{Na}_2\text{CO}_3$  concentration was obvious. Dispersed oil droplets gradually leave the water phase at higher salinity and alkaline concentrations. As **Figure 9** illustrated, when salinity increases to over 3,000 ppm, emulsion type inversion occurred and water dispersion in oil phase was favored. Simultaneously, the increase of  $\text{Na}_2\text{CO}_3$  concentration also facilitates the water dispersion into oil phase.

Thus, W/O emulsion is likely to be generated when salinity or alkaline concentration increased for the  $\text{Na}_2\text{CO}_3$  system. Therefore, it reveals that the difference between **Figures 4, 7** of the NaOH cases is mainly because of the quantity change of O/W emulsion.

## SANDPACK FLOODING TEST

Based on the data analysis, the modified bottle test has provided satisfactory results in analyzing the phase distribution of the multi-emulsion system. According to the orthogonal bottle tests, changing alkali types, alkaline concentration, and salinity alters the major emulsion type generation which determines the alkaline flooding mechanisms to be achieved for facilitating the oil recovery. In theory, it will be of great convenience to predict the possible emulsion generation and oil recovery mechanisms during the alkaline flooding process through the modified bottle test.

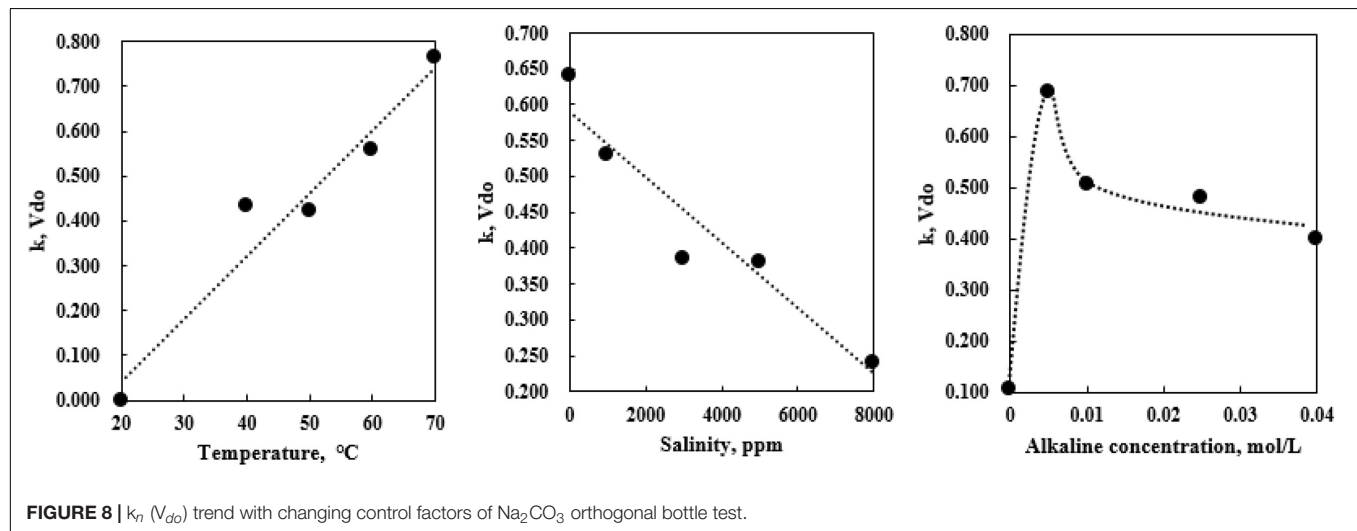
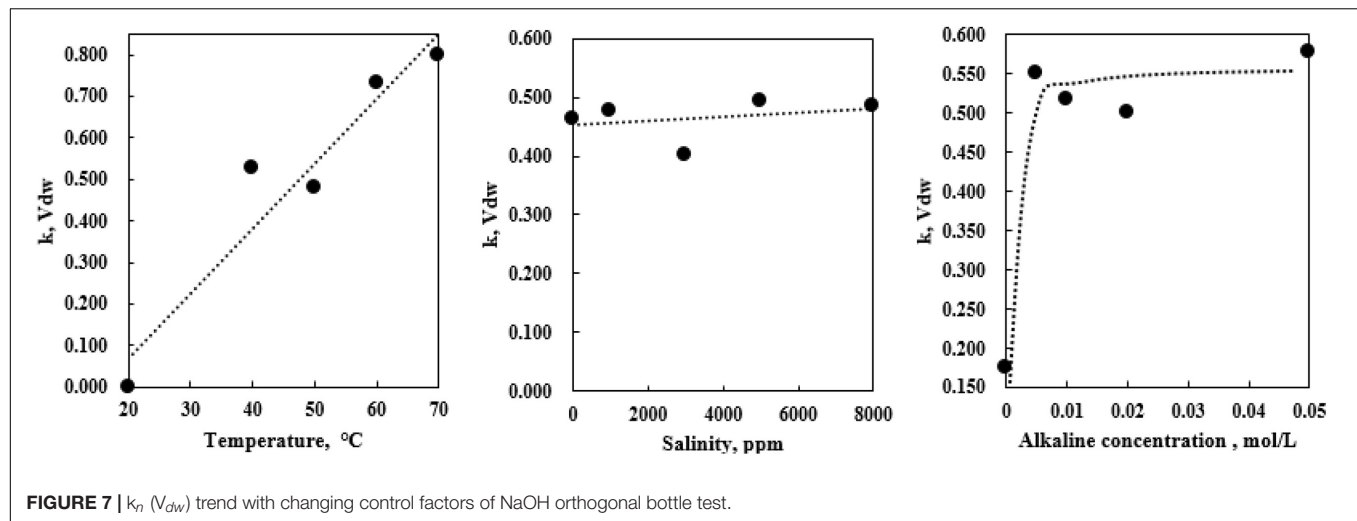
Several sandpack alkaline flooding tests were conducted in order to validate the feasibility of the above hypothesis. The operating condition of the flooding test was majorly based on

**TABLE 7 |** NaOH  $V_{dw}$  orthogonal data processing.

$V_{do}$	Temp.	Salinity	Aconc.
K1	0	2.312	0.874
K2	2.626	2.384	2.753
K3	2.395	2.013	2.582
K4	3.659	2.465	2.497
K5	4.000	2.424	2.892
k1	0.000	0.462	0.175
k2	0.525	0.477	0.551
k3	0.479	0.403	0.516
k4	0.732	0.493	0.499
k5	0.800	0.485	0.578
Range	0.732	0.090	0.404

**TABLE 8 |**  $\text{Na}_2\text{CO}_3$   $V_{do}$  orthogonal data processing.

$V_{dw}$	Temp.	Salinity	Aconc.
K1	0.000	3.205	0.537
K2	2.167	2.653	3.425
K3	2.115	1.926	2.533
K4	2.794	1.904	2.401
K5	3.813	1.201	1.994
k1	0.000	0.641	0.107
k2	0.433	0.531	0.685
k3	0.423	0.385	0.507
k4	0.559	0.381	0.480
k5	0.763	0.240	0.399
Range	0.763	0.401	0.578



the modified bottle test design and was aimed at using the smallest number of tests to verify the most representative bottle test emulsion generation phenomenon considering the sandpack preparation time. The same heavy oil sample was used in the flooding test. **Table 9** portrays the alkaline flooding strategy used in the sandpack experiments and the sandpack flooding schematic diagram is provided in **Figure 10**.

The 30 cm long and 4 cm diameter sandpack was vacuumed and weighted once fully packed by 80–120 mesh Ottawa sand. Then, deionized water/brine was sucked into the vertical oriented sandpack from the bottom and several PV of water/brine was injected to the sandpack afterward. The fully water-saturated sandpack was then weighed again to calculate the sandpack porosity. The absolute permeability of the sandpack was measured by injecting water/brine at different rates and monitoring the pressure drop at a steady state based on Darcy's law. Then, the sandpack was placed vertically again and oil was injected at 0.1 mL/min from the top to displace water at the bottom. The total discharged water volume was measured to calculate the initial water saturation.

As seen from **Table 9**, the measured porosity and permeability of the sandpack maintained relatively good consistency among different tests; thus, the repeatability of the flooding test can be assured. The sandpack has irreducible water saturation after the drainage process at 6~8% and the pore volume is approximately 150  $\text{cm}^3$ . The sandpack was flooded by water/brine at 1  $\text{cm}^3/\text{min}$  as the primary production stage until the effluent water cut was above 95%. Then, 0.7 pore volume (PV) of alkaline solution was injected followed by extended water/brine injection according to similar flooding test configurations by previous researchers (Castor et al., 1981; Pei et al., 2012). The flooding process stopped when water cut returned to 95% at the final water flooding stage.

**Figure 11** portrays the six alkaline flooding test results for NaOH and  $\text{Na}_2\text{CO}_3$ , respectively, in terms of oil recovery and pressure drop.

The abrupt hike of oil recovery after the alkali injection for all three NaOH cases is clear from **Figure 11A**. Either ambient temperature (20°C) or 70°C NaOH solution injection brought an extra 26~30% of OOIP recovered after water flooding. Similar to the previous bottle test results, alkaline flooding using NaOH

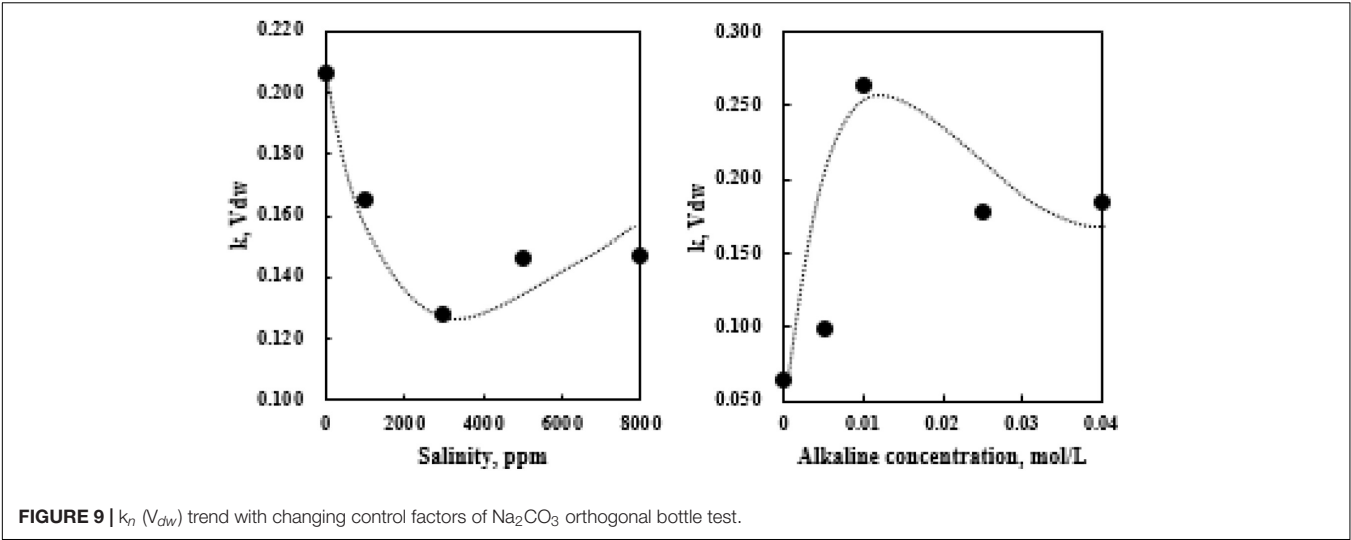
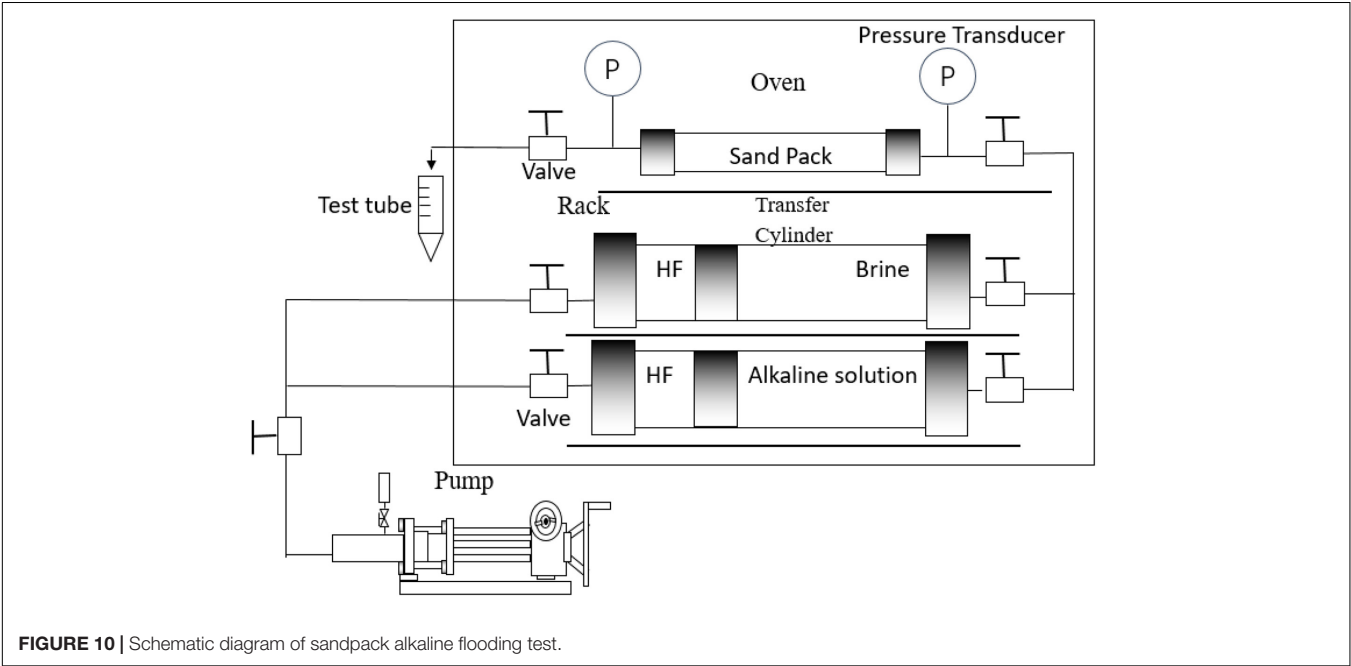
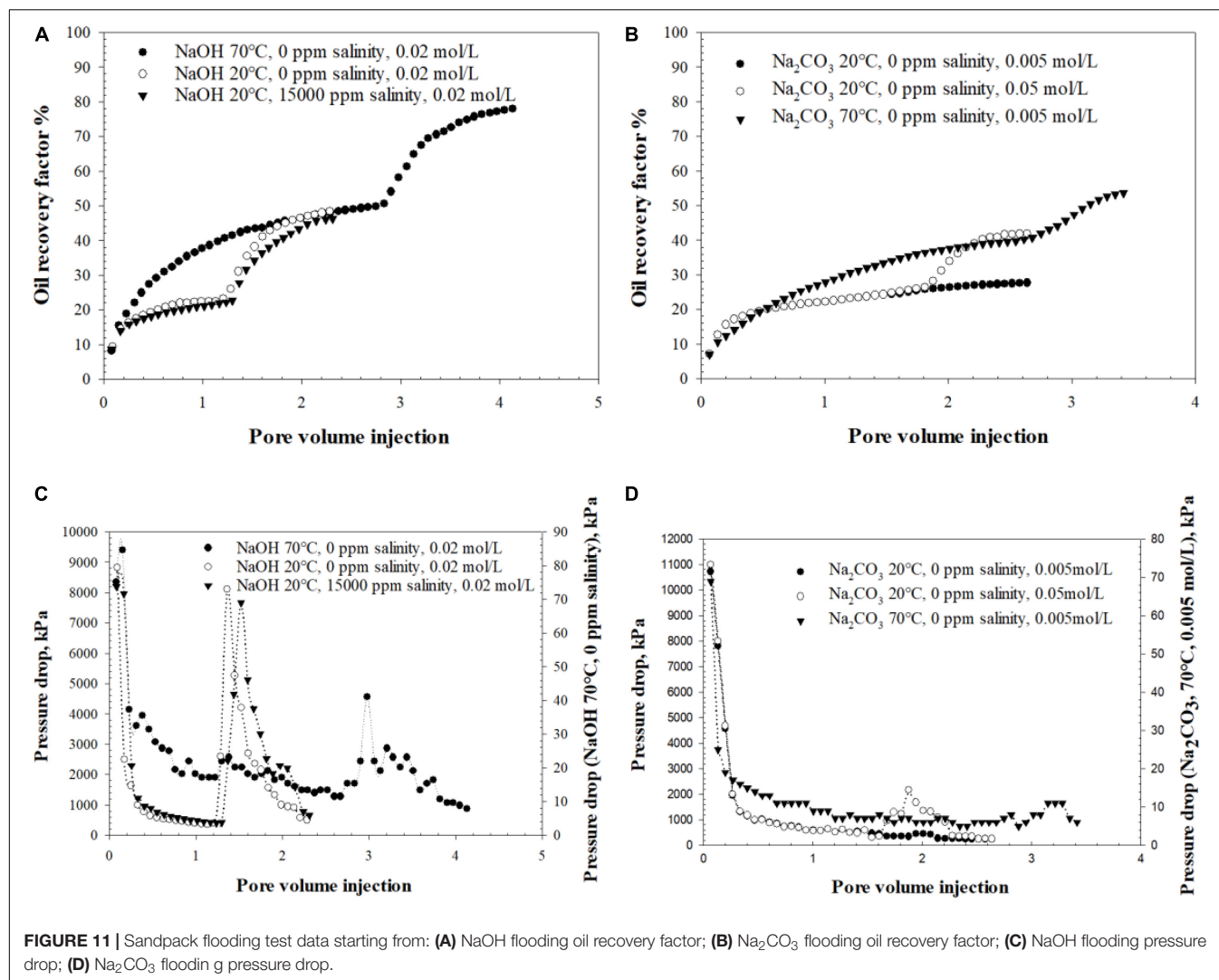


**TABLE 9** | Sandpack alkaline flooding test strategies.

Alkali	EXP	Temp, °C	Salinity, ppm	Concentration, mol/L	Porosity	Permeability, mD	Injection rate, mL/min
NaOH	1	70	0	0.02	0.32	4,568	1
	2	20	15,000	0.02	0.34	4,987	1
	3	20	0	0.02	0.35	4,611	1
$\text{Na}_2\text{CO}_3$	4	20	0	0.005	0.36	4,900	1
	5	20	0	0.05	0.36	4,694	1
	6	70	0	0.005	0.36	4,596	1



at 70°C produced large amounts of W/O emulsion with high viscosity. The effluent was also accompanied with noticeable oil dispersion in the water phase, as shown in **Figure 12A**, which can be confirmed with the turbidity change of produced water. NaOH flooding at ambient temperatures had only trace oil dispersion into the water phase as demonstrated by its crystal-clear water phase effluent in **Figure 12B**. After 0.23 PV of NaOH injection, the pressure at the injection end started to rebuild (**Figure 11C**) which indicates the formation of high viscous oil emulsion with possible wettability reversal inside of the porous media (Johnson,







1976). The oil emulsion broke through afterward when the produced oil color turned out to be brownish and different from the initial oil's dark black color. The oil emulsion was sampled by time and Karl Fischer titration showed sample water content was approximately 30 wt%. The water portion will be subtracted from the emulsion to determine the actual recovered oil volume. It is found that the oil recovery performance of strong basic solution is not sensitive to temperature change in the testing range no matter how much OOIP was produced by previous water flooding stage. High temperatures may slightly increase the *in situ* surfactants solubility to water, although its overall influence is negligible given the current temperature range (Karnanda et al., 2012).

The NaOH cases with brine of 15,000 ppm NaCl salinity had only 2% of OOIP difference to the deionized water case, which can be attributed to normal experimental deviation. The pressure build-up for both cases with and without salinity occurred within the same injection interval and their emulsion effluents had similar water contents. It proves one of the conclusions from the bottle test that the emulsification performance of strong alkali is not salinity sensitive. By analyzing the three NaOH flooding

cases, it is found that the formation of O/W emulsion does not critically affect oil recovery. The wettability reversal (water-wet to oil-wet) mechanism dominates oil recovery through NaOH flooding, which can be described by W/O emulsion generation as well as the pressure rebuild phenomenon. The viscosity of effluent W/O emulsion measured by a cone and plate viscometer was found to be over 200,000 cp, which is almost 10 times higher than the original heavy oil viscosity. Consequently, the W/O emulsion plays a similar role as polymer to control the mobility accompanying possible blockage of water droplets in high permeable channels to improve the sweep efficiency (Arhuoma et al., 2009).

Identical to the bottle test prediction, Na<sub>2</sub>CO<sub>3</sub> flooding tests showed different phenomena from the NaOH flooding tests. 0.7 PV of 0.005 mol/L alkaline injection at 70°C produced an extra 13% of OOIP after water flooding. However, there was no apparent pressure rebuild during the Na<sub>2</sub>CO<sub>3</sub> injection stage (Figure 11D) due to O/W emulsion generation, shown in Figure 12C. The produced oil during alkaline injection was sampled and its water content was lower than 7 wt%, thus the oil



Flooding EXP	A NaOH 70 °C 0.02 mol/L	B NaOH 20 °C 0.02 mol/L	C Na <sub>2</sub> CO <sub>3</sub> 70 °C 0.005 mol/L	D Na <sub>2</sub> CO <sub>3</sub> 20 °C 0.05 mol/L
Effluents after 0.35 PV of alkaline injection				
Emulsion type	O/W + W/O	W/O	O/W	W/O

**FIGURE 12** | Emulsion (upper or lower emulsion) type of effluent from sandpack. **(A)** Effluent collected after 0.35 PV of 0.02 mol/L NaOH flooding at 70 °C. **(B)** Effluent collected after 0.35 PV of 0.02 mol/L NaOH flooding at 20 °C. **(C)** Effluent collected after 0.35 PV of 0.005 mol/L Na<sub>2</sub>CO<sub>3</sub> flooding at 70 °C. **(D)** Effluent collected after 0.35 PV of 0.05 mol/L Na<sub>2</sub>CO<sub>3</sub> flooding at 20 °C.

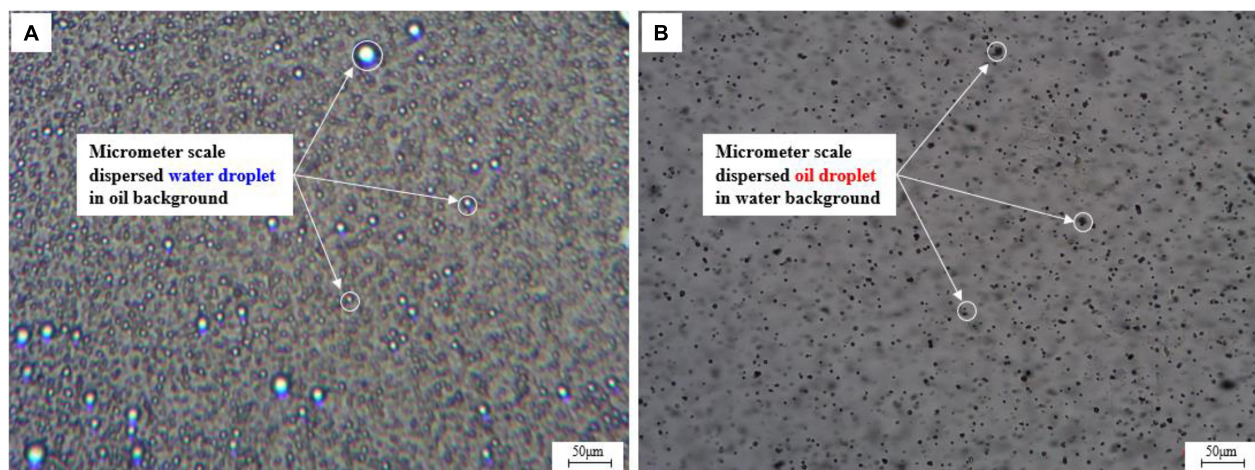
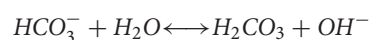
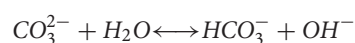
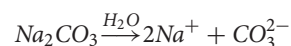


**FIGURE 13** | Sandpack flooding test effluents of **(A)** water in oil emulsion and **(B)** oil in water emulsion under microscopic view.

color is still black. There was a very slight pressure rebuild period during the final water flooding stage, which was also reported by Aminzadeh et al. (2016). It is believed to be induced by a small amount of trapped oil droplets in pore throats of the water dominant flow channel.

The temperature sensitivity test was also implemented to inject the same 0.005 mol/L Na<sub>2</sub>CO<sub>3</sub> solution after water flooding at 20°C. However, the oil recovery did not show any increase. The first reason is due to the high oil viscosity at low temperatures, which significantly reduces the oil dispersion possibility. A second reason is increased temperature is required to provide additional energy to facilitate the alkali dissociation in aqueous phase. As is known, the dissociation

of weak alkalis, like Na<sub>2</sub>CO<sub>3</sub>, normally undergoes multiple stages. The following chemical equations (Acevedo et al., 2001) were used to describe the generation of [OH<sup>-</sup>] group in two reversible reactions with postponement of [OH<sup>-</sup>] group generation.



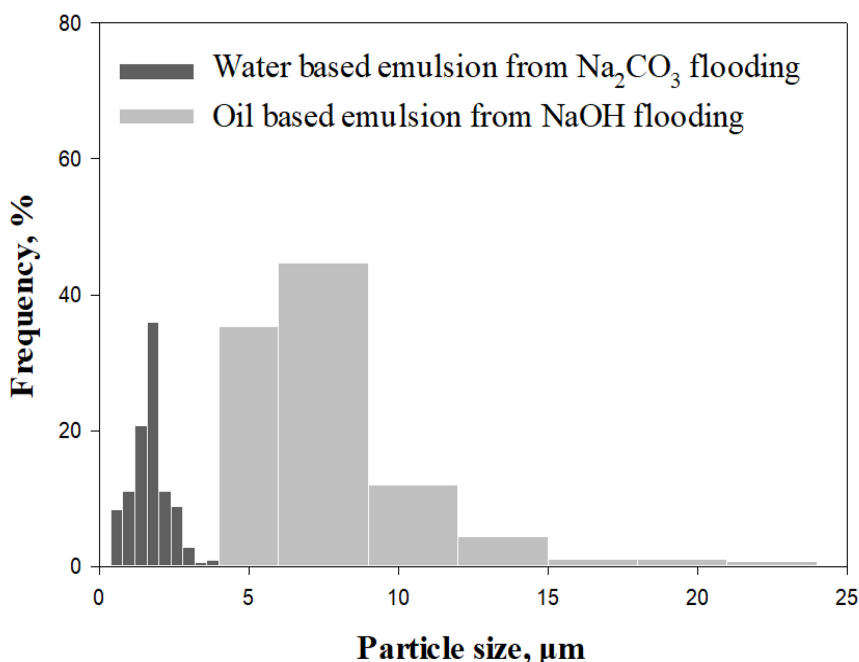


**FIGURE 14 |** Emulsion particle size distribution analysis.

High temperature conditions may favor the forward reaction to generate sufficient  $[\text{OH}^-]$  group in the system and consequently reduces the IFT to a lower level (Reardon, 1976).

Additionally, 0.05 mol/L of  $\text{Na}_2\text{CO}_3$  solution was injected after water flooding at an ambient temperature. Such a concentration is a bit off of the optimum  $\text{Na}_2\text{CO}_3$  concentration determined from the bottle test, but it is still workable for a saponification reaction since  $\text{Na}_2\text{CO}_3$  is an excellent buffer solution source. It can maintain the aqueous phase pH lower than 12 which is within the alkaline flooding working pH range (Rivas et al., 1997; Ashrafizadeh et al., 2012) that keeps asphaltenes and resins active with alkalis (Bryan and Kantzas, 2007). The flooding result fully matched with the previous bottle test result that W/O emulsion was generated at high  $\text{Na}_2\text{CO}_3$  concentration, as shown in **Figure 12D**. In this case, no oil dispersion in the water phase was observed from the effluent and the produced oil phase had more than 20 wt% of water content. The pressure from the injection end also rose after  $\text{Na}_2\text{CO}_3$  injection but it was not as high as that in the NaOH flooding case. According to Bryan and Kantzas (2007), Wang et al. (2010), and Dong et al. (2012) W/O emulsion viscosity increases with growing water content before converting to water-external emulsion. Since the water content of oil-external emulsion from a high  $\text{Na}_2\text{CO}_3$  concentration case is lower than NaOH cases, its lessened viscosity resulted in less pressure rebuild peak and therefore recovered less oil. The emulsion type reversal in sandpack flooding with increasing  $\text{Na}_2\text{CO}_3$  concentration is in good agreement with the  $\text{Na}_2\text{CO}_3$  orthogonal bottle test study (**Figure 9**).

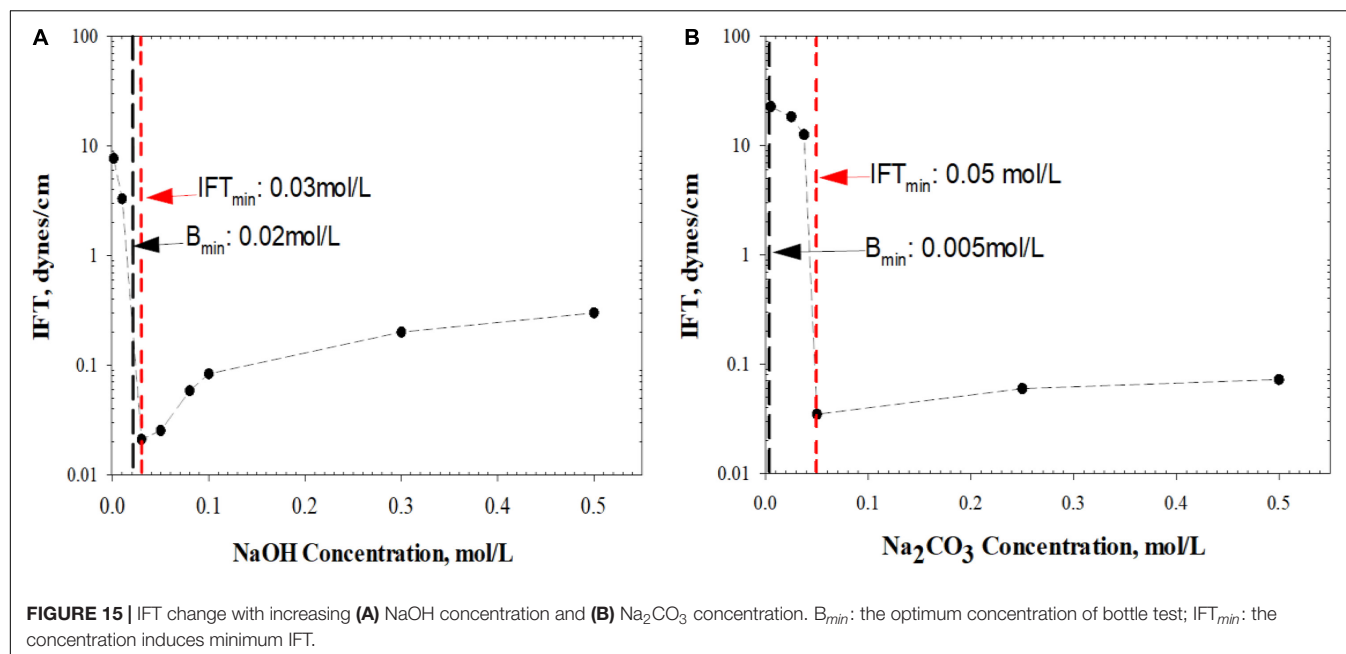
Generally, it can be concluded that a strong basic solution EOR like NaOH flooding showed better performance in oil

recovery relying on wettability reversal and high viscous W/O emulsion formation (Ding et al., 2010). Such Type II emulsion has been proven to have the highest economic efficiency by Aminzadeh et al. (2016).  $\text{Na}_2\text{CO}_3$  flooding on the other hand is more environmentally friendly due to its mild dissociation process. Appropriately low concentrations of  $\text{Na}_2\text{CO}_3$  solution injection under ideal temperatures and salinities can produce oil through emulsification and entrainment mechanisms. The essential difference between the two major types of emulsion produced after NaOH and  $\text{Na}_2\text{CO}_3$  solution injection can be manifested by microscopic observation, seen in **Figures 13A,B**.

The particle size distribution analysis based on microscopic images (**Figure 14**) shows that the water droplets in W/O emulsion have a larger radius than oil droplets in water emulsion. Therefore, the water droplets in oil-external emulsion have a higher possibility to plug the high permeable zone and thus improves the sweep efficiency and contributes to the pressure buildup as well.

The overall analysis of sandpack flooding tests has provided excellent consistency in emulsion type formation with modified bottle test prediction. It is believed that if the alkali dissociation rate is fast enough to bring sufficient  $[\text{OH}^-]$  group, the W/O emulsion tends to occur. Otherwise, if the alkali dissociation rate is slow, W/O emulsion still can be formed given the presence of plentiful salinity or alkaline concentration. The high concentration of weak alkali is able to compensate for its slow dissociation rate and thus achieve the similar emulsion type generation as strong alkalis. This phenomenon is also proven by the spinning drop IFT test at 70°C (**Figure 15**).

In **Figure 15A**, the NaOH concentration required to reach the minimum IFT is very close to the optimum concentration



obtained from modified bottle tests. On the contrary, there is a significant deviation of the two concentrations in **Figure 15B** for the Na<sub>2</sub>CO<sub>3</sub> case. This is because weak alkali introduced surfactants are more hydrophilic (Sun et al., 2017) so most of them stay in the aqueous phase rather than adhering to the interface. Such a fact explains the incapability of the IFT spinning drop test to predict the optimum weak alkali concentration when O/W emulsion is dominant.

## MODIFIED BOTTLE TEST TREND STUDY

As the feasibility of conducting an orthogonal modified bottle test for accurate prediction of emulsion generation during the flooding test was approved, a trend study using a modified bottle test was conducted to further verify the phase dispersion trend under the changing control factors. 70°C operating temperature was selected in order to improve the mixing quality while

**TABLE 10 |** NaOH concentration trend study experiment design.

EXPs	Temp, °C	Salinity, ppm	Aconc., mol/L
EXP1	70	0	0.001
EXP2	7	0	0.01
EXP3	70	0	0.03
EXP4	70	0	0.05
EXP5	70	0	0.08
EXP6	70	0	0.1
EXP7	70	0	0.3
EXP8	70	0	0.5

**TABLE 11 |** Na<sub>2</sub>CO<sub>3</sub> concentration trend study experiment design.

EXPs	Temp, °C	Salinity, ppm	Aconc., mol/L
EXP1	70	0	0.0005
EXP2	70	0	0.0025
EXP3	70	0	0.005
EXP4	70	0	0.0075
EXP5	70	0	0.025
EXP6	70	0	0.05
EXP7	70	0	0.25
EXP8	70	0	0.5

**TABLE 12 |** NaOH salinity trend study experiment design.

EXPs	Temp, °C	Salinity, ppm	Aconc., mol/L
EXP1	70	0	0.03
EXP2	70	500	0.03
EXP3	70	1,000	0.03
EXP4	70	3,000	0.0
EXP5	70	5,000	0.03
EXP6	70	7,000	0.03
EXP7	70	9,000	0.03
EXP8	70	12,000	0.03

**TABLE 13 |** Na<sub>2</sub>CO<sub>3</sub> salinity trend study experiment design.

EXPs	Temp, °C	Salinity, ppm	Aconc., mol/L
EXP1	70	0	0.005
EXP2	70	1,000	0.005
EXP3	70	3,000	0.005
EXP4	70	5,000	0.005
EXP5	70	7,000	0.005
EXP6	70	9,000	0.005
EXP7	70	12,000	0.005
EXP8	70	50,000	0.005

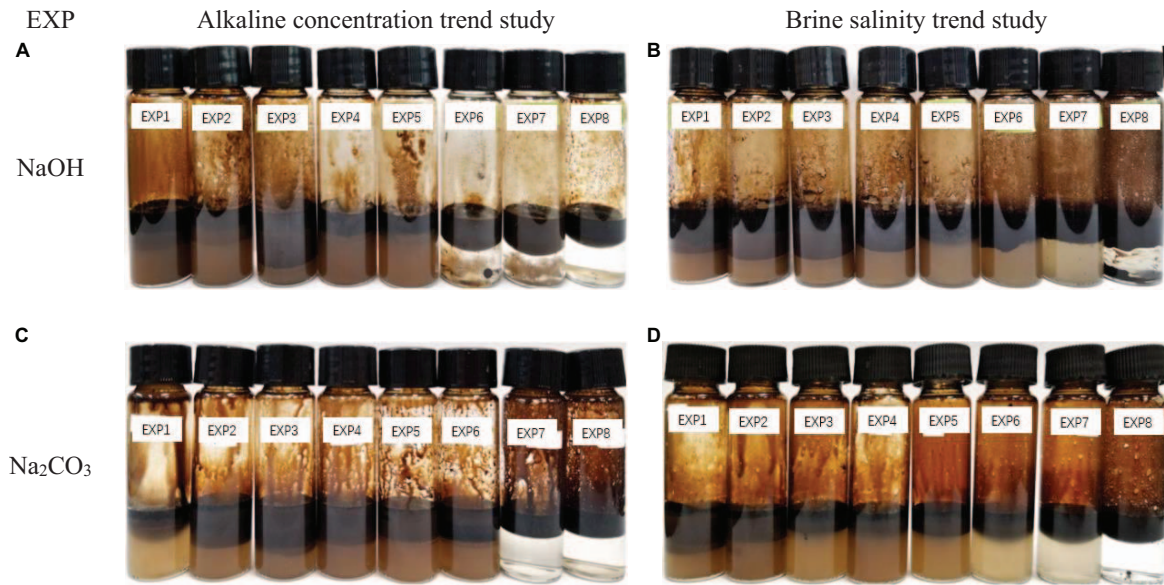


**FIGURE 16** | Bottle test trend study phases at equilibrium after 24 h. **(A)** NaOH concentration trend study. **(B)** NaOH salinity trend study. **(C)** Na<sub>2</sub>CO<sub>3</sub> concentration trend study. **(D)** Na<sub>2</sub>CO<sub>3</sub> salinity trend study.

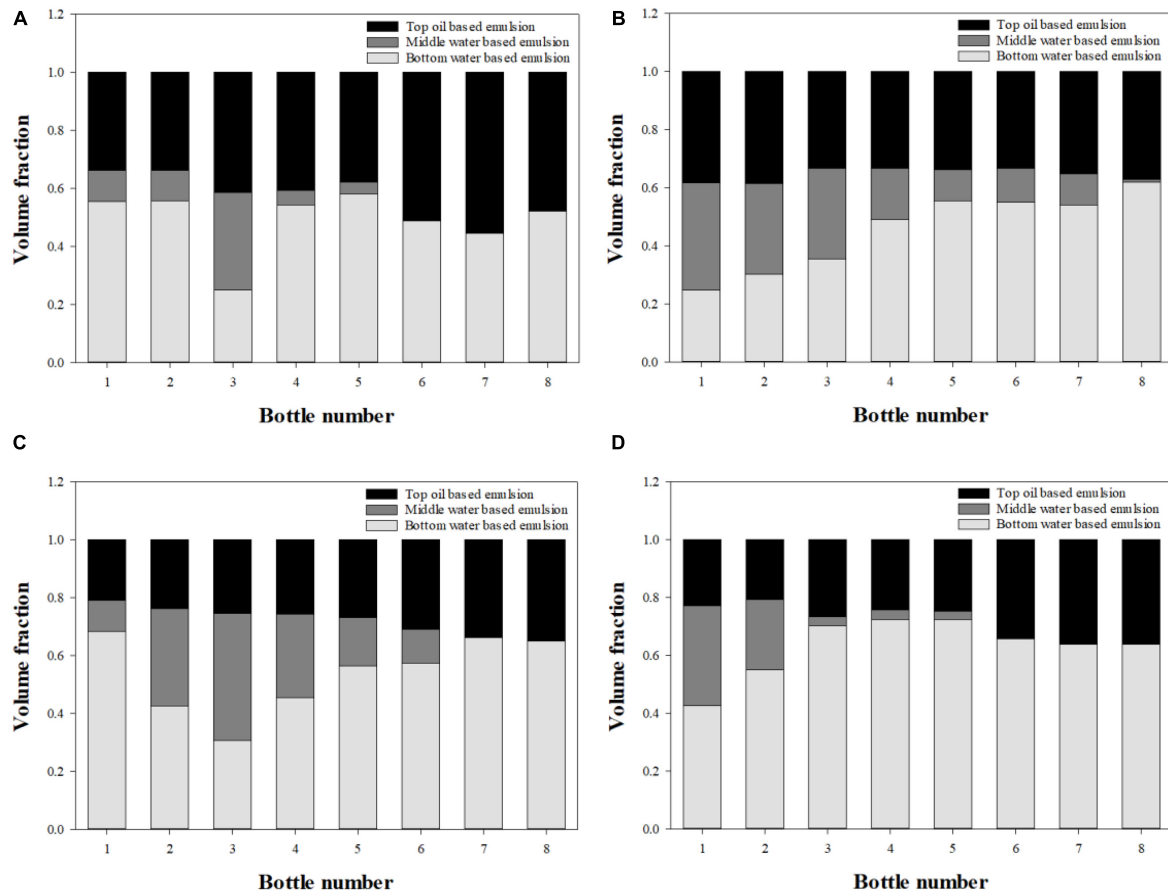


**FIGURE 17** | Three phase distribution of bottle test trend study after calibration starting from: **(A)** NaOH concentration trend study; **(B)** NaOH salinity trend study; **(C)** Na<sub>2</sub>CO<sub>3</sub> concentration trend study; **(D)** Na<sub>2</sub>CO<sub>3</sub> salinity trend study.



salinity and alkaline concentration trend tests were applied to both NaOH and Na<sub>2</sub>CO<sub>3</sub>. For each alkaline solution, alkaline concentration trend study was conducted primarily and the salinity was kept at 0 ppm to thoroughly exclude the salinity effect. Afterward, a salinity trend test was performed on the optimum alkaline concentration determined from the previous step. **Tables 10, 11** show the bottle test alkaline concentration trend study designs for NaOH and Na<sub>2</sub>CO<sub>3</sub> solutions and the salinity trend bottle test designs are provided in **Tables 12, 13**. In **Figure 16**, the observed bottle test results are given to show the phase variation tendency with changing salinity and alkaline concentration.

Accordingly, phase volume calibration by water content data was conducted through material balance to correct the observation error. Each emulsion's absolute volume was normalized into volume fraction in order to eliminate the natural volume difference between bottles. Therefore, the accurate emulsion type distribution can be derived in **Figure 17**. It can be seen that the imaged emulsion volume distribution in **Figure 17** reveals a more detailed and accurate depiction of the specific emulsion type volume fraction than the visualization results shown in **Figure 16**, especially in W/O emulsion quantification.

Based on **Figure 17**, the emulsion type generation tendency under various control factors which was concluded from previous orthogonal bottle test has been proven to have a good agreement with the trend study results. For strong alkalis like NaOH, it is found W/O emulsion dominated the total emulsion generation from **Figure 17A**. It can also be seen that additional NaOH concentration slightly improves the water dispersion in the oil phase. In addition, the brine salinity mainly affects the oil dispersion in the water phase other than the W/O emulsion for the NaOH case as shown in **Figure 17B**. On the other hand, the O/W emulsion in **Figure 17C** was found to be the dominant emulsion type for low concentrations (< 0.005 mol/L) of Na<sub>2</sub>CO<sub>3</sub> cases. When Na<sub>2</sub>CO<sub>3</sub> concentration is higher than 0.005 mol/L, the oil phase dispersion was suppressed and the volume of W/O emulsion became larger. A similar trend was shown in **Figure 17D** as O/W emulsion quantity gradually decreased in the higher salinity system. The major emulsion type inversion was observed in Na<sub>2</sub>CO<sub>3</sub> cases where O/W emulsion dominating system switched into W/O emulsion prevailing at high salinity and high alkaline concentration ranges. Such an emulsion type inversion was also proven through microscopic observation by Ge et al. (2012).

## CONCLUSION

This research mainly focused on the feasibility study of the modified bottle test in emulsion preparation to predict major emulsion type generation during oil recovery by alkaline flooding. Through the novel sampling practice and water content measurement, the phase volume distribution of the bottle tests using different alkalis at various alkaline concentrations, salinities, and temperatures can be more accurately quantified

than volume observation. The sandpack flooding tests conducted afterward verified the feasibility of the modified bottle test method as the effluent emulsion type was identical to the bottle test prediction. Considering the relationship between the driving mechanism of oil recovery by alkaline flooding and certain emulsion type generation, it will be practical to apply the modified bottle test to investigate the major emulsion type generation in order to predict the possible driving mechanisms that may occur during the alkaline flooding based on previous experience. Further study can focus on the correlation of shear energy to homogenizer rotation rate. By building the bridge between the bottle test and sandpack test, the accuracy of simulated emulsification process in the bottle test can be enhanced. Based on the current works, the following main conclusions can be drawn:

- (1) Given that the huge difference between the micrometer-scale porous media and bulk oil and water phases, sufficient shear energy is vital in the preparation of representative emulsion in the bottle test.
- (2) Due to the additional saponification process and complexity of *in situ* surfactants generation, the emulsification type and quality of different alkaline solutions are more unpredictable than artificial surfactants in regard to concentration and temperature change. By sampling individual phases from the bottle test and conducting water content measurement, a more detailed and accurate emulsion phase distribution in bottle test can be obtained that is more reliable than conventional volume observation.
- (3) The modified bottle test method is able to determine the major emulsion type potentially to be produced in flooding test and thus the outcome can be used to predict the related driving mechanism of the alkaline flooding based on previous experience. This modified method is especially suitable for cases when high viscous heavy oil is involved.
- (4) In respect of the driving mechanism study and prediction of alkaline flooding performance in oil recovery, the modified bottle test method is relatively more convenient and time-saving than the sandpack flooding test. Designed orthogonal experiments can be quickly conducted through bottle test and obtain emulsification tendency under various control factors.
- (5) The modified bottle test provided acceptable results for both strong and weak alkalis to show its adaptability. Other alkali or salt types can also be tested following a similar methodology to expand the modified bottle test application.

## DATA AVAILABILITY STATEMENT

The original contributions presented in the study are included in the article/supplementary material, further inquiries can be directed to the corresponding author/s.



## AUTHOR CONTRIBUTIONS

ZX: methodology, investigation, formal analysis, data collection, processing, and writing original draft. NJ: conceptualization, validation, resources, writing–review and editing, supervision, funding acquisition, and project administration. ES: resources and validation. All authors contributed to the article and approved the submitted version.

## REFERENCES

- Acevedo, S., Escobar, G., Gutiérrez, L., and Rivas, H. (1992). Isolation and characterization of natural surfactants from extra heavy crude oils, asphaltenes and maltenes. Interpretation of their interfacial tension-pH behaviour in terms of ion pair formation. *Fuel* 71, 619–623. doi: 10.1016/0016-2361(92)90163-i
- Acevedo, S., Gutierrez, X., and Rivas, H. (2001). Bitumen-in-water emulsions stabilized with natural surfactants. *J. Colloid Interface Sci.* 242, 230–238. doi: 10.1006/jcis.2001.7728
- Aminzadeh, B., Hoang, V., Inouye, A., Izgec, O., Walker, D., Chung, D., et al. (2016). “Improving recovery of a viscous oil using optimized emulsion viscosity,” in *Proceedings of the SPE Improved Oil Recovery Conference*, Tulsa, OK.
- Arhuoma, M., Dong, M., Yang, D., and Idem, R. (2009). Determination of water-in-oil emulsion viscosity in porous media. *Indust. Eng. Chem. Res.* 48, 7092–7102. doi: 10.1021/ie801818n
- Ashrafizadeh, S., Motae, E., and Hoshyargar, V. (2012). Emulsification of heavy crude oil in water by natural surfactants. *J. Pet. Sci. Eng.* 86–87, 137–143. doi: 10.1016/j.petrol.2012.03.026
- Athreya, S., and Venkatesh, Y. D. (2012). Application of taguchi method for optimization of process parameters in improving the surface roughness of lathe facing operation. *Intl. Refereed J. Eng. Sci.* 1, 13–19.
- Baek, K. H., Argüelles-Vivas, F. J., Okuno, R., Sheng, K., Sharma, H., and Weerasooriya, U. P. (2018). “Organic alkali as a steam additive for improved sagd: experimental study of emulsion phase behavior and viscosity,” in *Proceedings of the SPE Canada Heavy Oil Technical Conference*, Calgary, ALB.
- Bryan, J. L., and Kantzas, A. (2007). “Enhanced heavy-oil recovery by alkali-surfactant flooding,” in *Proceedings of the SPE Annual Technical Conference and Exhibition*, Anaheim, CA.
- Castor, T. P., Somerton, W. H., and Kelly, J. F. (1981). “Recovery Mechanisms of Alkaline Flooding,” in *Surface Phenomena in Enhanced Oil Recovery*, ed. D. O. Shah (Boston, MA: Springer), 249–291. doi: 10.1007/978-1-4757-0337-5\_14
- Chhabra, R. P., and Richardson, J. F. (2008). “Chapter 8 - Liquid mixing,” in *Non-Newtonian Flow and Applied Rheology Engineering Applications*, 2nd Edn, Amsterdam: Butterworth-Heinemann/Elsevier.
- Cooke, C., Williams, R., and Kolodzie, P. (1974). Oil recovery by alkaline waterflooding. *J. Pet. Technol.* 26, 1365–1374. doi: 10.2118/4739-pa
- Dehghan, A. A., Masihi, M., and Ayatollahi, S. (2013). Evaluation of chemicals interaction with heavy crude oil through water/oil emulsion and interfacial tension study. *Energy Fuels* 27, 5852–5860. doi: 10.1021/ef401361t
- Dhankhar, P. (2014). Homogenization fundamentals. *IOSR J. Eng.* 4, 1–8. doi: 10.1201/b18436-2
- Ding, B., Zhang, G., Ge, J., and Liu, X. (2010). Research on mechanisms of alkaline flooding for heavy oil. *Energy Fuels* 24, 6346–6352. doi: 10.1021/ef100849u
- Dong, M., Liu, Q., and Li, A. (2012). Displacement mechanisms of enhanced heavy oil recovery by alkaline flooding in a micromodel. *Particuology* 10, 298–305. doi: 10.1016/j.partic.2011.09.008
- Fan, D. Y., and Chen, Y. H. (1996). *Probability Theory and Mathematical Statistics*. China: Zhejiang University Press, 215.
- Ge, J., Feng, A., Zhang, G., Jiang, P., Pei, H., Li, R., et al. (2012). Study of the factors influencing alkaline flooding in heavy-oil reservoirs. *Energy Fuels* 26, 2875–2882. doi: 10.1021/ef3000906
- Homsy, G. (1987). Viscous fingering in porous media. *Annu. Rev. Fluid Mech.* 19, 271–311.
- Isaacs, E. E., and Chow, R. S. (1992). “Practical aspects of emulsion stability,” in *Emulsions Fundamentals and Applications in the Petroleum Industry*, ed.
- L. L. Schramm (Washington, DC: American Chemical Society), 51–77. doi: 10.1021/ba-1992-0231.ch002
- Johnson, C. (1976). Status of caustic and emulsion methods. *J. Pet. Technol.* 28, 85–92. doi: 10.2118/5561-pa
- Karnanda, W., Benzagouta, M. S., AlQuraishi, A., and Amro, M. M. (2012). Effect of temperature, pressure, salinity, and surfactant concentration on IFT for surfactant flooding optimization. *Arab. J. Geosci.* 6, 3535–3544. doi: 10.1007/s12517-012-0605-7
- Kokal, S., and Abdulaziz, A. (2010). “Enhanced oil recovery: challenges and opportunities,” in *World Petroleum Council: Official Publication 2010* (Global Energy Solutions), 64–69.
- Nelson, R., Lawson, J., Thigpen, D., and Stegemeier, G. (1984). “Cosurfactant-enhanced alkaline flooding,” in *Proceedings of SPE Enhanced Oil Recovery Symposium*, Tulsa, OK.
- Panthi, K., and Mohanty, K. K. (2013). Effect of alkaline preflush in an alkaline-surfactant-polymer flood. *Energy Fuels* 27, 764–771. doi: 10.1021/ef301847z
- Pei, H., Zhang, G., Ge, J., Tang, M., and Zheng, Y. (2012). Comparative effectiveness of alkaline flooding and alkaline-surfactant flooding for improved heavy-oil recovery. *Energy Fuels* 26, 2911–2919. doi: 10.1021/ef300206u
- Reardon, E. J. (1976). Dissociation constants for alkali earth and sodium borate ion pairs from 10 to 50°C. *Chem. Geol.* 18, 309–325. doi: 10.1016/0009-2541(76)90013-9
- Rivas, H., Gutierrez, X., Zirrit, J. L., Anto'n, R. E., and Salager, J. L. (1997). “Microemulsion and optimum formulation occurrence in PH dependent systems as found in alkaline enhanced oil recovery,” in *Industrial Applications of Microemulsions*, eds C. Solans and H. Kunieda (New York, NY: M. Dekker), 305–329.
- Sun, J., Sun, L., Liu, W., Liu, X., Li, X., and Shen, Q. (2008). Alkaline consumption mechanisms by crude oil: a comparison of sodium carbonate and sodium hydroxide. *Colloids Surf. A* 315, 38–43. doi: 10.1016/j.colsurfa.2007.07.009
- Sun, N., Jing, J., Jiang, H., An, Y., Wu, C., Zheng, S., et al. (2017). Effects of surfactants and alkalis on the stability of heavy-oil-in-water emulsions. *SPE J.* 22, 120–129. doi: 10.2118/181742-pa
- Wang, J., Dong, M., and Arhuoma, M. (2010). Experimental and numerical study of improving heavy oil recovery by alkaline flooding in sandpacks. *J. Can. Pet. Technol.* 49, 51–57. doi: 10.2118/134248-pa
- Xu, B., Kang, W., Wang, X., and Meng, L. (2013). Influence of water content and temperature on stability of W/O crude oil emulsion. *Pet. Sci. Technol.* 31, 1099–1108. doi: 10.1080/10916466.2010.551812
- Zhang, S., Zhao, L., Yue, X., Li, B., and Zhang, J. (2018). Density, viscosity, surface tension and spectroscopic studies for the liquid mixture of tetraethylene glycol+ N, N -dimethylformamide at six temperatures. *J. Mol. Liq.* 264, 451–457. doi: 10.1016/j.molliq.2018.04.017

## ACKNOWLEDGMENTS

We would like to thank the financial support for this project from Petroleum Technology Research Centre (PTRC) and Mitacs Accelerate Program. We also acknowledge the permission of CNRL and Husky to publish the experiment's data and results. Mr. Tian Jian's constructive suggestions in manuscript writing are highly appreciated as well.

**Conflict of Interest:** The authors declare that the research was conducted in the absence of any commercial or financial relationships that could be construed as a potential conflict of interest.

Copyright © 2021 Xi, Jia and Shirif. This is an open-access article distributed under the terms of the Creative Commons Attribution License (CC BY). The use, distribution or reproduction in other forums is permitted, provided the original author(s) and the copyright owner(s) are credited and that the original publication in this journal is cited, in accordance with accepted academic practice. No use, distribution or reproduction is permitted which does not comply with these terms.



# Effects of Fracturing Parameters on Fracture Unevenness During Large-Stage Multi-Cluster Fracturing in Horizontal Wells

Rui Yong<sup>1</sup>, Fu-Jian Zhou<sup>1\*</sup>, Ming-Hui Li<sup>1</sup>, Yi Song<sup>2</sup>, Xiao-Jin Zhou<sup>2</sup>, Zhi-Heng Zhao<sup>2</sup>, Ben Li<sup>1</sup> and Shi-Yong Qin<sup>3</sup>

<sup>1</sup> Unconventional Oil-Gas Science and Technology Research Institute, China University of Petroleum, Beijing, China, <sup>2</sup> Shale Gas Research Institute, PetroChina Southwest Oil & Gas Field Company, Chengdu, China, <sup>3</sup> PetroChina Tarim Oil & Gas Field Company, Xinjiang, China

## OPEN ACCESS

### Edited by:

Wei Yu,  
University of Texas at Austin,  
United States

### Reviewed by:

Peng Tan,  
CNPC Engineering Technology R&D  
Company Limited, China  
Tiankui Guo,  
China University of Petroleum  
(Huadong), China

### \*Correspondence:

Fu-Jian Zhou  
zhoufj@cup.edu.cn

### Specialty section:

This article was submitted to  
Advanced Clean Fuel Technologies,  
a section of the journal  
Frontiers in Energy Research

**Received:** 30 September 2020

**Accepted:** 10 March 2021

**Published:** 20 May 2021

### Citation:

Yong R, Zhou F-J, Li M-H,  
Song Y, Zhou X-J, Zhao Z-H, Li B and  
Qin S-Y (2021) Effects of Fracturing  
Parameters on Fracture Unevenness  
During Large-Stage Multi-Cluster  
Fracturing in Horizontal Wells.  
Front. Energy Res. 9:612486.  
doi: 10.3389/fenrg.2021.612486

Horizontal well with multi-cluster fracturing technology is an effective approach to exploit unconventional hydrocarbon reservoirs. The on-site diagnosis results indicate that multi-cluster fractures always tend to propagate unevenly due to stress interference, therefore it is very essential to study the effect of fracturing parameters on fracture propagation unevenness. In this paper, the unconventional fracturing model (UFM, Unconventional Fracturing Model) is used to study the effect of multi-cluster fracturing parameters on fracture unevenness in a large stage. This model has been validated with the actual fracturing case on-site in the Longmaxi shale. The investigated parameters include completion parameters (cluster spacing, number of perforations per cluster), pumping parameters (fluid injection intensity and proppant injection intensity). Our simulation results show that firstly reducing fracture spacing will increase stress interference, and hydraulic fractures exhibit a “radial” pattern. Secondly, reducing the perforation number of a single cluster can promote the more uniform propagation of multi-cluster fractures. Thirdly, increasing the fluid injection intensity will increase the fracture length, but will also increase the fracture unevenness. Besides, the injection strength of the proppant has a little effect on the average fracture length and the unevenness of the fracture length. Finally, setting a reasonable cluster spacing and injection fluid strength can obtain a more uniform fracture propagation. Meanwhile reducing the number of perforations per cluster can also reach the goal of propagating evenly. This paper provides a certain reference for the optimization of multi-cluster fracturing parameters in large-stage and multi-cluster wells.

**Keywords:** horizontal well, staged fracturing, fracture propagation, UFM model, uneven propagation

## INTRODUCTION

The unconventional reservoirs such as shale have nanoscale pore-spaces and very low permeability, so the traditional reservoir stimulation methods cannot satisfy their commercial exploitation (Jia et al., 2012). In recent decades, horizontal well drilling with multi-cluster fracturing technology has become the mainstream technology for the exploitation of unconventional reservoirs.

The implementation of this technology is to shoot multi-cluster perforations in the casing of a horizontal well and then to inject high-rate and high-pressure fracturing fluid into the wellbore. Multiple hydraulic fractures can initiate and propagate simultaneously, which increases the stimulation volume and greatly improves reservoir seepage conditions (Chen et al., 2010; Wu et al., 2011a,b).

With the increase in the burial depth of shale gas reservoirs, problems such as complex stratigraphic structure and large in-situ stress differences will emerge in the reservoirs, which makes it difficult to form multiple uniform and effective hydraulic fractures in the target formation (Xie, 2018; Xie et al., 2019; Ma et al., 2020). With the background of the low oil prices, the large-stage multi-cluster fracturing technology, increasing the stage length to reduce the amount of bridge plugs and reducing the cluster spacing to improve the reservoir contact, is the key technology to reduce the cost and improve production (Fan et al., 2019). However, recent studies have shown that reducing fracture spacing will perform stronger stress interference and more uneven fracture length are obtained (Pan et al., 2014; Zhao et al., 2015; Li et al., 2017; Zhou et al., 2019). Pan et al. (2014) established a three-dimensional finite element model to simulate the simultaneous propagation of multiple fractures in horizontal wells. Their results show that the number of perforation clusters and fracture spacing is the main factors affecting fracture propagation. The closer perforation clusters are distributed, the more serious the stress interference in one stage can be obtained. Zhao et al. (2015) established the simultaneous propagation model of multiple fractures using the displacement discontinuity method, and they studied the influence of the stress interference between fractures on the local stress field and initial fracture pressure. Their results show that induced stress may lead to the asymmetric propagation of the two wings of the fractures. Li et al. (2017) studied the influence of perforation erosion on the fracture propagation of multiple clusters by a comprehensive model that couples perforation erosion effect and hydraulic fracture propagation. Their results show that the proppant in the sand slurry will destroy the perforations, resulting in a huge limit-entry capacity reduction, which in turn leads to a wider variation among the length of fractures in one stage. Liu et al. (2020) explored multi-fracture propagation in shale strata based on the Lattice model, and their results show that middle fractures are suppressed by other adjacent fractures. Fracture spacing and in-situ stress difference are the key parameters to keep uniform fracture length from their results. Meanwhile their results (Liu et al., 2019) show that the application of zipper fracturing technology increases SRV when two horizontal wells exist. These above studies indicate that uneven fracture propagation is very common during the propagation of multiple fractures.

In multi-cluster fracturing field operations in the large stages, fracturing fluids with temporary plugging agents are usually used to plug the over-treated fractures and promote the uniform propagation of multi-cluster fractures (Wang et al., 2018; Murphree et al., 2020; Zhou et al., 2020). Zhou et al. (2020) studied the effect of temporary plugging ball on fracture propagation using a fully coupled model

of “wellbore-perforation-fracture propagation” based on the boundary element method. Their results show that the addition of temporary plugging agents helps to improve the non-uniform propagation of multi-cluster fractures. Li et al. (2020) studied the temporarily plugging staged fracturing (TPSF) using the cohesive zone method, and their results show that lateral fractures can break through the suppression from previous fractures and TPSF enhance the complexity of fracture network. Chen et al. (2020a) numerically investigated the optimization of the number of diverters and diverting time during near-wellbore diversion in a heterogeneous stress reservoir, and their results indicate that more ball sealers and the earlier diverting time are required for creating a new fracture in the formations with the high-stress zone. Some advanced monitoring methods in the oil-field also show the effectiveness of temporary plugging technology. Rahim et al. (2017) adopted post-job diagnostics and analyzed well performances in the cases in carbonate and sandstone reservoirs, and they proved that the diverters can successfully plug perforations. Panjaitan et al. (2018) carried out a comprehensive method including water hammer analysis, step-down test, and micro-seismic data in Haynesville Shale and their results show the diverters can divert the fluid to intended perforations and TPSF can promote uniform propagation of multiple fractures. Some other field researches also get similar results (Huang et al., 2018; Senters et al., 2018; Weddle et al., 2018). In TPSF operations, a key question is how uneven is the fractures at this point when the temporary plugging agents are injected. Fracturing parameters have an important impact on the unevenness of multi-cluster fracture propagation. Therefore, studying fracturing parameters on multi-cluster fracture length is of great significance to the design of the timing and dosage of the temporary plugging agents.

At present, there are few studies on the influence of multi-cluster fracturing parameters on the unevenness of multi-cluster fracture length in a large stage. In this paper, numerical simulation is conducted using the unconventional fracturing model (UFM) to analyze the sensitivity of fracturing design parameters. The first part of this study will briefly describe the mathematical model of the UFM model; In the second part, a large-scale multi-cluster fracturing simulation will be performed on the shale formation of the Longmaxi Formation in Changning, and compared with the real treatment pressure curve to verify the accuracy of the model; In the third part, numerical simulations will be carried out on different fracturing parameters to study the influence of fracturing parameters on the unevenness of fracture length. The main fracturing parameters studied include completion parameters (cluster spacing and the number of perforations per cluster); pumping injection parameters (fluid injection intensity and proppant injection intensity).

## MATHEMATICAL MODEL

The UFM model is used to simulate the propagation of multiple clusters of fractures. The UFM model is a complex

fracture model developed by Weng et al. based on a pseudo-three-dimensional plane hydraulic fracture model. The model can simulate the propagation of multiple fracture tips. The mathematical model is as follows (Nolte, 1991; Weng et al., 2011, 2012):

## Fluid Flow in Fractures

The flow equation of power-law fluid in a fracture follows Poiseuille's law (Nolte, 1991):

$$\frac{\partial p}{\partial s} = -\alpha_0 \frac{1}{\bar{w}^{2n'+1}} \frac{q}{h_{fl}} \left| \frac{q}{h_{fl}} \right|^{n'-1} \quad (1)$$

$$\alpha_0 = \frac{2K}{\varphi(n)^n} \left( \frac{4n+2}{n} \right)^n \quad (2)$$

$$\varphi(n) = \frac{2K}{h_{f1}} \int_{h_{f1}} \left( \frac{w(z)}{\bar{w}} \right)^{\frac{2n+1}{n}} dz \quad (3)$$

where,  $p$  is the fluid pressure;  $q$  is the local flow velocity in the fracture;  $h_{fl}$  is the fluid height in the fracture;  $\bar{w}$  is the average fracture width;  $w(z)$  is the depth-related fracture width;  $s$  is the distance along the fracture;  $n$  and  $K$  is the fluid power-law exponent and consistency coefficient, respectively.

The fluid in the fracture obeys the conservation of mass, and its continuity equation is:

$$\frac{\partial q}{\partial s} + \frac{\partial(H_{fl}\bar{w})}{\partial t} + q_L = 0 \quad (4)$$

$$q_L = \frac{2h_1 c_1}{\sqrt{t - \tau(s)}}, t > \tau(s) \quad (5)$$

where  $c_1$  is the total filtration coefficient;  $h_1$  is the filter loss zone height;  $\tau(s)$  is the time when the fracture unit first contacts the fracturing fluid.

Global volume balance equation:

$$\int_0^t Q(t)dt = \int_0^{L(t)} h\bar{w}ds + \int_0^{L(t)} \int_0^t q_L dtds \quad (6)$$

where  $Q(t)$  is the injection rate;  $L(t)$  is the total length of the entire fracture at time  $t$ ;  $h$  is the fracture height.

In the wellbore, the total injection rate should be equal to the sum of the rates flowing into the fractures, and its equation satisfies (Mack and Elbel, 1992):

$$\sum_i q_i(t) = Q(t) \quad (7)$$

where,  $q_i(t)$  is the injection rate of the  $i$ th fracture.

The 2D KPN model is used to describe the relationship between fracture width and pressure, and the equation is satisfied

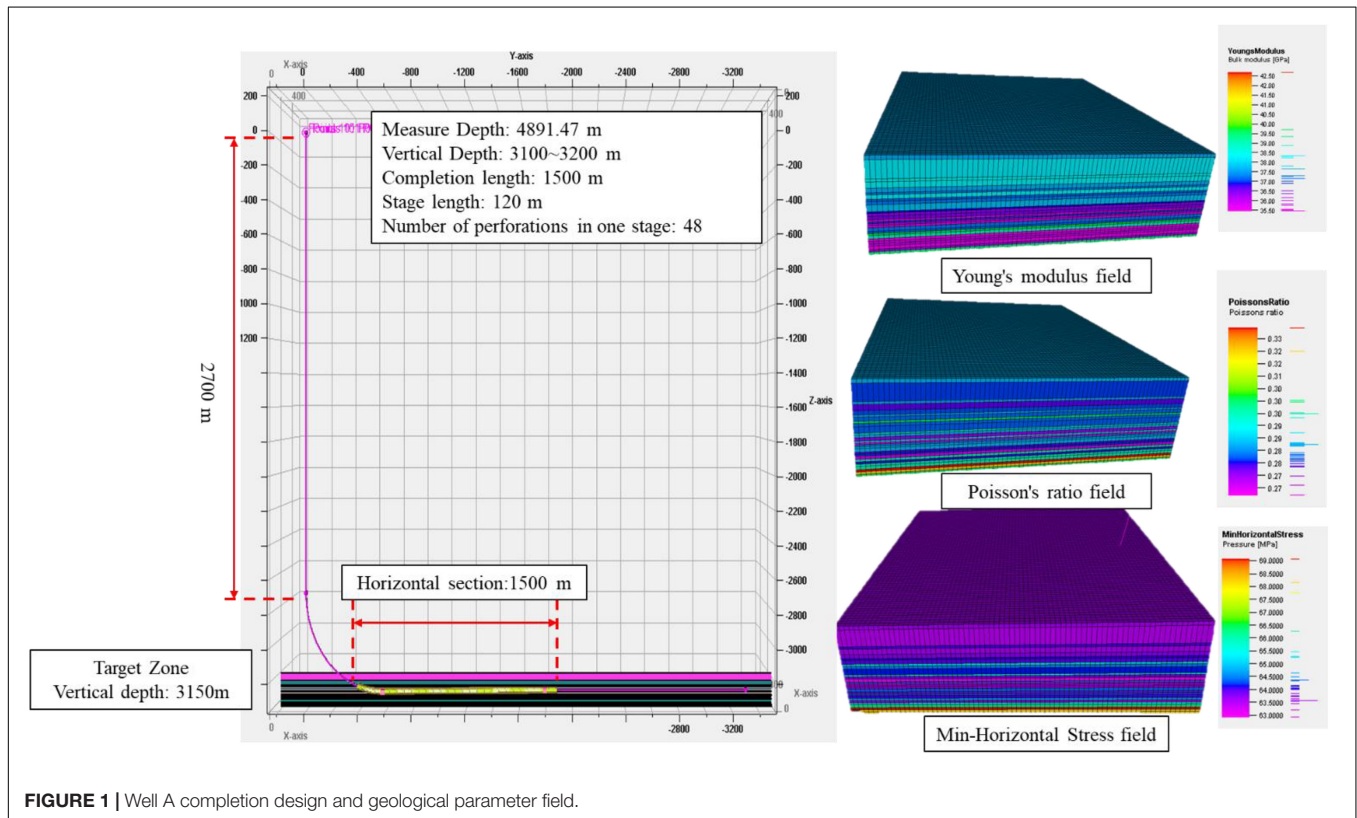
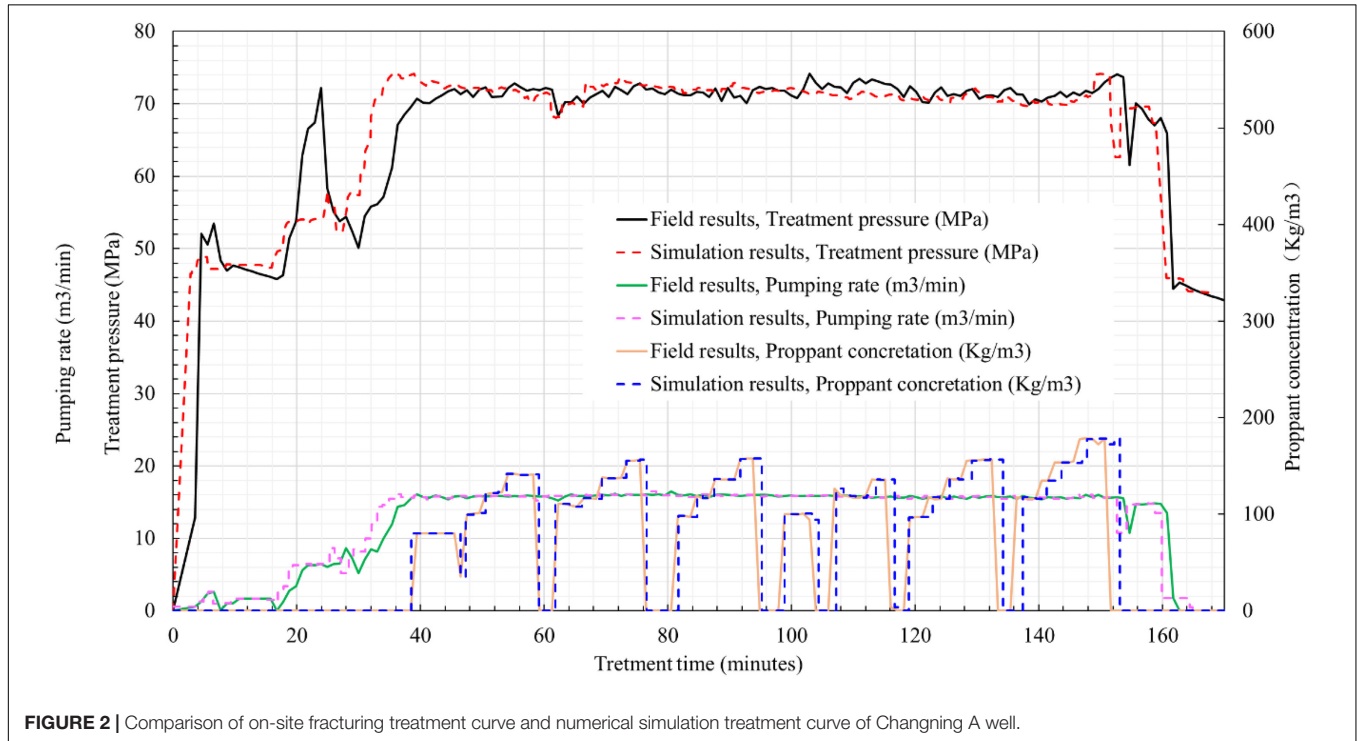


FIGURE 1 | Well A completion design and geological parameter field.



**TABLE 1** | Basic parameters of the numerical model.

Completion parameters	Value	Unit	Pumping parameters	Value	Unit/type
Fracture spacing	10	m	Total mass of the proppant	180	Tons
Number of perforation clusters	10	/	Proppant injection intensity	1.8	Tons/m
Perforation number per cluster	4	/	Total volume of the fluid	2400	m <sup>3</sup>
Perforation diameter	10	mm	Fluid injection intensity	24	m <sup>3</sup> /m
Stage length	100	m	Pumping rate	12	m <sup>3</sup> /min
Total number of perforations in one stage	40	/	Proppant type	40/70mesh	Quartz sand
Minimum horizontal principal stress	64.19	MPa	Vertical principal stress	72.5	MPa
Maximum horizontal principal stress	77.52	MPa			

**FIGURE 2** | Comparison of on-site fracturing treatment curve and numerical simulation treatment curve of Changning A well.

(Perkins and Kern, 1961; Nordgren, 1970):

$$\bar{w} = \frac{\pi H(p - \delta_n)}{2E'} \quad (8)$$

where  $E'$  is the plane strain rock modulus.

At the crack tip, the following boundary conditions are met:

$$p = \delta_n, w = 0, q = 0 \quad (9)$$

### Fracture Height Control Model

For the control of the fracture height, the UFM model uses a model like the pseudo-three-dimensional model (Weng et al., 2011). The pressure  $p$  in the fracture is:

$$p = p_{cp} + \rho_f g(h_{cp} - z) \quad (10)$$

where  $p_{cp}$  is the fracture pressure at the perforation depth (measured at the bottom of the fracture);  $\rho_f$  is the fluid density.

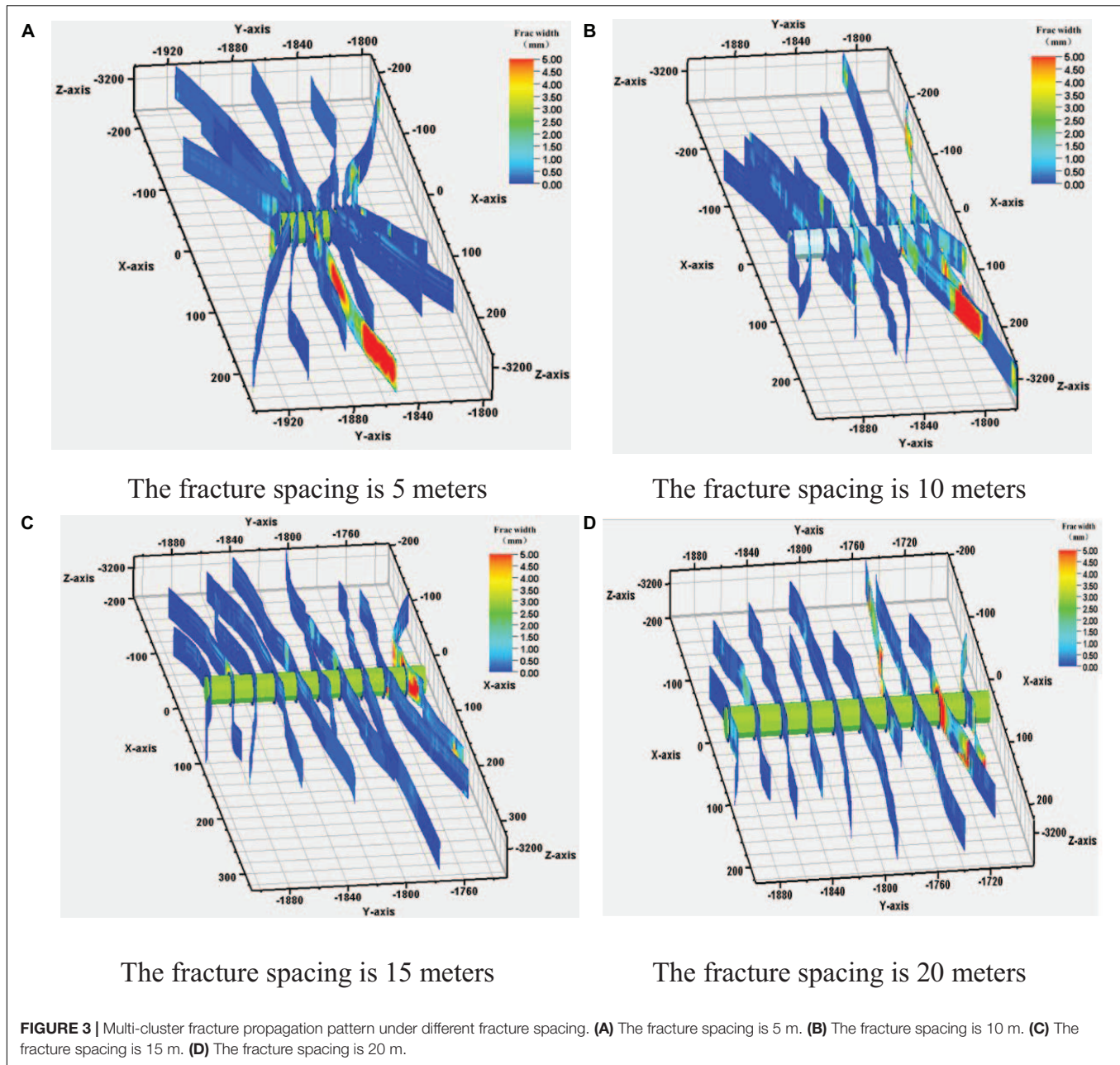
The fracture height is obtained by matching the stress intensity factor and fracture toughness. The intensity factors at the top

and bottom of the fracture tip can be obtained from the pressure in the fracture, fracture height, and local stress. The calculation equation for the stress intensity factor and fracture width at the top and bottom of the fracture tip is:

$$K_{Iu} = \sqrt{\frac{\pi h}{2}} \left[ p_{cp} - \delta_n + \rho_f g \left( h_{cp} - \frac{3}{4}h \right) \right] + \sqrt{\frac{2}{\pi h}} \sum_{i=1}^{n-1} (\delta_{i+1} - \delta_i) \left[ \frac{h}{2} \arccos \left( \frac{h - 2h_i}{h} \right) - \sqrt{h_i(h - h_i)} \right] \quad (11)$$

$$K_{Il} = \sqrt{\frac{\pi h}{2}} \left[ p_{cp} - \delta_n + \rho_f g \left( h_{cp} - \frac{1}{4}h \right) \right]$$





$$+ \sqrt{\frac{2}{\pi h}} \sum_{i=1}^{n-1} (\delta_{i+1} - \delta_i) \left[ \frac{h}{2} \arccos \left( \frac{h-2h_i}{h} \right) - \sqrt{h_i(h-h_i)} \right] \quad (12)$$

$$w(z) = \frac{4}{E'} [p_{cp} - \delta_n + \rho_{fg}(h_{cp} - z)] \sqrt{z(h-z)} + \frac{4}{\pi E'} \sum_{i=1}^n (\delta_{i+1} - \delta_i)$$

$$\left[ (h_i - z) \coth^{-1} \frac{z \left( \frac{h-2h_i}{h} \right) + h_i}{|z - h_i|} + \sqrt{z(h-z)} \arccos^{-1} \left( \frac{h-2h_i}{h} \right) \right] \quad (13)$$

where,  $K_{Iu}$  and  $K_{Ib}$  is the stress intensity factors at the top and bottom of the slit tip, respectively;  $\delta_n$  and  $\delta_i$  is the local stress at the top of the fracture tip and the bottom of the fracture tip, respectively;  $h$  is the fracture height;  $h_i$  is the height from the bottom of the seam tip to the top of the seam tip.

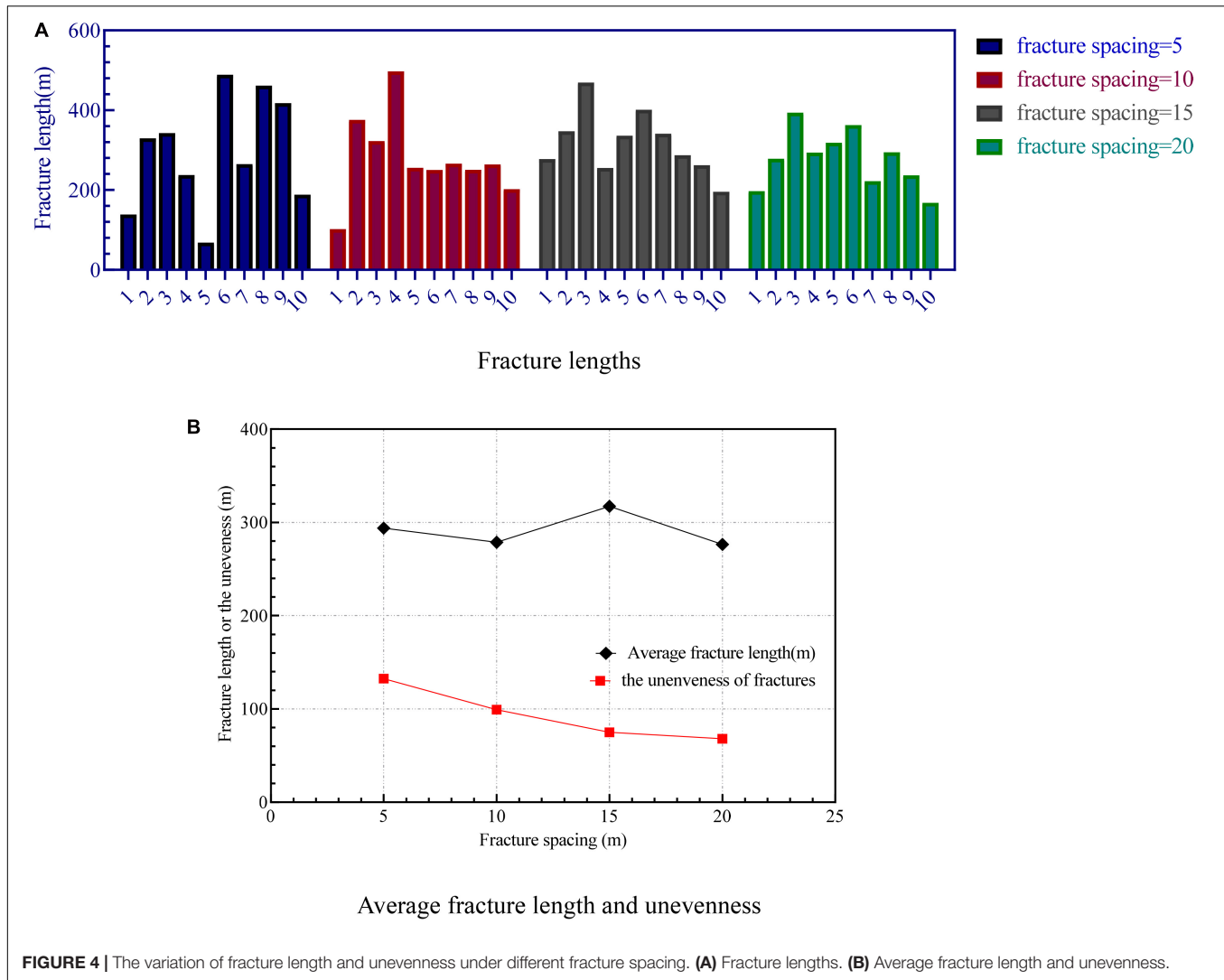


**FIGURE 4 |** The variation of fracture length and unevenness under different fracture spacing. **(A)** Fracture lengths. **(B)** Average fracture length and unevenness.

## Stress Interference Model

The 3D modified boundary element method is used to calculate the induced stress field (Crouch and Starfield, 1983; Olson, 2004):

$$\sigma_n^i = \sum_{j=1}^N A^{ij} C_{ns}^{ij} D_s^j + \sum_{j=1}^N A^{ij} C_{nn}^{ij} D_n^j \quad (14)$$

$$\sigma_s^i = \sum_{j=1}^N A^{ij} C_{ss}^{ij} D_s^j + \sum_{j=1}^N A^{ij} C_{sn}^{ij} D_n^j \quad (15)$$

$$A^{ij} = 1 - \frac{d_{ij}^\beta}{(d_{ij}^2 + (h/\alpha)^2)^{\beta/2}} \quad (16)$$

where  $A^{ij}$  is the 3D correction factor;  $h$  is the fracture height;  $d_{ij}$  is the distance between  $i_{th}$  element and  $j_{th}$  element;  $\alpha$  and  $\beta$  is the fitting parameters ( $\alpha = 1$ ,  $\beta = 3.2$ );  $C^{ij}$  is the influence coefficient of the discontinuous displacement of element  $j$  on the induced

stress on element  $i$ ;  $C_{ns}^{ij}$  indicates the influence coefficient of the shear discontinuous displacement of element  $j$  on the normal stress of element  $i$ ;  $C_{nn}^{ij}$  indicates the influence coefficient of the discontinuous displacement of the element  $j$  on the normal stress of the element  $i$ .

## Proppant Transport Model

The model determines the type of fluid and proppant by volume concentration, and the calculation equation for the average volume concentration in the fracture is as follows:

$$c_k = \frac{1}{\Delta x' w (h - h_{bank})} * \int_{h_{bank}}^h \int_{\frac{w}{2}}^{\frac{w}{2}} \int_{x'_c - \frac{\Delta x'}{2}}^{x'_c + \frac{\Delta x'}{2}} X_k(x', y', z) dx dy' dz \quad (17)$$

where  $X_k$  is the volume fraction of the  $k$  proppant;  $\Delta x'$  is the element length;  $h_{bank}$  is the stacking height;  $c_k$  is the concentration of the  $k$  proppant.

The horizontal transport model of proppant in fractures is a one-dimensional migration model, which only considers

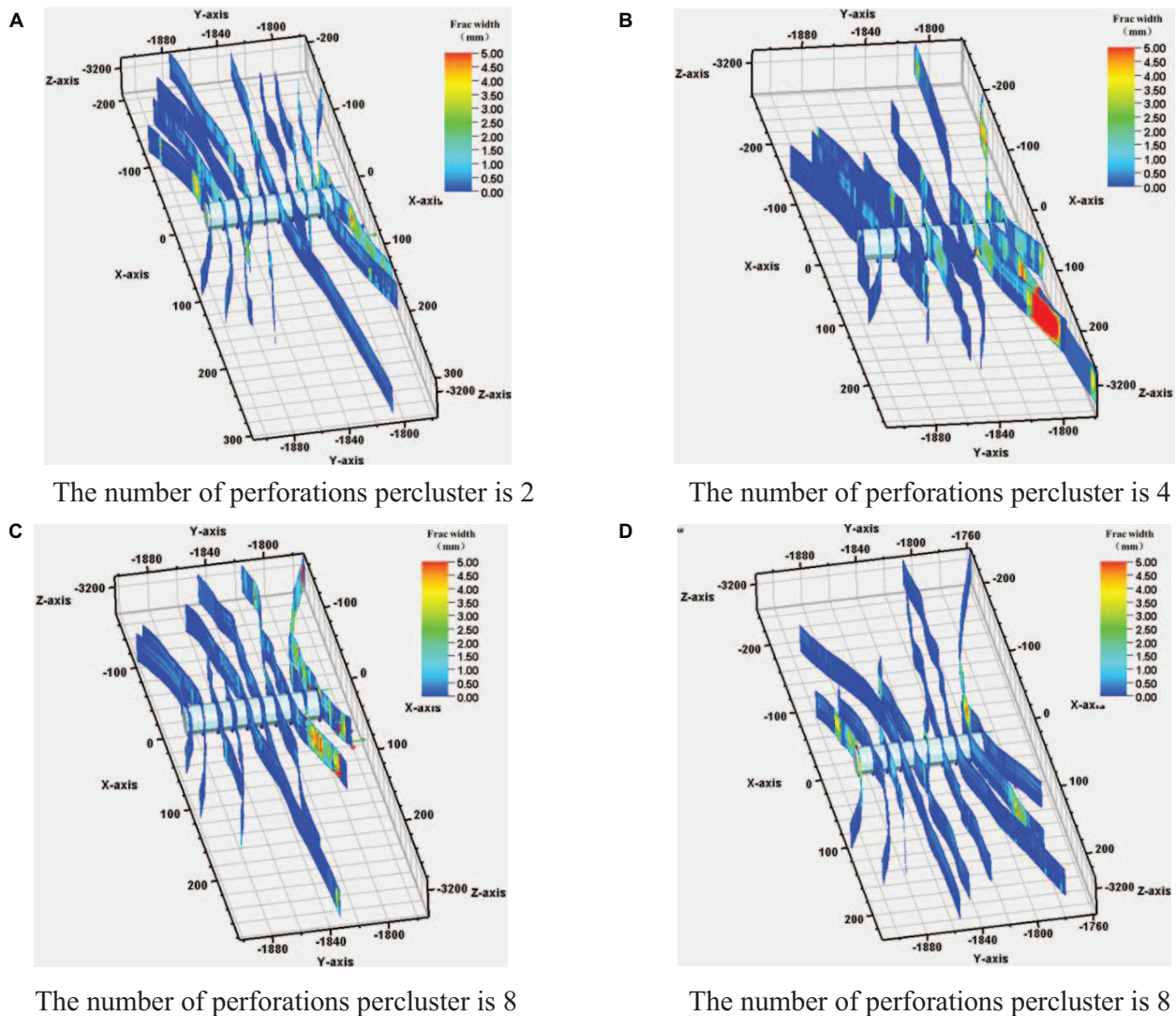


**FIGURE 5 |** Multi-cluster fracture propagation pattern under different numbers of perforations per cluster. **(A)** The number of perforations per cluster is 2. **(B)** The number of perforations per cluster is 4. **(C)** The number of perforations per cluster is 8. **(D)** The number of perforations per cluster is 8.

horizontal advection migration. The fluid concentration change equation is described as (Adachi et al., 2007):

$$\frac{\partial(h - h_{bank})\bar{w}c_{fl,k}}{\partial t} + \frac{\partial(q_{fl}c_{fl,k})}{\partial x} = -f_{leakoff}c_{fl,k} \quad (18)$$

where  $q_{fl}$  is the flow rate in the fracture;  $f_{leakoff}$  is the velocity of the fluid passing through the fracture wall;

The sedimentation velocity of the proppant in the vertical direction is described by the Stokes equation (Weng et al., 2011):

$$v_{set,k} = \left[ \frac{1}{3\pi'^{-1}18} \frac{(\rho_{prop,k} - \bar{\rho}_{fl})}{\bar{K}'} g D_k^{\bar{n}'+1} \right]^{1/\pi'} \quad (19)$$

Where  $v_{set,k}$  is the sedimentation velocity of the k proppant;  $\rho_{prop,k}$  is the density of the k proppant;  $D_k$  is the diameter of the k proppant;  $\bar{n}'$  and  $\bar{K}'$  is the rheological index and consistency coefficient weighted by the fluid concentration, respectively.

## Interaction Criterion Between Hydraulic Fractures and Natural Fractures

Natural fractures can be seen as the friction interface, Renshaw and Pollard (Weng et al., 2012) established the orthogonal interaction criterion of hydraulic fracture and natural fracture, and Gu et al. (Nolte, 1991) extended to the nonorthogonal criterion on Renshaw and Pollard's study. The detailed work can be seen in Gu's study. With a certain cohesion interface standard, the extended orthogonal formula is:

$$\frac{S_0/\mu - \sigma_H}{T_0 - \sigma_h} > \frac{0.35 + (0.35/\lambda)}{1.06} \quad (20)$$

where  $S_0$  is the cohesive force;  $\mu$  is the interfacial friction coefficient;  $T_0$  is the tensile strength of the rock;  $\sigma_H$ ,  $\sigma_h$

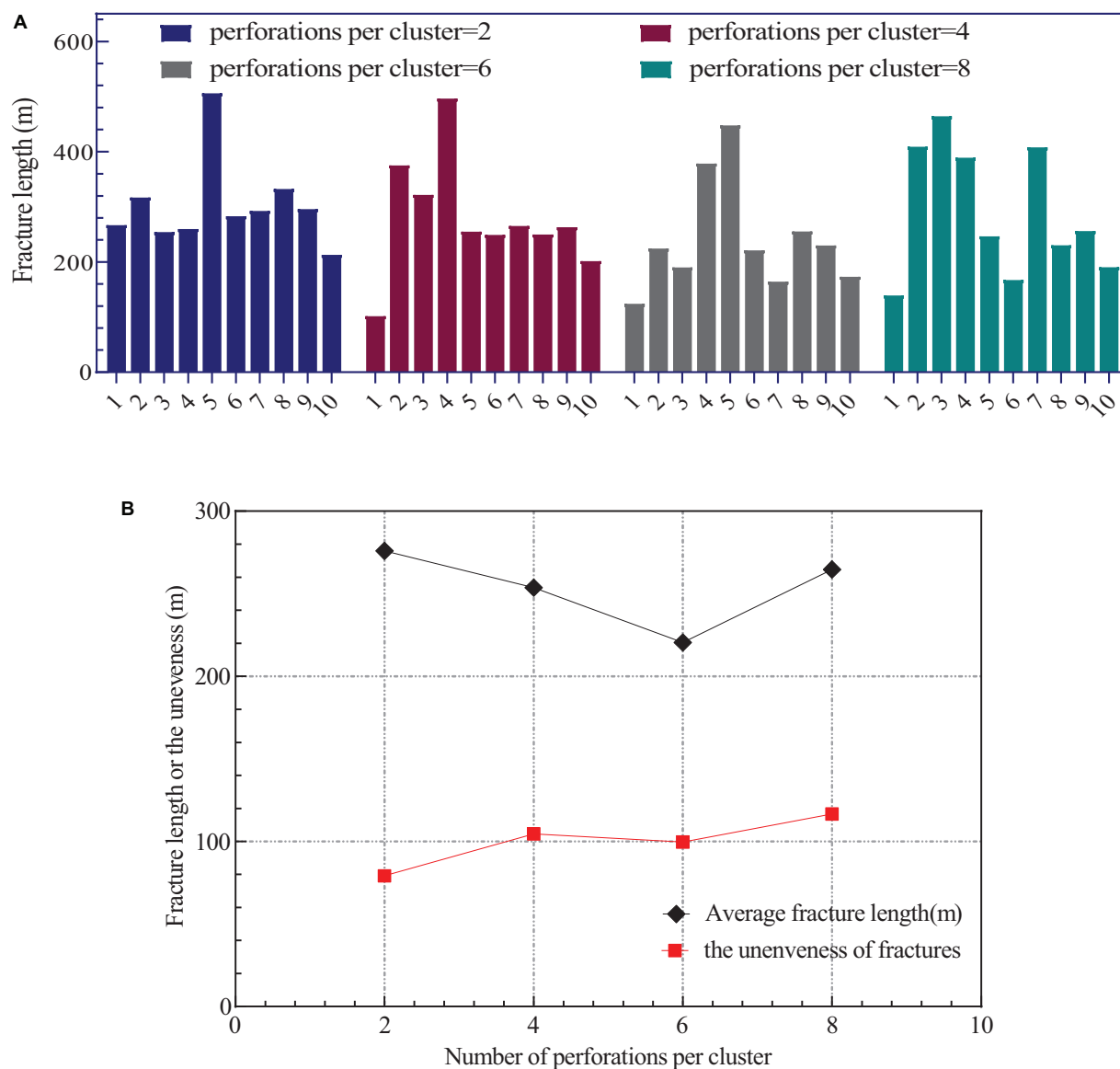


**FIGURE 6 |** The variation of fracture length and unevenness with different numbers of perforations per cluster. **(A)** Fracture length. **(B)** Average fracture length and unevenness.

are the horizontal maximum and minimum principal stresses, respectively.

## THE INFLUENCE OF FRACTURING PARAMETERS ON THE UNEVENNESS OF FRACTURE LENGTH

### Model Establishment and Model Verification

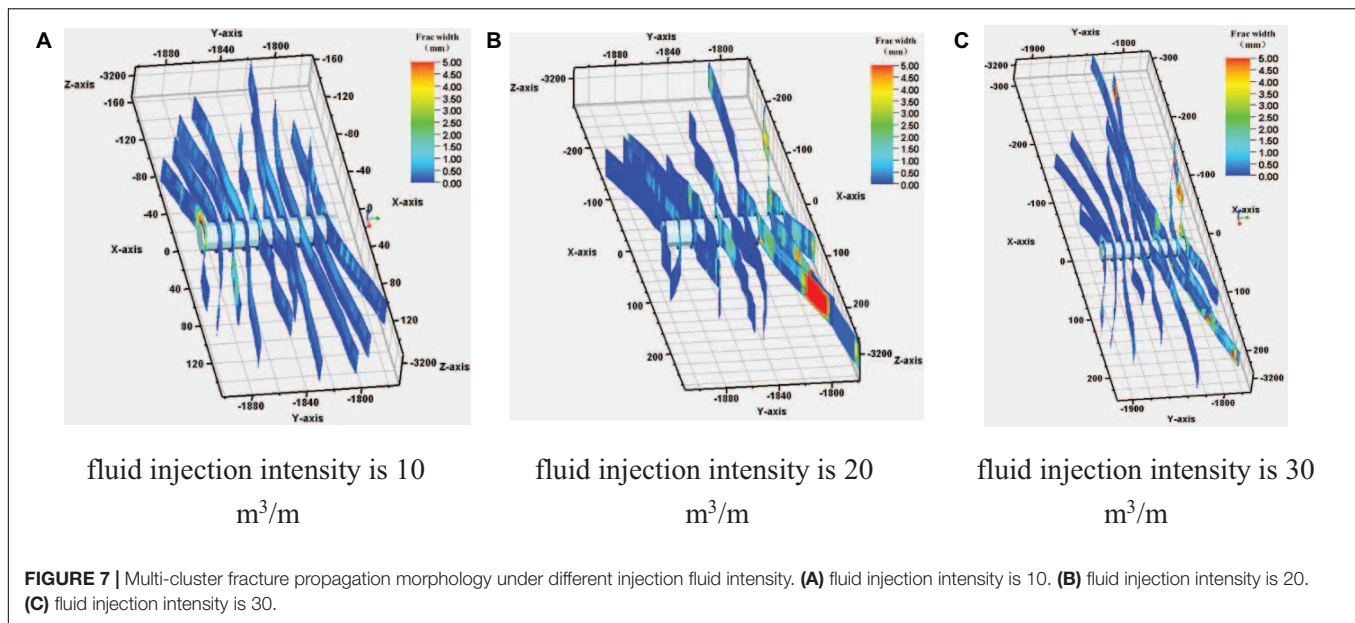
The UFM has been integrated into the Mangrove platform of the geological integrated software Petrel. The verification of the model and the analytical solution has been conducted

by Weng et al. (Murphree et al., 2020), so this study will not repeat.

In this section, based on the same/real logging data, injection procedures, completion measures, and fracturing design as well A, three-dimensional fracturing numerical simulation results are generated and compared with the on-site fracturing treatment pressure curve to verified the accuracy of the geological model and fracturing model.

As shown in **Figure 1**, the target zone of Well A is located in the Long 1 layer of the Longmaxi Formation in Changning, with a burial depth of 3060–3175 m. Logging interpretation results show that organic carbon content (TOC) is between 4 and 8%. Minimum horizontal principal stress ( $Sh_{min}$ ) is between 56.77 and 71.6 MPa. The maximum horizontal principal stress ( $Sh_{max}$ )





is between 71.34 and 83.69 MPa. And the vertical stress ( $S_v$ ) is between 71.83 and 73.17 MPa. The stress state belongs to a strike-slip fault. The measured depth of Well A is 4891.47 m, the vertical depth is 3100~3200 m, the horizontal completion section length is 1500 m, the average stage length is designed to be 120 m, the total number of perforations in one stage is 48 holes, and the number of clusters is 11 clusters and the cluster spacing is 10.9 m.

The average minimum horizontal, maximum horizontal and vertical stress is 64.19 MPa, 77.52 MPa and 72.5 MPa, respectively. X-axis, Y-axis, and Z-axis are the directions of horizontal minimum stress  $\sigma_h$ , horizontal maximum stress  $\sigma_H$  and vertical stress  $\sigma_V$ , respectively. In addition, the horizontal wellbore direction in this model is parallel to the direction of the minimum horizontal principal stress, so that multiple fractures can be generated in the horizontal wellbore perpendicular to the wellbore. In fact, this is a common practice in multi-cluster fracturing of horizontal wells. Sensitivity analysis is proposed to determine how uniform will the fractures distribute based on changes in certain fracturing parameter while the other parameters remain the basic model parameters. The basic model parameters are shown in Table 1.

Figure 2 shows the on-site treatment pressure and the simulated pressure are in good agreement. It should be noted that there are still some pressure disturbances in the pumping pressure curve, which are mainly ascribed to stratigraphic causes. However, it can be proved that simulating the Longmaxi section of the Changning block by this model can be fairly representative to some extent.

This section will study the fracturing parameters from the following two aspects: completion parameters (cluster spacing and the number of perforations per cluster); pumping parameters (fluid injection intensity and proppant injection intensity).

The unevenness of fracture length is defined as the length difference in the geometrical morphology of multiple clusters of fractures in the same stage. In this study, the fracture propagation geometry mainly refers to the fracture length, so we define the value of the fracture unevenness as the standard deviation of the fracture length of multiple clusters. The larger the value is, the more uneven the distribution of multiple clusters of fractures in the stage; otherwise, the more uniform fracture propagation can be obtained when the value is smaller. Its mathematical expression is:

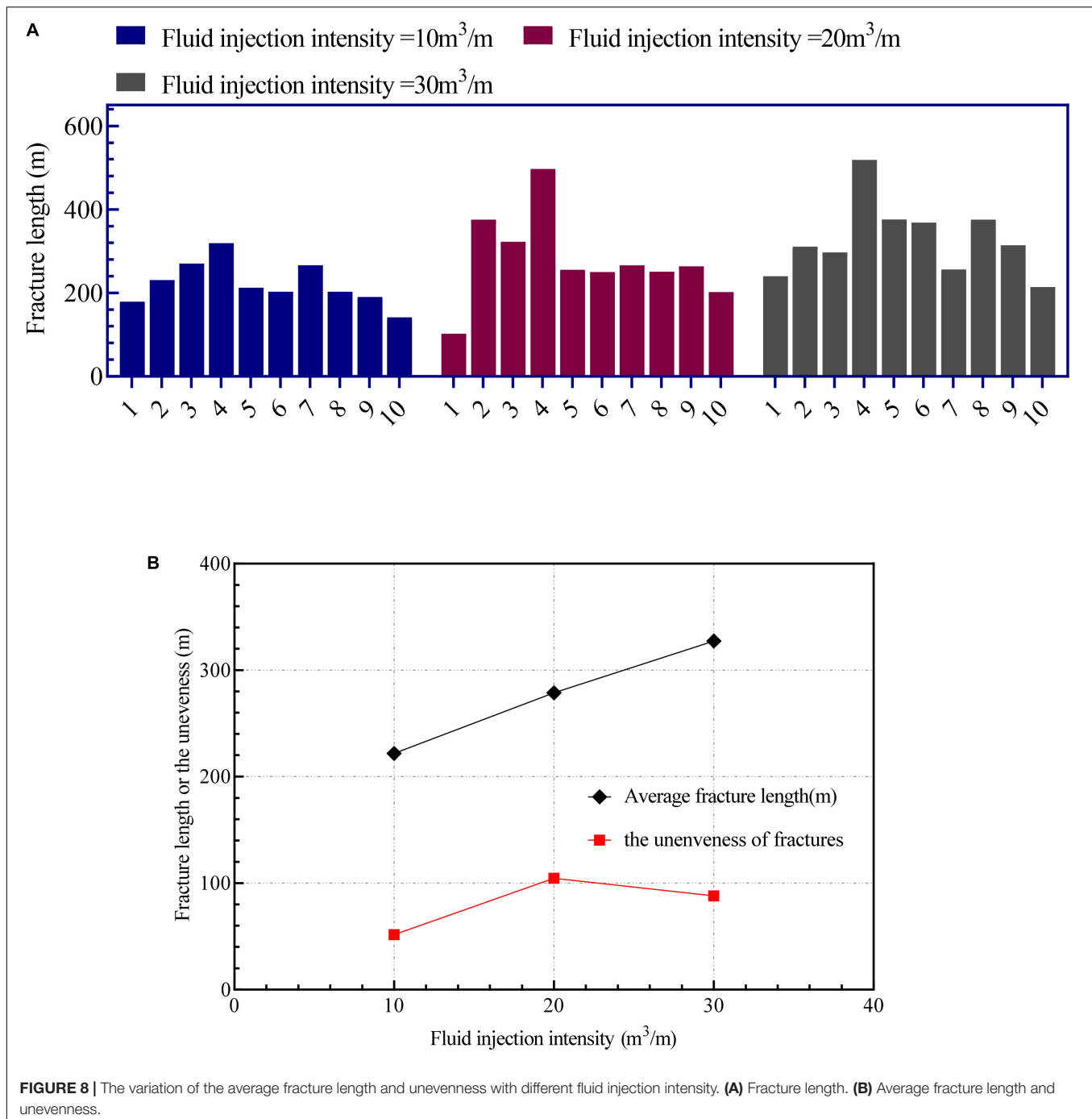
$$\sigma(L) = \sqrt{\frac{1}{N} \sum_{i=1}^N (L_i - \bar{L})^2} \quad (21)$$

where  $\sigma(L)$  is the length unevenness of multiple clusters of fractures;  $L_i$  is the fracture length of the  $i$ th fracture;  $\bar{L}$  is the average fracture length of multiple fractures.

## Fracture Spacing

The fracture spacing will be changed to 5 m, 10 m, 15 m, and 20 m, respectively, to explore the influence of the cluster spacing on the length unevenness of multi-cluster fracture propagation. As shown in Figure 3, when the fracture spacing is 5 m, 10 clusters of fracture propagate in a “radial shape”, and the strong stress interference under the narrow cluster spacing promotes the deflection of the clusters. With the continuous increase of the fracture spacing, when the fracture spacing is 20 m, the morphology of each fracture is almost parallel, which indicates that the increase of the cluster spacing can reduce the stress interference and the fracture morphology transitions from a strong fracture deflection to a mutual parallel fracture group. Fracture lengths of the cases in Figure 3 are analyzed, and the length unevenness of the cracks and the average value





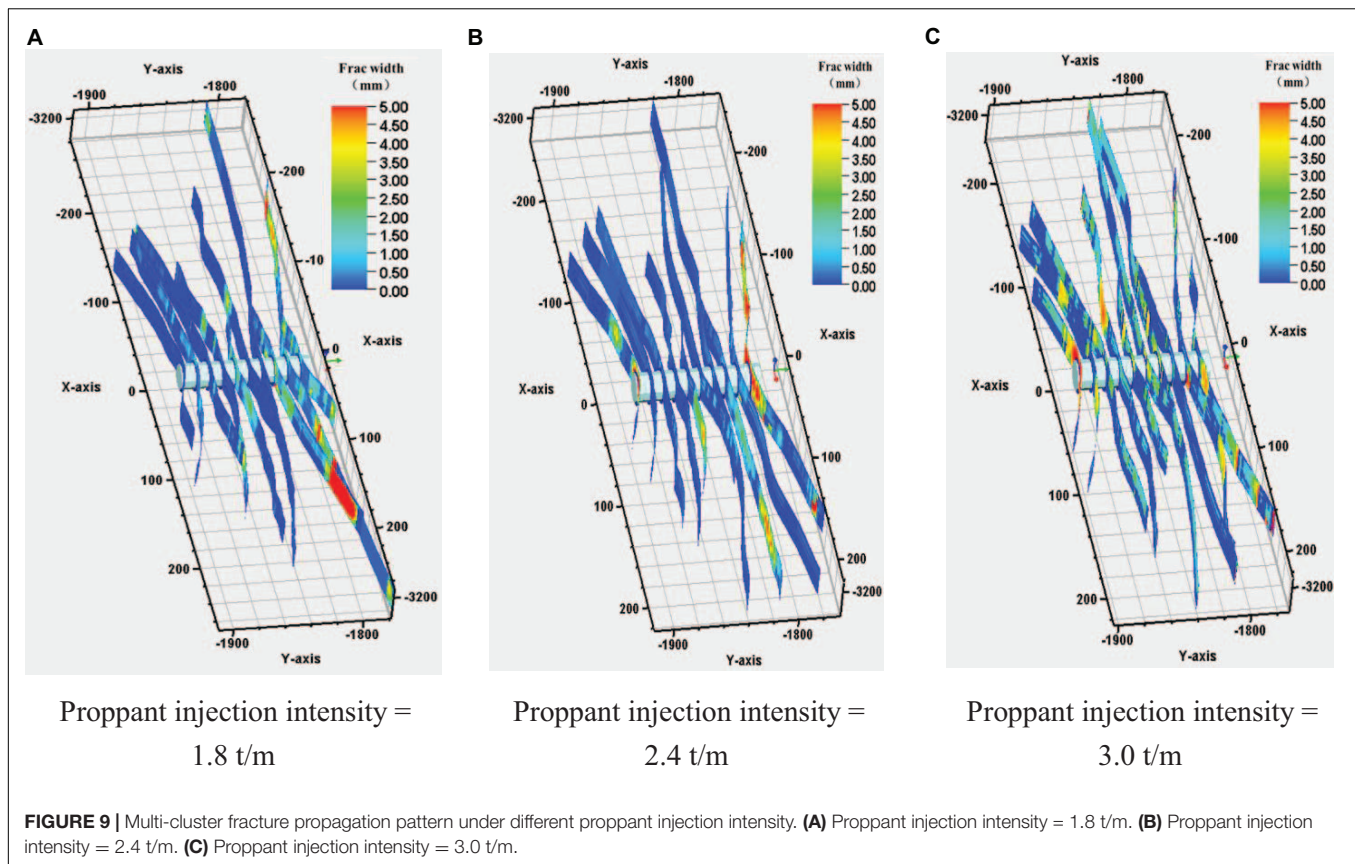
of the fracture lengths in each case according to formula (20) are calculated.

**Figure 4A** shows the fracture lengths in different fracture spacing cases. It can be seen from the figure that as the fracture spacing increases, the histogram of fracture length distribution gradually turns from uneven to even. **Figure 4B** shows the variation of the average fracture length and unevenness with the different fracture spacing. The results showed that the fracture spacing increased from 5 to 20 m, the unevenness of the

multi-cluster cracks decreased, and the average fracture length did not change much.

### Number of Perforations per Cluster

With the basic parameters unchanged, the number of single-cluster perforations is modified to 2 holes, 4 holes, 6 holes, and 8 holes, respectively. Influence of the number of perforations per cluster on the fracture propagation morphology and length unevenness are explored.



The fracture propagation pattern is shown in **Figure 5**. It can be seen from this figure that most of the fractures have a fracture width of less than 2 mm, and the overall crack width is small. The side fractures are affected by stress interference and the fracture length is reduced. The middle fractures are deflected due to stress interference, and multiple fractures merge into the main fracture within 100 m from the wellbore and continue to expand, which further increases the induced stress and promotes uneven fracture propagation.

The fracture lengths of the cracks in each case in **Figure 5** are counted, and the fracture length results are shown in **Figure 6A**. The results in **Figure 6A** do not reflect the changes in the uniformity of the cracks. Therefore, the unevenness calculation is performed, and the calculation result is shown in **Figure 6B**. It can be seen from **Figure 6B** that the average length of the fracture has a slight downward trend with the increase in the number of perforations per cluster. The unevenness of the fractures increases with the increase in the number of perforations per cluster. When the number of perforations per cluster is six, it is an abnormal point. This may be due to the influence of the calculation of the fracture length when multiple clusters of fractures merge, which interferes with the calculation result of unevenness. These results show that reducing the number of single-cluster perforations can help reduce the unevenness of cracks and improve the uniformity of cracks; at the same time, increase the average length of fractures slightly.

## Fluid Injection Intensity

With the basic parameters unchanged, the pump injection schedule is changed to alter the fluid injection intensity as: 10 m<sup>3</sup>/m, 20 m<sup>3</sup>/m, 30 m<sup>3</sup>/m, respectively. Influence of the injection fluid intensity on the fracture propagation morphology and length unevenness are explored.

**Figure 7** is the fracture morphology diagram. From **Figures 7A–C**, as the fluid injection intensity increases, the difference in fracture length of multiple clusters of fractures gradually increases, and the fracture propagation gradually becomes uneven, such as the longest fracture length in **Figure 7A** is 319.05 m, and the shortest fracture length is 141.894 m. In **Figure 7B**, they are 497.189 m and 102.252 m, respectively. This shows that the increase of the injection strength increases the unevenness of the fracture propagation. **Figure 8A** shows the fracture length distribution under different fluid injection intensity. **Figure 8B** shows the variation of unevenness and fracture length with fluid injection intensity. When the fluid injection intensity is 10 m<sup>3</sup>/m, the average fracture length is 221.7 m, and the unevenness is 51.53 m; while the injection intensity is 20 m<sup>3</sup>/m, 30 m<sup>3</sup>/m, the average fracture length is 278.7 m, 327.2 m, the unevenness of the cracks increased to 104.58 m and 88.02 m; This shows that the increase of the injection intensity increases the length of the fracture stimulation as a whole, but the unevenness of the fracture gradually increases, and there is the extreme value of the maximum unevenness of

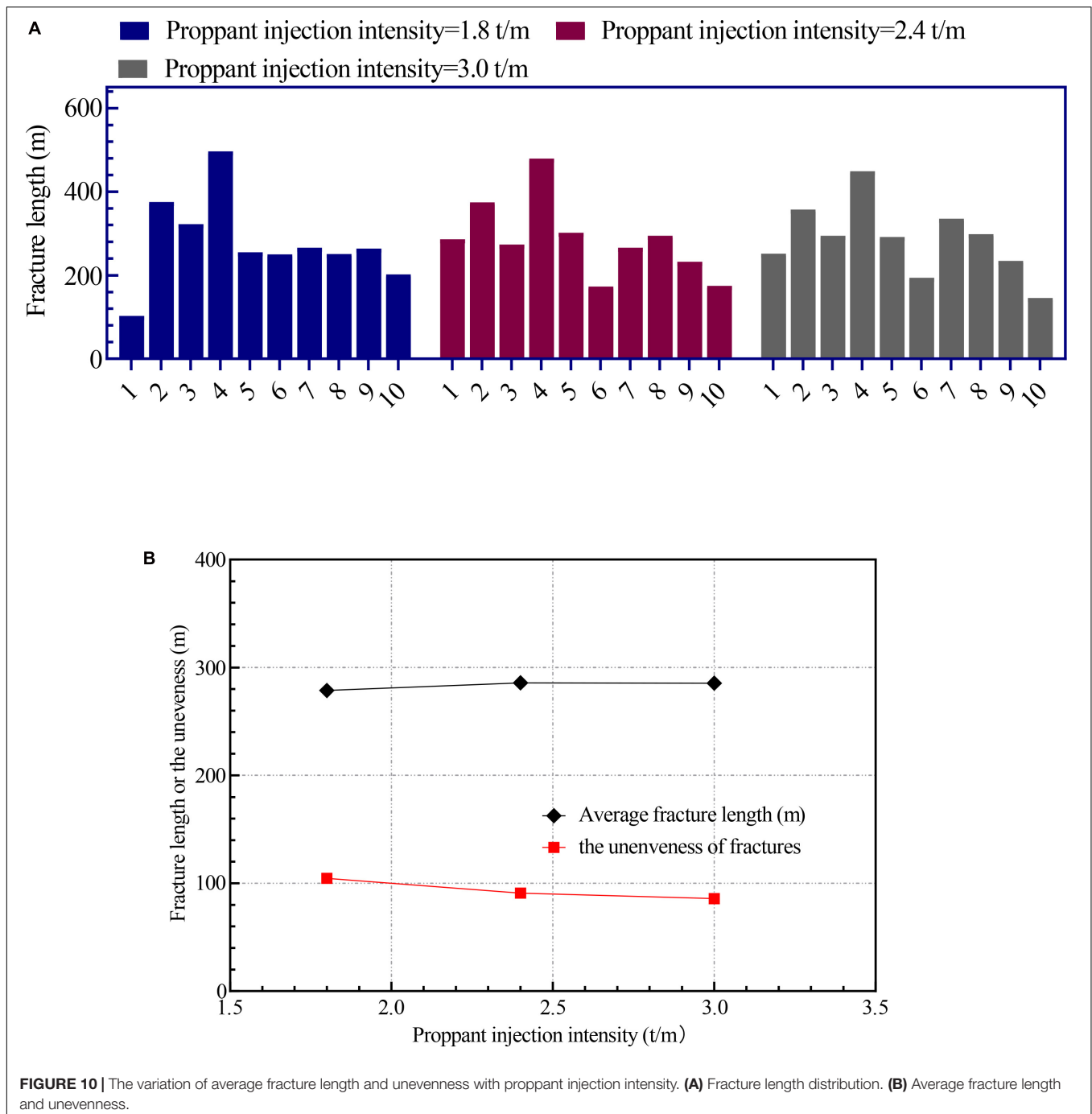


**FIGURE 10 |** The variation of average fracture length and unevenness with proppant injection intensity. **(A)** Fracture length distribution. **(B)** Average fracture length and unevenness.

the fracture. In our simulations, the injection intensity in the case with the maximum unevenness is  $20 \text{ m}^3/\text{m}$ .

### Proppant Injection Intensity

In this section, we will keep the basic parameters unchanged, and change the proppant injection intensity to 1.8 t/m, 2.4 t/m, and 3.0 t/m, respectively, and explore the influence of the proppant injection intensity on the fracture propagation pattern and the unevenness of fracture length. The fracture morphology diagram is shown in **Figure 9**. It can be seen from **Figures 9A–C** that when

the proppant injection intensity increases from 1.8 to 3.0 t/m, the average fracture width has been increased, and the average fracture width is 2.1 mm, 2.4 mm, and 3.0 mm, respectively. There is not much change in other geometric forms of fractures. **Figure 10A** shows the distribution of fracture lengths under different proppant injection intensity. **Figure 10B** shows the variation of average fracture length and the unevenness with the proppant injection intensity. The results show that when the injection proppant intensity increases, the average length of the fractures in each cluster hardly changes, which are 278.7 m,

**TABLE 2** | Basic parameters of natural fractures in different cases.

Case number	Approach angle (degree)	Natural fracture length (meters)	Natural crack spacing (meters)
Case 1	30 ± 5	30 ± 5	30 ± 5
Case 2	60 ± 5	30 ± 5	30 ± 5
Case 3	90 ± 5	30 ± 5	30 ± 5

285.8 m, and 285.4 m, respectively; the unevenness of the cracks gradually decreases to 104.6 m, 90.9 m, and 85.9 m, respectively. This shows that the change of the proppant injection intensity will not affect the average length of fractures or the scale of stimulation and meanwhile have a little effect on improving the uniformity of the fracture length.

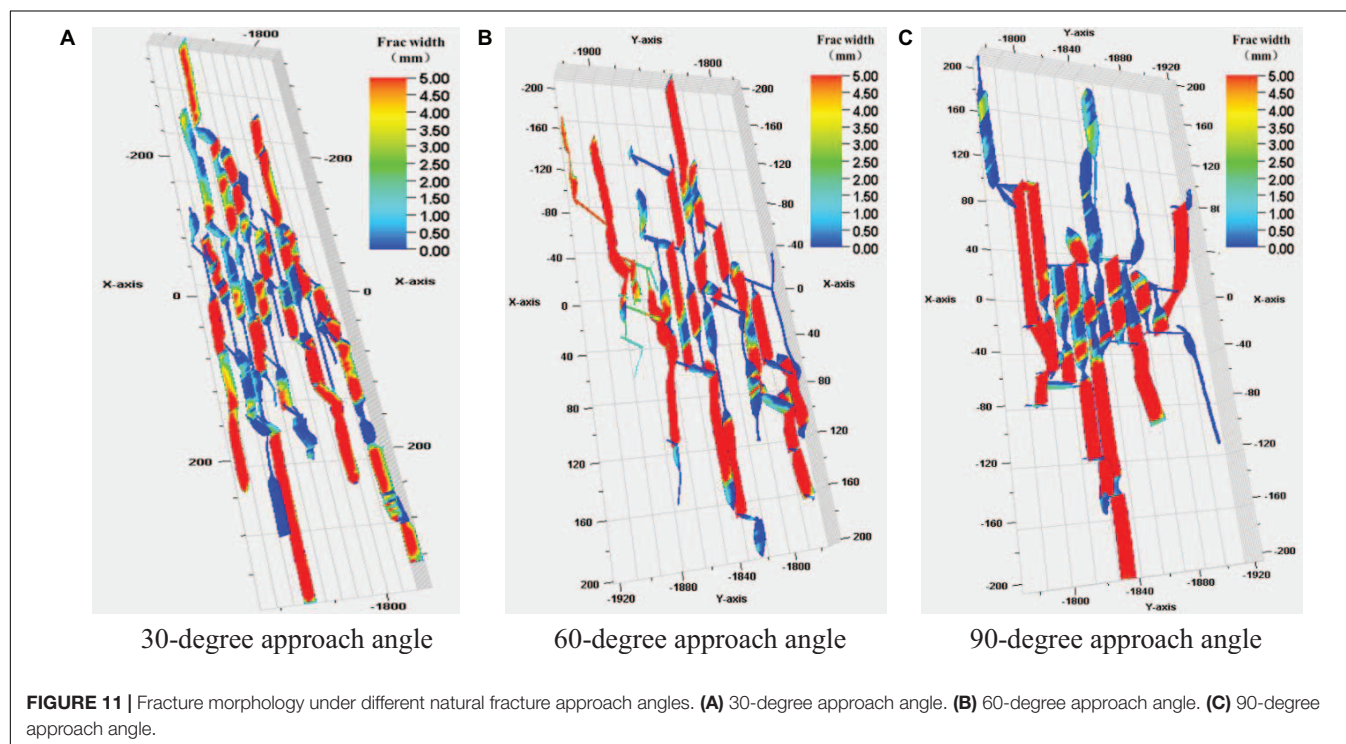
### Effect of Approach Angle When Natural Fractures Exist

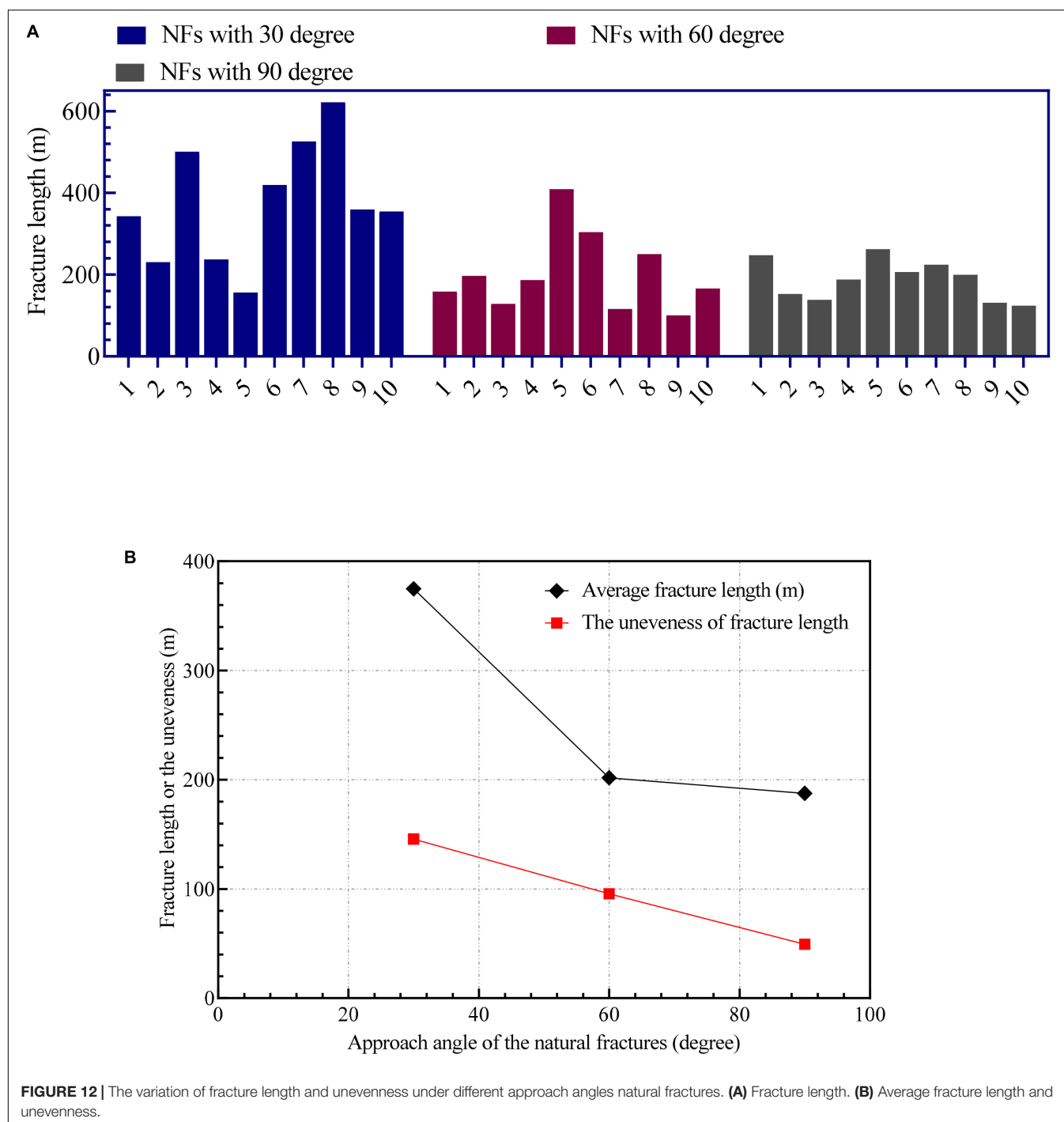
Complicated natural fractures (NF) and bedding usually exist in shale formations. Therefore, complex fracture networks are created when hydraulic fractures (HF) encounter natural fractures. The approach angle refers to the angle between hydraulic fractures and natural fractures, which is an important parameter that affects the interaction between hydraulic fractures and natural fractures. This section mainly describes the complex fracture network when the natural fractures are distributed under different approach angles. The approach angles for setting natural fractures are 30, 60, and 90 degrees. The basic setting parameters of natural fractures are shown in **Table 2**.

**Figure 11** shows the fracture networks with different natural fractures approach angles. Compared with the no-HF case,

the fracture morphology with NFs shows a more complicated fracture network. Due to the high fluid loss of natural fractures, the local fracture width shows wider hydraulic fractures. In addition, the fracture morphology of different approach angles is also quite different. When the natural fracture angle is 30 degrees, hydraulic fractures divert easily to the natural fractures, which show a highly complex fracture network in the near-wellbore region and far-field region. When the approach angle is 60 degrees, hydraulic fractures are captured by the natural fracture only at the near-wellbore region and a small amount of the fracture network was disturbed in the far-field region. This phenomenon is more obvious when the approach angle is 90°. There are only a few hydraulic fractures in the far-field region, and the figure shows that hydraulic fractures do not communicate with the natural fractures. The complex fracture network in the near-wellbore region is mainly due to the strong stress interference created by the simultaneous propagation of multiple fractures, which makes it easier for hydraulic fractures to divert to natural fractures. However, the stress interference is relatively weak in the far-field region. At low approach angles, hydraulic fractures in the far-field region can still divert to natural fractures to produce a more complex fracture network, as shown in **Figure 11A**; At high approach angles, the hydraulic fractures in the far-field region will directly cross the natural fractures, as shown in **Figure 11C**.

**Figure 12A** shows the fracture length under the conditions of different approach angles. It can be seen from this figure that natural fractures with low approach angles promote the propagation of hydraulic fractures. Although natural fractures cause the high fluid loss of fracturing fluid, natural fractures





provide a fast propagation path, which caused hydraulic fractures to spread to the far-field region. However, when the approach angle increases, natural fractures cut off the normal propagation path of hydraulic fractures to the far-field. Hence the shape of hydraulic fractures near the well section is complex, the length of hydraulic fractures gradually decreases. **Figure 12B** proves the above conclusion. When the approach angle is low, the average fracture length is the highest, the reservoir stimulation zone is the best, and the unevenness is the highest; when the approach

angle is high, the average fracture length is the shortest and the unevenness is the lowest.

## CONCLUSION

This study uses an UFM to carry out geological modeling and fracturing simulation of real Sichuan Changning shale. Comparing with field fracturing treatment pressure curve with



the simulation treatment pressure curve, the accuracy of this simulation can be verified. Through a series of numerical simulations of different fracturing parameters, the main conclusions as follows:

1. Small fracture spacing has a strong stress interference during fracturing in the horizontal wells, which will cause obvious uneven propagation of fractures. Its influencing factors include completion parameters (cluster spacing and the number of perforations per cluster) and pumping parameters (fluid injection intensity and proppant injection intensity).
2. Reducing the fracture spacing will increase the stress interference, causing the fracture to appear “radial style,” Meanwhile the unevenness of the fracture’s length increases with the decrease of the fracture spacing.
3. Reducing the number of perforations per cluster can promote more uniform propagation of multiple clusters of fractures and reduce the unevenness of fracture length.
4. Increasing the fluid injection intensity will increase the length of the fractures, but at the same time, it will increase the unevenness of the fracture length and cause the fractures to propagate more unevenly.
5. The increase of proppant injection intensity has little effect on the average length of fractures, while it has a little effect on improving the uniformity of the fracture length.
6. When natural fractures exist, the uniformity of fracture length increases with the decrease of approach angle in horizontal wells.
7. In horizontal large-stage multi-cluster wells, reasonable cluster spacing, and fluid injection intensity should be set to achieve a more effective stimulation effect, meanwhile reducing the number of perforations per cluster is also helpful to improve the uneven propagation.

## REFERENCES

- Adachi, J., Siebrits, E., Peirce, A., and Desroches, J. (2007). Computer simulation of hydraulic fractures. *Int. J. Rock Mech. Mining Sci.* 44, 739–757. doi: 10.1016/j.ijrmms.2006.11.006
- Chen, M., Zhang, S. C., Xu, Y., Ma, X. F., and Zou, Y. S. (2020a). A numerical method for simulating planar 3D multi-fracture propagation in multi-stage fracturing of horizontal wells. *Pet. Explor. Dev.* 47, 171–183. doi: 10.1016/s1876-3804(20)60016-7
- Chen, Z., Xue, C. J., Jiang, T. X., and Qin, Y. M. (2010). Application proposal of shale gas well volume fracturing technology in China[J]. *Nat. Gas Ind.* 30, 30–32. doi: 10.1016/j.wasman.2010.02.001
- Crouch, S. L., and Starfield, A. M. (1983). *Boundary Element Methods in Solid Mechanics: With Applications in Rock Mechanics and Geological Engineering*. London: George Allen & Unwin.
- Fan, Y., Zhou, X. J., Ceng, B., Song, Y., Zhou, N. Y., and Chen, Y. (2019). Application of intensive staged fracturing technology in deep shale gas well Zi-2[J]. *Xinjiang Pet. Geol.* 40, 117–124.
- Huang, J., Safari, R., and Fragachan, F. (2018). “Applications of self-degradable particulate diverters in wellbore stimulations: hydraulic fracturing and matrix acidizing case studies,” in *Paper Presented at the Proceedings of the SPE International Hydraulic Fracturing Technology Conference and Exhibition. Society of Petroleum Engineers*, (The Woodlands TX).

## DATA AVAILABILITY STATEMENT

The original contributions presented in the study are included in the article/Supplementary Material, further inquiries can be directed to the corresponding authors.

## AUTHOR CONTRIBUTIONS

RY wrote the first manuscript and designed the paper framework. F-JZ provided the funds and the research idea of this study. M-HL provided very helpful thoughts and opinions, and made the simulations. YS wrote the introduction and made grammatical modifications to the whole manuscript. X-JZ provided a large number of relevant references and made grammatical corrections to the manuscript. Z-HZ has provided a number of helpful suggestions for the idea of this manuscript. BL and S-YQ have done data analysis and equipment for the whole research for this manuscript. All authors contributed to the article and approved the submitted version.

## FUNDING

This work was financially supported by the Foundation of State Key Laboratory of Petroleum Resources and Prospecting (Grant No. PRP/indep-2-1704), the National Natural Science Foundation of China, the National Science and Technology Major Projects of China (Grant Nos. 2016ZX05051 and 2017ZX05030), and China University of Petroleum – Beijing School Startup Fund (No. ZX20190183).

- Jia, C. Z., Zheng, M., and Zhang, Y. F. (2012). Unconventional hydrocarbon resources in China and the prospect of exploration and development[J]. *Pet. Explor. Dev.* 39, 129–136.
- Li, J., Dong, S., Wen, H., Li, X. L., and Guo, T. K. (2020). Numerical Simulation of Temporarily Plugging Staged Fracturing (TPSF) based on cohesive zone method. *Comp. Geotechnics* 121:103453. doi: 10.1016/j.compgeo.2020.103453
- Li, Y. M., Chen, X. Y., Zhao, J. Z., Xu, W. J., Wu, J., and Fu, D. Y. (2017). Influence of perforation erosion on multiple growing hydraulic fractures in multi-stage fracturing[J]. *Nat. Gas Ind.* 37, 52–59. doi: 10.1016/j.ngib.2017.11.002
- Liu, X., Qu, Z., Guo, T., Sun, Y., Wang, Z., and Bakhshi, E. (2019). Numerical simulation of non-planar fracture propagation in multi-cluster fracturing with natural fractures based on lattice modelling[J]. *Eng. Fract. Mech.* 220:106625. doi: 10.1016/j.engfracmech.2019.106625
- Liu, X., Rasouli, V., Guo, T., Qu, Z., and Damjanac, B. (2020). Numerical simulation of stress shadow in multiple cluster hydraulic fracturing in horizontal wells based on lattice modelling[J]. *Eng. Fract. Mech.* 238:107278. doi: 10.1016/j.engfracmech.2020.107278
- Ma, X. H., Xie, J., and Yong, R. (2020). Geological characteristics and high production control factors of shale gas in silurian longmaxi formation, southern Sichuan Basin, SW China. *Pet. Explor. Dev.* 47, 901–915. doi: 10.1016/s1876-3804(20)60105-7

- Mack, M. G., and Elbel, J. L. (1992). "Numerical representation of multilayer hydraulic fracturing," in *Paper presented at the The 33rd U.S. Symposium on Rock Mechanics (USRMS)*, (Santa Fe).
- Murphree, C., Kintzing, M., Robinson, S., and Sepehri, J. (2020). Evaluating limited entry perforating & diverter completion techniques with ultrasonic perforation imaging & fiber Optic DTS warmbacks. *Paper presented at the SPE Hydraulic Fracturing Technology Conference and Exhibition, Society of Petroleum Engineers*, The Woodlands, Texas.
- Nolte, K. G. (1991). Fracturing-pressure analysis for nonideal behavior[J]. *J. Pet. Technol.* 43, 210–218. doi: 10.2118/20704-pa
- Nordgren, R. P. (1970). "Propagation of a vertical hydraulic fractures," in *Paper Presented at SPE 45th Annual Fall Meeting, SPE. 3009*, (Houston).
- Olson, J. E. (2004). "Predicting fracture swarms—the influence of subcritical crack growth and the crack-tip process zone on joint spacing in rock," in *The Initiation, Propagation, and Arrest of Joints and Other Fractures*, eds J. W. Cosgrove and T. Engelder (Bath: Special Publication, Geological Society Publishing House), 73–87. doi: 10.1144/gsl.sp.2004.231.01.05
- Pan, L. H., Zhang, S. C., Cheng, L. J., Lu, Z. H., and Liu, K. Y. A. (2014). numerical simulation of the inter-cluster interference in multi-cluster staged fracking for horizontal wells[J]. *Nat. Gas Ind.* 34, 74–79.
- Panjaitan, M., Moriyama, A., McMillan, D., Rutledge, L., Xu, J., and Parkhonyuk, S. (2018). "Qualifying diversion in multi clusters horizontal well hydraulic fracturing in haynesville shale using water hammer analysis, step-down test and micro-seismic data," in *Paper Presented at the Proceedings of the SPE Hydraulic Fracturing Technology Conference and Exhibition. Society of Petroleum Engineers*, (The Woodlands TX).
- Perkins, T. K., and Kern, L. R. (1961). "Widths of hydraulic fractures," in *Paper Presented at 36th Annual Fall Meeting of SPE*, Oct, 1961.
- Rahim, Z., Al-Kanaan, A., Taha, S., Crawford, E. M., Khalifa, M., Krich, D., et al. (2017). "Innovative diversion technology ensures uniform stimulation treatments and enhances gas production: example from carbonate and sandstone reservoirs," in *Paper Presented at the Proceedings of SPE Hydraulic Fracturing Technology Conference and Exhibition. Society of Petroleum Engineers*, (The Woodlands TX). doi: 10.2118/184840-MS
- Senters, C. W., Johnson, M. D., Leonard, R. S., Ramos, C. R., Squires, C. L., et al. (2018). "Diversion optimization in new well completions," in *Paper presented at the Proceedings of the SPE Hydraulic Fracturing Technology Conference and Exhibition. Society of Petroleum Engineers*, (The Woodlands TX). doi: 10.2118/189900-MS
- Wang, B., Zhou, F. J., Zou, Y. S., Gao, L. Y., Hu, J., and Gu, X. L. (2018). Numerical simulation method of fracture interaction during temporary plugging staged fracturing[J]. *Fault Block Oil Gas Field* 25, 506–509.
- Weddle, P., Griffin, L., and Pearson, C. (2018). "Mining the bakken II - pushing the envelope with extreme limited entry perforating," in *Paper presented at the Proceedings of the SPE Hydraulic Fracturing Technology Conference and Exhibition. Society of Petroleum Engineers*, (The Woodlands TX). doi: 10.2118/189880-MS
- Weng, X., Kresse, O., Cohen, C., Wu, R., and Gu, H. (2012). "Numerical modeling of hydraulic fractures interaction in complex naturally fractured formations," in *Paper Presented at the 46th U.S. Rock Mechanics/Geomechanics Symposium*, (Chicago, IL: American Rock Mechanics Association).
- Weng, X., Kresse, O., Cohen, C.-E., Wu, R., and Gu, H. (2011). Modeling of hydraulic-fracture-network propagation in a naturally fractured formation. *Soc. Pet. Eng.* 26, 368–380. doi: 10.2118/140253-PA
- Wu, Q., Xu, Y., Liu, Y. Z., Ding, Y. H., Wang, X. Q., and Wang, T. F. (2011a). The current situation of stimulated reservoir volume for shale in U.S. and its inspiration to China[J]. *Oil Drilling Prod. Technol.* 33, 1–7.
- Wu, Q., Xu, Y., Wang, T. F., and Wang, X. Q. (2011b). Significant revolution in the concept of increasing production - Introduction to volume stimulation technology[J]. *Nat. Gas Ind.* 31, 7–12.
- Xie, J. (2018). Practices and achievements of the changning-wei yuan shale gas national demonstration project construction[J]. *Nat. Gas Ind.* 38, 1–7. doi: 10.1016/j.ngib.2017.07.001
- Xie, J., Xian, C. G., Wu, J. F., and Zhao, C. D. (2019). Optimal key elements of geoen지니어링 integration in changning national shale gas demonstration zone[J]. *China Pet. Explor.* 24, 174–185.
- Zhao, J. Z., Chen, X. Y., Liu, C. Y., Li, Y. M., Li, H., and Cao, X. J. (2015). The analysis of crack interaction in multi-stage horizontal fracturing[J]. *Nat. Gas Ind.* 26, 533–538.
- Zhou, T., Chen, M., Zhang, S. C., Li, Y. Z., Li, F. X., and Zhang, C. (2020). Simulation of fracture propagation and optimization of ball-sealer in-stage diversion under the effect of heterogeneous stress field[J]. *Nat. Gas Ind.* 40, 82–91.
- Zhou, T., Zhang, S. C., Chen, M., and Huang, Z. W. (2019). Competitive propagation of multi-fractures and their control on multi-clustered fracturing of horizontal wells (in Chinese). *Sci. Sin. Tech.* 49, 469–478. doi: 10.1360/n092018-00059

**Conflict of Interest:** YS, X-JZ and Z-HZ were employed by company PetroChina Southwest Oil & Gas Field Company. S-YQ was employed by company PetroChinaTarim Oil & Gas Field Company.

The remaining authors declare that the research was conducted in the absence of any commercial or financial relationships that could be construed as a potential conflict of interest.

Copyright © 2021 Yong, Zhou, Li, Song, Zhou, Zhao, Li and Qin. This is an open-access article distributed under the terms of the Creative Commons Attribution License (CC BY). The use, distribution or reproduction in other forums is permitted, provided the original author(s) and the copyright owner(s) are credited and that the original publication in this journal is cited, in accordance with accepted academic practice. No use, distribution or reproduction is permitted which does not comply with these terms.

# Advantages of publishing in Frontiers



## OPEN ACCESS

Articles are free to read  
for greatest visibility  
and readership



## FAST PUBLICATION

Around 90 days  
from submission  
to decision



## HIGH QUALITY PEER-REVIEW

Rigorous, collaborative,  
and constructive  
peer-review



## TRANSPARENT PEER-REVIEW

Editors and reviewers  
acknowledged by name  
on published articles

## Frontiers

Avenue du Tribunal-Fédéral 34  
1005 Lausanne | Switzerland

**Visit us:** [www.frontiersin.org](http://www.frontiersin.org)

**Contact us:** [frontiersin.org/about/contact](http://frontiersin.org/about/contact)



## REPRODUCIBILITY OF RESEARCH

Support open data  
and methods to enhance  
research reproducibility



## DIGITAL PUBLISHING

Articles designed  
for optimal readership  
across devices



## FOLLOW US

@frontiersin



## IMPACT METRICS

Advanced article metrics  
track visibility across  
digital media



## EXTENSIVE PROMOTION

Marketing  
and promotion  
of impactful research



## LOOP RESEARCH NETWORK

Our network  
increases your  
article's readership